

1-1-2009

An Investigation For Optimal Tool Kinematics In Powder Compaction Cycle To Minimize Density Gradient In Green Powder Compacts

Orest Kostiv
Ryerson University

Follow this and additional works at: <http://digitalcommons.ryerson.ca/dissertations>



Part of the [Aerospace Engineering Commons](#)

Recommended Citation

Kostiv, Orest, "An Investigation For Optimal Tool Kinematics In Powder Compaction Cycle To Minimize Density Gradient In Green Powder Compacts" (2009). *Theses and dissertations*. Paper 1540.

This Thesis is brought to you for free and open access by Digital Commons @ Ryerson. It has been accepted for inclusion in Theses and dissertations by an authorized administrator of Digital Commons @ Ryerson. For more information, please contact bcameron@ryerson.ca.

AN INVESTIGATION FOR OPTIMAL TOOL KINEMATICS IN
POWDER COMPACTION CYCLE TO MINIMIZE DENSITY
GRADIENT IN GREEN POWDER COMPACTS

by

Orest Kostiv, B.Eng
Ryerson University, Toronto, 2007

A thesis presented to Ryerson University
in partial fulfillment of the requirements for the degree of
Master of Applied Science
in the Program of
Aerospace Engineering

Toronto, Ontario, Canada, 2009

© Orest Kostiv 2009

Author's Declaration

I hereby declare that I am the sole author of this thesis.

I authorize Ryerson University to lend this thesis to other institutions or individuals for the purpose of scholarly research.

I further authorize Ryerson University to reproduce this thesis by photocopying or by other means, in total or in part, at the request of other institutions or individuals for the purpose of scholarly research.

AN INVESTIGATION FOR OPTIMAL TOOL KINEMATICS IN POWDER COMPACTION CYCLE TO MINIMIZE DENSITY GRADIENT IN GREEN POWDER COMPACTS

Master of Applied Science, Aerospace Engineering,
Ryerson University, 2009

Orest Kostiv

Abstract

The major disadvantage of powder metallurgy (PM) is the density variation throughout the powder compact. During the compaction process, due to the existence of friction at powder-tool interfaces, the contact surfaces experience a non-uniform stress distribution having to do with a variable friction coefficient and tool kinematics, consequently resulting in density gradient throughout the green powder compact. This represents a serious problem in terms of reliability and performance as it may contribute to a crack-defect generation during the compaction and ejection cycle, and more importantly a non-uniform powder compact shrinkage during the sintering process. The geometrical distortion caused by non-uniform shrinkage may require secondary operations, thus, compromising the competitiveness of PM technology. Simulation analyses, consisting of two parts, were conducted to study and suppress the causes of density variation. First, simulation analyses were conducted using a newly proposed friction-assisted compaction technique for compaction of cylindrical parts. Second study extended to a more complex geometry, consisting of a multi-stepped part, which indirectly used friction-assisted compaction by varying the tool kinematics of the press system. The overall focus of both studies was to establish optimal tool kinematics in powder compaction cycle to minimize density gradient in both cylindrical and multi-stepped green powder compacts. Consequently, optimal tool kinematics were determined producing the least variation in density throughout the corresponding powder compacts.

Acknowledgments

To begin with, I would like to express my gratitude to both of my supervisors, to Professor Kamran Behdinin for his continual support and guidance throughout the process of completing this thesis, and to Dr. Seyed M. Hashemi for believing in me and his persistent enthusiasm and encouragement, without his support this thesis would not be possible. Also, I would like to thank both of them for providing me with a rare opportunity to participate in Canada - EU Student Exchange Program in Aerospace Engineering, through which I have realized new prospects and have made new friends. Further, I would like to kindly thank Dr. Hamid Ghaemi for his technical support and continual willingness to help.

Next, I would like to thank all of my friends who stood by me all these years and encouraged me in my academic endeavours, you know who you are. I thank you all for all the times spend together and would like to apologize for all the times missed.

Lastly, but most importantly, I would like to express my extensive gratitude to my family and Diana, without whose love, patience, support, encouragement, and belief, I would not have come this far. You mean a world to me and I dedicate this thesis to you.

Table of Contents

| | |
|---|-------|
| Author's Declaration | ii |
| Abstract..... | iii |
| Acknowledgments..... | iv |
| List of Tables | xii |
| List of Figures | xiii |
| Nomenclature | xviii |
| 1.0 Introduction | 1 |
| 1.1 Powder Metallurgy | 1 |
| 1.2 Problem Statement..... | 8 |
| 1.3 Objective | 9 |
| 1.4 Thesis Organization..... | 9 |
| 2.0 Powder Constitutive Model | 12 |
| 2.1 Yield Criterion | 12 |
| 2.2 Constitutive Equations | 15 |
| 2.3 Determination of β and γ Material Parameters | 17 |
| 2.4 Modification of Original Yield Criterion | 20 |
| 3.0 Material Properties and Friction in PM | 21 |
| 3.1 Material Properties for Powder and Porous Materials | 21 |
| 3.1.1 Material Properties Provided by Pavier and Doremus | 21 |
| 3.1.2 Material Properties Provided by Shima | 27 |
| 3.1.3 Material Properties Provided by Koval'chenko | 29 |
| 3.1.4 Shear Viscosity for Iron-based Powder..... | 33 |
| 3.2 Friction in Powder Compaction | 35 |

| | |
|--|----|
| 3.2.1 Friction Measurement Using Instrumented-die Device | 35 |
| 3.2.2 Friction Measurement Using Shear-plate Device | 38 |
| 3.2.3 Friction Measurement Using Tribological Device | 44 |
| 4.0 The Effect of Tool Kinematics on Density Gradient of Green Powder Compacts | 47 |
| 4.1 Friction-assisted Compaction of Cylindrical Parts | 47 |
| 4.1.1 Friction-assisted Compaction Experiments | 48 |
| 4.1.2 Experimental Results Using Friction-assisted Compaction..... | 49 |
| 4.2 Compaction of a Multi-stepped Part | 51 |
| 4.2.1 Analyses of a Multi-stepped Part..... | 51 |
| 4.2.2 Analyses Results for a Multi-stepped Part..... | 54 |
| 4.2.2.1 Occurrence of Slip-Crack Defects..... | 54 |
| 4.2.2.2 Effect of Velocity Ratio on Green Density Variation | 55 |
| 5.0 Finite Element Approach | 57 |
| 5.1 Mesh Generation | 57 |
| 5.2 Friction-assisted Compaction of Cylindrical Parts | 58 |
| 5.3 Compaction of a Multi-stepped Part | 61 |
| 5.4 Powder Material Model..... | 65 |
| 5.5 Contact Definition and Control..... | 66 |
| 5.5.1 Motion of Contact Bodies | 67 |
| 5.5.2 Initial Conditions | 67 |
| 5.5.3 Contact Detection | 68 |
| 5.5.4 Contact Separation | 69 |
| 5.6 Friction Modelling..... | 69 |
| 5.6.1 Coulomb Friction..... | 70 |

| | |
|---|-----|
| 5.6.2 Bilinear Model..... | 71 |
| 5.6.3 Limitations of the Coulomb Friction Model..... | 74 |
| 5.7 Friction Coefficient Used for Simulation Analyses..... | 75 |
| 5.8 Automatic Global Remeshing | 77 |
| 5.8.1 Remeshing Criteria..... | 80 |
| 5.8.2 Remeshing Technique..... | 80 |
| 5.9 Element Type | 81 |
| 5.10 Units Used for Simulation Analyses | 83 |
| 5.11 Further Considerations for Nonlinear Analysis..... | 83 |
| 5.12 Full Newton-Raphson Algorithm | 84 |
| 5.13 Selection of Load Increment Size..... | 85 |
| 5.14 Convergence Control | 86 |
| 6.0 Simulation Results and Discussion of Friction-Assisted Compaction of Cylindrical Parts | 88 |
| 6.1 Effect of Die to Upper-Punch Velocity Ratio on Density Gradient of Cylindrical Parts with Compact Height-to-Diameter Ratio of 1.50..... | 89 |
| 6.1.1 Using Material Properties Provided by Pavier and Doremus | 89 |
| 6.1.2 Using Material Properties Provided by Koval'chenko | 93 |
| 6.2 Effect of Die to Upper-Punch Velocity Ratio on Density Gradient of Cylindrical Parts with Compact Height-to-Diameter Ratio of 1.00..... | 96 |
| 6.2.1 Using Material Properties Provided by Pavier and Doremus | 96 |
| 6.2.2 Using Material Properties Provided by Koval'chenko | 100 |
| 6.3 Effect of Die to Upper-Punch Velocity Ratio on Density Gradient of Cylindrical Parts with Compact Height-to-Diameter Ratio of 0.50..... | 104 |
| 6.3.1 Using Material Properties Provided by Pavier and Doremus | 104 |
| 6.3.2 Using Material Properties Provided by Koval'chenko | 108 |

| | |
|---|-----|
| 6.4 Summary and Discussion of Results | 112 |
| 7.0 Simulation Results and Discussion of Compaction of a Multi-stepped Part | 117 |
| 7.1 Effect of Lower-Inner-Punch to Upper-Punch Velocity Ration on Density Variation..... | 121 |
| 7.1.1 Using Material Properties Provided by Shima | 121 |
| 7.1.2 Using Material Properties Provided by Pavier and Doremus | 122 |
| 7.1.3 Using Material Properties Provided by Koval'chenko | 123 |
| 7.1.4 Summary and Discussion of Results | 124 |
| 7.2 Effect of Die to Upper-Punch Velocity Ration on Density Variation..... | 129 |
| 7.2.1 Using Material Properties Provided by Shima | 129 |
| 7.2.2 Using Material Properties Provided by Pavier and Doremus | 130 |
| 7.2.3 Using Material Properties Provided by Koval'chenko | 131 |
| 7.2.4 Summary and Discussion of Results | 132 |
| 7.3 Effect of Die & Core-Rod to Upper-Punch Velocity Ration on Density Variation..... | 136 |
| 7.3.1 Using Material Properties Provided by Shima | 136 |
| 7.3.2 Using Material Properties Provided by Pavier and Doremus | 137 |
| 7.3.3 Summary and Discussion of Results | 138 |
| 8.0 Conclusion..... | 141 |
| 8.1 Friction-assisted Compaction of Cylindrical Parts | 141 |
| 8.2 Compaction of a Multi-stepped Part | 142 |
| 8.3 Specific Contribution..... | 143 |
| 8.4 Future Work | 145 |
| 9.0 References | 147 |
| Appendix A. Effect of Die to Upper-Punch Velocity Ratio on Density Distribution of Cylindrical Parts with Compact Height-to-Diameter Ratio of 1.50 | 158 |

| | |
|--|-----|
| A.1 Using Material Properties Provided by Pavier and Doremus..... | 158 |
| A.1.1 Using Constant Friction Coefficient of 0.1..... | 158 |
| A.1.2 Using Variable Friction Coefficient, $\mu(\sigma_n, v_r)$ | 160 |
| A.2 Using Material Properties Provided by Koval'chenko | 162 |
| A.2.1 Using Constant Friction Coefficient of 0.1..... | 162 |
| A.2.2 Using Variable Friction Coefficient, $\mu(\sigma_n, v_r)$ | 164 |
| Appendix B. Effect of Die to Upper-Punch Velocity Ratio on Density Distribution of Cylindrical Parts with Compact Height-to-Diameter Ratio of 1.00 | 166 |
| B.1 Using Material Properties Provided by Pavier and Doremus..... | 166 |
| B.1.1 Using Constant Friction Coefficient of 0.1..... | 166 |
| B.1.2 Using Variable Friction Coefficient, $\mu(\sigma_n, v_r)$ | 167 |
| B.2 Using Material Properties Provided by Koval'chenko | 169 |
| B.2.1 Using Constant Friction Coefficient of 0.1..... | 169 |
| B.2.2 Using Variable Friction Coefficient, $\mu(\sigma_n, v_r)$ | 170 |
| Appendix C. Effect of Die to Upper-Punch Velocity Ratio on Density Distribution of Cylindrical Parts with Compact Height-to-Diameter Ratio of 0.50 | 172 |
| C.1 Using Material Properties Provided by Pavier and Doremus..... | 172 |
| C.1.1 Using Constant Friction Coefficient of 0.1..... | 172 |
| C.1.2 Using Variable Friction Coefficient, $\mu(\sigma_n, v_r)$ | 173 |
| C.2 Using Material Properties Provided by Koval'chenko | 175 |
| C.2.1 Using Constant Friction Coefficient of 0.1..... | 175 |
| C.2.2 Using Variable Friction Coefficient, $\mu(\sigma_n, v_r)$ | 176 |
| Appendix D. Effect of Lower-Inner-Punch to Upper-Punch Velocity Ration on Density Distribution of a Multi-stepped Part..... | 178 |
| D.1 Using Material Properties Provided by Shima..... | 178 |

| | |
|---|-----|
| D.1.1 Using Constant Friction Coefficient of 0.08..... | 178 |
| D.1.2 Using Constant Friction Coefficient of 0.12..... | 180 |
| D.1.3 Using Constant Friction Coefficient of 0.20..... | 182 |
| D.1.4 Using Variable Friction Coefficient, $\mu(\sigma_n, v_r)$ | 184 |
| D.2 Using Material Properties Provided by Pavier and Doremus..... | 186 |
| D.2.1 Using Constant Friction Coefficient of 0.08..... | 186 |
| D.2.2 Using Constant Friction Coefficient of 0.12..... | 188 |
| D.2.3 Using Constant Friction Coefficient of 0.20..... | 190 |
| D.2.4 Using Variable Friction Coefficient, $\mu(\sigma_n, v_r)$ | 192 |
| D.3 Using Material Properties Provided by Koval'chenko | 194 |
| D.3.1 Using Constant Friction Coefficient of 0.08..... | 194 |
| D.3.2 Using Constant Friction Coefficient of 0.12..... | 196 |
| D.3.3 Using Constant Friction Coefficient of 0.20..... | 198 |
| D.3.4 Using Variable Friction Coefficient, $\mu(\sigma_n, v_r)$ | 200 |
| Appendix E. Effect of Die to Upper-Punch Velocity Ration on Density Distribution of a Multi- stepped Part..... | 202 |
| E.1 Using Material Properties Provided by Shima | 202 |
| E.1.1 Using Constant Friction Coefficient of 0.08 | 202 |
| E.1.2 Using Constant Friction Coefficient of 0.12 | 204 |
| E.1.3 Using Constant Friction Coefficient of 0.20 | 206 |
| E.1.4 Using Variable Friction Coefficient, $\mu(\sigma_n, v_r)$ | 208 |
| E.2 Using Material Properties Provided by Pavier and Doremus | 210 |
| E.2.1 Using Constant Friction Coefficient of 0.08 | 210 |
| E.2.2 Using Constant Friction Coefficient of 0.12 | 212 |

| | |
|--|-----|
| E.2.3 Using Constant Friction Coefficient of 0.20 | 214 |
| E.2.4 Using Variable Friction Coefficient, $\mu(\sigma_n, v_r)$ | 216 |
| E.3 Using Material Properties Provided by Koval'chenko | 218 |
| E.3.1 Using Constant Friction Coefficient of 0.08 | 218 |
| E.3.2 Using Constant Friction Coefficient of 0.12 | 220 |
| E.3.3 Using Constant Friction Coefficient of 0.20 | 222 |
| E.3.4 Using Variable Friction Coefficient, $\mu(\sigma_n, v_r)$ | 224 |
| Appendix F. Effect of Die & Core-Rod to Upper-Punch Velocity Ration on Density Distribution of a Multi-stepped Part | 226 |
| F.1 Using Material Properties Provided by Shima | 226 |
| F.1.1 Using Constant Friction Coefficient of 0.08 | 226 |
| F.1.2 Using Constant Friction Coefficient of 0.12 | 228 |
| F.1.3 Using Constant Friction Coefficient of 0.20 | 230 |
| F.1.4 Using Variable Friction Coefficient, $\mu(\sigma_n, v_r)$ | 232 |
| F.2 Using Material Properties Provided by Pavier and Doremus | 234 |
| F.2.1 Using Constant Friction Coefficient of 0.08 | 234 |
| F.2.2 Using Constant Friction Coefficient of 0.12 | 236 |
| F.2.3 Using Constant Friction Coefficient of 0.20 | 238 |
| F.2.4 Using Variable Friction Coefficient, $\mu(\sigma_n, v_r)$ | 240 |
| Appendix H. UFRIC User-subroutine | 245 |

List of Tables

| | |
|--|-----|
| Table 1. Powder data for an atomized iron-based powder - Distaloy AE | 22 |
| Table 2. Evaluation of material properties for given values of powder density | 24 |
| Table 3. Summary of material properties..... | 26 |
| Table 4. Evaluation of elastic modulus for given values of powder density | 27 |
| Table 5. Summary of material properties..... | 28 |
| Table 6. Evaluation of material properties for given values of powder density | 32 |
| Table 7. Summary of material properties..... | 33 |
| Table 8. Parameter values for equations (43) and (44)..... | 45 |
| Table 9. Tool kinematics | 53 |
| Table 10. Summary of tool kinematics for all case studies | 60 |
| Table 11. Detailed data and nomenclature for all powder fill FE models for cylindrical parts.... | 60 |
| Table 12. Summary of tool kinematics for all three case studies..... | 63 |
| Table 13. Detailed data and nomenclature for FE model of the multi-stepped part..... | 64 |
| Table 14. Friction coefficient values used for simulation analyses | 77 |
| Table 15. Basic steps for automatic global remeshing employed in MSC.Marc Mentat | 79 |
| Table 16. Quick reference for Element 10..... | 82 |
| Table 17. Set of self-congruent units employed for simulation analyses..... | 83 |
| Table 18. Load step increment sizes used | 86 |
| Table 19. Summary of simulation runs for all cylindrical parts | 89 |
| Table 20. Summary of simulation runs for the multi-stepped part..... | 120 |
| Table 21. Evaluated values of v_3/v_1 at minimum density variation and critical velocity ratio, v_c | 125 |
| Table 22. Difference between maximum and minimum relative density values..... | 127 |
| Table 23. Average relative density of the final multi-stepped compacts..... | 128 |
| Table 24. Difference between maximum and minimum relative density values..... | 134 |
| Table 25. Average relative density of the final multi-stepped compacts..... | 135 |
| Table 26. Difference between maximum and minimum relative density values..... | 139 |
| Table 27. Average relative density of the final multi-stepped compacts..... | 140 |

List of Figures

| | |
|---|----|
| Figure 1. Particle shape and texture of different iron-based powder grades..... | 2 |
| Figure 2. The conventional cold-die compaction cycle: (1) filling the die cavity with powder, done by automatic feed in production, (2) initial, and (3) final position of upper and lower punches during compaction, and (4) ejection of green powder compact..... | 3 |
| Figure 3. Comparison of iron and steel powder consumption (relative use of unity) and other metal powder consumption on a logarithmic mass scale | 4 |
| Figure 4. North American iron powder shipments..... | 6 |
| Figure 5. International iron/steel powder shipments | 6 |
| Figure 6. North American shipments of iron powder for PM versus year | 6 |
| Figure 7. A collection of typical PM parts..... | 7 |
| Figure 8. 2D illustration of yield surfaces for powder (or porous) material..... | 13 |
| Figure 9. 3D view progression of Shima and Oyane yield function in principal stress space for values of relative density, $\bar{\rho}$, (a) 0.5, (b) 0.7, and (c) 1.0 | 14 |
| Figure 10. The degree of influence of powder material parameter (a) β on the hydrostatic stress, and (b) γ on the yield stress, $\bar{\sigma}$, with respect to relative density, $\bar{\rho}$ | 19 |
| Figure 11. Kinematics of (a) isotropic, (b) consolidated, and (c) overconsolidated triaxial tests carried out with triaxial cell in the q - p stress plane; where q is the deviatoric stress, $q = -(\sigma_z - \sigma_r)$; p is the mean stress, $p = -\frac{1}{3}(2\sigma_r - \sigma_z)$; p_c is the pressure of consolidation for overconsolidated test; σ_z is the axial stress; and the confining pressure is the radial stress, σ_r , during a triaxial loading | 21 |
| Figure 12. Evaluation of (a) elastic modulus and (b) bulk modulus as a function of density..... | 23 |
| Figure 13. Evaluation of Poisson's ration as a function of density | 23 |
| Figure 14. Yield limit reached using consolidated and overconsolidated tests with triaxial cell apparatus | 25 |
| Figure 15. Evaluation of deviatoric stress as a function of axial strain at different radial stresses | 26 |
| Figure 16. Evaluation of elastic modulus as a function of relative density | 27 |

| | |
|---|----|
| Figure 17. Dependence of (a) elastic modulus and (b) Poisson's ratio on relative density of sintered iron-based powder compacts..... | 31 |
| Figure 18. Dependence of shear viscosity on relative density for porous material..... | 32 |
| Figure 19. Dependence of shear viscosity on relative density for iron-based powder compact. | 34 |
| Figure 20. Instrumented-die with illustration of different instruments used to measure radial-pressure. | 35 |
| Figure 21. Stress balance on a cylindrical compact. | 36 |
| Figure 22. Compacted powder with measured upper punch (σ_{ua}) and lower punch (σ_{la}) stresses, and radial stress (σ_r), axial stress (σ_a), and frictional shear stress (τ) distribution..... | 37 |
| Figure 23. A shear-plate device consisting of: (1) optical transducer, (2) transducer, (3) powder compact disc, (4) parallelepipedic slab, (5) force transducer, (6) hydraulic press, (7) cylindrical die, and (8) press..... | 39 |
| Figure 24. Evaluation of friction coefficient versus normal stress, under the following conditions: sliding velocity, $v_r = 0.35$ mm/s; density, $\rho = 7.30$ g/cm ³ ; and temperature, $T = 20^\circ\text{C}$ | 40 |
| Figure 25. Evaluation of friction coefficient versus density, under the following conditions: sliding velocity, $v_r = 0.35$ mm/s; normal stress, $\sigma_n = 150$ MPa; and temperature, $T = 20^\circ\text{C}$ | 41 |
| Figure 26. Evaluation of friction coefficient versus sliding velocity, under the following conditions: density, $\rho = 7.30$ g/cm ³ ; normal stress, $\sigma_n = 150$ MPa; and temperature, $T = 20^\circ\text{C}$. | 41 |
| Figure 27. Friction of powder compacted sample at (a) low and (b) high density on tungsten carbide tool wall. | 42 |
| Figure 28. Evaluation of friction coefficient versus temperature, $T(^{\circ}\text{C})$, under the following conditions: density, $\rho = 7.02$ g/cm ³ ; sliding velocity, $v_r = 0.35$ mm/s; and normal stress, $\sigma_n = 150$ MPa. | 43 |
| Figure 29. Evaluation of friction coefficient versus temperature, $T(^{\circ}\text{C})$, under the following conditions: density, $\rho = 7.30$ g/cm ³ ; sliding velocity, $v_r = 10$ mm/s; and normal stress, $\sigma_n = 150$ MPa. | 43 |
| Figure 30. Friction coefficient with respect to sliding velocity and pressure..... | 44 |
| Figure 31. Functions relating the friction coefficient to the powder density and the sliding velocity..... | 46 |

| | |
|--|----|
| Figure 32. Friction model fitted to experimental values | 46 |
| Figure 33. Friction-assisted press system consisting of: (1) upper-punch, (2) powder, (3) movable die, and (4) lower-punch..... | 48 |
| Figure 34. Relative density distribution for compact height-to-diameter ratio of 1.50..... | 50 |
| Figure 35. Relative density distribution for compact height-to-diameter ratio of 1.00..... | 50 |
| Figure 36. Relative density distribution for compact height-to-diameter ratio of 0.50..... | 51 |
| Figure 37. Shape and dimensions of powder compact schematic. All dimensions are in mm | 52 |
| Figure 38. Press system consisting of: (1) upper-punch, (2) lower-outer-punch, (3) lower-inner-punch, (4) die, and (5) core-rod | 52 |
| Figure 39. Shape and density distribution of the multi-stepped compact after Stage 2 of compaction cycle | 54 |
| Figure 40. Density variation due to movement of tools 1 and 3, where • refers to minimum green density variation, and × refers to critical velocity ratio at which formation of slip-crack defect is initiated | 55 |
| Figure 41. Density variation due to movement of tools 1 and 4..... | 56 |
| Figure 42. Axisymmetric FE model of the powder fill for cylindrical part used for case study (1) | 59 |
| Figure 43. Axisymmetric FE model of the powder fill for cylindrical part used for case study (2) | 59 |
| Figure 44. Axisymmetric FE model of the powder fill for cylindrical part used for case study (3) | 59 |
| Figure 45. Axisymmetric FE model of the powder fill for multi-stepped part used for all case studies..... | 64 |
| Figure 46. Definition of a rigid body for 2-D or axisymmetric analysis using a curve | 66 |
| Figure 47. Contact tolerance..... | 68 |
| Figure 48. Trial displacement with penetration | 68 |
| Figure 49. Coulomb friction model | 71 |
| Figure 50. Bilinear model | 72 |
| Figure 51. Linear Coulomb friction model versus observed behaviour | 75 |

| | |
|---|-----|
| Figure 52. Mesh distortion example | 78 |
| Figure 53. Penetration of deformable body (powder) through rigid body (lower-inner-punch) at lower-inner-punch (3) to upper-punch (1) velocity ratio, v_3/v_1 , of 0.48 | 79 |
| Figure 54. Advancing front meshing | 81 |
| Figure 55. Integration points for Element 10 | 82 |
| Figure 56. Illustration of Full Newton-Raphson method | 85 |
| Figure 57. Density distribution over the compact height for a range of v_{die}/v_{u-p} values, using constant friction coefficient..... | 90 |
| Figure 58. Density distribution over the compact height for a range of v_{die}/v_{u-p} values, using variable friction coefficient, $\mu(\sigma_n, v_r)$ | 91 |
| Figure 59. Density variation with respect to v_{die}/v_{u-p} , using constant friction coefficient | 92 |
| Figure 60. Density variation with respect to v_{die}/v_{u-p} , using variable friction coefficient, $\mu(\sigma_n, v_r)$ | 92 |
| Figure 61. Density distribution over the compact height for a range of v_{die}/v_{u-p} values, using constant friction coefficient..... | 93 |
| Figure 62. Density distribution over the compact height for a range of v_{die}/v_{u-p} values, using variable friction coefficient, $\mu(\sigma_n, v_r)$ | 94 |
| Figure 63. Density variation with respect to v_{die}/v_{u-p} , using constant friction coefficient | 95 |
| Figure 64. Density variation with respect to v_{die}/v_{u-p} , using variable friction coefficient, $\mu(\sigma_n, v_r)$ | 96 |
| Figure 65. Density distribution over the compact height for a range of v_{die}/v_{u-p} values, using constant friction coefficient..... | 97 |
| Figure 66. Density distribution over the compact height for a range of v_{die}/v_{u-p} values, using variable friction coefficient, $\mu(\sigma_n, v_r)$ | 98 |
| Figure 67. Density variation with respect to v_{die}/v_{u-p} , using constant friction coefficient | 99 |
| Figure 68. Density variation with respect to v_{die}/v_{u-p} , using variable friction coefficient, $\mu(\sigma_n, v_r)$ | 99 |
| Figure 69. Density distribution over the compact height for a range of v_{die}/v_{u-p} values, using constant friction coefficient..... | 101 |

| | |
|--|-----|
| Figure 70. Density distribution over the compact height for a range of v_{die}/v_{u-p} values, using variable friction coefficient, $\mu(\sigma_n, v_r)$ | 102 |
| Figure 71. Density variation with respect to v_{die}/v_{u-p} , using constant friction coefficient | 103 |
| Figure 72. Density variation with respect to v_{die}/v_{u-p} , using variable friction coefficient, $\mu(\sigma_n, v_r)$ | 103 |
| Figure 73. Density distribution over the compact height for a range of v_{die}/v_{u-p} values, using constant friction coefficient..... | 105 |
| Figure 74. Density distribution over the compact height for a range of v_{die}/v_{u-p} values, using variable friction coefficient, $\mu(\sigma_n, v_r)$ | 106 |
| Figure 75. Density variation with respect to v_{die}/v_{u-p} , using constant friction coefficient | 107 |
| Figure 76. Density variation with respect to v_{die}/v_{u-p} , using variable friction coefficient, $\mu(\sigma_n, v_r)$ | 107 |
| Figure 77. Density distribution over the compact height for a range of v_{die}/v_{u-p} values, using constant friction coefficient..... | 109 |
| Figure 78. Density distribution over the compact height for a range of v_{die}/v_{u-p} values, using variable friction coefficient, $\mu(\sigma_n, v_r)$ | 110 |
| Figure 79. Density variation with respect to v_{die}/v_{u-p} , using constant friction coefficient | 111 |
| Figure 80. Density variation with respect to v_{die}/v_{u-p} , using variable friction coefficient, $\mu(\sigma_n, v_r)$ | 111 |
| Figure 81. Compact shape and density distribution after Stage 2 of compaction cycle | 117 |
| Figure 82. Density variation due to movement of tools 1 and 3..... | 121 |
| Figure 83. Density variation due to movement of tools 1 and 3..... | 122 |
| Figure 84. Density variation due to movement of tools 1 and 3..... | 123 |
| Figure 85. Density variation due to movement of tools 1 and 4..... | 129 |
| Figure 86. Density variation due to movement of tools 1 and 4..... | 130 |
| Figure 87. Density variation due to movement of tools 1 and 4..... | 131 |
| Figure 88. Density variation due to movement of tools 1, 4, and 5..... | 136 |
| Figure 89. Density variation due to movement of tools 1, 4, and 5..... | 137 |

Nomenclature

Roman letters:

| | |
|----------------------------------|--|
| a_1, a_2, a_3 | constants for load path dependent yield stress |
| $A^{(t)}, A^{(t+\delta t)}$ | nodal position at point (t) and point (t+ δt), respectively |
| b_1, b_2, b_3, b_4 | constants for β powder material parameter |
| c | material parameter that correlates with Poisson's ratio |
| d | powder compact diameter |
| \mathbf{D} | matrix relating rate of change of friction force vector and component of rate of relative elastic (stick) tangential displacement vector |
| \mathbf{D}^* | non-symmetric matrix |
| D_{ijkl}^e | fourth-order elastic modulus tensor |
| e | friction force tolerance |
| E | elastic modulus for powder (or porous) material |
| E_0 | elastic modulus for powder constitutive material |
| f_n | normal force |
| f_t | tangential (friction) force |
| \dot{f}_t | rate of change of friction force vector |
| f_v | Wikman's function of relative sliding velocity |
| f_{v0} | Wikman's equivalent static friction coefficient |
| f_ρ | Wikman's function of local density |
| F | external nodal-load vector |
| F_n, F_t | normal and tangential force for Pavier and Doremus's friction experiments |
| F_p | punch force |
| F_{residual} | residual force vector |
| $\ F_{\text{residual}}\ _\infty$ | component of residual force vector with highest absolute value |
| \mathbf{F}_t | current total friction force vector (collection of all nodal contributions) |
| \mathbf{F}_t^p | total friction force vector of previous iteration |
| g, m | constants for β powder material parameter |
| G | shear modulus for powder (or porous) material |
| G_0 | shear modulus for powder constitutive material |
| h | height of powder compact |
| h_f | final height of powder compact |
| h_i | initial height of powder fill prior to compaction |
| h/d | height-to-diameter ratio |
| k | structural imperfection index |
| K | bulk (volumetric) modulus for powder (or porous) material |
| K_0 | bulk (volumetric) modulus for powder constitutive material |
| \mathbf{K} | tangent-stiffness matrix |
| M_{residual} | residual moment vector |
| n | increment number |
| N | total number of elements |
| p | hydrostatic (mean) stress tensor |

| | |
|------------------------|---|
| p_c | consolidation pressure |
| P | axial pressure acting at specific radius, r |
| P_0 | axial pressure acting at the center of compact's cross-sectional area ($r = 0$) |
| q | deviatoric (effective or shear) stress tensor |
| q_1, q_2, q_3, q_4 | constants for γ powder material parameter |
| r | radius |
| R | internal nodal load vector due to internal stresses |
| R_a | average surface roughness |
| s | constant for γ powder material parameter |
| t | incremental state |
| \mathbf{t} | tangential vector in direction of relative velocity |
| T | temperature |
| TOL_1, TOL_2 | control tolerances for residual checking convergence criterion |
| u | nodal-displacement vector |
| \mathbf{u}_t | relative tangential (slip) displacement vector |
| $\dot{\mathbf{u}}_t$ | rate of relative tangential (slip) displacement vector |
| $\dot{\mathbf{u}}_t^e$ | rate of relative elastic (stick) tangential displacement vector component |
| $\dot{\mathbf{u}}_t^p$ | rate of relative plastic (slip) tangential displacement vector component |
| δu | incremental nodal-displacement vector |
| δu^i | approximate solution at iteration number i |
| Δu_n | incremental displacement at increment number n |
| Δu_t | incremental tangential relative displacement |
| v | velocity |
| v_c | critical velocity ratio at which slip-crack defect initiates |
| v_{die} | die velocity in compaction of cylindrical parts |
| v_r | relative sliding velocity |
| v_{u-p} | upper-punch velocity in compaction of cylindrical parts |
| v_0 | Wikman's reference velocity |
| v_1 | upper-punch velocity in compaction of a multi-stepped part |
| v_3 | lower-inner-punch velocity in compaction of a multi-stepped part |
| v_4 | die velocity in compaction of a multi-stepped part |
| v_5 | core-rod velocity in compaction of a multi-stepped part |
| v_{die}/v_{u-p} | die to upper-punch velocity ratio |
| v_3/v_1 | lower-inner-punch to upper-punch velocity ratio |
| v_4/v_1 | die to upper-punch velocity ratio |
| $v_{4,5}/v_1$ | die and core-rod to upper-punch velocity ratio |
| w_1, w_2, w_3 | Wikman's friction model parameters |
| x | point location at which friction is calculated |
| z | radial stress to axial stress (transmission) ratio |
| W | plastic work done per unit volume of powder (or porous) body |

Greek letters:

| | |
|-----------------|---|
| β, γ | material parameters for powder (or porous) material |
| δ | small quantity, variation, slip threshold |

| | |
|--|---|
| Δ | increment |
| $\varepsilon_1, \varepsilon_2, \varepsilon_3$ | principal normal strains |
| $d\varepsilon_1, d\varepsilon_2, d\varepsilon_3$ | principal normal strain increments |
| $d\varepsilon_v$ | volumetric strain increment |
| $\bar{\varepsilon}$ | effective plastic strain of powder (or porous) material |
| $d\bar{\varepsilon}$ | effective strain increment |
| $\dot{\bar{\varepsilon}}$ | effective plastic strain rate of powder (or porous) material |
| $\dot{\varepsilon}_{ij}$ | strain rate tensor for elastic-plastic deformation of powder (or porous) material |
| $\dot{\varepsilon}_{ij}^e$ | elastic strain rate tensor for deformation of powder (or porous) material |
| $\dot{\varepsilon}_{ij}^p$ | plastic strain rate tensor for deformation of powder (or porous) material |
| ζ | volumetric viscosity for powder (or matrix of porous) material |
| η | shear viscosity for powder (or porous) material |
| η_0 | shear viscosity for powder constitutive material |
| θ | porosity of powder (or porous) material |
| $\dot{\lambda}$ | a positive proportionality constant (or plastic multiplier) |
| $\dot{\Lambda}$ | slip displacement rate magnitude |
| μ | friction coefficient at powder-tool interface |
| μ_B | Wikman's base friction constant |
| ν | Poisson's ratio for powder (or porous) material |
| ν_0 | Poisson's ratio for powder constitutive material |
| ρ | powder density |
| ρ_m | average (mean) relative density of green compact |
| ρ_{ref} | Wikman's model limit value for density dependent friction |
| ρ_{var} | density variation throughout green compact |
| ρ_0 | density of powder constitutive material |
| $\bar{\rho}$ | relative density of powder (or porous) material |
| $\bar{\rho}_i$ | relative density of element i |
| $d\bar{\rho}$ | relative density increment |
| $\dot{\bar{\rho}}$ | rate of relative density of powder (or porous) material |
| σ_a, σ_z | axial stress |
| σ_m | hydrostatic (mean) stress tensor |
| σ_n | normal stress |
| σ_r | radial stress |
| σ_t | tangential friction (shear) stress |
| σ_{la} | axial stress on lower punch |
| σ_{ua} | axial stress on upper punch |
| $\sigma_1, \sigma_2, \sigma_3$ | principal normal stresses |
| $\bar{\sigma}$ | yield stress of powder (or porous) material |
| τ | tangential friction shear stress |
| φ | friction slip surface |
| $\dot{\varphi}$ | rate of change of friction slip surface |
| Φ | Shima and Oyane yield criterion for powder (or porous) material |
| Ψ | slip flow potential |

Abbreviations:

| | |
|-----|----------------------------|
| CAD | computer aided design |
| CAE | computer aided engineering |
| FE | finite element |
| FEA | finite element analysis |
| FEM | finite element method |
| HIP | hot isostatic pressing |
| PM | powder metallurgy |

1.0 Introduction

1.1 Powder Metallurgy

Powder metallurgy (PM) is a manufacturing process that involves production of parts from metallic or ceramic powders, or combination of both. The complete process consists of the following primary operations: (i) production of powder; (ii) blending or mixing of powder; (iii) compaction, in which powder is pressed into the desired shape; and (iv) sintering, which involves heat treatment below melting point temperature to procure inter-particle bonding and strengthening of the compact [1, 4, 26, 30]. Among manufacturing methods of metal treatment, PM occupies a distinctive place, successfully competing with casting, machining and other methods.

There are three principal commercial powder production methods: (i) atomization, which involves conversion of molten metal droplets into powder particles; (ii) chemical synthesis, where chemical reaction is used to reduce metallic compound into powder particles; and (iii) electrolysis, where electrolytic cell is used to dissolve metal, which acts as an anode under application of voltage [4, 26, 30]. The produced powder is distinct in shape and texture, depending on the production method; see Figure 1. The particle sizes vary as well, typically falling in a range of 25 - 300 μm (0.001 and 0.012 in) [1, 26, 30].

The blending and mixing process is performed to homogenize powder and improve the subsequent processing. Particles of identical or different chemical composition and varying in size are evenly intermingled to obtain more uniform blend. This process is achieved by mechanical means and usually involves addition of ingredients other than powder, exclusively to improve compaction and sintering. The lubricants are added to reduce friction on the inter-particle level and between the powder and the tooling surfaces. In addition, binders are sometimes added, depending on the powder used, to improve the strength of ejected compacts [1, 4, 30].

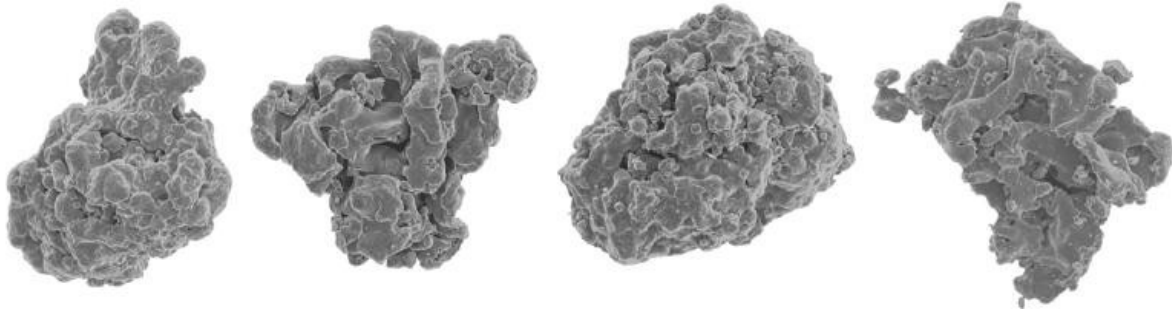


Figure 1. Particle shape and texture of different iron-based powder grades [42].

The compaction process consists of pressing of powder at high pressures into a desired shape using a die and appropriate pressing tools. The pressure during compaction varies depending on powder, typically ranging from 70 MPa, for lower yield powder, to 700 MPa for ferrous powders [4, 26, 30]. The design complexity of the die and pressing tools and their kinematics chiefly depend on part geometry. The conventional cold-die compaction cycle, shown in Figure 2, consists of three stages: (i) filling of the die, where the powder is in a loose state; (ii) pressing, due to displacement of punches; and (3) ejection of compact from the die.

After filling powder into the die, the powder is in a loose state and has apparent density value much lower than theoretical density of its constitutive material; that is the density at a fully solid state. Typical apparent density values for most ferrous powders fall in a range of 0.3 - 0.6 of the theoretical density or 2.3 - 4.7 g/cm³ [4, 26]. Most commonly the PM parts are produced using the cold-die compaction method, which is carried out at ambient temperatures and consists of a uniaxial compaction. The pressing cycle involves the following: (i) displacement of upper punch(es); or (ii) simultaneous displacement of upper and lower punches; or (iii) synchronized displacement of all pressing tools, depending on complexity of the part. The pressing itself may be subdivided into three stages: (I) the initial pressure is low causing sliding and rearrangement of powder particles, and an increase in contact points; (II) the pressure is increased causing plastic deformation and fracture of particles, and an increase in inter-particle contact area leading to a steep increase in density and, thus, decrease in porosity; (III) the pressure become very high switching to a moderate increase in density, yet never reaching theoretical density [4, 27, 30].

After pressing, the compact is ejected from the die and is in what is called a green state, meaning not yet fully processed. The density of green compact is much greater than apparent density of the powder fill, typically reaching values 0.85 to 0.92 of theoretical density for ferrous powders, although relative density of up to 0.98 is possible, depending on the applied pressure and its applications [26]. Before sintering, the ejected green compact is only adequate for handling due to its low strength and can only sustain low stresses. Upon sintering high mechanical strength and hardness is achieved due contact point bonding and expansion of contact area, thus, causing further decline in pores and evaporation of impurities (binders and lubricants). As a result, the powder compact is converted into a porous body consisting of a matrix material, which is composed of the powder constitutive material, and randomly distributed and shaped porous voids. The sintering process is conducted for a specific period of time at temperatures typically between 0.7 and 0.9 of the melting point, depending on constitutive material of powder [30]. It is important to note that some shrinkage does occur during the sintering process due to the reduction of pores, yet is generally predictable and accounted for in the design of a die.

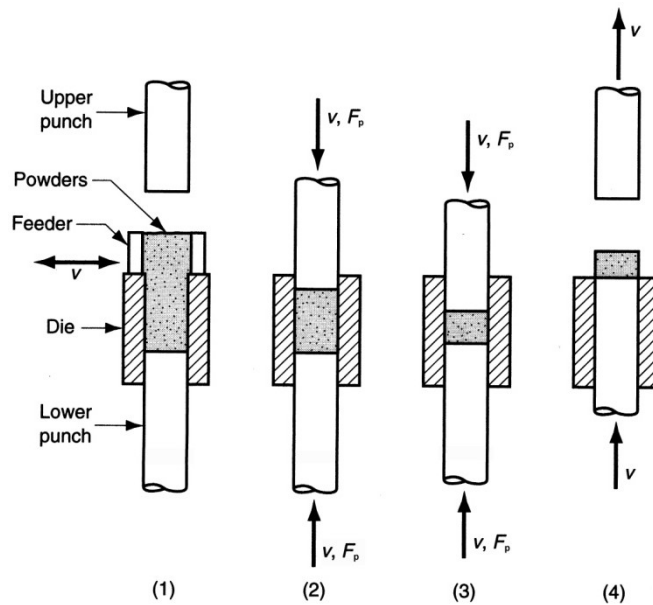


Figure 2. The conventional cold-die compaction cycle: (1) filling the die cavity with powder, done by automatic feed in production, (2) initial, and (3) final position of upper and lower punches during compaction, and (4) ejection of green powder compact [30].

In terms of weight, most of PM products fall in a range of 1 g to 2.2 kg, although parts weighting as little as 0.02 g and as much as 1 ton are known to have been successfully produced [26, 30]. Most common metal powders used in PM are alloys of iron, steel, and aluminum, out of which 85-90% is consumed by ferrous powders; see Figure 3. Others include copper, nickel, and refractory metals such a molybdenum and tungsten [26, 30].

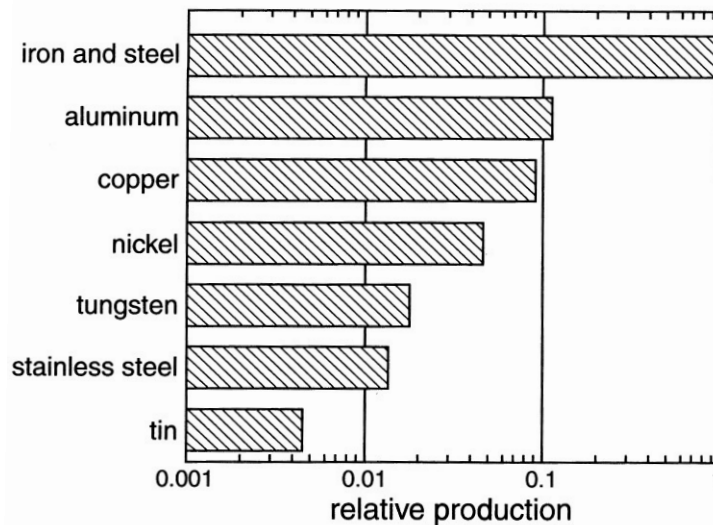


Figure 3. Comparison of iron and steel powder consumption (relative use of unity) and other metal powder consumption on a logarithmic mass scale [26].

PM technology has a vast number of applications, such that it is difficult to provide a brief listing. The prevailing applications in the past were, and still are, for the automotive sector and are mainly associated with engine and power transmission, where some of the most common components include: gears, sprockets, shock absorber compression valves, connecting rods, bearing pads, water and oil pumps, lifters, sensors, rockers, powder steering pump, flanges, fuel filters, injectors, valve seats and braking pads [26]. However, recent advancement in PM technology targets applications in industries such as aerospace, medical field, electronics, and sports, some of which include: jet engine components, biomedical implants, medical diagnostics, wear structures, electronic systems, electrical contacts, batteries, instrumentation, and sporting equipment [26]. Specifically in the aerospace industry, the problems associated with forging and machining of titanium alloy components have greatly influenced the use of PM technology as an alternative [35, 64]. More importantly, the advancements in hot isostatic

pressing (HIP), which is a branch of PM technology, led to its general acceptance as the main choice for the production of high-performance aircraft landing gears [26].

To give a sense of economical growth and trends seen in recent years in both North American and world-scale market, PM has sustained an average growth rate of 8 - 10% [26, 96-98, 117-122]; see Figures 4 and 5. The North American market alone, has seen a steep increase in demand in terms of powder supply over the last few decades, where on the of tonnage, the annual average growth rate is estimated at 7%; see Figure 6.

One of the main advantages of PM technology is that it allows for mass production of net shape parts, often eliminating or reducing the need for secondary operations. It compares favourably with conventional methods in terms of dimension control, with dimensional tolerances near the ones associated with machining [26, 30]. The process itself leaves marginal waste, typically utilizing 97% of starting materials, thus favourably competing with conventional manufacturing processes, such as casting and machining, which tend to produce more waste [4, 26, 30]. Further, the process allows for porosity control, which although judged as a disadvantage for certain applications, yet is favourable for others. For example, pores may serve as lubricant reservoirs, which allows for production of oil-impregnated gears and bearings with increased life span due to their reduction in wear [26, 30]. Furthermore, PM technology is a cheaper alternative when it comes to production of parts composed of refractory metals, which is costly when using traditional methods due to their high melting points. Also, PM technology allows for production of unusual metal alloys or combination of metal alloy with ceramic materials, allowing for production of cutting tools, which is simply not possible by other means [30]. Lastly, the process is highly automated, thus allowing for much higher production rates than conventional manufacturing processes, such as casting and machining [26, 30].

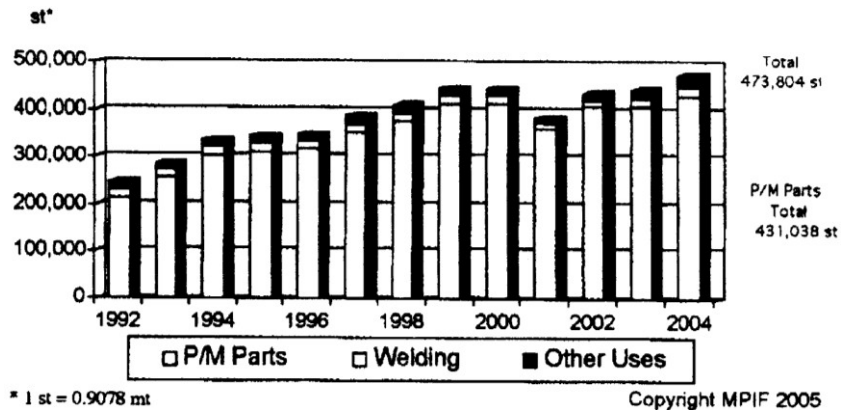


Figure 4. North American iron powder shipments [96].

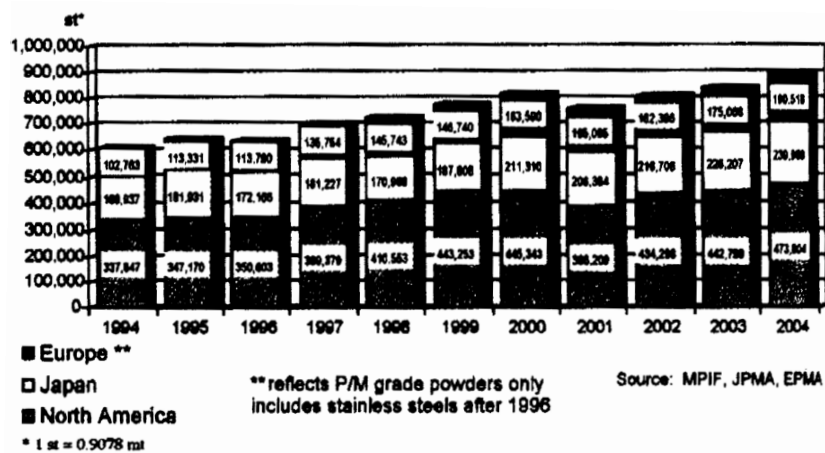


Figure 5. International iron/steel powder shipments [96].

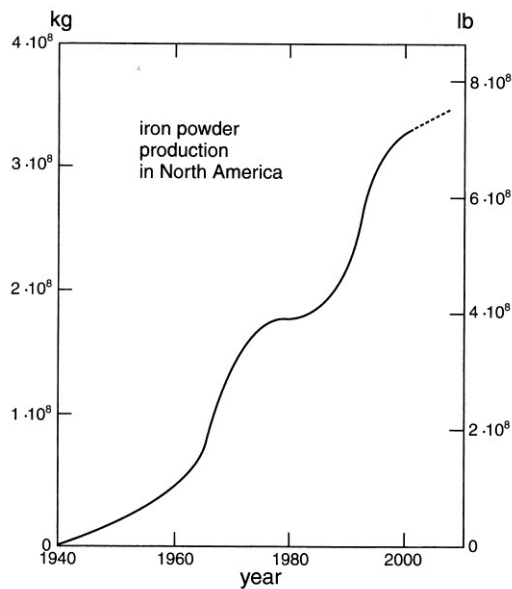


Figure 6. North American shipments of iron powder for PM versus year [26].

There are limitations and disadvantages in PM technology. One major limitation is the part geometry. Unlike molten metal, upon compression the powder does not readily flow and evenly distribute itself, particularly in lateral direction. Thus, certain design guidelines must be followed such that geometry of the part can permit its ejection from the die, thus, limiting features along its sides. Nevertheless, stepped geometry is permissible and very common among typical PM parts; see Figure 7 [4, 26, 30]. Besides, more detailed geometric side features are possible, however, requiring secondary operations. As a general rule, cold-die compaction is best suited for production of moderately complex components with dimensional tolerances near the ones associated with machining [26]. Nevertheless, the advancements in PM technology, specifically efficiency improvements of the pressing tools, have significantly contributed to a decrease in complexity barriers.



Figure 7. A collection of typical PM parts [30].

1.2 Problem Statement

One of the major disadvantages of PM is the density variation throughout the green powder compacts. During the compaction cycle, due to the existence of friction at powder-tool interfaces, the contact surfaces experience a non-uniform stress distribution mainly having to do with a variable friction coefficient and tool kinematics of a press system, consequently resulting in the density gradient throughout a compact body [10, 15, 20, 43, 44, 45, 49, 48, 70, 80, 88-90,101, 102]. Density variation in a green powder compact represents a serious problem in terms of its reliability and performance as it may contribute to a crack-defect generation during the compaction cycle, depending on part's geometrical complexity, and more importantly a non-uniform shrinkage of a powder compact during the sintering process [4, 10, 20, 26, 44, 48, 49, 70, 88-90, 101, 102]. The geometrical distortion caused by non-uniform shrinkage may require secondary operations, such as machining, thus, compromising the competitiveness of PM technology.

Until now, the measures taken to reduce density variation have primarily concentrated on the reduction of friction by development of enhanced lubricants and their implementation into the powder blend, as well as their application onto the tooling surfaces. However, excessive addition of lubricants undermines the mechanical properties of the final PM components, due to the increased porosity upon sintering. More importantly, a double-action compaction has generally been put into practice to further reduce the effects of friction. However, the problems associated with friction cannot be eliminated by the above measures, but can only be reduced [20, 44, 49, 48, 70, 102]. In addition, different isostatic pressing methods have been introduced to further reduce the effects of friction. However, as geometrical complexity of a part increases the corresponding shape cannot be achieved with uniform pressure due to the imposed geometrical constrains. Consequently, the key to further reduction of heterogeneity in green compacts lies in an efficient design of a press system. The most influential practices that have demonstrated to improve the efficiency of a press system consist of optimizing the compaction cycle, primarily the optimization of tool kinematics, such that the resultant green compacts have a minimal density variation throughout their volume [15, 20, 44, 48, 49, 70, 88, 90, 101, 102].

Traditionally, the efficiency of a new press system heavily depended on engineer's experience and involved lengthy and expensive trial-and-error design process. Yet, the consistent research of process associated parameters and development of powder constitutive models throughout the last three decades, and their implementation into the Finite Element Method (FEM) and Computer Aided Engineering (CAE) software, has established a ground for simulation of powder compaction process and consequently a more efficient way for future development of PM equipment. Now, with the help of FEM and CAE, engineers have the ability to conduct appropriate simulation analysis to establish optimal conditions during the design stage of a new press system or to optimize the pressing cycle of existing equipment.

1.3 Objective

The focus of this research is to investigate the parameters contributing to density variation in green powder compacts and specifically to establish optimal tool kinematics during powder compaction cycle to minimize density gradient in both cylindrical and multi-stepped compacts. Using simulation analyses, a newly proposed friction-assisted compaction technique was employed for compaction of cylindrical parts. This was further extended to a more complex geometry, consisting of a multi-stepped part, by indirectly using the friction-assisted compaction technique by varying the tool kinematics of a press system. Further, for all case studies, experimentally derived material properties and a variable friction coefficient were implemented into the corresponding simulation models to assimilate more realistic material behaviour and process associated conditions, respectively.

1.4 Thesis Organization

In Chapter 2, the powder constitutive model is discussed which was employed for all the simulation analyses conducted for the present study. It covers the powder yield criterion and the corresponding constitutive equations and parameters associated with the powder and porous material behaviour.

Chapter 3 consists of two sections covering the material properties and friction in powder metallurgy, respectively. First section summarizes three sets of material properties, all experimentally derived using the iron-based powder and porous material, and their dependence on the process associated parameters. All corresponding sets were implemented into the FE models. Second section covers three different experimental methods used to measure friction at powder-tool interfaces and the corresponding derived relationships for the variable friction coefficient.

Chapter 4 consists of two main sections. First, a newly proposed friction-assisted compaction technique is discussed for the compaction of cylindrical parts. In the second section, the discussion is extended to the compaction of a more complex geometry, consisting of a multi-stepped part, which indirectly uses the friction-assisted compaction technique by varying the tool kinematics of the press system. The information presented in both sections was adopted for the simulation analyses of the present study.

Chapter 5 discusses the finite element approach employed for the simulation analyses of the present study. It covers the employed FE models for the analyses of the friction-assisted compaction of cylindrical parts and the multi-stepped part. Specifically, it covers the definition of powder, pressing tools, remeshing techniques used, and the process associated parameters such as contact definition and control, friction modelling, and more.

Chapter 6 presents the simulation results and discussion of the friction-assisted compaction of the cylindrical parts. It consists of three main sections, each covering the effect of die to upper-punch velocity ratio on the density gradient of the cylindrical green powder compacts with three different compact height-to-diameter ratio values of 1.50, 1.00, and 0.50, respectively, using two sets of material properties.

Chapter 7 consists of the simulation results and discussion of compaction of a multi-stepped part. The chapter is divided into three case studies, each covering the effect of different velocity ratios of specific pressing tools on the green powder compact density variation: (i) lower-inner-punch to upper-punch velocity ratio, (ii) die to upper-punch velocity ratio, and (iii)

die and core-rod to upper-punch velocity ratio. The results are presented for different sets of material properties.

Chapter 8 consists of concluding remarks with regards to the simulation results obtained for the friction-assisted compaction of the cylindrical parts and compaction of the multi-stepped part. The chapter ends with a discussion on specific contribution and future work.

2.0 Powder Constitutive Model

2.1 Yield Criterion

Until now, there have been developed a number of powder constitutive models to represent the yield criterion for powder material. The one adapted for this analysis was Shima and Oyane model. Initially developed as a yield criterion for porous metals, in other words sintered powder compacts; it has been successfully adapted over the years for compaction analysis of both metal and ceramic powders, yielding consistent results for various compact geometries [16, 43, 48, 49, 50, 70, 83, 101, 102]. The Shima and Oyane yield criterion, Φ , is based on the von-Mises criterion with implemented influence of hydrostatic stress on yielding. Unlike other constitutive material models, its main advantage is that its yield surface is expressed using a single function as [106]

$$\Phi = \frac{1}{\gamma} \left[\frac{1}{2} \{ (\sigma_1 - \sigma_2)^2 + (\sigma_2 - \sigma_3)^2 + (\sigma_3 - \sigma_1)^2 \} + \left(\frac{\sigma_m}{\beta} \right)^2 \right]^{1/2} - \bar{\sigma} \quad (1)$$

or in a more concise form as [43, 44, 50, 70, 71, 74, 75]

$$\Phi = q^2 + \left(\frac{p}{\beta} \right)^2 - (\gamma \bar{\sigma})^2 \quad (2)$$

where: β, γ – material parameters for powder (or porous) material

$\sigma_1, \sigma_2, \sigma_3$ – principal normal stresses

σ_m or $p(\sigma_{kk}/3)$ – hydrostatic (mean) stress tensor

$q (= \sqrt{3\sigma_{ij}\sigma_{ij}/2})$ – deviatoric (shear) stress tensor

$\bar{\sigma}$ – yield stress of powder (or matrix of porous) material.

Both γ and β are functions of relative density, $\bar{\rho}$, which is defined as the density of powder, ρ , with respect to the theoretical density of powder constitutive material (fully solid state), ρ_0 , expressed as

$$\bar{\rho} = \frac{\rho}{\rho_0} \quad (3)$$

Unlike, isotropic material which only yields due to deviatoric stress tensor, the yielding of powder is caused by both deviatoric and hydrostatic stress tensors. Consequently, material parameter β represents the degree of influence of hydrostatic stress component on the onset of yielding of powder (or porous) material, whereas γ represents the ratio of the apparent stress applied to the powder (or porous) body and the yield stress, $\bar{\sigma}$, applied to the powder particles (or matrix of porous material) [43, 106]; see Figure 10.

In a two dimensional view, the yield surface of Shima and Oyane model for powder material with a relative density, $\bar{\rho}$, has the form of an ellipsoid whose major axis coincides with hydrostatic stress axis, as shown in Figure 8. In a three dimensional view, the yield criterion represents a prolate spheroid in principal stress space with a smooth, convex, bounded surface; see Figure 9. Moreover, as relative density, $\bar{\rho}$, approaches unity, the yield surface matches that of the von-Mises criterion beyond which point yielding may still progress, yet strictly due to deviatoric stress [45, 106].

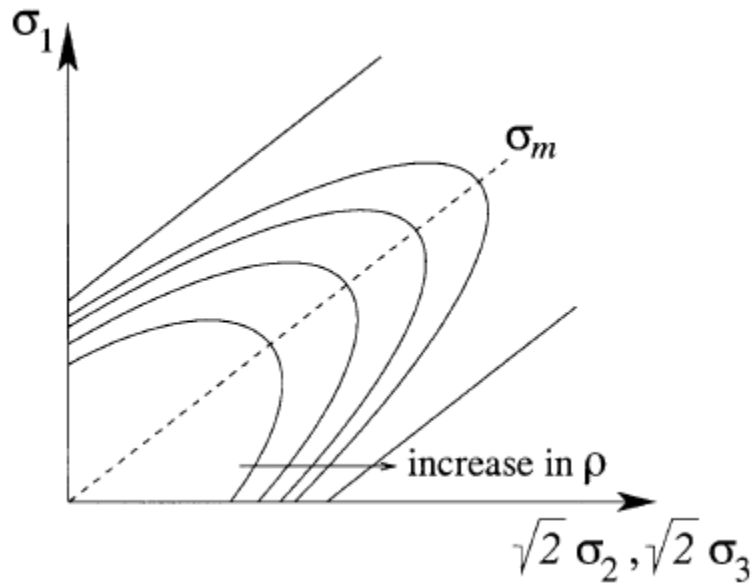


Figure 8. 2D illustration of yield surfaces for powder (or porous) material [45, 106].

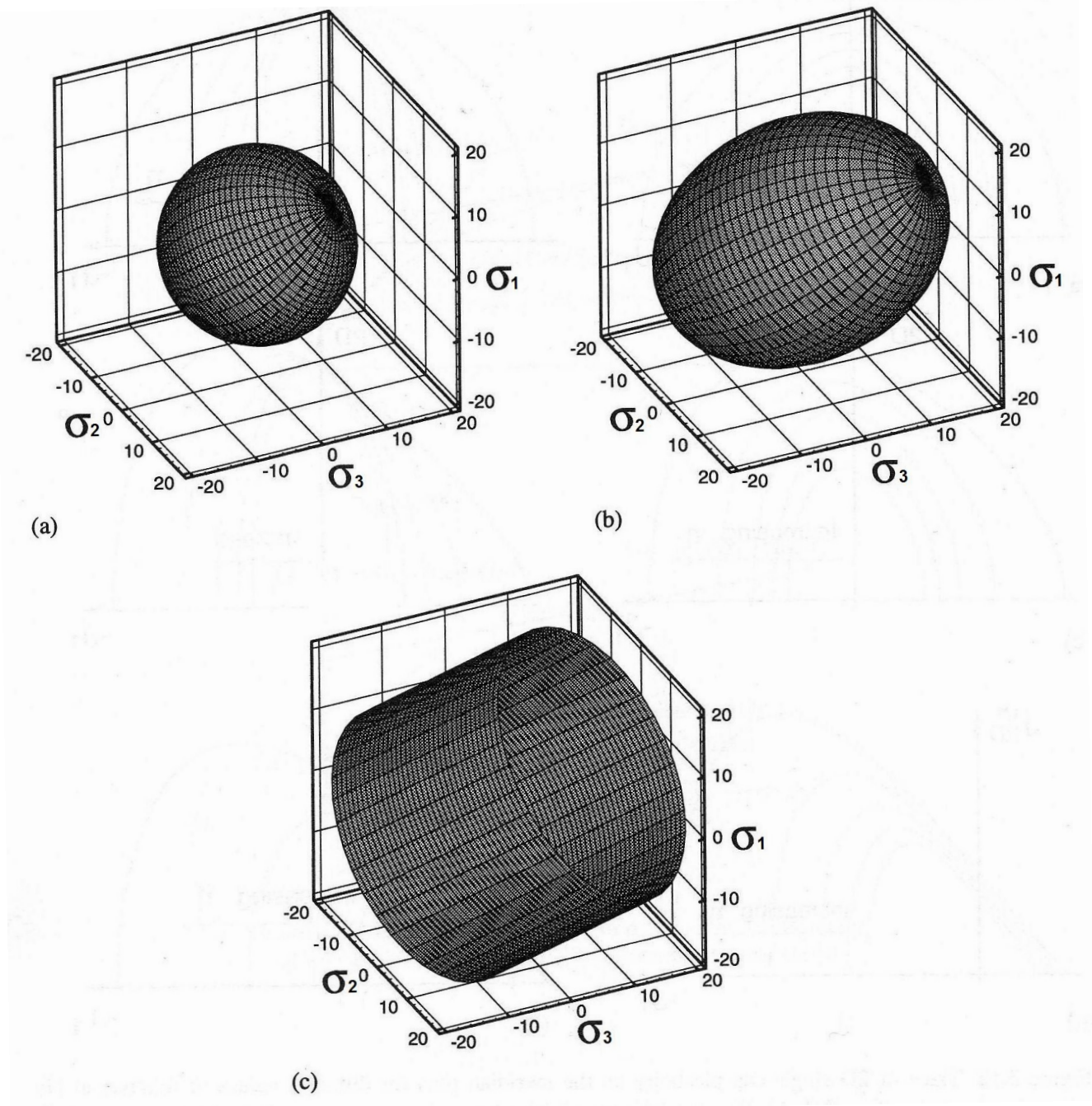


Figure 9. 3D view progression of Shima and Oyane yield function in principal stress space for values of relative density, $\bar{\rho}$, (a) 0.5, (b) 0.7, and (c) 1.0 [45].

2.2 Constitutive Equations

The strain rate tensor for elastic-plastic deformation of powder (or porous) material is expressed as

$$\dot{\epsilon}_{ij} = \dot{\epsilon}_{ij}^e + \dot{\epsilon}_{ij}^p \quad (4)$$

where $\dot{\epsilon}_{ij}^e$ and $\dot{\epsilon}_{ij}^p$ are elastic and plastic strain rate tensors, respectively [17, 43, 45, 50]. The plastic strain rate tensor $\dot{\epsilon}_{ij}^p$ is expressed as

$$\dot{\epsilon}_{ij}^p = \dot{\lambda} \frac{\partial \Phi}{\partial \sigma_{ij}} \quad (5)$$

or in alternative form as

$$\dot{\epsilon}_{ij}^p = \frac{1}{\eta} \left(\frac{\Phi}{\bar{\sigma}} \right) \quad (6)$$

where $\dot{\lambda}$ is a positive proportionality constant, to be determined later; Φ is Shima and Oyane's yield function for powder (or porous) material; and η is the shear viscosity for powder constitutive (or matrix of porous) material [17, 43, 45, 50, 75].

Assuming that the constitutive material (or matrix) is incompressible, the rate of relative density, $\dot{\bar{\rho}}$, is expressed as

$$\dot{\bar{\rho}} = \bar{\rho} \dot{\epsilon}_{kk}^p \quad (7)$$

The stress tensor can be written in the form of Hooke's law as

$$\sigma_{ij} = D_{ijkl}^e \dot{\epsilon}_{ij}^e \quad (8)$$

where D_{ijkl}^e is a fourth-order elastic modulus tensor [17, 43, 45, 50]. Further, it is assumed that plastic work done on powder (or porous) body is equivalent to that of the matrix material, such that

$$\bar{\rho} \dot{\bar{\epsilon}} = \sigma_{ij} \dot{\epsilon}_{ij}^p \quad (9)$$

where again $\bar{\sigma}$ is the yield stress and $\dot{\bar{\epsilon}}$ is the effective plastic strain rate of powder (or matrix of porous) body [43, 50]. In this study, the effective plastic strain, $\bar{\epsilon}$, is referred to frequently, which in the rate form is defined as

$$\dot{\bar{\epsilon}} = \sqrt{\frac{2}{3} \dot{\epsilon}_{ij}^p \dot{\epsilon}_{ij}^p} \quad (10)$$

where $\dot{\epsilon}_{ij}^p$ is the plastic strain rate tensor expressed by equations (5) and (6) [45].

Assuming Φ to be a plastic potential, then by its partial differentiation with respect to σ_1 , σ_2 , and σ_3 we obtain the following principal strain increments $d\epsilon_1$, $d\epsilon_2$, and $d\epsilon_3$, respectively [106]

$$\begin{aligned} d\epsilon_1 &= d\lambda' \frac{\partial \Phi}{\partial \sigma_1} = d\lambda \left\{ \sigma_1 - \left(1 - \frac{2}{9} \beta^2\right) \sigma_m \right\} \\ d\epsilon_2 &= d\lambda' \frac{\partial \Phi}{\partial \sigma_2} = d\lambda \left\{ \sigma_2 - \left(1 - \frac{2}{9} \beta^2\right) \sigma_m \right\} \\ d\epsilon_3 &= d\lambda' \frac{\partial \Phi}{\partial \sigma_3} = d\lambda \left\{ \sigma_3 - \left(1 - \frac{2}{9} \beta^2\right) \sigma_m \right\} \end{aligned} \quad (11)$$

Consequently, the volumetric strain increment is expressed as [106]

$$d\epsilon_v = d\epsilon_1 + d\epsilon_2 + d\epsilon_3 = -\frac{d\bar{\rho}}{\bar{\rho}} = d\lambda \left(\frac{2}{9} \beta^2 \right) \sigma_m \quad (12)$$

Further, the plastic work, dW , done per unit volume of powder (or porous) body may be expressed as a function of yield stress, $\bar{\sigma}$, and effective strain increments, $d\bar{\epsilon}$, as [106]

$$dW = \sigma_1 d\epsilon_1 + \sigma_2 d\epsilon_2 + \sigma_3 d\epsilon_3 = \bar{\rho} \bar{\sigma} d\bar{\epsilon} \quad (13)$$

This is because a unit volume of powder (or porous) body with relative density $\bar{\rho}$ consists of the matrix material of volume $\bar{\rho}$, thus, dW is not directly equivalent to $\bar{\sigma} d\bar{\epsilon}$ [106].

By substituting equation (11) into (13) and further rearranging, we obtain proportionality constant as [106]

$$d\lambda = \frac{3\bar{\rho}}{2\gamma^2} \frac{d\bar{\epsilon}}{\bar{\sigma}} \quad (14)$$

In addition, by elimination of σ_m from equation (11) and (12) and rearrangement of σ_1 , σ_2 , and σ_3 we may express the effective strain increment, $d\bar{\epsilon}$, in terms of $d\epsilon_1$, $d\epsilon_2$, $d\epsilon_3$, and $d\epsilon_v$, as [106]

$$d\bar{\epsilon} = \frac{\gamma}{\bar{\rho}} \left[\frac{2}{9} \{ (d\epsilon_1 + d\epsilon_2)^2 + (d\epsilon_2 + d\epsilon_3)^2 + (d\epsilon_3 + d\epsilon_1)^2 \} + (\beta d\epsilon_v)^2 \right]^{1/2} \quad (15)$$

2.3 Determination of β and γ Material Parameters

Both functions for β and γ material parameters can be determined from a uniaxial compression test using sintered powder compacts, compacted to various densities [45, 81, 106]. By substitution of $\sigma_1 = \sigma_2 = 0$ and $\sigma_m = \sigma_1/3$ into equations (11) and (12), thus, having uniaxial stress condition, and their rearrangement, we obtain [106]

$$\beta = \frac{\sqrt{2}}{3} \left(\frac{d\epsilon_1 - d\epsilon_2}{d\epsilon_v} \right)^{1/2} \quad (16)$$

Using equation (16) we may determine β by experimental means by determining changes in relative density through application of incremental load using simple compression and tension tests [106].

Similarly, by substitution of $\sigma_1 = \sigma_2 = 0$ into equation (1), we obtain [106]

$$\bar{\sigma} = \frac{|\sigma_1|}{\gamma} \left(1 + \frac{1}{9} \beta^2 \right)^{1/2} \quad (17)$$

Using equation (17) we may extract the relationship for γ by plotting yield stress with respect to relative density [106]. Thus, using the above steps Shima and Oyane have derived the following functions for representation of β and γ as [43, 48, 49, 81, 101, 106]

$$\beta = \frac{1}{g(1 - \bar{\rho})^m} \quad (18)$$

$$\gamma = \bar{\rho}^s \quad (19)$$

where $\bar{\rho}$ is the relative density; and g , m , and s are all material parameter constants that vary depending on powder. Using the specified procedure, the above material parameter constants g , m , and s were determined for iron-based powder as 2.49, 0.514, and 2.5, respectively [43, 48, 49, 50, 106]. Substituting these values into equation (18) and (19) we have complete representation of β and γ for iron-based powder material as

$$\beta = \frac{1}{2.49(1 - \bar{\rho})^{0.514}} \quad (20)$$

$$\gamma = \bar{\rho}^{2.5} \quad (21)$$

For an illustrative representation of β as the degree of influence of the hydrostatic stress on the onset of yielding of powder, and the degree of influence of γ on the yield stress, $\bar{\sigma}$, see Figure 10.

It is argued, that material parameters obtained based on uniaxial test using sintered specimens do not truly represent the behaviour of a non-sintered green compact, and their derivation may be difficult to perform on the lower density range specimens [45]. An alternative is the triaxial (three-dimensional) test or a closed-die compaction test, with earlier being able to control and measure both axial and lateral pressures. However, the triaxial apparatus is rather expensive and the material parameters β and γ derived using triaxial method were not found in the literature. Nevertheless, Shima et al. have later confirmed the earlier derived material parameter values for iron-based powder using closed-die compaction test. More importantly, in numerous powder compaction simulation studies conducted by Shima and other researchers, using material parameters presented in equations (20) and (21), results agreeable with experimental data have been attained [16, 43, 48, 49, 50, 81, 83, 101, 102]. Therefore, these parameters were adopted for all simulation analyses.

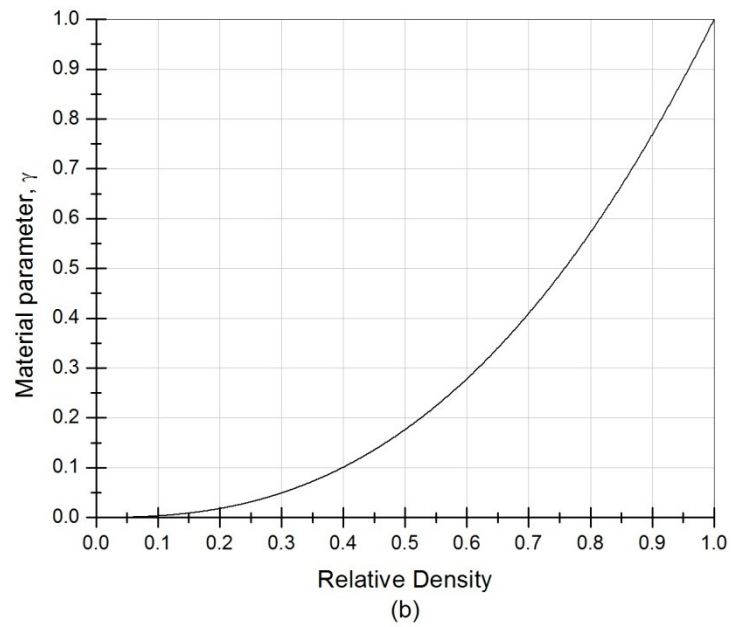
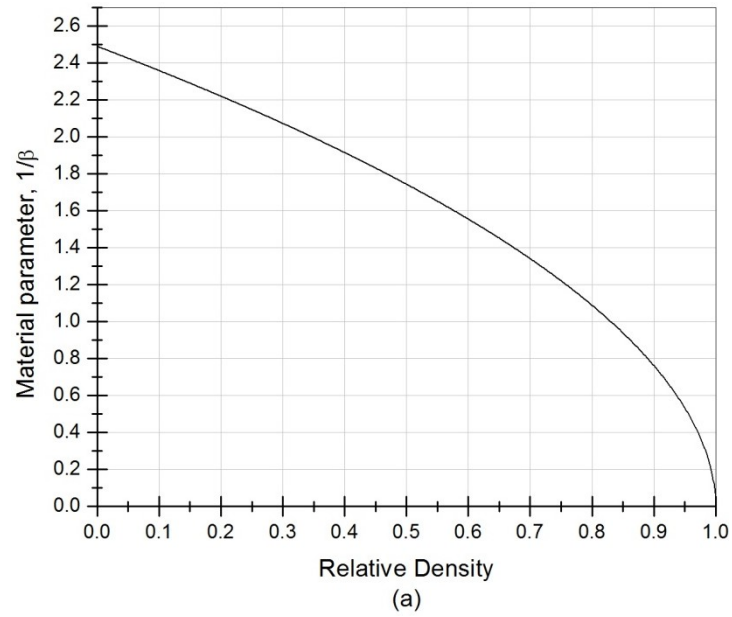


Figure 10. The degree of influence of powder material parameter (a) β on the hydrostatic stress, and (b) γ on the yield stress, $\bar{\sigma}$, with respect to relative density, $\bar{\rho}$.

2.4 Modification of Original Yield Criterion

One of the major limitations of the originally proposed yield criterion by Shima and Oyane is that it does not fully incorporate the effect of work-hardening associated with the densification process, having a constant yield stress, $\bar{\sigma}$, value, even though this is one of the main features in the process [43, 45, 48, 49, 50, 70, 102, 104, 106]. Later, Shima et al., proposed an updated yield criterion in the form of equation (1), but with a load path dependent yield stress, $\bar{\sigma}$, relationship, thus, expressed as a function of effective strain, $\bar{\epsilon}$,

$$\bar{\sigma} = a_1 + a_2(\bar{\epsilon})^{a_3} \quad (22)$$

where constants a_1 , a_2 , and a_3 should be determined for each powder material individually [104]. In fact, this was further confirmed and improved upon by a number of separate studies conducted by various researchers, having the yield stress expressed as

$$\bar{\sigma} = \bar{\sigma}(\bar{\epsilon}, \dot{\bar{\epsilon}}, T) \quad (23)$$

where $\bar{\epsilon}$, $\dot{\bar{\epsilon}}$, and T are the effective strain, effective strain rate, and temperature, respectively [22, 43, 46, 47, 48, 49, 50, 71, 82, 84, 85, 87]. It is important to note that the simulation software utilized for the present study limits the definition of yield stress to a function of temperature or as a constant value for powder material [72, 73]. Since the compaction process consists of cold-die compaction, with both powder and tools at ambient temperatures, the influence of temperature was ignored. For these reasons, a constant value for the yield stress had to be adopted. Thus, due to the specified limitations the above suggested modification could not be implemented into finite element (FE) model.

3.0 Material Properties and Friction in PM

3.1 Material Properties for Powder and Porous Materials

Contrary to fully dense (solid) isotropic materials, material properties for powder and porous (sintered powder compact) materials vary with respect to relative density. Thus, for accurate simulation of the powder behaviour, derivation of the appropriate constitutive material parameters and both elastic and plastic properties is essential. Various experimental studies conducted over the years have confirmed that material properties such as: (i) elastic, bulk (volumetric), and shear moduli; (ii) Poisson's ratio; (iii) yield stress; (iv) shear and volumetric viscosity; and (v) material hardness; all depend on relative density of tested powder (or porous) materials [7, 10, 11, 22, 23, 29, 36-43, 45-47, 48-50, 52-60, 62, 63, 67, 68, 81, 84, 85, 87, 91-96, 104, 127, 128]. The material property sets adopted for simulation analysis were the ones derived by most prominent researchers who have spent extensive number of years, studying and modelling the behaviour of powder and porous materials.

3.1.1 Material Properties Provided by Pavier and Doremus

To date, the best available experimental apparatus for characterisation of mechanical behaviour of powder materials is the triaxial cell [10, 22, 45, 84, 85, 87, 112]. Using triaxial cell, Pavier and Doremus have conducted extensive analyses on iron-based powder by subjecting it to the isotropic, consolidated, and overconsolidated tests; see Figure 11.

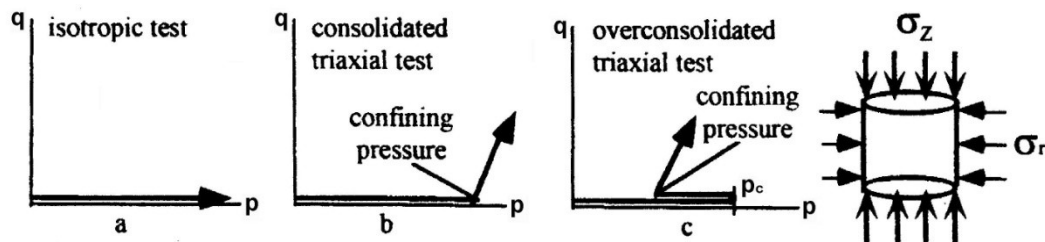


Figure 11. Kinematics of (a) isotropic, (b) consolidated, and (c) overconsolidated triaxial tests carried out with triaxial cell in the q - p stress plane; where q is the deviatoric stress, $q = -(\sigma_z - \sigma_r)$; p is the mean stress, $p = -\frac{1}{3}(2\sigma_r - \sigma_z)$; p_c is the pressure of consolidation for overconsolidated test; σ_z is the axial stress; and the confining pressure is the radial stress, σ_r , during a triaxial loading [87].

The powder used for the study was an atomised iron-based powder, Distaloy AE, supplied by leading powder producer Höganäs AB. The reason for selection of this particular metal powder is the fact that it is one of the most commonly used powder grade in PM, due to its high end applications that require high strength and wear resistance, such as production of gears, and synchronizing and oil pump parts [36]. In addition, this powder grade is most favourable for parts where good dimensional control is critical [36]. The atomised powder particles have a size ranging from 20 to 180 μm . The apparent density of powder (at uncompressed state) is 3.04 g/cm^3 , while the theoretical density, which corresponds to the fully dense powder compact with lubricant additives, is 7.33 g/cm^3 . The complete data on Distaloy AE material composition is shown in Table 1.

Table 1. Powder data for an atomized iron-based powder - Distaloy AE [36, 48, 84, 85, 87].

| Powder Density, ρ [g/cm^3] | | Chemical Composition [in %] | | | | | |
|---|-------------|-----------------------------|------|------|-------|-------|---------|
| Apparent | Theoretical | Ni | Mo | Cu | C | O-tot | Fe |
| 3.04 | 7.33 | 4.00 | 0.50 | 1.50 | <0.01 | 0.11 | balance |

From their studies, Pavier and Doremus have produced a detailed account of mechanical behaviour of iron-based powder. Based on this experimental data, it was made possible to derive a relationship for the elastic modulus as a function of density, written as

$$E(\text{MPa}) = (E_0 + E_1\rho)e^{\left(\frac{\rho}{\rho_0}\right)^a} \quad (24)$$

with $E_0 = -28000$ MPa, $E_1 = 10020$ MPa, $a = 6$, and $\rho_0 = 6.8$ g/cm^3 ; for bulk modulus, as

$$K(\text{MPa}) = (K_0 + K_1\rho)e^{\left(\frac{\rho}{\rho_0}\right)^b} \quad (25)$$

with $K_0 = -10500$ MPa, $K_1 = 3750$ MPa, $b = 6$, and $\rho_0 = 6.55$ g/cm^3 ; and for Poisson's ratio, as

$$\nu = 0.5 - \frac{E}{6K} \quad (26)$$

where E and K are elastic and bulk moduli, given by equation (24) and (25), respectively [10, 84]. However, it must be noted that due to the small strain and transducer sensitivity variations experienced upon cyclic loading, there is an uncertainty margin of 10% and 30% for deduced elastic and bulk moduli, respectively [10, 84, 85, 87]. Upon implementation of the above

functions into the simulation model, the uncertainty level may have an influence on final results. Nevertheless, the triaxial test is the most accurate experimental method to date, and the ensuing uncertainty is relatively small in comparison to alternative methods.

Evaluation of equations (24) to (26) with respect to density shows identical trend where all three properties experience exponential increase with density; see Figures 12 and 13.

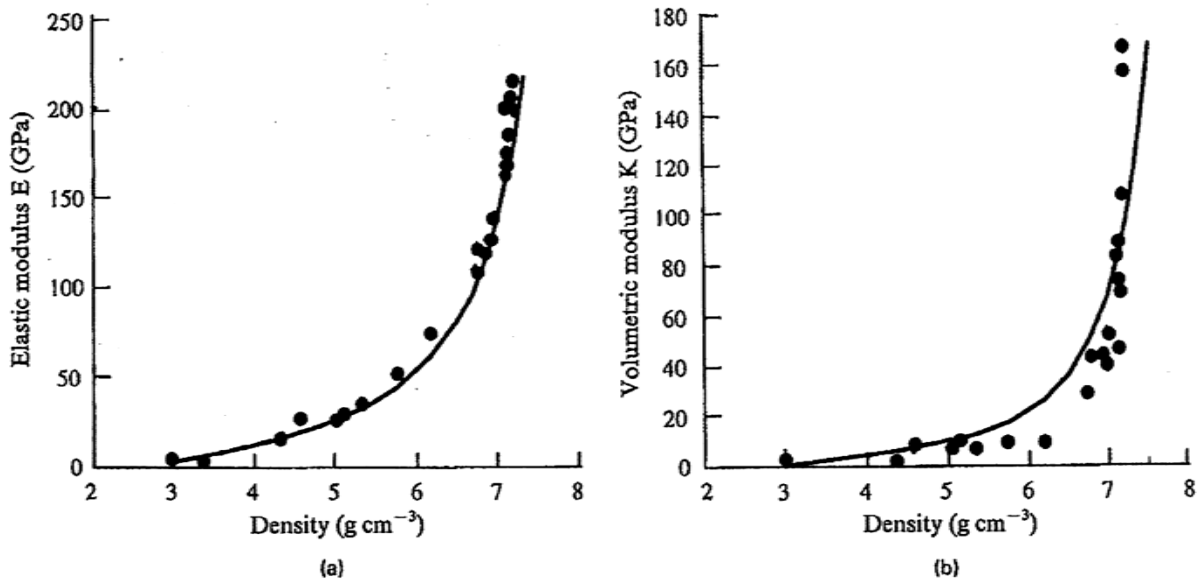


Figure 12. Evaluation of (a) elastic modulus and (b) bulk modulus as a function of density [84].

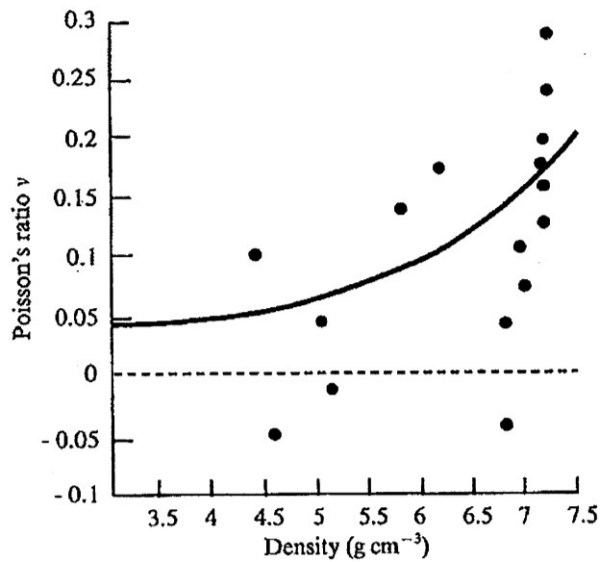


Figure 13. Evaluation of Poisson's ratio as a function of density [84].

Further, equations (24) to (26) were evaluated for apparent and theoretical density values to give a better perspective of the actual initial and final magnitudes, respectively; see Table 2.

Table 2. Evaluation of material properties for given values of powder density.

| Powder Density, ρ [g/cm ³] (Relative Density, $\bar{\rho}$) | Material Properties | | |
|--|--------------------------|-----------------------|------------------------|
| | Elastic Modulus, E [GPa] | Bulk Modulus, K [GPa] | Poisson's ratio, ν |
| Apparent, 3.04 (0.42) | 2.481 | 909.041E-3 | 45.212E-3 |
| Theoretical, 7.33 (1.00) | 218.186 | 121.102 | 199.722E-3 |

For determination of the yield stress, $\bar{\sigma}$, Pavier and Doremus had first compared the plastic behaviour of the powder with that of the powder particle constitutive material, through application of stress, to establish whether it forms similar behavioural pattern. The plastic behaviour of particle constitutive material is best represented by von-Mises criterion. The uniaxial compression yield limit, $\bar{\sigma}$, of the constitutive material can be determined based on particle hardness, using the following expression

$$10.58HV = 3\bar{\sigma} \quad (27)$$

Based on the data provided by Hoğanäs for Distaloy AE, HV0.025 = 105, giving it a compressive yield limit, $\bar{\sigma}$, of 370 MPa [10, 84, 85, 87]. To confirm this, Pavier and Doremus have carried out a series of their own microhardness tests on powder particles arising from a specimen compressed with a confining pressure of 400 MPa. Their results have revealed the same microhardness value (105±5 HV0.03) [84, 85, 87]. Therefore, in the deviatoric stress, q , versus hydrostatic stress, p , plane, the iron yield limit, $\bar{\sigma}$, crosses the deviatoric axis at 370 MPa, at which level the plastic behaviour of the powder is similar to that of the particle constitutive material; see Figure 14.

Further investigation by Pavier and Doremus using a consolidated test, with varied confining pressure, has revealed that powder yields at lower stress levels than constitutive material [84, 87]; see Figure 15. Only upon reaching a deviatoric stress value of 370 MPa, with confining pressure of 400 MPa, the powder flows with constant density. Based on this, it can be concluded that plastic behaviour for iron powder depends on the loading path, which has a pattern similar to that expressed by equations (22) or (23) [48, 49, 50, 104], and whose yielding

exhibits work-hardening effect initiated at stress levels lower than that of the constitutive material. However, upon reaching a deviatoric stress level of 370 MPa the powder flows with constant density, exhibiting the same plastic behaviour as the constitutive material [84, 85, 87].

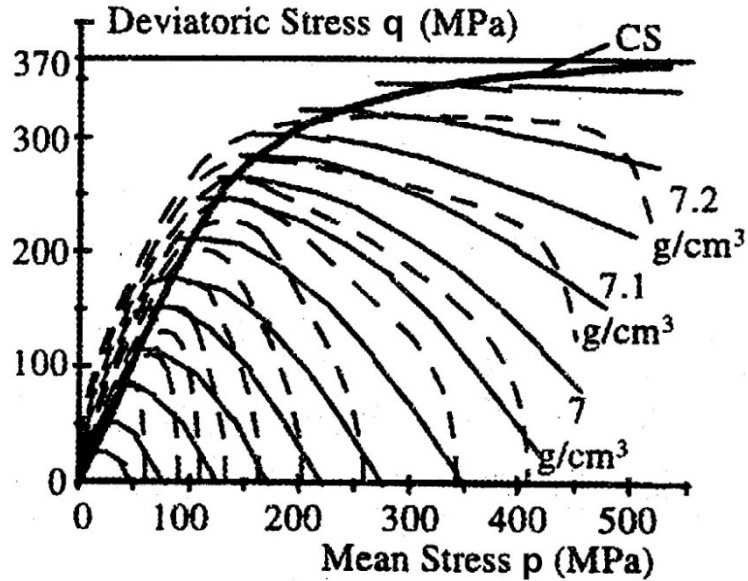


Figure 14. Yield limit reached using consolidated and overconsolidated tests with triaxial cell apparatus [84].

It is important to note that due to the earlier specified software limitations, a constant yield value had to be employed [72, 74, 76, 77]. Thus, for simulation analyses the yield limit of 370 MPa was used, under which the powder has the same plastic behaviour as the constitutive material of powder particles [48, 84, 85, 86]; refer to Figures 14 and 15. For a complete summary of material properties provided by Pavier and Doremus and the set adopted for simulation analyses, see Table 3; where the listed material parameters β and γ were provided in the former section, see section 2.3, and the shear viscosity, η , is discussed in the subsequent sections.

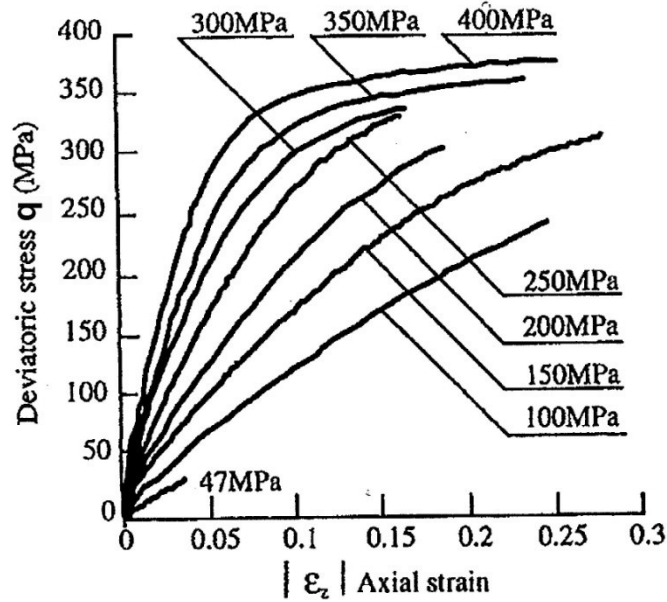


Figure 15. Evaluation of deviatoric stress as a function of axial strain at different radial stresses [84].

Table 3. Summary of material properties.

| Material properties provided by Pavier and Doremus | | |
|---|----------|----------------------------|
| Material Property | Type | Provided relation or value |
| Elastic modulus, E [MPa] | Variable | Equation (24) |
| Poisson's ratio, ν | Variable | Equation (26) |
| Yield Stress, $\bar{\sigma}$ [MPa] | Variable | Equation (22) or (23) |
| Material properties adopted for simulation analyses | | |
| Material Property | Type | Used relation or value |
| Elastic modulus, E [MPa] | Variable | Equation (24) |
| Poisson's ratio, ν | Variable | Equation (26) |
| Yield Stress, $\bar{\sigma}$ [MPa] | Constant | 370 |
| Shear viscosity, η [MPa · s] | Constant | 2 |
| Material parameter, β | Variable | Equation (20) |
| Material parameter, γ | Variable | Equation (21) |

3.1.2 Material Properties Provided by Shima

Shima et al. have obtained the relationship for elastic modulus for the same iron-based powder, Distaloy AE (refer to Table 1), through the analysis of stress-strain curves, derived based on green compacts subjected to simple compression test [101, 102]. The compressive plastic strain was measured through the help of strain gauges affixed to a free surface of the corresponding green compacts. The relationship for elastic modulus was derived as

$$E(\text{MPa}) = 896e^{(5.31\bar{\rho})} \quad (28)$$

where $\bar{\rho}$ is a relative density of green compact, and elastic modulus, E , is in units of MPa. Evaluation of equation (28) with respect to relative density shows an exponential increase in the elastic modulus with density; see Figure 16.

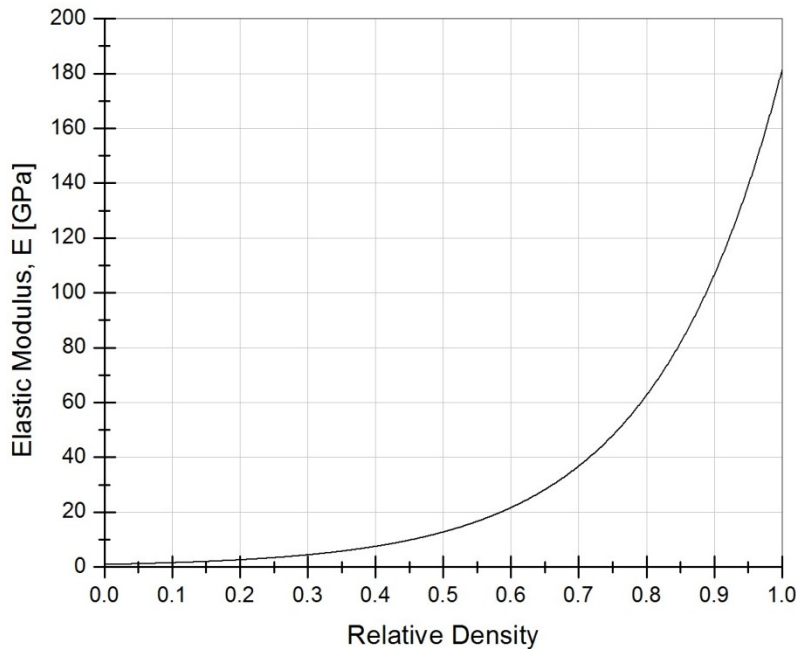


Figure 16. Evaluation of elastic modulus as a function of relative density.

For exact values of elastic modulus evaluated at apparent and theoretical densities using equation (28), see Table 4.

Table 4. Evaluation of elastic modulus for given values of powder density.

| Powder Density, ρ [g/cm^3] (Relative Density, $\bar{\rho}$) | Elastic Modulus, E [GPa] |
|---|----------------------------|
| Apparent, 3.04 (0.42) | 8.105 |
| Theoretical, 7.33 (1.00) | 183.306 |

The measured Poisson’s ratio, ν , was found to somewhat fluctuate with relative density. Yet, a constant Poisson’s ratio value of 0.25 was assumed for simulation analysis. The yield stress, $\bar{\sigma}$, value of 1926 MPa was suggested for a relative density range of $\bar{\rho} \leq 0.62$, and 598.9 MPa, for $\bar{\rho} > 0.62$. However, as mentioned earlier, due to software limitations, allowing only for definition of a constant value, a yield stress of 598.9 MPa was adopted, as it reflects more closely the value suggested by Pavier and Doremus, determined using triaxial cell, and encompasses a wider range of the relative density. For a complete summary of material properties provided by Shima and the set adopted for simulation analyses, see Table 5; where the listed material parameters β and γ were provided in the former section, see section 2.3, and the adopted shear viscosity, η , is discussed in the subsequent sections.

Table 5. Summary of material properties.

| Material properties provided by Shima | | |
|--|-------------|---|
| Material Property | Type | Provided relation or value |
| Elastic modulus, E [MPa] | Variable | Equation (28) |
| Poisson’s ratio, ν | Constant | 0.25 |
| Yield stress, $\bar{\sigma}$ [MPa] | Variable | 1926 for $\bar{\rho} \leq 0.62$ and 598.9 for $\bar{\rho} > 0.62$ |
| Material properties adopted for simulation analyses | | |
| Material Property | Type | Used relation or value |
| Elastic modulus, E [MPa] | Variable | Equation (28) |
| Poisson’s ratio, ν | Constant | 0.25 |
| Yield stress, $\bar{\sigma}$ [MPa] | Constant | 598.9 |
| Shear viscosity, η [MPa · s] | Constant | 2 |
| Material parameter, β | Variable | Equation (20) |
| Material parameter, γ | Variable | Equation (21) |

3.1.3 Material Properties Provided by Koval'chenko

It is important to note that Shima and Oyane yield criterion is based on porous material, in other words sintered powder compacts. For this reason, material properties derived based on sintered powder compacts were also employed for simulation analyses, specifically to make comparison between their results and those attained using properties based on powder material or green compact specimens.

Over the last three decades Koval'chenko et al. have conducted an extensive amount of research on behaviour of porous materials. It was determined that material properties for porous bodies tend to depend on their relative density [53-60]. Koval'chenko has derived approximate relations for elastic properties of various porous materials on the basis of analysing the dependence of pore shape and experimental data, and also taking into an account the mesostructural imperfection encountered in powder bodies [54]. In his derivation, it was assumed that dependence of elastic properties on relative density should represent as closely as possible the experimental data determined for high porosity powder compacts, whereas for lower porosity compacts, it should represent both the experimental data and theoretical relationships [54]. As a result, the following relationships were suggested for

$$\text{Elastic modulus, as } E(\text{GPa}) = 2G_0(1 + \nu_0\bar{\rho})\bar{\rho}^{\frac{c-(1-k^2)\bar{\rho}}{(1-k^2)\bar{\rho}}} \quad (29)$$

$$\text{Shear modulus, as } G(\text{GPa}) = G_0\bar{\rho}^{\frac{c-(1-k^2)\bar{\rho}}{(1-k^2)\bar{\rho}}} \quad (30)$$

$$\text{Bulk modulus, as } K(\text{GPa}) = \frac{E}{3(1 - 2\nu)} \quad (31)$$

$$\text{Poisson's ratio, as } \nu = \nu_0\bar{\rho}^{\frac{3}{(1-k^2)\bar{\rho}}} \quad (32)$$

where: ν_0 – Poisson's ratio for powder constitutive material; for iron 0.28 [54]

$\bar{\rho}$ – relative density

E_0 – elastic modulus for powder constitutive material; for iron 211 GPa [54]

G_0 – shear modulus for powder constitutive material; for iron 82.4219 GPa [54]

K_0 – bulk modulus for powder constitutive material

c – material parameter, which correlates with Poisson’s ratio; values of 2 for metal and 2.5 for ceramic materials

k – structural imperfection index.

For an illustration of dependence of elastic modulus and Poisson’s ratio on relative density of sintered iron-based powder compacts, see Figure 17. Further, equations (29) to (32) were evaluated at relative apparent and theoretical density values to give a better perspective of the actual magnitudes; see Table 6.

The structural imperfection index, k, is chiefly introduced as a quantitative characteristic to account for a degree of mesostructural imperfection of porous bodies, attributed to randomly shaped and distributed pores [54]. The recommended values of k ranges from 0, for perfect, to 0.65, for imperfect materials; and the values of c are 2 for metallic materials (iron, nickel), and 2.5 for ceramic materials (boron carbide) [54]. For imperfection index, k, a value of 0.65 was selected for analysis as it correlates closest to metal porous bodies, and tends to reflect more closely the elastic relations based on other studies [84, 85, 87, 101, 102].

From the above elastic properties, it is possible to derive dependence of rheological properties, such as shear and volumetric viscosity, on relative density, $\bar{\rho}$, based on the condition that the matrix of the porous body is incompressible. The relation for shear viscosity is expressed as

$$\eta = \eta_0 \bar{\rho}^{\frac{2-(1-k^2)\bar{\rho}}{(1-k^2)\bar{\rho}}} \quad (33)$$

and volumetric viscosity as

$$\zeta = \frac{1}{3} \eta_0 \left(\frac{2 + \bar{\rho}}{1 - \bar{\rho}} \right) \bar{\rho}^{\frac{2-(1-k^2)\bar{\rho}}{(1-k^2)\bar{\rho}}} \quad (34)$$

where η_0 is the shear viscosity for a fully dense (solid) material, and $\bar{\rho}$ and k are relative density and imperfection index, respectively. However, for simulation analysis of powder compaction only shear viscosity function is required; refer to equation (6). For the illustration of dependence of shear viscosity on relative density for porous material, see Figure 18. It is worth noting that due to software limitations, it was not possible to implement a variable shear

viscosity function into FE model [72, 73, 74, 76, 77]. Thus, a constant shear viscosity value for iron-based powder was employed for simulation analyses.

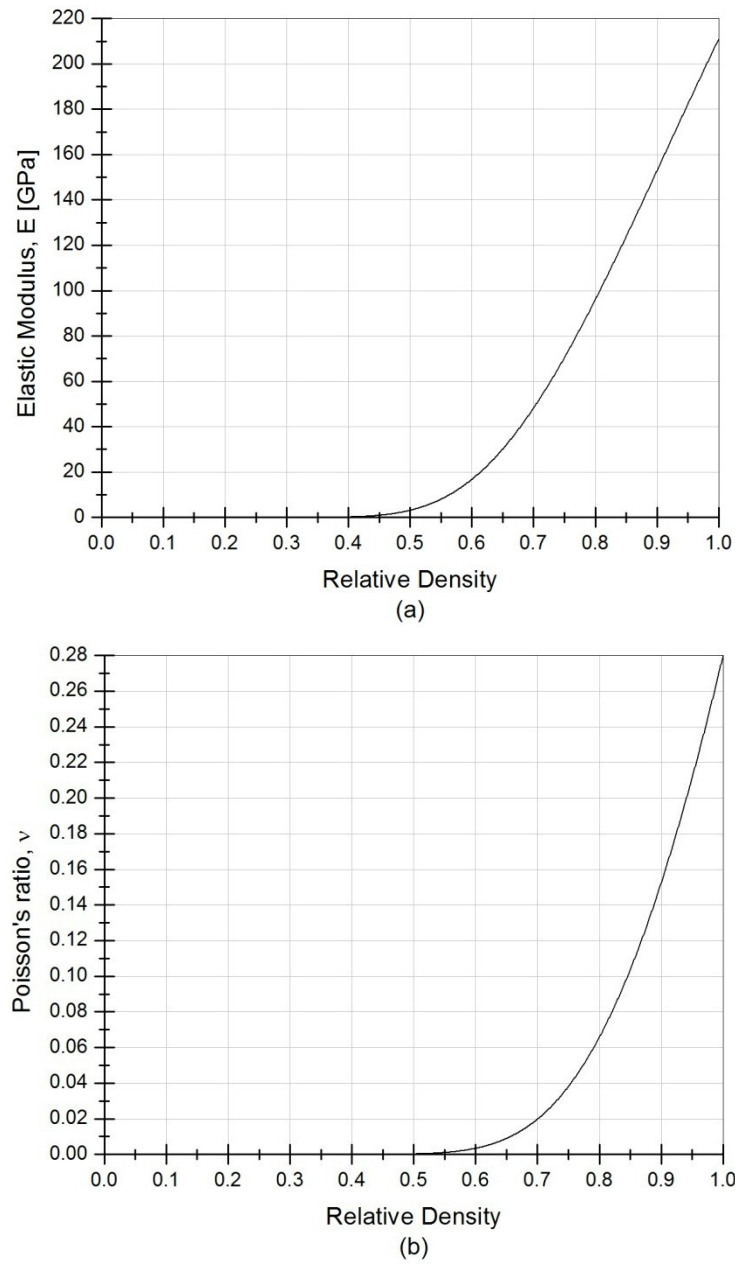


Figure 17. Dependence of (a) elastic modulus and (b) Poisson's ratio on relative density of sintered iron-based powder compacts.

Table 6. Evaluation of material properties for given values of powder density.

| Powder Density, ρ [g/cm ³] (Relative Density, $\bar{\rho}$) | Elastic Modulus, E [GPa] | Shear Modulus, G [GPa] | Bulk Modulus, K [GPa] | Poisson's Ratio, ν |
|--|-----------------------------|---------------------------|--------------------------|---------------------------|
| Apparent, 3.04 (0.42) | 343.185E-3 | 153.536E-3 | 114.396E-3 | 6.128E-6 |
| Theoretical, 7.33 (1.00) | 211.0 | 82.422 | 159.848 | 0.28 |

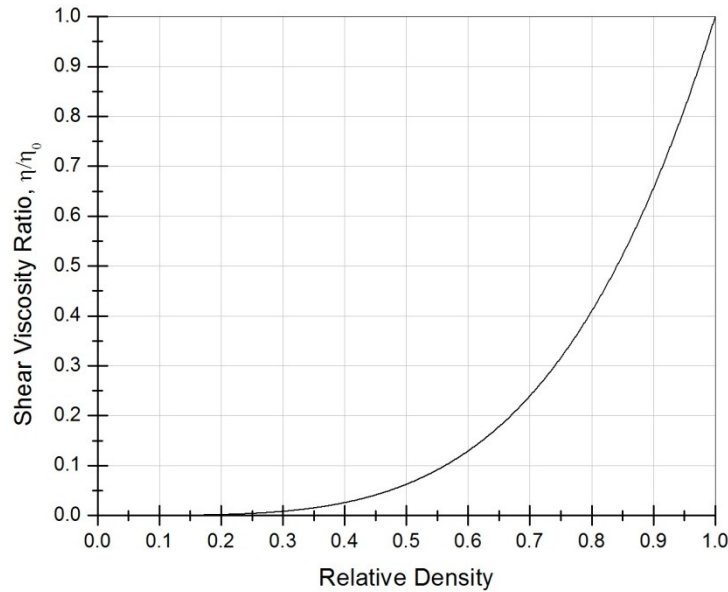


Figure 18. Dependence of shear viscosity on relative density for porous material.

Further, in Koval'chenko's work on the above listed elastic properties, nothing is mentioned on plastic behaviour of porous material [54]. However, many of his earlier studies have concluded that plastic behaviour for porous iron material depends on its loading path, corresponding to a yield stress relationship expressed by equations (22) or (23) [53, 55, 56, 58, 59]. Once again, it is important to emphasize that due to software limitations a constant yield stress value had to be employed for simulation analyses. A yield stress value of 420 MPa was used, based on the data provide by Höganäs for Distaloy AE sintered powder compact [36]. For a complete summary of material properties provided by Koval'chenko and the set adopted for simulation analyses, see Table 7; where the listed material parameters β and γ were provided in the former section, see section 2.3, and the adopted shear viscosity, η , is discussed in the following section.

Table 7. Summary of material properties.

| Material properties provided by Koval'chenko | | |
|--|-------------|-----------------------------------|
| Material Property | Type | Provided relation or value |
| Elastic modulus, E [MPa] | Variable | Equation (29) |
| Poisson's ratio, ν | Variable | Equation (32) |
| Yield stress, $\bar{\sigma}$ [MPa] | Variable | Equations (22) or (23) |
| Shear viscosity, η [MPa · s] | Variable | Equation (33) |
| Imperfection index, k | Constant | 0.65 |
| Material parameter, c | Constant | 2 |
| Material properties adopted for simulation analyses | | |
| Material Property | Type | Used relation or value |
| Elastic modulus, E [MPa] | Variable | Equation (29) |
| Poisson's ratio, ν | Variable | Equation (32) |
| Yield stress, $\bar{\sigma}$ [MPa] | Constant | 420 |
| Shear viscosity, η [MPa · s] | Constant | 2 |
| Imperfection index, k | Constant | 0.65 |
| Material parameter, c | Constant | 2 |
| Material parameter, β | Variable | Equation (20) |
| Material parameter, γ | Variable | Equation (21) |

3.1.4 Shear Viscosity for Iron-based Powder

Based on experimental analyses, a number of researchers have determined that rheological properties, such as shear and volumetric viscosity, depend on relative density of the powder compact [54, 62, 63, 93, 96]. However, as mentioned earlier, for simulation analysis of powder compaction only shear viscosity relation is required; refer to equation (6). Specifically derived for Shima and Oyane yield criterion, a relationship for shear viscosity, η , as a function of relative density, $\bar{\rho}$, is expressed as

$$\eta = \eta_0 \bar{\rho}^4 \quad (35)$$

or as a function of porosity, θ , where $\theta = 1 - \bar{\rho}$, is expressed as

$$\eta = \eta_0 (1 - \theta)^4 \quad (36)$$

where η_0 is a shear viscosity value for powder constitutive material, such that porosity is zero, $\theta = 0$ [62].

There is no single standard method for determination of η_0 . In fact, this area lacks research and the available relevant literature is very scarce. The available experimental data are based on both dynamic and static methods, and are scattered considerably by several orders of magnitude, particularly for iron based material, from 0 to 10^6 Pa · s [63, 96]. Nonetheless, based on experimental investigation of the internal friction of iron powder, Polyakov and Alekseev were successful in estimating a more consistent value using the Voigt rheological model [93]. Based on their experiments the estimated shear viscosity for iron powder was $2 \cdot 10^6$ Pa · s and showed dependence on relative density, similar to the behaviour of elastic and shear moduli [93]. For representation of shear viscosity dependence on relative density for iron-based powder using equation (35) with estimated value of η_0 , by Polyakov and Alekseev, see Figure 19.

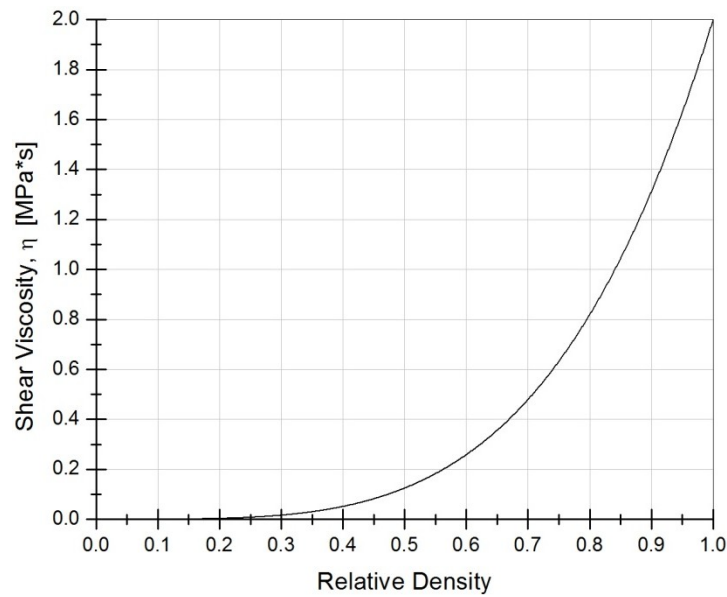


Figure 19. Dependence of shear viscosity on relative density for iron-based powder compact.

It is important to note that due to the software limitations, it was not possible to implement the corresponding variable shear viscosity relation into the FE model [72, 72, 74, 76, 77]. For simulation analysis, a constant value had to be employed; consequently a value of $2 \cdot 10^6$ Pa · s was used. Thus, equations (33) to (36) were simply stated to inform the reader that rheological properties do in fact vary with relative density for powder material and sintered porous compacts, even though it was not possible to implement them into the simulation model.

3.2 Friction in Powder Compaction

Friction is considered as one of the major limiting factors in the powder compaction process as it is a primary cause for density variation in green compact and occurrence of crack defects during compaction and ejection cycle. Thus, knowing frictional behaviour at powder-tool interfaces is essential for controlling these limiting factors. At present there are a number of friction measuring devices among which the most commonly used are the instrumented-die and the shear-plate device [10, 13, 19, 21, 31, 45, 86, 89].

3.2.1 Friction Measurement Using Instrumented-die Device

The instrumented-die apparatus typically consists of a uniaxial press with a series of strain gauges affixed along the height of the die wall and both upper and lower punches to measure radial stress distribution and corresponding axial loads, respectively; see Figure 20. Due to the existence of friction between powder and tool surfaces, the radial stress has a non-uniform distribution along the die-wall and there is a gradual drop in axial stress between the active upper-punch and the stationary lower-punch [10, 24, 25, 27, 45]; see Figures 20 and 21.

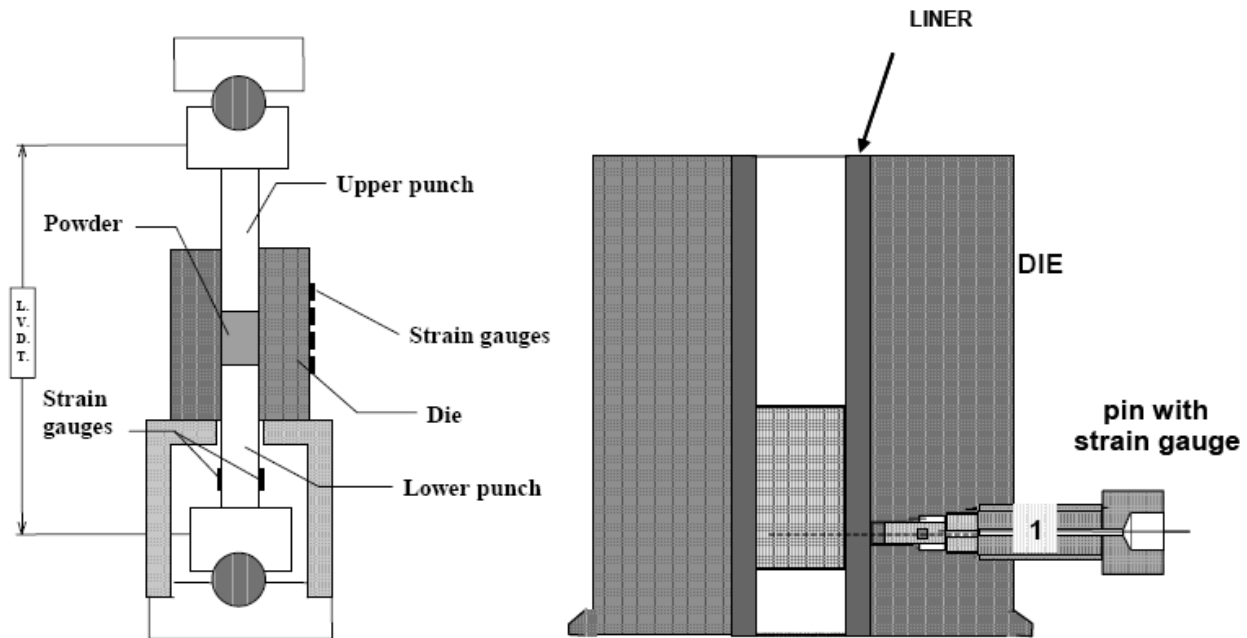


Figure 20. Instrumented-die with illustration of different instruments used to measure radial-pressure [10].

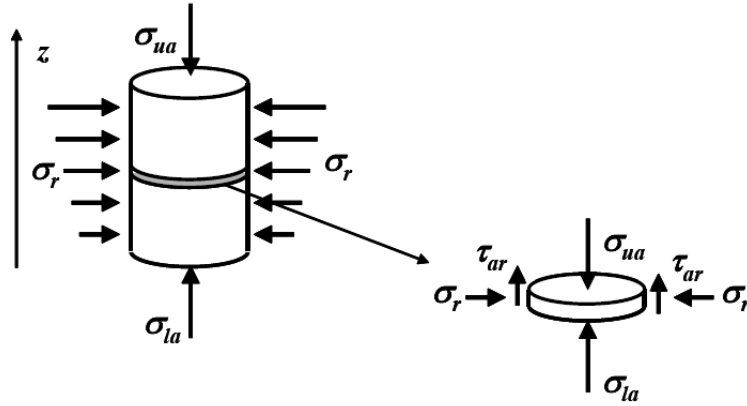


Figure 21. Stress balance on a cylindrical compact [10].

Based on experimental measurement by instrumented-die, a mean friction coefficient, μ , may be derived through a force balance integrated over the height of the compact [10, 86], leading to the following expression

$$\mu = \frac{d}{4zh} (\ln \sigma_{ua} - \ln \sigma_{la}) \quad (37)$$

where: μ – friction coefficient at powder-tool interface

d – diameter of powder compact

h – height of powder compact

σ_{ua} – axial stress on upper punch

σ_{la} – axial stress on lower punch

z – radial stress, σ_r , to axial stress, σ_a , ratio expressed as

$$z = \frac{\sigma_r}{\sigma_a} \quad (38)$$

In addition, the pressure over the upper and lower punch faces varies with respect to the radius, thus, leading to a variable friction coefficient. Application of similar approach to a flat disc allows for determination of friction coefficient using the following expression

$$\mu = \frac{zh(\ln P_0 - \ln P)}{2r} \quad (39)$$

where: μ – friction coefficient at powder-tool interface

h – height of powder compact

P_0 – axial pressure acting at the center of the compacting area ($r = 0$)

P – axial pressure acting at a certain radius, r

r – radius

However, it is important to pointed out that there are practical difficulties associated with the two above methods in measurement of friction coefficient [10, 31, 86, 89, 114]. First of all, for a successful evaluation of friction coefficient it is essential to know both radial and axial stresses for determination of process parameter z . For simplification purposes, the value of z is often assumed to be a constant, however, this is not exactly true as experimental data shows that both radial stress, σ_r , and axial stress, σ_a , vary during the compression process over the height of the compact [10, 24, 25, 27, 31, 45, 86, 89, 111, 114, 124]; see Figure 22. Thus, it is difficult to establish a correct relationship for both radial and axial stresses and generally requires some assumptions. As a general rule, the instrumented-die method is more practical for investigation of friction along the powder-die interface for long cylinders as it allows for easy radial stress measurement, and is less feasible for determination of friction along punch faces as it is impractical to measure radial stress variation for a flat disc [10].

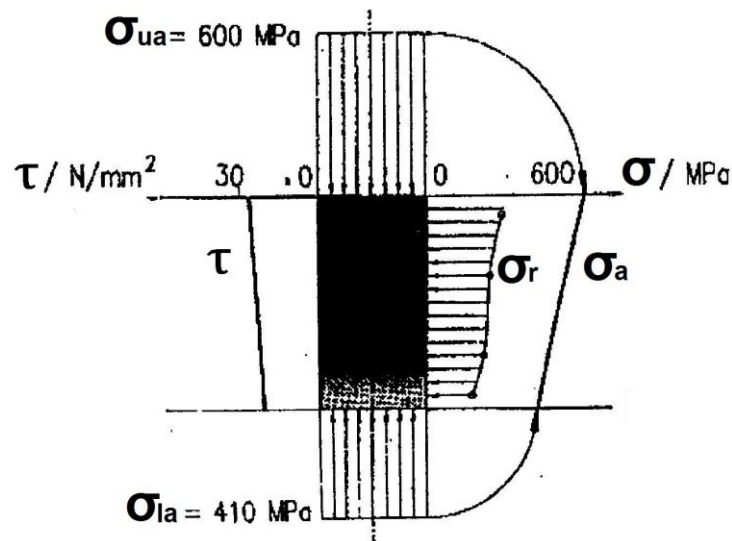


Figure 22. Compacted powder with measured upper punch (σ_{ua}) and lower punch (σ_{la}) stresses, and radial stress (σ_r), axial stress (σ_a), and frictional shear stress (τ) distribution [24].

In addition, with instrumented-die apparatus it is difficult to investigate the influence of material hardness and die surface-roughness parameters as the die-wall container is either fixed or not easy to change [10, 31, 89, 111, 114]. More importantly, the accuracy of the instrumented-die greatly depends on the sensitivity of its measuring instruments, which is influenced by die-wall thickness. There are two most common variants for the instrumented-die design: (i) a cylindrical die with affixed strain gauges to its outer surface for measurement of hoop stress, for indirect measurement of radial stress; and (ii) one that comprises of a thick cylinder with inner liner against which rests a preloaded instrumented pin, for a more direct measurement of radial stress; refer to Figure 20. Both variants require laborious calibration process to account for the dilation of the die and other factors influencing the accuracy of the measuring instrument. Other limitation of the instrumented-die is its inability to account for the change in compact's height as some strain gauges or pins may end up outside the measuring range as their location is fixed along the height. Consequently, this further limits a detailed measurement of the radial stress gradient, which is non-linear in nature.

The major limitation of the method is that the obtained friction coefficient is a function of only two parameters, axial and radial stresses, which in fact are both normal stresses experienced between the powder and tool surfaces. However, based on numerous studies it has been determined that upon powder compaction friction coefficient tends to vary and is a function of several process parameters, such as powder density, normal stress, sliding velocity, temperature, displacement, tool surface-roughness, and material hardness [10, 13, 19, 21, 31, 86, 88-90, 113, 114]. Most importantly, in the case of an instrumented-die, only a mean friction coefficient value may be derived; however, the local friction coefficient value varies over the height of the compact [3, 10, 13, 19, 21, 31, 85, 89, 90, 111, 113, 114].

3.2.2 Friction Measurement Using Shear-plate Device

Shear-plate device overcomes the limitations experienced with instrumented-die. It allows for exploration of a wider range of parameters which influence the coefficient of friction between powder and tool surfaces. In general, it provides a more direct and accurate measurement of friction. A typical shear-plate apparatus consists of eight primary components; see Figure 23.

Using this shear-plate device, Pavier and Doremus have successfully measured variation of friction coefficient for iron-based powder with respect to a range of parameters. Their device consisted of a parallelepipedic slab (4), measuring 200 x 20 x 20 mm in size, to represent the tool surface, which was fixed on moving rolls (with friction coefficient of 0.001) [19, 21, 86]. The slab was connected through a force transducer (5) to a hydraulic press (6). The powder was compacted against the slab to a disc shaped compact (3) of 2 mm in height, leaving a gap of 0.05 mm between the die and the slab [19, 21, 86]. The load was then applied by the press (8) and measured by transducer (2), registering the applied force, F_n , by the compact onto the slab. The relative displacement between the slab and the powder disc was controlled at desired velocity, and the tangential force, F_t , was measured through the transducer (5). As a result, this test assimilates the conditions of compressing powder against the tool surface, with friction coefficient defined as

$$\mu = \frac{F_t}{F_n} \quad (40)$$

Consequently, the versatility of the test conditions allows for studying the influence of different parameters, such as the applied normal stress, density of the powder compact, temperature, sliding displacement, and velocity.

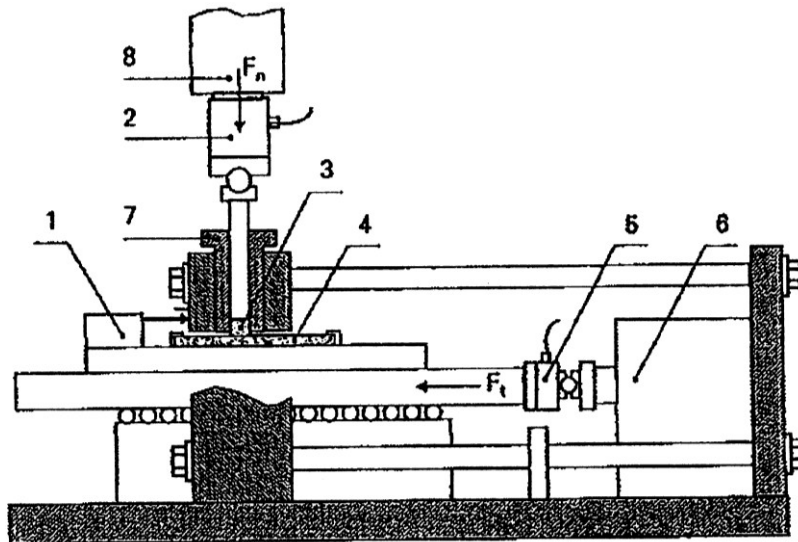


Figure 23. A shear-plate device consisting of: (1) optical transducer, (2) transducer, (3) powder compact disc, (4) parallelepipedic slab, (5) force transducer, (6) hydraulic press, (7) cylindrical die, and (8) press [19].

All tests were performed on a slab composed of tungsten carbide (91.5%WC and 8.5% Co), with a hardness of $HV_1 = 1520$ and a surface-roughness average, R_a , of $0.1 \mu\text{m}$, which is the most common material composition for the die-wall [19, 21, 84-87]. The powder used was an atomised iron-based powder, Distaloy AE, supplied by Höganäs; same as the one used for determination of material properties. The test conditions were kept close to the manufacturing conditions of iron parts. For the tests performed, the densities ranged from 4.75 to 7.20 g/cm^3 , normal stresses from 50 to 800 MPa , sliding velocities from 0.35 to 100 mm/s , and temperature from ambient to 80°C [19, 21, 86]. Using these conditions the friction coefficient was evaluated according to the normal stress, the density, and the relative velocity of the slab; see Figures 24, 25, and 26.

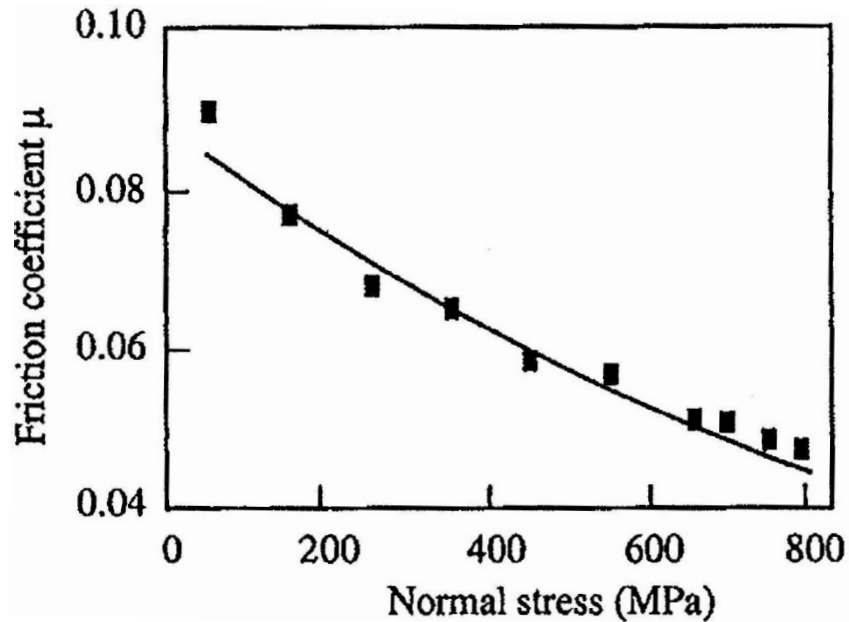


Figure 24. Evaluation of friction coefficient versus normal stress, under the following conditions: sliding velocity, $v_r = 0.35 \text{ mm/s}$; density, $\rho = 7.30 \text{ g/cm}^3$; and temperature, $T = 20^\circ\text{C}$ [19, 21, 86].

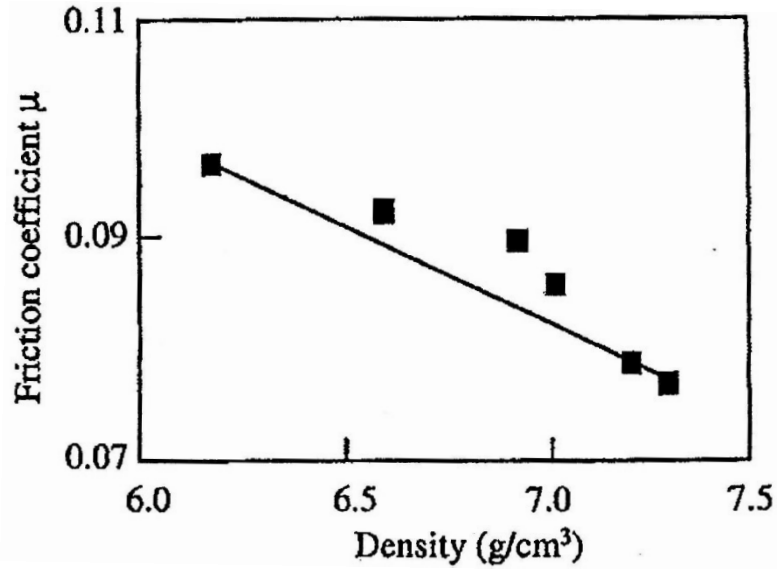


Figure 25. Evaluation of friction coefficient versus density, under the following conditions: sliding velocity, $v_r = 0.35$ mm/s; normal stress, $\sigma_n = 150$ MPa; and temperature, $T = 20^\circ\text{C}$ [19, 21, 86].

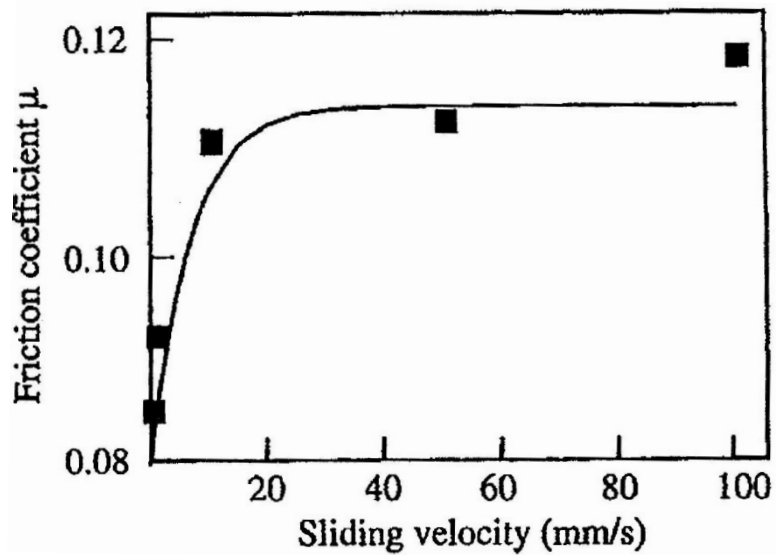


Figure 26. Evaluation of friction coefficient versus sliding velocity, under the following conditions: density, $\rho = 7.30$ g/cm³; normal stress, $\sigma_n = 150$ MPa; and temperature, $T = 20^\circ\text{C}$ [19, 21, 86].

From the presented results it can be observed that the friction coefficient decreases with an increase of normal stress or density of the powder compact, and a steep increase in friction coefficient is observed with increase of sliding velocity from 0 to roughly 30 mm/s, after which point it becomes relatively steady. Similar trends were observed in other studies [10, 13, 24, 25, 33, 51, 66, 80, 89, 90, 109, 110, 111, 114, 124-126]. The reasons for decrease of friction coefficient upon increase of density and normal stress may be explained by an illustration

presented in Figure 27. During the initial stages of compaction the powder consists of a rough contact surface with lubricant trapped inside its pores, leading to local unlubricated contacts; see Figure 8 (a). As compaction progresses, there is a continuous increase of normal stress and the pores are closed due to plastic deformation of local contacts leading to the ejection of the lubricant from compact cavities and inter-particles, and thus progressively resulting in smoother surface. Consequently, upon further progression of compaction a layer of lubricant film is created between the compacted powder and the tool surface, further reducing friction coefficient; see Figure 8 (b). Based on these experiments, a single expression for the friction coefficient was derived as

$$\mu(\sigma_n, \rho, v_r) = e^{\left(\frac{-\sigma_n}{1169}\right)} \times \left(-0.14 \times \frac{\rho}{7.33} + 0.224\right) \times \left(1.437 \times \tanh\left(\frac{v_r}{12.6} + 0.886\right)\right) \quad (41)$$

where: σ_n – normal stress between powder and tool surface, in [MPa]
 ρ – density of compacted powder, in [g/cm³]
 v_r – relative sliding velocity between powder and tool surface, in [mm/s].

Equation (41) is expressed by a curve in Figures 24, 25, and 26.

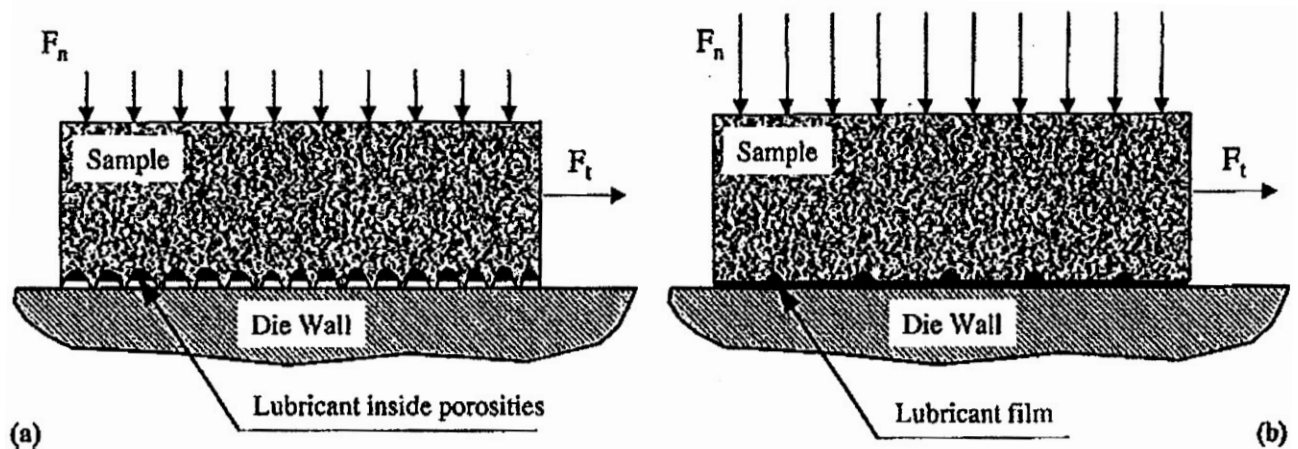


Figure 27. Friction of powder compacted sample at (a) low and (b) high density on tungsten carbide tool wall [19].

Further, the influence of temperature on friction coefficient was studied. For this the slab was fitted with thermal resistors and several tests were conducted between 20 and 80°C to assimilate manufacturing conditions, where due friction and high production rate, temperature

of the tools and the ejected green compact may reach close to 70°C [19, 21, 27, 86]. The experimental data showed that friction coefficient is independent of the temperature under the specified test conditions; see Figure 28 and 29.

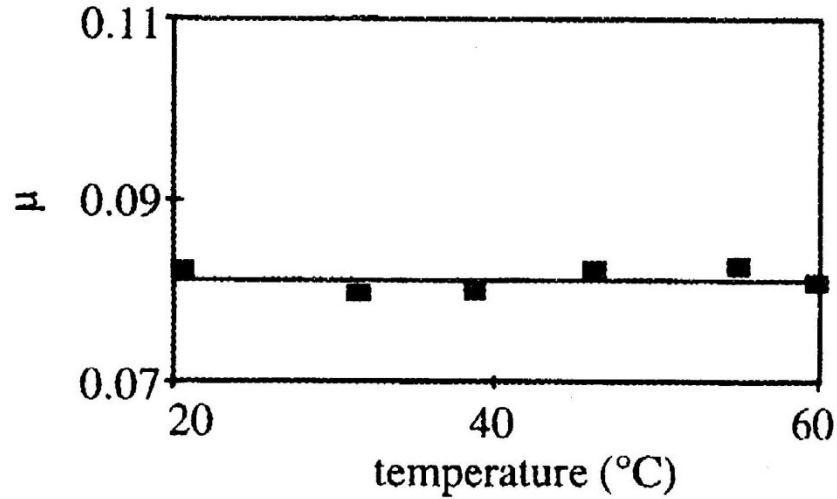


Figure 28. Evaluation of friction coefficient versus temperature, $T(^{\circ}\text{C})$, under the following conditions: density, $\rho = 7.02 \text{ g/cm}^3$; sliding velocity, $v_r = 0.35 \text{ mm/s}$; and normal stress, $\sigma_n = 150 \text{ MPa}$ [21].

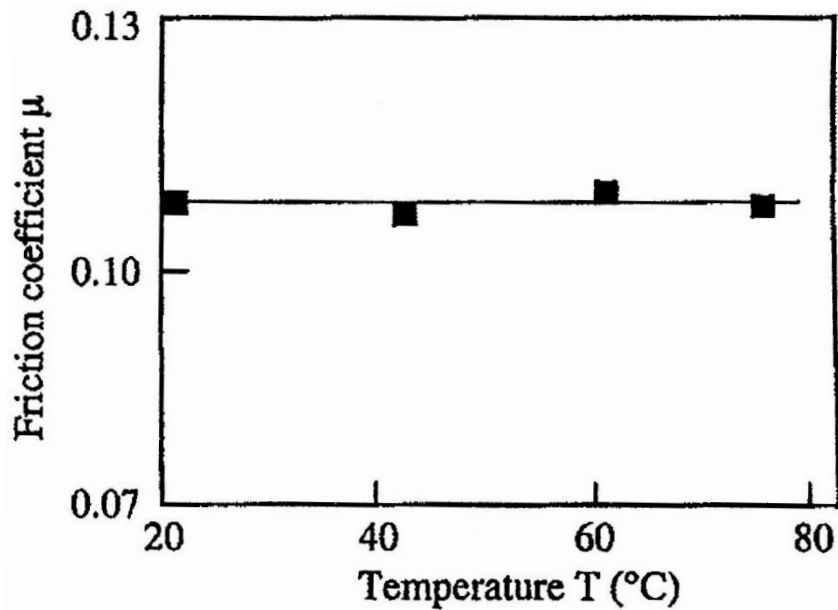


Figure 29. Evaluation of friction coefficient versus temperature, $T(^{\circ}\text{C})$, under the following conditions: density, $\rho = 7.30 \text{ g/cm}^3$; sliding velocity, $v_r = 10 \text{ mm/s}$; and normal stress, $\sigma_n = 150 \text{ MPa}$ [19].

3.2.3 Friction Measurement Using Tribological Device

Using a tribological device, Wikman et al. [79, 125] have conducted experimental study on the coefficient of friction. The same atomized iron-based powder, Distaloy AE, was used, admixed with additional lubricant, 0.5%C and 1% Hoechst Microwax, where the content is given in wt-% [80, 124, 126]. The tribological device consisted of a sliding cylinder on a flat plate covered with powder. The plate material was the same as used in pressing experiments. Tests were performed within a range of sliding velocity of 50 to 200 mm/s, and within a range of normal stress of 100 to 700 MPa [80]. Selected experimental results using different sliding velocities were presented over the range of normal contact pressure; see Figure 30.

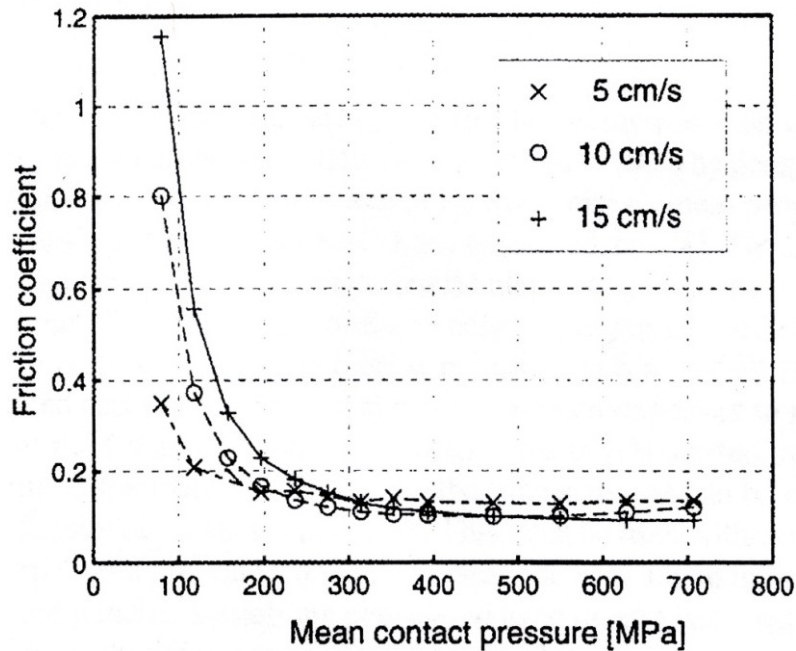


Figure 30. Friction coefficient with respect to sliding velocity and pressure [80, 126].

Based on experimental results presented in Figure 30, Wikman et al. have derived an expression for the friction coefficient as

$$\mu = \mu_B (1 + f_v \cdot f_p) \quad (42)$$

where μ_B is a base friction constant, and f_v and f_p are both functions of relative sliding velocity and the local density, respectively [80, 124- 126]. The two functions are defined as

$$f_v = \frac{v_r(v_r/v_0 - 1)}{v_r + w_1 v_0} + f_{v0} \quad (43)$$

$$f_p = w_2 e^{\left(-\frac{(\rho/\rho_0 - \rho_{ref}/\rho_0)^2}{w_3}\right)} \quad (44)$$

where: v_r – relative sliding velocity
 v_0 – reference velocity
 ρ – powder density
 ρ_0 – density of powder constitutive material (fully solid state)
 ρ_{ref} – model limit value for density dependent friction
 f_{v0} – equivalent static friction coefficient
 a, b, c - model parameters.

The values for above parameters are shown in Table 8. The symbol $\langle x - x_0 \rangle$ means that $\langle x - x_0 \rangle = 0$ if $x < x_0$ and $\langle x - x_0 \rangle = x - x_0$ if $x \geq x_0$.

Table 8. Parameter values for equations (43) and (44).

| Parameter | μ_B | f_{v0} | w_1 | w_2 | w_3 | ρ_{ref}/ρ_0 | v_0 |
|---------------------|---------|----------|-------|-------|-------|---------------------|---------|
| Corresponding value | 0.1 | 0.05 | 1.0 | 1.5 | 0.01 | 0.65 | 11 mm/s |

In their first study, the dependence of friction coefficient on the sliding velocity and the powder density were studied separately; see Figure 31. Both functions were based on the measurements presented in Figure 30. To relate pressure to density, the contact pressure was converted to powder density based on the isotropic test data, obtained using triaxial cell. Thus, it was assumed that the stress state at the point of contact is hydrostatic. In their second study, Wikman et al. have extrapolated the behaviour of the friction coefficient at relative densities below 0.7, showing a decrease in friction coefficient with density; see Figure 32. However, for this case a density cut off limit was assumed below which the friction coefficient just depends on the sliding velocity [126].

The limitation of equation (42) is that it expresses the friction coefficient as a function of two parameters only, the relative sliding velocity and powder density. Further, the assumption of

hydrostatic stress at the point of contact does not reflect true representation of the actual conditions. In addition, in the second study it was noted that numerical analyses produced higher friction forces compared to experimental results at the initial stage of the compaction, when using the proposed variable friction coefficient expression [126].

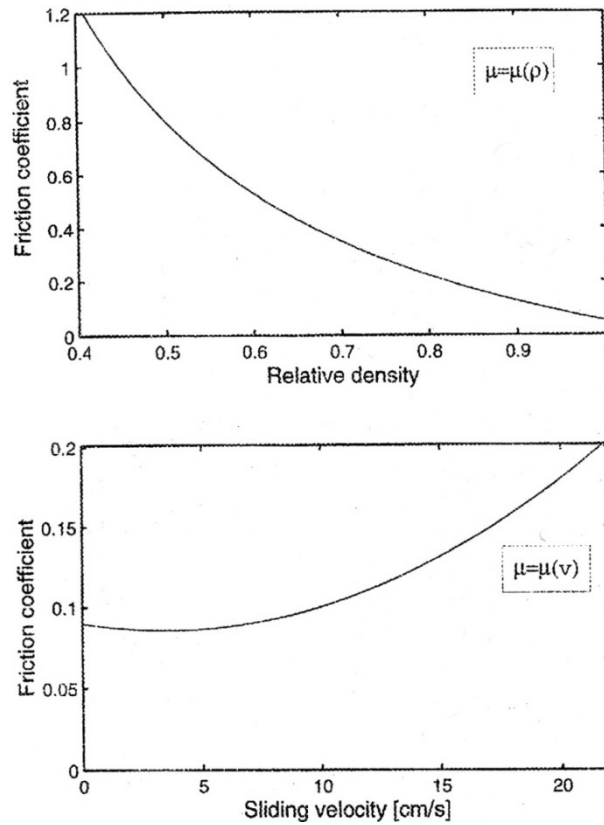


Figure 31. Functions relating the friction coefficient to the powder density and the sliding velocity.

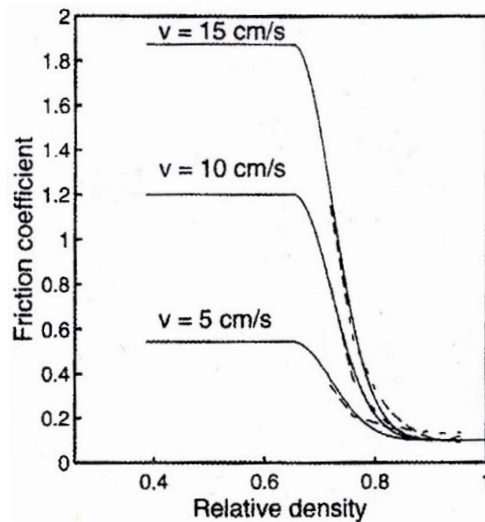


Figure 32. Friction model fitted to experimental values.

4.0 The Effect of Tool Kinematics on Density Gradient of Green Powder Compacts

4.1 Friction-assisted Compaction of Cylindrical Parts

As already mentioned, the existence of friction at powder-tool interfaces causes the occurrence of density gradient and crack-defects in PM components during the cold-die compaction and ejection cycle. For this reason, friction is seen as an undesirable factor, which degrades the competitiveness of the PM technology. Traditionally, the desire to reduce frictional effects has led to the implementation of enhanced powder lubricants. However, excessive addition of lubricants undermines the mechanical properties of the final PM components, due to increased porosity upon sintering.

However, a newly proposed powder compaction technique has demonstrated that friction may actually assist rather than undermine the compaction process. The proposed technique is applicable to uniaxial compaction, which uses friction as an active pressing force at powder-die interfaces. Unlike the traditional cold-die compaction process, which consists of a stationary die, the proposed method uses a moving die in the parallel direction to the punch; see Figure 33. By displacing the die at specific velocity and in the same direction of the moving punch the friction changes into an active force and assists in the compaction process. Using the proposed technique in their experimental studies, Canta and Frunza [15] have shown that density gradient over the compact height can be considerably reduced by varying the die to upper-punch velocity ratio, $v_{\text{die}}/v_{\text{u-p}}$. Thus, even though the friction force cannot be eliminated, changing its sense may prove to be beneficial to the compaction process.

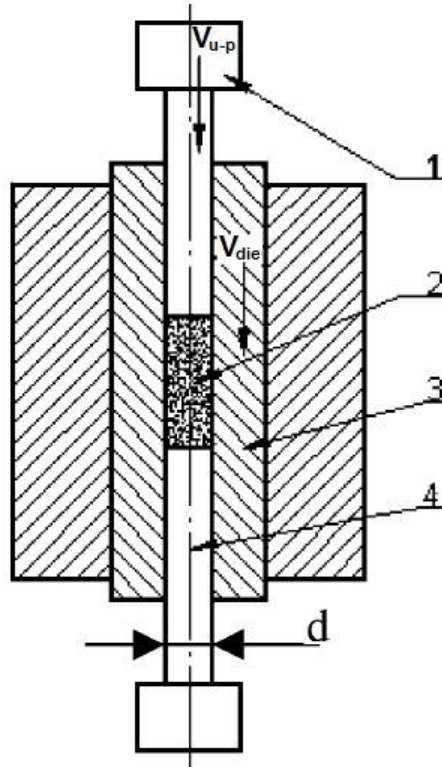


Figure 33. Friction-assisted press system consisting of: (1) upper-punch, (2) powder, (3) movable die, and (4) lower-punch [15].

4.1.1 Friction-assisted Compaction Experiments

For their experiments, Canta and Frunza have used gas atomized 316L stainless powder [15]. More detailed powder data was not provided. Cylindrically shaped specimens were compacted at ambient temperature to three different height-to-diameter ratio, h/d , values of 1.50, 1.00, and 0.50, with constant diameter of 12 mm, using a 200 kN press [15]. No inter-particle powder lubricant was added, however, some lubricant was applied onto the surface of die. The powder was compacted using the axial pressures of 380 to 400 MPa.

The experiments consisted of three tests using a press setup shown in Figure 33. For the first test the upper-punch (1) was displaced at specific velocity, while the die (3) was kept stationary, thus, having the die to upper-punch velocity ratio, v_{die}/v_{u-p} , of 0. For the second and third test both the upper-punch and the die were displaced in the same direction at v_{die}/v_{u-p} values of 0.33 and 0.5, respectively. During the compaction process both the punch and the die displacement versus time were recorded, and the loads exerted by the upper punch and

experienced by the die were evaluated. However, the recorded information was not published. After each test, the compact's dimensions and mass were measured to determine relative density, $\bar{\rho}$. Further, partial machining had been used in order to find local relative density along the compact's height.

4.1.2 Experimental Results Using Friction-assisted Compaction

Following the measurements, the relative density versus point location of the specimen's height was separately plotted for each test: fixed die, $v_{\text{die}}/v_{\text{u-p}} = 0$; and movable die with $v_{\text{die}}/v_{\text{u-p}}$ of 0.33 and 0.50, respectively. In total, for specimens with h/d of 1.50, eight location points were used, and for specimens with h/d of 1.00 and 0.50, three location points were used, representing the top, middle, and bottom sections of the compact, respectively; see Figures 34, 35, and 36.

The figures show density distribution over the height of the compact for all three tool kinematics scenarios. From observation, the least variation in density was recorded for $v_{\text{die}}/v_{\text{u-p}}$ of 0.50, for all three compact h/d specimens. For $v_{\text{die}}/v_{\text{u-p}}$ of 0.50, the density was found to be the highest at the top and bottom of the compact, and the lowest in the vicinity of its center. This is similar to the density distribution produced in the double-action compaction process. An increase in density gradient is observed for the lower value of $v_{\text{die}}/v_{\text{u-p}} = 0.33$. However, for the fixed die, $v_{\text{die}}/v_{\text{u-p}} = 0$, the density gradient was found to be the highest, with a declining relative density from top to bottom of the compact. It is important to note that the density gradient is reduced as the h/d decreases. This phenomenon is attributed to the reduction of the total friction area imposed by the die-wall and will be discussed in more detail in subsequent sections.

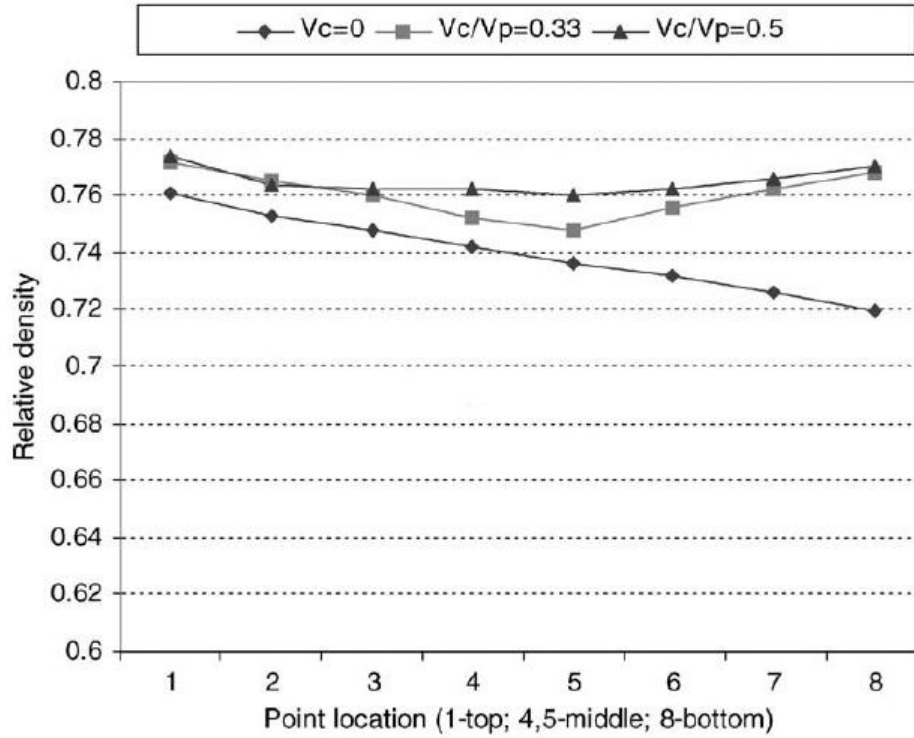


Figure 34. Relative density distribution for compact height-to-diameter ratio of 1.50 [15].

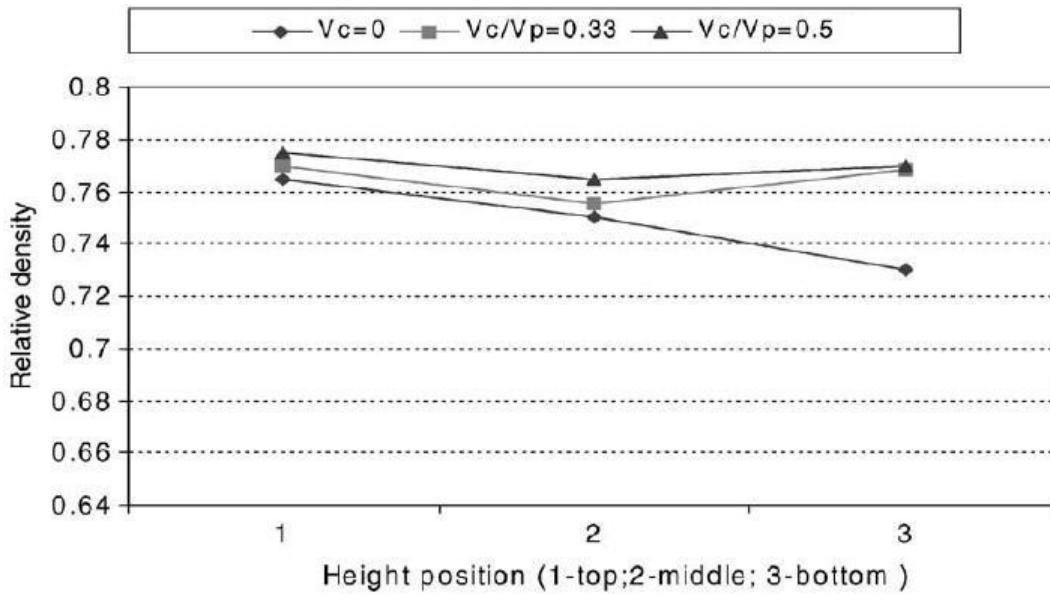


Figure 35. Relative density distribution for compact height-to-diameter ratio of 1.00 [15].

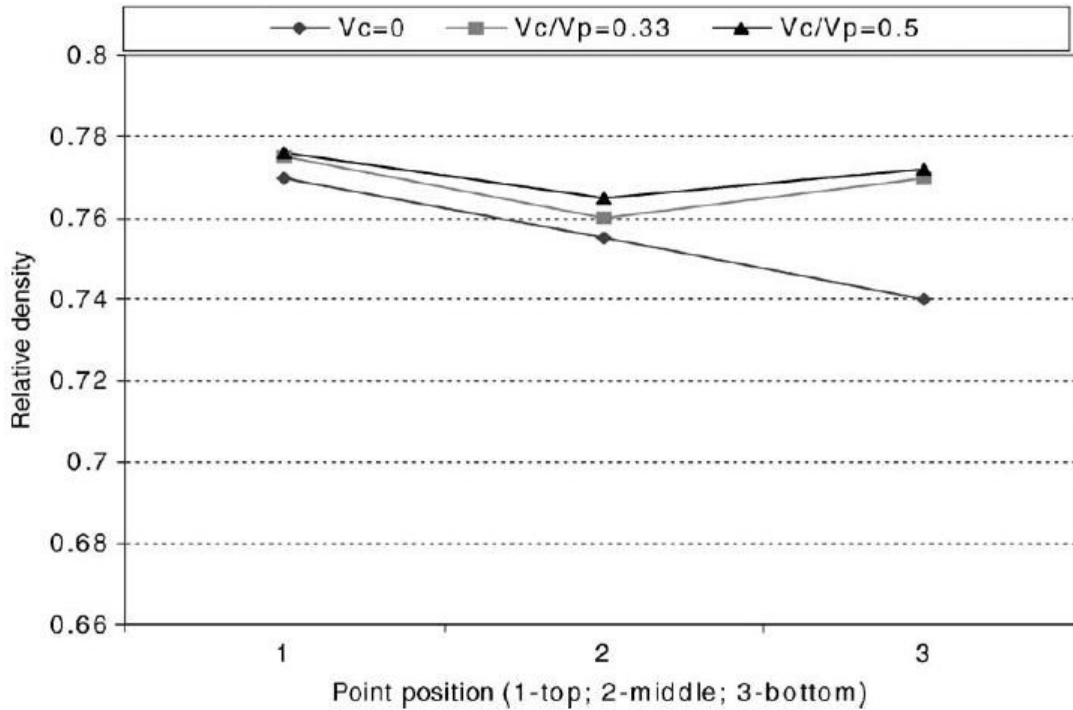


Figure 36. Relative density distribution for compact height-to-diameter ratio of 0.50 [15].

4.2 Compaction of a Multi-stepped Part

Although friction-assisted compaction proves to be beneficial in production of cylindrically shaped PM components, it is not directly applicable to more complex geometries. Both experimental and finite element analyses (FEA) of powder compaction of axisymmetric multi-stepped parts, were carried out by a number of researchers [20, 44, 45, 70, 88, 101, 102]; all parts consisted of identical general shape.

4.2.1 Analyses of a Multi-stepped Part

A study conducted by Shima et al. [101, 102] consisted of powder compaction analyses of a multi-stepped part, with dimensions presented in Figure 37, where the initial values of h_1 and h_2 were 5 and 10 mm, respectively, and all the other dimensions were kept constant. In this study the press has consisted of several moving tools; see Figure 38. The compression was carried out by displacing the upper-punch (1) and lower-inner-punch (3) at relative velocity ratio, v_3/v_1 , while the lower-outer-punch (2), the die (4), and the core-rod (5) were all kept stationary throughout the process. Overall, the analysis consisted of two parts. First, the

simulation was conducted to investigate the occurrence of the slip-crack defects adopting the conditions similar to those used by other researchers [20, 44, 70, 88]. However, the main focus of the analyses was to investigate the effect of tool kinematics on the green density variation. For this, two sets of analyses were conducted. First, the velocity ratio, v_3/v_1 , of the tools was varied by changing the velocity of the lower-inner-punch (3), v_3 , and keeping the velocity of the upper-punch (1), v_1 , constant; and for the second analyses, the velocity ratio, v_4/v_1 , of the tools was varied by changing the velocity of the die (4), v_4 , and keeping the velocity of both the upper-punch (1), v_1 , and lower-inner-punch (3), v_3 , constant. All other tools were kept stationary.

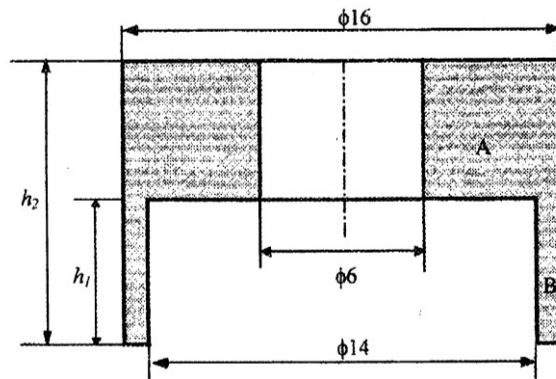


Figure 37. Shape and dimensions of powder compact schematic. All dimensions are in mm [100, 101].

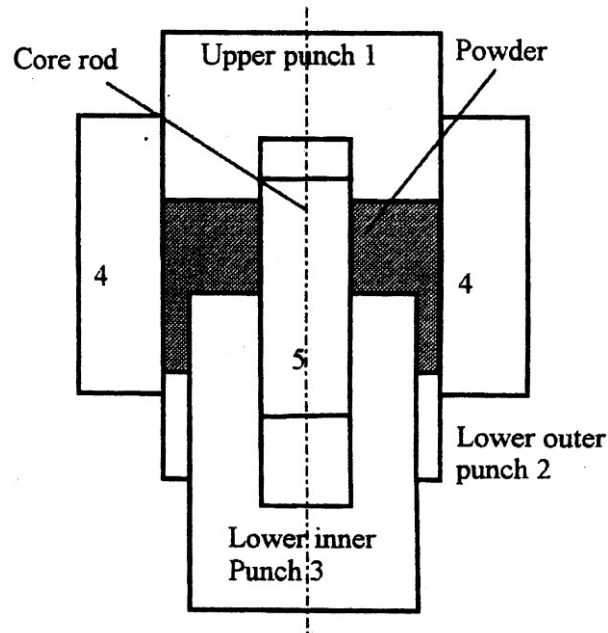


Figure 38. Press system consisting of: (1) upper-punch, (2) lower-outer-punch, (3) lower-inner-punch, (4) die, and (5) core-rod [101, 102].

For the presented multi-stepped part, it was suggested that if $h_1/h_2 = v_3/v_1$, then the compression ratio in the rim (zone B) would be equal to that in the hub (zone A); otherwise, both areas would experience a difference in the compression ratios; refer to Figure 37 [101]. To account for friction, the Coulomb model was used. For simplification purposes, different constant friction coefficient values of 0.08, 0.12, and 0.20 were assumed for the tool-powder interfaces to encompass a range of possible frictional conditions [101, 102]. The value of 0.40 was used as the initial relative density which is typical for iron-based powder [20, 26, 36, 44, 70, 88-90]. Linear triangular element was employed for FE mesh.

For the first part of the analyses, the tool kinematics consisted of two stages listed in Table 9, including the height ratio at the beginning of each stage. Identical tool kinematics were employed in other experimental and simulation analyses studies [20, 22, 44, 70, 88]. At each stage all tools moved at the specified constant velocity, moving in the same direction. Only constant friction coefficient value of 0.08 was employed for the first part of the analyses.

Table 9. Tool kinematics.

| Stage | 1 | | 2 | |
|-----------------------|-----------------|-------------------|-----------------|-------------------|
| Tool | velocity [mm/s] | displacement [mm] | velocity [mm/s] | displacement [mm] |
| Upper-punch (1) | 1 | 1.84 | 1 | 2.35 |
| Lower-outer-punch (2) | 0 | 0 | 0 | 0 |
| Lower-inner-punch (3) | 0.470 | 0.865 | 0.696 | 1.635 |
| Die (4) | 0 | 0 | 0.567 | 5.62 |
| Core-rod (5) | 0 | 0 | 0 | 0 |
| h_1/h_2 | 0.5 | | 0.507 | |

For the evaluation of relative density variation throughout the compact body, Shima et al. have employed the following expression

$$\rho_{var} = \sqrt{\frac{1}{N} \sum_{i=1}^N (\bar{\rho}_i - \bar{\rho}_m)^2} \quad (45)$$

where: N – number of elements
 $\bar{\rho}_i$ – relative density of element i
 $\bar{\rho}_m$ – average relative density of green compact.

4.2.2 Analyses Results for a Multi-stepped Part

4.2.2.1 Occurrence of Slip-Crack Defects

The shape and green density distribution after completion of the second stage of tool kinematics is shown in Figure 39. Since the friction coefficient implemented into the FE model was relatively small, the main cause of density variation is due to the tool kinematics [101, 102]. Because of the uneven compression ratio, $h_1/h_2 = v_3/v_1$, experienced in both stages of compaction, there was uneven compression of the hub (zone A) and the rim (zone B) during stages one and two of the compaction, respectively. In stage one with velocity ratio, v_3/v_1 , slightly lower than the initial height ratio, h_1/h_2 , the compression in the hub (zone A) was slightly larger than in the rim [101, 102]. However, in stage two as v_3/v_1 was much higher than the initial h_1/h_2 , thus, resulting in higher compression of the rim (zone B) as opposed to the hub (zone A) as experienced during the first stage of compaction [101, 102]. Due to a much higher compression of the rim (zone B), it experiences a higher local level of densification and thus resulting in the constrained powder pushing itself upwards against the rim-hub junction to a lower density region in the hub (zone A). Consequently, a slip-crack defect occurs at the corner of the left side of the rim-hub junction [20, 44, 70, 88, 101, 102]; see Figure 39.

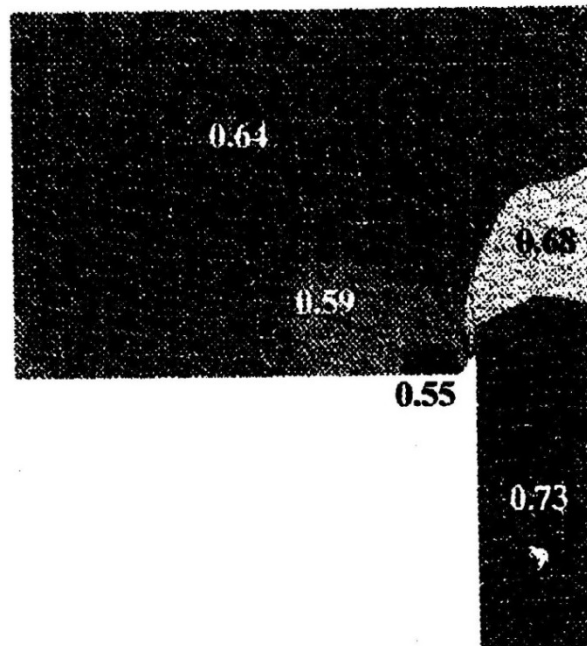


Figure 39. Shape and density distribution of the multi-stepped compact after Stage 2 of compaction cycle [101, 102].

4.2.2.2 Effect of Velocity Ratio on Green Density Variation

The evaluated relationship between green density variation and the velocity ratio, v_3/v_1 , for the first set of analyses, using different friction coefficient values, is shown in Figure 40. Depending on the imposed friction condition, the green density variation was found to be minimum at a certain velocity ratio, v_3/v_1 . The least variation in density was observed in the vicinity of the v_3/v_1 of 0.50, and was found to increase with friction coefficient. Figure 40 also shows the recorded critical velocity ratio, v_3/v_1 , values at which the initiation of a slip-crack defect was observed. Thus, by avoiding further increase in v_3/v_1 , the slip-crack defect may be prevented.

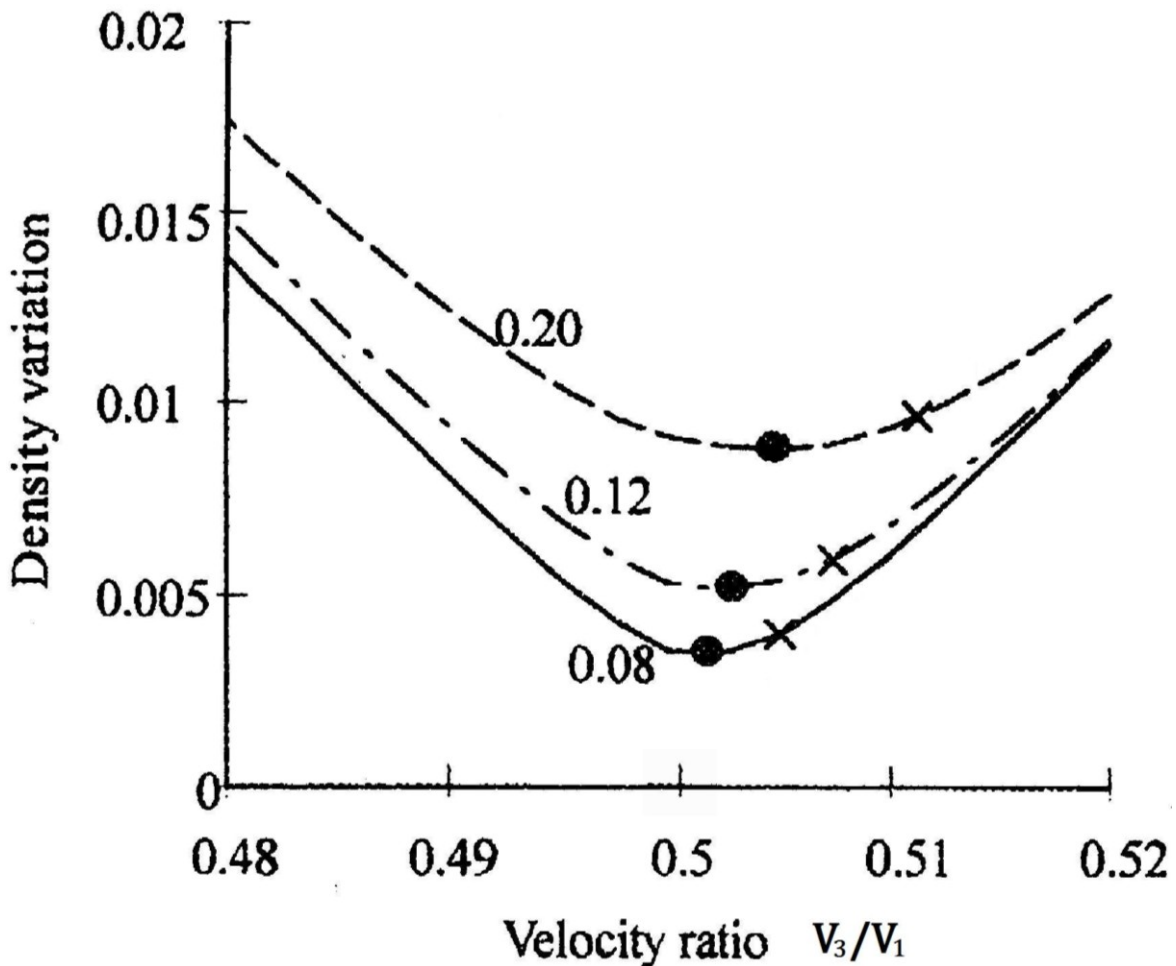


Figure 40. Density variation due to movement of tools 1 and 3, where • refers to minimum green density variation, and x refers to critical velocity ratio at which formation of slip-crack defect is initiated [101, 102].

For the second set of analyses, the evaluated relationship between green density variation and the velocity ratio, v_4/v_1 , using again different friction coefficient values, is shown in Figure 41. For this test the lower-inner-punch to upper-punch velocity ratio, v_3/v_1 , was kept constant at 0.50, while the die to upper-punch velocity ratio, v_4/v_1 was varied by changing the velocity of the die (4), v_4 , and keeping the velocity of the upper-punch (1), v_1 , constant. Both tools moved in the same direction, while all the other tools were kept stationary. From Figure 41 it is observed that moving the die has actually a negative effect of on homogeneity of the green compact, where the density variation is observed to increase with v_4/v_1 , regardless of the friction coefficient value.

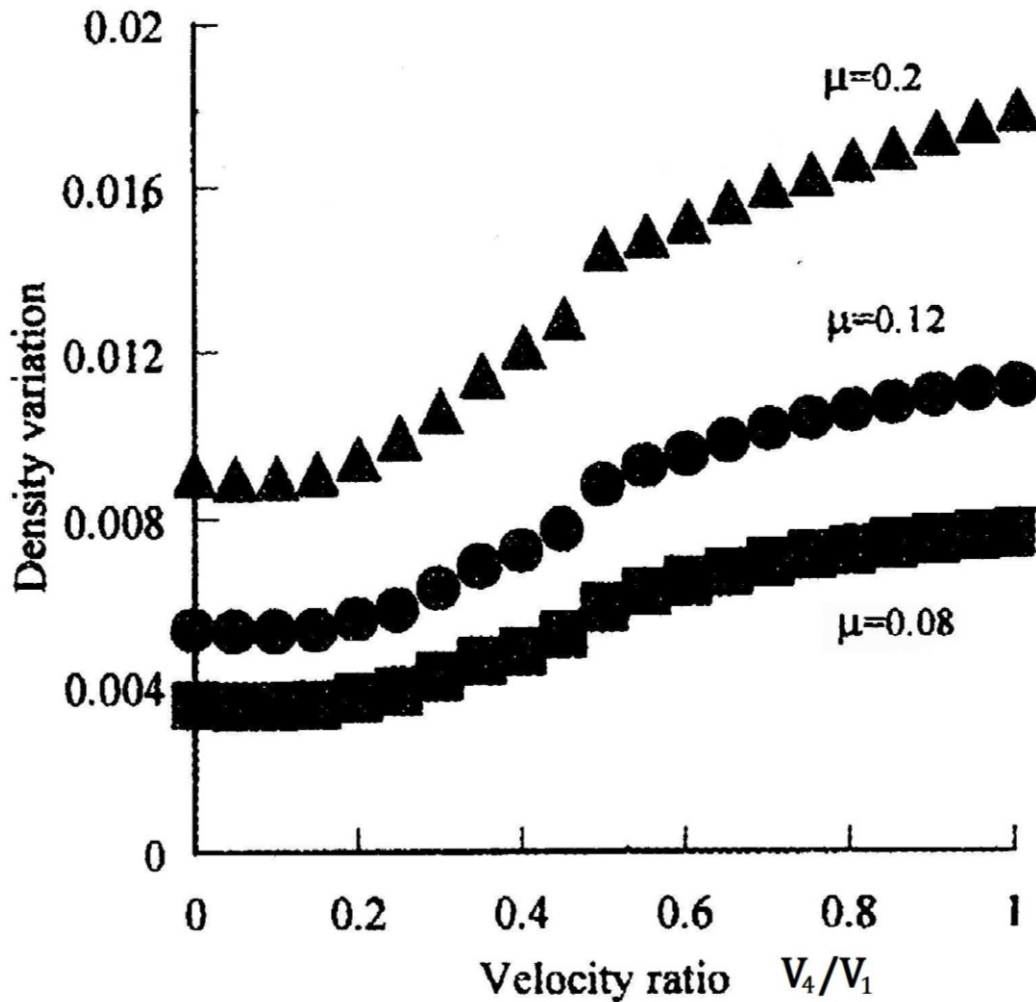


Figure 41. Density variation due to movement of tools 1 and 4 [101, 102].

5.0 Finite Element Approach

Sophisticated nonlinear FEA software was required for successful simulation analyses of powder compaction due to the nature of the PM process, which primarily involves a highly plastic deformation of powder, thus, resulting in a large nonlinear strain. For this, implicit nonlinear FEA software, MSC.Marc Mentat, was used which provides a relatively easy to use and robust capabilities for contact and large strain analysis. Other software such as ABAQUS and ANSYS were considered, however, both lack the equivalent non-linear capability offered by the employed software, especially when it comes to the analyses of powder compaction of complex geometry parts; see section 5.8 Automatic Global Remeshing [49, 88].

In this study the simulation analyses consisted of two parts. First, simulation analyses were conducted using friction-assisted compaction technique employed by Canta and Frunza [15] in their experimental studies on compaction of cylindrical parts. For the second part, simulation analyses were extended to a more complex geometry consisting of a multi-stepped part, identical to the one adopted by Shima et al. for their analyses, where friction-assisted compaction was indirectly used by varying the kinematics of specific pressing tools.

5.1 Mesh Generation

Due to the circumferential symmetry of both cylindrical and multi-stepped parts, used in simulation analyses, all parts were modelled as 2-D axisymmetric models. It is important to note, that this by no mean undermines the final simulation results [27, 43, 45, 48, 49, 50, 65, 70, 88, 101, 102, 125, 126]. Consequently, this eliminated the need for the use of CAD software, as all models were conveniently modelled in the pre-processor MSC.Mentat using the built-in modelling tools under MESH GENERATION option. All FE models are presented in the two following sections.

5.2 Friction-assisted Compaction of Cylindrical Parts

For simulation analyses of the cylindrical parts, three different dimensional sets were used. The experimental specimen data presented by Canta and Frunza [15] was adopted, where the final green compact height-to-diameter ratio, h/d , was specified as 1.50, 1.00, and 0.50, with constant diameter of 12 mm. Thus, the actual final height of the corresponding compact specimens was 18, 12, and 6 mm, respectively.

It is important to note that since no information was provided on the initial powder fill height or its initial relative density, the initial height was assumed to be twice the final height for each FE model and initial relative density was assumed to be 0.42. This relative density value represents the typical values encountered for iron-based powder fills in the industry [26, 27, 36, 88-90].

In addition, it is important to note, that aside from the specified velocity ratio values and that velocity of the upper-punch was kept constant at all times, no specific speed values were provided for all the active tools, which includes the upper-punch and the die, while the lower-punch was kept stationary. For this reason, all simulation analyses of cylindrical parts were carried out using compaction speeds representative of the industrial practices, which typically range from 1 to 5 mm/s [27]. Specifically, the velocity of the upper-punch was kept constant at all times at 5 mm/s, while the velocity of the die corresponded to the desired die-to-punch velocity ratio, v_{die}/v_{u-p} , varying from 0 to 5 mm/s. For a complete summary of tool kinematics for each case study, see Table 10.

In total three FE models were used, which are shown in Figures 42, 43, and 44. For reasons already discussed, all three were modelled as axisymmetric models, consisting of the cross-sectional area with the constant radius multiplied by height of the corresponding cylinder. For detailed information on each FE model, see Table 11.

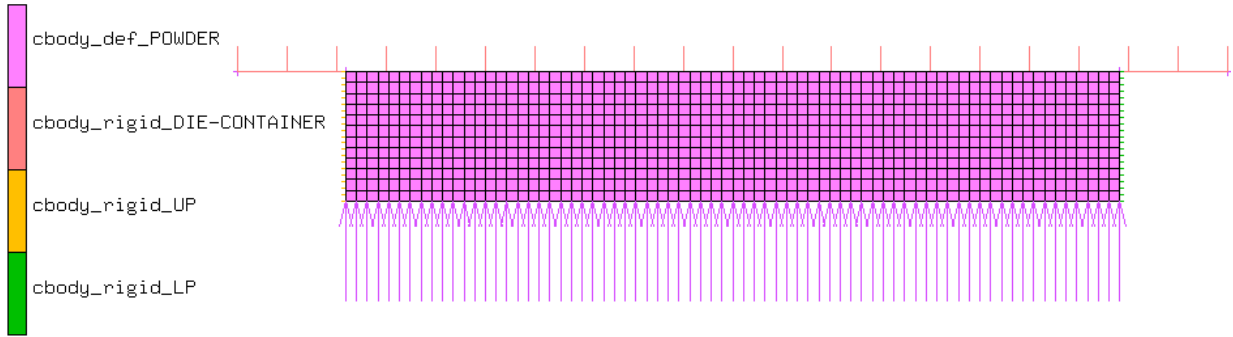


Figure 42. Axisymmetric FE model of the powder fill for cylindrical part used for case study (1).

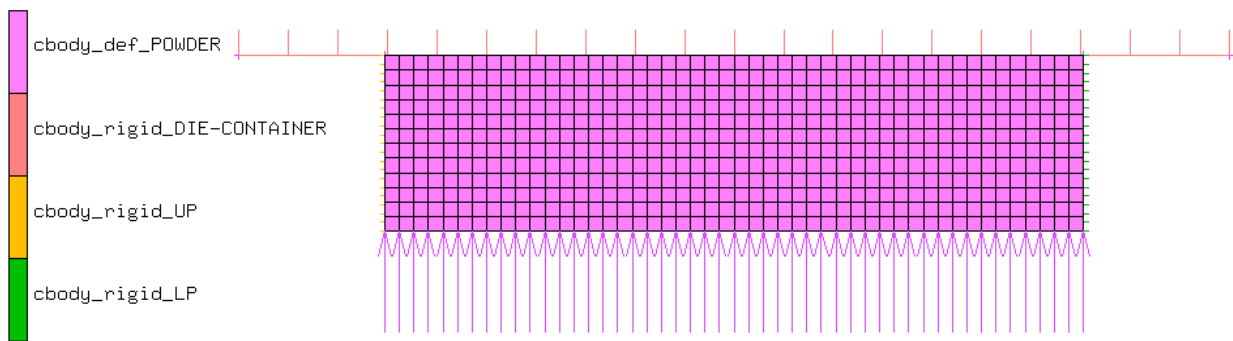


Figure 43. Axisymmetric FE model of the powder fill for cylindrical part used for case study (2).

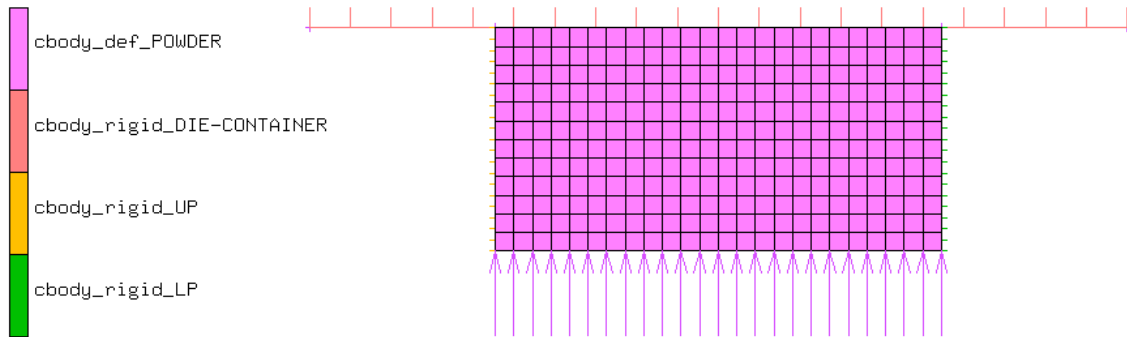


Figure 44. Axisymmetric FE model of the powder fill for cylindrical part used for case study (3).

Table 10. Summary of tool kinematics for all case studies.

| Case Study (1): | | Compact Height-to-Diameter Ratio, h/d = 1.50 | | |
|------------------------|----------|---|-------------------|---------------------|
| Tool | Type | Tool Velocity [mm/s] | Displacement [mm] | Total Load Time [s] |
| Upper-punch (1) | Constant | 5 | 18 | 3.6 |
| Lower-punch (4) | Constant | 0 | 0 | 3.6 |
| Die (3) | Variable | 0 to 5 | 0 to 18 | 3.6 |
| Case Study (2): | | Compact Height-to-Diameter Ratio, h/d = 1.00 | | |
| Tool | Type | Tool Velocity [mm/s] | Displacement [mm] | Total Load Time [s] |
| Upper-Punch (1) | Constant | 5 | 12 | 2.4 |
| Lower-Punch (4) | Constant | 0 | 0 | 2.4 |
| Die (3) | Variable | 0 to 5 | 0 to 12 | 2.4 |
| Case Study (3): | | Compact Height-to-Diameter Ratio, h/d = 0.50 | | |
| Tool | Type | Tool Velocity [mm/s] | Displacement [mm] | Total Load Time [s] |
| Upper-Punch (1) | Constant | 5 | 6 | 1.2 |
| Lower-Punch (4) | Constant | 0 | 0 | 1.2 |
| Die (3) | Variable | 0 to 5 | 0 to 6 | 1.2 |

Table 11. Detailed data and nomenclature for all powder fill FE models for cylindrical parts.

| Model Parameters | Compact Height-to-Diameter Ratio, h/d | | |
|------------------------------|--|---------------------------------------|----------------------|
| | 0.50 | 1.00 | 1.50 |
| Initial height, h_i [mm] | 12 | 24 | 36 |
| Compacted height, h_f [mm] | 6 | 12 | 18 |
| Radius, r [mm] | 6 | 6 | 6 |
| Total number of elements | $24 \times 12 = 288$ | $48 \times 12 = 576$ | $72 \times 12 = 864$ |
| Total number of nodes | 325 | 637 | 949 |
| Nomenclature | | | |
| Contact Body Acronym | Type | Description | |
| cbody_def_POWDER | deformable | Body of elements representing powder. | |
| cbody_rigid_DIE-CONTAINER | rigid | Die tool. | |
| cbody_rigid_UP | rigid | Upper-punch tool. | |
| cbody_rigid_LP | rigid | Lower-punch tool. | |

For each FE model, all the listed tools were defined to be rigid (i.e. not meshed). For powder compaction simulation analysis, the use of rigid bodies for representation of the pressing tools is realistic due to high difference in rigidity between the tools and the ferrous-based powder [43, 45, 48, 49, 50, 70, 101, 102, 112]. Typically, the tools are much more rigid as the punches

are made of hardened steels and the dies compose of tungsten carbide to reduce wear [30]. Just for comparison, the hardness of a tungsten carbide composition (91.5%WC, 8.5%Co), typically used for construction of dies, is measured at $HV_1 = 1520$, whereas for iron-based powder, Distaloy AE, $HV_{0.025} = 105$ [19, 21, 83, 84, 85, 86], i.e., a difference of about 14 ½ times.

5.3 Compaction of a Multi-stepped Part

For simulation analyses of the multi-stepped part, a single set of initial dimensions for depiction of powder fill were used; refer to Figure 37. For this, the data presented by Shima et al. [101, 102] was adopted, where the initial height for the rim, h_1 , and the hub, $h_2 - h_1$, was defined at 5 mm. Both corresponding height dimensions varied upon studying the effect of tool velocity ratio on green density distribution for all cases of simulation analyses. All the other (horizontal) dimensions were kept constant.

It is important to note that before carrying out any simulation studies, the initial tool kinematics adopted by Shima et al. for occurrence of slip-crack defects study, presented in Table 9, were employed as the starting point for powder compaction simulation. Using the proposed tool kinematics, succession of initial simulations were run to compare the ensuing density distribution results to those presented by Shima et al. in Figure 39. Upon satisfaction of the obtained results, three sets of simulations were conducted to study the effect of tool velocity ratio on green density distribution using the following three case studies: (i) lower-inner-punch to upper-punch velocity ratio, v_3/v_1 ; (ii) die to upper-punch velocity ratio, v_4/v_1 ; and (iii) die and core-rod to upper-punch velocity ratio, $v_{4,5}/v_1$. For the nomenclature of press tools, refer back to Figure 38. It is important to note that only case studies (i) and (ii) were carried out by Shima et al., while case (iii) was done by the present author as an extension to their work.

For case (i), the velocity of the upper-punch (1) was kept constant at all times, while the velocity of the lower-inner-punch (3) was varied corresponding to v_3/v_1 . In total, eleven runs were conducted with v_3/v_1 ranging from 0.45 to 0.55 in increments of 0.01. All other tools were kept stationary throughout the process.

For case (ii), the velocity of the upper-punch (1) was kept constant at all times, while the velocity of the die (4) was varied corresponding to v_4/v_1 . Additionally, the lower-inner-punch was displaced at a constant velocity with a lower-inner-punch (3) to upper-punch (1) velocity ratio, v_3/v_1 , of 0.50. Once again, eleven runs were conducted with v_4/v_1 ranging from 0 to 1.00 in increments of 0.1. All other tools were kept stationary throughout the process.

For case (iii), the velocity of the upper-punch (1) was kept constant at all times while the velocity of the die (4) and core-rod (5) varied corresponding to $v_{4,5}/v_1$. Again, the lower-inner-punch was displaced at a constant velocity with a constant lower-inner-punch (3) to upper-punch (1) velocity ratio, v_3/v_1 , of 0.50. Eleven more runs were conducted with $v_{4,5}/v_1$ ranging from 0 to 1.00 in increments of 0.1. All other tools were kept stationary throughout the process.

It is worth noting that for all the case studies conducted by Shima et al. [101], aside from specification of velocity ratio values and constant velocity of the upper-punch, no specific speed for all the active tools was provided. For this reason, the velocity of the upper punch of 1 mm/s was adopted from the occurrence of slip-crack defects study by Shima et al. [101, 102], presented in Table 9. All the other velocity values varied corresponding to the velocity ratios of the active tools. Similarly, for the two case studies conducted by Shima et al. [101], studying the influence of velocity ratios v_3/v_1 and v_4/v_1 on green density distribution, the total load time was not specified. Therefore, for the three case studies conducted by the present author, the total load time of 4.19 s was used, again adopted from Table 9, as the total load time for all active tools. For a complete summary of tool kinematics for each case study, refer to Table 12. All simulation analyses were carried out using compaction speeds representative of the industrial practices, which typically range from 1 to 5 mm/s [27]. The initial relative density value of 0.40 was adopted for all cases of study, as suggested by Shima et al. [101, 102].

Table 12. Summary of tool kinematics for all three case studies.

| Case Study (1): Lower-Inner-Punch to Upper-Punch Velocity Ratio, v_3/v_1 | | | | |
|---|----------|----------------------|-------------------|---------------------|
| Tool | Type | Tool Velocity [mm/s] | Displacement [mm] | Total Load Time [s] |
| Upper-Punch (1) | Constant | 1 | 4.19 | 4.19 |
| Lower-Outer-Punch (2) | Constant | 0 | 0 | 4.19 |
| Lower-Inner-Punch (3) | Variable | 0.45 to 0.55 | 1.8855 to 2.3045 | 4.19 |
| Die (4) | Constant | 0 | 0 | 4.19 |
| Core-Rod (5) | Constant | 0 | 0 | 4.19 |
| Case Study (2): Die to Upper-Punch Velocity Ratio, v_4/v_1 | | | | |
| Tool | Type | Tool Velocity [mm/s] | Displacement [mm] | Total Load Time [s] |
| Upper-Punch (1) | Constant | 1 | 4.19 | 4.19 |
| Lower-Outer-Punch (2) | Constant | 0 | 0 | 4.19 |
| Lower-Inner-Punch (3) | Constant | 0.5 | 2.095 | 4.19 |
| Die (4) | Variable | 0 to 1 | 0 to 4.19 | 4.19 |
| Core-Rod (5) | Constant | 0 | 0 | 4.19 |
| Case Study (3): Die and Core-Rod to Upper Punch Velocity Ratio, $v_{4,5}/v_1$ | | | | |
| Tool | Type | Tool Velocity [mm/s] | Displacement [mm] | Total Load Time [s] |
| Upper-Punch (1) | Constant | 1 | 4.19 | 4.19 |
| Lower-Outer-Punch (2) | Constant | 0 | 0 | 4.19 |
| Lower-Inner-Punch (3) | Constant | 0.5 | 2.095 | 4.19 |
| Die (4) | Variable | 0 to 1 | 0 to 4.19 | 4.19 |
| Core-Rod (5) | Variable | 0 to 1 | 0 to 4.19 | 4.19 |

For all simulation analyses a single axisymmetric FE model was used, see Figure 45. For detailed summary and nomenclature of the corresponding FE model, see Table 13. Further, for all three case studies, equation (45), employed by Shima et al., was used for the evaluation of relative density variation.

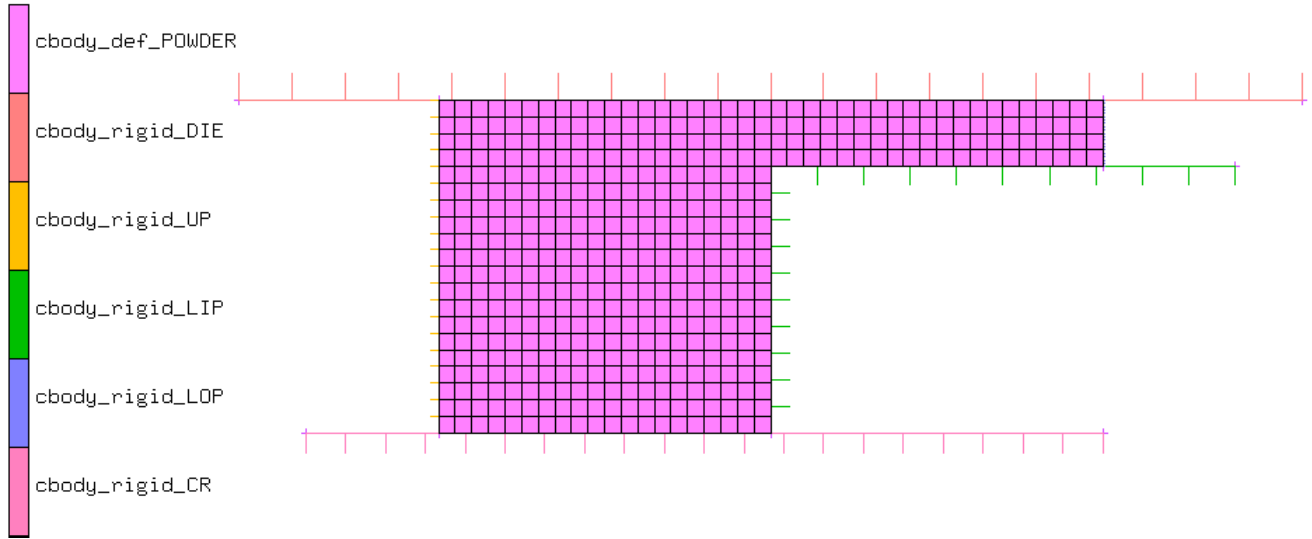


Figure 45. Axisymmetric FE model of the powder fill for multi-stepped part used for all case studies.

Table 13. Detailed data and nomenclature for FE model of the multi-stepped part.

| Model Parameters | Type | Value |
|--|-------------|---------------------------------------|
| Initial rim height, $h_{1,i}$ [mm] | Constant | 50 |
| Initial hub height, $h_{2,i} - h_{1,i}$ [mm] | Constant | 50 |
| Compacted rim height, $h_{1,f}$ [mm] | Variable | Varied depending on velocity ratio. |
| Compacted hub height, $h_{2,f} - h_{1,f}$ [mm] | Variable | Varied depending on velocity ratio. |
| Initial number of elements | Constant | 480 |
| Final number of elements | Variable | Varied due to global remeshing. |
| Initial number of nodes | Constant | 541 |
| Final number of nodes | Variable | Varied due to global remeshing. |
| Contact Body Acronym | Type | Description |
| cbody_def_POWDER | deformable | Body of elements representing powder. |
| cbody_rigid_DIE | rigid | Die tool. |
| cbody_rigid_UP | rigid | Upper-punch tool. |
| cbody_rigid_LIP | rigid | Lower-inner-punch tool. |
| cbody_rigid_LOP | rigid | Lower-outer-punch tool. |
| cbody_rigid_CR | rigid | Core-rod tool. |

5.4 Powder Material Model

To analyse powder material, MSC.Marc Mentat uses Shima and Oyane yield function presented by equations (1) and (2) [74, 76, 77]. The yield stress, $\bar{\sigma}$, for this model can be defined as a constant value or a function of temperature only [72, 77]. The shear viscosity, η , of the powder constitutive material can only be defined as a constant value; refer to equation (6) [77]. In MSC.Marc Mentat, for the sake of numerical convenience, the material parameters β and γ are defined as

$$\beta = (b_1 + b_2 \bar{\rho}^{b_3})^{b_4} \quad (46)$$

$$\gamma = (q_1 + q_2 \bar{\rho}^{q_3})^{q_4} \quad (47)$$

where $\bar{\rho}$ is the relative density, and b_i and q_i are material parameter constants to be defined by the user. Equations (46) and (47) do not match the format of equations (20) and (21), respectively. Therefore, in order to input appropriate data into each FE model, the constants of the original equations presented by Shima et al. had to be converted to correspond to equations (46) and (47). For the detailed conversion procedure, see Appendix G.

It is worth noting that MSC.Marc Mentat allows for the input of the elastic properties as a function of relative density, such as the elastic modulus and Poisson's ratio. Thus, all the corresponding suggested elastic properties by (i) Pavier and Doremus, (ii) Shima, and (iii) Koval'chenko, were implemented into each FE model. All variable material properties were defined using TABLE option.

It is important to note that as both parts of the simulation analyses focused on cold-die compaction, any effects of temperature on material properties or corresponding parameters were ignored. All input data concerning powder material, such as material properties and corresponding parameters, were entered through the POWDER option. The initial relative density was entered through the RELATIVE DENSITY option.

5.5 Contact Definition and Control

MSC.Marc Mentat allows for definition of two types of contact bodies, deformable and rigid. The deformable bodies consist of a collection of a 2-D or 3-D finite elements, which may change in dimension and shape. The rigid bodies do not deform and may be composed of curves (2-D) or surfaces (3-D). Conveniently, in MSC.Marc Mentat, for 2-D or axisymmetric analysis, a rigid body may be defined simply by a curve as shown in Figure 46. The curves and surfaces are used to describe the outer edges or faces of the body whose nodes may become in contact with another body. For this reason, all curves and surfaces are treated as potential contact segments, and each of their corresponding nodes are treated as potential contact nodes [74].

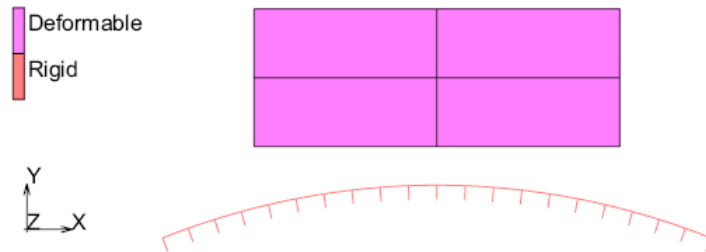


Figure 46. Definition of a rigid body for 2-D or axisymmetric analysis using a curve [74].

For these analyses, all deformable and rigid bodies were defined using CONTACT option for each FE model. The advantage of using this option is that it does not require an individual selection of each node of the corresponding curve or surface, as this is done automatically upon selection of geometric entities of corresponding deformable or rigid bodies. Further, MSC.Marc Mentat has a convenient CONTACT TABLE model option, allowing for the user to designate more detailed information on the interaction of the bodies, as opposed to the general CONTACT option. Using this option allows for the user to easily indicate which particular body will or will not contact (or possibly become in contact with) another body [74]. Also, this may be used to indicate whether the body will or will not come in contact with itself. Overall, the CONTACT TABLE option extremely simplifies the computation process upon creating simulation model of any nature, thus, this option was utilized for all FE models.

5.5.1 Motion of Contact Bodies

In MSC.Marc Mentat, the motion or deformation of deformable bodies is prescribed by applying displacement, force or distributed load onto the corresponding bodies. It is not recommended to apply displacement or point load onto a deformable body which may come into contact with rigid bodies [74]. For this reason, for all FE models, the prescribed displacement of a deformable body (powder) was imposed by introduction of a number of rigid bodies (punches) and by application of motion to these rigid bodies.

Using CONTACT option in MSC.Marc Mentat, there are four ways to prescribe motion to the rigid bodies – velocity, position, load, and scaling [74]. For the present simulation analyses, the kinematics of all rigid bodies (pressing tools) was prescribed using velocity option. Due to complex kinematics of the tools, TABLE option was used for definition of motion for each active rigid body using velocity versus time curves. In this software, for any simulation analysis, a fictitious total analysis time and desired time increment is always assigned by a user input using the LOADCASE option, even-for static rate-independent analysis. Upon simulation, the motion during a time increment is considered to be linear and the position of the assigned bodies is determined by an explicit forward integration of the corresponding velocity curves based upon the current time step [74].

5.5.2 Initial Conditions

For all parts of the simulation analyses, all the rigid bodies (pressing tools) were modelled and assigned to be in contact with deformable body (powder), before the start of each analysis. Thus, it was assumed that all the punches and dies were already in contact with the powder fill before the start off of each pressing cycle. In MSC.Marc Mentat, before the actual analysis commences, i.e., at time increment zero, first the initialization procedure takes place that brings together all the active rigid bodies, in this case the pressing tools, with the deformable body – powder [74]. It is important to note that at this moment no actual distortion in the deformable body (powder) takes place. Distortion begins only at time increment one.

There is a possibility of the contact not being perfect, due to mesh discretization, when multiple bodies are initially in contact [74]; which was the case for this analysis. This could result in

induction of stresses. To avoid this problem, for each FE model, stress-free initial contact was flagged using CONTACT TABLE option. This causes node coordinates to relocate on the designated curve/surface to avoid the occurrence of initial stress condition [74].

5.5.3 Contact Detection

It is unlikely that a node belonging to a designated body will exactly contact the curve/surface of the opposing body during the contact [74]. For this reason, in MSC.Marc, a contact tolerance is associated with a designated curve/surface; see Figure 47.

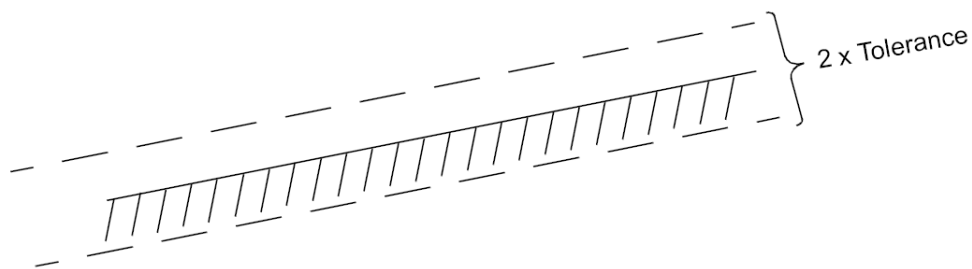


Figure 47. Contact tolerance [74].

During incremental procedure, if node A moves from location $A^{(t)}$ to location $A^{(t+\delta t)}$, the node is considered to have penetrated the body, as location $A^{(t+\delta t)}$ is beyond the contact tolerance; see Figure 48 [74]. Since in most cases the FE model consists of a large number of nodes and elements, MSC.Marc has efficient algorithms to speed up the contact and penetration detection process. One most commonly employed is a bounding box algorithm [74].

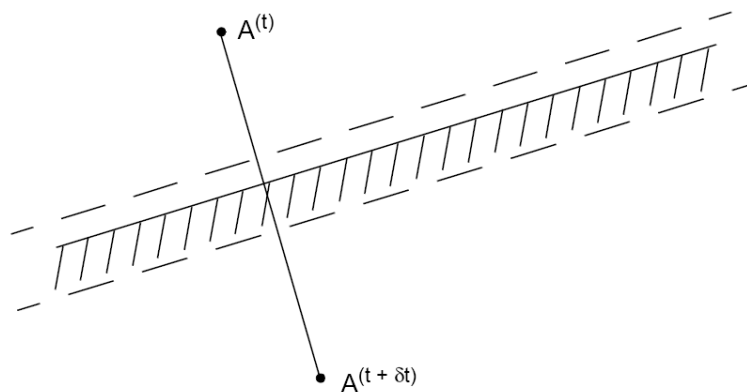


Figure 48. Trial displacement with penetration [74].

During each iteration process, the motion of each node is checked whether it is within the designated tolerance or it has penetrated the opposing body by extending over the tolerance.

By default, the contact tolerance is determined as the 5% of the smallest element side for solid elements [74]. In general, the size of the contact tolerance has a significant impact on the accuracy of the solution; especially in some cases when contact tolerance happens to be too large, where nodes are considered to be in contact prematurely, thus leading to a loss of accuracy or more recycling due to separation [74]. For present simulation analyses the default values for contact tolerance were employed, as recommended in MSC.Marc Mentat manual, to avoid a possibility of accuracy loss [74]. Also, to reduce the possibility of separation, the number of allowed recycling cycles was increased from default value of 10 to a new value of 20.

5.5.4 Contact Separation

There is always a possibility for the node in contact to separate in a subsequent iteration or increment. Theoretically, the node should be considered to have separated when the force or stress between the node and the contacted body is tensile in nature [74]. MSC.Mentat allows for the separation criterion to be based on either nodal stresses or nodal forces, which is flagged through user input. Force based separation criterion was selected for the present analyses, predicting separation based on the force threshold value between the node and the contacted body. The user specified threshold value was defined to be zero.

5.6 Friction Modelling

In general, friction is a complex physical phenomenon, even more so when it come to powder compaction, where based on numerous experimental analyses it has been shown to be a function of various physical and material parameters. The actual physics of friction and its numerical representation are still debatable and under research [45, 74], particularly so when it comes to PM application. Simply put, there are many factors involved and to account for all of them is very difficult especially when most of the parameters involved are indirectly related to each other.

Presently, MSC.Marc Mentat has two types of built-in models – the Coulomb and shear friction model. Generally, the Coulomb friction model is more commonly used, as the experimentally derived friction factor values for the shear model are not readily available in the literature [45].

5.6.1 Coulomb Friction

The general Coulomb friction model written in terms of the nodal stresses is presented as [74]

$$\|\sigma_t\| < \mu\sigma_n \text{ (stick)} \quad \text{and} \quad \sigma_t = -\mu\sigma_n \cdot \mathbf{t} \text{ (slip)} \quad (48)$$

where: σ_t - tangential (friction) stress

σ_n - normal stress

μ - friction coefficient

\mathbf{t} - tangential vector in the direction of the relative velocity, such that

$$\mathbf{t} = \frac{\mathbf{v}_r}{\|\mathbf{v}_r\|} \quad (49)$$

where \mathbf{v}_r is the relative velocity. Similarly, in term of nodal forces [74]

$$\|\mathbf{f}_t\| < \mu f_n \text{ (stick)} \quad \text{and} \quad \mathbf{f}_t = -\mu f_n \cdot \mathbf{t} \text{ (slip)} \quad (50)$$

where: \mathbf{f}_t - tangential (friction) force

f_n - normal force

Therefore, MSC.Marc allows for the use of either the nodal stress-based or force-based Coulomb friction model. When the nodal stress-based model is employed, the integration point stresses are first extrapolated to the nodal points and then transformed, such that a direct component is normal to the contacted surface [74]. The tangential stress is then evaluated and a consistent nodal force is determined based on the corresponding normal stress and relative sliding velocity values.

For a resulting normal stress or normal force, the corresponding friction stress or force has a step function behaviour based upon the value of the relative sliding velocity, v_r , or the tangential relative incremental displacement, Δu_t ; see Figure 49 [74]. Both the relative velocity and incremental displacement are scalar in nature.

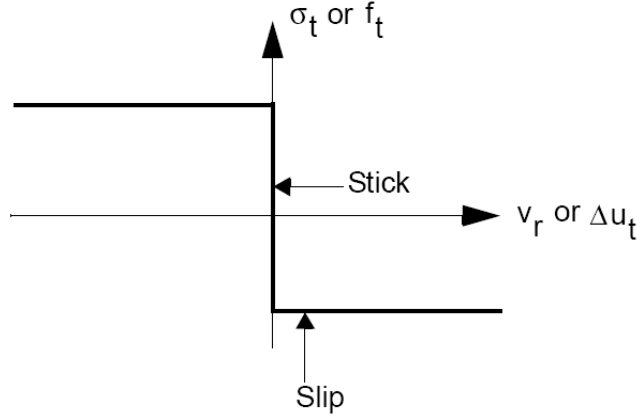


Figure 49. Coulomb friction model [74].

Due to step-like behaviour of the friction model, numerical difficulties may easily be encountered [74]. To resolve this problem, three different approximations of the friction step function have been implemented into the MSC.Marc: (i) arctangent model, (ii) stick-slip model, and (iii) bilinear model. The one employed for the present study was bilinear model, due to its noted superior performance in simulation of powder forming process [45].

5.6.2 Bilinear Model

The bilinear model is based on relative tangential displacements. Unlike in alternative models, where special constraints to enforce sticking conditions are defined, the bilinear model assumes that the stick-and-slip conditions correspond to reversible (elastic) and permanent (plastic) relative displacements, respectively [45, 74]. The bilinear model incorporates the theory of elasto-plasticity, such that the Coulomb's law of friction is expressed by the following slip surface, φ

$$\varphi = \|\mathbf{f}_t\| - \mu f_n \quad (51)$$

for which the stick or elastic domain is given by $\varphi < 0$, while $\varphi > 0$ is physically impossible [45, 74]. The rate of the relative tangential displacement vector, $\dot{\mathbf{u}}_t$, is split into an elastic (stick), $\dot{\mathbf{u}}_t^e$, and a plastic (slip), $\dot{\mathbf{u}}_t^p$, contribution [45, 74] as

$$\dot{\mathbf{u}}_t = \dot{\mathbf{u}}_t^e + \dot{\mathbf{u}}_t^p \quad (52)$$

The elastic tangential displacement is related to the rate of change of friction force vector as

$$\dot{\mathbf{f}}_t = \mathbf{D}\dot{\mathbf{u}}_t^e \quad (53)$$

in which matrix \mathbf{D} is given by

$$\mathbf{D} = \begin{bmatrix} \frac{\mu f_n}{\delta} & 0 \\ 0 & \frac{\mu f_n}{\delta} \end{bmatrix} \quad (54)$$

where δ is the slip threshold or relative sliding displacement below which sticking occurs, see Figure 50. By default, in MSC.Marc Mentat, the value of δ is determined by the program as 0.0025 times the average edge length of the finite elements defining the deformable contact bodies [74].

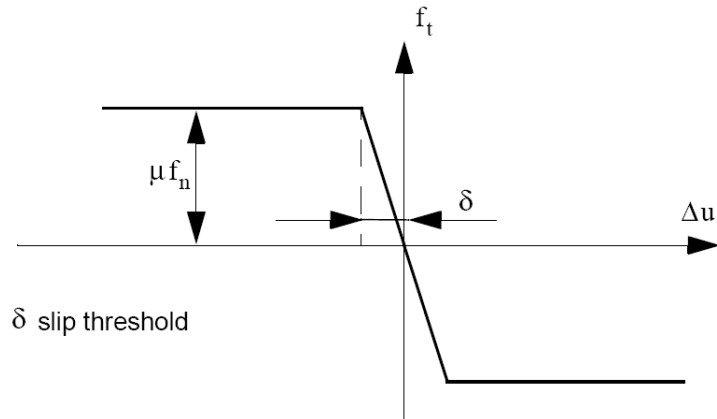


Figure 50. Bilinear model [74].

However, given a tangential displacement vector, \mathbf{u}_t , the evolution for tangential force, \mathbf{f}_t , leads to a physically impossible situation, such that $\varphi > 0$. To overcome this problem, the plastic or slip contribution must be determined. By substitution of equation (52) into (53)

$$\dot{\mathbf{f}}_t = \mathbf{D}(\dot{\mathbf{u}}_t - \dot{\mathbf{u}}_t^p) \quad (55)$$

Further, it is assumed that the direction of the slip displacement rate, $\dot{\mathbf{u}}_t$, is given by the normal to the slip flow potential, Ψ , which is expressed as [45, 74]

$$\Psi = \|\mathbf{f}_t\| \quad (56)$$

As a result, the plastic tangential displacement rate, $\dot{\mathbf{u}}_t^p$, with the slip displacement rate magnitude, $\dot{\Lambda}$, is expressed as

$$\dot{\mathbf{u}}_t^p = \dot{\Lambda} \frac{\partial \Psi}{\partial \mathbf{f}_t} \quad (57)$$

with the slip surface, φ , different from the slip flow potential, Ψ , an analogy to non-associative plasticity can be observed [45, 74].

Further, the following requirement is imposed, since a force point can never be outside the slip surface [45, 74]

$$\dot{\varphi} = \left(\frac{\partial \varphi}{\partial \mathbf{f}_t} \right)^T \dot{\mathbf{f}}_t = 0 \quad (58)$$

This way, the magnitude of the slip rate can be determined [45, 74]. Further, by combining and manipulating the above equations

$$\left(\frac{\partial \varphi}{\partial \mathbf{f}_t} \right)^T \mathbf{D} \left(\dot{\mathbf{u}}_t - \dot{\Lambda} \frac{\partial \Psi}{\partial \mathbf{f}_t} \right) = 0 \quad (59)$$

or

$$\dot{\Lambda} = \frac{\left(\frac{\partial \varphi}{\partial \mathbf{f}_t} \right)^T \mathbf{D} \dot{\mathbf{u}}_t}{\left(\frac{\partial \varphi}{\partial \mathbf{f}_t} \right)^T \mathbf{D} \frac{\partial \Psi}{\partial \mathbf{f}_t}} \quad (60)$$

Combining the above equations, the final set of rate equations is expressed as [74]

$$\dot{\mathbf{f}}_t = \left(\mathbf{D} - \frac{\mathbf{D} \frac{\partial \Psi}{\partial \mathbf{f}_t} \left(\frac{\partial \varphi}{\partial \mathbf{f}_t} \right)^T \mathbf{D}}{\left(\frac{\partial \varphi}{\partial \mathbf{f}_t} \right)^T \mathbf{D} \frac{\partial \Psi}{\partial \mathbf{f}_t}} \right) \dot{\mathbf{u}}_t = (\mathbf{D} - \mathbf{D}^*) \dot{\mathbf{u}}_t \quad (61)$$

Matrix \mathbf{D}^* will generally be non-symmetric, just as for non-associative plasticity [74]. However, the software utilizes a special procedure which converts the non-symmetric matrix \mathbf{D}^* into a symmetric matrix, while maintaining sufficient numerical stability and rate of convergence [74].

In addition, the built-in bilinear model uses an additional check on the convergence of the friction forces [74]

$$\frac{|\|\mathbf{F}_t\| - \|\mathbf{F}_t^p\||}{\|\mathbf{F}_t\|} \leq e \quad (62)$$

where: \mathbf{F}_t – current total friction force vector (collection of all nodal contributions)

\mathbf{F}_t^p – total friction force vector of the previous iteration

e – friction force tolerance, which has a default value of 0.05.

Therefore, the convergence is achieved upon satisfying the condition imposed by equation (62).

If a node coming into contact with a body results in stress-free condition, then the friction stiffness matrix will still be zero. Such condition may result in an ill-conditioned system during the next solution of the global set of equations [74]. To avoid this problem, the initial friction stiffness is based on the average contact body stiffness, which is determined during increment 0 of the analysis [74].

5.6.3 Limitations of the Coulomb Friction Model

Although, Coulomb based friction representation is most commonly adopted, it is not without flaws. For many cases, Coulomb model does not correlate well with experimental observations; see Figure 51 [74]. Due to its linear nature, it may over-estimate the value of shear stress upon exertion of a very high normal load, as it may exceed the yield stress of the material, which is physically not possible. In order to overcome this limitation, use of a nonlinear friction coefficient is recommended [74]. Thus, for this analysis, both constant and variable friction coefficient values were employed to try to encompass various frictional conditions and assimilate more realistic frictional behaviour without compromising the results due to the specified limitation. The variable friction coefficient used for present simulation analyses was defined using UFRIC user-subroutine in MSC.Marc Mentat.

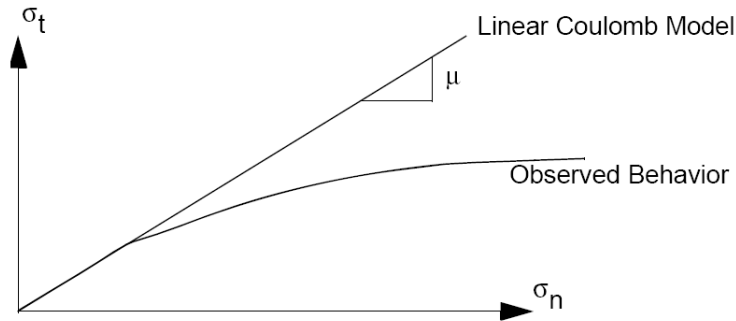


Figure 51. Linear Coulomb friction model versus observed behaviour [74].

5.7 Friction Coefficient Used for Simulation Analyses

As explained in previous sections, the friction coefficient at powder-tool interfaces is a function of various physical and material parameters, and is nonlinear in nature. Generally, for simulation analysis of metal powder compaction, an average friction coefficient value is employed [23, 43, 45, 48, 49, 50, 70, 88, 90, 101, 102, 112, 129]. The typical recommended friction coefficient value for simulation of iron-based powder compaction is 0.1 [27, 90, 111]. This is consistent with numerous experimental data, where the friction coefficient was found to vary within the range of 0.4 to 0.17, having an approximate average value of 0.1 [10, 13, 27, 31, 89-90, 111, 114].

It is important to note that using a constant friction coefficient does not provide true representation of frictional conditions. Traditionally, this approach is adopted because of inconsistent or incomplete experimental data, or due to imposed software limitations. For most cases, the derived friction coefficient relations presented in literature cannot be directly used as an input data for the friction model designated for simulation analysis. Just like material properties, the friction coefficient is dependent on powder constitutive material, and thus, when derived for specific powder materials, it cannot be directly adopted for the analysis of a powder composed of different constitutive material, or for the case of identical powder, but with different lubricant mixture [80]. For this reason, all experiments must be conducted using identical powder and lubricant composition. For experiments conducted by Pavier and Doremus [19, 21, 84-87], when deriving both the material properties and the friction coefficient relation,

identical iron-based powder, Distaloy AE, was used. For this reason, equation (41) was adopted for simulation analysis of powder compaction.

To encompass various frictional conditions and assimilate more realistic powder behaviour, both constant and variable friction coefficients were employed. More specifically, for simulation analyses of the cylindrical parts, a constant friction coefficient value of 0.1 was used, and a modified version of equation (41) was employed as a variable friction coefficient. For simulation analyses of the multi-stepped part, three constant friction coefficient values of 0.08, 0.12, and 0.20, as well as a variable friction coefficient evaluated using a modified version of equation (41), were employed. For a complete summary, see Table 14.

In MSC.Marc Mentat, the variable friction coefficient may be defined using the UFRIC user-subroutine, through a user supplied FORTRAN code. Using this subroutine, a user is allowed to define the friction coefficient as [74]

$$\mu = \mu(x, f_n, T, v_r, \bar{\sigma}) \quad (63)$$

where:

- x – point location at which friction is calculated
- f_n – normal force at point location at which friction is calculated
- T – temperature at point location at which friction is calculated
- v_r – relative sliding velocity at contact point of opposing bodies
- $\bar{\sigma}$ – yield stress at point location at which friction is calculated.

Based on presented information, the UFRIC user-subroutine does not allow for the definition of friction coefficient as a function of density, ρ . This was further confirmed by MSC.Marc technical support [72]. For this reason, the density term, ρ , in equation (41) had to be dropped. As a compromise, the following function for variable friction coefficient

$$\mu(\sigma_n, v_r) = e^{\left(\frac{-\sigma_n}{1169}\right)} \times (0.224) \times \left(1.437 \times \tanh\left(\frac{v_r}{12.6} + 0.886\right)\right) \quad (64)$$

was adopted for the present simulation analyses, where:

- σ_n – normal stress at point location at which friction is calculated

v_r – relative sliding velocity at contact point of opposing bodies.

Table 14. Friction coefficient values used for simulation analyses.

| Cylindrical Parts | | |
|---------------------------|----------|-----------------------------|
| Condition | Type | Friction Coefficient, μ |
| 1 | constant | 0.1 |
| 2 | variable | Equation (64) |
| Multi-stepped Part | | |
| Condition | Type | Friction Coefficient, μ |
| 1 | constant | 0.08 |
| 2 | constant | 0.12 |
| 3 | constant | 0.20 |
| 4 | variable | Equation (64) |

The reasons for not adopting the alternative friction coefficient relation presented by Wikman et al., equation (42), were due to its limiting factors. Equation (42) expresses the friction coefficient as a function of two parameters only - the relative sliding velocity and powder density. Further, in its derivation, the assumption of hydrostatic stress was assumed at the point of contact; however, this does not give a true representation of the actual conditions. Most importantly, in the study conducted by Wikman et al., it was noted that their simulation analysis had produced higher friction forces compared to experimental results at the initial stage of compaction cycle, when using the proposed variable friction coefficient expression [126].

5.8 Automatic Global Remeshing

For common forming methods in manufacturing, involving either the forming of a solid body or powder, the material initially takes a relatively simple shape and is often formed to a more complex one. Due to this, when the forming process imposes high levels of deformation and especially where high curvature or radical change in geometry is present, the initially designated mesh for the FE model may become highly distorted and further unsuitable for a successful continuation of the simulation analysis; see Figure 52 [45, 49, 65, 74, 88, 90]. This was particularly experienced in powder compaction analyses of the multi-stepped part, where

at the left side corner of the hub-rim junction, a high level of penetration of the meshed deformable body (powder) through the rigid body (lower-inner punch) was observed; see Figure 53.

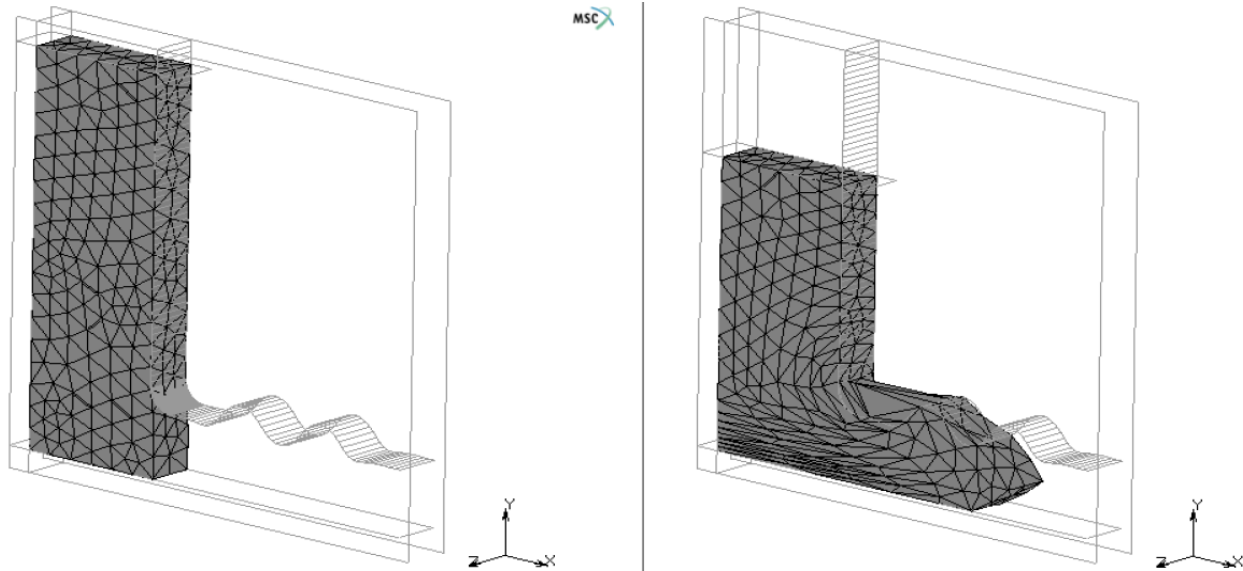


Figure 52. Mesh distortion example [74].

To overcome this problem, remeshing/rezoning of the FE model must be used during the analysis process. Based on numerous simulation studies, it has been concluded that due to high level of deformation and complicated tool kinematics a successful powder compaction simulation of a multi-stepped (or more complex) part is just not possible without employing some sort of remeshing procedure [45, 49, 88, 90]. MSC.Marc Mentat has the remeshing/rezoning option available using which global remeshing can be done manually or automatically. However, automatic global remeshing procedure is recommended as it makes sure that contact conditions are preserved and undesired penetration is removed [74]. The basic steps for automatic global remeshing are listed in Table 15.

In MSC.Marc Mentat, when remeshing/rezoning in 2-D (applies to axisymmetric models), the outline of the deformable body that needs to be rezoned is first found and then possible penetration is removed [74]. Based on the refined outline, it then calls the mesher to create a new mesh. It is important to note that by default, the Updated Lagrange formulation is used for the automatic remeshing/rezoning feature, where the coordinates of the FE mesh is forced to update for every load increment [45, 74].

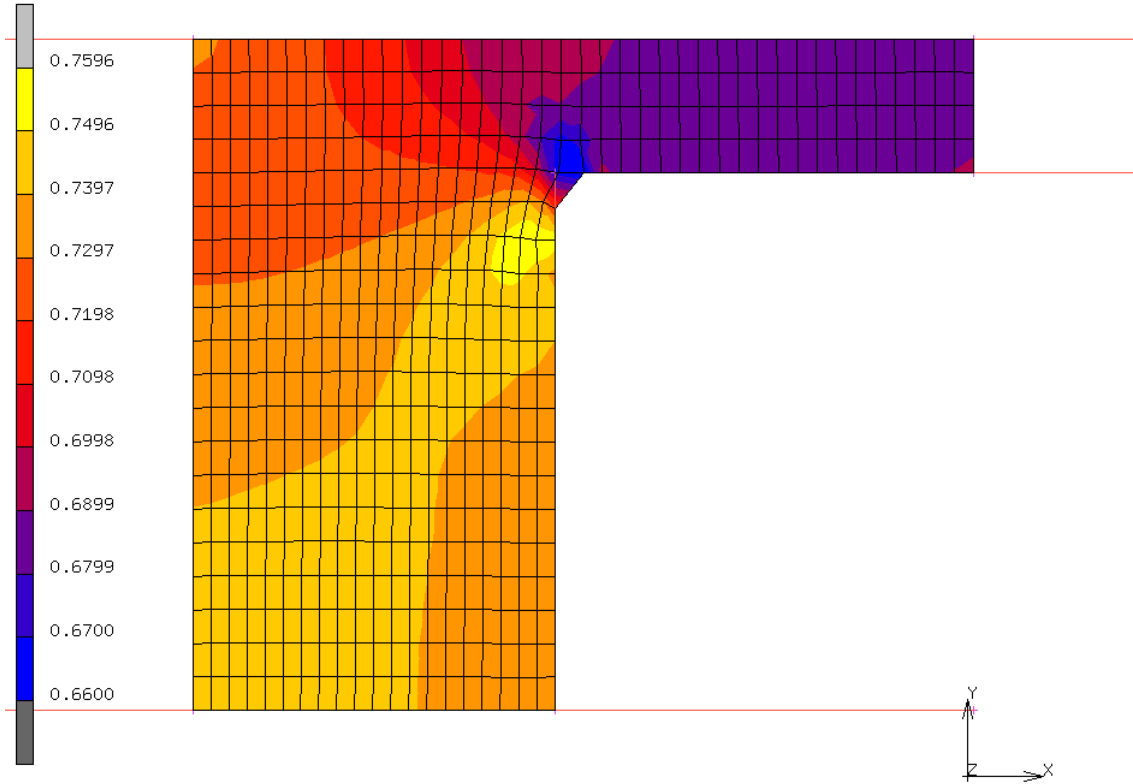


Figure 53. Penetration of deformable body (powder) through rigid body (lower-inner-punch) at lower-inner-punch (3) to upper-punch (1) velocity ratio, v_3/v_1 , of 0.48.

Table 15. Basic steps for automatic global remeshing employed in MSC.Marc Mentat [74].

| Step | Description |
|------|--|
| 1. | Analysis checks remeshing criteria at the end of each increment. When one of the remeshing criteria is met, analysis starts the remeshing procedure. |
| 2. | The deformed shape of the contact body is extracted. A new mesh is created by calling a stand-alone mesher or an internal mesher. |
| 3. | The new mesh is checked and corrected to avoid any penetration or contact loss to other contact bodies. |
| 4. | A data mapping is performed to transfer necessary data from the old deformed mesh to the new mesh. |
| 5. | The contact tolerance is recalculated (if not specified by you) and the contact conditions are redefined. |
| 6. | Boundary conditions, if any, are transferred to the new mesh. |
| 7. | The analysis completes global remeshing and continues its computation based on the new mesh. |

In general, it is recommended that frequent remeshing should be avoided for an effective analysis to take place, as each remeshing and subsequent rezoning step consists of

interpolation and extrapolation of element variables [45, 74]. Thus, there is a possibility of accumulating a numerical error over the progression of analysis. For this reason, for the analyses of a multi-stepped part, each remeshing criteria were carefully selected to keep remeshing to a minimum.

5.8.1 Remeshing Criteria

MSC.Marc Mentat has a selection of remeshing criteria, all of which may be used simultaneously. However, only two were employed for the powder compaction analyses of the multi-stepped part: the element distortion and the contact penetration criterion.

Using element distortion criterion, the deformable body is remeshed when the distortion in the elements becomes too large. For 2-D (including axisymmetric) analysis, the distortion check is based on element corner angles and the remeshing is performed if the following conditions are met: (i) any inner element angle is greater than 175° or less than 5° , or (ii) any inner element angle change is greater than the user specified value [74]. For the present analyses, the user specified option was selected with the limiting inner angle change of no more than 40° (initial recommended value).

Using contact penetration, the deformable body is remeshed when the curvature of the contact body is such that the current mesh cannot accurately detect penetration [74]. For 2-D (including axisymmetric) analysis, the penetration criterion is based on examining the distance between the edge of an element and the contacted body [74]. Remeshing is activated when the penetration distance reaches or exceeds a default or user specified penetration tolerance. By default, in MSC.Marc, the remeshing is executed if the penetration is greater than twice the contact tolerance and less than the target element size, where the default contact tolerance is 5% of the smallest element length and the target element size is the element size for remeshing [74]. The default contact tolerance, which can be changed by user input, was left unchanged for the analyses of the multi-stepped part.

5.8.2 Remeshing Technique

The MSC.Marc's remeshing technique, for 2-D and axisymmetric analysis, consists of the outline extraction and repair, followed by the call of a mesh generator to create a new mesh. There are

a number of build-in mesh generators available in MSC.Marc; however, the one most applicable for this analysis was the advancing front mesher [74]. The advancing front mesher is a 2-D mesher, which creates either triangular or quadrilateral mesh, or combination of both. It begins by creating a new layer of elements along the given boundary outline, resulting in a new boundary front; see Figure 54. The boundary front progresses inward until the complete enclosed region is meshed. In general, the advancing front mesher works with any enclosed geometry [74], which was the case for all FE models used in present analyses.

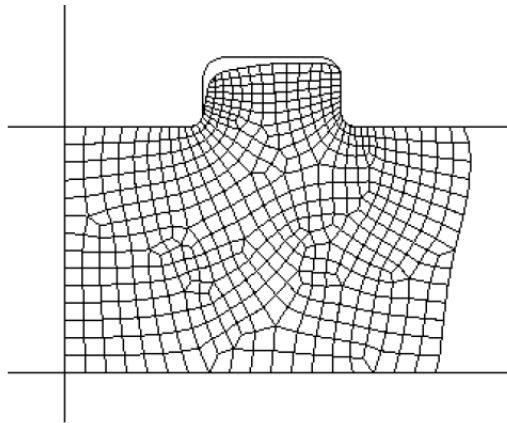


Figure 54. Advancing front meshing [73].

5.9 Element Type

Element type 10, in MSC.Marc Mentat, was employed for the simulation analyses of both the cylindrical and multi-stepped parts. Element 10 is an arbitrary four-noded quadrilateral, isoparametric element, specifically written for axisymmetric applications [75]; see Figure 55. It consists of four nodes per element, which are numbered in a counter-clockwise direction. For a quick reference on the element details, see Table 16.

This element is recommended over higher-order elements (meaning higher number of degrees of freedom) when used in a contact analysis, because of its ability to represent large distortion [74, 75]. However, in general, a larger number of these lower-order elements than the higher-order elements are required to obtain good results. Thus, for each FE model a very fine mesh was used, consisting of four elements per each 1 mm^2 area of the corresponding models.

For this element, four-point Gaussian integration is used to form its stiffness; see to Figure 55. All subjected pressures are positive when directed into the element. Further, point loads can be applied at the nodes with the magnitude corresponding to the load integrated around the circumference.

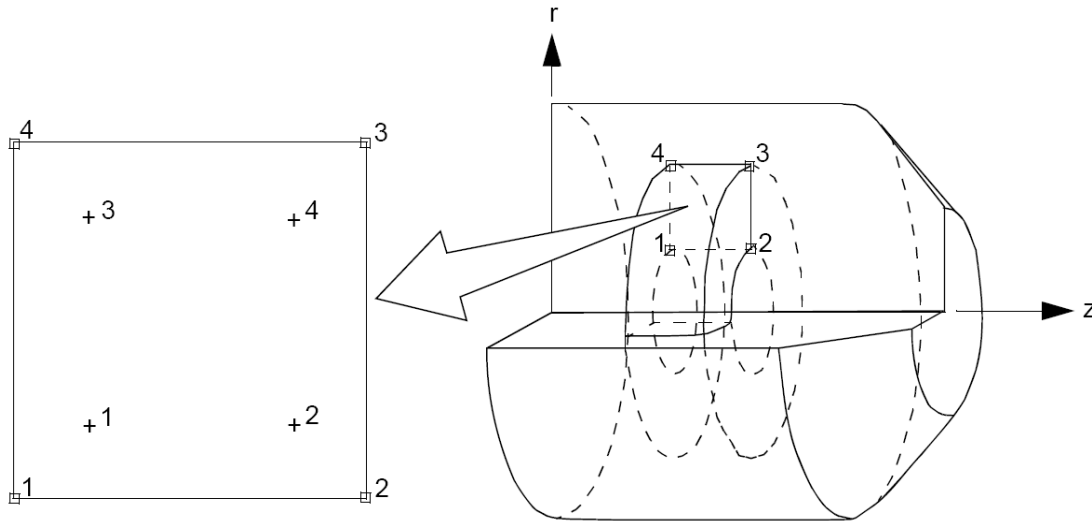


Figure 55. Integration points for Element 10 [75].

Table 16. Quick reference for Element 10 [75].

| | Description |
|--|--|
| Type 10 | Axisymmetric, arbitrary ring with a quadrilateral cross section. |
| Connectivity | Four nodes per element. Node numbering must be counter-clockwise. |
| Geometry | Particularly useful for analysis of approximately incompressible materials, and for analysis of structures in the fully plastic range. It is also recommended for creep problems in which it is attempted to obtain the steady-state solution. |
| Coordinates | Two coordinates in the global z- and r-direction. |
| Degrees of Freedom | 1 = u (displacement in the global z-direction) 2 = v (displacement in the global r-direction). |
| Output of Strains | Output of strains at the centroid of the element in global coordinates is: 1 = ϵ_{zz} , 2 = ϵ_{rr} , 3 = $\epsilon_{\theta\theta}$, 4 = γ_{rz} . |
| Output of Stresses | Same as for Output of Strains. |
| Transformation | Two global degrees of freedom can be transformed into local coordinates. |
| Output Points | Output is available at the centroid or at the four Gaussian points; refer to Figure 55. |
| Updated Lagrange Procedure and Finite Strain Plasticity | Capability is available – stress and strain output in global coordinate directions. Reduced volume strain integration recommended. (See Geometry.) |

In certain cases of FEA, the calculated displacements are some orders of magnitude smaller than they should be. When this happens, the elements are said to be locking. Locking usually occurs in lower order elements, due to some element's limited kinematics ability. Thus, upon definition of each FE model in MSC.Marc Mentat, the constant dilatation method was flagged through the GEOMETRY option to eliminate the potential of element locking [75].

5.10 Units Used for Simulation Analyses

Like many other FEA software, MSC.Marc Mentat has no units build into it. Thus, the units employed for any analysis must be self-consistent in order for the final output to be in correct or desired units. There are a number of self-congruent sets of units supported by MSC.Marc Mentat, however, the one adopted for this simulation was mm/tonnes/s/K or SI-mm, which are listed in Table 17.

Table 17. Set of self-congruent units employed for simulatin analyses [76].

| Quantity | SI-mm (mm/tonnes/s/K) |
|----------------------|--|
| Length | mm |
| Time | s |
| Mass | Mg (tonne) |
| Force | N (tonne-mm/s ²) |
| Density | Mg/mm ³ (tonne/mm ³) |
| Stress | MPa or N/mm ² or (tonne/mm/s ²) |
| Energy | MJ or N-mm (tonne-mm ² /s ²) |
| Temperature | °C |
| Spec. Heat Capacity | mm ² /s ² /°C |
| Heat Convection | N/s/°K/mm (tonne/s ³ /°C) |
| Thermal Conductivity | N/s/K (tonne-mm/s ³ /°C) |
| Thermal Expansion | mm/mm/°C |

5.11 Further Considerations for Nonlinear Analysis

A nonlinear problem cannot be successfully analysed using a set of linear equations [45, 74]. For example, superposition cannot be applied to linear equations to solve a nonlinear problem, without compromising the validity of results. In some cases when only a minor nonlinearity is experienced, the problem can be solved using linear approach with some level of error.

However, as powder compaction involves a large strain, an elasto-plastic nonlinear approach must be used.

In general, a nonlinear problem requires an incremental solution method and sometimes iterations (or recycles) within each load/time increment to ensure the satisfaction of equilibrium condition at the end of each time step [74]. The iterative schemes supported in MSC.Marc are: Full Newton-Raphson, Modified Newton-Raphson, Newton-Raphson with strain correction, and direct substitution. However, the Full Newton-Raphson method was employed for the powder compaction analyses as it provides good results for most nonlinear problems [74]. A detailed explanation of the Full Newton-Raphson method is presented in the following section.

5.12 Full Newton-Raphson Algorithm

The Full Newton-Raphson is the default method in MSC.Marc. The basis of this method is that the equilibrium condition must be satisfied when applied to nonlinear structural analysis [74]. To explain the method, first consider the following equation

$$\mathbf{K}(u)\delta u = F - R(u) \quad (65)$$

where \mathbf{K} is the tangent-stiffness matrix, u is the nodal-displacement vector, F is the external nodal-load vector, and R is the internal nodal load vector from the internal stresses [74]. The internal nodal-load vector, R , is obtained from the internal stresses of a specific element using the following relation [73]

$$R = \sum_{\text{element}} \int_V \beta^T \sigma \, dv \quad (66)$$

Both \mathbf{K} and R are functions of u in equations (65) and (66). In many cases F is also a function of u . For example, if F is determined from pressure loads, the nodal load vector is a function of the orientation of the structure [74].

Presume that the last obtained approximate solution is termed as δu^i , where i stands for the iteration number. Now, the equation (65) can be rewritten as [74]

$$\mathbf{K}(u_{n+1}^{i-1})\delta u = F - R(u_{n+1}^{i-1}) \quad (67)$$

The equation (67) is then solved for δu^i and the next corresponding solution is determined as

$$\Delta u^i = \Delta u^{i-1} + \delta u^i \quad \text{and} \quad u_{n+1}^i = u_n + \Delta u^i \quad (68)$$

where the subscript n denotes the increment number representing the state $t = n$, and unless stated otherwise, the subscript $n + 1$ is dropped with all quantities referring to the present state [74]. Upon solving equation (68) the first iteration is complete. By repeating the above steps the process can be repeated again; see Figure 56.

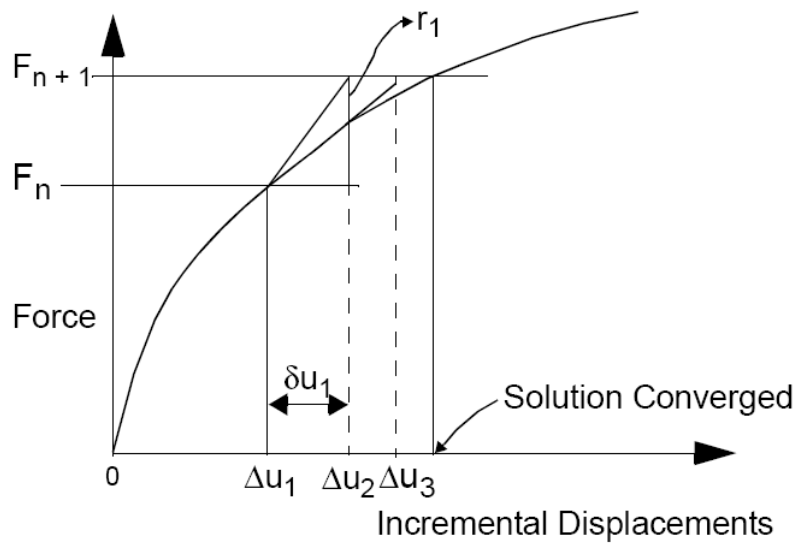


Figure 56. Illustration of Full Newton-Raphson method [74].

In general, the full Newton-Raphson method provides good results for most nonlinear problems, yet is expensive for large, three-dimensional problems, when the direct solver is used [74]. However, the computational problem is less significant when the iterative solvers are used, which are available in MSC.Marc.

5.13 Selection of Load Increment Size

One of the important aspects of a nonlinear solution scheme is to select a proper load step increment. As large steps can lead to too many iterations (or recycles) per increment, and more importantly, can result in inaccuracies and non-convergence [74], relatively small steps were selected for all cases of powder compaction analyses. The mechanical increment load type was

employed, using static mechanical approach. For a detailed list of all the load increment sizes used, see Table 18.

In addition, it is important to note, that the AUTO STEP option was selected, as it is recommended and appropriate for most applications [74]. This option allows for selection of a number of optional user-specified physical criteria, used to additionally control the load step. One criterion was modified using the AUTO STEP option – the recycling criterion. Using the recycling criterion, the user specifies a desired or allowed number of recycles (iterations). At times, for problems with severe nonlinearities, it is necessary to increase this number [74]. Thus, for the case of powder compaction, the number of recycles was increased from 10 to 20. However, it is worth noting that for all simulation runs, the observed number of recycles did not exceed a value of 10.

Table 18. Load step increment sizes used.

| Cylindrical Parts | | | |
|---|---------------------|----------------------|----------------------------------|
| Case Study | Total Load Time [s] | Number of Increments | Corresponding Load Step Size [s] |
| h/d = 0.50 | 1.2 | 100 | 0.012 |
| h/d = 1.00 | 2.4 | 100 | 0.024 |
| h/d = 1.50 | 3.6 | 100 | 0.036 |
| Multi-Stepped Part | | | |
| Case Study | Total Load Time [s] | Number of Increments | Corresponding Load Step Size [s] |
| Stage 1 & 2 | 11.75 | 200 | 0.1175 |
| Lower-Inner-Punch to Upper-Punch velocity ratio, v_3/v_1 | 4.19 | 100 | 0.0419 |
| Die to Upper-Punch velocity ratio, v_4/v_1 | 4.19 | 100 | 0.0419 |
| Die and Core-Rod to Upper Punch velocity ratio, $v_{4,5}/v_1$ | 4.19 | 100 | 0.0419 |

5.14 Convergence Control

For the analysis of powder compaction, MSC.Marc's default procedure for convergence criterion was used. This procedure is based on the magnitude of the maximum residual load compared to the maximum reaction force. This method is the most appropriate since the residuals measure the out-of-equilibrium force, which should be minimized as much as possible

[74]. This method has an additional benefit such that at times the convergence can be satisfied even without iteration [74].

The basic procedures for residual checking convergence criterion are outlined as follows [74]

$$\frac{\|F_{\text{residual}}\|_{\infty}}{\|F_{\text{reaction}}\|_{\infty}} < \text{TOL}_1 \quad (69)$$

$$\frac{\|F_{\text{residual}}\|_{\infty}}{\|F_{\text{reaction}}\|_{\infty}} < \text{TOL}_1 \quad \text{and} \quad \frac{\|M_{\text{residual}}\|_{\infty}}{\|M_{\text{reaction}}\|_{\infty}} < \text{TOL}_2 \quad (70)$$

$$\|F_{\text{residual}}\|_{\infty} < \text{TOL}_1 \quad (71)$$

$$\|F_{\text{residual}}\|_{\infty} < \text{TOL}_1 \quad \text{and} \quad \|M_{\text{residual}}\|_{\infty} < \text{TOL}_2 \quad (72)$$

where: F_{residual} – residual force vector

M_{residual} – residual moment vector

TOL_1 and TOL_2 – control tolerances

$\|F_{\text{residual}}\|_{\infty}$ - indicates the component of F_{residual} with the highest absolute value.

The default control tolerance value of 0.1 was used for all powder compaction analyses.

It is important to note that residual checking convergence criterion does have its limitations. It is not recommended if the CENTROID parameter (element quantities, such as stresses and strains are computed at the centroid of the element) is used, as the residuals and reactions are not calculated accurately [74]. Also, in problems involving free thermal expansion, there are no reaction forces, thus the residual checking cannot be used [74]. However, for the analyses of powder compaction the ALL POINT (element quantities calculated at each integration point of the element) parameter as opposed to the CENTROID parameter was used, and all simulation problems consisted of the fully constrained FE models with no thermal effects. Thus, the selection of residual checking convergence criterion is fully justified.

6.0 Simulation Results and Discussion of Friction-Assisted Compaction of Cylindrical Parts

In total, three cases of cylindrically shaped parts were analysed, with descending order of compact height-to-diameter ratio, h/d , of 1.50, 1.00, and 0.50, with constant diameter of 12 mm. The use of different height-to-diameter ratio, h/d , was employed to study the effects of compact height on final density distribution. For each case study the velocity ratio of the die to the upper-punch, v_{die}/v_{u-p} , was varied from 0 to 0.5 (0 to 1.0 for compact h/d of 1.50), in increments of 0.1, to study its effect on density distribution over the height of the compact.

All three cases were analyzed using two sets of material properties provided by: (i) Pavier and Doremus [10, 84], based on triaxial cell tests conducted on granular powder material; and (ii) Koval'chenko [54], based on simple-compression tests conducted on pre-sintered powder compact specimens. Further, both corresponding sets were specifically selected to see how their simulation results compare with each other. Specifically, it was interesting to see how the results match using the material properties derived from the granular powder material - set (i), and those derived using the pre-sintered powder compact specimens - set (ii). In addition, it is important to note that the material properties provided by Pavier and Doremus - set (i), were specifically chosen due to their consistency and fullness, where both the material properties and the variable friction coefficient expression were derived using identical iron-based powder composition, thus, providing the complete database for simulation analysis. Also, since Shima and Oyane's powder yield criterion [106] was derived based on porous material, the material properties derived using the pre-sintered powder compact specimens (porous material) – set (ii), provided by Koval'chenko, were selected. In addition, all cases were analysed using two frictional conditions by employing the constant friction coefficient of 0.1 and the variable friction coefficient expressed by equation (64). For a summary of simulation runs, see Table 19.

After completion of all simulation runs, relative density data was extracted based on which an average relative density value was evaluated per each mm of the final compact height. This data was then plotted as the average relative density versus location of each mm of the compact height for all corresponding values of v_{die}/v_{u-p} and compact h/d . Further, using

equation (45), proposed by Shima et al. [101, 102], density variation, ρ_{var} , for each corresponding v_{die}/v_{u-p} , was evaluated and plotted for all three cases of compact h/d.

Table 19. Summary of simulation runs for all cylindrical parts.

| Using material properties provided by Pavier and Doremus | | | | | | |
|---|------|------|------|--------------------------------------|------|------|
| Friction coefficient | 0.1 | | | $\mu(\sigma_n, v_r)$, equation (64) | | |
| Compact height-to-diameter ratio, h/d | 1.50 | 1.00 | 0.50 | 1.50 | 1.00 | 0.50 |
| Number of simulation runs, one for each corresponding velocity ratio, v_{die}/v_{u-p} , 0 to 0.5 (1.0 for h/d = 1.50), in increments of 0.1 | 11 | 6 | 6 | 11 | 6 | 6 |
| Total number of simulation runs | 23 | | | 23 | | |
| Using material properties provided by Koval'chenko | | | | | | |
| Friction coefficient | 0.1 | | | $\mu(\sigma_n, v_r)$, equation (64) | | |
| Compact height-to-diameter ratio, h/d | 1.50 | 1.00 | 0.50 | 1.50 | 1.00 | 0.50 |
| Number of simulation runs, one for each corresponding velocity ratio, v_{die}/v_{u-p} , 0 to 0.5 (1.0 for h/d = 1.50), in increments of 0.1 | 11 | 6 | 6 | 11 | 6 | 6 |
| Total number of simulation runs | 23 | | | 23 | | |

6.1 Effect of Die to Upper-Punch Velocity Ratio on Density Gradient of Cylindrical Parts with Compact Height-to-Diameter Ratio of 1.50

6.1.1 Using Material Properties Provided by Pavier and Doremus [10, 84]

From Figure 57, representing density distribution over the point location of each mm of the compact height using constant friction coefficient, a symmetric trend in density distribution is observed over the compact height when the die to the upper-punch velocity ratio, v_{die}/v_{u-p} , is varied from 0 to 1.0. When v_{die}/v_{u-p} increases from 0 to 0.5, a decrease in density gradient is observed, identical to the trend recorded in experimental study conducted by Canta and Frunza [15], and simulation analyses conducted by Wang et al. [115]. However, upon further increase of v_{die}/v_{u-p} from 0.5 to 1.0, a reverse trend is observed, with gradual increase in overall density gradient over the compact height; similar trend was also recorded by Wang et al. [115]. The maximum density gradient is observed at v_{die}/v_{u-p} of 0 and 1.0, with an equivalent difference between the recorded maximum and minimum relative density values of 0.0273. Further, the minimum density gradient is observed at v_{die}/v_{u-p} of 0.5, with the smallest difference between

the maximum and minimum relative density values of 0.0111. Thus, as v_{die}/v_{u-p} deviates from a value of 0.5, an increase in density gradient over the compact height is observed.

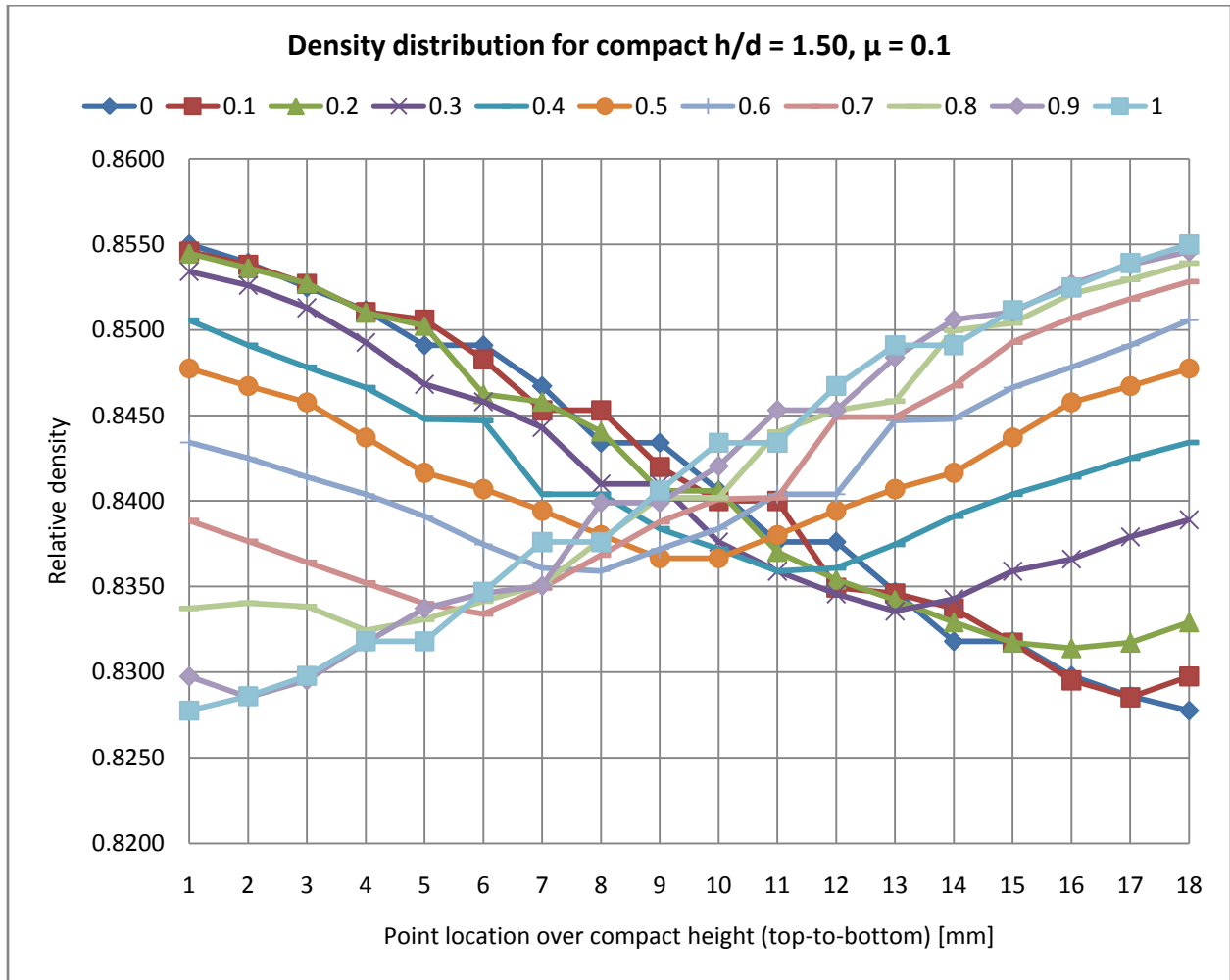


Figure 57. Density distribution over the compact height for a range of v_{die}/v_{u-p} values, using constant friction coefficient.

In Figure 58, derived using the variable friction coefficient, a higher overall gradient in density is observed, roughly twice of that obtained using the constant friction coefficient shown in Figure 57, for all corresponding values of v_{die}/v_{u-p} . Similar symmetric trend in density distribution over the compact height, with respect to Figure 57, is observed, however, with a gradual increase in density gradient for the second half of the corresponding velocity ratio range, $0.5 \leq v_{die}/v_{u-p} \leq 1.0$. Again, the maximum density gradient is observed at v_{die}/v_{u-p} of 0 and 1.0, with corresponding difference between the maximum and minimum relative density values of 0.0510 and 0.0690, respectively. The minimum density gradient is observed at v_{die}/v_{u-p} of 0.5,

with the smallest difference between the maximum and minimum relative density values of 0.0257.

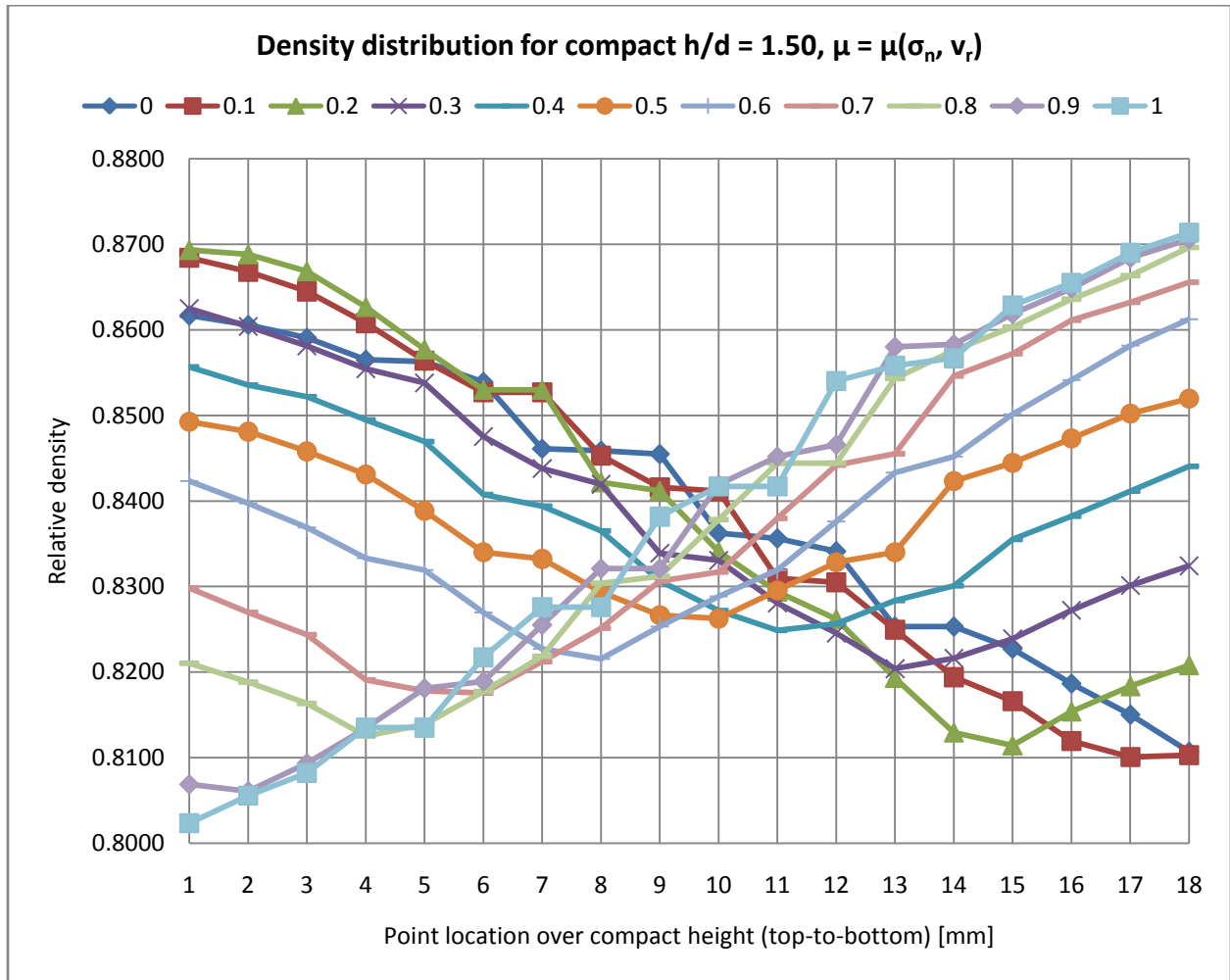


Figure 58. Density distribution over the compact height for a range of v_{die}/v_{u-p} values, using variable friction coefficient, $\mu(\sigma_n, v_r)$.

The density variation, encompassing the overall cross-sectional area of the compact, is observed to be the lowest at v_{die}/v_{u-p} of 0.5, when using both constant and variable friction coefficients; see Figures 59 and 60. When using constant friction coefficient, the density variation followed a symmetrical trend, with an initial value of 0.00937 at v_{die}/v_{u-p} of 0, declining to a value of 0.00454 at v_{die}/v_{u-p} of 0.5. Similar to density distribution trend, observed in Figures 57 and 58, the density variation was found to increase upon increasing or decreasing v_{die}/v_{u-p} from 0.5. When using variable friction coefficient, the density variation was observed to initially increase from 0.01693 to 0.02086 for corresponding v_{die}/v_{u-p} of 0 to 0.2, respectively, and then

decline to a minimum value of 0.01022 at v_{die}/v_{u-p} of 0.5. Based on Figures 59 and 60, for all corresponding values of v_{die}/v_{u-p} , the overall density variation obtained using the variable friction coefficient is roughly double of that obtained using the constant friction coefficient.

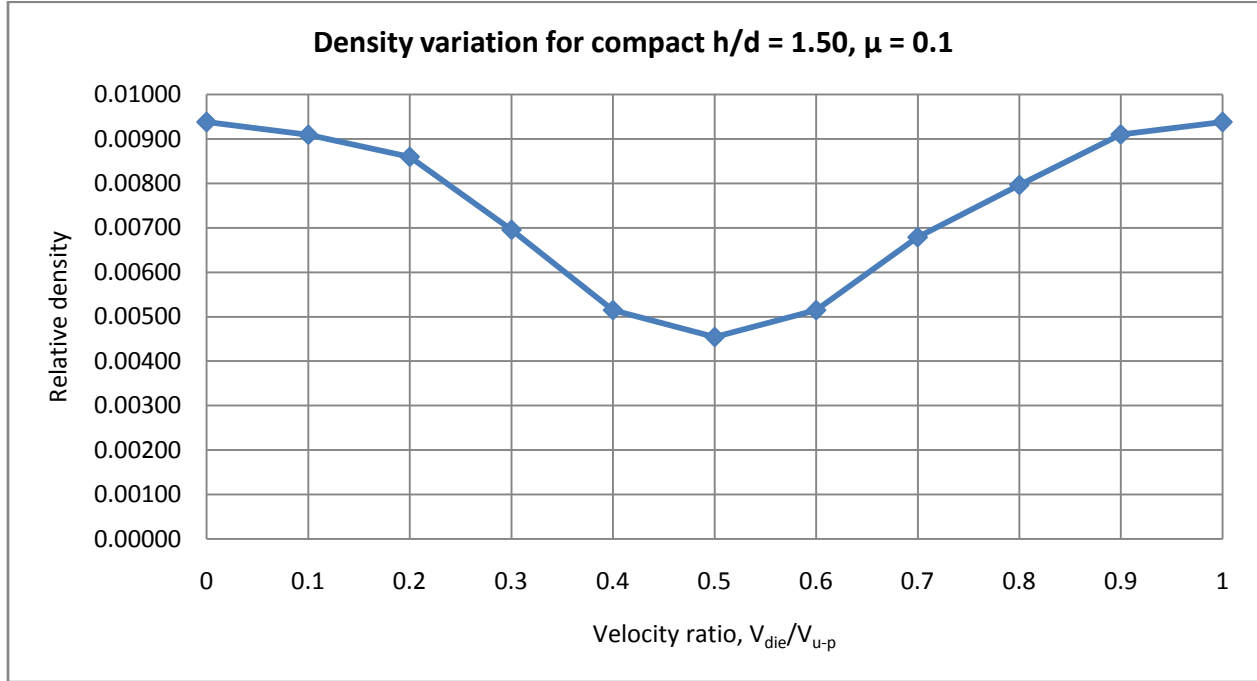


Figure 59. Density variation with respect to v_{die}/v_{u-p} , using constant friction coefficient.

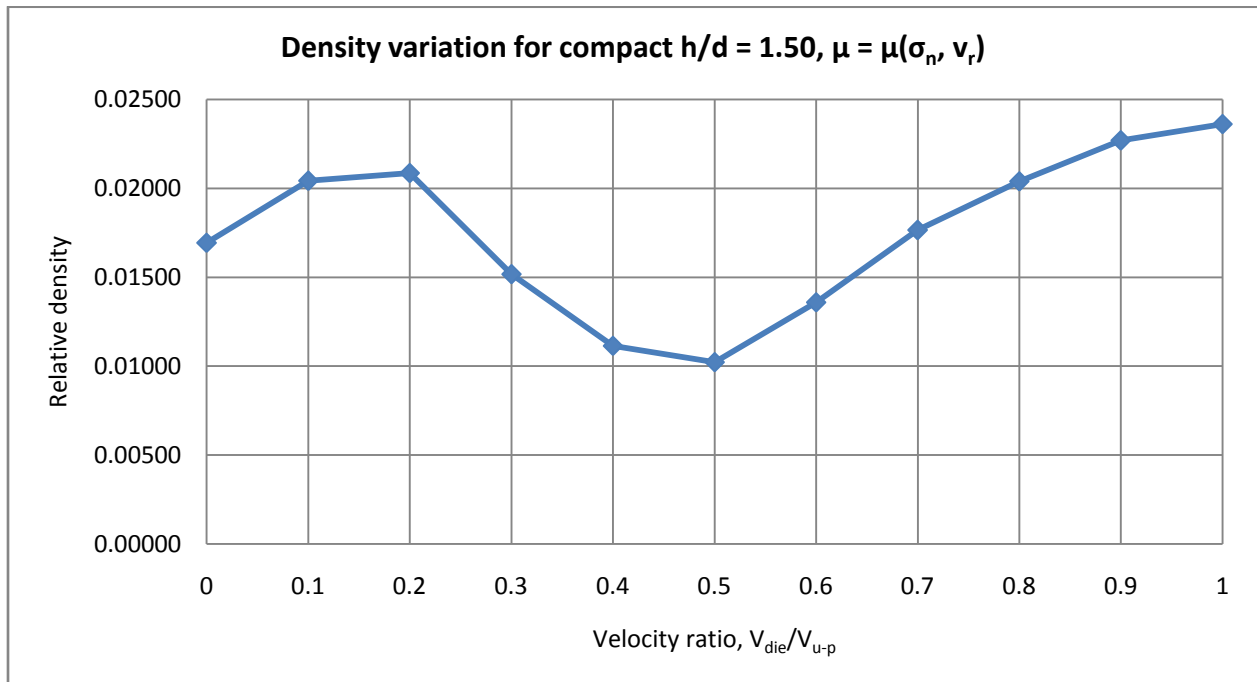


Figure 60. Density variation with respect to v_{die}/v_{u-p} , using variable friction coefficient, $\mu(\sigma_n, v_r)$.

6.1.2 Using Material Properties Provided by Koval'chenko [54]

Based on observation, Figure 61 shows identical trend to the one observed in Figure 57, where a symmetrical trend in density distribution is observed over the compact height upon variation of v_{die}/v_{u-p} from 0 to 1.0. An overall decrease and increase in density gradient is observed upon increase of v_{die}/v_{u-p} from 0 to 0.5 and from 0.5 to 1.0, respectively. The maximum density gradient is observed at v_{die}/v_{u-p} of 0 and 1.0, with an equivalent difference between the maximum and minimum relative density values of 0.0261. The minimum density gradient is observed at v_{die}/v_{u-p} of 0.5, with the smallest difference between the maximum and minimum relative density values of 0.0107.

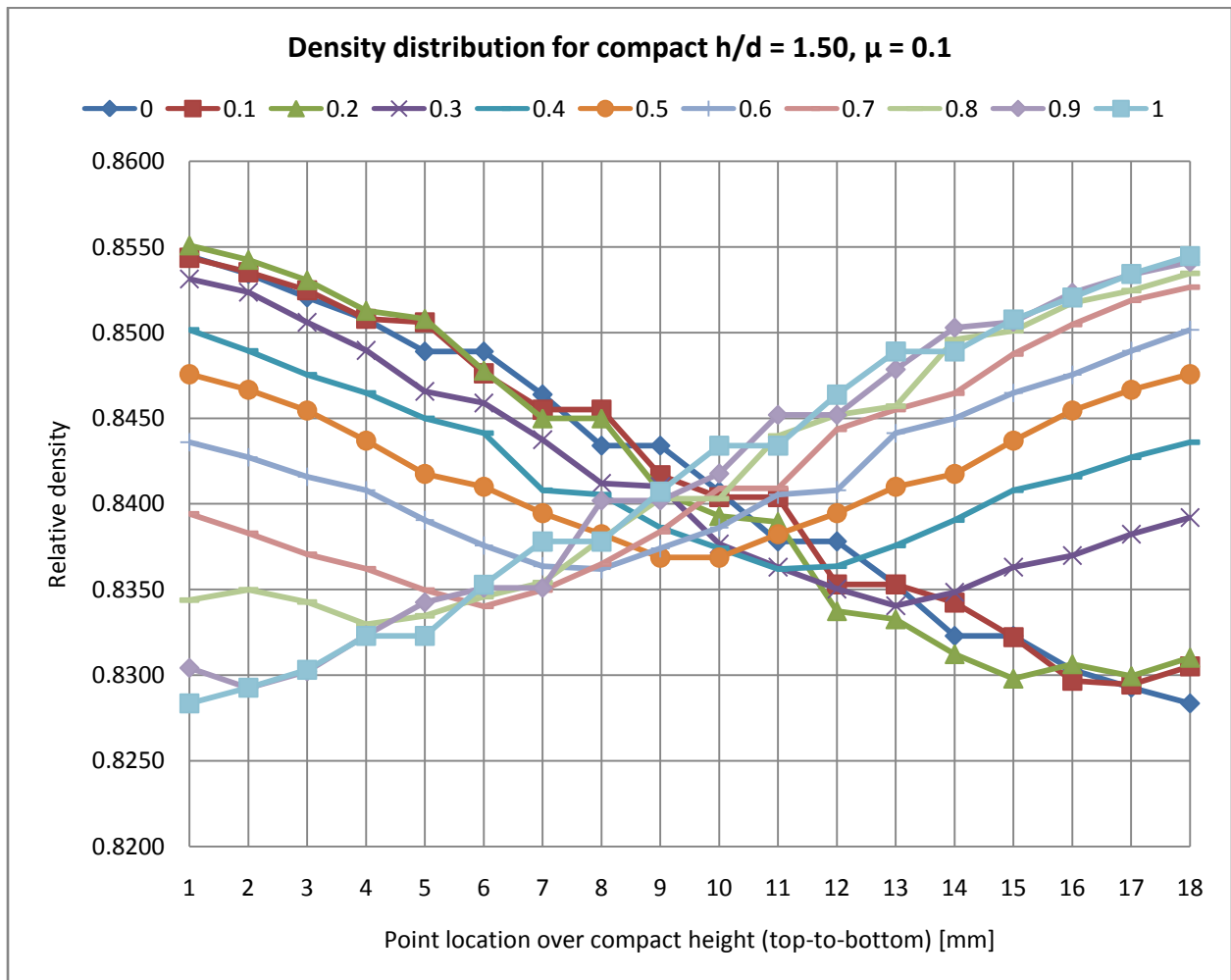


Figure 61. Density distribution over the compact height for a range of v_{die}/v_{u-p} values, using constant friction coefficient.

In Figure 62, derived using the variable friction coefficient, a higher overall gradient in density is observed, roughly twice of that obtained using the constant friction coefficient shown in Figure 61, for all corresponding values of v_{die}/v_{u-p} . Again, a symmetric trend in density distribution over the compact height is observed, however, with a gradual increase in density gradient for the second half of the corresponding velocity ratio range, $0.5 \leq v_{die}/v_{u-p} \leq 1.0$. Again, the maximum density gradient is observed at v_{die}/v_{u-p} of 0 and 1.0, with corresponding difference between the maximum and minimum relative density values of 0.0486 and 0.0652, respectively. The minimum density gradient is observed at v_{die}/v_{u-p} of 0.5, with the smallest difference between the maximum and minimum relative density values of 0.0247.

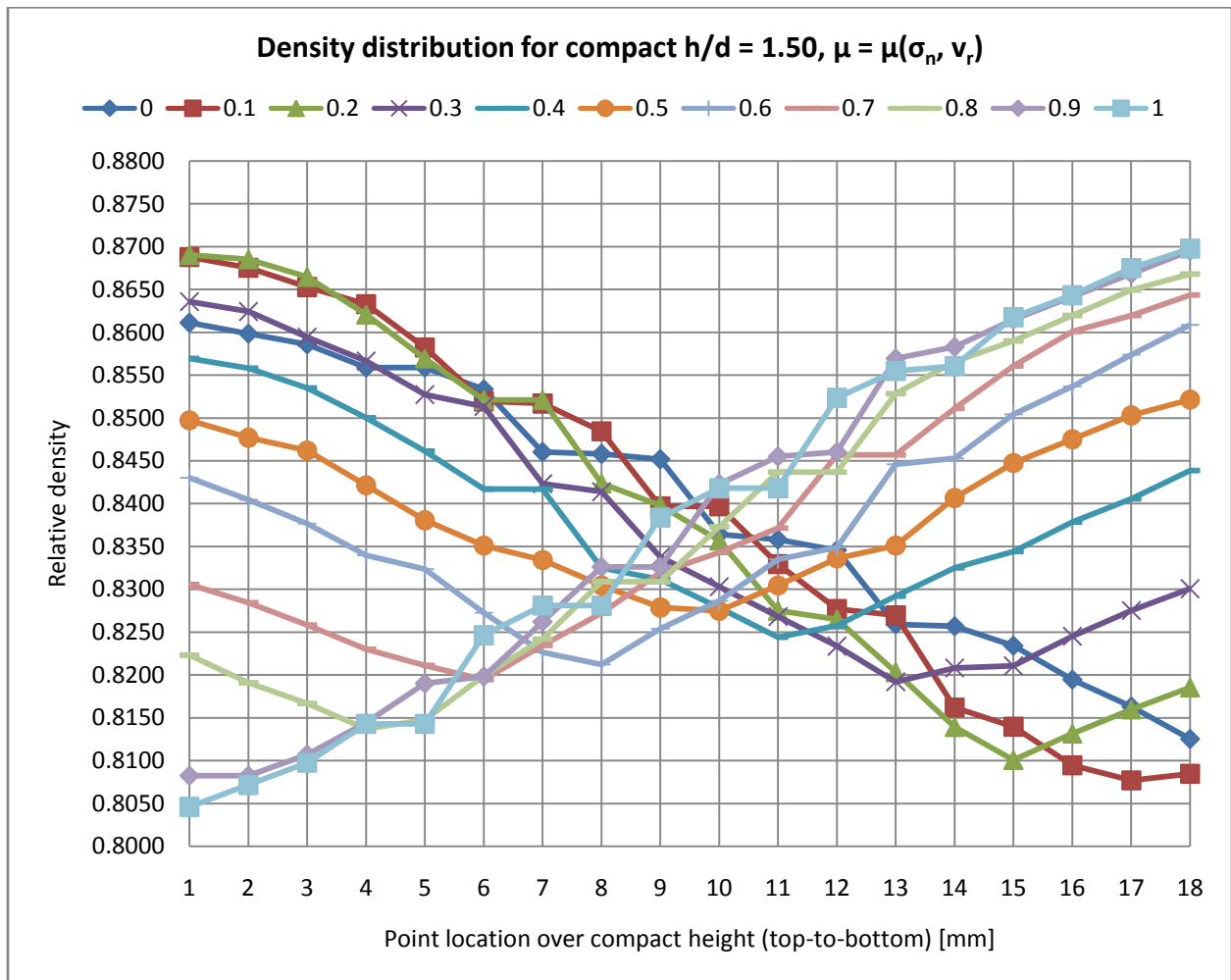


Figure 62. Density distribution over the compact height for a range of v_{die}/v_{u-p} values, using variable friction coefficient, $\mu(\sigma_n, v_r)$.

Using Koval'chenko's material properties, the density variation is observed to be the lowest at v_{die}/v_{u-p} of 0.5, when using both constant and variable friction coefficients; see Figure 63 and 64. Upon using constant friction coefficient, the density variation was relatively steady for v_{die}/v_{u-p} range 0 to 0.2, with corresponding value of 0.00897, 0.00872, and 0.00947, respectively, declining to its minimum value of 0.00439 at v_{die}/v_{u-p} of 0.5. When using variable friction coefficient, the density variation was observed to initially increase from 0.01630 to 0.02168 for corresponding v_{die}/v_{u-p} values of 0 to 0.1, respectively, and then decline to a minimum value of 0.00980 at v_{die}/v_{u-p} of 0.5. Based on Figures 63 and 64, for all corresponding values of v_{die}/v_{u-p} , the overall density variation obtained using the variable friction coefficient is roughly double of that obtained using the constant friction coefficient.

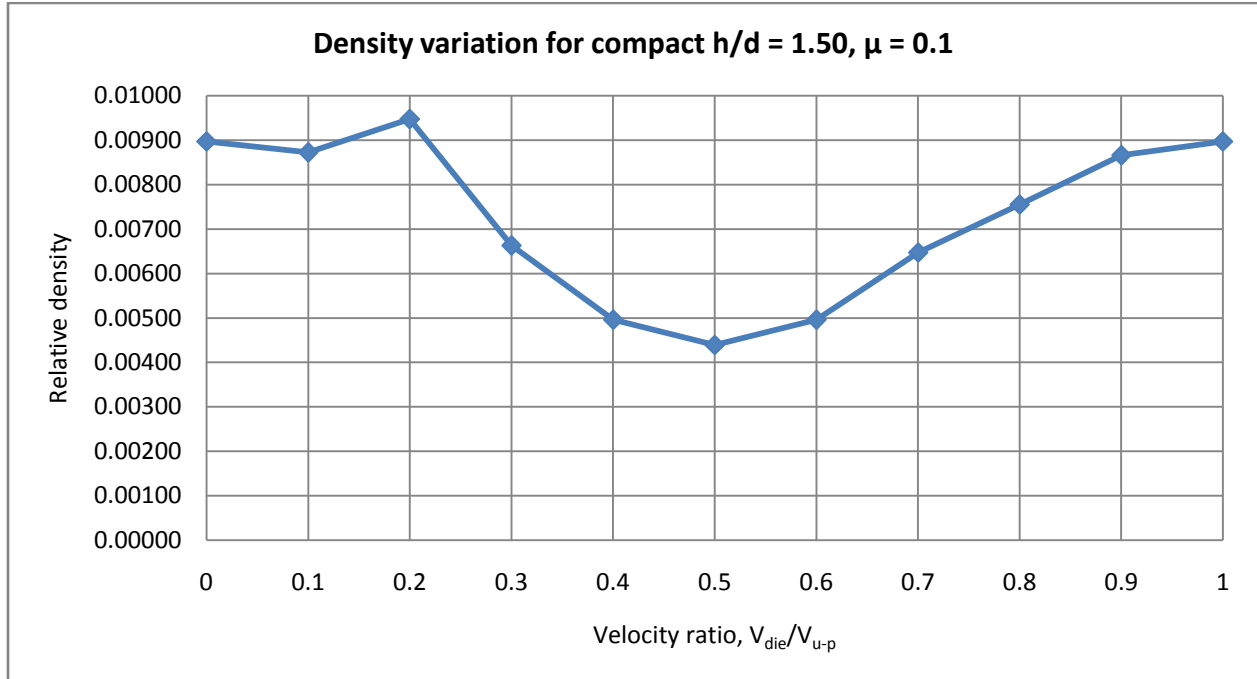


Figure 63. Density variation with respect to v_{die}/v_{u-p} , using constant friction coefficient.

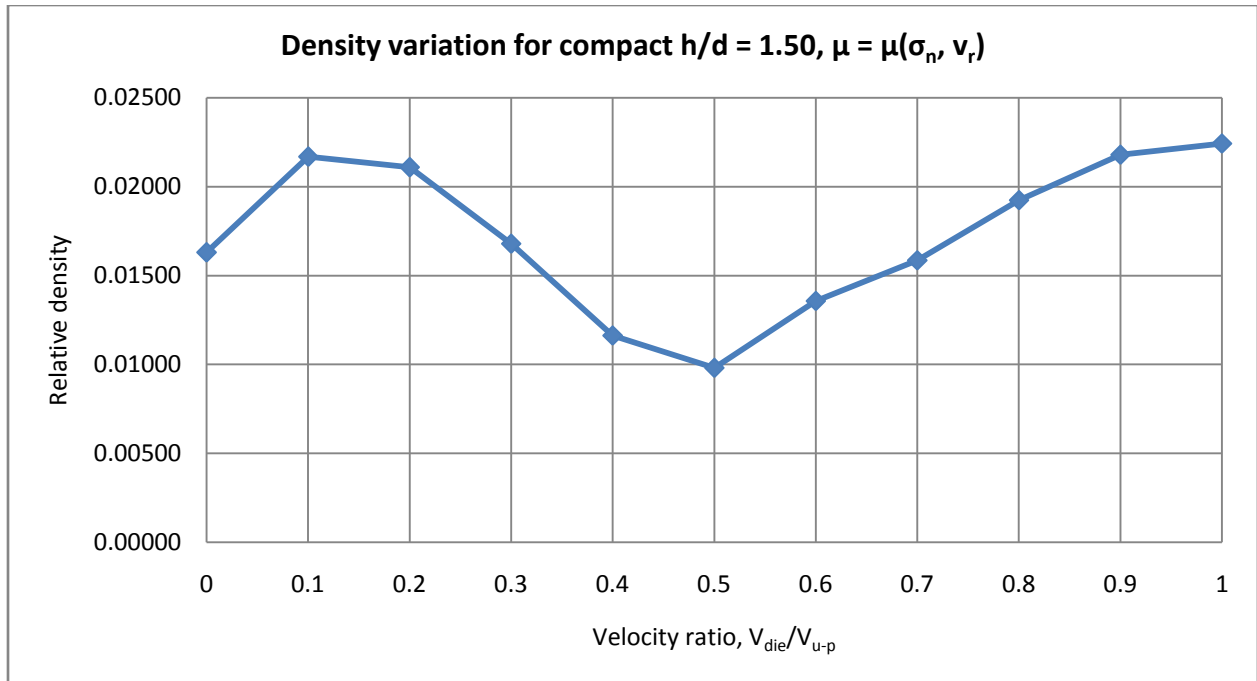


Figure 64. Density variation with respect to v_{die}/v_{u-p} , using variable friction coefficient, $\mu(\sigma_n, v_r)$.

6.2 Effect of Die to Upper-Punch Velocity Ratio on Density Gradient of Cylindrical Parts with Compact Height-to-Diameter Ratio of 1.00

6.2.1 Using Material Properties Provided by Pavier and Doremus [10, 84]

From Figure 65, similar trend in density distribution is observed as for the compact height-to-diameter ratio, h/d , of 1.50, however, with a smaller overall density gradient for v_{die}/v_{u-p} values of 0 to 0.5; refer to Figure 57. A gradual decrease in density gradient is observed upon increasing v_{die}/v_{u-p} from 0 to 0.5. The maximum density gradient is observed at v_{die}/v_{u-p} of 0, with a difference between the maximum and minimum relative density values of 0.0170. Further, the minimum density gradient is observed at v_{die}/v_{u-p} of 0.5, with the smallest difference between the maximum and minimum relative density values of 0.0058. It is important to note that the overall decline in density gradient with respect to the results obtained for h/d of 1.50 is due to the reduction in friction area imposed by the die-wall. Similar decrease was observed in experimental studies conducted by Canta and Frunza [15].

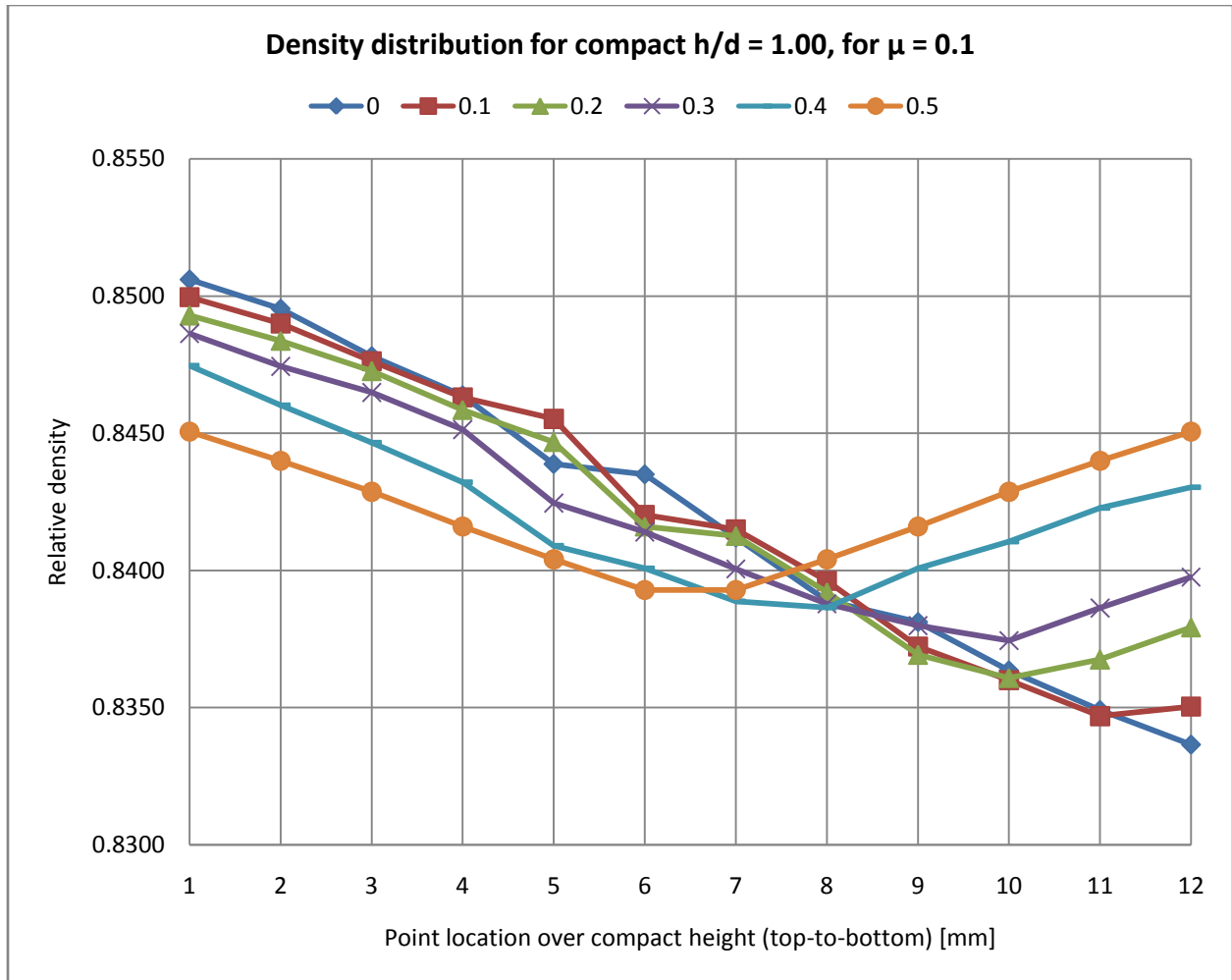


Figure 65. Density distribution over the compact height for a range of v_{die}/v_{u-p} values, using constant friction coefficient.

In Figure 66, derived using the variable friction coefficient, a higher overall gradient in density is observed, roughly twice of that obtained using the constant friction coefficient shown in Figure 65, for all corresponding values of v_{die}/v_{u-p} . A gradual decrease in density gradient is observed upon increasing v_{die}/v_{u-p} from 0 to 0.5. Again, the maximum density gradient is observed at v_{die}/v_{u-p} of 0, with a difference between the maximum and minimum relative density values of 0.0308. The minimum density gradient is observed at v_{die}/v_{u-p} of 0.5, with the smallest difference between the maximum and minimum relative density values of 0.0140.

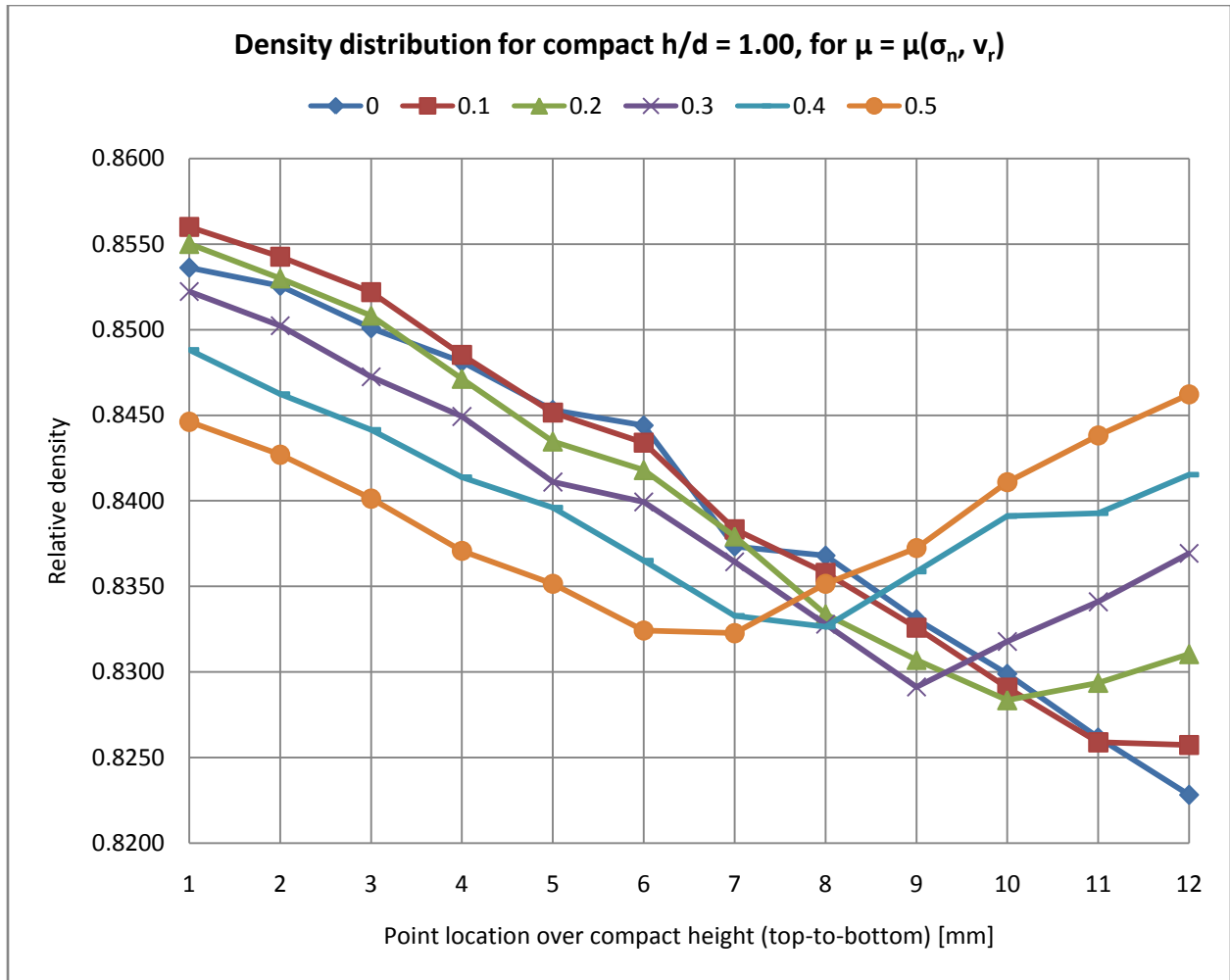


Figure 66. Density distribution over the compact height for a range of v_{die}/v_{u-p} values, using variable friction coefficient, $\mu(\sigma_n, v_r)$.

The density variation, for h/d of 1.00, was found to be the lowest at v_{die}/v_{u-p} of 0.5, when using both constant and variable friction coefficients; see Figure 67 and 68. When using constant friction coefficient the density variation was observed to decrease with an initial value of 0.00615 at v_{die}/v_{u-p} of 0, declining to a minimum value of 0.00333 at v_{die}/v_{u-p} of 0.5. When using variable friction coefficient, the density variation was observed to decrease starting from 0.01138 at v_{die}/v_{u-p} of 0.1, to a minimum value of 0.00767 at v_{die}/v_{u-p} of 0.5. As observed in previous cases, for all corresponding values of v_{die}/v_{u-p} , the overall density variation obtained using the variable friction coefficient is roughly double of that obtained using the constant friction coefficient.

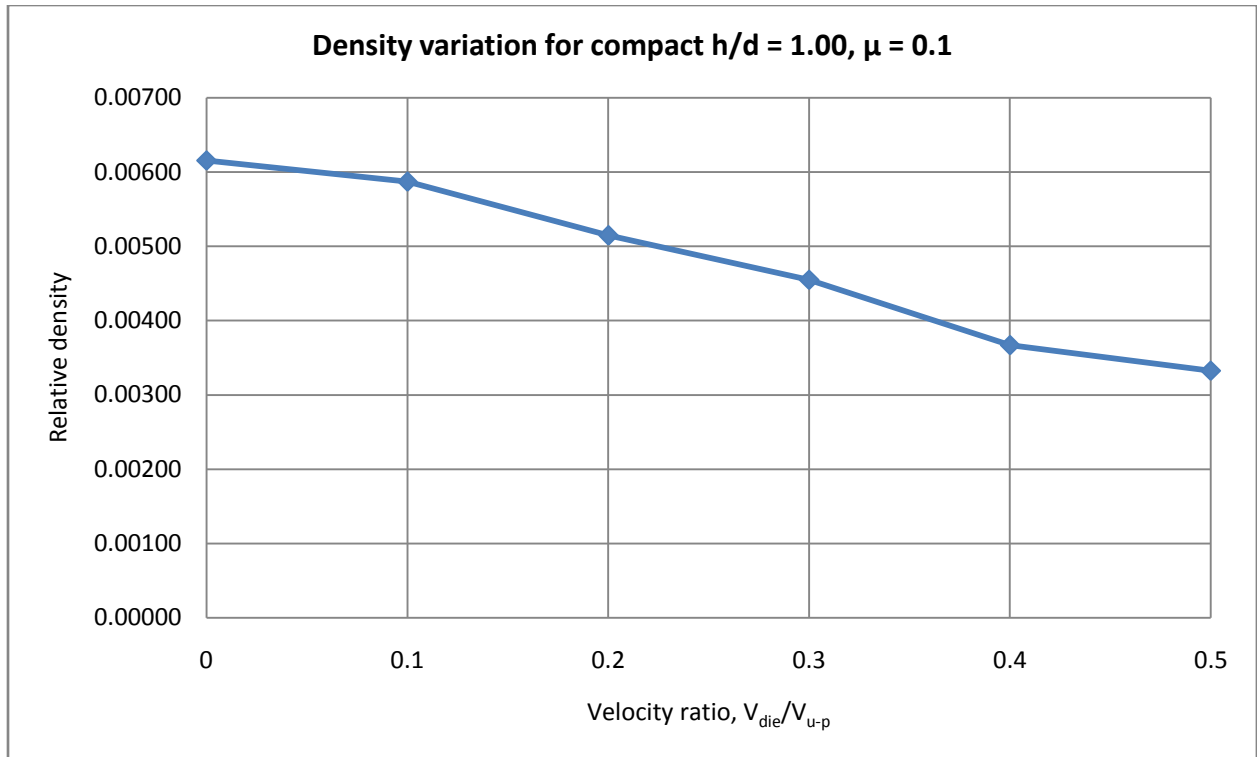


Figure 67. Density variation with respect to v_{die}/v_{u-p} , using constant friction coefficient.

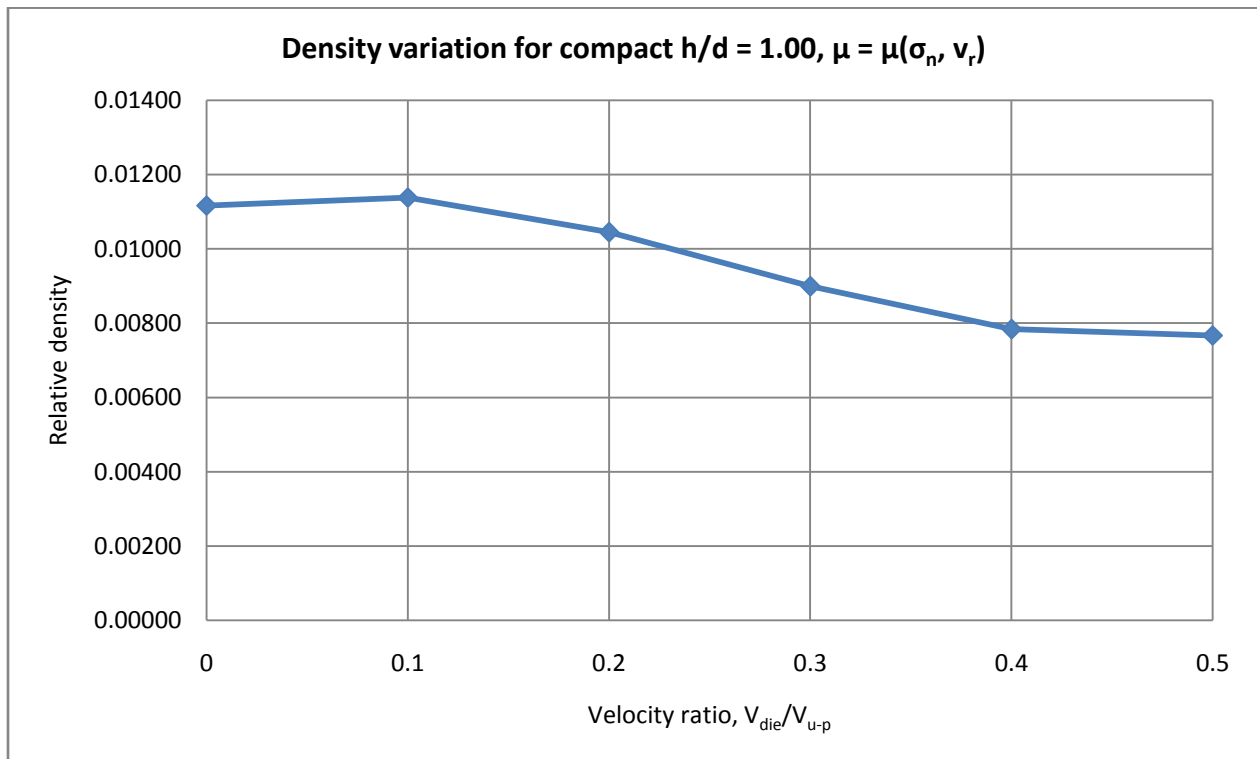


Figure 68. Density variation with respect to v_{die}/v_{u-p} , using variable friction coefficient, $\mu(\sigma_n, v_r)$.

6.2.2 Using Material Properties Provided by Koval'chenko [54]

In Figure 69, similar trend in density distribution is observed as for the compact h/d of 1.50, however, with a smaller overall density gradient for v_{die}/v_{u-p} values of 0 to 0.5; refer to Figure 61. Further, a gradual decrease in density gradient is observed upon increasing v_{die}/v_{u-p} from 0 to 0.5. The maximum density gradient is observed at v_{die}/v_{u-p} of 0, with a difference between the maximum and minimum relative density values of 0.0164. The minimum density gradient is observed at v_{die}/v_{u-p} of 0.5, with the smallest difference between the maximum and minimum relative density values of 0.0054. Furthermore, the overall observed decline in density gradient with respect to the results obtained for h/d of 1.50 is due to the reduction in friction area imposed by the die-wall. Again, similar decrease was observed in experimental studies conducted by Canta and Frunza [15].

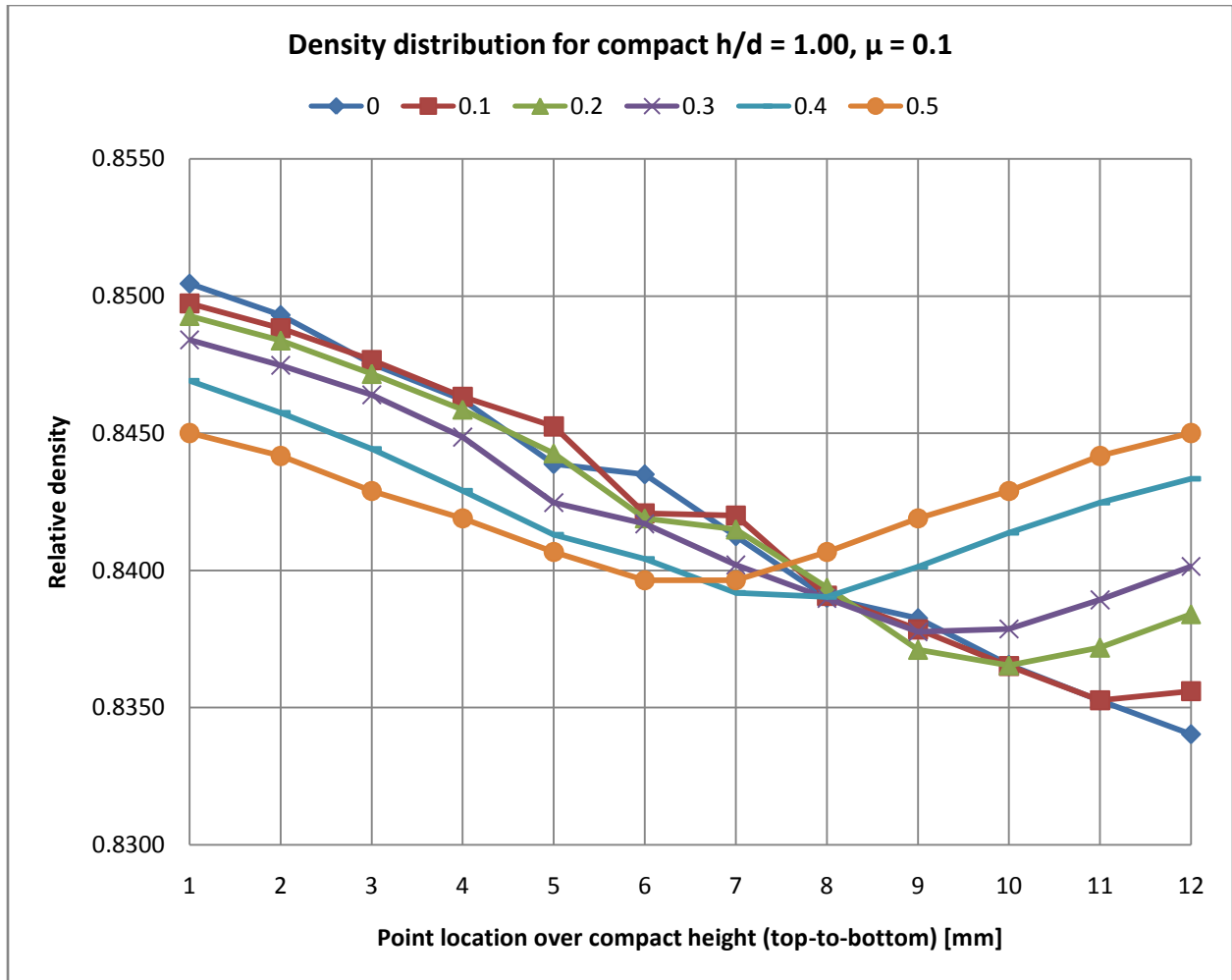


Figure 69. Density distribution over the compact height for a range of v_{die}/v_{u-p} values, using constant friction coefficient.

In Figure 70, derived using the variable friction coefficient, a higher overall gradient in density is observed, roughly twice of that obtained using the constant friction coefficient shown in Figure 69, for all corresponding values of v_{die}/v_{u-p} . In general, similar trend in density distribution over the compact height is observed. Once again, the maximum density gradient is observed at v_{die}/v_{u-p} of 0, with a difference between the maximum and minimum relative density values of 0.0297. The minimum density gradient is observed at v_{die}/v_{u-p} of 0.5, with the smallest difference between the maximum and minimum relative density values of 0.0134.

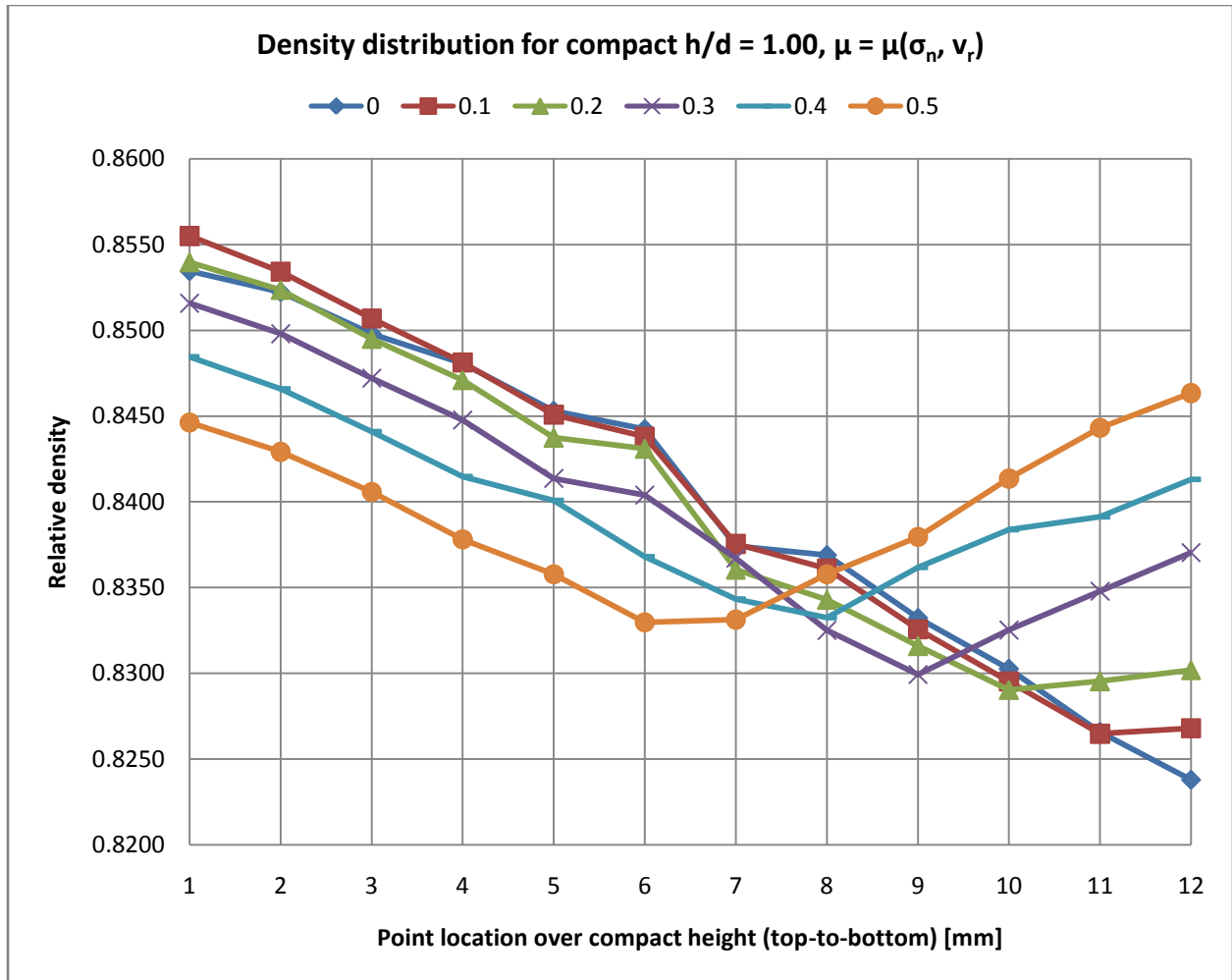


Figure 70. Density distribution over the compact height for a range of v_{die}/v_{u-p} values, using variable friction coefficient, $\mu(\sigma_n, v_r)$.

Again, the density variation is observed to be the lowest at v_{die}/v_{u-p} of 0.5, when using both constant and variable friction coefficients; see Figure 71 and 72. When using constant friction, the density variation was observed to decrease with initial value of 0.00596 at v_{die}/v_{u-p} of 0, declining to a minimum value of 0.00317 at v_{die}/v_{u-p} of 0.5. When using variable friction coefficient, the density variation was observed to decrease starting from 0.01106 at v_{die}/v_{u-p} of 0.1, to a minimum value of 0.00737 at v_{die}/v_{u-p} of 0.5. Similar to previous cases, for all corresponding values of v_{die}/v_{u-p} , the overall density variation obtained using the variable friction coefficient is roughly double of that obtained using the constant friction coefficient.

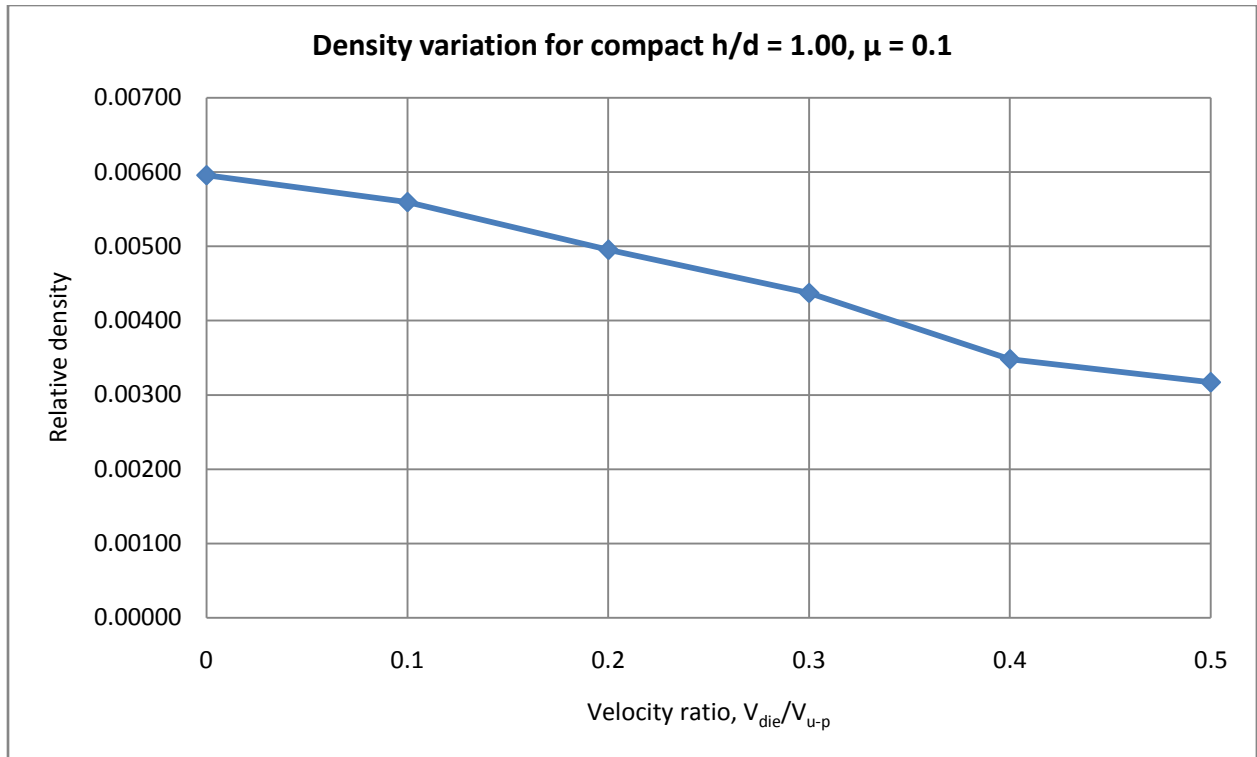


Figure 71. Density variation with respect to v_{die}/v_{u-p} , using constant friction coefficient.

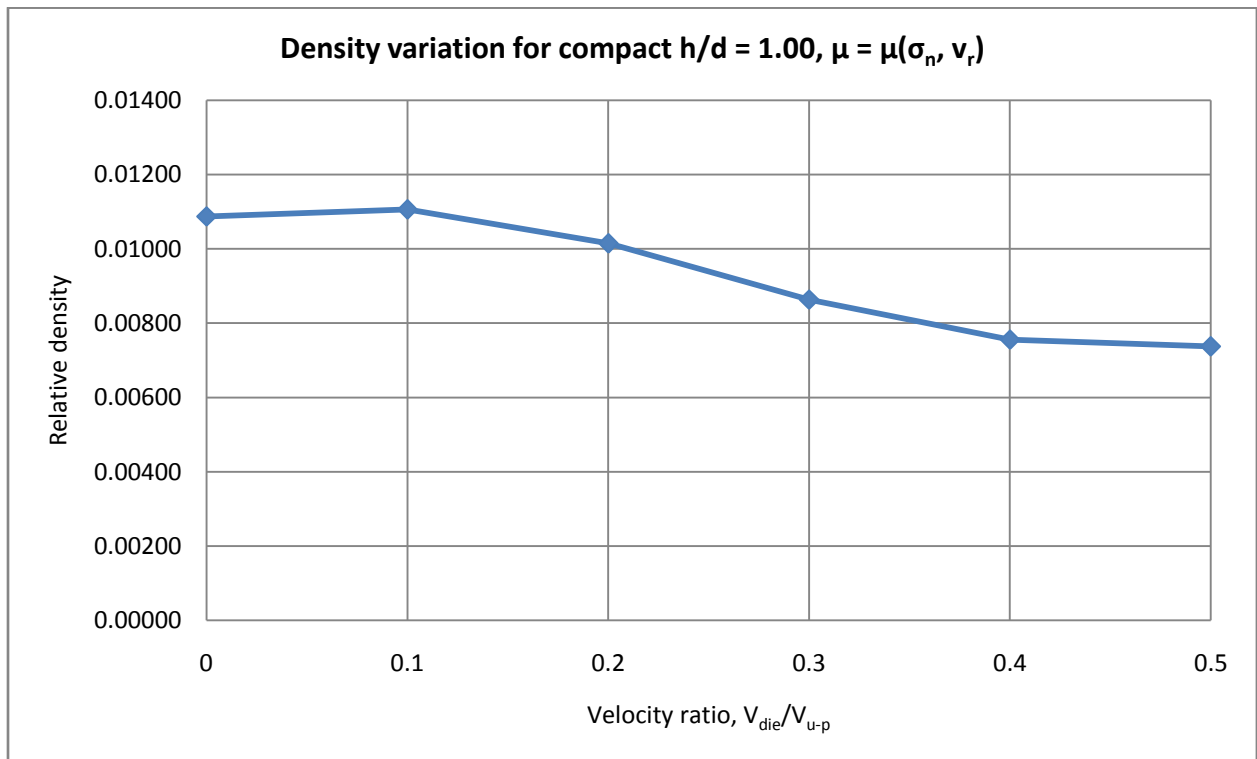


Figure 72. Density variation with respect to v_{die}/v_{u-p} , using variable friction coefficient, $\mu(\sigma_n, v_r)$.

6.3 Effect of Die to Upper-Punch Velocity Ratio on Density Gradient of Cylindrical Parts with Compact Height-to-Diameter Ratio of 0.50

6.3.1 Using Material Properties Provided by Pavier and Doremus [10, 84]

In Figure 73, similar trend in density distribution is observed as for the compact h/d of 1.50 and 1.00, however, with the lowest overall density gradient for v_{die}/v_{u-p} values of 0 to 0.5; refer to Figures 57 and 65. Again, a decrease in density gradient is observed upon increasing v_{die}/v_{u-p} from 0 to 0.5. Overall, the relative density gradient is insignificant with respect to the trends observed for compact h/d of 1.50 and 1.00. The maximum density gradient is observed to be at v_{die}/v_{u-p} of 0, with a minor difference between the maximum and minimum relative density values of 0.0055. Even more so, the minimum density gradient, observed at v_{die}/v_{u-p} of 0.5, has a negligible difference between the maximum and minimum relative density values of 0.0021. It is important to note that the additional decline in density gradient in comparison to the compact h/d of 1.00, is due to a further reduction in friction area imposed by the die-wall. Similar decrease was observed in experimental studies conducted by Canta and Frunza [15].

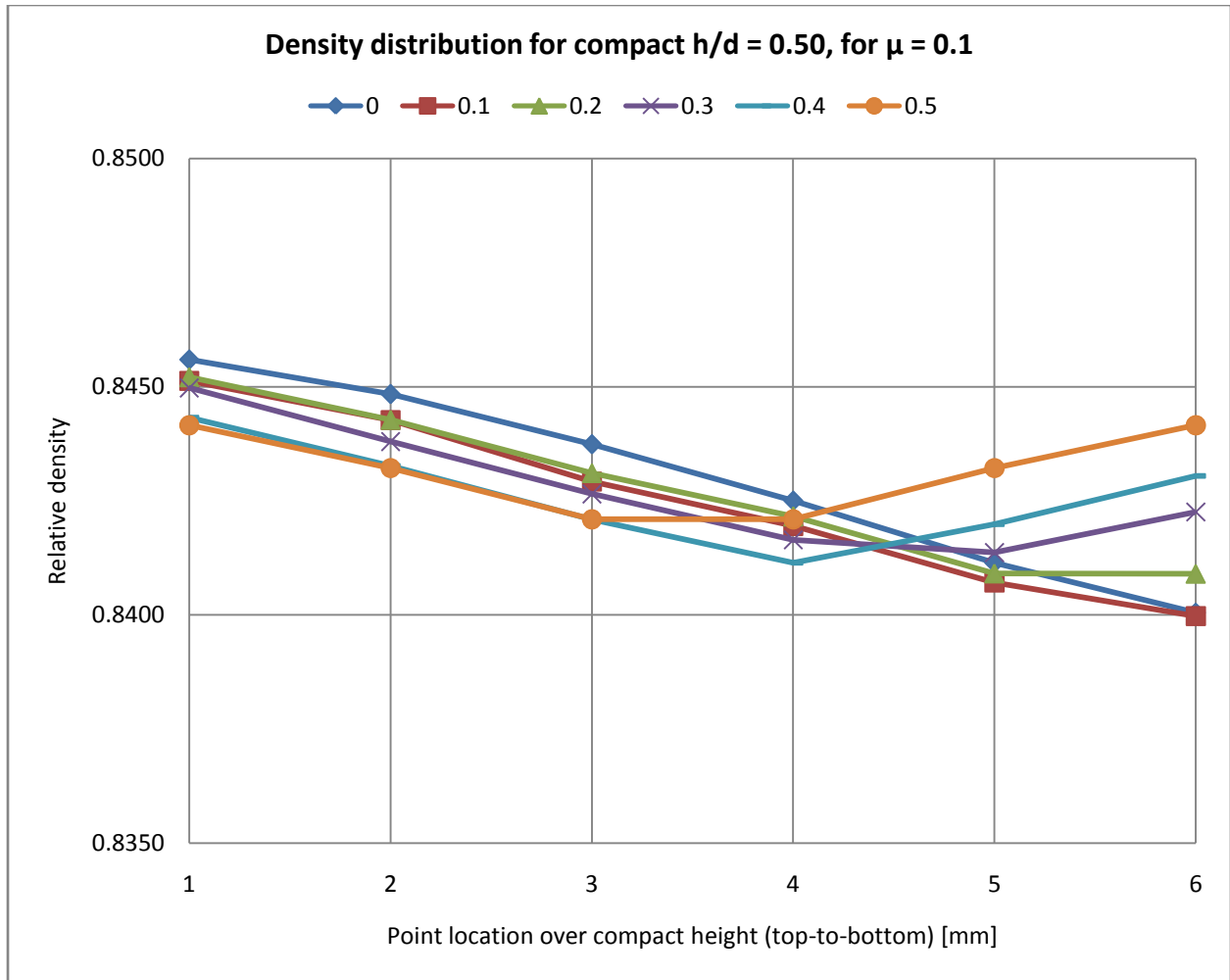


Figure 73. Density distribution over the compact height for a range of v_{die}/v_{u-p} values, using constant friction coefficient.

In Figure 74, derived using the variable friction coefficient, a higher overall gradient in density is observed, roughly twice of that obtained using the constant friction coefficient shown in Figure 73, for all corresponding values of v_{die}/v_{u-p} . Nevertheless, the overall density gradient is relatively minor in comparison to the results obtained for the higher compact h/d values; refer to Figures 58 and 66. Overall, similar trend in density distribution over the compact height is observed. Again, the maximum density gradient is observed at v_{die}/v_{u-p} of 0, with a difference between the maximum and minimum relative density values of 0.0093. The minimum density gradient observed at v_{die}/v_{u-p} of 0.5 has a minor difference between the maximum and minimum relative density values of 0.0049.

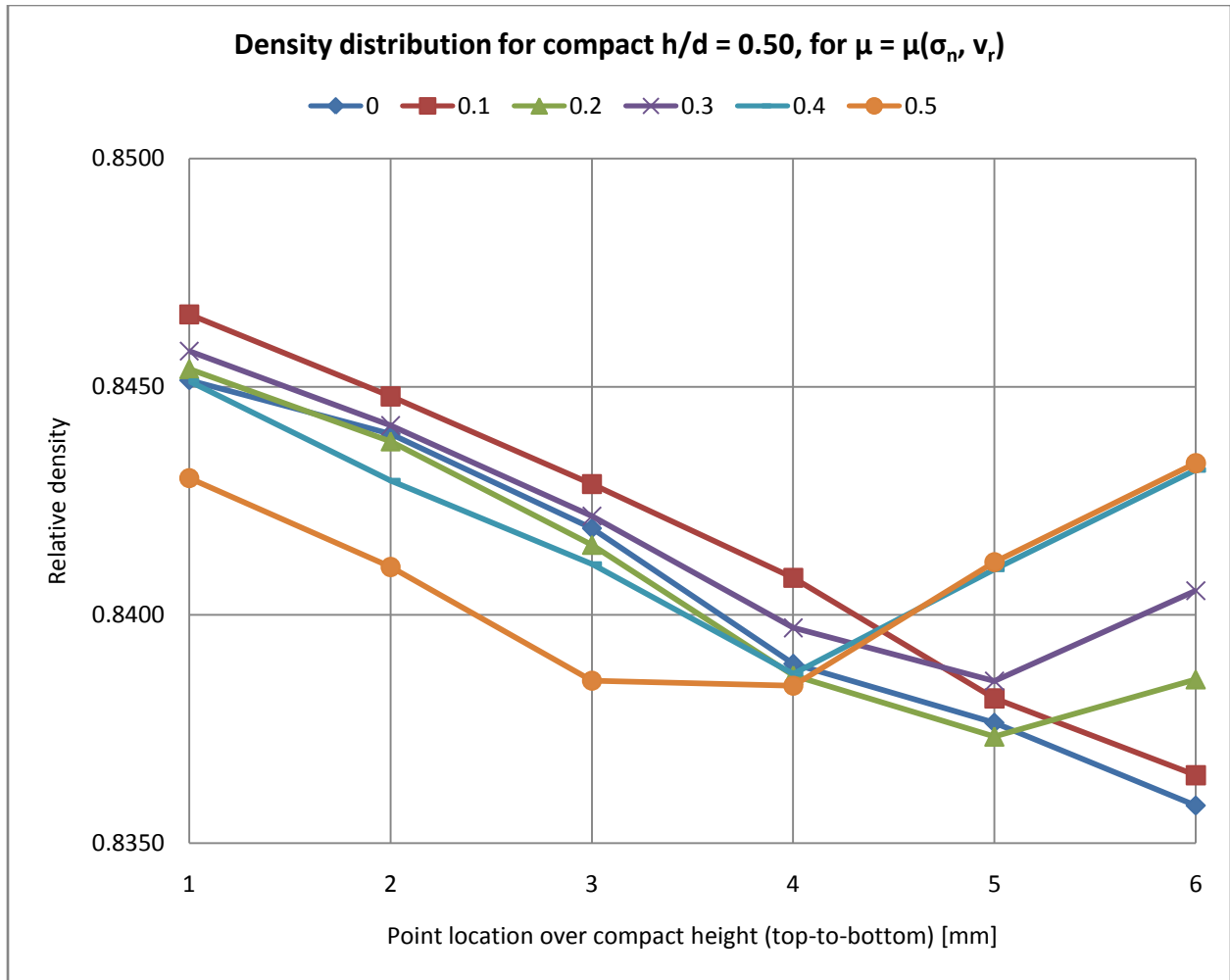


Figure 74. Density distribution over the compact height for a range of v_{die}/v_{u-p} values, using variable friction coefficient, $\mu(\sigma_n, v_r)$.

As observed in the previous two case studies, for the compact h/d of 1.50 and 1.00, the least density variation is observed at v_{die}/v_{u-p} of 0.5, when using both constant and variable friction coefficients; see Figures 75 and 76. When using constant friction coefficient, the evaluated density variation was observed to decrease with an initial value of 0.00330 at v_{die}/v_{u-p} of 0, declining to a minimum value of 0.00198 at v_{die}/v_{u-p} of 0.5. However, when using variable friction coefficient, the density variation was observed to decrease from initial value of 0.00632 at v_{die}/v_{u-p} of 0, to a minimum value of 0.00457 at v_{die}/v_{u-p} of 0.4. Similar to previous cases, for all corresponding values of v_{die}/v_{u-p} , the overall density variation obtained using the variable friction coefficient is roughly double of that obtained using the constant friction coefficient.

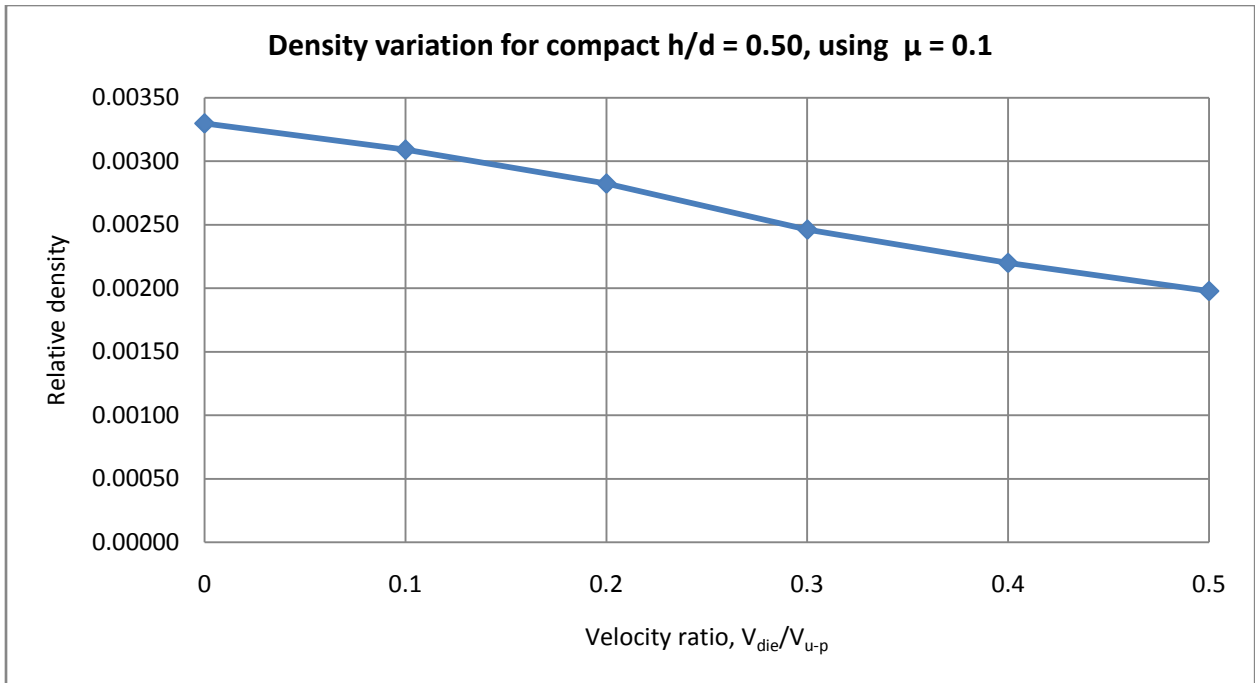


Figure 75. Density variation with respect to v_{die}/v_{u-p} , using constant friction coefficient.

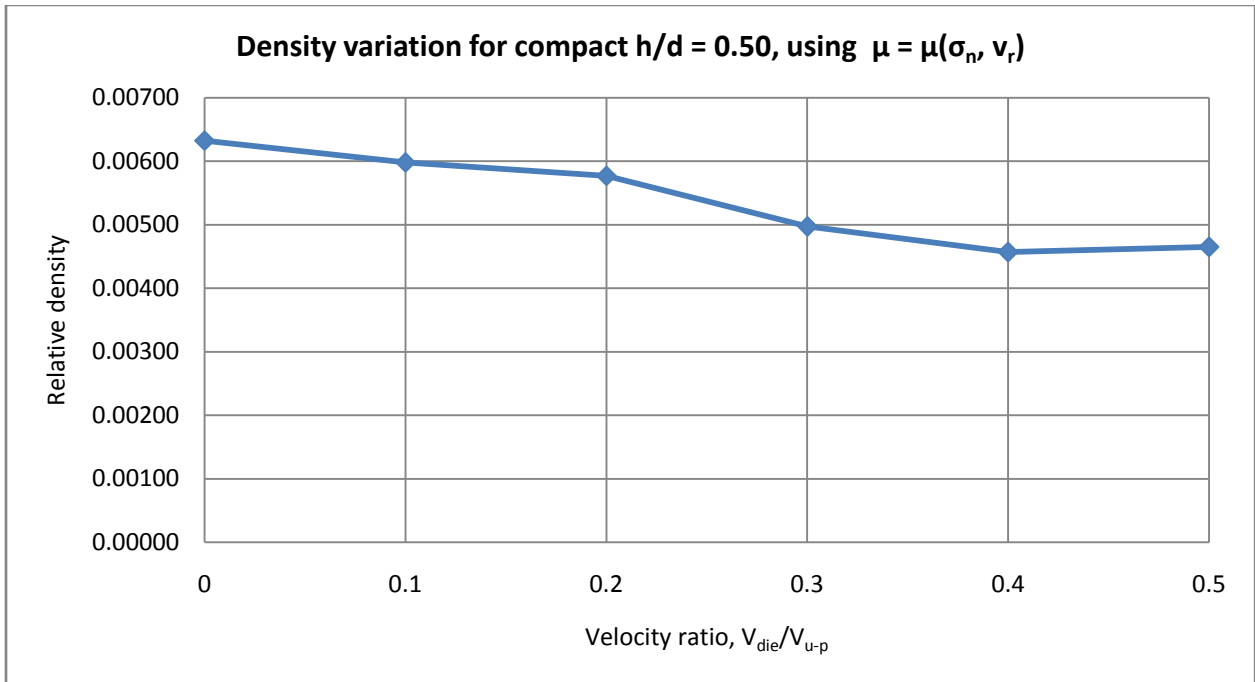


Figure 76. Density variation with respect to v_{die}/v_{u-p} , using variable friction coefficient, $\mu(\sigma_n, v_r)$.

6.3.2 Using Material Properties Provided by Koval'chenko [54]

In Figure 77, similar trend in density distribution is observed as for compact h/d of 1.50 and 1.00, however, with the lowest overall density gradient for v_{die}/v_{u-p} values of 0 to 0.5; refer to Figures 63 and 69. Again, a decrease in density gradient is observed upon increasing v_{die}/v_{u-p} from 0 to 0.5. Overall, the relative density gradient is insignificant with respect to the trends observed for compact h/d of 1.50 and 1.00. The maximum density gradient is observed at v_{die}/v_{u-p} of 0, with a minor difference between the maximum and minimum relative density values of 0.0055. Further, the minimum density gradient observed at v_{die}/v_{u-p} of 0.5 has a negligible difference between the maximum and minimum relative density values of 0.0020. It is important to note that the additional decline in density gradient in comparison to the compact h/d of 1.00, is due to a further reduction in friction area imposed by the die-wall. Similar decrease was observed in experimental studies conducted by Canta and Frunza [15].

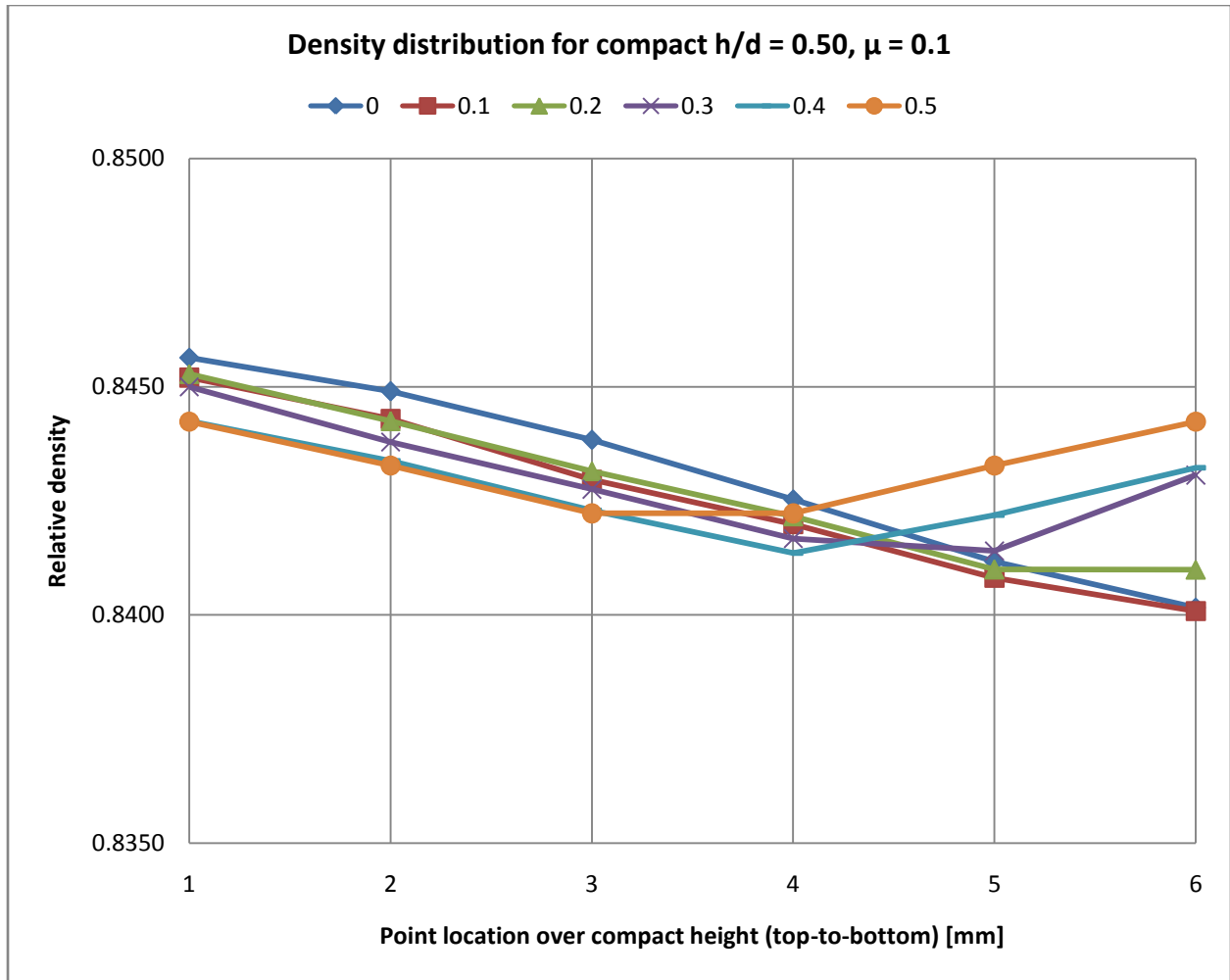


Figure 77. Density distribution over the compact height for a range of v_{die}/v_{u-p} values, using constant friction coefficient.

In Figure 78, derived using the variable friction coefficient, a higher overall gradient in density is observed, roughly twice of that obtained using the constant friction coefficient shown in Figure 77, for all corresponding values of v_{die}/v_{u-p} . Nevertheless, the overall density gradient is relatively minor in comparison to the results obtained for the higher compact h/d values; refer to Figures 62 and 70. Overall, similar trend in density distribution over the compact height is observed. Again, the maximum density gradient is observed at v_{die}/v_{u-p} of 0, with a difference between the maximum and minimum relative density values of 0.0089. The minimum density gradient is observed at v_{die}/v_{u-p} of 0.5 and has a minor difference between the maximum and minimum relative density values of 0.0046.

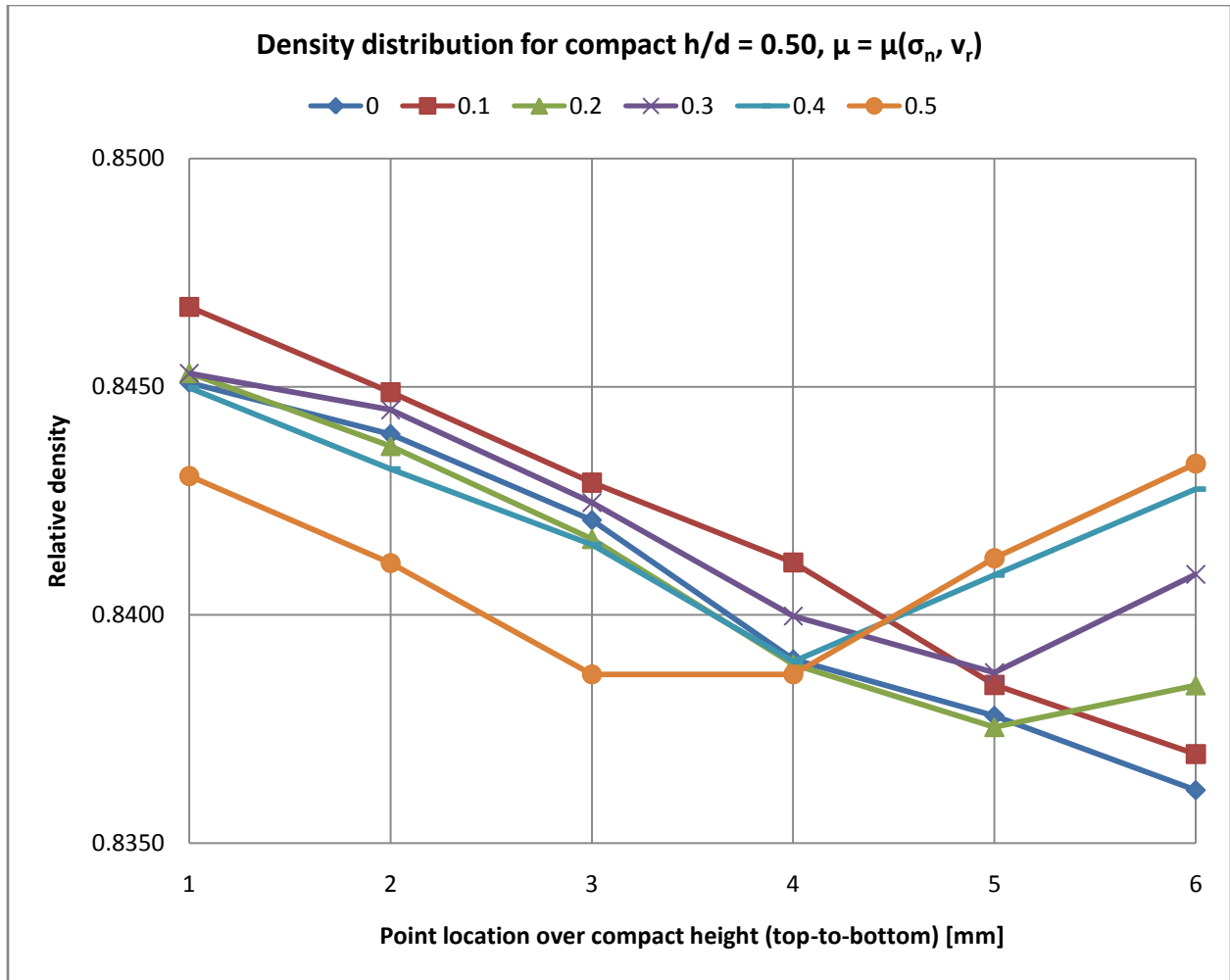


Figure 78. Density distribution over the compact height for a range of v_{die}/v_{u-p} values, using variable friction coefficient, $\mu(\sigma_n, v_r)$.

As observed in the previous two case studies, for the compact h/d of 1.50 and 1.00, the density variation is observed to be the lowest at v_{die}/v_{u-p} of 0.5, when using both constant and variable friction coefficients; see Figures 79 and 80. When using constant friction coefficient, the density variation was observed to decrease with an initial value of 0.00327 at v_{die}/v_{u-p} of 0, declining to a minimum value of 0.00194 at v_{die}/v_{u-p} of 0.5. However, when using variable friction coefficient, the density variation was observed to decrease from a value of 0.00616 at v_{die}/v_{u-p} of 0, to a minimum value of 0.00449 at v_{die}/v_{u-p} of 0.4. Similar to previous cases, for all corresponding values of v_{die}/v_{u-p} , the overall density variation obtained using the variable friction coefficient is roughly double of that obtained using the constant friction coefficient.

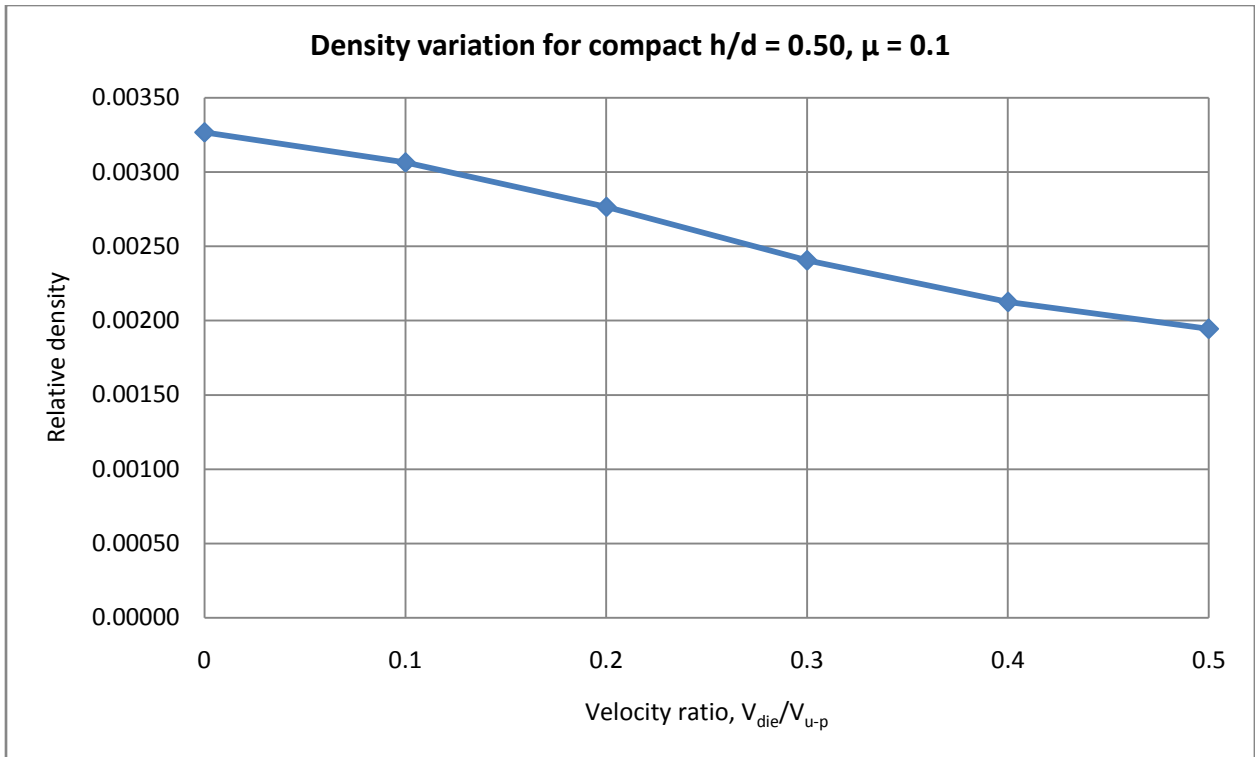


Figure 79. Density variation with respect to v_{die}/v_{u-p} , using constant friction coefficient.

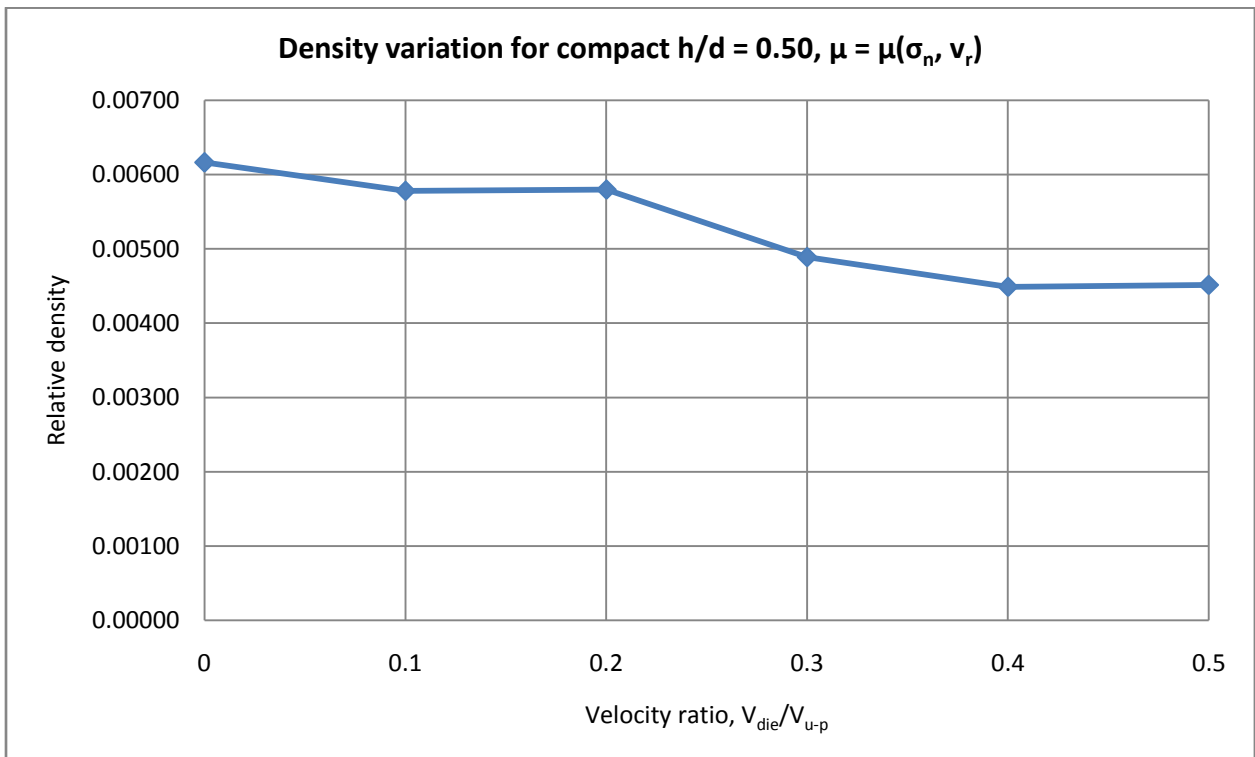


Figure 80. Density variation with respect to v_{die}/v_{u-p} , using variable friction coefficient, $\mu(\sigma_n, v_r)$.

6.4 Summary and Discussion of Results

Based on the overall observations the average relative density distribution over the final compact height is more uniform at the die-to-upper-punch velocity ratio, $v_{\text{die}}/v_{\text{u-p}}$, of 0.5, for all the cases of compact height-to-diameter ratio, h/d . Consequently, upon increase of $v_{\text{die}}/v_{\text{u-p}}$ from 0 to 0.5, a decrease in density gradient is observed, identical to the trend recorded in experimental study conducted by Canta and Frunza [15], and simulation analyses conducted by Wang et al. [115].

Likewise, the evaluated density variation, encompassing the overall cross-sectional area of the compact, is observed to be the lowest at $v_{\text{die}}/v_{\text{u-p}}$ of 0.5, for all cases of the compact h/d . Upon increase of $v_{\text{die}}/v_{\text{u-p}}$ from 0 to 0.5, a decrease in density variation is observed. Thus, as $v_{\text{die}}/v_{\text{u-p}}$ increases from 0 to 0.5, a decrease in both the non-uniformity of density distribution over the compact height and the evaluated density variation is observed, hence, confirming an overall decline in density gradient over the compact height.

Upon further increase of $v_{\text{die}}/v_{\text{u-p}}$ from 0.5 to 1.0, for the compact h/d of 1.50, a reverse trend in density distribution is observed, with a gradual increase in non-uniformity of density distribution over the compact height. Likewise, the evaluated density variation is observed to follow a reverse trend, where an increase in density variation is observed. Thus, upon further increase of $v_{\text{die}}/v_{\text{u-p}}$ from 0.5 to 1.0, the overall density gradient is observed to increase; similar observations were made using simulation analyses conducted by Wang et al. [115]. However, the presented results beyond $v_{\text{die}}/v_{\text{u-p}}$ of 0.5 are inconclusive as no experimental data is available to support these results.

Moreover, as the compact h/d decreases, from 1.50 to 0.50, the overall density distribution becomes more uniform and the evaluated density variation is observed to decrease, generally resulting in a lower density gradient over the compact height for each corresponding $v_{\text{die}}/v_{\text{u-p}}$. Similar trend was observed in experimental studies conducted by Canta and Frunza [15], and other studies [24, 25, 27], where the overall heterogeneity over the compact height was observed to decrease upon reduction of compact h/d .

The decline in density gradient with compact h/d is explained due to the reduction in friction area imposed by the die-wall. A cylindrically shaped powder compact has two types of surfaces: (i) the punch face, with cross-sectional area constituted by its diameter, d ; and (ii) the sliding envelope surface, constituted by its height, h [24, 25]. Thus, as compact h/d decreases this leads to a reduction of the total friction area of the enclosed sliding envelope, upon which the opposing friction force is generated, in truth leading to the obstruction of uniform powder flow.

Further, it is important to note that when using the variable friction coefficient, $\mu(\sigma_n, v_r)$, as opposed to the constant value of 0.1, the overall gradient in density distribution and the evaluated density variation is observed to roughly double for all the corresponding values of compact h/d and v_{die}/v_{u-p} . More importantly, the observed higher density gradient, achieved using the variable friction coefficient, compares better with experimental data reported by Canta and Frunza [15], as opposed to the results obtained using the constant friction coefficient, which are found to slightly underestimate the level of heterogeneity in the overall density distribution over the compact height.

Furthermore, for the compact h/d of 1.50, when using the constant friction coefficient, a symmetrical trend is observed in both the density distribution over the compact height and the evaluated density variation over the corresponding v_{die}/v_{u-p} range. However, upon using the variable friction coefficient, $\mu(\sigma_n, v_r)$, a gradual increase is observed in both the overall gradient in density distribution and the evaluated density variation for the second half of velocity ratio range, $0.5 \leq v_{die}/v_{u-p} \leq 1.0$. Nevertheless, it is important to note again that the presented results beyond v_{die}/v_{u-p} of 0.5 are inconclusive as no experimental data is available to support these results.

It is interesting to point out that a minor difference is observed in the overall results attained using the two sets of material properties provided by Pavier and Doremus, and Koval'chenko. In general, the obtained density distribution and the evaluated density variation using both of the material property sets are virtually indistinguishable, with a slightly lower values obtained upon using Koval'chenko's material properties, where the observed difference is of the order of magnitude of roughly 1.0^{-3} and 1.0^{-4} for the density distribution and the evaluated density variation, respectively, for each corresponding compact h/d and v_{die}/v_{u-p} .

A better visual observation can be made by consulting Appendices A to C, where illustration of the relative density distribution over the cross-sectional area of the cylindrical compacts is presented for each corresponding compact h/d and v_{die}/v_{u-p} . Regardless of the compact h/d , it is observed that for the initial velocity ratio, v_{die}/v_{u-p} , of 0, where the die is kept stationary, the resultant relative density distribution over the compact height corresponds to that of a single-action pressing. Due to the existence of the opposing friction force imposed by the stationary die-wall surface, the transmission of axial pressure, exerted by the upper-punch, is progressively diminished over the compact height, leaving the bottom of the compact, in the vicinity of the lower-punch, at a lower pressure level. Thus, as the pressing progresses, more powder accumulates in the vicinity of the moving upper-punch due to higher levels of pressure, further resulting in higher and lower levels of relative density at the top and the bottom of the compact, respectively. Consequently, at v_{die}/v_{u-p} , of 0, the final green compact has an uneven density distribution throughout its height; consult Appendices A to C.

Further, based on the observation, at v_{die}/v_{u-p} of 0, the highest and lowest density levels are located at the corner-edges of the upper-punch-and-die interface and the lower-punch-and-die interface, respectively. The highest density level at the top edge of the green powder compact may be explained due to the fact that the friction effect in the vicinity of the upper-punch-and-die interface is more significant. Due to the existence of friction at the powder-tool interfaces and the fact that the distance between corresponding tool surfaces at the vicinity of the top corner-edge is relatively small, higher accumulation of powder takes place in the surrounding volume as the pressing progresses. Similarly, the lowest level of relative density at the bottom corner-edge may be explained due to the gradual reduction in axial pressure over the compact height, leaving the bottom of the powder compact, particularly the corner-edge, exposed to the lowest pressure level.

Further, it is observed that upon moving the die, thus increasing v_{die}/v_{u-p} , the effect of the friction force imposed by the surface of the die is minimized. Upon increasing v_{die}/v_{u-p} from 0 to 0.5, the overall density gradient throughout the compact height is reduced, where the initial minimum relative density level, located at the bottom corner-edge, is gradually displaced upwards to the center of the cylinder's enveloping surface. Consequently, upon reaching v_{die}/v_{u-p} .

ρ of 0.5, the density distribution corresponds to that of a double-action pressing, where the highest relative density levels are observed to be located at the top and bottom of the compact, both roughly equivalent in magnitude. Moreover, the overall density distribution is observed to be symmetrical over the compact volume with respect to the cross-sectional plane Y-Z located at the center of the compact; see Appendices A to C.

The overall decrease in density gradient upon increase of $v_{\text{die}}/v_{\text{u-p}}$ from 0 to 0.5 is accounted to the active friction force imposed by the surface of the die. Upon increase of $v_{\text{die}}/v_{\text{u-p}}$, the die is displaced in the same direction as the upper-punch, thus causing a gradual reduction of the initially opposing friction force. Eventually, upon reaching $v_{\text{die}}/v_{\text{u-p}}$ of 0.5, the direction of the friction force is reversed, thus, diverting the roles of the friction force from the opposing to the assisting force in powder compaction.

However, upon further increase of $v_{\text{die}}/v_{\text{u-p}}$ from 0.5 to 1.0, for the compact h/d of 1.50, a reverse trend is observed where the density gradient is increased, such that the minimum density level, located at the center of the cylinder's enveloping surface, further progresses upwards towards the top corner-edge. Consequently, upon reaching $v_{\text{die}}/v_{\text{u-p}}$ of 1.0, the density distribution again corresponds to that of a single-action pressing; however, with the reversed locations of the higher and lower density levels, located at the bottom and the top edge of the powder compact, respectively. Thus, the overall resultant density distribution over the compact height obtained at $v_{\text{die}}/v_{\text{u-p}}$ of 1.0 is fully reversed with respect to the results obtained at $v_{\text{die}}/v_{\text{u-p}}$ of 0; similar observations were made using simulation analyses conducted by Wang et al. [115]. It is crucial to note that these results were obtained using the displacement control method, by assigning velocity to the appropriate tools, and not a force or distributed load method; refer to section 5.5.1.

The complete reverse in density distribution, may be explained by the fact that upon reaching $v_{\text{die}}/v_{\text{u-p}}$ of 1.0, both the upper-punch and the die are moving at the same velocity. As a result, the role of both punches is reversed, such that the lower-punch may be assumed as the active pressing tool, moving with respect to the stationary upper-punch and the die. Consequently, the direction of friction force, imposed by the die, is fully reversed, thus causing a reverse effect in density distribution. However, as already noted, the above argument must only be accepted

as a premise as no experimental data is available to support the presented results beyond v_{die}/v_{u-p} of 0.5.

Further, consulting Appendices A to C, it is observed that by decreasing compact h/d has a diminishing effect on the overall cross-sectional area exposed to the high density gradient. Particularly, at v_{die}/v_{u-p} of 0.5, the high density gradient area, concentrated along of the die edge, is observed to gradually shrink in size upon reduction of compact h/d from 1.50 to 0.50. This further explains why the evaluated density distribution over the compact height becomes more uniform and the evaluated density variation is observed to decrease upon reduction of the compact h/d . Similar trend was observed in experimental studies conducted by other researchers where an overall heterogeneity over the compact height was observed to decrease upon reduction of the compact h/d [24, 25, 27].

7.0 Simulation Results and Discussion of Compaction of a Multi-stepped Part

Before carrying out any simulation analyses to study the effect of velocity ratio on green density variation in the proposed multi-stepped part, the two-stage tool kinematics, adopted by Shima et al. [101, 102] for the occurrence of slip-crack defect study, were employed as a starting point; refer to Table 9. Using the proposed tool kinematics and the provided set of material properties, a preliminary simulation run was made to compare the obtained results for the density distribution and the occurrence of slip-crack defect to those presented by Shima et al.; refer to Figure 39. The results from the preliminary simulation run are presented in Figure 81, with the data obtained by Shima et al. presented in the brackets.

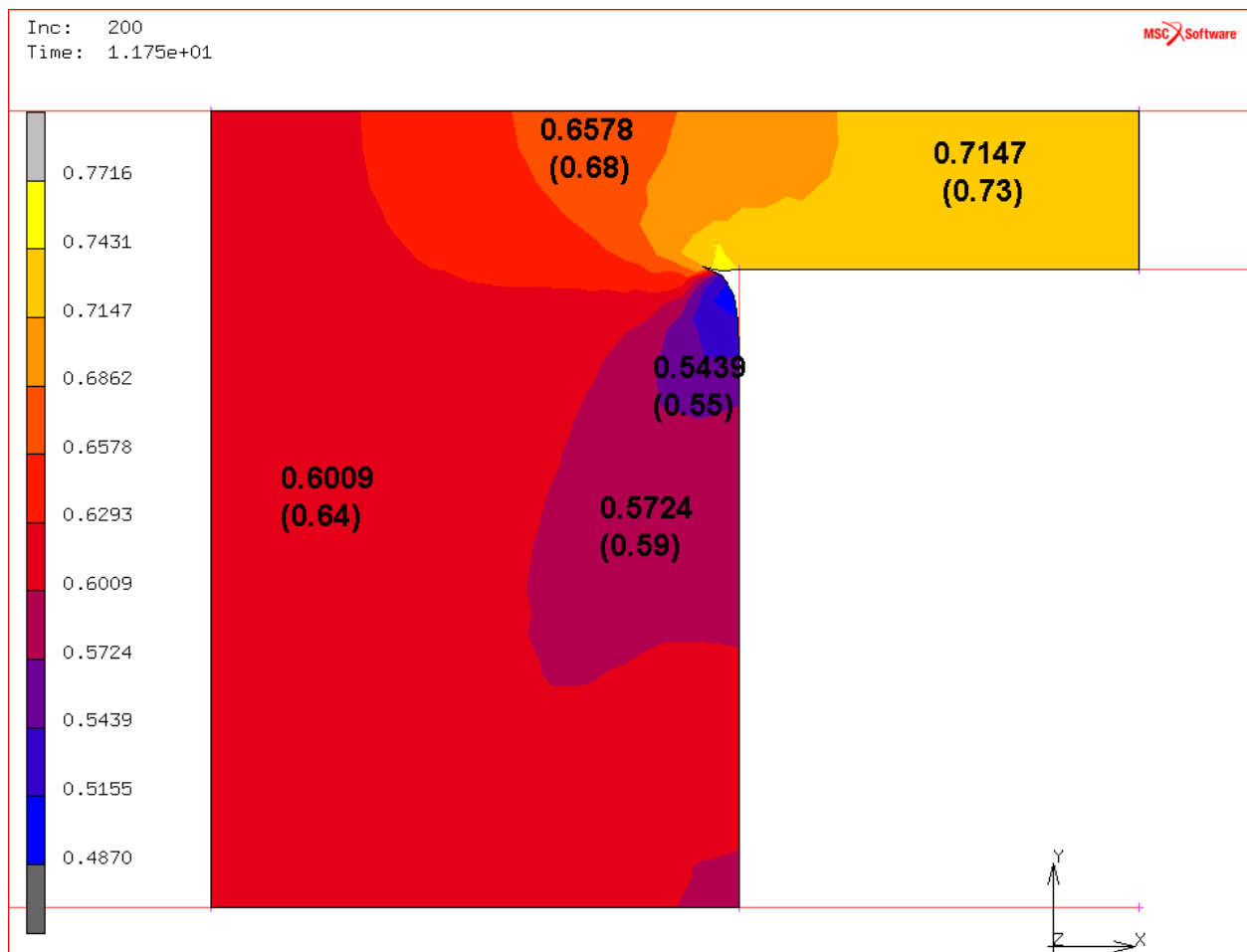


Figure 81. Compact shape and density distribution after Stage 2 of compaction cycle.

Although it was not possible to employ the exact set of material properties provided by Shima, due to software limitations, it is fair to say that the above results are within close proximity of those attained by Shima et al. [101, 102]. Further, it is important to note that similar slip-crack defect had resulted at the corner of the left side of the rim-hub junction as the one obtained in the analysis conducted by Shima et al. [101, 102]; refer to Figure 39. The details on the occurrence of slip-crack defect were explained in the previous section; see section 4.2.2.1.

Upon acquirement of satisfying results, the next step was to carry out simulation analyses to study the effect of velocity ratio of specific tools on green density variation using the following three case studies: (1) lower-inner-punch to upper-punch velocity ratio, v_3/v_1 ; (2) die to upper-punch velocity ratio, v_4/v_1 ; and (3) die and core-rod to upper-punch velocity ratio, $v_{4,5}/v_1$. Again, one should note that only case studies (1) and (2) were carried out by Shima et al. [101, 102], while case study (3) was done by the present author as an extension to their work.

All three case studies were conducted using three sets of material properties provided by: (i) Shima [101, 102], derived based on simple compression tests conducted on powder compact specimens; (ii) Pavier and Doremus [10, 84], based on triaxial cell tests conducted on granular powder material; and (iii) Koval'chenko [54], based on simple-compression tests conducted on pre-sintered powder compact specimens. More specifically, for case study (1) and (2) all three material property sets, (i) to (iii), were employed; however, for case study (3) only sets (i) and (ii) were employed. Material property set (i), provided by Shima [101, 102], was used as a comparative base to the results attained by Shima et al. [101, 102].

The reason for using more than one material property set was to see how their simulation results compare with each other. Specifically, it was interesting to see how the results match using the material properties derived from the granular powder material - set (ii), and those derived from the pre-sintered powder compact specimens - set (iii). In addition, it is important to note that material properties provided by Pavier and Doremus - set (ii), were specifically chosen due to their consistency and completeness, where both the material properties and the variable friction coefficient expression were derived using the same iron-based powder composition, thus, providing the complete database for simulation analysis.

All case studies were analysed using different frictional conditions by employing: (i) a set of constant friction coefficients - 0.08, 0.12, and 0.20, proposed by Shima et al. [101, 102]; and (ii) the variable friction coefficient expressed by equation (64), provided by Pavier and Doremus [19, 21, 86]. For a complete summary of simulation runs, see Table 20.

Upon completion of all simulation runs, the relative density data was manually extracted from the results of each individual simulation run based on which the density variation was evaluated and then plotted for all three case studies, for each corresponding velocity ratio, using equation (45) proposed by Shima et al. [101, 102].

Table 20. Summary of simulation runs for the multi-stepped part.

| Case Study (1): Lower-Inner-Punch to Upper-Punch Velocity Ratio, v_3/v_1 | | | | |
|---|------|------|------|----------------------|
| Using material properties provided by Shima | | | | |
| Friction coefficient | 0.08 | 0.12 | 0.20 | $\mu(\sigma_n, v_r)$ |
| Number of simulation runs, one for each corresponding velocity ratio, v_3/v_1 , 0.45 to 0.55, in increments of 0.01 | 11 | 11 | 11 | 11 |
| Using material properties provided by Pavier and Doremus | | | | |
| Friction coefficient | 0.08 | 0.12 | 0.20 | $\mu(\sigma_n, v_r)$ |
| Number of simulation runs, one for each corresponding velocity ratio, v_3/v_1 , 0.45 to 0.55, in increments of 0.01 | 11 | 11 | 11 | 11 |
| Using material properties provided by Koval'chenko | | | | |
| Friction coefficient | 0.08 | 0.12 | 0.20 | $\mu(\sigma_n, v_r)$ |
| Number of simulation runs, one for each corresponding velocity ratio, v_3/v_1 , 0.45 to 0.55, in increments of 0.01 | 11 | 11 | 11 | 11 |
| Total number of simulation runs | 132 | | | |
| Case Study (2): Die to Upper-Punch Velocity Ratio, v_4/v_1 | | | | |
| Using material properties provided by Shima | | | | |
| Friction coefficient | 0.08 | 0.12 | 0.20 | $\mu(\sigma_n, v_r)$ |
| Number of simulation runs, one for each corresponding velocity ratio, v_4/v_1 , 0 to 1.0, in increments of 0.1 | 11 | 11 | 11 | 11 |
| Using material properties provided by Pavier and Doremus | | | | |
| Friction coefficient | 0.08 | 0.12 | 0.20 | $\mu(\sigma_n, v_r)$ |
| Number of simulation runs, one for each corresponding velocity ratio, v_4/v_1 , 0 to 1.0, in increments of 0.1 | 11 | 11 | 11 | 11 |
| Using material properties provided by Koval'chenko | | | | |
| Friction coefficient | 0.08 | 0.12 | 0.20 | $\mu(\sigma_n, v_r)$ |
| Number of simulation runs, one for each corresponding velocity ratio, v_4/v_1 , 0 to 1.0, in increments of 0.1 | 11 | 11 | 11 | 11 |
| Total number of simulation runs | 132 | | | |
| Case Study (3): Die and Core-Rod to Upper Punch Velocity Ratio, $v_{4,5}/v_1$ | | | | |
| Using material properties provided by Shima | | | | |
| Friction coefficient | 0.08 | 0.12 | 0.20 | $\mu(\sigma_n, v_r)$ |
| Number of simulation runs, one for each corresponding velocity ratio, $v_{4,5}/v_1$, 0 to 1.0, in increments of 0.1 | 11 | 11 | 11 | 11 |
| Using material properties provided by Pavier and Doremus | | | | |
| Friction coefficient | 0.08 | 0.12 | 0.20 | $\mu(\sigma_n, v_r)$ |
| Number of simulation runs, one for each corresponding velocity ratio, $v_{4,5}/v_1$, 0 to 1.0, in increments of 0.1 | 11 | 11 | 11 | 11 |
| Total number of simulation runs | 88 | | | |

7.1 Effect of Lower-Inner-Punch to Upper-Punch Velocity Ratio on Density Variation

7.1.1 Using Material Properties Provided by Shima [101, 102]

The evaluated relationship between the green density variation and the lower-inner-punch (3) to upper-punch (1) velocity ratio, v_3/v_1 , using the first set of material properties and different frictional conditions, is shown in Figure 82. Depending on the imposed frictional condition, the green density variation was found to be minimum at a certain velocity ratio, v_3/v_1 . The least variation in density was observed in the vicinity of $v_3/v_1 = 0.50$ and the corresponding value of v_3/v_1 , evaluated at the point of minimum density variation, was found to slightly increase with the friction coefficient.

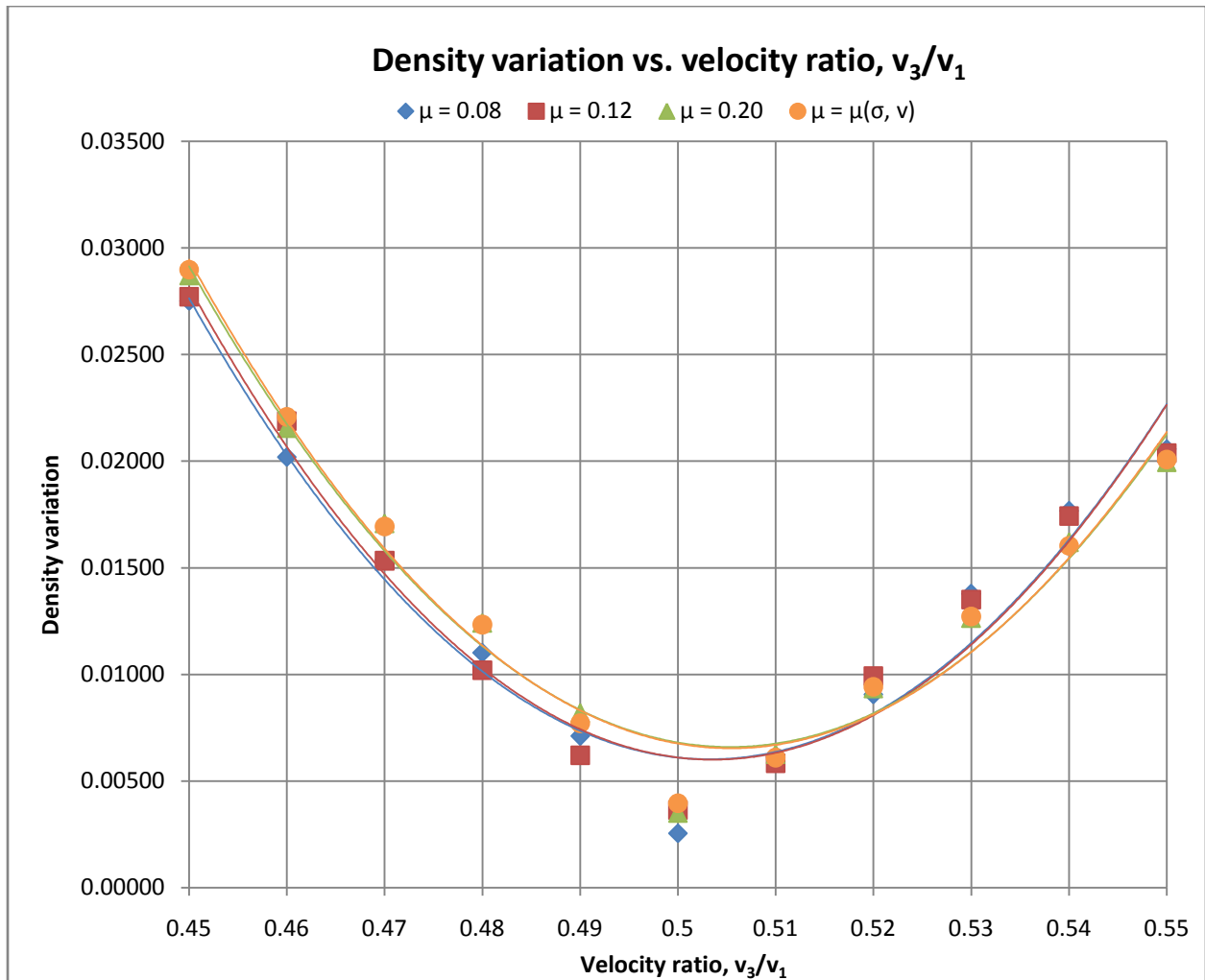


Figure 82. Density variation due to movement of tools 1 and 3.

7.1.2 Using Material Properties Provided by Pavier and Doremus [10, 84]

The evaluated relationship between the green density variation and the lower-inner-punch (3) to upper-punch (1) velocity ratio, v_3/v_1 , using the second set of material properties and different frictional conditions, is shown in Figure 83. Depending on the imposed frictional condition, the green density variation was found to be minimum at a certain velocity ratio, v_3/v_1 . The least variation in density was observed in the vicinity of $v_3/v_1 = 0.50$ and the corresponding value of v_3/v_1 , evaluated at the point of minimum density variation, was found to slightly increase with the friction coefficient.

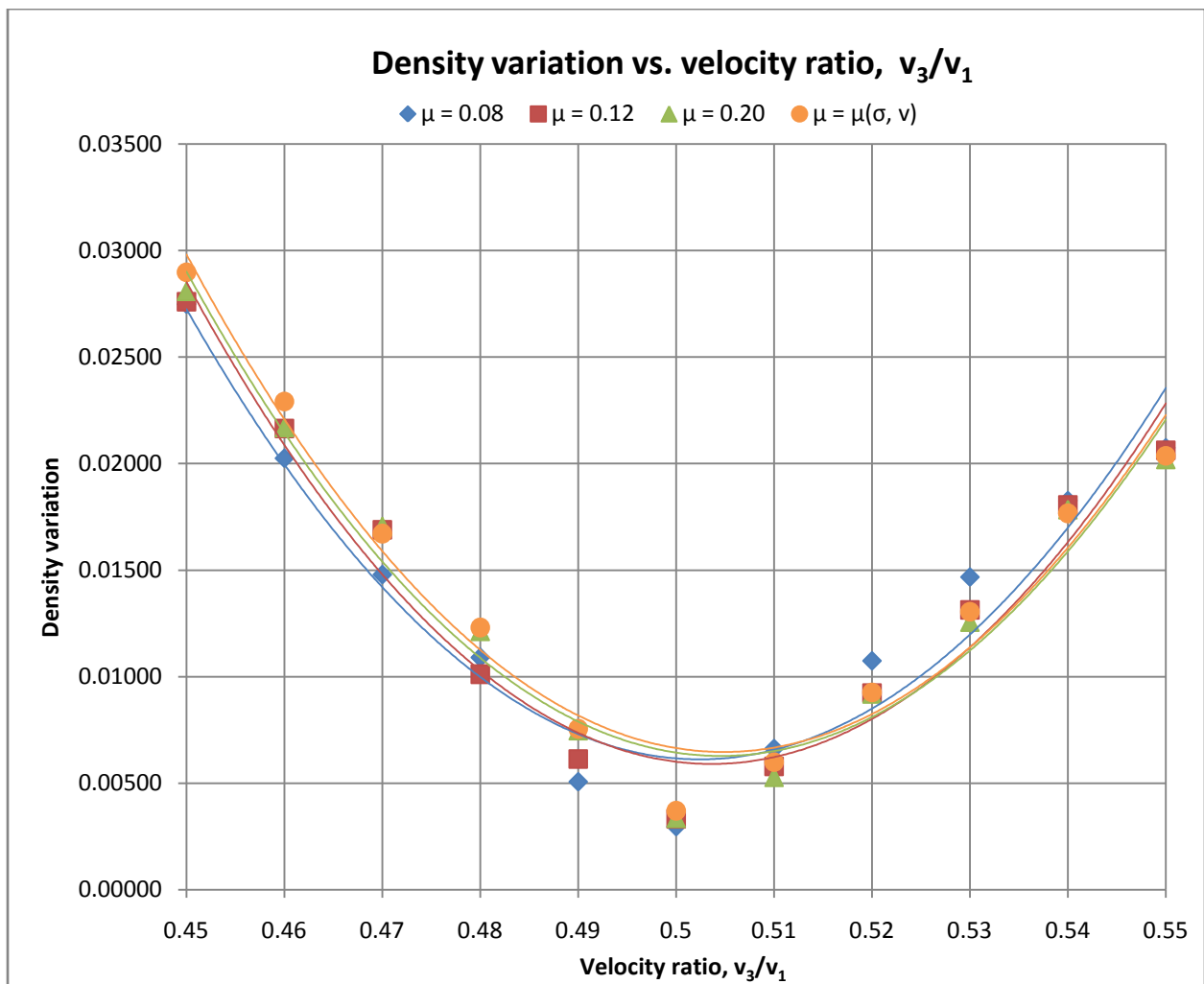


Figure 83. Density variation due to movement of tools 1 and 3.

7.1.3 Using Material Properties Provided by Koval'chenko [54]

The evaluated relationship between the green density variation and the lower-inner-punch (3) to upper-punch (1) velocity ratio, v_3/v_1 , using the third set of material properties and different frictional conditions, is shown in Figure 84. Depending on the imposed frictional condition, the green density variation was found to be minimum at a certain velocity ratio, v_3/v_1 . The least variation in density was observed in the vicinity of $v_3/v_1 = 0.50$ and the corresponding value of v_3/v_1 , evaluated at the point of minimum density variation, was found to slightly increase with the friction coefficient.

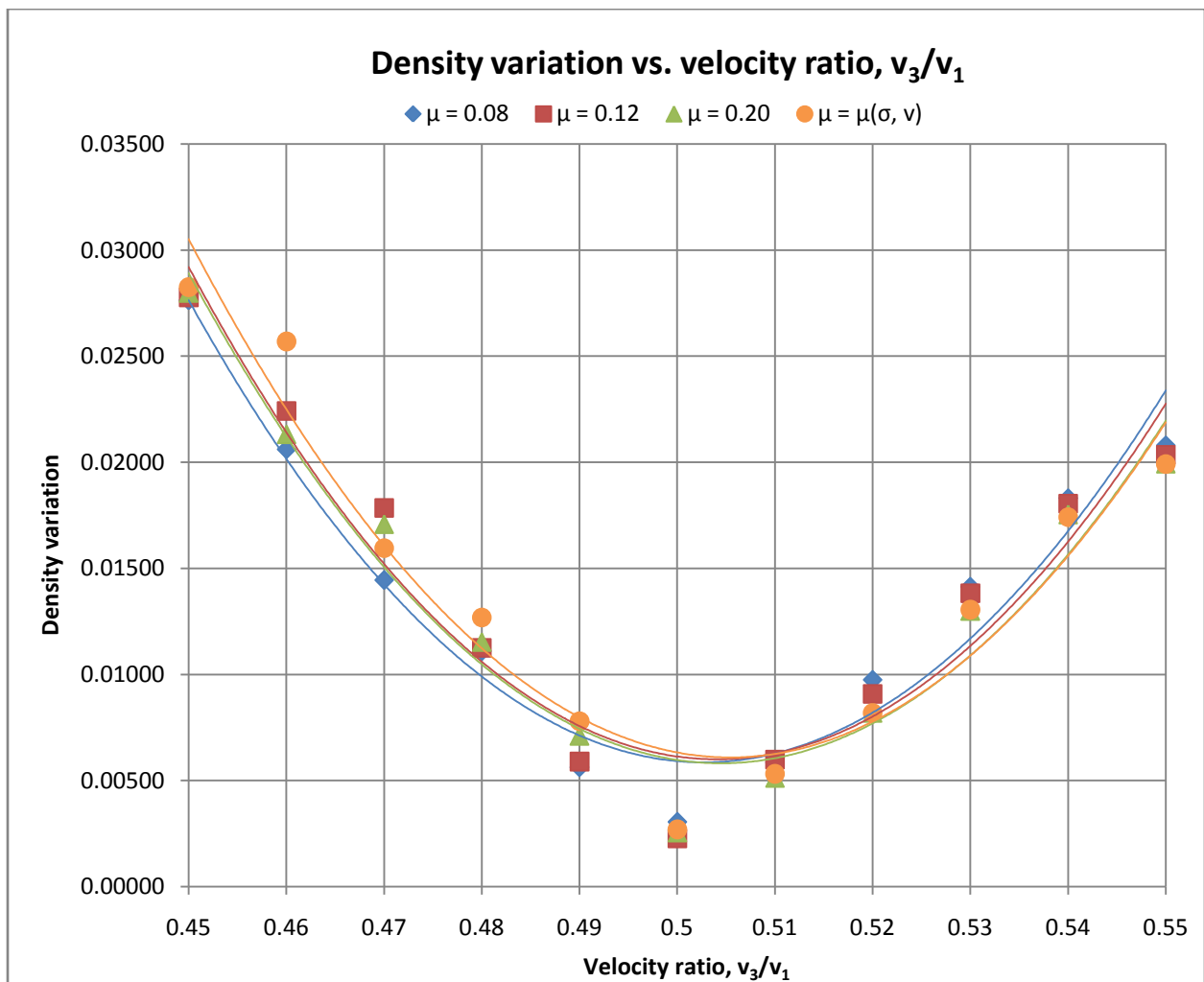


Figure 84. Density variation due to movement of tools 1 and 3.

7.1.4 Summary and Discussion of Results

Throughout the compaction cycle, the density in the rim should be kept at a certain level, considering that the higher is the velocity ratio, v_3/v_1 , the higher is the average density in the rim relative to the hub. For all three sets of material properties, the green density variation was found to be minimum at a certain velocity ratio, v_3/v_1 , depending on the friction coefficient. In Figures 82 to 84, using appropriate polynomial functions, best-fit-curves were plotted through the evaluated density variation values to illustrate a general trend in relative density variation with respect to v_3/v_1 , for each corresponding friction coefficient. Based on these curves, values of v_3/v_1 were determined at the point of minimum density variation. Consequently, the least variation in density was observed in the vicinity of v_3/v_1 of 0.50, and the corresponding value of v_3/v_1 was found to slightly increase with the friction coefficient for all the sets of material properties employed; see Table 21. Similar trend was observed in the analyses conducted by Shima et al. [101, 102]; refer to Figure 40.

It is important to note that the highest value of v_3/v_1 , representing the minimum density variation, was recorded for the variable friction coefficient, $\mu(\sigma_n, v_r)$, for all the sets of material properties; see Table 21. Also, based on Figures 82 to 84, the use of the variable friction coefficient has generally resulted in a slightly higher green density variation values for the first half of the velocity ratio range, $v_3/v_1 \leq 0.50$.

Further, although not shown in Figures 82 to 84, the values of critical velocity ratio, $v_c = v_3/v_1$, were recorded at which the initiation of a slip-crack defect was observed; see Table 21. Upon avoiding the increase of v_3/v_1 beyond the specified critical velocity ratio, v_c , for corresponding friction coefficient, the occurrence of a slip-crack defect is prevented. It is important to note, that based on the analyses conducted by Shima et al. [101, 102], all critical velocity ratio, v_c , values happened to surpass the ones evaluated at the minimum density variation points; refer to Figure 40. However, this proved not to be the case in the present study, regardless of the material property set used. In Table 21, it is shown that certain critical velocity ratio values, for corresponding frictional conditions and material property sets, are actually lower than the ones evaluated at the minimum density variation points. The discrepancy in results may be attributed to the software limitations, due to which a constant yield stress value as opposed to

the strain dependent relationship had to be implemented into all of the simulation models. Another possibility is the fact that the quadrilateral element type was employed for the present study as opposed to the linear triangular type used by Shima et al. [101, 102]. Further, the actual software employed by Shima et al. [101, 102] is unknown, thus, adding to the list of possible factors contributing to the overall discrepancy in the results. Nevertheless, considering the minor differences between the simulation models and the above factors, it is fair to say that the results attained in the present study compare well with the ones presented by Shima et al. [101, 102].

Table 21. Evaluated values of v_3/v_1 at minimum density variation and critical velocity ratio, v_c .

| Using material properties provided by Shima | | | | |
|--|---------|---------|---------|----------------------|
| Friction coefficient | 0.08 | 0.12 | 0.20 | $\mu(\sigma_n, v_r)$ |
| Value of velocity ratio, v_3/v_1 , at the point of minimum density variation | 0.50328 | 0.50362 | 0.50537 | 0.50543 |
| Critical velocity ratio, $v_c = v_3/v_1$, at which slip-crack defect is initiated | 0.504 | 0.503 | 0.504 | 0.503 |
| Using material properties provided by Pavier and Doremus | | | | |
| Friction coefficient | 0.08 | 0.12 | 0.20 | $\mu(\sigma_n, v_r)$ |
| Value of velocity ratio, v_3/v_1 , at the point of minimum density variation | 0.50240 | 0.50362 | 0.50452 | 0.50490 |
| Critical velocity ratio, $v_c = v_3/v_1$, at which slip-crack defect is initiated | 0.501 | 0.503 | 0.503 | 0.523 |
| Using material properties provided by Koval'chenko | | | | |
| Friction coefficient | 0.08 | 0.12 | 0.20 | $\mu(\sigma_n, v_r)$ |
| Value of velocity ratio, v_3/v_1 , at the point of minimum density variation | 0.50274 | 0.50403 | 0.50450 | 0.50541 |
| Critical velocity ratio, $v_c = v_3/v_1$, at which slip-crack defect is initiated | 0.504 | 0.503 | 0.504 | 0.524 |

Further observation can be made by consulting Appendix D, where illustration of the relative density distribution over the cross-sectional area of the multi-stepped compact is presented for each corresponding velocity ratio - v_3/v_1 , friction coefficient, and material property set. It is observed that upon increase of v_3/v_1 , from 0.45 to 0.50, an overall density variation over the cross-sectional area of the compact is reduced for each corresponding friction coefficient and material property set. However, upon further increase of v_3/v_1 , from 0.50 to 0.55, and increase in density variation is observed. More importantly, by examining of relative density values for

each corresponding velocity ratio and the imposed frictional condition, it is observed that the difference between the highest and the lowest relative density values is drastically reduced upon increase of v_3/v_1 from 0.45 to 0.50, thus, constituting an overall reduction in the density gradient. However, upon further increase of v_3/v_1 , from 0.50 to 0.55, the difference between the highest and the lowest relative density values is reversed, meaning that the overall density gradient is increased; see Table 22.

Lastly, it is important to note that the evaluated average relative density of the final multi-stepped compact is observed to decrease with v_3/v_1 for each corresponding friction coefficient and material property set. The complete summary of the evaluated average relative density values is presented in Table 23.

Table 22. Difference between maximum and minimum relative density values.

| Using material properties provided by Shima | | | | |
|---|---|--------------------------------|--------------------------------|--|
| Velocity ratio, v_3/v_1 | Friction coefficient, μ | | | |
| | $\mu = 0.08$ | $\mu = 0.12$ | $\mu = 0.20$ | $\mu = \mu(\sigma_n, v_r)$ |
| 0.45 | 0.1658 | 0.1680 | 0.1688 | 0.1706 |
| 0.46 | 0.1271 | 0.1426 | 0.1347 | 0.1322 |
| 0.47 | 0.1058 | 0.0992 | 0.1001 | 0.0993 |
| 0.48 | 0.0943 | 0.0804 | 0.0931 | 0.0915 |
| 0.49 | 0.0741 | 0.0619 | 0.0958 | 0.0669 |
| 0.50 | 0.0468 | 0.0669 | 0.0524 | 0.0466 |
| 0.51 | 0.0566 | 0.0903 | 0.0792 | 0.0798 |
| 0.52 | 0.0623 | 0.0792 | 0.0771 | 0.0773 |
| 0.53 | 0.0858 | 0.0864 | 0.0866 | 0.0866 |
| 0.54 | 0.1142 | 0.1131 | 0.1044 | 0.1040 |
| 0.55 | 0.1368 | 0.1353 | 0.1326 | 0.1449 |
| Using material properties provided by Pavier and Doremus | | | | |
| Velocity ratio, v_3/v_1 | Friction coefficient, μ | | | |
| | $\mu = 0.08$ | $\mu = 0.12$ | $\mu = 0.20$ | $\mu = \mu(\sigma_n, v_r)$ |
| 0.45 | 0.1664 | 0.1666 | 0.1651 | 0.1727 |
| 0.46 | 0.1256 | 0.1430 | 0.1342 | 0.1306 |
| 0.47 | 0.1056 | 0.1068 | 0.1004 | 0.0996 |
| 0.48 | 0.0940 | 0.0787 | 0.0923 | 0.0886 |
| 0.49 | 0.0653 | 0.0612 | 0.0699 | 0.0656 |
| 0.50 | 0.0494 | 0.0650 | 0.0513 | 0.0563 |
| 0.51 | 0.0776 | 0.0634 | 0.0611 | 0.0626 |
| 0.52 | 0.0748 | 0.0755 | 0.0761 | 0.0763 |
| 0.53 | 0.0922 | 0.0857 | 0.0860 | 0.0907 |
| 0.54 | 0.1194 | 0.1180 | 0.1164 | 0.1160 |
| 0.55 | 0.1532 | 0.1517 | 0.1487 | 0.1473 |
| Using material properties provided by Koval'chenko | | | | |
| Velocity ratio, v_3/v_1 | Friction coefficient, μ | | | |
| | $\mu = 0.08$ | $\mu = 0.12$ | $\mu = 0.20$ | $\mu = \mu(\sigma_n, v_r)$ |
| 0.45 | 0.1691 | 0.1690 | 0.1639 | 0.1620 |
| 0.46 | 0.1300 | 0.1464 | 0.1288 | 0.2088 |
| 0.47 | 0.1058 | 0.1863 | 0.1056 | 0.0902 |
| 0.48 | 0.0880 | 0.0874 | 0.0994 | 0.0977 |
| 0.49 | 0.0801 | 0.0588 | 0.0615 | 0.0571 |
| 0.50 | 0.0475 | 0.0419 | 0.0382 | 0.0333 |
| 0.51 | 0.0582 | 0.0507 | 0.0559 | 0.0450 |
| 0.52 | 0.0669 | 0.0680 | 0.0533 | 0.0532 |
| 0.53 | 0.0881 | 0.0879 | 0.0876 | 0.0872 |
| 0.54 | 0.1195 | 0.1181 | 0.1162 | 0.1159 |
| 0.55 | 0.1537 | 0.1521 | 0.1495 | 0.1482 |

Table 23. Average relative density of the final multi-stepped compacts.

| Using material properties provided by Shima | | | | |
|---|---|--------------------------------|--------------------------------|--|
| Velocity ratio, v_3/v_1 | Friction coefficient, μ | | | |
| | $\mu = 0.08$ | $\mu = 0.12$ | $\mu = 0.20$ | $\mu = \mu(\sigma_n, v_r)$ |
| 0.45 | 0.7154 | 0.7157 | 0.7161 | 0.7161 |
| 0.46 | 0.7133 | 0.7123 | 0.7128 | 0.7131 |
| 0.47 | 0.7061 | 0.7064 | 0.7061 | 0.7069 |
| 0.48 | 0.7001 | 0.7004 | 0.7006 | 0.7008 |
| 0.49 | 0.6936 | 0.6940 | 0.6915 | 0.6937 |
| 0.50 | 0.6885 | 0.6882 | 0.6882 | 0.6885 |
| 0.51 | 0.6815 | 0.6796 | 0.6802 | 0.6811 |
| 0.52 | 0.6748 | 0.6739 | 0.6741 | 0.6742 |
| 0.53 | 0.6676 | 0.6681 | 0.6686 | 0.6685 |
| 0.54 | 0.6608 | 0.6607 | 0.6620 | 0.6619 |
| 0.55 | 0.6531 | 0.6535 | 0.6540 | 0.6541 |
| Using material properties provided by Pavier and Doremus | | | | |
| Velocity ratio, v_3/v_1 | Friction coefficient, μ | | | |
| | $\mu = 0.08$ | $\mu = 0.12$ | $\mu = 0.20$ | $\mu = \mu(\sigma_n, v_r)$ |
| 0.45 | 0.7162 | 0.7159 | 0.7159 | 0.7161 |
| 0.46 | 0.7135 | 0.7122 | 0.7126 | 0.7125 |
| 0.47 | 0.7055 | 0.7057 | 0.7061 | 0.7068 |
| 0.48 | 0.6999 | 0.7006 | 0.7004 | 0.6998 |
| 0.49 | 0.6940 | 0.6945 | 0.6947 | 0.6938 |
| 0.50 | 0.6891 | 0.6877 | 0.6880 | 0.6876 |
| 0.51 | 0.6805 | 0.6808 | 0.6819 | 0.6818 |
| 0.52 | 0.6743 | 0.6750 | 0.6745 | 0.6744 |
| 0.53 | 0.6674 | 0.6679 | 0.6685 | 0.6682 |
| 0.54 | 0.6604 | 0.6604 | 0.6608 | 0.6610 |
| 0.55 | 0.6546 | 0.6543 | 0.6543 | 0.6542 |
| Using material properties provided by Koval'chenko | | | | |
| Velocity ratio, v_3/v_1 | Friction coefficient, μ | | | |
| | $\mu = 0.08$ | $\mu = 0.12$ | $\mu = 0.20$ | $\mu = \mu(\sigma_n, v_r)$ |
| 0.45 | 0.7144 | 0.7154 | 0.7158 | 0.7161 |
| 0.46 | 0.7131 | 0.7115 | 0.7132 | 0.7075 |
| 0.47 | 0.7051 | 0.7029 | 0.7060 | 0.7069 |
| 0.48 | 0.6995 | 0.6992 | 0.6991 | 0.6997 |
| 0.49 | 0.6942 | 0.6948 | 0.6941 | 0.6949 |
| 0.50 | 0.6880 | 0.6889 | 0.6886 | 0.6897 |
| 0.51 | 0.6823 | 0.6821 | 0.6823 | 0.6824 |
| 0.52 | 0.6749 | 0.6755 | 0.6759 | 0.6758 |
| 0.53 | 0.6675 | 0.6679 | 0.6687 | 0.6686 |
| 0.54 | 0.6597 | 0.6599 | 0.6608 | 0.6608 |
| 0.55 | 0.6543 | 0.6542 | 0.6539 | 0.6538 |

7.2 Effect of Die to Upper-Punch Velocity Ratio on Density Variation

7.2.1 Using Material Properties Provided by Shima [101, 102]

The evaluated relationship between the green density variation and the die (4) to upper-punch (1) velocity ratio, v_4/v_1 , using the first set of material properties and different frictional conditions, is shown in Figure 85. It is observed that moving the die has a negative effect on the overall homogeneity of the green compact, where the density variation is observed to increase with v_4/v_1 regardless of the frictional condition imposed.

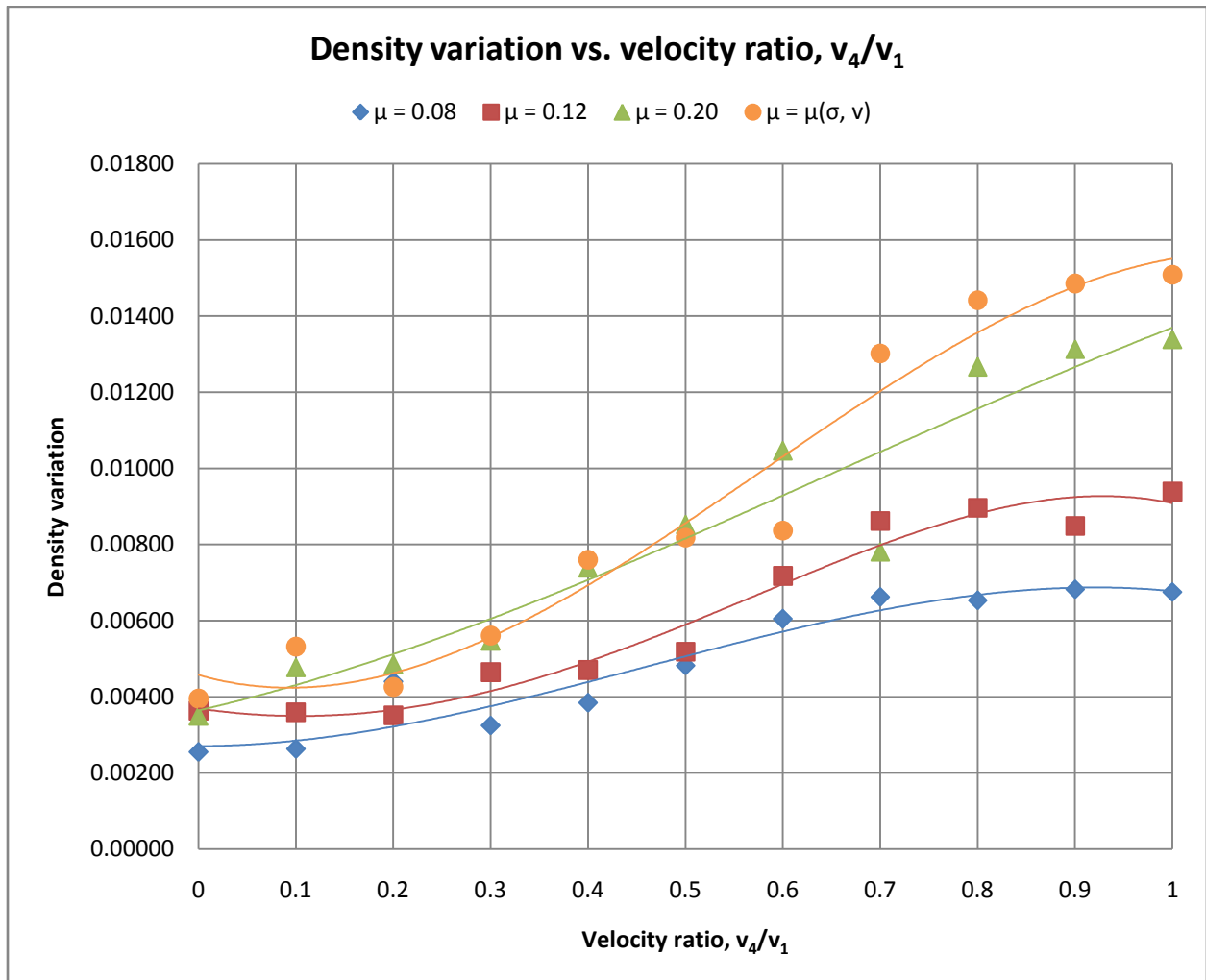


Figure 85. Density variation due to movement of tools 1 and 4.

7.2.2 Using Material Properties Provided by Pavier and Doremus [10, 84]

The evaluated relationship between the green density variation and the die (4) to upper-punch (1) velocity ratio, v_4/v_1 , using the second set of material properties and different frictional conditions, is shown in Figure 86. It is observed that moving the die has a negative effect on the overall homogeneity of the green compact, where the density variation is observed to increase with v_4/v_1 regardless of the frictional condition imposed.

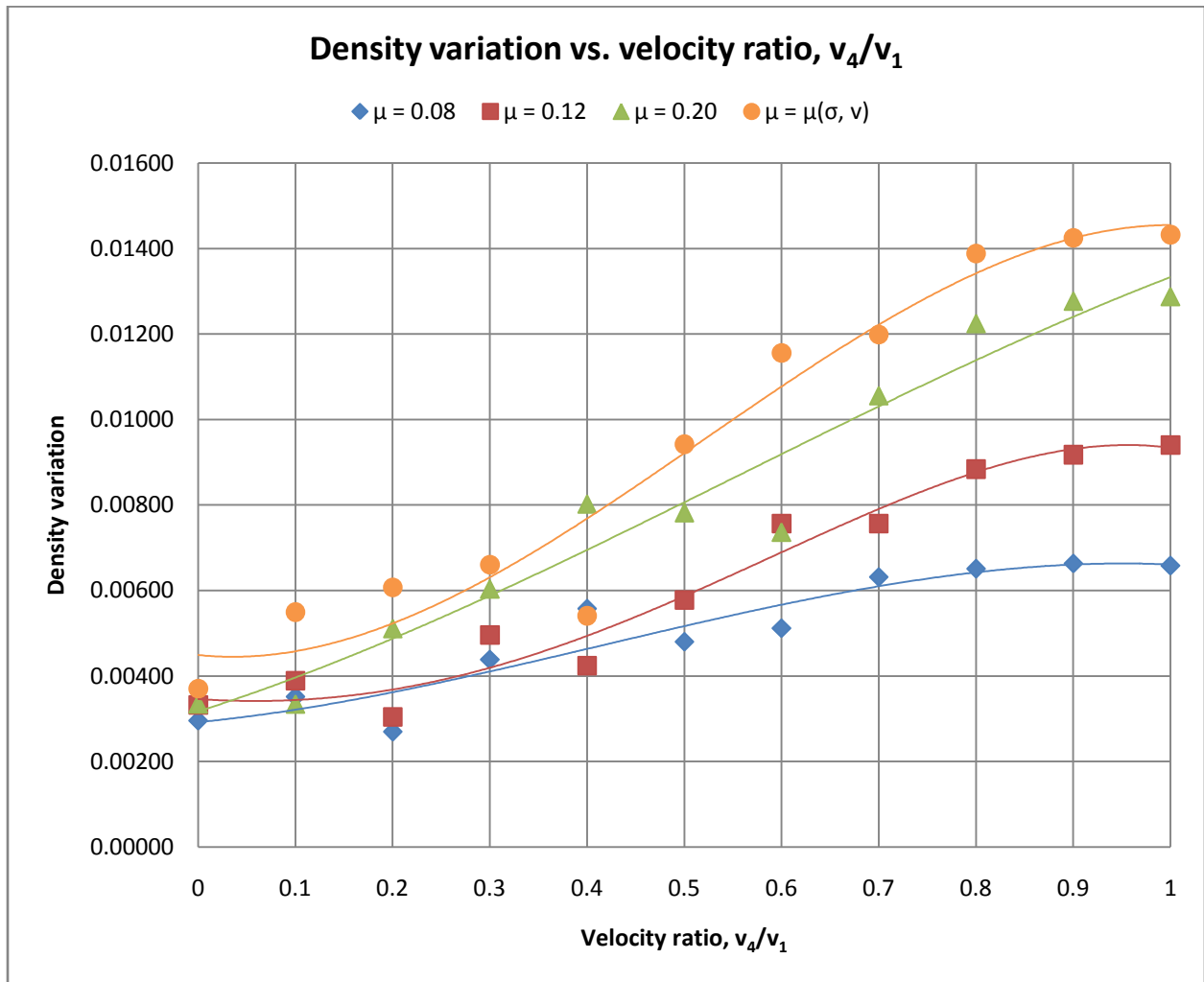


Figure 86. Density variation due to movement of tools 1 and 4.

7.2.3 Using Material Properties Provided by Koval'chenko [54]

The evaluated relationship between the green density variation and the die (4) to upper-punch (1) velocity ratio, v_4/v_1 , using the third set of material properties and different frictional conditions, is shown in Figure 87. Once again, moving the die is observed to have a negative effect on the overall homogeneity of the green compact, where the density variation is observed to increase with v_4/v_1 , predominantly beyond a value of 0.2, regardless of the frictional condition imposed.

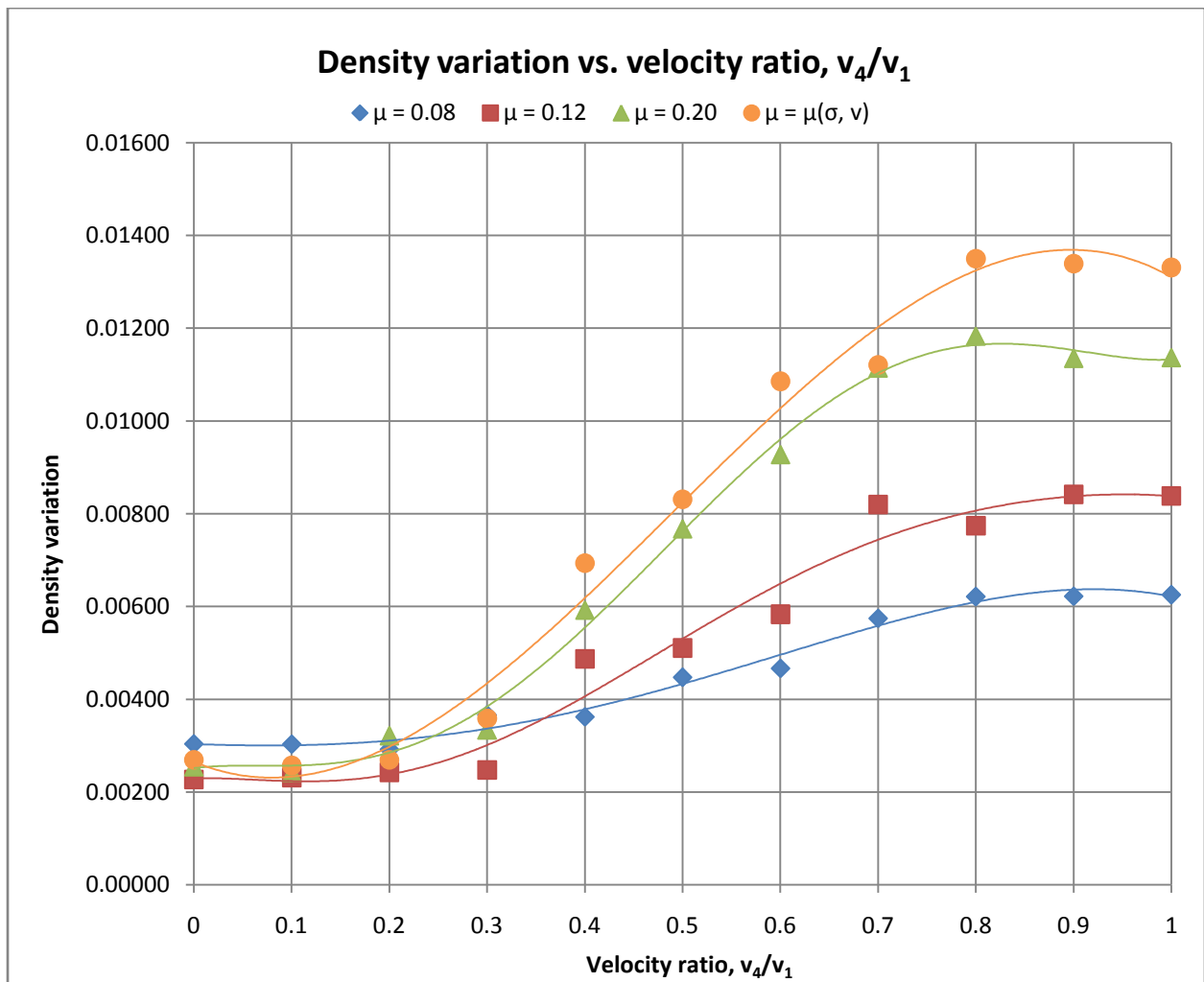


Figure 87. Density variation due to movement of tools 1 and 4.

7.2.4 Summary and Discussion of Results

In the first case study, conducted to determine the relationship between the green density variation and the lower-inner-punch to upper-punch velocity ratio, v_3/v_1 , the least density variation was found to be in the vicinity of $v_3/v_1 = 0.50$. Thus, for the second case study, the value of v_3/v_1 was kept constant at 0.50, while the die to upper-punch velocity ratio, v_4/v_1 , was varied in a range from 0 to 1.0. Using the specified tool kinematics, the relationship between the green density variation and the die to upper-punch velocity ratio, v_4/v_1 , was evaluated using the three sets of material properties and different frictional conditions.

From Figures 85 to 87, representing the corresponding simulation results using all three sets of material properties, it was observed that moving the die had actually a negative effect of on the overall homogeneity of the green compact. By simultaneously moving the die and the upper-punch, the density variation was observed to steadily increase, predominantly beyond a value of $v_4/v_1 = 0.2$, regardless of the friction coefficient or the material property set employed, thus, contributing to a higher overall density gradient. Overall, the magnitude of the evaluated density variation with respect to v_4/v_1 was observed to increase with the friction coefficient, predominantly beyond a value of $v_4/v_1 = 0.2$. Similar observations were made in the analyses conducted by Shima et al. [102]; refer to Figure 41. Also, it is important to note that, generally, the highest magnitude in density variation was observed when using the variable friction coefficient, $\mu(\sigma_n, v_r)$, for all sets of material properties employed.

Further, it is important to note that although the general trend observed in Figures 85 to 87, closely reflects the results presented by Shima et al. [102], there is a noticeable discrepancy in the magnitude of the evaluated density variation for corresponding v_4/v_1 range, for all sets of material properties; refer to Figure 41. Again, the discrepancy in results may be attributed to the software limitations, due to which a constant yield stress value as opposed the strain dependent relationship had to be implemented into all of the simulation models. Another possibility is the fact that the quadrilateral element type was employed for the present study as opposed to the linear triangular type used by Shima et al. [101, 102]. Further, the actual software employed by Shima et al. [101, 102] is unknown, thus, adding to the list of possible factors contributing to the overall discrepancy in the results. Nevertheless, considering the

minor differences between the simulation models and the above factors, it is fair to say that the results attained in the present study compare well with the ones presented by Shima et al. [101, 102].

Further observation can be made by consulting Appendix E, where illustration of the relative density distribution over the cross-sectional area of the multi-stepped compact is presented for each corresponding velocity ratio - v_4/v_1 , friction coefficient, and material property set. It is observed that upon increase of v_4/v_1 , from 0 to 1.0, an overall density variation over the cross-sectional area of the compact is shown to increase for each corresponding friction coefficient and material property set. The overall rate of change in density variation is observed to increase with friction coefficient, with the highest rate observed for the constant friction coefficient of 0.20 and the variable friction coefficient, $\mu(\sigma_n, v_r)$, for all the material property sets.

More importantly, close observation of relative density values for each corresponding v_4/v_1 and the imposed frictional condition, it is observed that the difference between the highest and the lowest relative density values generally increases with v_4/v_1 , thus, constituting an overall increase in the density gradient; see Table 24. Lastly, it is important to note that the evaluated average relative density of the final multi-stepped compacts is observed to remain steady with respect to v_4/v_1 for each corresponding friction coefficient and material property set. The complete summary of the evaluated average relative density is presented in Table 25.

Table 24. Difference between maximum and minimum relative density values.

| Using material properties provided by Shima | | | | |
|---|---|--------------------------------|--------------------------------|--|
| Velocity ratio, v_4/v_1 | Friction coefficient, μ | | | |
| | $\mu = 0.08$ | $\mu = 0.12$ | $\mu = 0.20$ | $\mu = \mu(\sigma_n, v_r)$ |
| 0 | 0.0468 | 0.0669 | 0.0524 | 0.0466 |
| 0.1 | 0.0467 | 0.0668 | 0.0719 | 0.0775 |
| 0.2 | 0.0549 | 0.0502 | 0.0627 | 0.0419 |
| 0.3 | 0.0503 | 0.0538 | 0.0613 | 0.0703 |
| 0.4 | 0.0439 | 0.0485 | 0.0703 | 0.0762 |
| 0.5 | 0.0455 | 0.0546 | 0.0945 | 0.0769 |
| 0.6 | 0.0773 | 0.0603 | 0.1048 | 0.0760 |
| 0.7 | 0.0867 | 0.0879 | 0.0712 | 0.1085 |
| 0.8 | 0.0800 | 0.0952 | 0.1086 | 0.1055 |
| 0.9 | 0.0745 | 0.0710 | 0.1134 | 0.1219 |
| 1.0 | 0.0690 | 0.0924 | 0.1130 | 0.1101 |
| Using material properties provided by Pavier and Doremus | | | | |
| Velocity ratio, v_4/v_1 | Friction coefficient, μ | | | |
| | $\mu = 0.08$ | $\mu = 0.12$ | $\mu = 0.20$ | $\mu = \mu(\sigma_n, v_r)$ |
| 0 | 0.0494 | 0.0650 | 0.0513 | 0.0563 |
| 0.1 | 0.0704 | 0.0666 | 0.0504 | 0.0850 |
| 0.2 | 0.0467 | 0.0409 | 0.0720 | 0.0769 |
| 0.3 | 0.0543 | 0.0539 | 0.0736 | 0.0780 |
| 0.4 | 0.0735 | 0.0459 | 0.0980 | 0.0639 |
| 0.5 | 0.0477 | 0.0524 | 0.0842 | 0.0884 |
| 0.6 | 0.0478 | 0.0829 | 0.0696 | 0.1080 |
| 0.7 | 0.0829 | 0.0765 | 0.0775 | 0.0858 |
| 0.8 | 0.0788 | 0.0865 | 0.0857 | 0.1180 |
| 0.9 | 0.0795 | 0.0931 | 0.1075 | 0.1149 |
| 1.0 | 0.0541 | 0.0963 | 0.1036 | 0.1136 |
| Using material properties provided by Koval'chenko | | | | |
| Velocity ratio, v_4/v_1 | Friction coefficient, μ | | | |
| | $\mu = 0.08$ | $\mu = 0.12$ | $\mu = 0.20$ | $\mu = \mu(\sigma_n, v_r)$ |
| 0 | 0.0475 | 0.0419 | 0.0382 | 0.0333 |
| 0.1 | 0.0473 | 0.0434 | 0.0351 | 0.0363 |
| 0.2 | 0.0430 | 0.0379 | 0.0452 | 0.0362 |
| 0.3 | 0.0499 | 0.0376 | 0.0360 | 0.0462 |
| 0.4 | 0.0521 | 0.0545 | 0.0646 | 0.0681 |
| 0.5 | 0.0461 | 0.0557 | 0.0742 | 0.0837 |
| 0.6 | 0.0608 | 0.0668 | 0.0857 | 0.0901 |
| 0.7 | 0.0481 | 0.0826 | 0.1002 | 0.0970 |
| 0.8 | 0.0515 | 0.0631 | 0.0910 | 0.1044 |
| 0.9 | 0.0653 | 0.0607 | 0.0952 | 0.0882 |
| 1.0 | 0.0656 | 0.0603 | 0.1000 | 0.0850 |

Table 25. Average relative density of the final multi-stepped compacts.

| Using material properties provided by Shima | | | | |
|---|---|--------------------------------|--------------------------------|--|
| Velocity ratio, v_4/v_1 | Friction coefficient, μ | | | |
| | $\mu = 0.08$ | $\mu = 0.12$ | $\mu = 0.20$ | $\mu = \mu(\sigma_n, v_r)$ |
| 0 | 0.6885 | 0.6882 | 0.6882 | 0.6885 |
| 0.1 | 0.6885 | 0.6880 | 0.6875 | 0.6869 |
| 0.2 | 0.6883 | 0.6879 | 0.6878 | 0.6895 |
| 0.3 | 0.6892 | 0.6886 | 0.6885 | 0.6881 |
| 0.4 | 0.6892 | 0.6890 | 0.6869 | 0.6861 |
| 0.5 | 0.6881 | 0.6880 | 0.6858 | 0.6861 |
| 0.6 | 0.6864 | 0.6876 | 0.6857 | 0.6864 |
| 0.7 | 0.6859 | 0.6861 | 0.6872 | 0.6852 |
| 0.8 | 0.6869 | 0.6856 | 0.6850 | 0.6852 |
| 0.9 | 0.6874 | 0.6873 | 0.6847 | 0.6846 |
| 1.0 | 0.6871 | 0.6858 | 0.6848 | 0.6849 |
| Using material properties provided by Pavier and Doremus | | | | |
| Velocity ratio, v_4/v_1 | Friction coefficient, μ | | | |
| | $\mu = 0.08$ | $\mu = 0.12$ | $\mu = 0.20$ | $\mu = \mu(\sigma_n, v_r)$ |
| 0 | 0.6891 | 0.6877 | 0.6880 | 0.6876 |
| 0.1 | 0.6873 | 0.6868 | 0.6880 | 0.6858 |
| 0.2 | 0.6885 | 0.6894 | 0.6871 | 0.6868 |
| 0.3 | 0.6888 | 0.6879 | 0.6865 | 0.6864 |
| 0.4 | 0.6874 | 0.6889 | 0.6863 | 0.6874 |
| 0.5 | 0.6887 | 0.6884 | 0.6872 | 0.6854 |
| 0.6 | 0.6881 | 0.6867 | 0.6863 | 0.6839 |
| 0.7 | 0.6860 | 0.6875 | 0.6866 | 0.6864 |
| 0.8 | 0.6871 | 0.6865 | 0.6864 | 0.6849 |
| 0.9 | 0.6867 | 0.6853 | 0.6852 | 0.6852 |
| 1.0 | 0.6882 | 0.6849 | 0.6854 | 0.6838 |
| Using material properties provided by Koval'chenko | | | | |
| Velocity ratio, v_4/v_1 | Friction coefficient, μ | | | |
| | $\mu = 0.08$ | $\mu = 0.12$ | $\mu = 0.20$ | $\mu = \mu(\sigma_n, v_r)$ |
| 0 | 0.6880 | 0.6889 | 0.6886 | 0.6897 |
| 0.1 | 0.6880 | 0.6885 | 0.6891 | 0.6894 |
| 0.2 | 0.6883 | 0.6885 | 0.6881 | 0.6892 |
| 0.3 | 0.6878 | 0.6887 | 0.6889 | 0.6892 |
| 0.4 | 0.6881 | 0.6875 | 0.6885 | 0.6869 |
| 0.5 | 0.6878 | 0.6880 | 0.6861 | 0.6855 |
| 0.6 | 0.6884 | 0.6872 | 0.6865 | 0.6864 |
| 0.7 | 0.6882 | 0.6861 | 0.6853 | 0.6860 |
| 0.8 | 0.6880 | 0.6878 | 0.6855 | 0.6847 |
| 0.9 | 0.6876 | 0.6879 | 0.6863 | 0.6855 |
| 1.0 | 0.6877 | 0.6879 | 0.6852 | 0.6859 |

7.3 Effect of Die & Core-Rod to Upper-Punch Velocity Ration on Density Variation

7.3.1 Using Material Properties Provided by Shima [101, 102]

The evaluated relationship between the green density variation and the die (4) and core-rod (5) to upper-punch (1) velocity ratio, $v_{4,5}/v_1$, using the first set of material properties and different frictional conditions, is shown in Figure 88. From Figure 88 it is observed that simultaneously moving the die and the core-rod appears to have a negative effect on the overall homogeneity of the green compact, where the density variation is observed to increase with $v_{4,5}/v_1$ regardless of the frictional condition imposed.

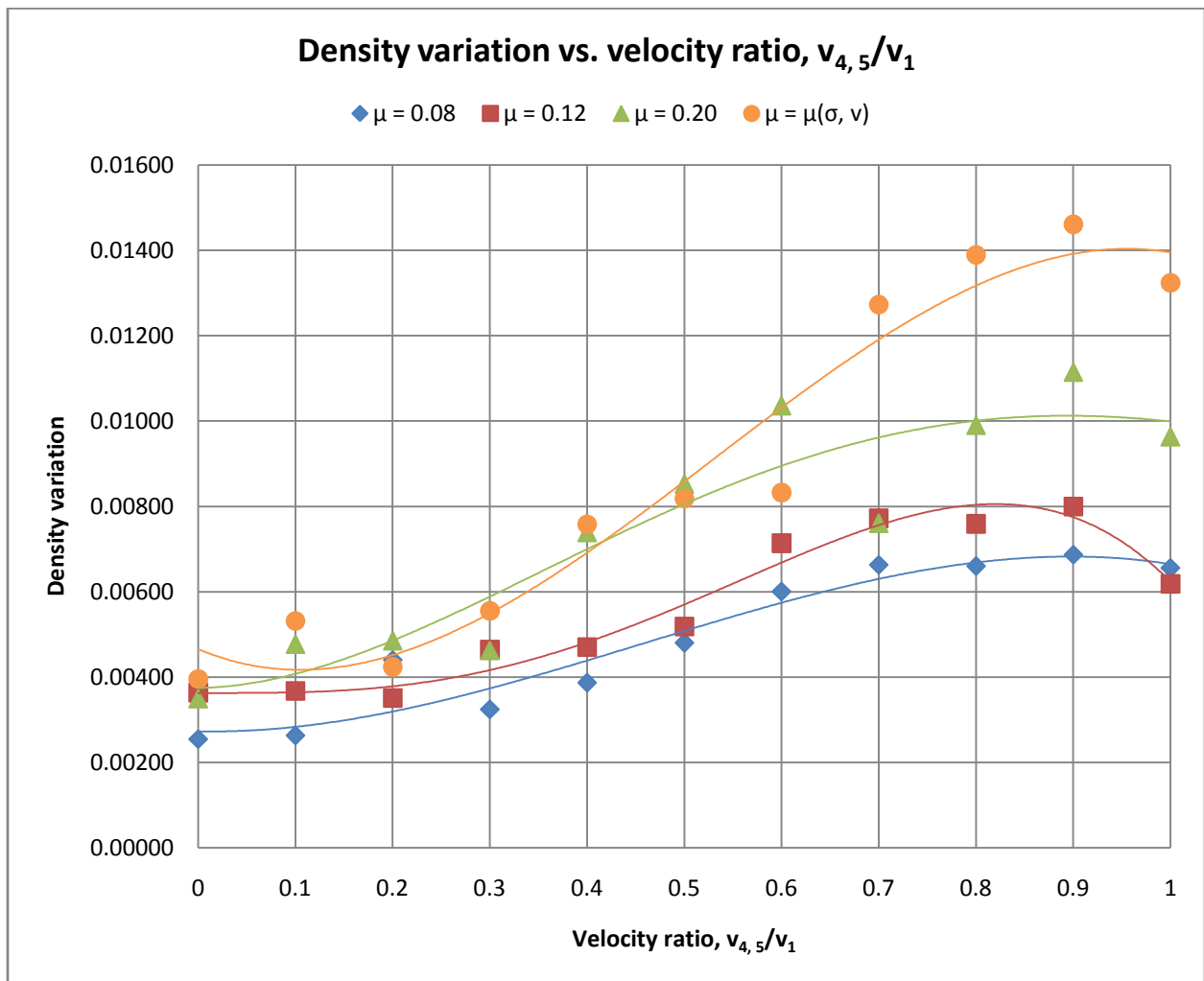


Figure 88. Density variation due to movement of tools 1, 4, and 5.

7.3.2 Using Material Properties Provided by Pavier and Doremus [10, 84]

The evaluated relationship between the green density variation and the die (4) and core-rod (5) to upper-punch (1) velocity ratio, $v_{4,5}/v_1$, using the second set of material properties and different frictional conditions, is shown in Figure 89. It is observed that simultaneously moving the die and the core-rod has a negative effect on the overall homogeneity of the green compact, where the density variation is observed to increase with $v_{4,5}/v_1$ regardless of the frictional condition imposed.

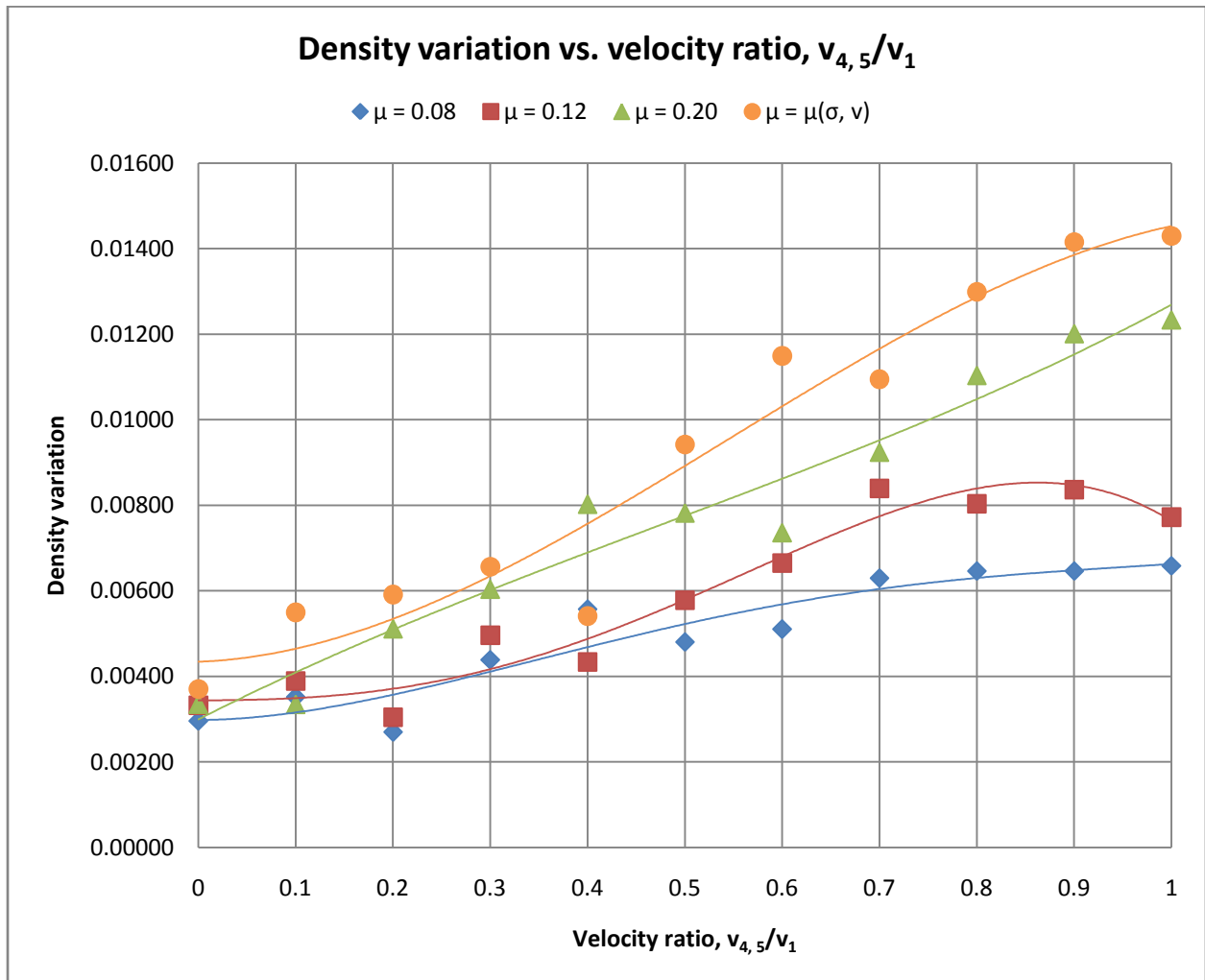


Figure 89. Density variation due to movement of tools 1, 4, and 5.

7.3.3 Summary and Discussion of Results

In the third case study, identical tool kinematics as in the former case study were employed. However, this time both the core-rod (5) and the die (4) were simultaneously set into motion at the same velocity, which was determined by the die and core-rod to upper-punch velocity ratio, $v_{4,5}/v_1$. Using the specified tool kinematics, the relationship between the green density variation and the velocity ratio, $v_{4,5}/v_1$, was evaluated using two sets of material properties and different frictional conditions.

Based on the results presented in Figures 88 and 89, it was observed that moving both the die and the core-rod has actually a negative effect of on the overall homogeneity of the green compact. By simultaneously moving the both tools with respect to the upper-punch, the density variation was observed to steadily increase with $v_{4,5}/v_1$, regardless of the friction coefficient or the material property set employed, thus, contributing to a higher density gradient. Overall, the magnitude of the evaluated density variation with respect to $v_{4,5}/v_1$ was observed to increase with the friction coefficient. Also, it is important to note that, generally, the highest magnitude in density variation was observed when using the variable friction coefficient, $\mu(\sigma_n, v_r)$, for all sets of material properties employed. Furthermore, it is important to note that no direct comparison of the above presented results can be made at this point as the study conducted by Shima et al. [101, 102] did not look into the influence of core-rod motion on the density variation of the multi-stepped part.

Further observation can be made by consulting Appendix F, where illustration of the relative density distribution over the cross-sectional area of the multi-stepped compact is presented for each corresponding velocity ratio, $v_{4,5}/v_1$, friction coefficient, and material property sets (i) and (ii). It is observed that upon increase of $v_{4,5}/v_1$, from 0 to 1.0, the overall density variation over the cross-sectional area of the compact increases for each corresponding friction coefficient and material property set. The rate of change of density variation is observed to increase with the friction coefficient, with the highest rate observed for the constant friction coefficient of 0.20 and the variable friction coefficient, $\mu(\sigma_n, v_r)$, for both material property sets.

More importantly, close examination of relative density values for each corresponding $v_{4,5}/v_1$ and the imposed frictional condition, reveals that the difference between the highest and the lowest relative density values generally increases with $v_{4,5}/v_1$, thus, constituting an overall increase in the density gradient; see Table 26. Lastly, it is important to note that the evaluated average relative density of the final multi-stepped compact is observed to remain steady with respect to $v_{4,5}/v_1$ for each corresponding friction coefficient and material property set. The complete summary of the evaluated average relative density is presented in Table 27.

Table 26. Difference between maximum and minimum relative density values.

| Using material properties provided by Shima | | | | |
|---|---|--------------------------------|--------------------------------|--|
| Velocity ratio, $v_{4,5}/v_1$ | Friction coefficient, μ | | | |
| | $\mu = 0.08$ | $\mu = 0.12$ | $\mu = 0.20$ | $\mu = \mu(\sigma_n, v_r)$ |
| 0 | 0.0468 | 0.0669 | 0.0524 | 0.0466 |
| 0.1 | 0.0467 | 0.0668 | 0.0719 | 0.0775 |
| 0.2 | 0.0549 | 0.0502 | 0.0627 | 0.0419 |
| 0.3 | 0.0503 | 0.0538 | 0.0542 | 0.0703 |
| 0.4 | 0.0439 | 0.0485 | 0.0703 | 0.0762 |
| 0.5 | 0.0455 | 0.0546 | 0.0945 | 0.0769 |
| 0.6 | 0.0771 | 0.0603 | 0.1048 | 0.0762 |
| 0.7 | 0.0545 | 0.0746 | 0.0710 | 0.1150 |
| 0.8 | 0.0859 | 0.0759 | 0.0919 | 0.1189 |
| 0.9 | 0.0731 | 0.0804 | 0.0968 | 0.1204 |
| 1.0 | 0.0805 | 0.0653 | 0.0854 | 0.1072 |
| Using material properties provided by Pavier and Doremus | | | | |
| Velocity ratio, $v_{4,5}/v_1$ | Friction coefficient, μ | | | |
| | $\mu = 0.08$ | $\mu = 0.12$ | $\mu = 0.20$ | $\mu = \mu(\sigma_n, v_r)$ |
| 0 | 0.0468 | 0.0669 | 0.0524 | 0.0466 |
| 0.1 | 0.0467 | 0.0668 | 0.0719 | 0.0775 |
| 0.2 | 0.0549 | 0.0502 | 0.0627 | 0.0419 |
| 0.3 | 0.0503 | 0.0538 | 0.0542 | 0.0703 |
| 0.4 | 0.0439 | 0.0485 | 0.0703 | 0.0762 |
| 0.5 | 0.0455 | 0.0546 | 0.0945 | 0.0769 |
| 0.6 | 0.0771 | 0.0603 | 0.1048 | 0.0762 |
| 0.7 | 0.0545 | 0.0746 | 0.071 | 0.115 |
| 0.8 | 0.0859 | 0.0759 | 0.0919 | 0.1189 |
| 0.9 | 0.0731 | 0.0804 | 0.0968 | 0.1204 |
| 1.0 | 0.0805 | 0.0653 | 0.0854 | 0.1072 |

Table 27. Average relative density of the final multi-stepped compacts.

| Using material properties provided by Shima | | | | |
|---|---|--------------------------------|--------------------------------|--|
| Velocity ratio, $v_{4,5}/v_1$ | Friction coefficient, μ | | | |
| | $\mu = 0.08$ | $\mu = 0.12$ | $\mu = 0.20$ | $\mu = \mu(\sigma_n, v_r)$ |
| 0 | 0.6885 | 0.6882 | 0.6882 | 0.6885 |
| 0.1 | 0.6885 | 0.6880 | 0.6875 | 0.6869 |
| 0.2 | 0.6883 | 0.6879 | 0.6878 | 0.6895 |
| 0.3 | 0.6892 | 0.6886 | 0.6880 | 0.6881 |
| 0.4 | 0.6892 | 0.6890 | 0.6869 | 0.6861 |
| 0.5 | 0.6881 | 0.6880 | 0.6858 | 0.6861 |
| 0.6 | 0.6864 | 0.6875 | 0.6858 | 0.6865 |
| 0.7 | 0.6876 | 0.6876 | 0.6872 | 0.6850 |
| 0.8 | 0.6860 | 0.6867 | 0.6849 | 0.6855 |
| 0.9 | 0.6878 | 0.6874 | 0.6862 | 0.6852 |
| 1.0 | 0.6868 | 0.6874 | 0.6858 | 0.6860 |
| Using material properties provided by Pavier and Doremus | | | | |
| Velocity ratio, $v_{4,5}/v_1$ | Friction coefficient, μ | | | |
| | $\mu = 0.08$ | $\mu = 0.12$ | $\mu = 0.20$ | $\mu = \mu(\sigma_n, v_r)$ |
| 0 | 0.6891 | 0.6877 | 0.6880 | 0.6876 |
| 0.1 | 0.6873 | 0.6868 | 0.6880 | 0.6858 |
| 0.2 | 0.6885 | 0.6894 | 0.6871 | 0.6868 |
| 0.3 | 0.6888 | 0.6879 | 0.6865 | 0.6864 |
| 0.4 | 0.6874 | 0.6889 | 0.6863 | 0.6874 |
| 0.5 | 0.6887 | 0.6884 | 0.6872 | 0.6854 |
| 0.6 | 0.6880 | 0.6876 | 0.6862 | 0.6839 |
| 0.7 | 0.6859 | 0.6862 | 0.6869 | 0.6869 |
| 0.8 | 0.6871 | 0.6865 | 0.6873 | 0.6858 |
| 0.9 | 0.6872 | 0.6865 | 0.6870 | 0.6836 |
| 1.0 | 0.6878 | 0.6867 | 0.6870 | 0.6844 |

8.0 Conclusion

8.1 Friction-assisted Compaction of Cylindrical Parts

From powder compaction simulation analyses of cylindrical parts, it was shown that the overall homogeneity of the corresponding green powder compacts may be considerably improved upon using the friction-assisted compaction technique, consisting of an active upper-punch and a die. Based on the overall observation of simulation results, the average relative density distribution over the final compact height was found to be more uniform at the die-to-upper-punch velocity ratio, $v_{\text{die}}/v_{\text{u-p}}$, of 0.5, reflecting density distribution of a double-action pressing, for all cases of the compact height-to-diameter ratio, h/d , and the material property sets employed. Thus, upon increasing $v_{\text{die}}/v_{\text{u-p}}$ from 0 to 0.5, an overall reduction in density gradient was observed.

The observed reduction in density gradient was further confirmed upon evaluation of the density variation, encompassing the overall cross-sectional area of the compact, which was observed to be the lowest at $v_{\text{die}}/v_{\text{u-p}}$ of 0.5, for all cases of the compact h/d . Upon increasing $v_{\text{die}}/v_{\text{u-p}}$ from 0 to 0.5, a decrease in density variation was observed. Thus, as $v_{\text{die}}/v_{\text{u-p}}$ was increased from a value of 0 to 0.5, a decrease in both the non-uniformity of density distribution over the compact height and the evaluated density variation was observed, hence, confirming an overall decline in density gradient over the compact height.

Moreover, as the compact h/d was reduced from 1.50 to 0.50, the overall uniformity of the density distribution over the compact volume was observed to improve. Likewise, the magnitude of the evaluated density variation was observed to decrease, generally, resulting in a lower density gradient over the compact height, for each corresponding $v_{\text{die}}/v_{\text{u-p}}$.

Upon using the variable friction coefficient, $\mu(\sigma_n, v_r)$, as opposed to the constant value of 0.1, the overall gradient in both the density distribution and the evaluated density variation was observed to roughly double for all corresponding values of the compact h/d and $v_{\text{die}}/v_{\text{u-p}}$. More importantly, the observed higher density gradient, attained using the variable friction coefficient, compared better with the experimental data as opposed to the results obtained using the constant friction coefficient, which was found to slightly underestimate the level of

non-uniformity in the overall density distribution over the compact height. Finally, it is interesting to point out that a minor difference was observed in the overall results attained using the two sets of material properties provided by Pavier and Doremus [10, 84], and Koval'chenko [54].

8.2 Compaction of a Multi-stepped Part

From simulation analyses of the multi-stepped part, studying the effect of the lower-inner-punch (3) to the upper-punch (1) velocity ratio, v_3/v_1 , on green density distribution, and using three sets of material properties, the evaluated density variation was found to be the lowest at a certain value of v_3/v_1 . The least variation in the overall density was observed in the vicinity of $v_3/v_1 = 0.50$, and the corresponding value of v_3/v_1 was generally found to slightly increase with the friction coefficient for all the sets of material properties employed. The highest value of v_3/v_1 , at the point of minimum density variation, was recorded for the variable friction coefficient, $\mu(\sigma_n, v_r)$.

More importantly, upon close examination of relative density values for each corresponding v_3/v_1 and the imposed frictional condition, it was observed that the difference between the highest and the lowest relative density levels had significantly decreased upon increase of v_3/v_1 from 0.45 to 0.50, thus, constituting an overall reduction in the density gradient. However, upon further increase of v_3/v_1 , from 0.50 to 0.55, the difference between the highest and the lowest relative density levels was observed to increase, thus, resulting in the increase of density gradient. Further, for each corresponding friction coefficient and material property set employed, the evaluated average relative density of the final multi-stepped compact was observed to decrease with v_3/v_1 .

Furthermore, using simulation analyses, it was possible to determine the values of critical velocity ratio, $v_c = v_3/v_1$, at which the initiation of a slip-crack defect was observed. Consequently, the occurrence of a slip-crack defect may be prevented upon avoiding further increase of v_3/v_1 beyond the determined value of the critical velocity ratio, v_c .

Studying the effect of the die (4) to upper-punch (1) velocity ratio, v_4/v_1 , on the green density variation, using three sets of material properties, it was observed that moving the die has actually a negative effect on the overall homogeneity of the green powder compact. Upon moving the die, the evaluated density variation was observed to progressively increase, predominately beyond v_4/v_1 of 0.2, regardless of the imposed friction coefficient, thus, contributing to a higher density gradient. Overall, the magnitude of the evaluated density variation with respect to v_4/v_1 was observed to increase with friction coefficient, where generally the highest magnitude was observed for the variable friction coefficient, $\mu(\sigma_n, v_r)$, for all the sets of material properties employed.

Similarly, studying the effect of the die (4) and core-rod (5) to upper-punch (1) velocity ratio, $v_{4,5}/v_1$, on the green density variation, using two sets of material properties, it was observed that moving the die and core-rod has a negative effect on the overall homogeneity of the green powder compact. Upon moving both corresponding tools, the density variation was observed to increase with $v_{4,5}/v_1$ regardless of the imposed friction coefficient, thus, contributing to a higher density gradient. Overall, the magnitude of the evaluated density variation with respect to $v_{4,5}/v_1$ was observed to increase with friction coefficient, where generally the highest magnitude was observed for the variable friction coefficient, $\mu(\sigma_n, v_r)$, for all the sets of material properties employed.

Lastly, closer observation of relative density values, studying the effects of both v_4/v_1 and $v_{4,5}/v_1$ on the density variation, revealed that the difference between the highest and the lowest relative density values generally increases with the corresponding velocity ratios, thus, confirming an overall increase in density gradient.

8.3 Specific Contribution

One major contribution of the present research was the implementation of three sets of material properties, all of which were experimentally derived using iron-based granular powder and pre-sintered specimens (porous material), into all of the corresponding FE models. All corresponding material properties showed dependence on the density. It is important to note

that in most of the simulation studied covered in literature, the variance of material properties is overlooked, i.e., constant values are employed. This, however, is unacceptable as it fails to assimilate a realistic material behaviour.

Employing more than one material property set made it possible to examine the sensitivity of the obtained simulation results. Specifically, it was interesting to see how the results match using the material properties derived from the granular powder and those derived from the pre-sintered powder compact specimens. This was important as the employed powder constitutive model – Shima and Oyane [106], was originally derived for the analysis of porous material.

Another major contribution was the implementation of the variable friction coefficient provided by Pavier and Doremus [19, 21, 86]. Although, a modified version of the corresponding variable friction coefficient expression had to be employed, the ensuing simulation results compared more closely with the experimental results for the friction-assisted compaction of the cylindrical parts, presented by Canta and Frunza [15]. It is important to note that most of the simulation studies presented in the literature had employed a constant friction coefficient value [13, 27, 31, 48, 49, 70, 89, 101, 102, 110, 112, 115, 124, 129]. However, as was shown earlier in this report, based on experimental studies, the friction coefficient tends to vary and is a function of several parameters. In total, only four literature sources were found which had employed the variable friction coefficient relation proposed by Wikman et al. [80, 88, 125, 126]; however, as discussed earlier, this relation does not give true representation of the actual conditions; see section 3.2.3.

Further, equation (45) proposed by Shima et al. [101, 102] for the evaluation of density variation, encompassing the overall cross-sectional area of the green powder compact, was employed to further confirm an overall decline in the density gradient for the analyses of the friction-assisted compaction of cylindrical parts. Lastly, simulation analyses were conducted to look into the influence of the core-rod motion on density variation of the multi-stepped part as an extension to the work presented by Shima et al. [101, 102],.

8.4 Future Work

For future work, the primary focus should be in overcoming all the encountered software limitations presented in the present study, that is:

- Implementation of the variable friction coefficient relation, $\mu(\sigma_n, \rho, v_r)$, into the simulation models, as derived by Pavier and Doremus [19, 21, 86], expressed as a function of all the primary dependent variables – normal stress, powder density, and relative sliding velocity, respectively.
- Implementation of a load path dependent yield stress, $\bar{\sigma}(\bar{\epsilon}, \dot{\bar{\epsilon}})$, to fully account for the work-hardening effect in the compressed powder during the compaction cycle.

Other possibilities include:

- To test the alternative powder constitutive models to see how their simulation results compare with each other and to the available experimental data. Specifically, considering the Cap-model, which in the last decade has been gaining more popularity.
- Another possibility is to develop a new powder constitutive model which overcomes the limitations presented by the existing models.
- Conduct FEA of a more complex geometry such as a gear or a jet engine component, using a 3-D model.
- More focus into the parameters causing a crack-defect initiation and derivation of optimization techniques to limit their occurrence.
- Investigate possible optimization techniques of the sintering process to lower the effect of geometry distortion due to the density gradient and thus limit the possible need for secondary machining operations.
- Conduct simulation analyses using powders of non-ferrous composition, particularly aluminum and refractory alloys, such as titanium, which are more commonly used for the aerospace applications.

- Investigate other branches of PM technology and their optimization, such as hot isostatic pressing (HIP), which due to its advancements in the last two decades has led to its general acceptance as the main choice for the production of high-performance aircraft landing gears.
- Lastly, consider the effect of preheating both powder and pressing tools on the final density of the compact. Recent research shows that doing so may increase the overall final density of the green powder compact.

9.0 References

- [1] *Handbook of Powder Science & Technology*, (1997). 2nd Ed., Chapman & Hall, New York, Toronto.
- [2] Al-Qureshi, H., Soares, M. R. F., Hotza, D., Alves, M. C., Klein, A. N. (2008). "Analyses of the Fundamental Parameters of Cold Die Compaction of Powder Metallurgy." *Journal of Materials Processing Tech*, 199(1-3), 417-424.
- [3] Amin, K. E. (1987). "Friction in Metal Powders." *International Journal of Powder Metallurgy (Princeton NJ)*, 23(2), 83-93.
- [4] Asthana, R., Kumar, A., Dahotre, N. B. (2006). *Materials Processing and Manufacturing Science*, Elsevier Academic Press, Amsterdam, Boston.
- [5] Bocchini, G. F. (1995). "Friction effects in metal powder compaction. Part one - theoretical aspects." *Proc., Part 1 (of 3)*, Metal Powder Industries Federation, 2, 115-140.
- [6] Bocchini, G. F., Fontanari, V., Molinari, A. (1995). "Friction effects in metal powder compacting. Part two - experimental results." *Proc., Part 1 (of 3)*, Metal Powder Industries Federation, 2, 141-151.
- [7] Boitsov, O. F., Chernyshev, L. I., Solonin, S. M. (2006). "Effect of the Structure of the Pore Space on the Mechanical Properties of Highly Porous Materials Produced with Pore-Forming Agents." *Powder Metallurgy and Metal Ceramics*, 45(9-10), 409-414.
- [8] Bonnefoy, V., Doremus, P., Puente, G. (2003). "Investigations on Friction Behaviour of Treated and Coated Tools with Poorly Lubricated Powder Mixes." *Powder Metallurgy*, 46(3), 224-228.
- [9] Boresi, A. P., and Schmidt, R. J. (2003). *Advanced Mechanics of Materials*, 6th Ed., John Wiley & Sons, Inc., USA.
- [10] Brewin, P. R., Coube, O., Doremus, P., Tweed, J. H. (2008). *Modelling of Powder Die Compaction*, Springer, London.
- [11] Buchatskii, L. M., Stolin, A. M., Khudyaev, S. I. (1986). "Kinetics of the Change of Density Distribution in Hot One-Sided Pressing of a Viscous Porous Body." *Soviet Powder Metallurgy and Metal Ceramics*, 25(9), 733-737.
- [12] Callister, W. D. J. (2003). *Material Science and Engineering: An Introduction*, 6th Ed., John Wiley & Sons, Inc., USA.

- [13] Cameron, I. M., Gethin, D. T., Tweed, J. H. (2002). "Friction Measurement in Powder Die Compaction by Shear Plate Technique." *Powder Metallurgy*, 45(4), 345-353.
- [14] Cameron, I. M., and Gethin, D. T. (2001). "Exploration of Die Wall Friction for Powder Compaction using a Discrete Finite Element Modelling Technique." *Modell. Simul. Mater. Sci. Eng.*, 9(4), 289-307.
- [15] Canta, T., and Frunza, D. (2003). "Friction-assisted pressing of PM components." *Proc., Journal of Materials Processing Technology*, 143-144(1), 645-650.
- [16] Cedergren, J., Sorensen, N. J., Bergmark, A. (2002). "Three-Dimensional Analysis of Compaction of Metal Powder." *Mech. Mater.*, 34(1), 43-59.
- [17] Chen, W. F., and Han, D. J. (1988). *Plasticity for Structural Engineers*, Springer-Verlag, New York, USA.
- [18] Cocoz , G., Bellet , M., Lecot , R., Ackermann , L., Häggblad, H. A. (1994). "Cold Compaction of Iron Powder: Experiments and Simulation." *Powder Metallurgy World Congress*, 1, 709-712.
- [19] Doremus, P., Toussaint, F., Pavier, E. (2001). "Investigation of Iron Powder Friction on Tungsten Carbide Tool Wall." *Powder Metallurgy*, 44(3), 243-247.
- [20] Doremus, P., Pavier, E., Kergadallan, J., Puente, G. (1999). "Axisymmetric Part Compaction: Data Base for Numerical Simulation." *Int. J. Powder Metall. (Princeton NJ)*, 35(3), 63-69.
- [21] Doremus, P., and Pavier, E. (1998). "Friction: Experimental Equipment and Measuring." *1998 PM World Congress Powder Compaction*, 114-119.
- [22] Doremus, P., Geindreau, C., Martin, A., Debove, L., Lecot, R., Dao, M. (1995). "High Pressure Triaxial Cell for Metal Powder." *Powder Metallurgy*, 38(4), 284-287.
- [23] Drachinskii, A. S., Kushchevskii, A. E., Podrezov, Y. N., Firstov, S. A. (1984). "Strain Hardening and Failure of Powder Metallurgy Iron." *Soviet Powder Metallurgy and Metal Ceramics*, 23(10), 805-809.
- [24] Ernst, E., and Barnekow, D. (1994). "Pressure, Friction and Density during Axial Powder Compaction." *PM'94: World Congress on Powder Metallurgy*, 1, 673-676.

- [25] Ernst, E., Thummler, F., Beiss, P., Wahling, R., Arnhold, V. (1991). "Friction Measurements during Powder Compaction." *Powder Metallurgy International*, 23(2), 77-78.
- [26] German, R. M. (1998). *Powder Metallurgy of Iron and Steel*, Wiley, New York.
- [27] Gethin, D. T., Tran, V. D., Lewis, R. W., Ariffin, A. K. (1994). "An Investigation of Powder Compaction Processes." *Int. J. Powder Metall. (Princeton NJ)*, 30(4), 385-398.
- [28] Gillia, O., and Bouvard, D. (2001). "Continuum Modelling of Sintering of Powder Compacts." *Recent Developments in Computer Modeling of Powder, Metallurgy Processes*, 176, 122-134.
- [29] Griffiths, T. J., and Ghanizadeh, A. (1986). "Determination of Elastic Constants for Porous Sintered Iron Powder Compacts." *Powder Metallurgy*, 29(2), 129-133.
- [30] Groover, M. P. (2007). *Fundamentals of Modern Manufacturing: Materials, Processes, and Systems*, 3rd Ed., Wiley, USA.
- [31] Guyoncourt, D. M. M., Tweed, J. H., Gough, A., Dawson, J., Pater, L. (2001). "Constitutive Data and Friction Measurements of Powders using Instrumented Die." *Powder Metallurgy*, 44(1), 25-33.
- [32] Haggblad, H.-A., and Oldenburg, M. (1994). "Modelling and Simulation of Metal Powder Die Pressing with use of Explicit Time Integration." *Modell. Simul. Mater. Sci. Eng.*, 2(4), 893-911.
- [33] Haggblad, H.-A., Doremus, P., Bouvard, D. (1996). "An International Research Program on the Mechanics of Powder Metal Forming." *Adv. Powder Metallurgy & Particulate Matls.*, 2(PART 7), 179-192.
- [34] Haggblad, H.-A., Doremus, P., Bouvard, D. "An International Research Programme on the Mechanics of Metal Powder Forming." *Mechanics of Metal Powder Forming*, 7, 179-192.
- [35] Henriques, V. A. R., de Campos, P. P., Cairo, C. A. A., Bressiani, J. C. (2005). "Production of Titanium Alloys for Advanced Aerospace Systems by Powder Metallurgy." *Materials Research*, 8(4), 443-446.
- [36] Höganäs AB. (2008). "Product data handbook: Diffusion-alloyed powder grades > distalloy AE > typical data.pdf." <http://stage.hoganas.com/en/Products--Applications/Sintered-Components/Product-Data-Handbook/>>.

- [37] Höganäs AB. (2008). "Product data handbook: Powder grades & sintered properties > diffusion-alloyed powder grades > distaloy AE > sintered properties > distaloy AE (density vs. compaction pressure).pdf." <<http://stage.hoganas.com/en/Products--Applications/Sintered-Components/Product-Data-Handbook/>>.
- [38] Höganäs AB. (2008). "Product data handbook: Powder grades & sintered properties > diffusion-alloyed powder grades > distaloy AE > sintered properties > distaloy AE + C.pdf." <<http://stage.hoganas.com/en/Products--Applications/Sintered-Components/Product-Data-Handbook/>>.
- [39] Höganäs AB. (2008). "Product data handbook: Powder grades & sintered properties > diffusion-alloyed powder grades > distaloy AE > sintered properties > distaloy AE + 5% C (various sintering temp.).pdf." <<http://stage.hoganas.com/en/Products--Applications/Sintered-Components/Product-Data-Handbook/>>.
- [40] Höganäs AB. (2008). "Product data handbook: Powder grades & sintered properties > diffusion-alloyed powder grades > distaloy AE > sintered properties > distaloy AE + 5% C (various sintering time).pdf." <<http://stage.hoganas.com/en/Products--Applications/Sintered-Components/Product-Data-Handbook/>>.
- [41] Höganäs AB. (2008). "Product data handbook: Powder grades & sintered properties > diffusion-alloyed powder grades > distaloy AE > sintered properties > distaloy AE + C (vs. carbon content).pdf." <<http://stage.hoganas.com/en/Products--Applications/Sintered-Components/Product-Data-Handbook/>>.
- [42] Höganäs AB. (2008). "Powder selection guides: Höganäs iron and steel powders for sintered components > POWDER SELECTION GUIDE.pdf." <<http://stage.hoganas.com/en/Products--Applications/Sintered-Components/Powder-Selection-Guides/>>.
- [43] Kang, C. S., Kim, K. T., Lee, S. C., Rozenberg, O. (2007). "Densification Behavior of Iron Powder during Cold Stepped Compaction." *Materials Science & Engineering A (Structural Materials: Properties, Microstructure and Processing)*, 452-453, 359-366.
- [44] Kergadallan, J., Puente, G., Doremus, P., Pavier, E. (1997). "Compression of an Axisymmetric Part with an Instrumented Press." *Proceedings of the International Workshop on Modelling of Metal Powder Forming Processes*, 277-285.

- [45] Khoei, A. R. (2005). *Computational Plasticity in Powder Forming Processes*, 1st Ed., Elsevier Ltd., UK.
- [46] Kim, K. T., and Kim, J. S. (1998). "Stage 1 Compaction Behaviour of Tool Steel Powder Under Die Pressing." *Powder Metallurgy*, 41(3), 199-204.
- [47] Kim, K. T., and Suh, J. (1989). "Elastic-Plastic Strain Hardening Response of Porous Metals." *Int. J. Eng. Sci.*, 27(7), 767-78.
- [48] Know, Y. S., Chung, S. H., Sanderow, H. I., Kim, K. T., German, R. M. (2003). "Numerical Analysis and Optimization of Die Compaction Process." *Advances in Powder Metallurgy and Particulate Materials*, 4, 37-50.
- [49] Know, Y. S., Chung, S. H., Binet, C. B., Zhang, R., Engel, R. S., Salamon, N. J., German, R. M. (2002). "Application of Optimization Technique in the Powder Compaction and Sintering Process." 9, 131-146.
- [50] Know, Y. S., Lee, H. T., Kim, K. T. (1997). "Analysis for Cold Die Compaction of Stainless-Steel Powder." *Journal of Engineering Materials and Technology*, 119, 366-373.
- [51] Korachkin, D., Gethin, D. T., Lewis, R. W., Tweed, J. H. (2008). "Friction Measurement and Lubrication in Unloading and Ejection Stages in Powder Pressing Cycle." *Powder Metallurgy*, 51(1), 14-30.
- [52] Korachkin, D., Gethin, D. T., Lewis, R. W., Tweed, J. H., Guyoncourt, D. M. M. (2008). "Measurement of Young's Modulus and Tensile Failure Properties of Green Powder Compacts." *Powder Metallurgy*, 51(2), 150-159.
- [53] Koval'chenko, M. S., and Ochkas, L. F. (2008). "Densification Dynamics of Copper and Iron Powder Billets in Hot Shock Compaction: Simulation and Analysis." *Powder Metallurgy and Metal Ceramics*, 47(5-6), 273-283.
- [54] Koval'chenko, M. S. (2003). "Elasticity and viscosity of isotropic porous materials." *Proc., International Conference 'Nanomaterials and Coatings in Biomedicine and Sensors'*, Kluwer Academic/Consultants Bureau, 81-87.
- [55] Koval'chenko, M. S. (1997). "Dynamics of Mechanical Actions on Materials. VI. Periodic and Aperiodic Movements of the Autonomous Dynamic System." *Poroshkovaya Metallurgiya*, (3-4), 113-122.
- [56] Koval'chenko, M. S. (1996). "Mechanical Properties of Isotropic Porous Materials. IV. the Effect of Mesostructural Defects." *Powder Metallurgy and Metal Ceramics*, 35(9-10), 561-568.

- [57] Koval'chenko, M. S. (1993). "The Mechanical Properties of Porous Materials I. Elastic and Rheological Properties." *Poroshkovaya Metallurgiya*, (3), 89-96.
- [58] Koval'chenko, M. S. (1993). "Mechanical Properties of Isotropic Porous Materials. III. Strain-Hardening and Failure." *Powder Metallurgy and Metal Ceramics*, 32(5), 432-436.
- [59] Koval'chenko, M. S. (1993). "Mechanical Properties of Isotropic Porous Materials. II. Uniaxial Tensile and Compressive Yield Points." *Powder Metallurgy and Metal Ceramics*, 32(4), 366-370.
- [60] Koval'chenko, M. S. (1993). "The Dynamics of Mechanical Actions on Materials. I. General Theory." *Powder Metallurgy and Metal Ceramics*, 32(7), 596-601.
- [61] Kwon, Y. S., Chung, S. H., Sanderow, H. I., Kim, K. T., German, R. M. (2003). "Numerical Analysis and Optimization of Die Compaction Process." *Proceedings of the 2003 International Conference on Powder Metallurgy & Particulate Materials*, (PART 4), 37-50.
- [62] Lee, Y.-S. (2002). "Development of constitutive equations for plastic deformation of a porous material using numerical experiments." *Proc., Second International Conference on Advanced Forming and Die Manufacturing Technology*, Elsevier, 130-131, 161-167.
- [63] Li Y.-L., Liu F.-S., Zhang M.-J., Ma X.-J., Li Y.-L., Zhang J.-C. (2009). "Measurement on Effective Shear Viscosity Coefficient of Iron Under Shock Compression at 100 GPa." *Chinese Physics Letters*, 26(3), 038301 (3 pp.).
- [64] Liu, Y., Chen, L. F., Tang, H. P., Liu, C. T., Liu, B., Huang, B. Y. (2006). "Design of Powder Metallurgy Titanium Alloys and Composites." *Materials Science & Engineering A (Structural Materials: Properties, Microstructure and Processing)*, 418(1-2), 25-35.
- [65] Logan, D. L. (2002). *A First Course in Finite Element Method*, 3rd Ed., Bools/Cole, Thomson Learning, USA.
- [66] Mair, G. (1991). "Correlation between Axial Density and Friction in the Compaction and Ejection of PM Shapes." *Metal Powder Report*, 46(9), 60-64.
- [67] Mineev, V. N., and Funtikov, A. I. (2006). "Measurements of the Viscosity of Iron and Uranium Under Shock Compression." *High Temperature*, 44(6), 941-949.
- [68] Moon, J. R. (1989). "Elastic Moduli of Powder Metallurgy Steels." *Powder Metallurgy*, 32(2), 132-139.

- [69] Mori, K., Shima, S., Osakada, K. (1980). "Finite Element Method for the Analysis of Plastic Deformation of Porous Metals." *Bulletin of the JSME*, 23(178), 516-522.
- [70] Mosbah, P., Shima, S., Habraken, A.-M., Charlier, R. (1999). "Numerical Simulation of Compacting Process of a Multi-Stepped Part with Comparison to Experiments." *Funtai Oyobi Fummatsu Yakin*, 46(7), 696-704.
- [71] Mosbah, P., and Bouvard, D. (1996). "Finite Element Simulation of Die Compaction and Ejection of Iron Powder." *Advances in Powder Metallurgy and Particulate Materials*, 2, 23.
- [72] MSC.Marc Technical Support, Personal email correspondence.
- [73] MSC. Software Corporation. (2008). "Marc 2008r1 User's Guide." U.S.A.
- [74] MSC. Software Corporation. (2008). "Marc 2008r1, Volume A: Theory and User Information." U.S.A.
- [75] MSC. Software Corporation. (2008). "Marc 2008r1, Volume B: Element Library." U.S.A.
- [76] MSC. Software Corporation. (2008). "Marc 2008r1, Volume C: Program Input." U.S.A.
- [77] MSC. Software Corporation. (2008). "Marc 2008r1, Volume D: User Subroutines and Special Routines." U.S.A.
- [78] MSC. Software Corporation. (2008). "Marc 2008r1, Volume E: Demonstration Problems." U.S.A.
- [79] MSC. Software Corporation. (2003). "MSC. Marc Advanced Course." U.S.A.
- [80] Oldenburg , M., Häggblad, H.-A., Wikman, B. (1996). "A Friction Model for Iron Powder Pressing Based on a Tribological Approach." *Advances in Powder Metallurgy and Particulate Materials*, 7, 329-340.
- [81] Oyane, M., Shima, S., Tabata, T. (1978). "Consideration of Basic Equations, and their Application, in the Forming of Metal Powders and Porous Metals." *Journal of Mechanical Working Technology*, 1, 325-341.
- [82] Park, J. J. (1995). "Constitutive Relations to Predict Plastic Deformations of Porous Metals in Compaction." *Int. J. Mech. Sci.*, 37(7), 709-719.

- [83] Pavanachand, C., and Krishnakumar, R. (1997). "Yield Function Parameters for Metal Powder Compaction Based on Unit Cell Studies." *Acta Materialia*, 45(4), 1425-1444.
- [84] Pavier, E., and Doremus, P. (1999). "Triaxial Characterisation of Iron Powder Behaviour." *Powder Metallurgy*, 42(4), 345-352.
- [85] Pavier, E., and Doremus, P. (1997). "Comparison between Constitutive Equations. Modelling the Compaction of Iron Powder and Experimental Data obtained with Triaxial Tests." *International Workshop on Modelling of Metal Powder Forming Processes*, 1-8.
- [86] Pavier, E., and Doremus, P. (1997). "Friction Behaviour of an Iron Powder Investigated with Two Different Apparatus." *International Workshop on Modelling of Metal Powder Forming Processes*, 345-350.
- [87] Pavier, E., and Doremus, P. (1996). "Mechanical Behavior of a Lubricated Iron Powder." *Advances in Powder Metallurgy and Particulate Materials*, 2(PART 6), 27-40.
- [88] PM Modnet Computer Modeling Group. (1999). "Comparison of Computer Models Representing Powder Compaction Process." *Powder Metallurgy*, 42(4), 301-311.
- [89] PM Modnet Methods and Measurements Group. (2000). "Measurement of Friction for Powder Compaction Modelling-Comparison between Laboratories." *Powder Metallurgy*, 43(4), 364-374.
- [90] PM Modnet Research Group. (2002). "Numerical Simulation of Powder Compaction for Two Multilevel Ferrous Parts, Including Powder Characterisation and Experimental Validation." *Powder Metallurgy*, 45(4), 335-344.
- [91] Podrezov, Y. N., Shtyka, L. G., Verbylo, D. G. (2000). "Strain Hardening of Porous Iron Under Uniaxial Compression." *Powder Metallurgy and Metal Ceramics*, 39(1-2), 92-96.
- [92] Podrezov, Y. N., Chernyshev, L. I., Lugovoi, N. I., Verbilo, D. G. (1999). "Structural Sensitivity of the Ultimate Mechanical Properties of Biporous Materials Prepared using a Pore-Former." *Powder Metallurgy and Metal Ceramics*, 38(7-8), 403-407.
- [93] Polyakov, V. V., and Alekseev, A. N. (1994). "Porosity Dependence of the Internal Friction and Elastic Characteristics of Iron Powder." *Powder Metallurgy and Metal Ceramics*, 33(3-4), 192-193.

- [94] Polyakov, V. V., and Alekseev, A. N. (1994). "Dependence of Inner Friction and Elastic Characteristics of Powder Iron on Porosity." *Poroshkovaya Metallurgiya*, (3-4), 91-92.
- [95] Radchenko, A. K. (2004). "Mechanical Properties of Unsintered Pressings. I. Phenomenological Relations for Unsintered Pressing Strength." *Powder Metallurgy and Metal Ceramics*, 43(9-10), 447-460.
- [96] Savenkov, G. G., and Meshcheryakov, Y. I. (2002). "Structural Viscosity of Solid Bodies." *Fizika Goreniya i Vzryva*, 38(3), 113-118.
- [97] Schaefer, D. L., and Trombino, C. J. (2005). "State of the North American P/M Industry-2005." *Int. J. Powder Metall. (Princeton NJ)*, 41(4), 27-32.
- [98] Schaefer, D. L., and Trombino, C. J. (2004). "State of the North American P/M Industry - 2004." *Int. J. Powder Metall. (Princeton NJ)*, 40(4), 27-32.
- [99] Schaefer, D. L., and Trombino, C. J. (2003). "State-of-the-North American P/M Industry - 2003." *Int. J. Powder Metall. (Princeton NJ)*, 39(5), 31-36.
- [100] Schneider, L. C. R., and Cocks, A. C. F. (2002). "Experimental Investigation of Yield Behaviour of Metal Powder Compacts." *Powder Metallurgy*, 45(3), 237-245.
- [101] Shima, S. (2002). "Finite Element Simulation of Compaction." *Int. J. Powder Metall. (Princeton NJ)*, 38(2), 41-47.
- [102] Shima, S., Kotera, H., Yamamoto, Y. (2000). "Finite Element Simulation of Compacting Process of Multi-Stepped Part." *Funtai Oyobi Fummatsu Yakin*, 47(12), 1312-1317.
- [103] Shima, S., and Kotera, H. (1998). "A Study of Constitutive Behaviour of Powders for Application to Simulation of Compaction Processes." *Proceedings of the 1998 Powder Metallurgy World Congress & Exhibition, Special Interest Seminar*, 25-32.
- [104] Shima, S., Kotera, H., Hong, Z., Funato, M. (1996). "A Study of Iron Powders by Three Dimensional Compaction." *Advances in Powder Metallurgy and Particulate Materials*, 2(7), 193-205.
- [105] Shima, S., and Kotera, H. (1994). "Constitutive equations for granular materials undergoing compaction with internal friction." *Proc., Part 7 (of 7)*, Metal Powder Industries Federation, 71-71.
- [106] Shima, S., and Oyane, M. (1976). "Plasticity Theory for Porous Metals." *Int. J. Mech. Sci.*, 18(6), 285-291.

- [107] Shima, S., Tabata, T., Oyane, M., Kawakami, T. (1976). "Upper Bound Theory for Deformation of Porous Materials." *Memoirs of the Faculty of Engineering, Kyoto University*, 38, 117-137.
- [108] Skorokhod, V. V., Shtern, M. B., Martynova, I. F. (1987). "Theory of Nonlinearly Viscous and Plastic Behavior of Porous Materials." *Soviet Powder Metallurgy and Metal Ceramics*, 26(8), 621-626.
- [109] Solimanjad, N. (2003). "New Method for Measuring and Characterisation of Friction Coefficient at Wide Range of Densities in Metal Powder Compaction." *Powder Metallurgy*, 46(1), 49-54.
- [110] Solimanjad, N., and Larsson, R. (2003). "Die Wall Friction and Influence of some Process Parameters on Friction in Iron Powder Compaction." *Materials Science and Technology*, 19(12), 1777-1782.
- [111] Taniguchi, Y., Dohda, K., Wang, Z. (2005). "Lubricating Effect on Density Distribution in Uniaxial Powder Compaction." *Mater Forum*, 29, 356-362.
- [112] Trasorras, J. R. L., Parameswaran, R., Cocks, A. C. F. (1998). "Mechanical Behavior of Metal Powders and Compaction Modeling." *ASM Handbook*, 7, 326-342.
- [113] Turenne, S., Godère, C., Thomas, Y. (2000). "Effect of Temperature on the Behaviour of Lubricants during Powder Compaction." *Powder Metallurgy*, 43(2), 139-142.
- [114] Turenne, S., Godere, C., Thomas, Y., Mongeon, P.-E. (1999). "Evaluation of Friction Conditions in Powder Compaction for Admixed and Die Wall Lubrication." *Powder Metallurgy*, 42(3), 263-268.
- [115] Wang D.-G., Wu Y.-C., Jiao M.-H., Ting, X., Yu J.-W. (2008). "Research of Favorable Conversion of Friction during Powder Compaction." *Material Science Forum*, 575-578(1), 443-448.
- [116] Wei, D., Yang, X., Wang, Y. (2008). "Model for Calculating the Reliability of Powder Metallurgy Turbine Disk Based on Distribution of Defects." *Jixie Gongcheng Xuebao/Chinese Journal of Mechanical Engineering*, 44(11), 132-137.
- [117] Wei, D.-S., and Wang, Y.-R. (2008). "Lifing Methodology of Crack Propagation in Powder Metallurgy Turbine Disk." *Tuijin Jishu/Journal of Propulsion Technology*, 29(6), 753-758.
- [118] White, D. G. (2002). "State-of-the-North American P/M Industry - 2002." *Int. J. Powder Metall. (Princeton NJ)*, 38(5), 31-37.

- [119] White, D. G. (2001). "State-of-the-North American P/M Industry - 2001." *Int. J. Powder Metall. (Princeton NJ)*, 37(4), 33-41.
- [120] White, D. G. (2000). "State-of-the-North American P/M Industry - 2000." *Int. J. Powder Metall. (Princeton NJ)*, 36(5), 41-47.
- [121] White, D. G. (1999). "State-of-the-P/M Industry in North America - 1999." *Int. J. Powder Metall. (Princeton NJ)*, 35(5), 25-29.
- [122] White, D. G. (1998). "Challenges of Growth: State-of-the-P/M Industry: North America." *Int. J. Powder Metall. (Princeton NJ)*, 34(5), 27-35.
- [123] White, D. G. (1993). "State of the North American P/M Industry." *Int. J. Powder Metall. (Princeton NJ)*, 1-12.
- [124] Wikman, B., Solimannezhad, N., Larsson, R., Oldenburg, M., Häggblad, H.-A. (2000). "Wall Friction Coefficient Estimation through Modelling of Powder Die Pressing Experiment." *Powder Metallurgy*, 43(2), 132-138.
- [125] Wikman, B., Oldenburg, M., Häggblad, H.-A. (1998). "Modelling Methods in Pressing Simulations of Metal Powder Components." *Simulation of Material Processing: Theory, Methods and Applications*, Huetink & Baaijens, 397-402.
- [126] Wikman, B., Oldenburg, M., Häggblad, H.-A. (1997). "Modelling of Powder-Wall Friction for Simulation of Iron Powder Pressing." *Proceedings of the International Workshop on Modelling of Metal Powder Forming Processes*, 149-157.
- [127] Zhao, Y. H., Tandon, G. P., Weng, G. J. (1989). "Elastic Moduli for a Class of Porous Materials." *Aeta Mechanica*, 76, 105-131.
- [128] Zherdin, A. G., Podrezov, Y. N., Firstov, S. A., Shtyka, L. G. (1989). "Effect of Porosity on Microplastic Deformation of Iron Base Powder Materials." *Soviet Powder Metallurgy and Metal Ceramics*, 28(7), 579-584.
- [129] Zhou, Z. Y., Zhao, W. B., Chen, P. Q., Chen, W. P., Shao, M., Wang, J. W. (2002). "Simulation of Die Wall Friction Effect on Density Distribution in Metallic Powder Compaction." *Trans. Nonferrous Met. Soc. China*, 12(5), 890-893.

Appendix A. Effect of Die to Upper-Punch Velocity Ratio on Density Distribution of Cylindrical Parts with Compact Height-to-Diameter Ratio of 1.50

A.1 Using Material Properties Provided by Pavier and Doremus [10, 84]

A.1.1 Using Constant Friction Coefficient of 0.1

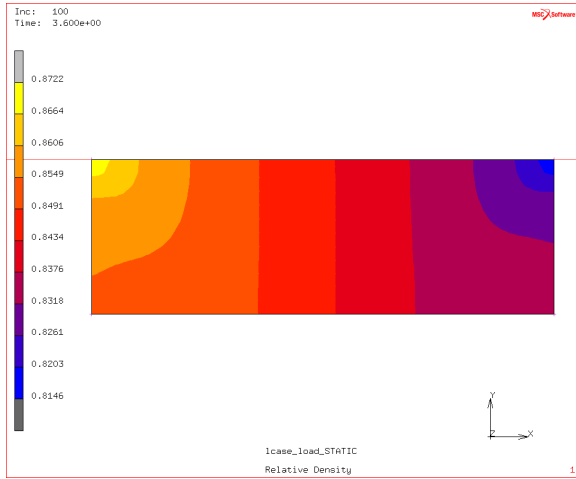


Figure 90. Relative density distribution at $v_{die}/v_{U-p} = 0$

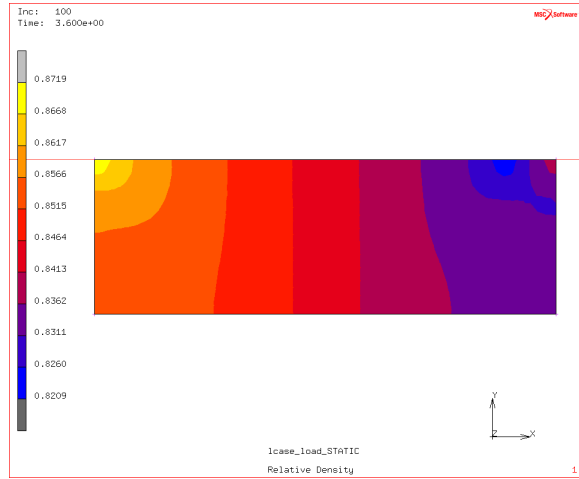


Figure 91. Relative density distribution at $v_{die}/v_{U-p} = 0.1$

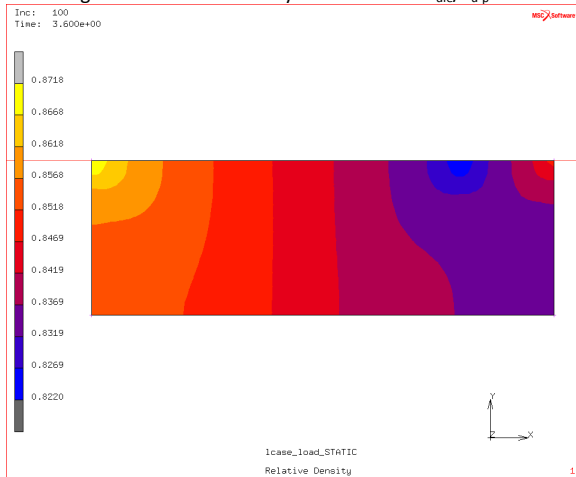


Figure 92. Relative density distribution at $v_{die}/v_{U-p} = 0.2$

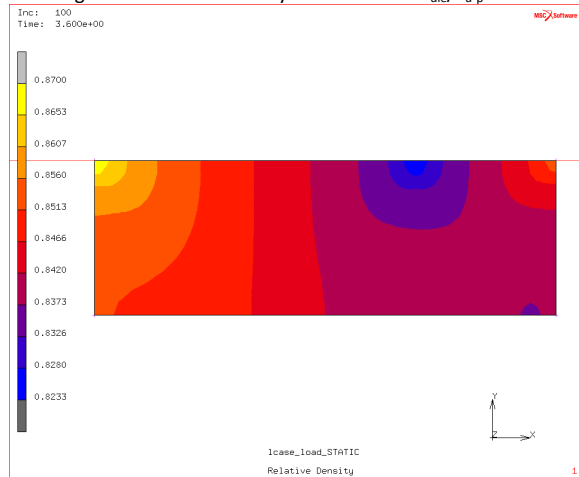


Figure 93. Relative density distribution at $v_{die}/v_{U-p} = 0.3$

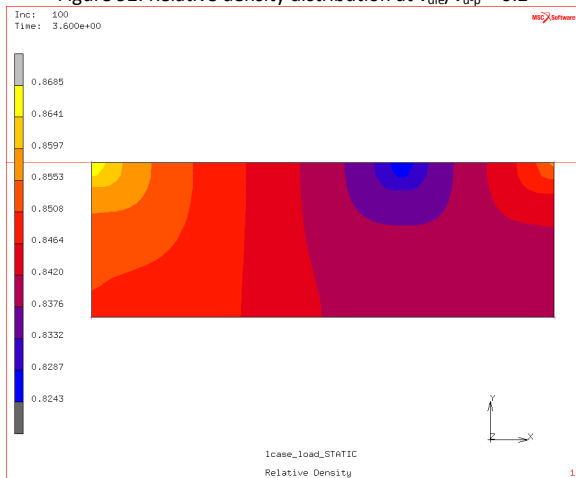


Figure 94. Relative density distribution at $v_{die}/v_{U-p} = 0.33$

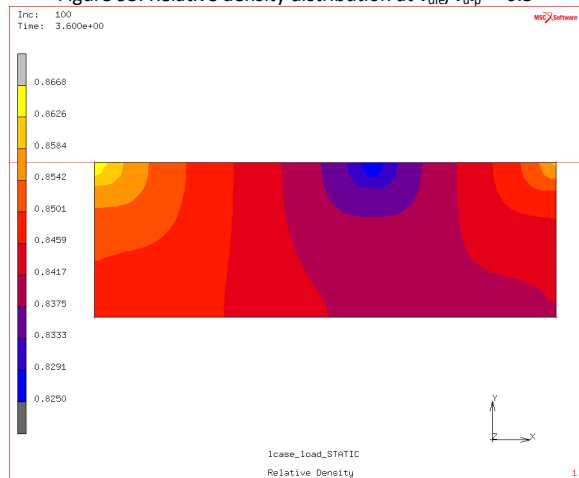


Figure 95. Relative density distribution at $v_{die}/v_{U-p} = 0.4$

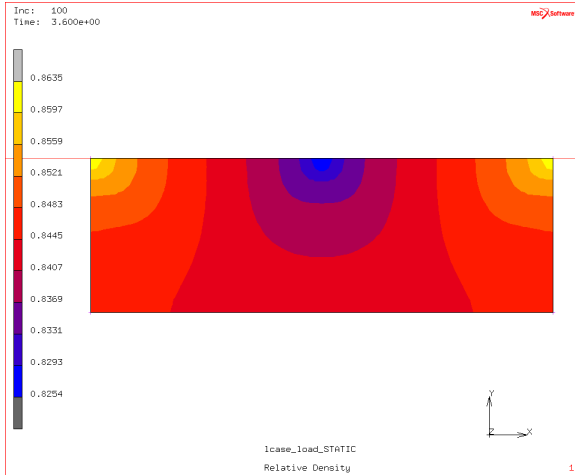


Figure 96. Relative density distribution at $v_{die}/v_{u-p} = 0.5$

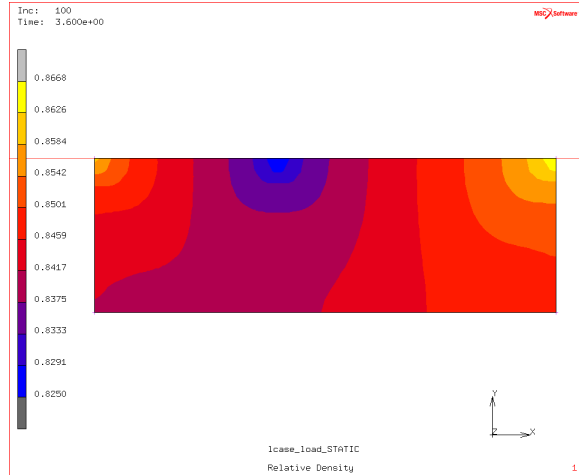


Figure 97. Relative density distribution at $v_{die}/v_{u-p} = 0.6$

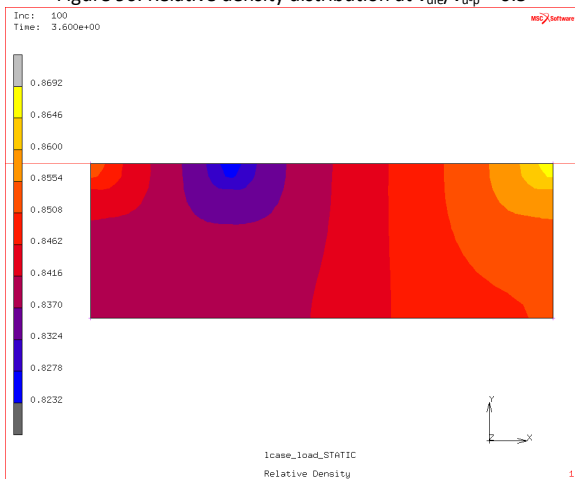


Figure 98. Relative density distribution at $v_{die}/v_{u-p} = 0.7$

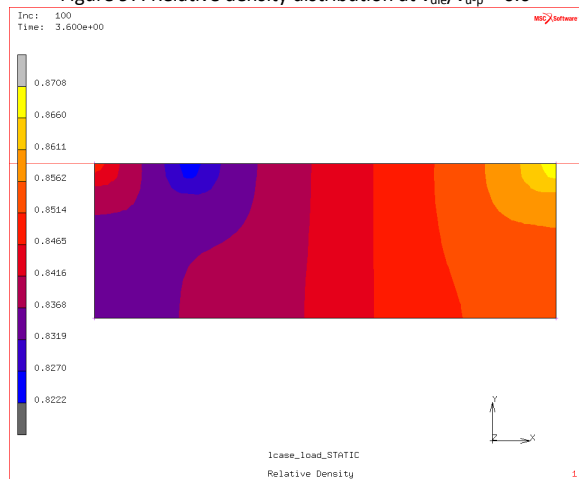


Figure 99. Relative density distribution at $v_{die}/v_{u-p} = 0.8$

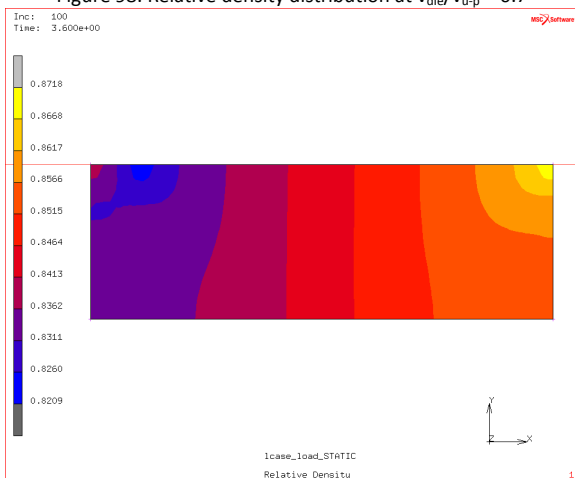


Figure 100. Relative density distribution at $v_{die}/v_{u-p} = 0.9$

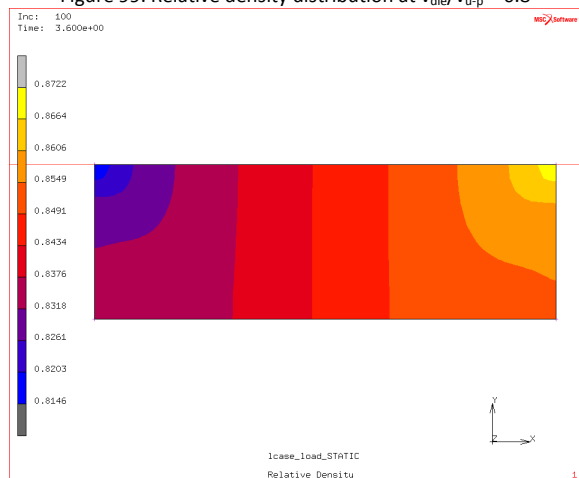


Figure 101. Relative density distribution at $v_{die}/v_{u-p} = 1.0$

A.1.2 Using Variable Friction Coefficient, $\mu(\sigma_n, v_r)$

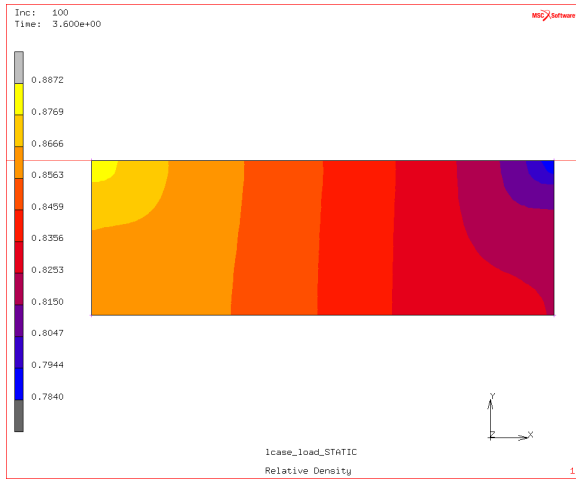


Figure 102. Relative density distribution at $v_{die}/v_{u-p} = 0$

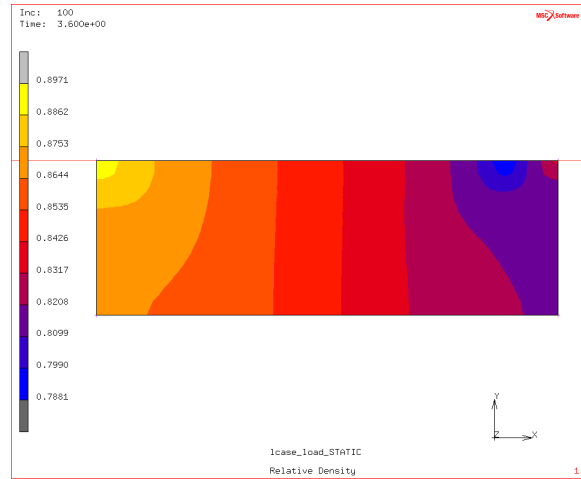


Figure 103. Relative density distribution at $v_{die}/v_{u-p} = 0.1$

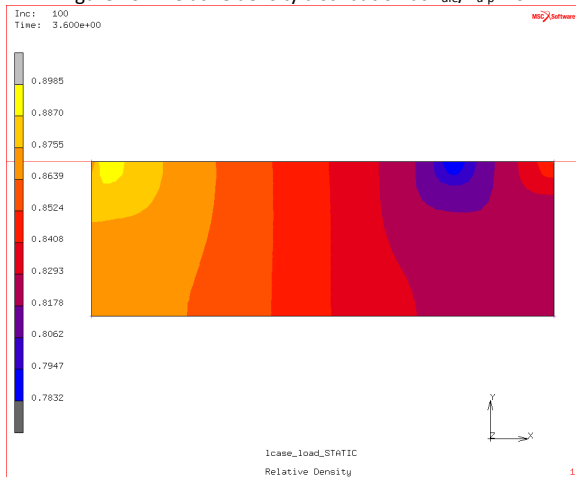


Figure 104. Relative density distribution at $v_{die}/v_{u-p} = 0.2$

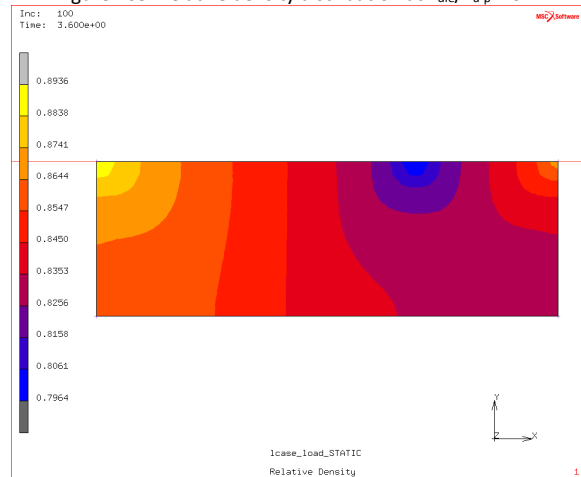


Figure 105. Relative density distribution at $v_{die}/v_{u-p} = 0.3$

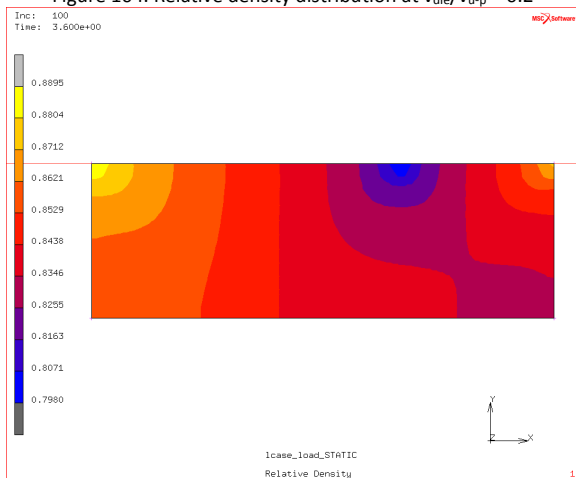


Figure 106. Relative density distribution at $v_{die}/v_{u-p} = 0.33$

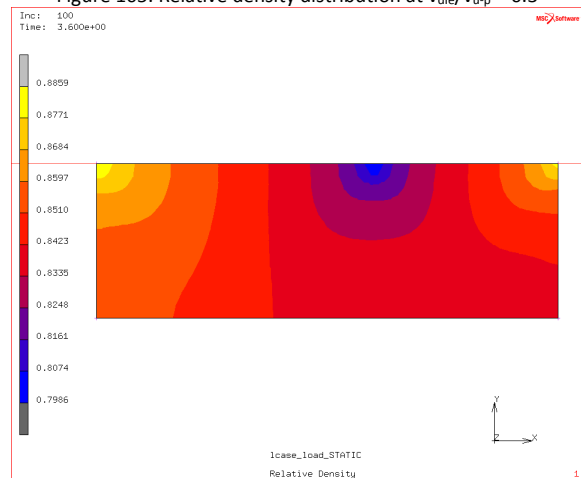


Figure 107. Relative density distribution at $v_{die}/v_{u-p} = 0.4$

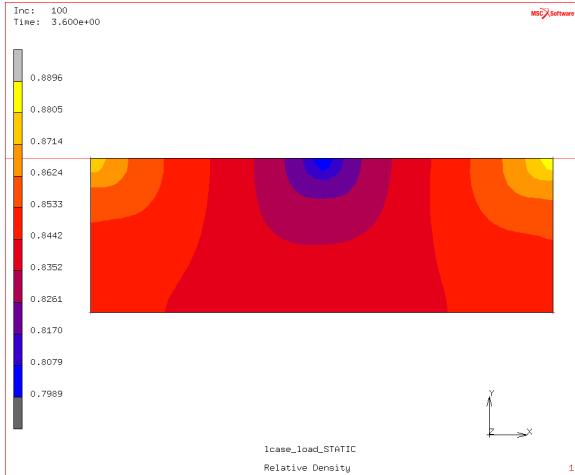


Figure 108. Relative density distribution at $v_{die}/v_{u-p} = 0.5$

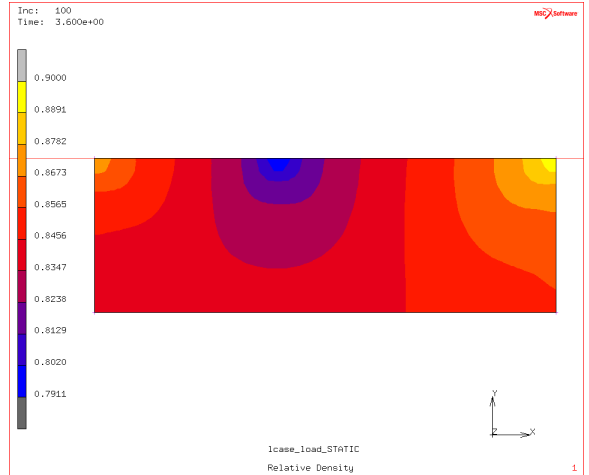


Figure 109. Relative density distribution at $v_{die}/v_{u-p} = 0.6$

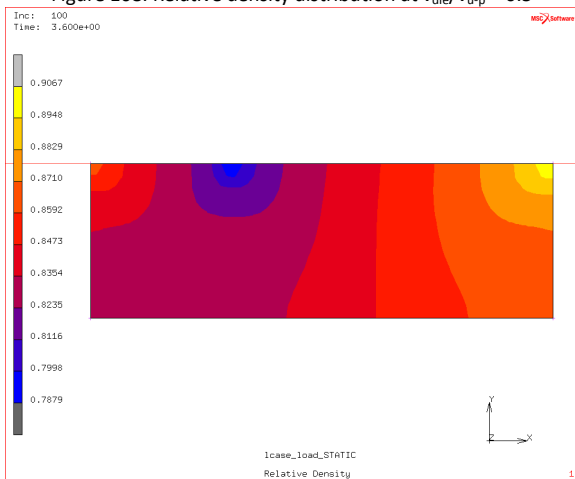


Figure 110. Relative density distribution at $v_{die}/v_{u-p} = 0.7$

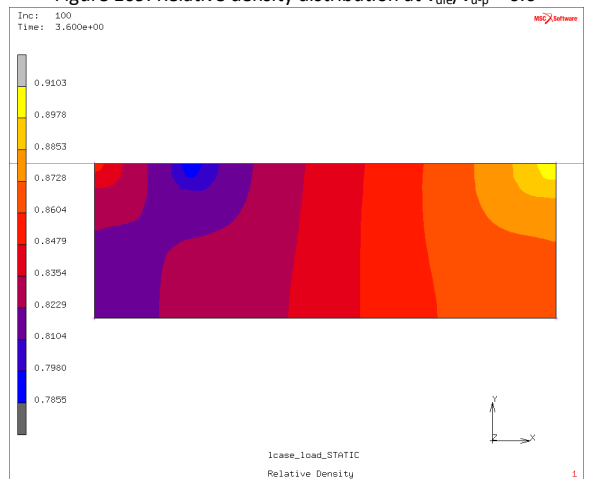


Figure 111. Relative density distribution at $v_{die}/v_{u-p} = 0.8$

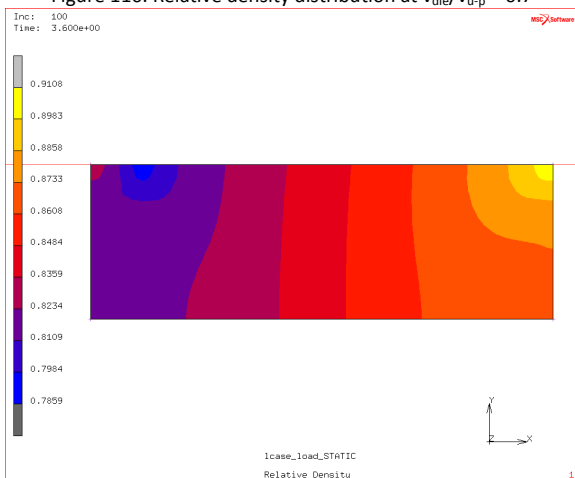


Figure 112. Relative density distribution at $v_{die}/v_{u-p} = 0.9$

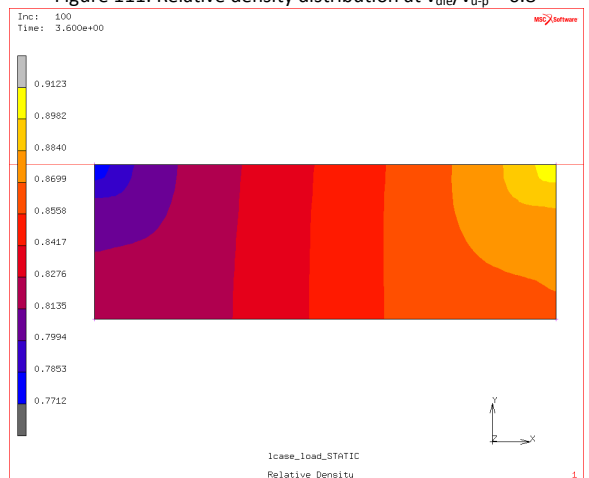


Figure 113. Relative density distribution at $v_{die}/v_{u-p} = 1.0$

A.2 Using Material Properties Provided by Koval'chenko [54]

A.2.1 Using Constant Friction Coefficient of 0.1

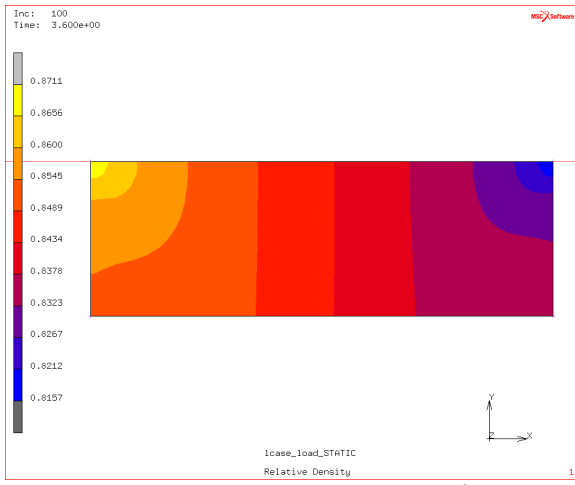


Figure 114. Relative density distribution at $v_{die}/v_{u-p} = 0$

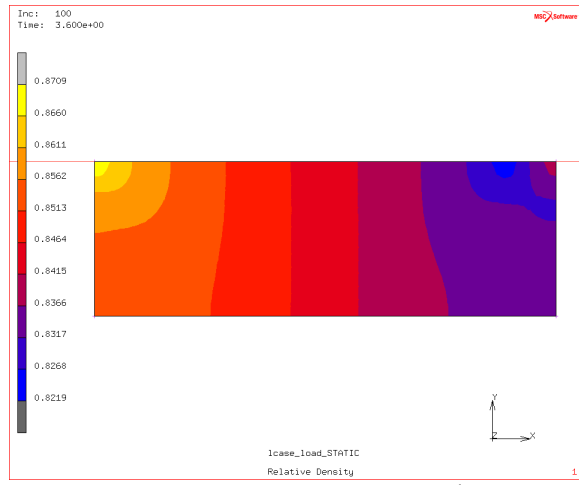


Figure 115. Relative density distribution at $v_{die}/v_{u-p} = 0.1$

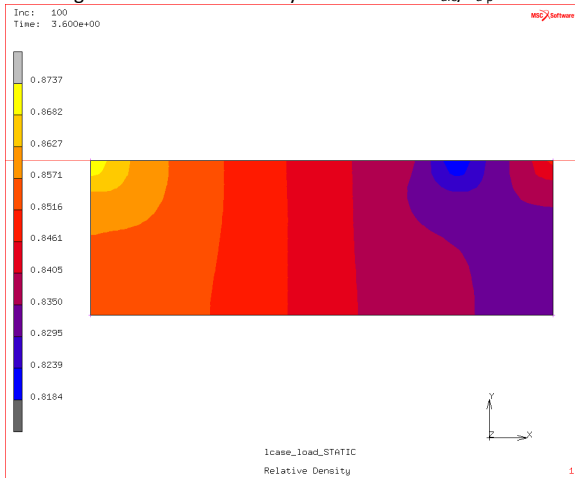


Figure 116. Relative density distribution at $v_{die}/v_{u-p} = 0.2$

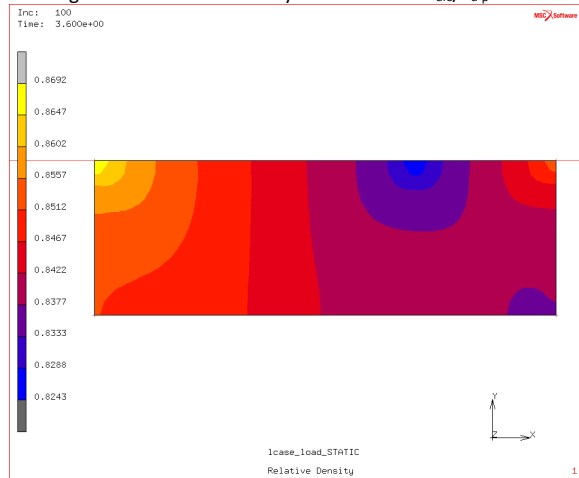


Figure 117. Relative density distribution at $v_{die}/v_{u-p} = 0.3$

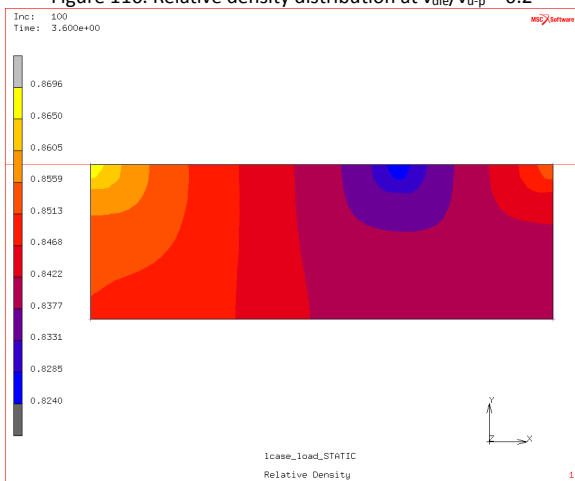


Figure 118. Relative density distribution at $v_{die}/v_{u-p} = 0.33$

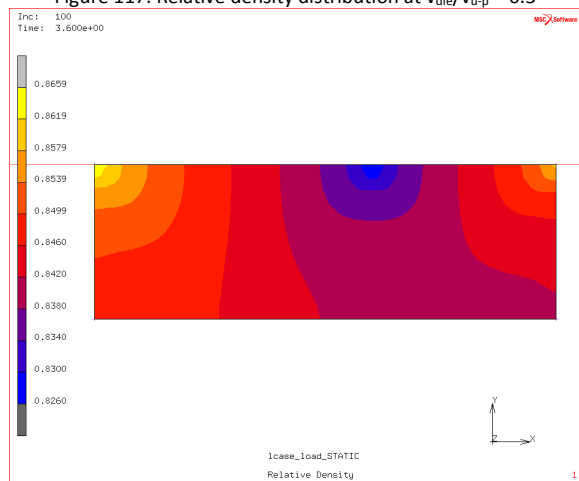


Figure 119. Relative density distribution at $v_{die}/v_{u-p} = 0.4$

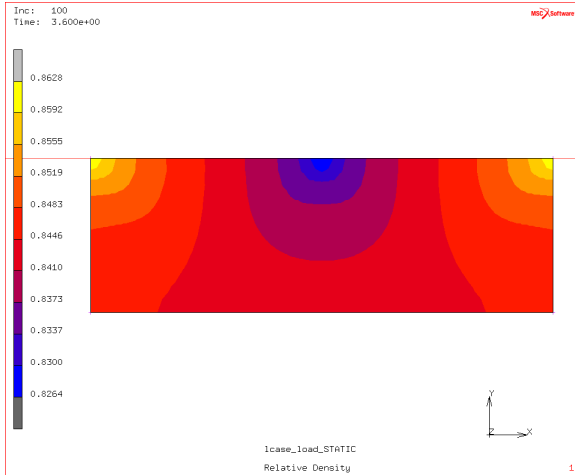


Figure 120. Relative density distribution at $v_{die}/v_{U-p} = 0.5$

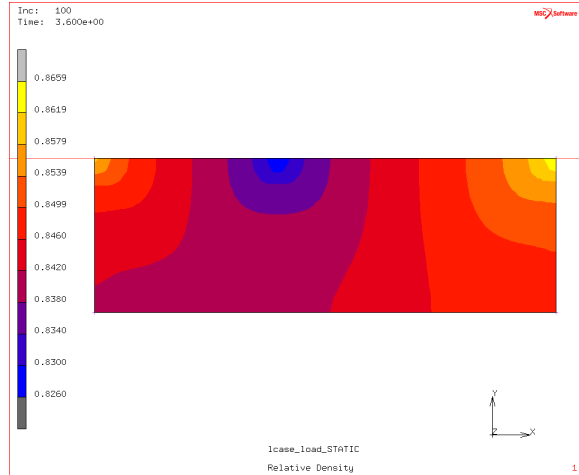


Figure 121. Relative density distribution at $v_{die}/v_{U-p} = 0.6$

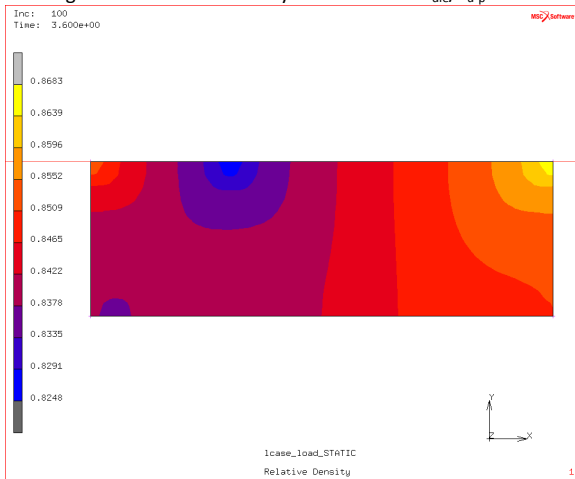


Figure 122. Relative density distribution at $v_{die}/v_{U-p} = 0.7$

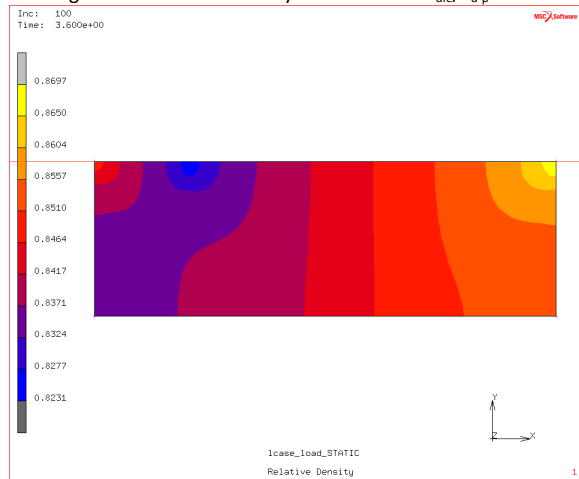


Figure 123. Relative density distribution at $v_{die}/v_{U-p} = 0.8$

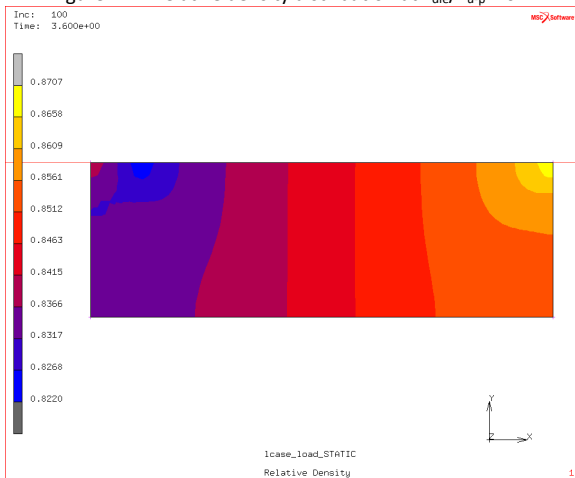


Figure 124. Relative density distribution at $v_{die}/v_{U-p} = 0.9$

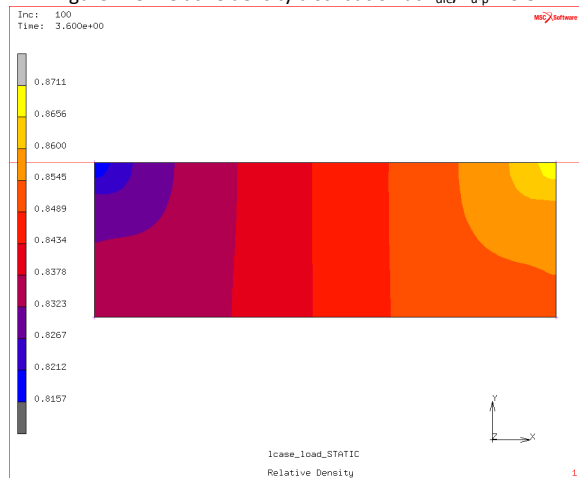


Figure 125. Relative density distribution at $v_{die}/v_{U-p} = 1.0$

A.2.2 Using Variable Friction Coefficient, $\mu(\sigma_n, v_r)$

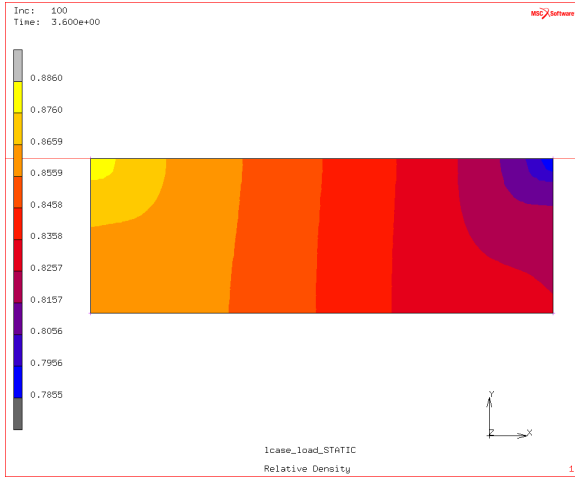


Figure 126. Relative density distribution at $v_{die}/v_{u-p} = 0$

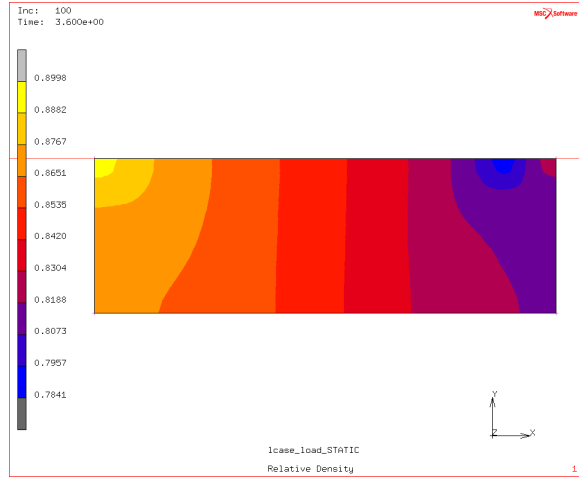


Figure 127. Relative density distribution at $v_{die}/v_{u-p} = 0.1$

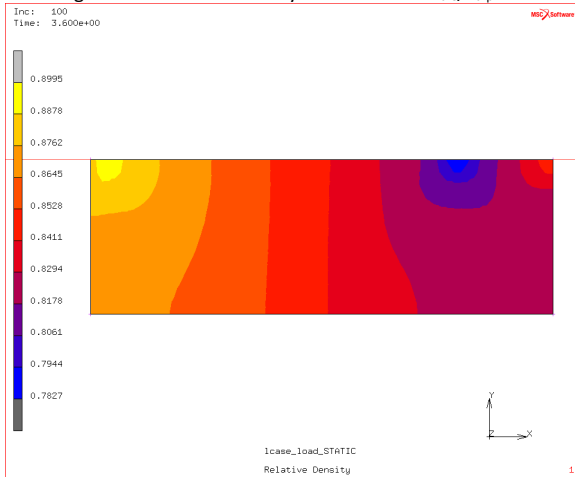


Figure 128. Relative density distribution at $v_{die}/v_{u-p} = 0.2$

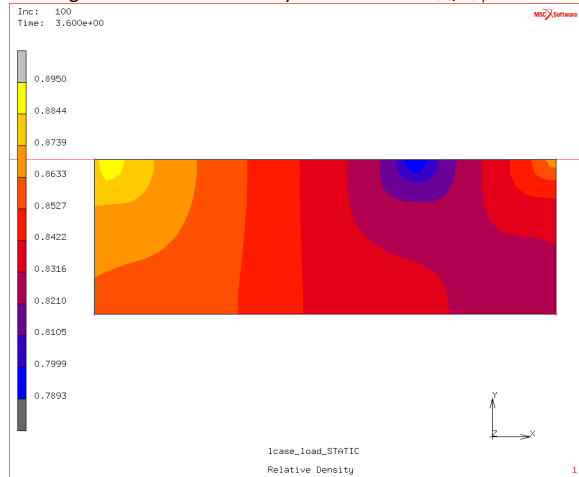


Figure 129. Relative density distribution at $v_{die}/v_{u-p} = 0.3$

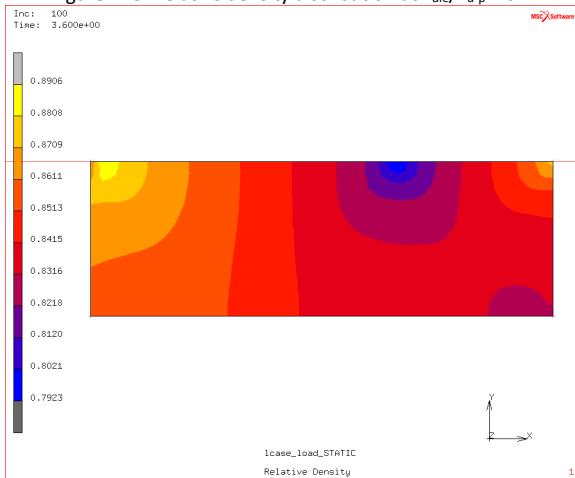


Figure 130. Relative density distribution at $v_{die}/v_{u-p} = 0.33$

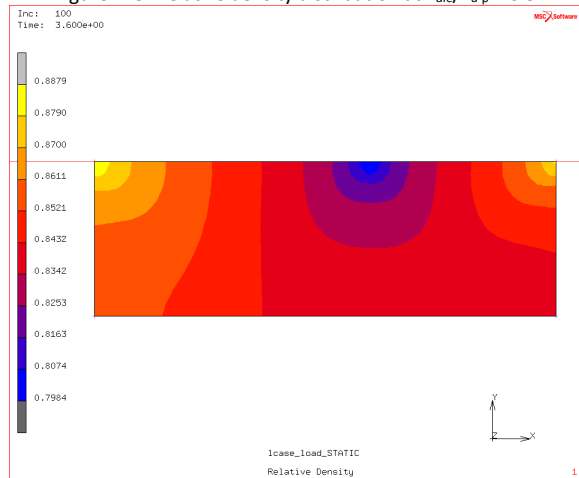


Figure 131. Relative density distribution at $v_{die}/v_{u-p} = 0.4$

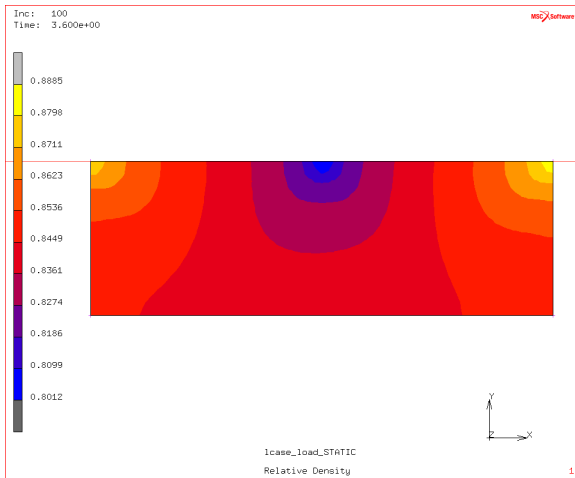


Figure 132. Relative density distribution at $v_{die}/v_{u-p} = 0.5$

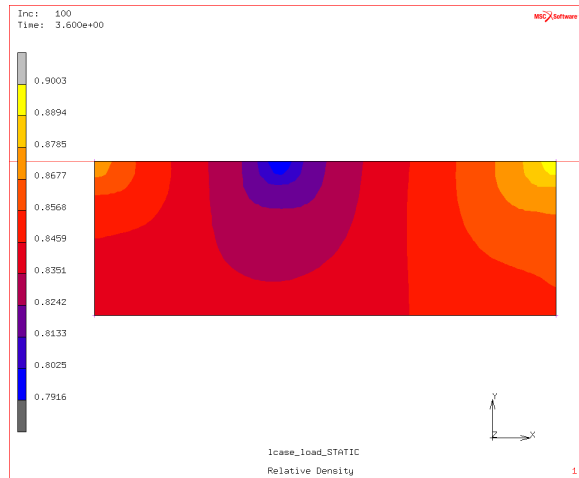


Figure 133. Relative density distribution at $v_{die}/v_{u-p} = 0.6$

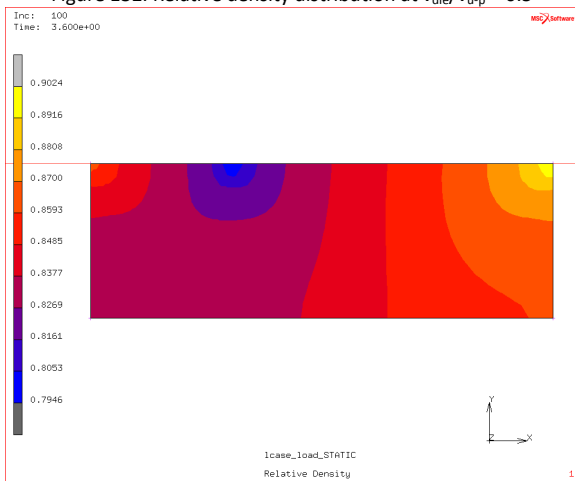


Figure 134. Relative density distribution at $v_{die}/v_{u-p} = 0.7$

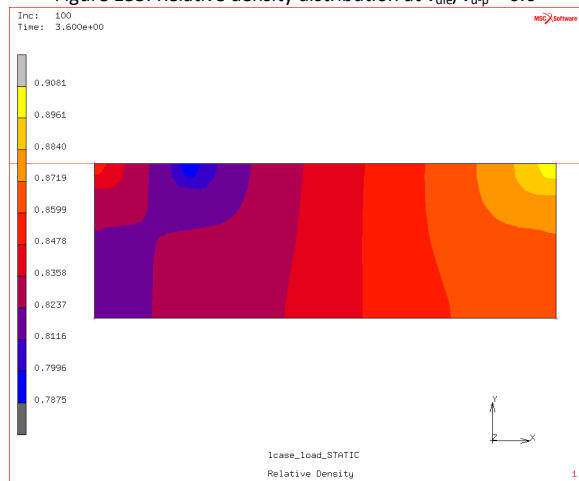


Figure 135. Relative density distribution at $v_{die}/v_{u-p} = 0.8$

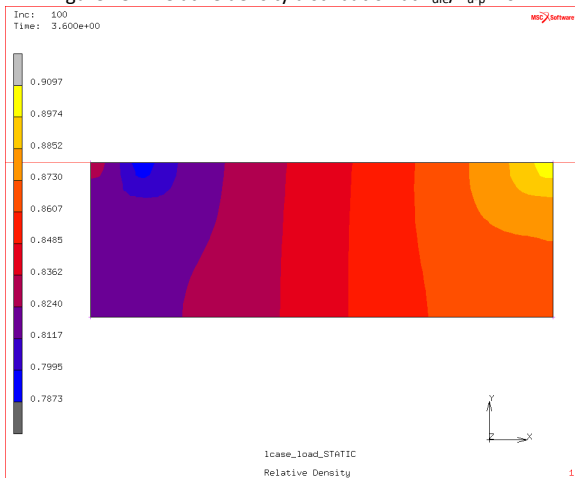


Figure 136. Relative density distribution at $v_{die}/v_{u-p} = 0.9$

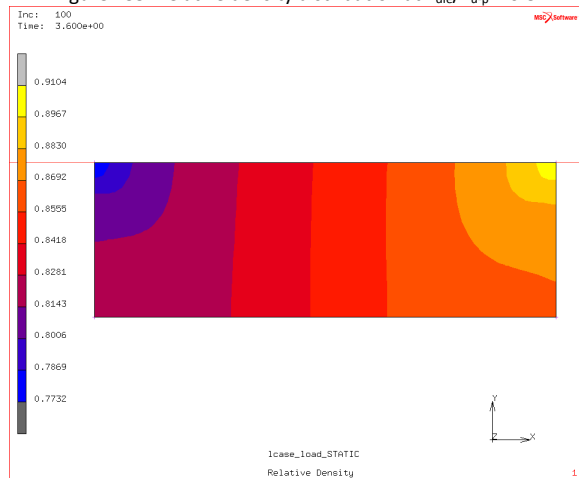


Figure 137. Relative density distribution at $v_{die}/v_{u-p} = 0.9$

Appendix B. Effect of Die to Upper-Punch Velocity Ratio on Density Distribution of Cylindrical Parts with Compact Height-to-Diameter Ratio of 1.00

B.1 Using Material Properties Provided by Pavier and Doremus [10, 84]

B.1.1 Using Constant Friction Coefficient of 0.1

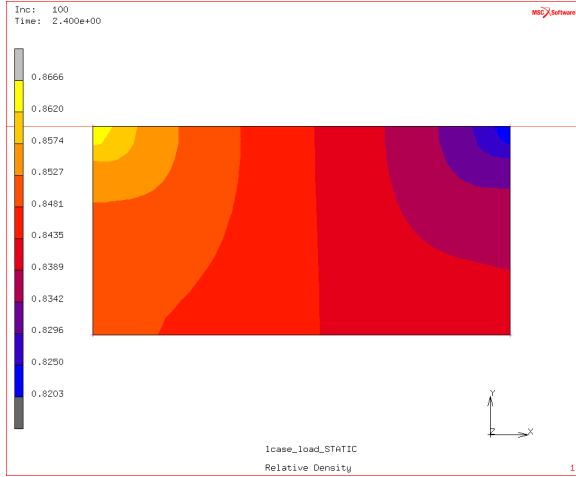


Figure 138. Relative density distribution at $v_{die}/v_{u-p} = 0$

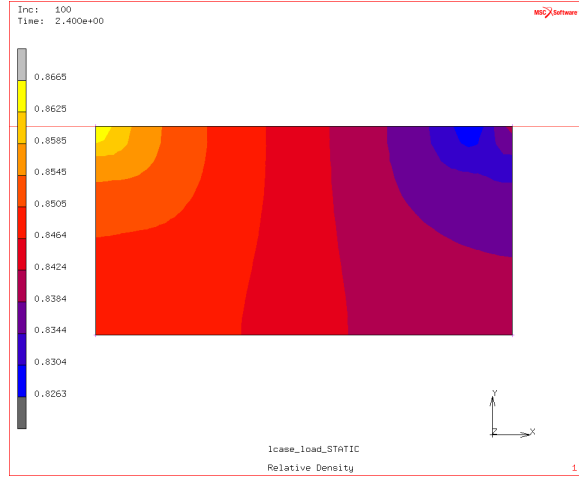


Figure 139. Relative density distribution at $v_{die}/v_{u-p} = 0.1$

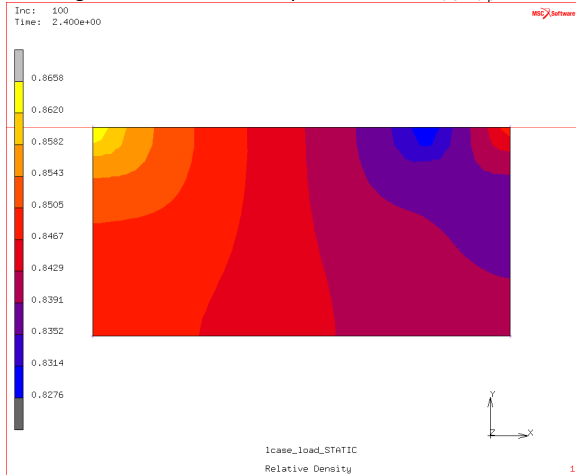


Figure 140. Relative density distribution at $v_{die}/v_{u-p} = 0.2$

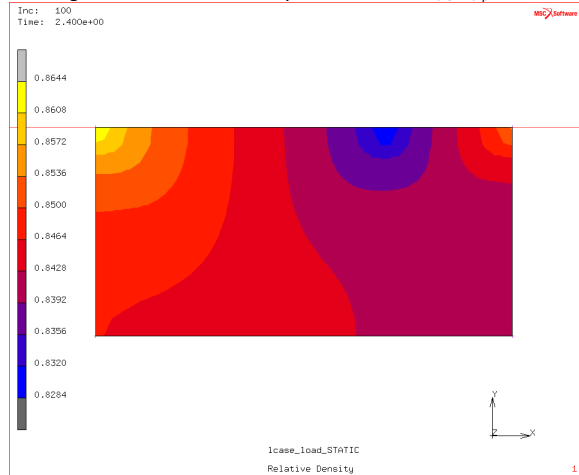


Figure 141. Relative density distribution at $v_{die}/v_{u-p} = 0.3$

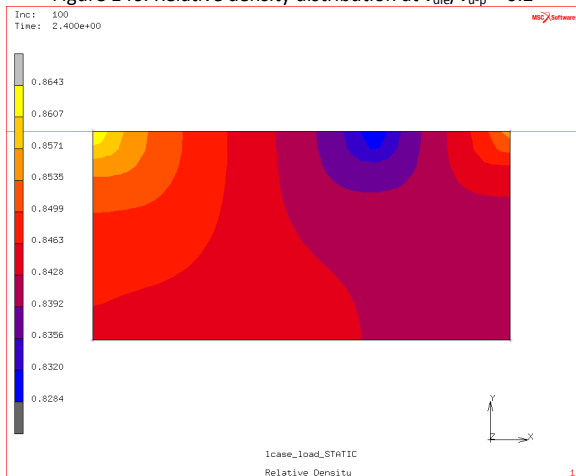


Figure 142. Relative density distribution at $v_{die}/v_{u-p} = 0.33$

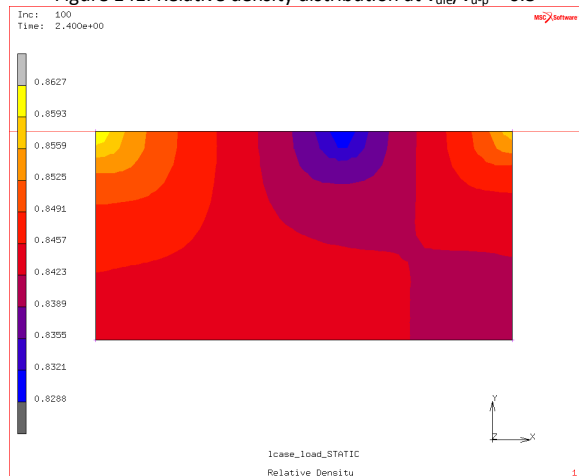


Figure 143. Relative density distribution at $v_{die}/v_{u-p} = 0.4$

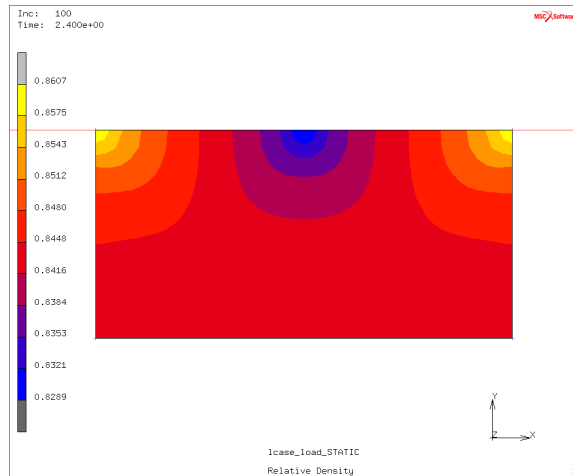


Figure 144. Relative density distribution at $v_{die}/v_{u-p} = 0.5$

B.1.2 Using Variable Friction Coefficient, $\mu(\sigma_n, v_r)$

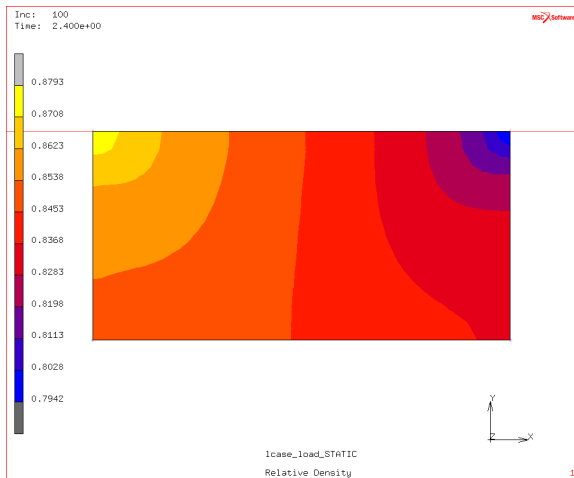


Figure 145. Relative density distribution at $v_{die}/v_{u-p} = 0$

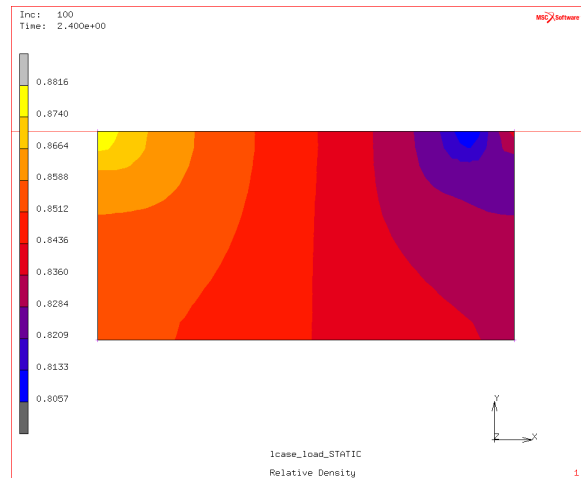


Figure 146. Relative density distribution at $v_{die}/v_{u-p} = 0.1$

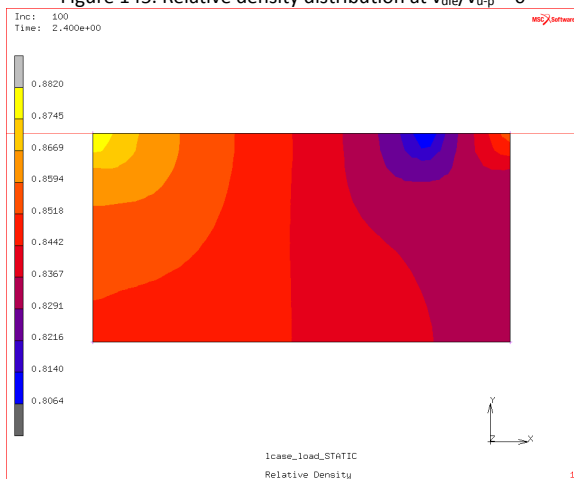


Figure 147. Relative density distribution at $v_{die}/v_{u-p} = 0.2$

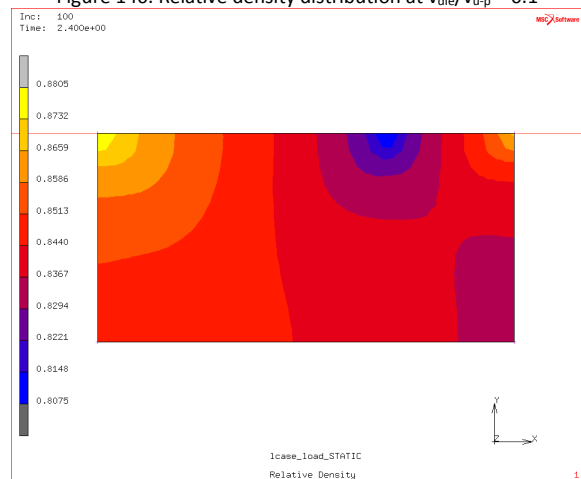


Figure 148. Relative density distribution at $v_{die}/v_{u-p} = 0.3$

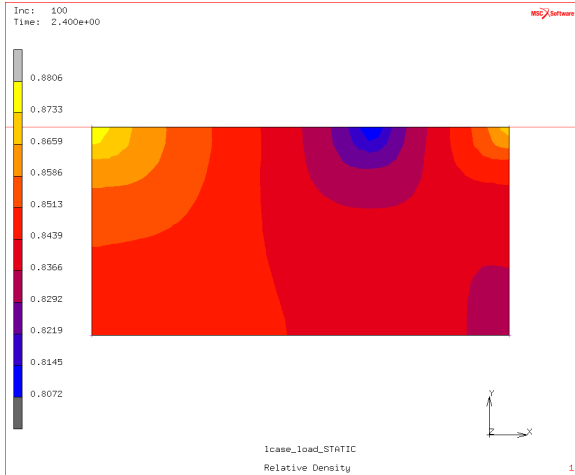


Figure 149. Relative density distribution at $v_{die}/v_{u-p} = 0.33$

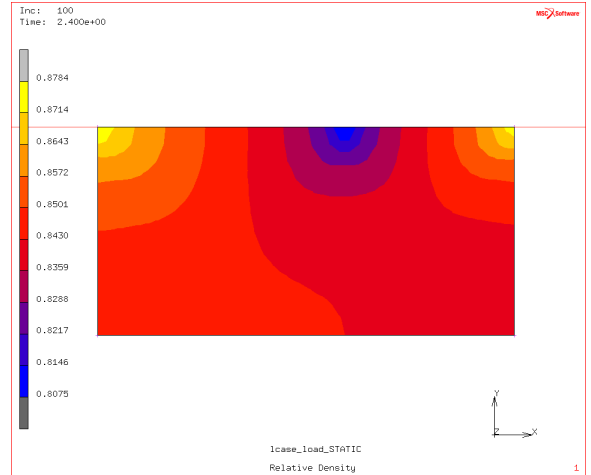


Figure 150. Relative density distribution at $v_{die}/v_{u-p} = 0.4$

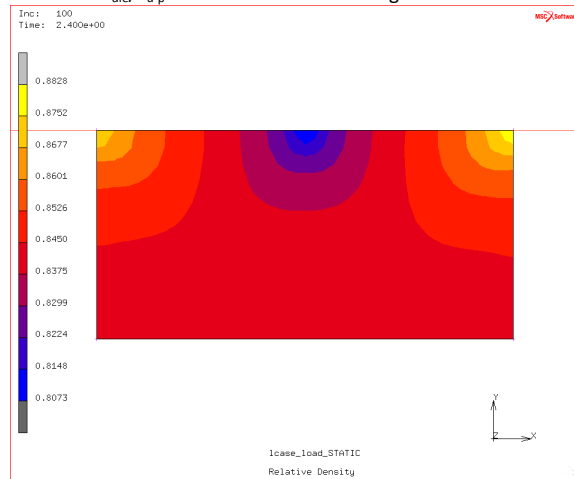


Figure 151. Relative density distribution at $v_{die}/v_{u-p} = 0.5$

B.2 Using Material Properties Provided by Koval'chenko [54]

B.2.1 Using Constant Friction Coefficient of 0.1

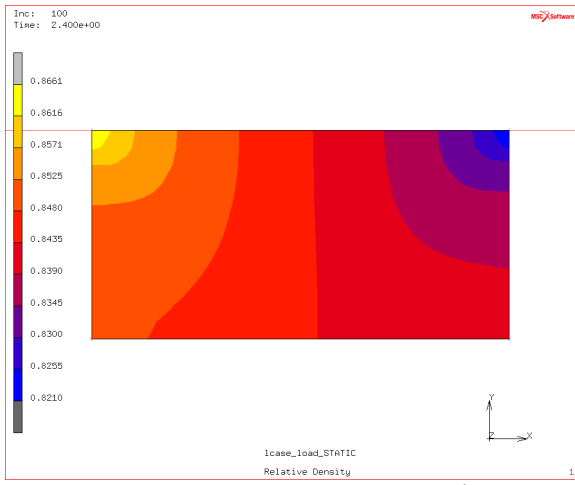


Figure 152. Relative density distribution at $v_{die}/v_{u-p} = 0$

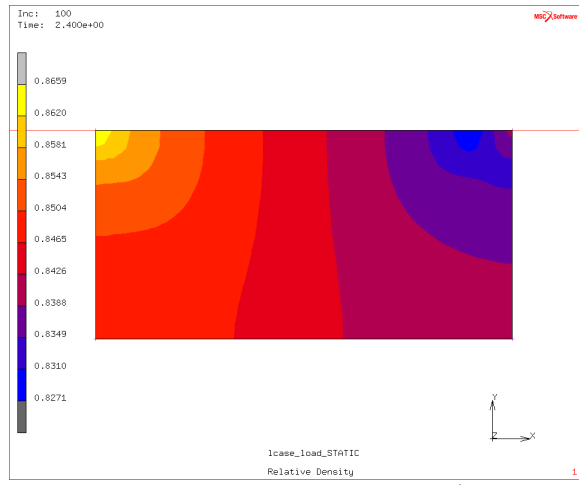


Figure 153. Relative density distribution at $v_{die}/v_{u-p} = 0.1$

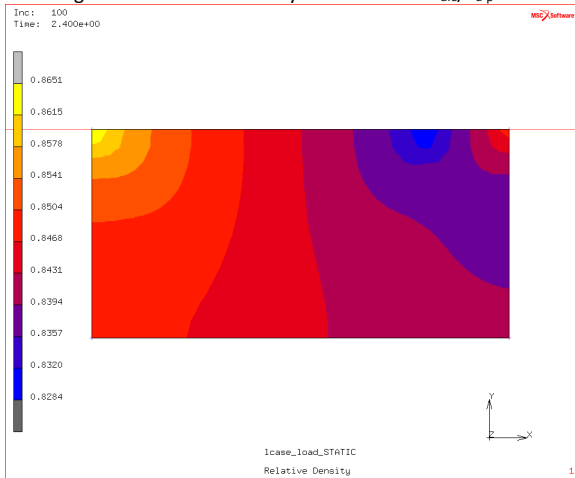


Figure 154. Relative density distribution at $v_{die}/v_{u-p} = 0.2$

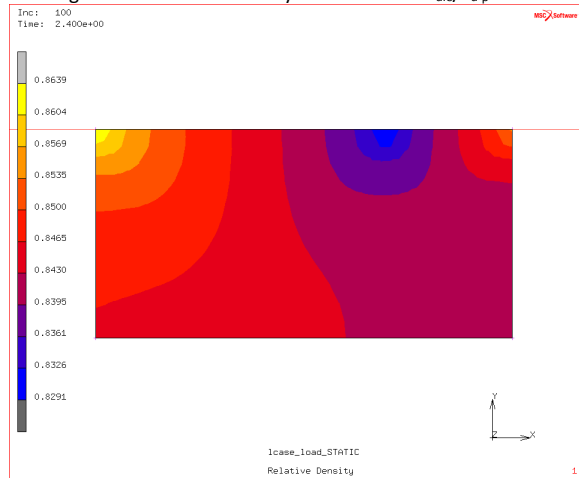


Figure 155. Relative density distribution at $v_{die}/v_{u-p} = 0.3$

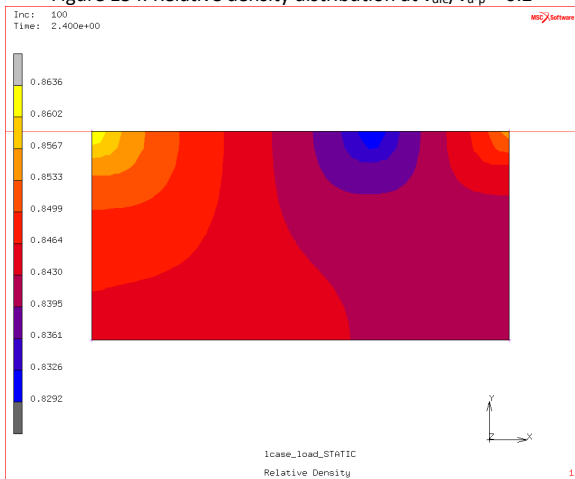


Figure 156. Relative density distribution at $v_{die}/v_{u-p} = 0.33$

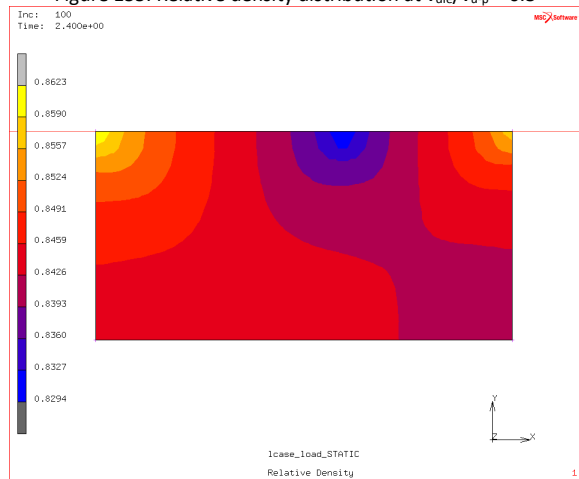


Figure 157. Relative density distribution at $v_{die}/v_{u-p} = 0.4$

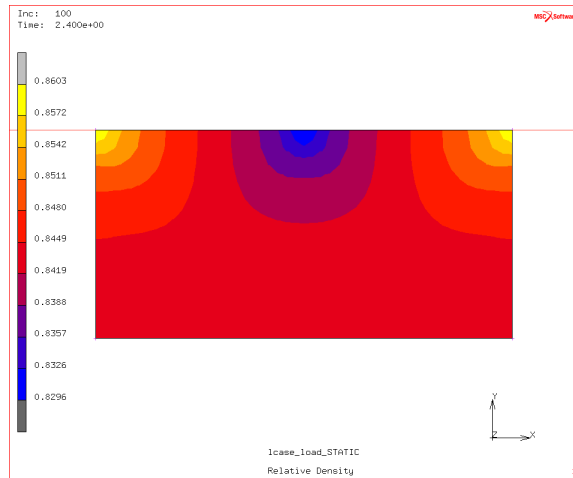


Figure 158. Relative density distribution at $v_{die}/v_{u-p} = 0.5$

B.2.2 Using Variable Friction Coefficient, $\mu(\sigma_n, v_r)$

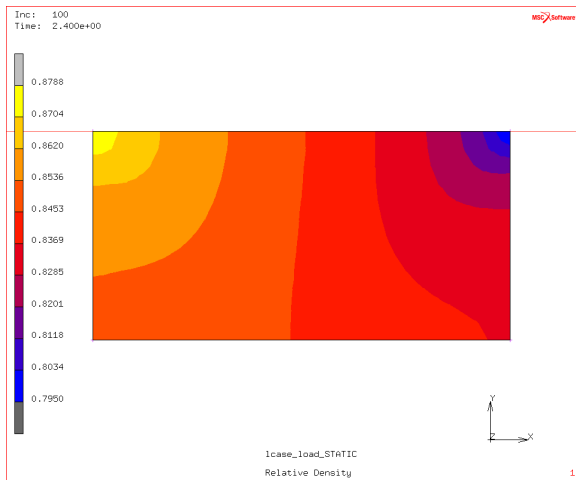


Figure 159. Relative density distribution at $v_{die}/v_{u-p} = 0$

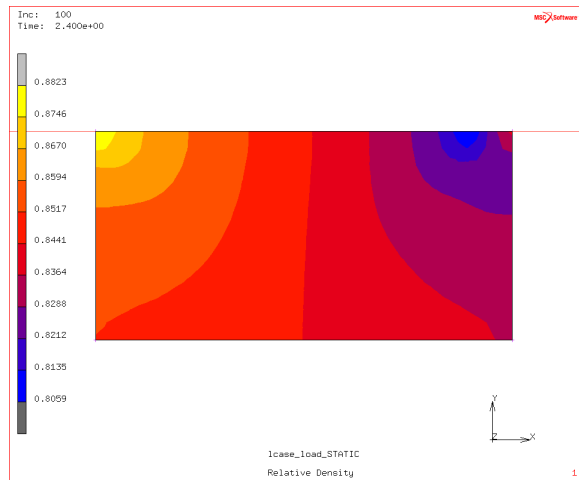


Figure 160. Relative density distribution at $v_{die}/v_{u-p} = 0.1$

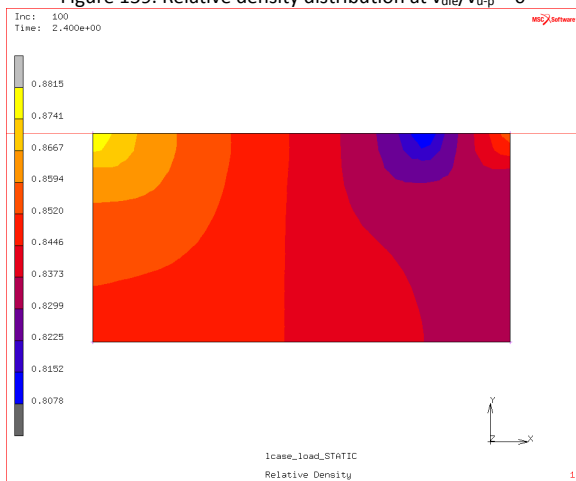


Figure 161. Relative density distribution at $v_{die}/v_{u-p} = 0.2$

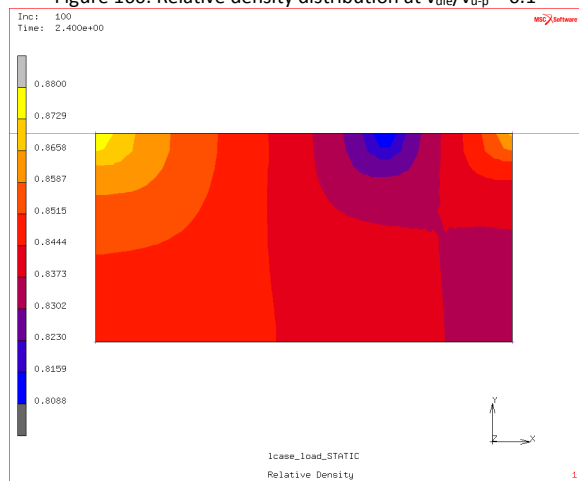


Figure 162. Relative density distribution at $v_{die}/v_{u-p} = 0.3$

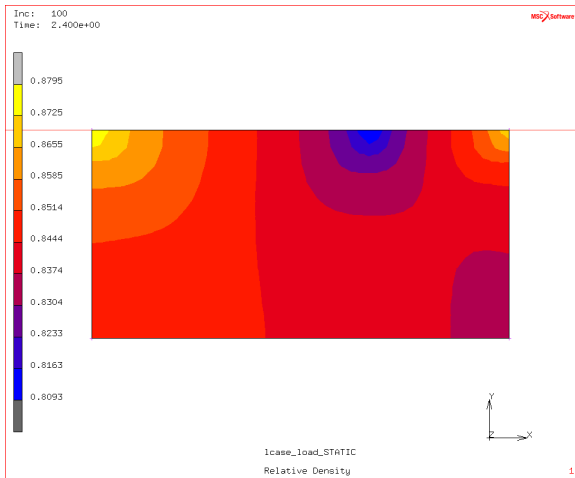


Figure 163. Relative density distribution at $v_{die}/v_{u-p} = 0.33$

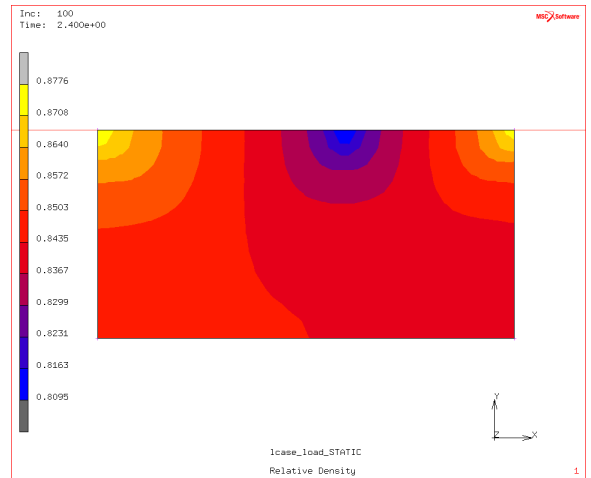


Figure 164. Relative density distribution at $v_{die}/v_{u-p} = 0.4$

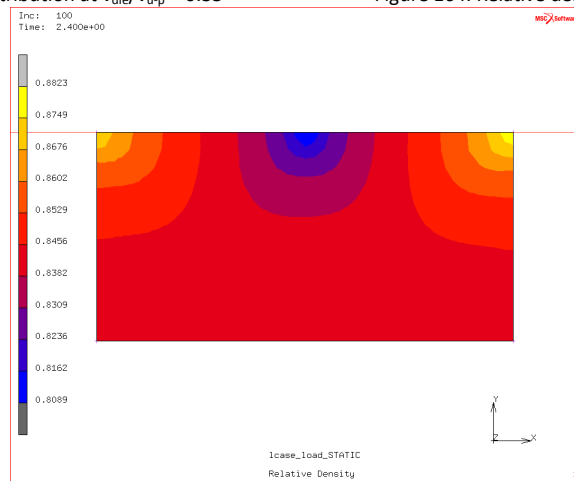


Figure 165. Relative density distribution at $v_{die}/v_{u-p} = 0.5$

Appendix C. Effect of Die to Upper-Punch Velocity Ratio on Density Distribution of Cylindrical Parts with Compact Height-to-Diameter Ratio of 0.50

C.1 Using Material Properties Provided by Pavier and Doremus [10, 84]

C.1.1 Using Constant Friction Coefficient of 0.1

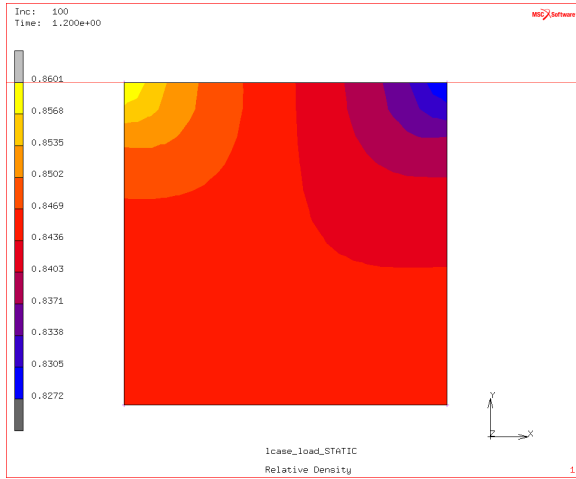


Figure 166. Relative density distribution at $v_{die}/v_{u-p} = 0$

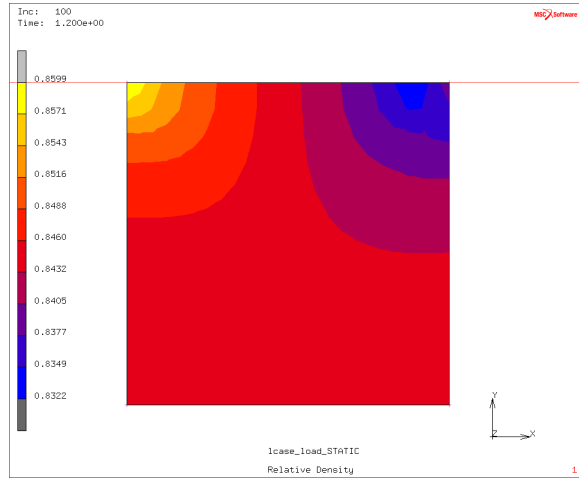


Figure 167. Relative density distribution at $v_{die}/v_{u-p} = 0.1$

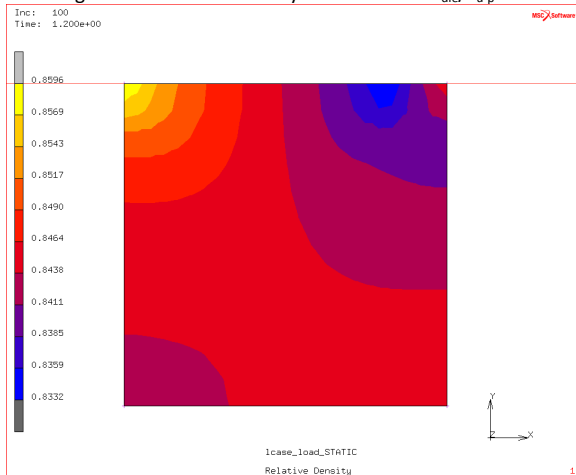


Figure 168. Relative density distribution at $v_{die}/v_{u-p} = 0.2$

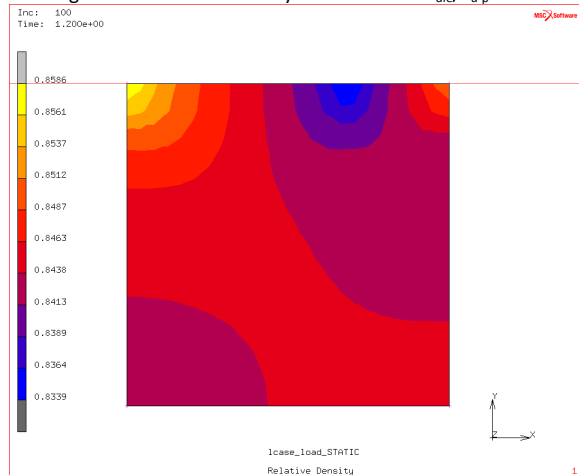


Figure 169. Relative density distribution at $v_{die}/v_{u-p} = 0.3$

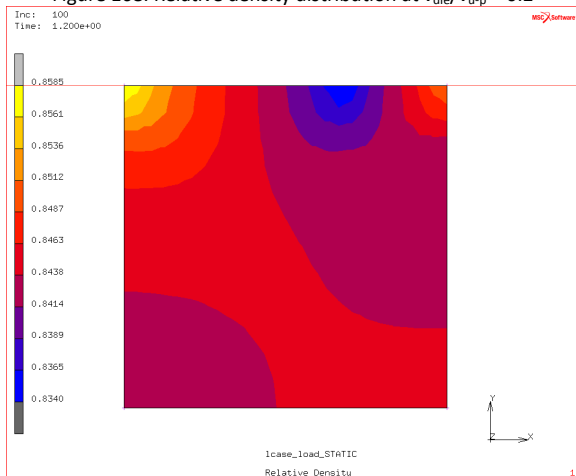


Figure 170. Relative density distribution at $v_{die}/v_{u-p} = 0.33$

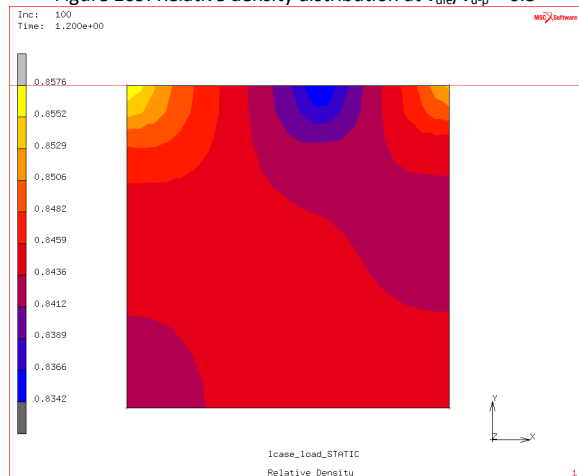


Figure 171. Relative density distribution at $v_{die}/v_{u-p} = 0.4$

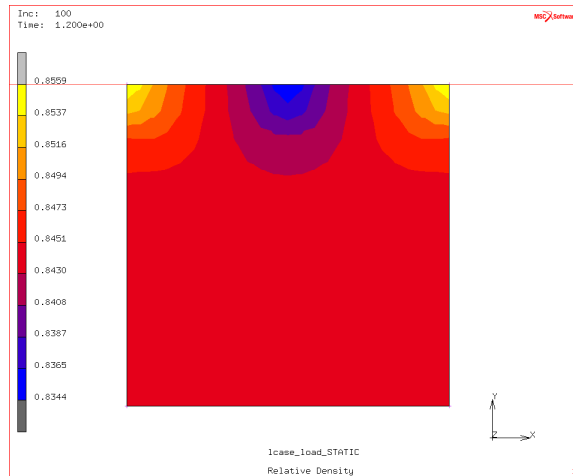


Figure 172. Relative density distribution at $v_{die}/v_{u-p} = 0.5$

C.1.2 Using Variable Friction Coefficient, $\mu(\sigma_n, v_r)$

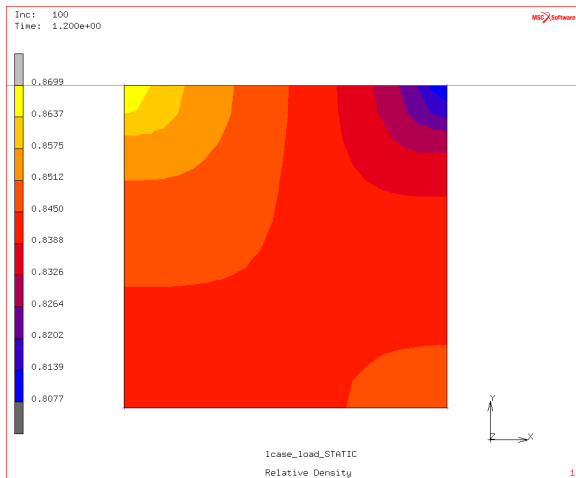


Figure 173. Relative density distribution at $v_{die}/v_{u-p} = 0$

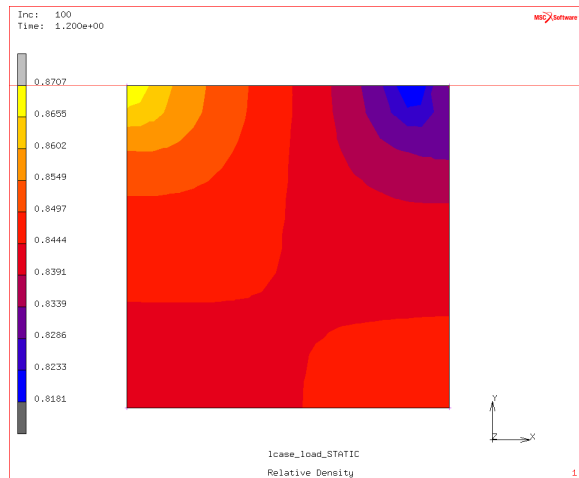


Figure 174. Relative density distribution at $v_{die}/v_{u-p} = 0.1$

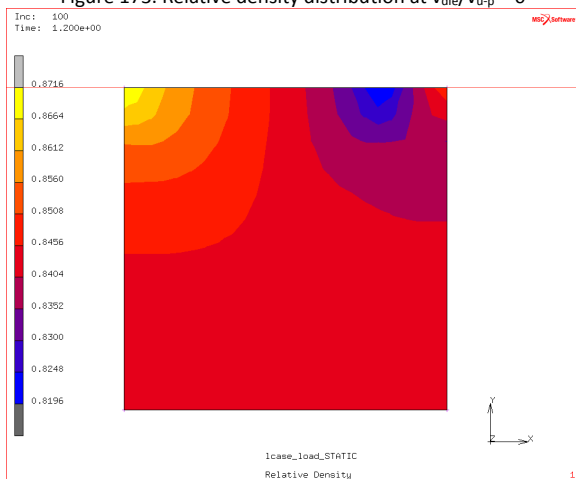


Figure 175. Relative density distribution at $v_{die}/v_{u-p} = 0.2$

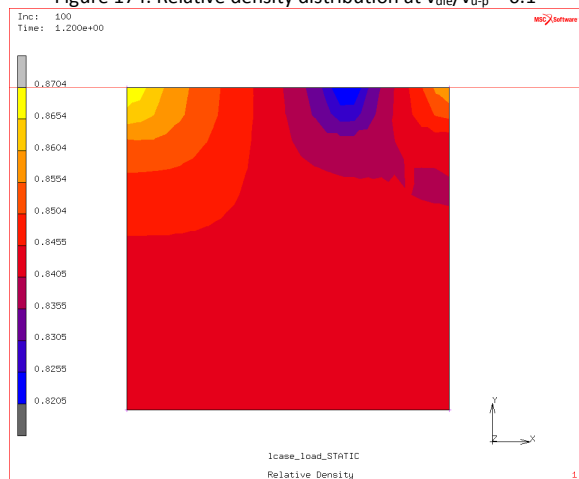


Figure 176. Relative density distribution at $v_{die}/v_{u-p} = 0.3$

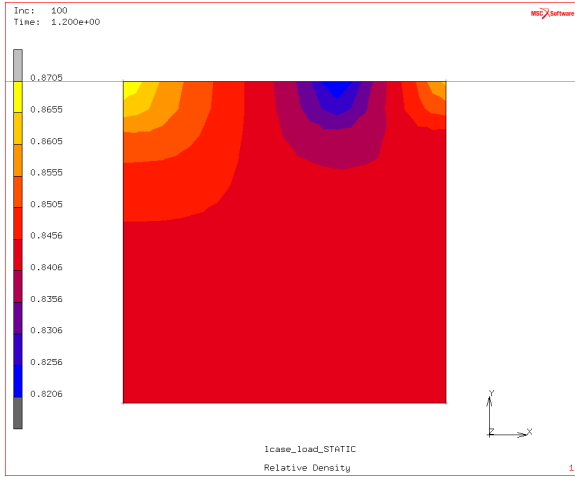


Figure 177. Relative density distribution at $v_{die}/v_{u-p} = 0.33$

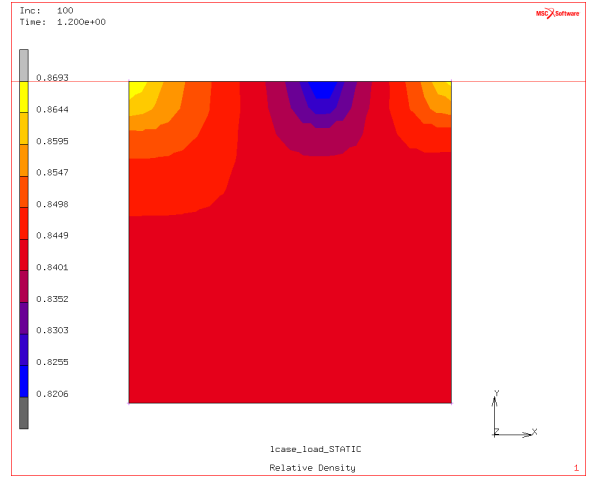


Figure 178. Relative density distribution at $v_{die}/v_{u-p} = 0.4$

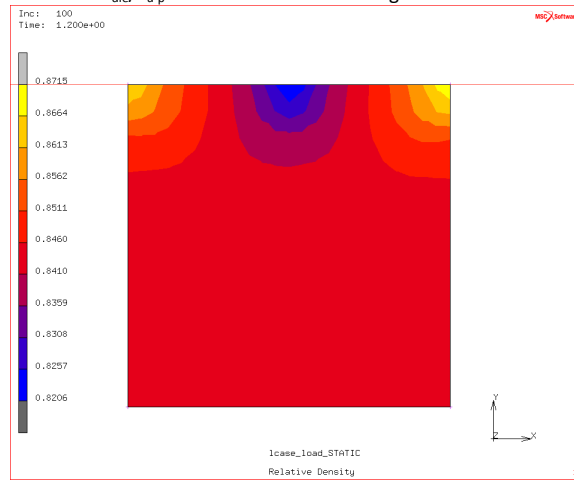


Figure 179. Relative density distribution at $v_{die}/v_{u-p} = 0.5$

C.2 Using Material Properties Provided by Koval'chenko [54]

C.2.1 Using Constant Friction Coefficient of 0.1

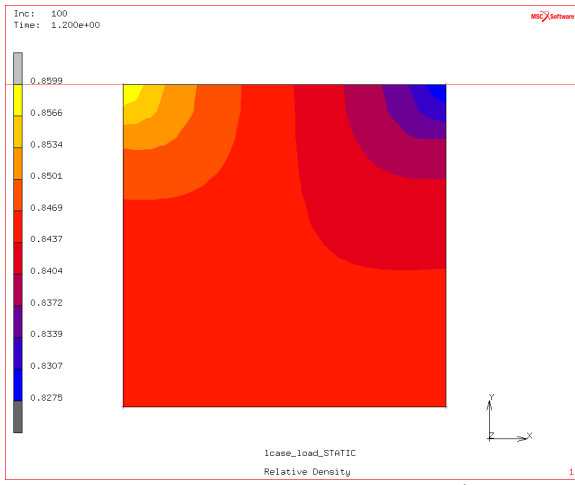


Figure 180. Relative density distribution at $v_{die}/v_{u-p} = 0$

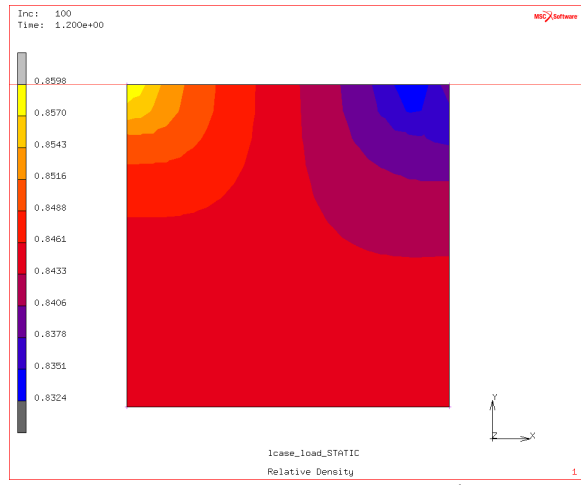


Figure 181. Relative density distribution at $v_{die}/v_{u-p} = 0.1$

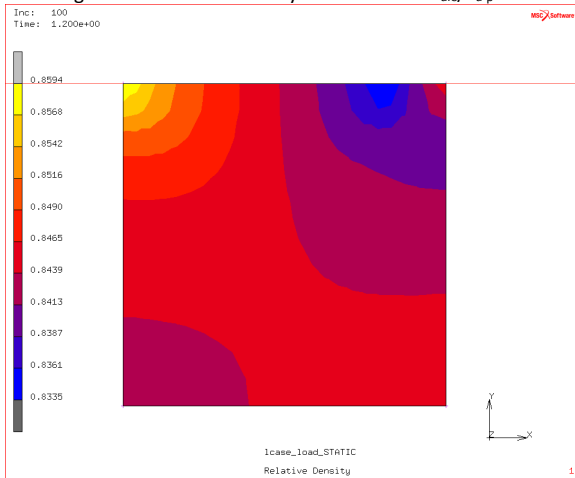


Figure 182. Relative density distribution at $v_{die}/v_{u-p} = 0.2$

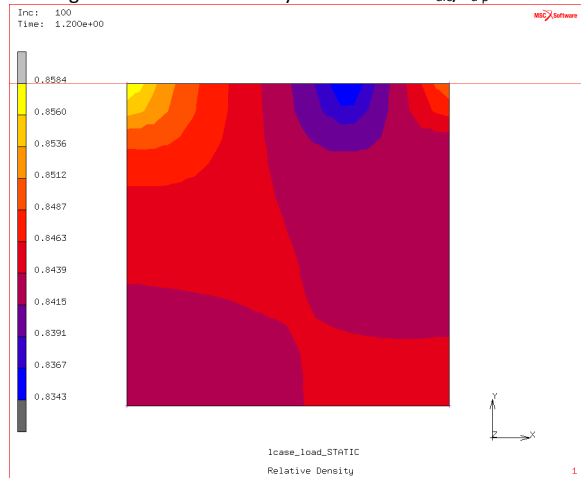


Figure 183. Relative density distribution at $v_{die}/v_{u-p} = 0.3$

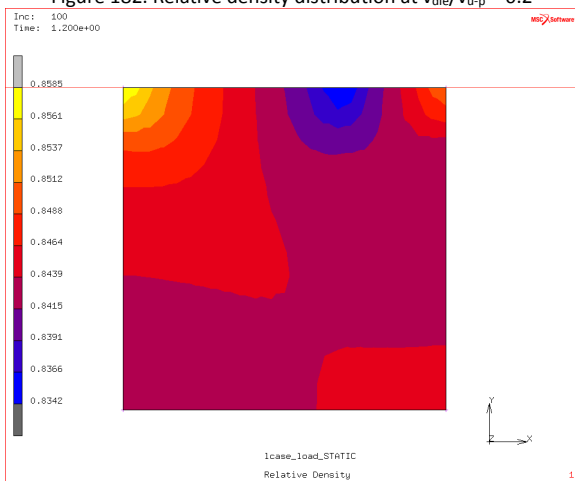


Figure 184. Relative density distribution at $v_{die}/v_{u-p} = 0.33$

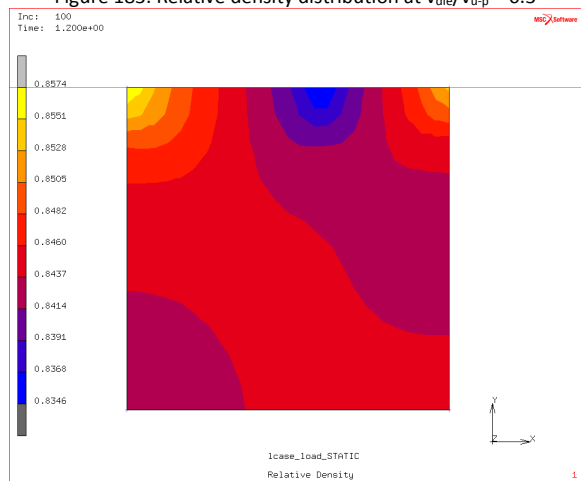


Figure 185. Relative density distribution at $v_{die}/v_{u-p} = 0.4$

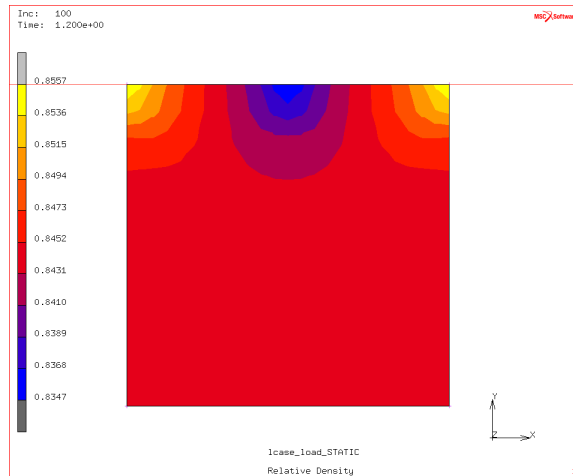


Figure 186. Relative density distribution at $v_{die}/v_{u-p} = 0.5$

C.2.2 Using Variable Friction Coefficient, $\mu(\sigma_n, v_r)$

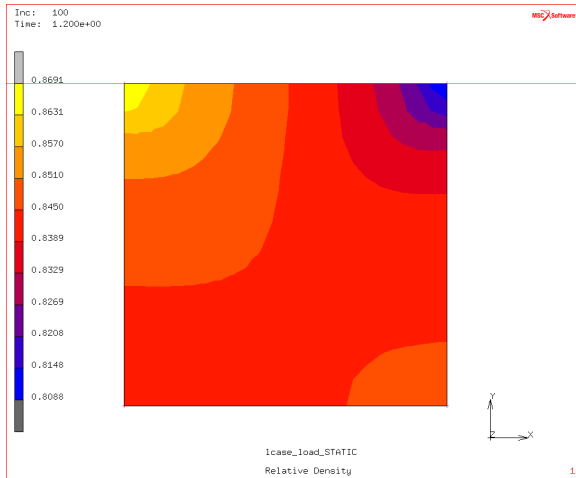


Figure 187. Relative density distribution at $v_{die}/v_{u-p} = 0$

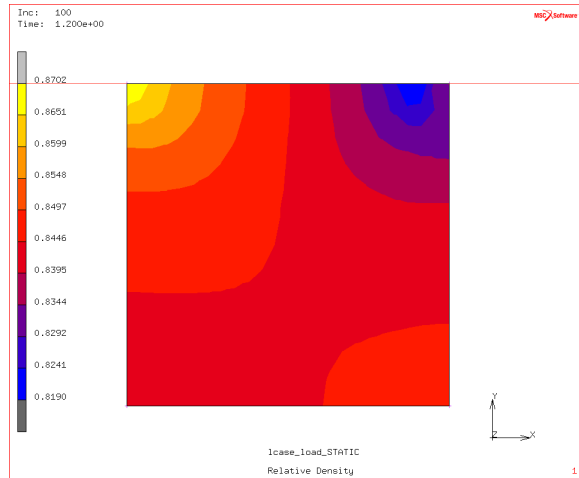


Figure 188. Relative density distribution at $v_{die}/v_{u-p} = 0.1$

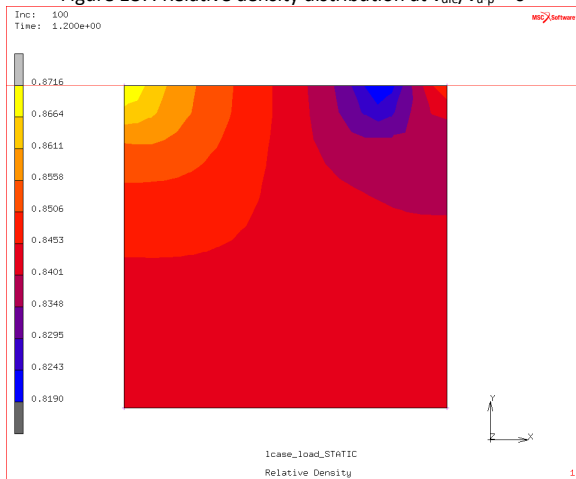


Figure 189. Relative density distribution at $v_{die}/v_{u-p} = 0.2$

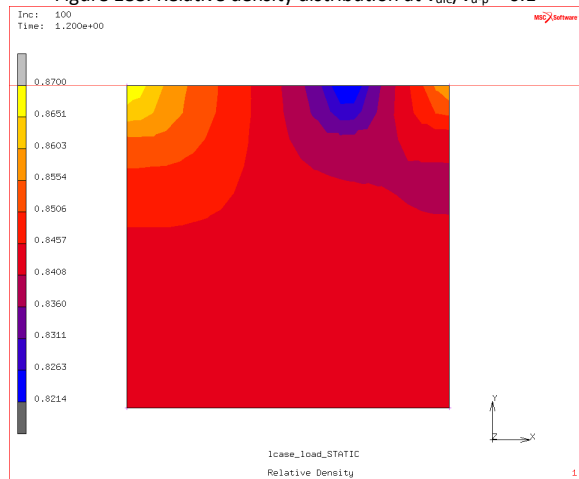


Figure 190. Relative density distribution at $v_{die}/v_{u-p} = 0.3$

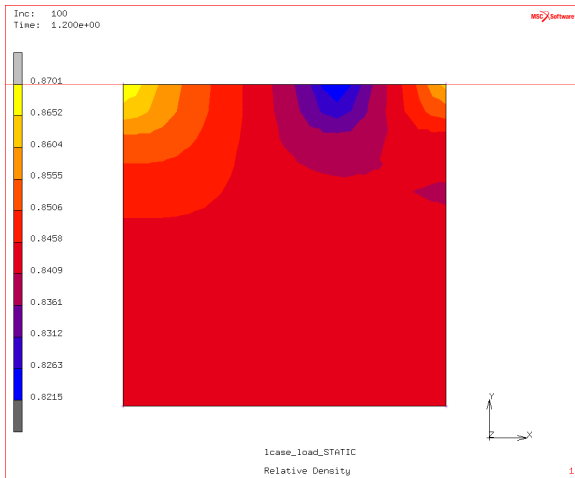


Figure 191. Relative density distribution at $v_{die}/v_{u-p} = 0.33$

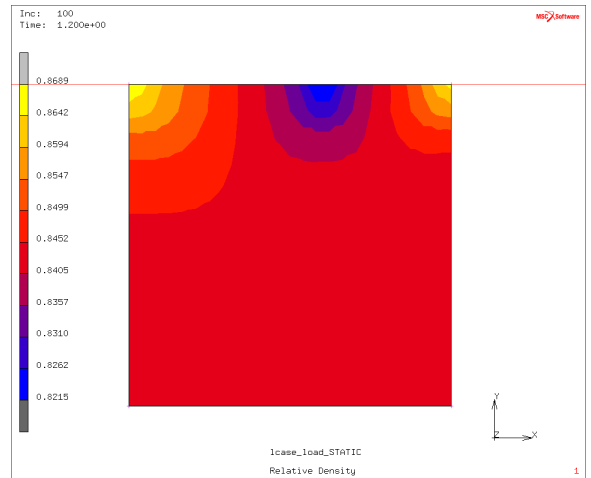


Figure 192. Relative density distribution at $v_{die}/v_{u-p} = 0.4$

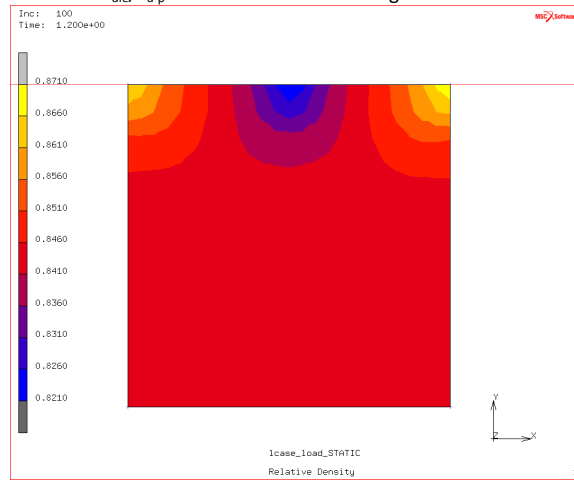


Figure 193. Relative density distribution at $v_{die}/v_{u-p} = 0.5$

Appendix D. Effect of Lower-Inner-Punch to Upper-Punch Velocity Ratio on Density Distribution of a Multi-stepped Part

D.1 Using Material Properties Provided by Shima [101, 102]

D.1.1 Using Constant Friction Coefficient of 0.08

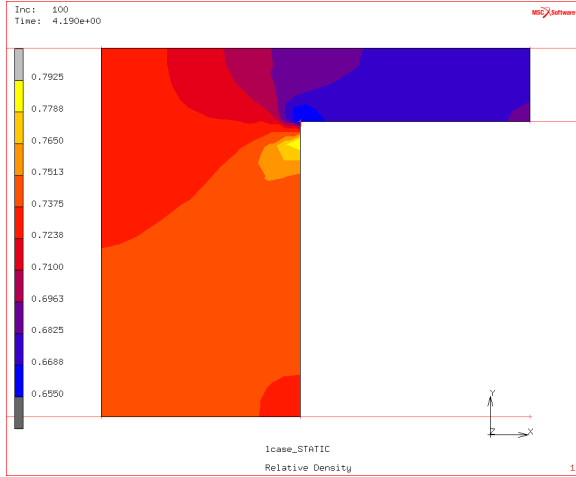


Figure 194. Relative density distribution for $v_3/v_1 = 0.45$

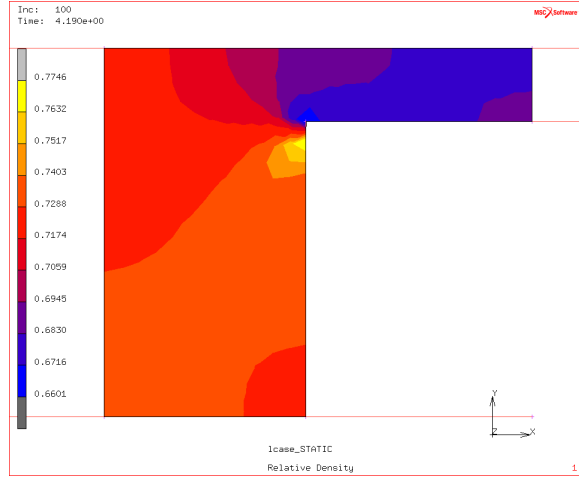


Figure 195. Relative density distribution for $v_3/v_1 = 0.46$

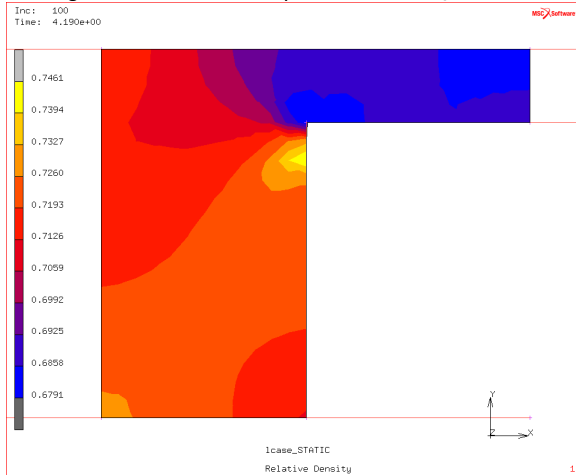


Figure 196. Relative density distribution for $v_3/v_1 = 0.47$

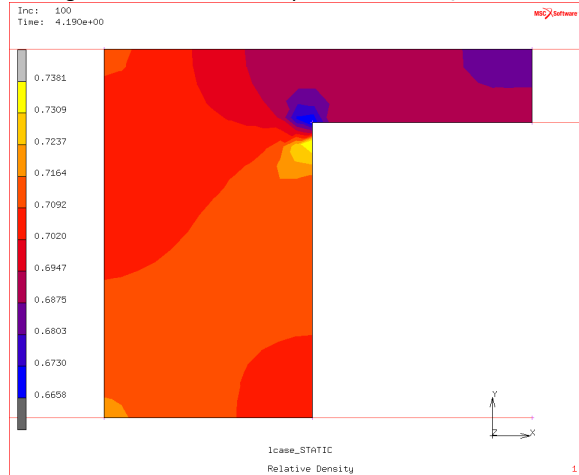


Figure 197. Relative density distribution for $v_3/v_1 = 0.48$

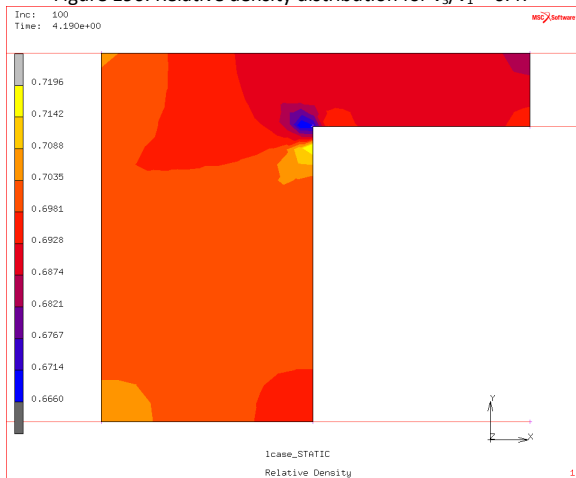


Figure 198. Relative density distribution for $v_3/v_1 = 0.49$

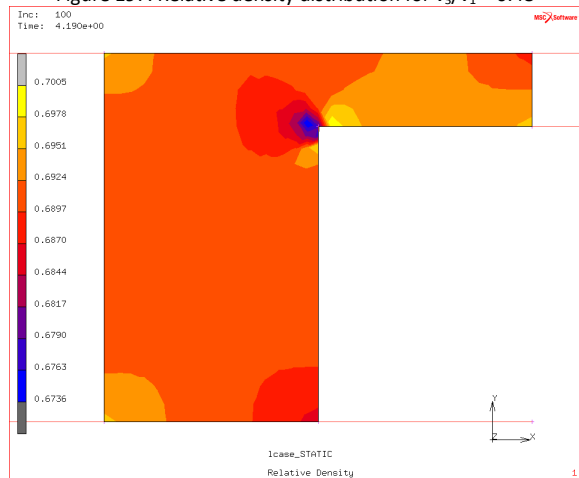


Figure 199. Relative density distribution for $v_3/v_1 = 0.50$

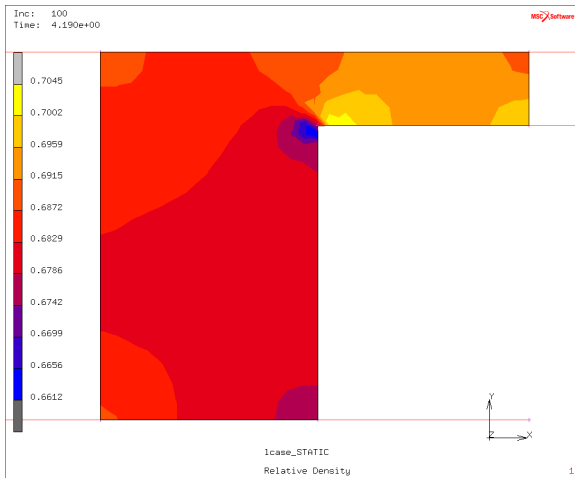


Figure 200. Relative density distribution for $v_3/v_1 = 0.51$

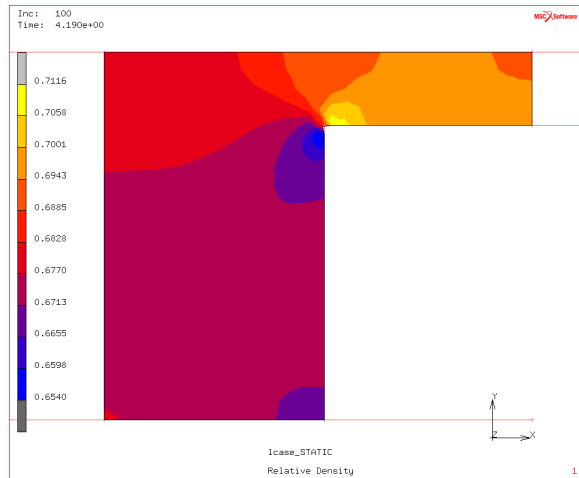


Figure 201. Relative density distribution for $v_3/v_1 = 0.52$

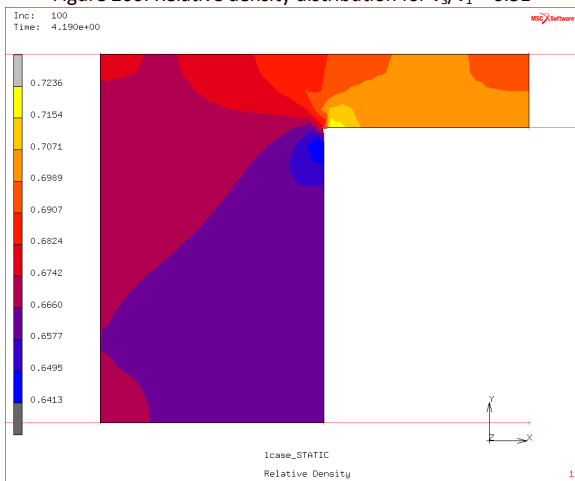


Figure 202. Relative density distribution for $v_3/v_1 = 0.53$

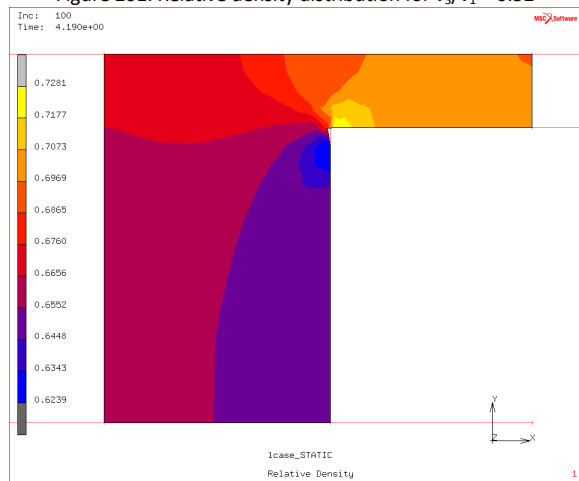


Figure 203. Relative density distribution for $v_3/v_1 = 0.54$

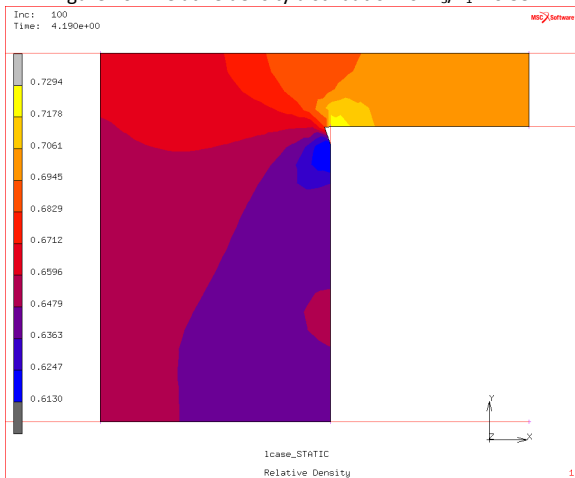


Figure 204. Relative density distribution for $v_3/v_1 = 0.55$

D.1.2 Using Constant Friction Coefficient of 0.12

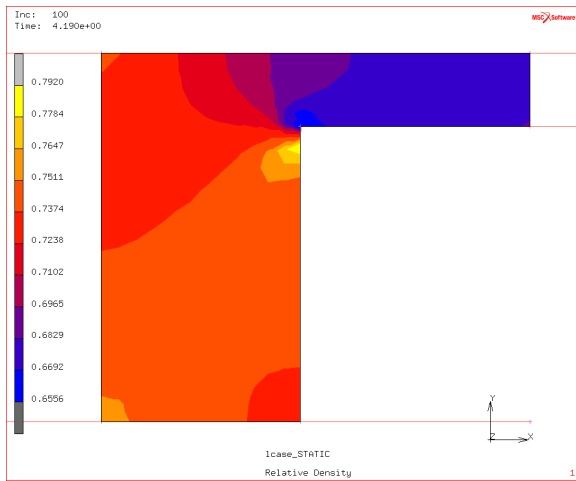


Figure 205. Relative density distribution for $v_3/v_1 = 0.45$

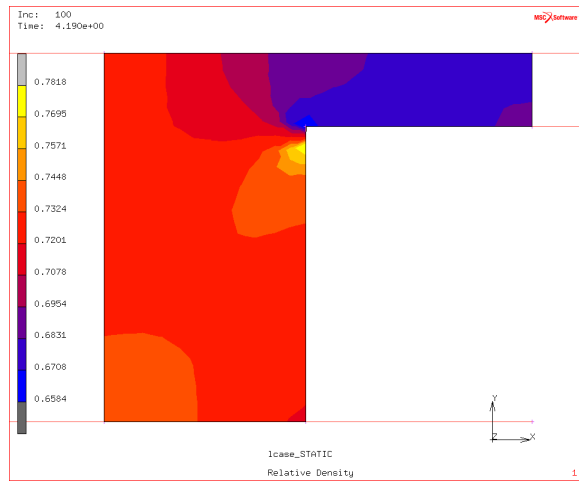


Figure 206. Relative density distribution for $v_3/v_1 = 0.46$

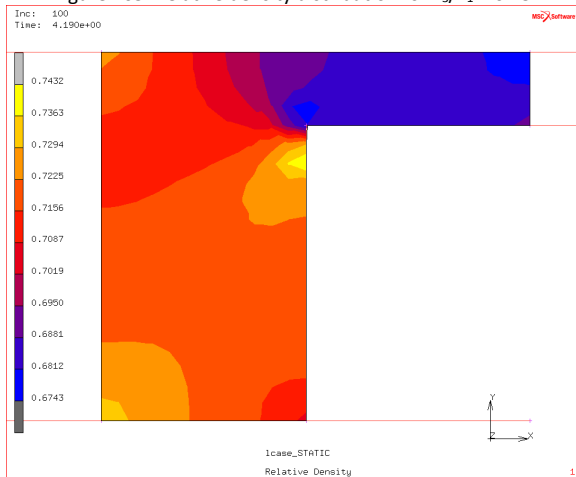


Figure 207. Relative density distribution for $v_3/v_1 = 0.47$

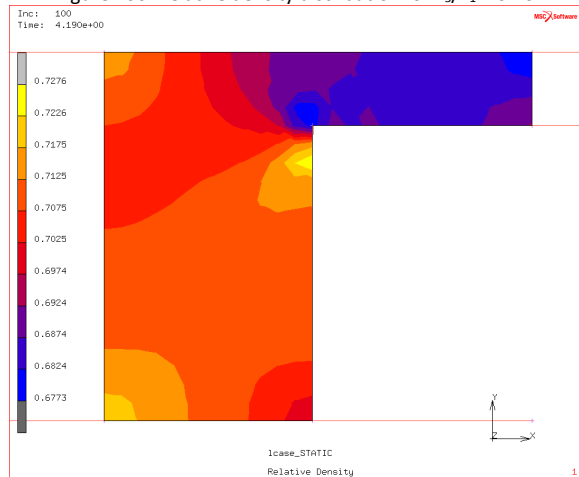


Figure 208. Relative density distribution for $v_3/v_1 = 0.48$

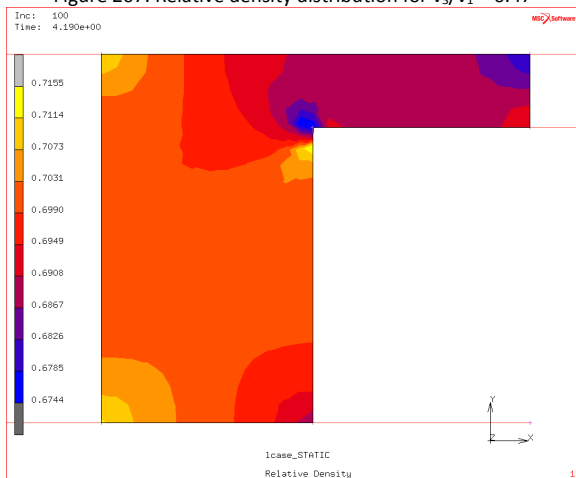


Figure 209. Relative density distribution for $v_3/v_1 = 0.49$

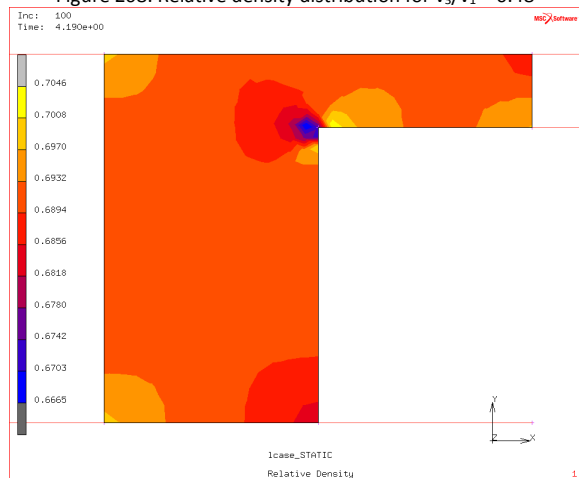


Figure 210. Relative density distribution for $v_3/v_1 = 0.50$

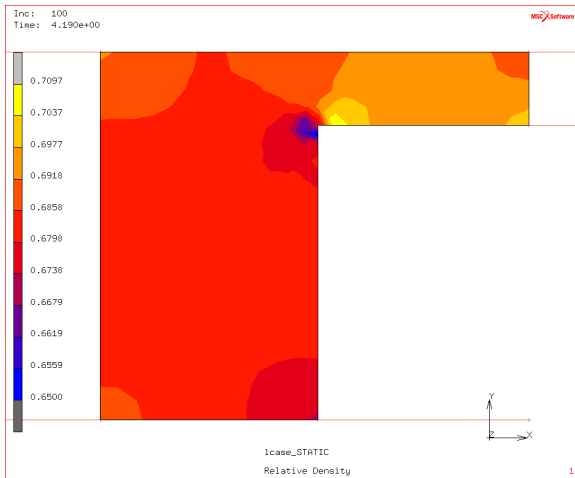


Figure 211. Relative density distribution for $v_3/v_1 = 0.51$

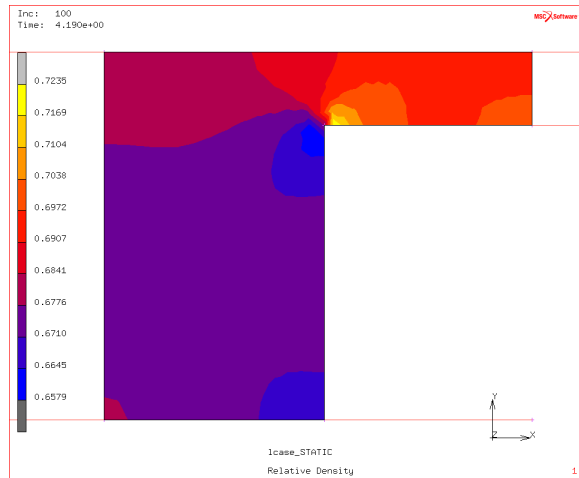


Figure 212. Relative density distribution for $v_3/v_1 = 0.52$

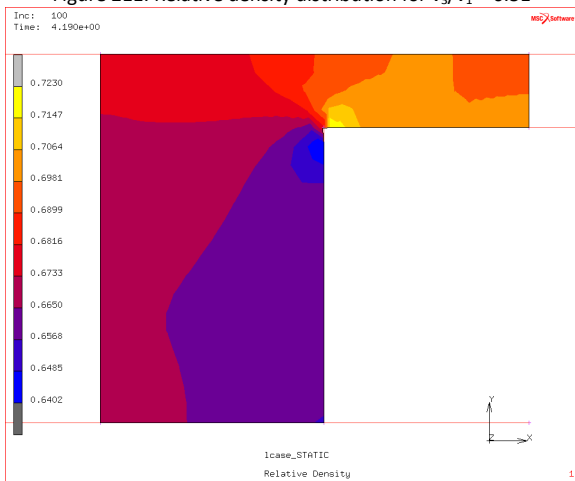


Figure 213. Relative density distribution for $v_3/v_1 = 0.53$

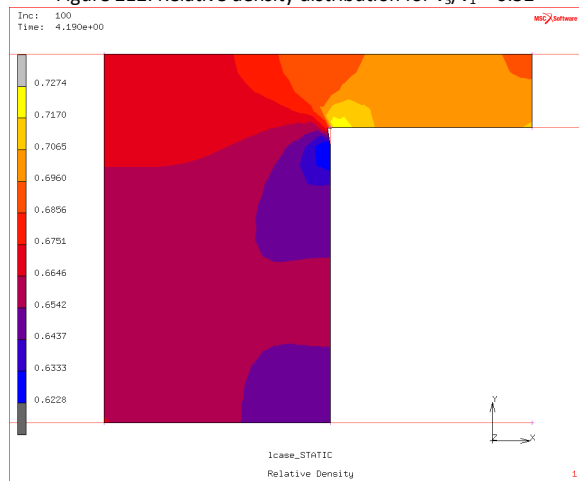


Figure 214. Relative density distribution for $v_3/v_1 = 0.54$

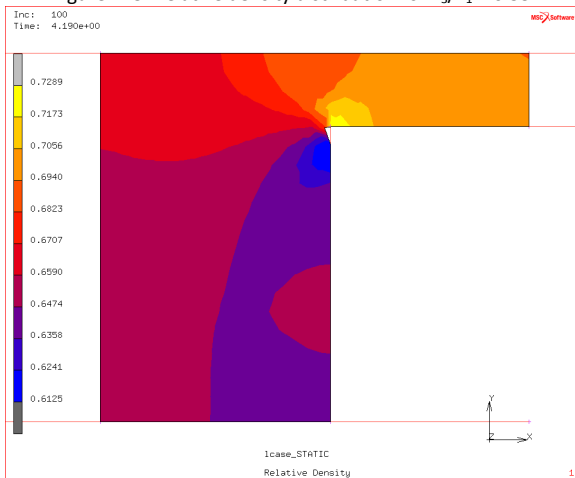


Figure 215. Relative density distribution for $v_3/v_1 = 0.55$

D.1.3 Using Constant Friction Coefficient of 0.20

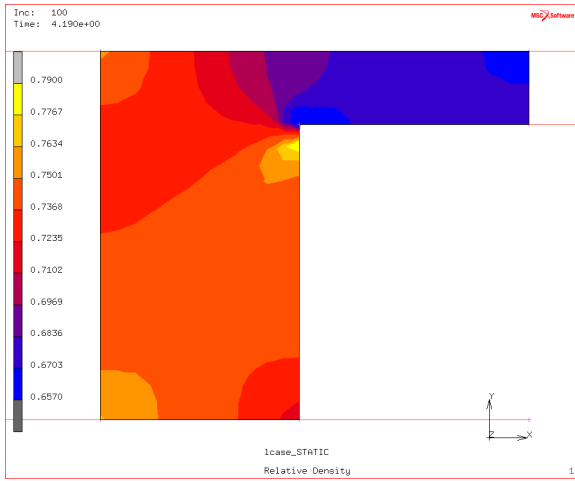


Figure 216. Relative density distribution for $v_3/v_1 = 0.45$

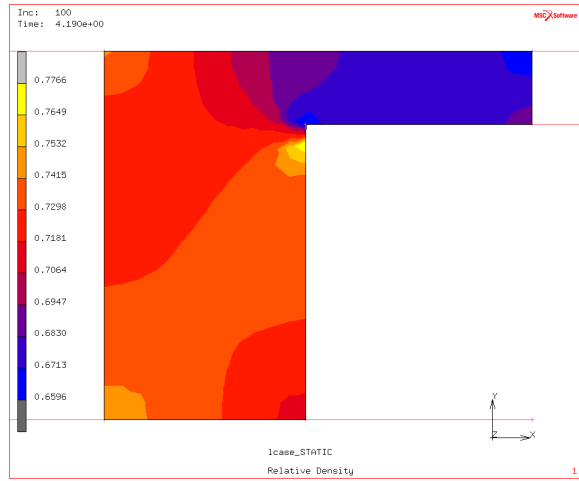


Figure 217. Relative density distribution for $v_3/v_1 = 0.46$

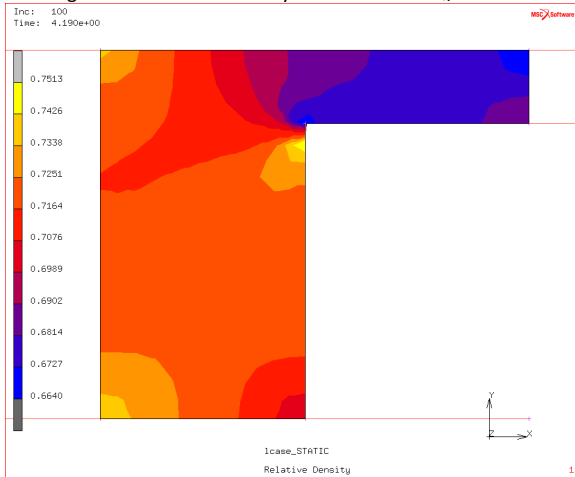


Figure 218. Relative density distribution for $v_3/v_1 = 0.47$

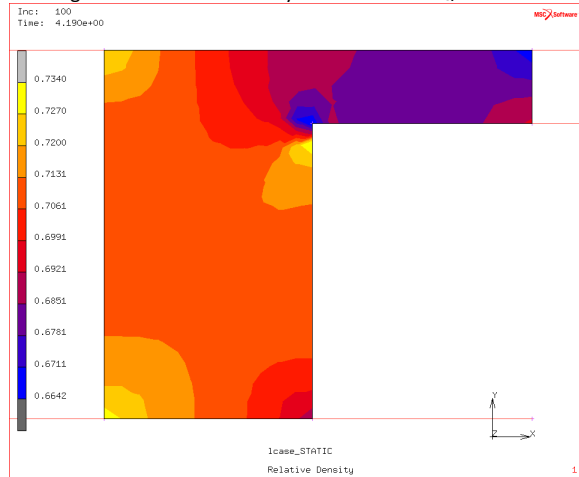


Figure 219. Relative density distribution for $v_3/v_1 = 0.48$

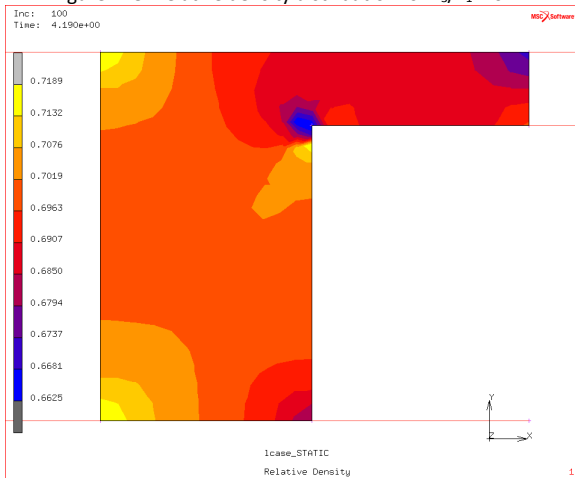


Figure 220. Relative density distribution for $v_3/v_1 = 0.49$

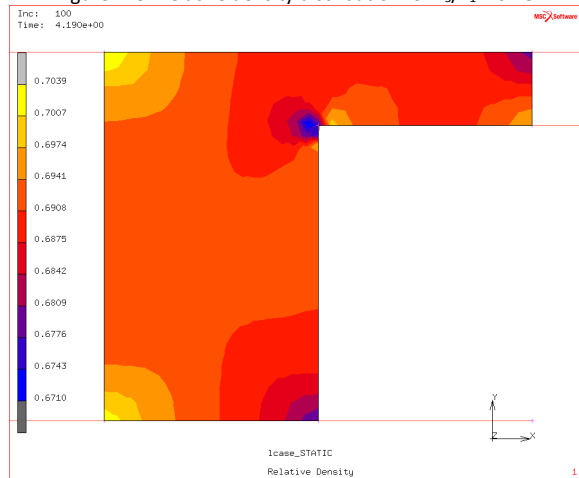


Figure 221. Relative density distribution for $v_3/v_1 = 0.50$

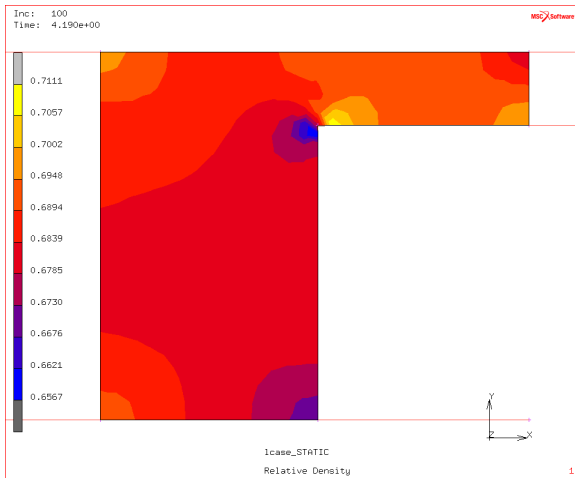


Figure 222. Relative density distribution for $v_3/v_1 = 0.51$

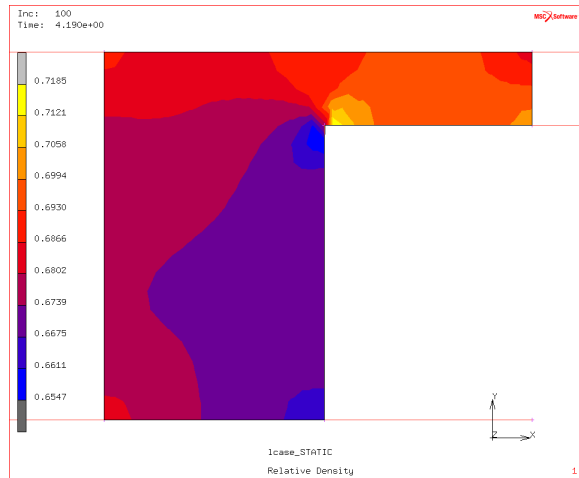


Figure 223. Relative density distribution for $v_3/v_1 = 0.52$

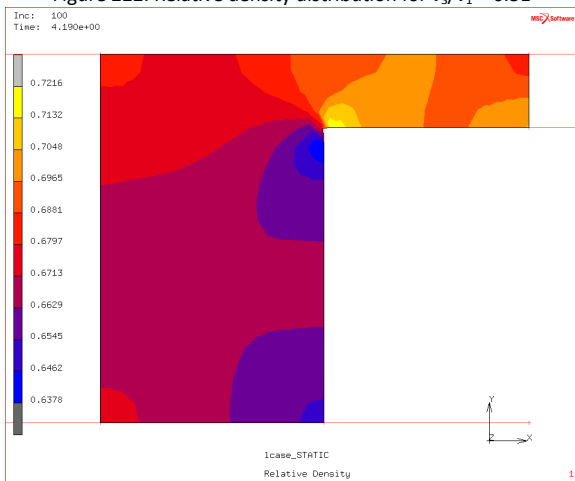


Figure 224. Relative density distribution for $v_3/v_1 = 0.53$

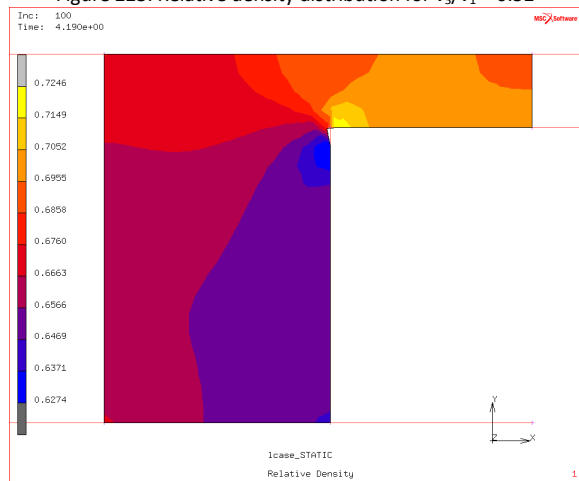


Figure 225. Relative density distribution for $v_3/v_1 = 0.54$

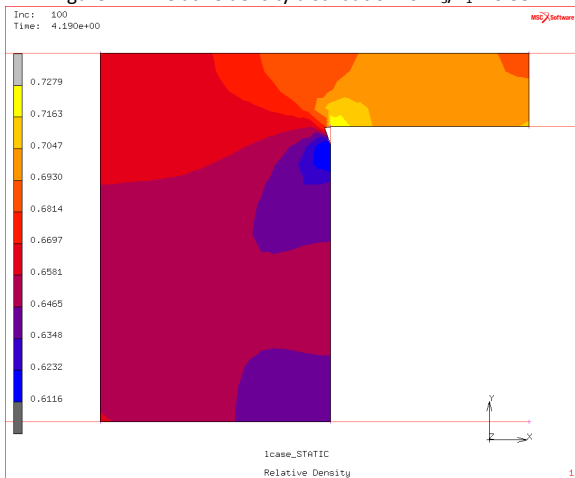


Figure 226. Relative density distribution for $v_3/v_1 = 0.55$

D.1.4 Using Variable Friction Coefficient, $\mu(\sigma_n, v_r)$

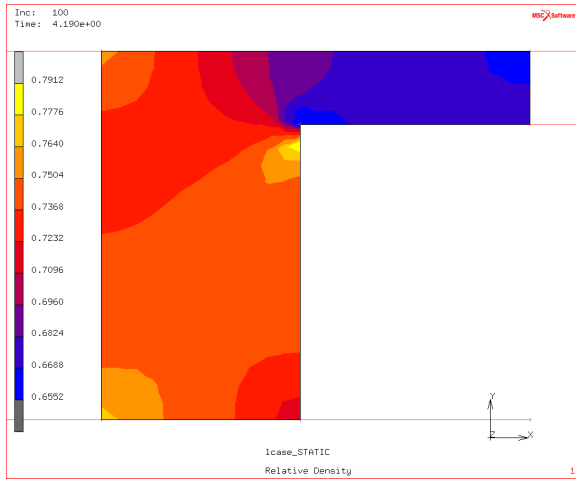


Figure 227. Relative density distribution for $v_3/v_1 = 0.45$

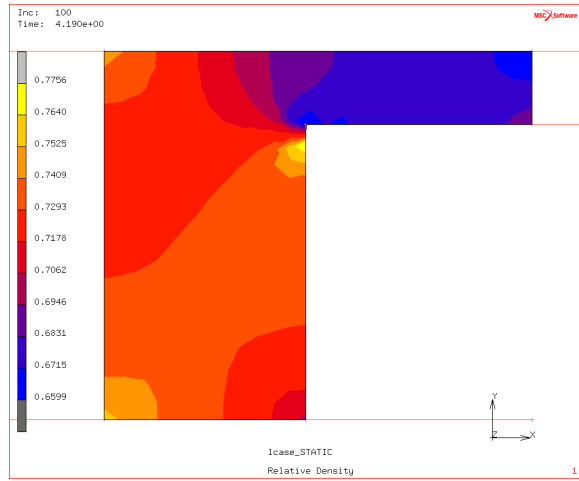


Figure 228. Relative density distribution for $v_3/v_1 = 0.46$

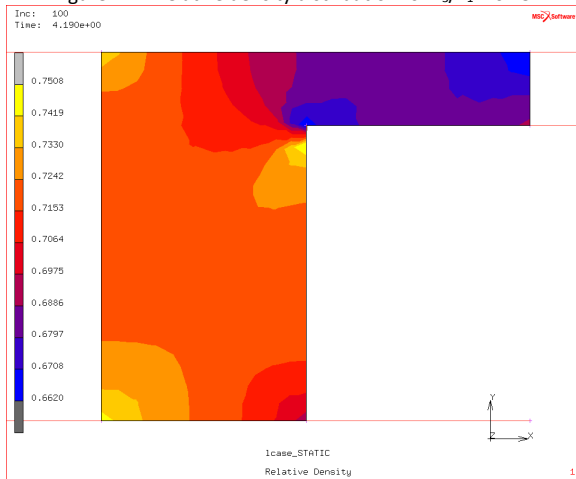


Figure 229. Relative density distribution for $v_3/v_1 = 0.47$

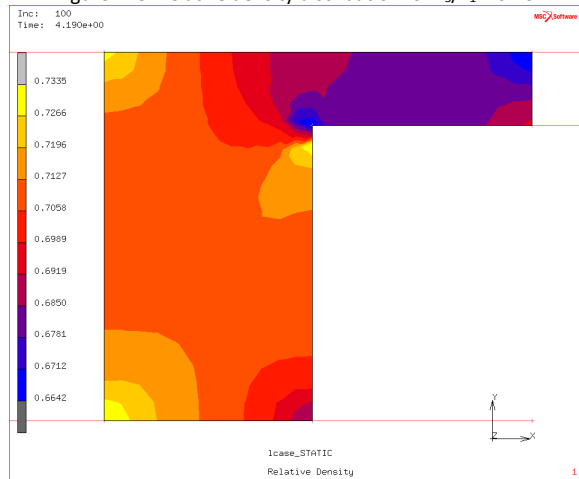


Figure 230. Relative density distribution for $v_3/v_1 = 0.48$

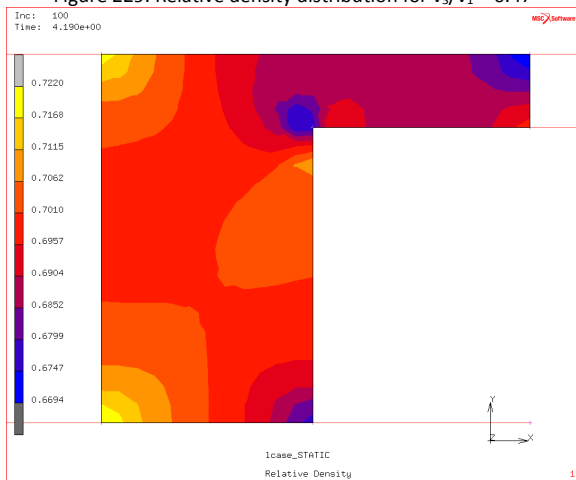


Figure 231. Relative density distribution for $v_3/v_1 = 0.49$

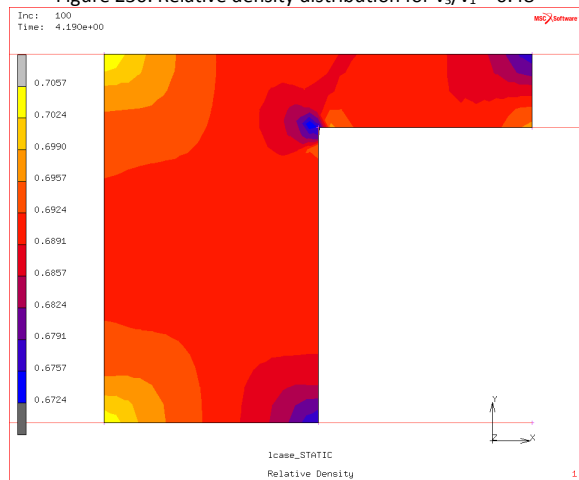


Figure 232. Relative density distribution for $v_3/v_1 = 0.50$

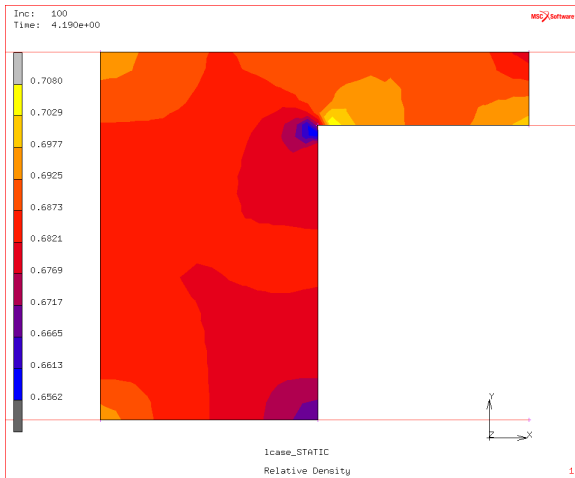


Figure 233. Relative density distribution for $v_3/v_1 = 0.51$

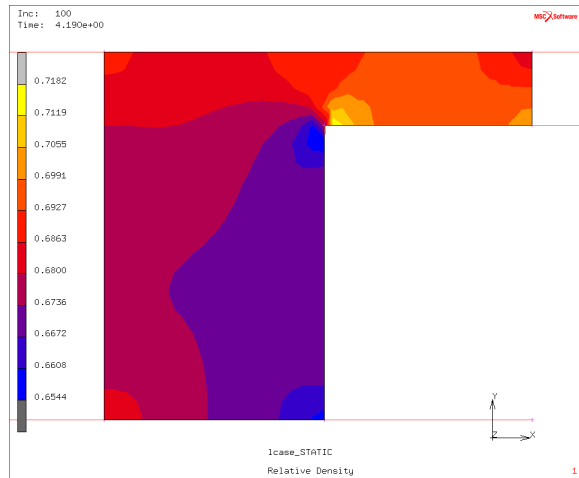


Figure 234. Relative density distribution for $v_3/v_1 = 0.52$

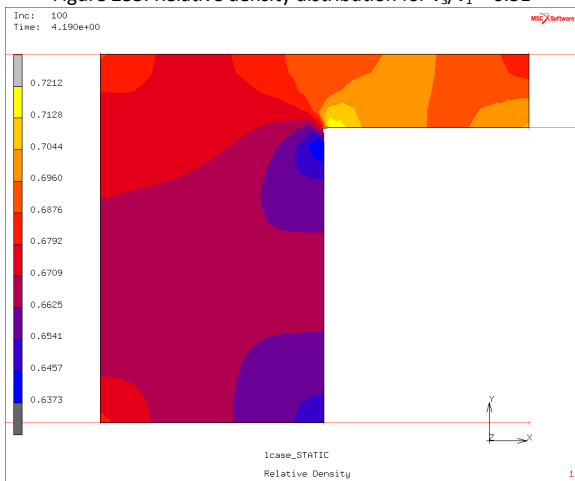


Figure 235. Relative density distribution for $v_3/v_1 = 0.53$

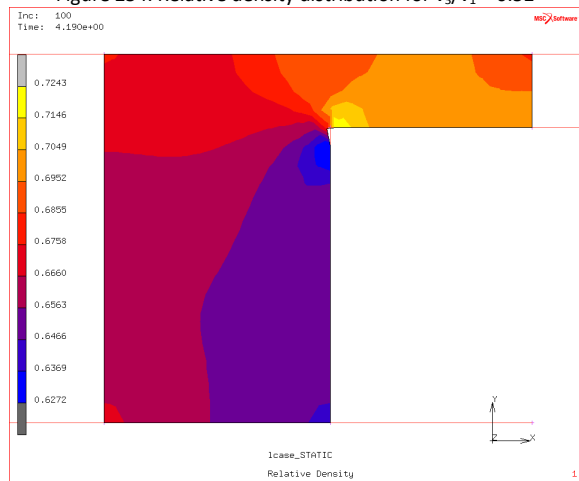


Figure 236. Relative density distribution for $v_3/v_1 = 0.54$

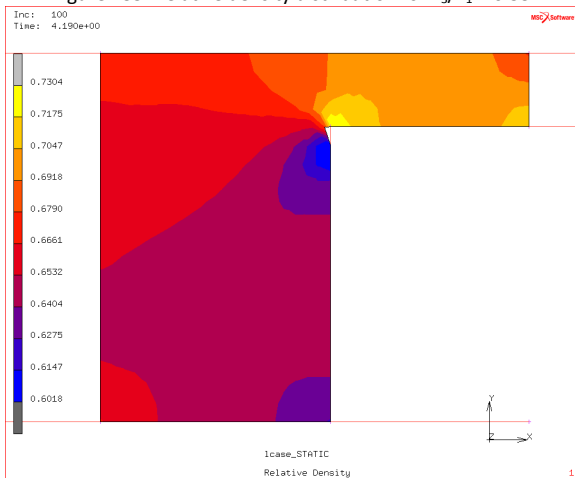


Figure 237. Relative density distribution for $v_3/v_1 = 0.55$

D.2 Using Material Properties Provided by Pavier and Doremus [10, 84]

D.2.1 Using Constant Friction Coefficient of 0.08

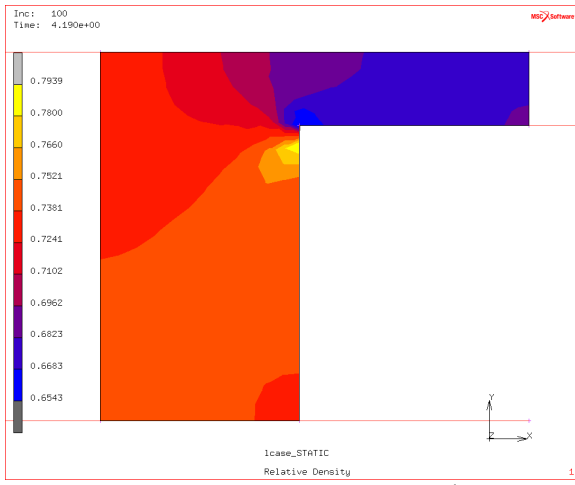


Figure 238. Relative density distribution for $v_3/v_1 = 0.45$

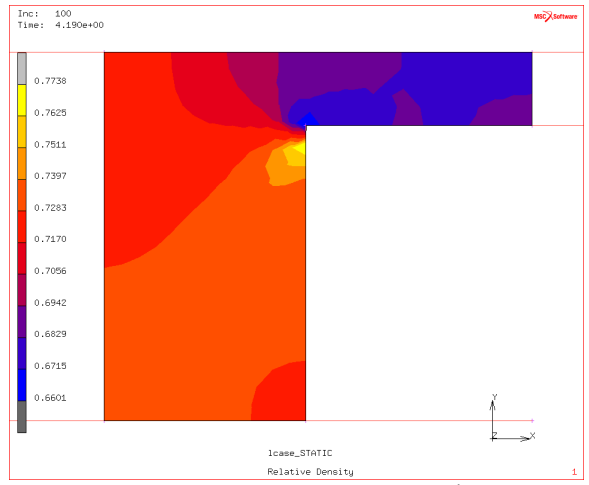


Figure 239. Relative density distribution for $v_3/v_1 = 0.46$

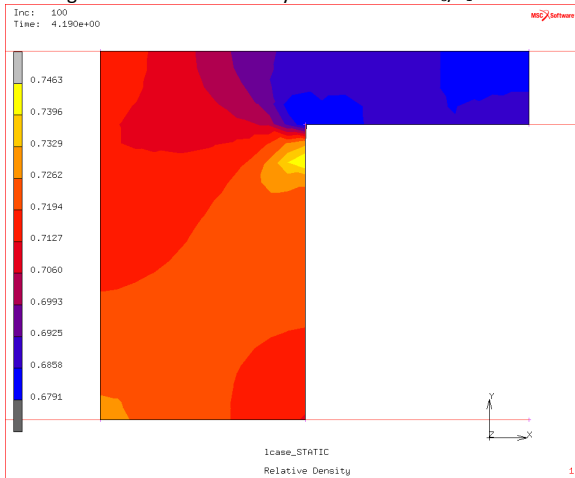


Figure 240. Relative density distribution for $v_3/v_1 = 0.47$

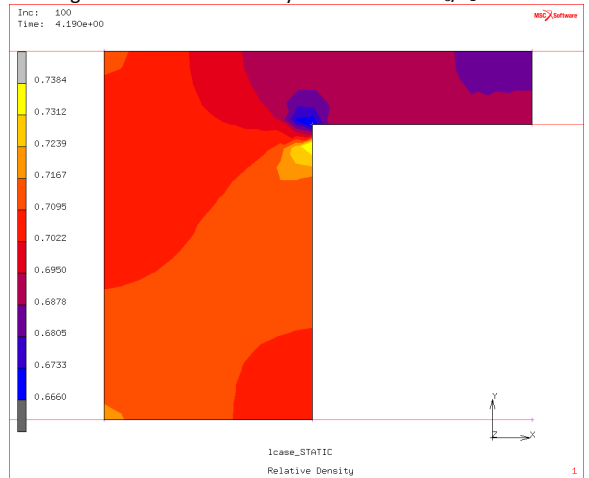


Figure 241. Relative density distribution for $v_3/v_1 = 0.48$

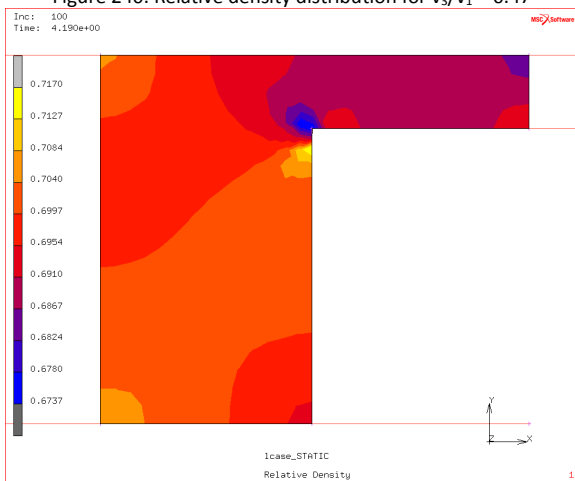


Figure 242. Relative density distribution for $v_3/v_1 = 0.49$

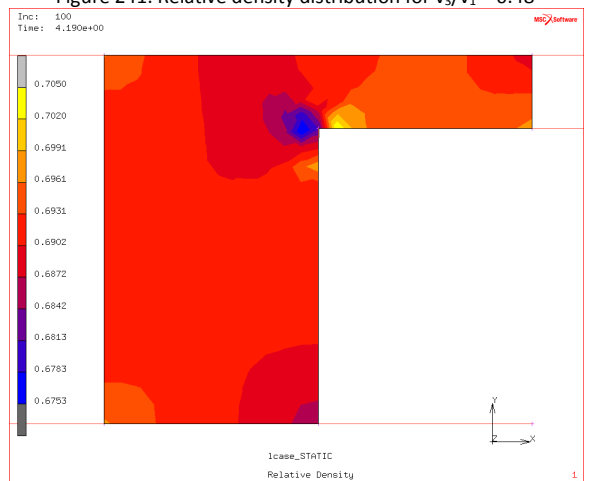


Figure 243. Relative density distribution for $v_3/v_1 = 0.50$

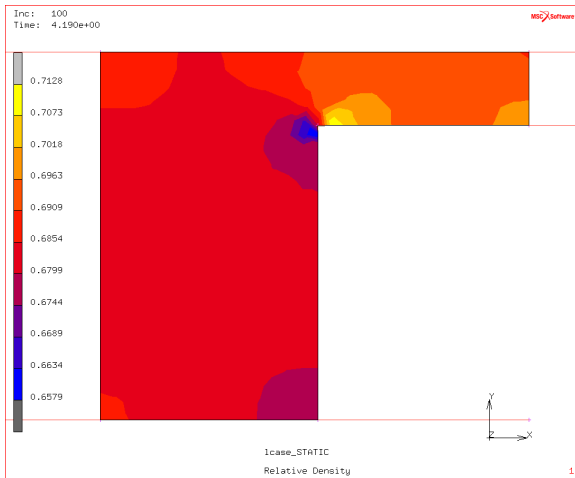


Figure 244. Relative density distribution for $v_3/v_1 = 0.51$

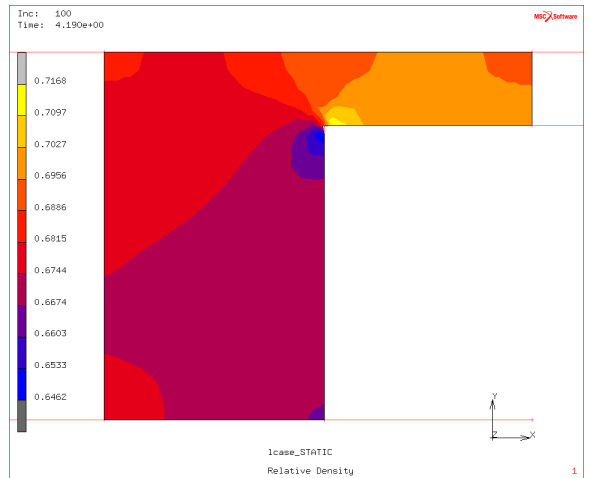


Figure 245. Relative density distribution for $v_3/v_1 = 0.52$

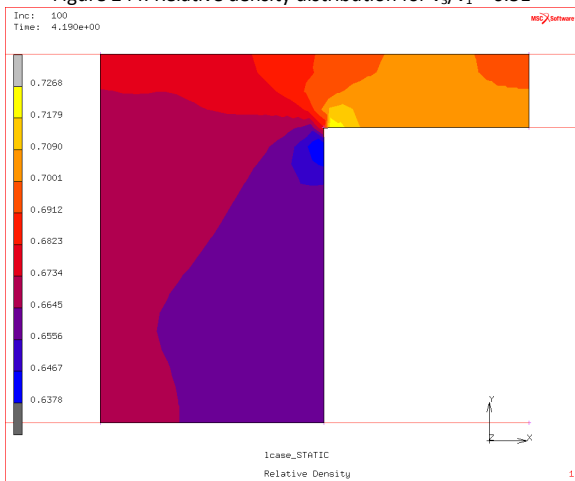


Figure 246. Relative density distribution for $v_3/v_1 = 0.53$

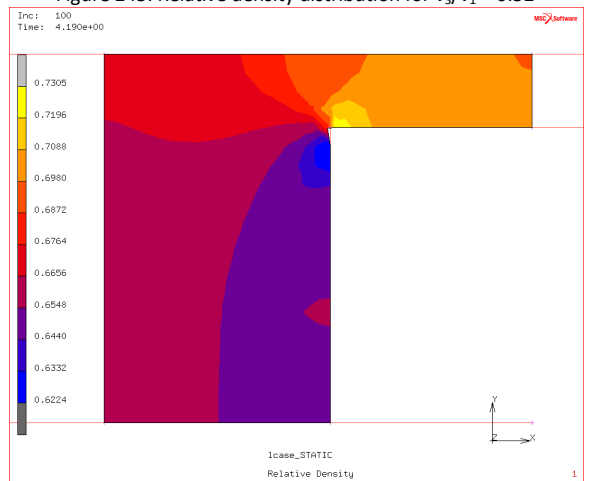


Figure 247. Relative density distribution for $v_3/v_1 = 0.54$

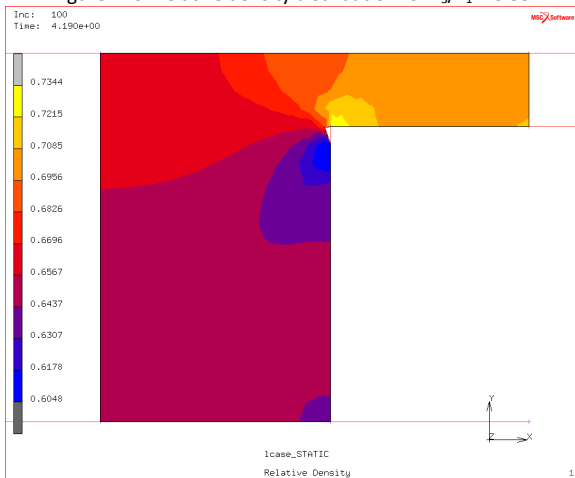


Figure 248. Relative density distribution for $v_3/v_1 = 0.55$

D.2.2 Using Constant Friction Coefficient of 0.12

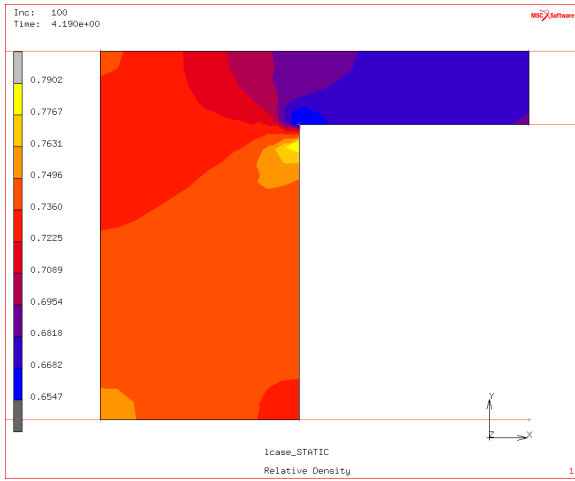


Figure 249. Relative density distribution for $v_3/v_1 = 0.45$

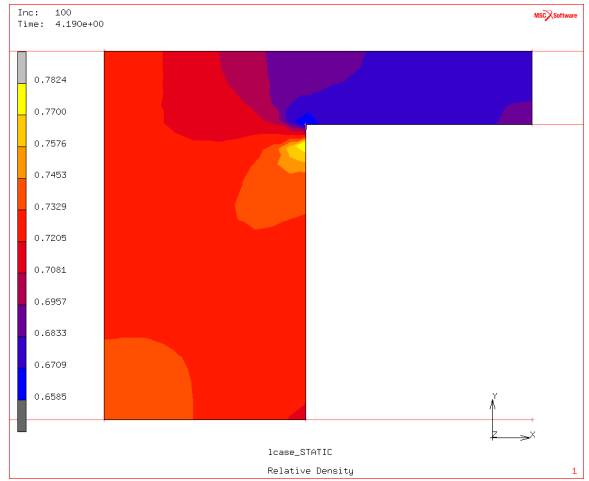


Figure 250. Relative density distribution for $v_3/v_1 = 0.46$

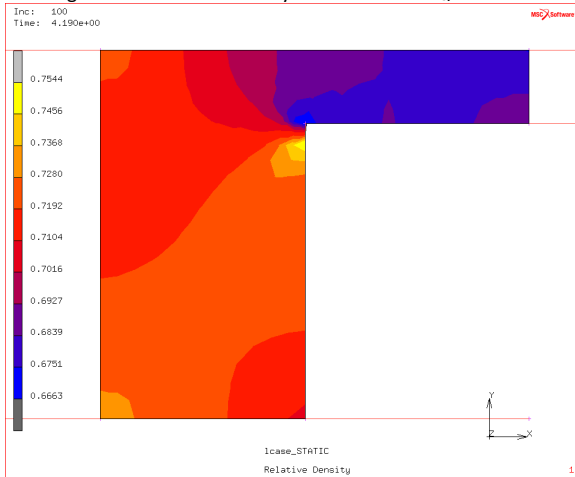


Figure 251. Relative density distribution for $v_3/v_1 = 0.47$

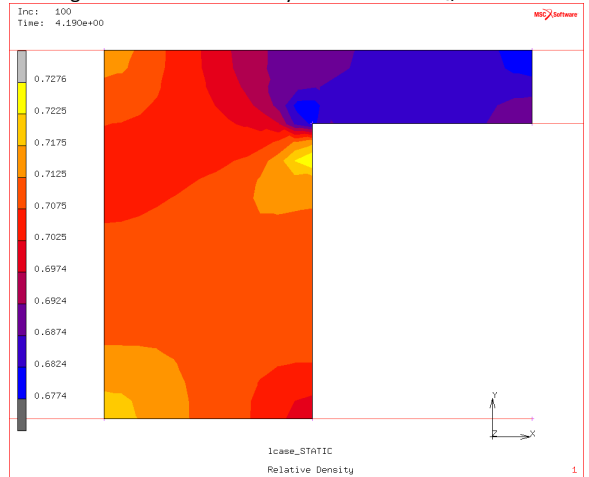


Figure 252. Relative density distribution for $v_3/v_1 = 0.48$

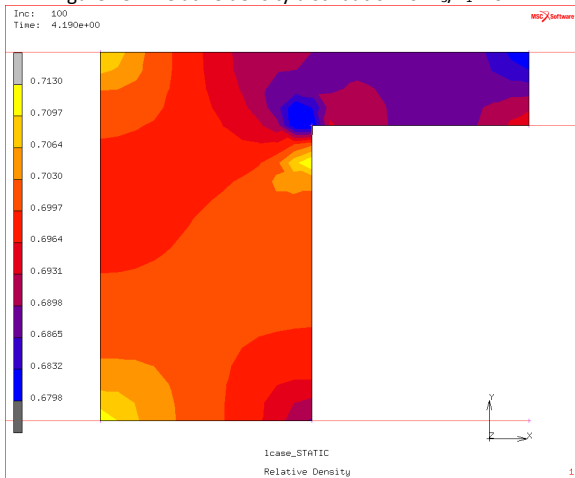


Figure 253. Relative density distribution for $v_3/v_1 = 0.49$

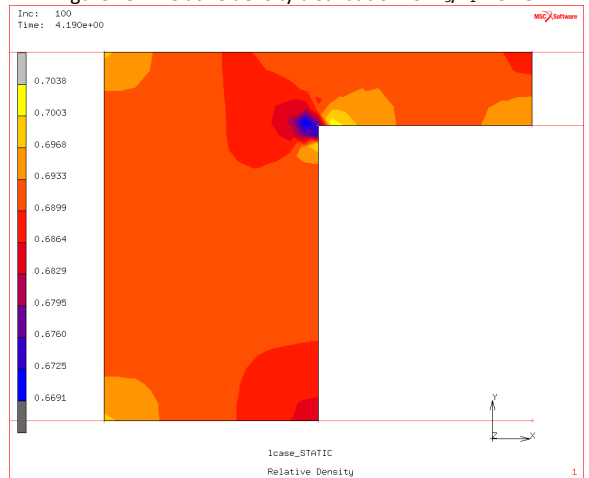


Figure 254. Relative density distribution for $v_3/v_1 = 0.50$

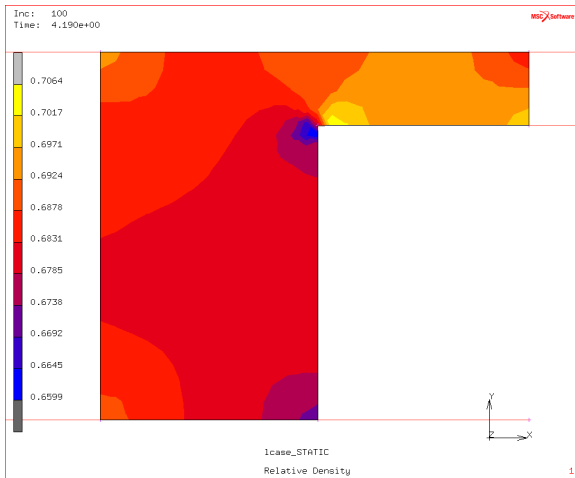


Figure 255. Relative density distribution for $v_3/v_1 = 0.51$

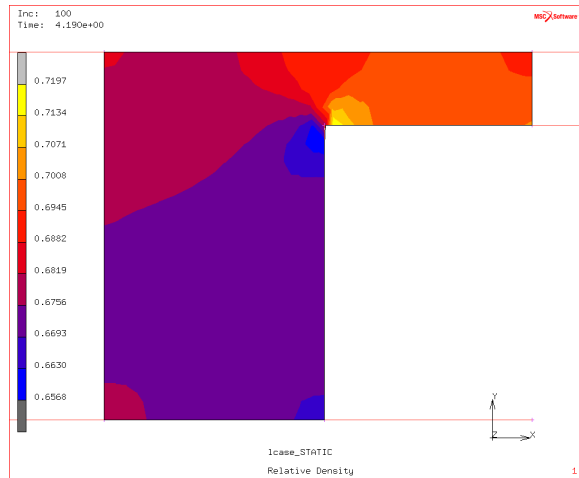


Figure 256. Relative density distribution for $v_3/v_1 = 0.52$

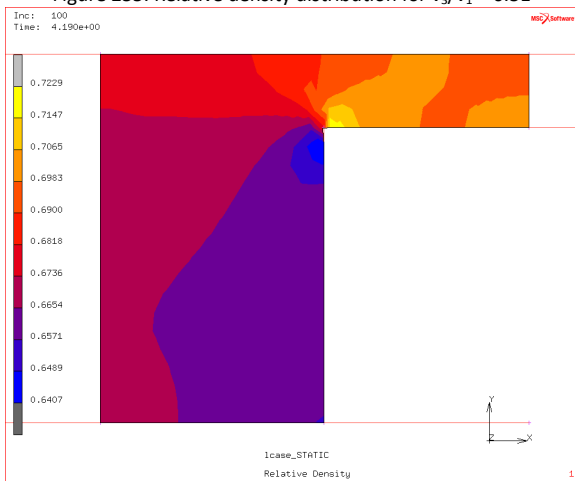


Figure 257. Relative density distribution for $v_3/v_1 = 0.53$

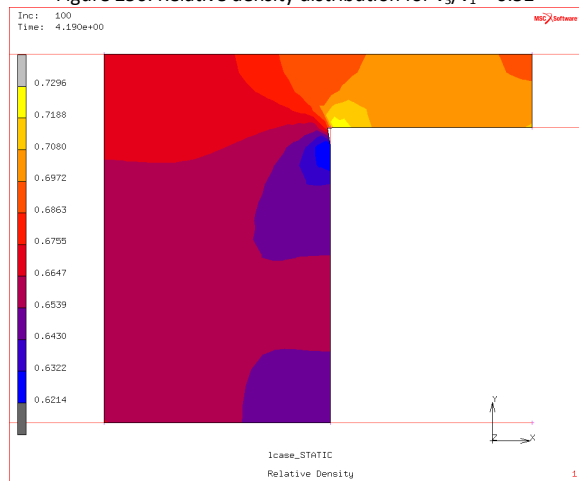


Figure 258. Relative density distribution for $v_3/v_1 = 0.54$

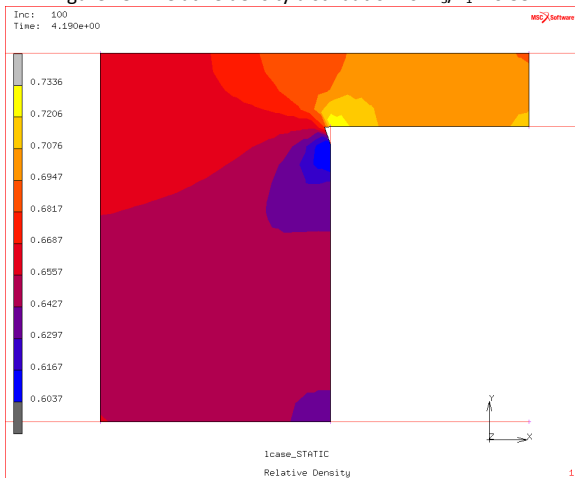


Figure 259. Relative density distribution for $v_3/v_1 = 0.55$

D.2.3 Using Constant Friction Coefficient of 0.20

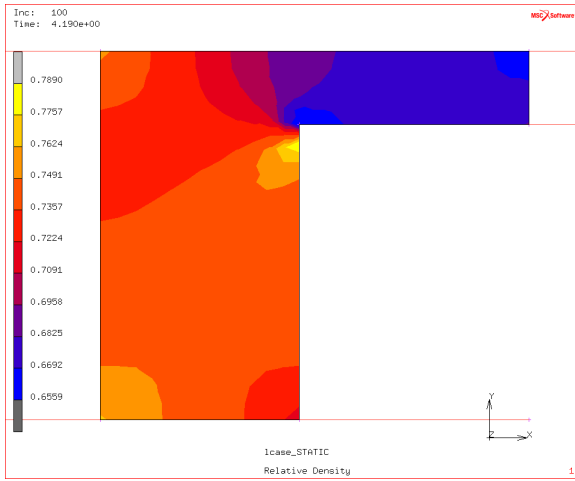


Figure 260. Relative density distribution for $v_3/v_1 = 0.45$

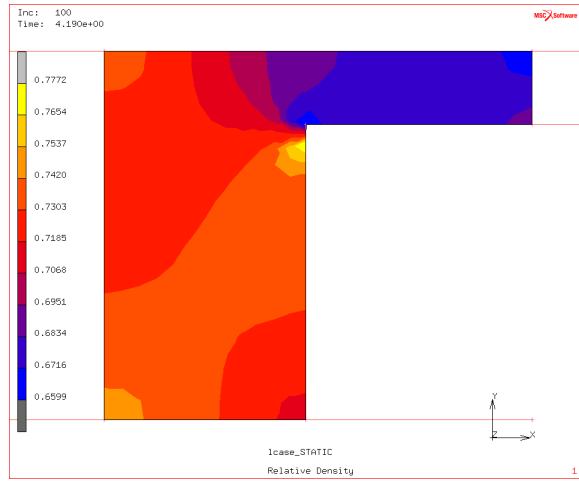


Figure 261. Relative density distribution for $v_3/v_1 = 0.46$

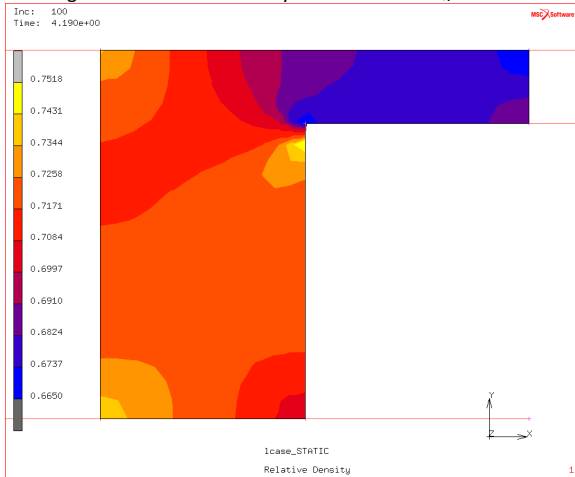


Figure 262. Relative density distribution for $v_3/v_1 = 0.47$

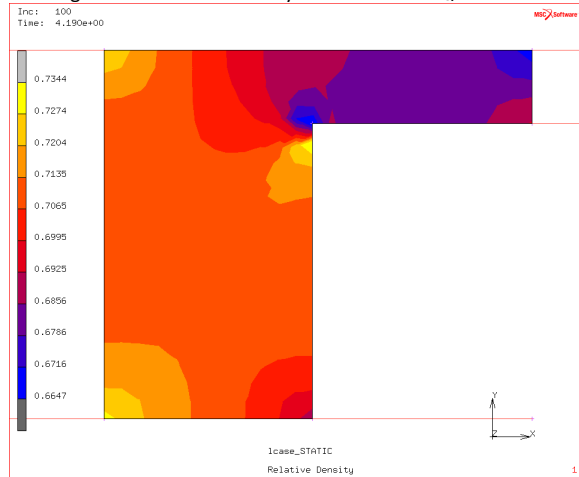


Figure 263. Relative density distribution for $v_3/v_1 = 0.48$

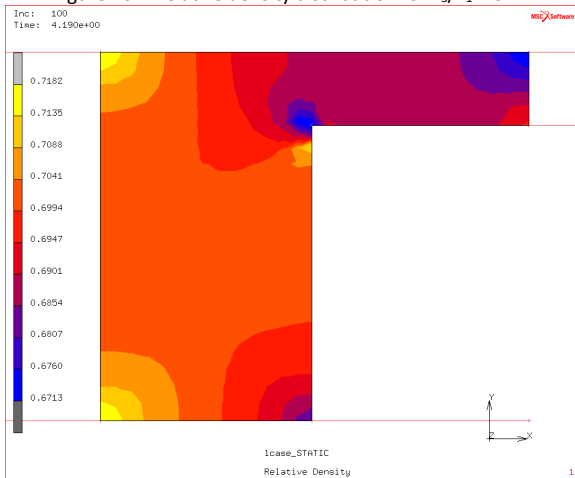


Figure 264. Relative density distribution for $v_3/v_1 = 0.49$

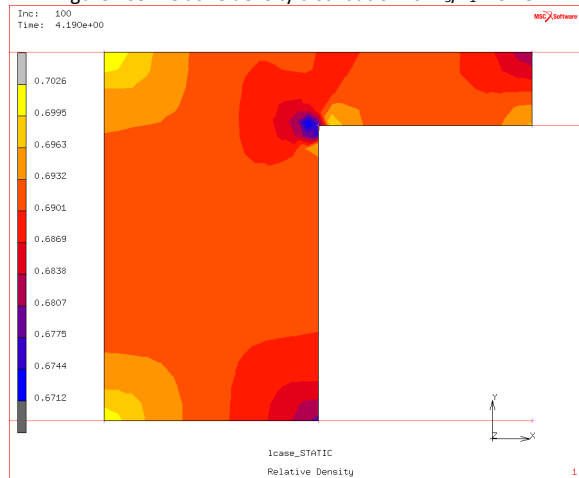


Figure 265. Relative density distribution for $v_3/v_1 = 0.50$

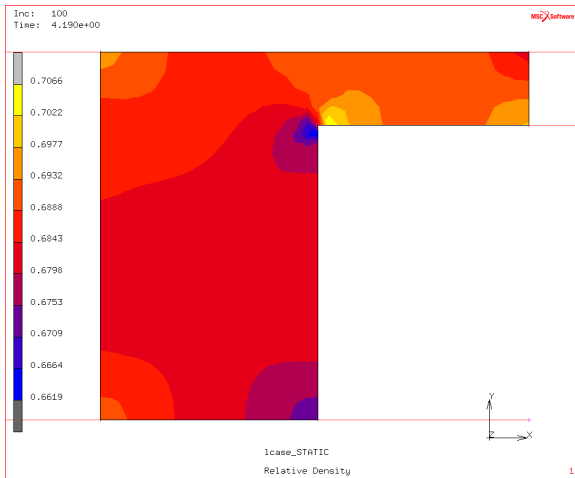


Figure 266. Relative density distribution for $v_3/v_1 = 0.51$

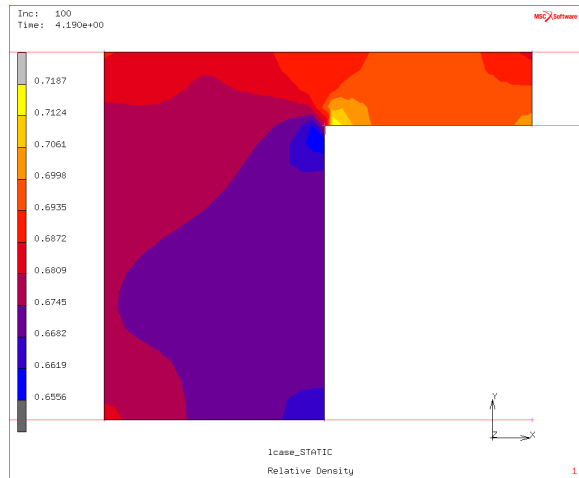


Figure 267. Relative density distribution for $v_3/v_1 = 0.52$

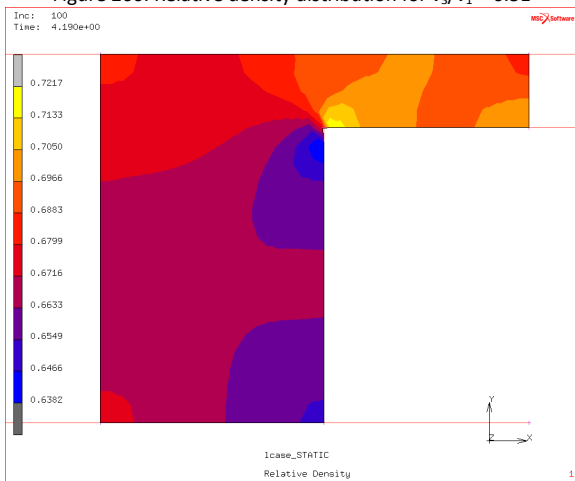


Figure 268. Relative density distribution for $v_3/v_1 = 0.53$

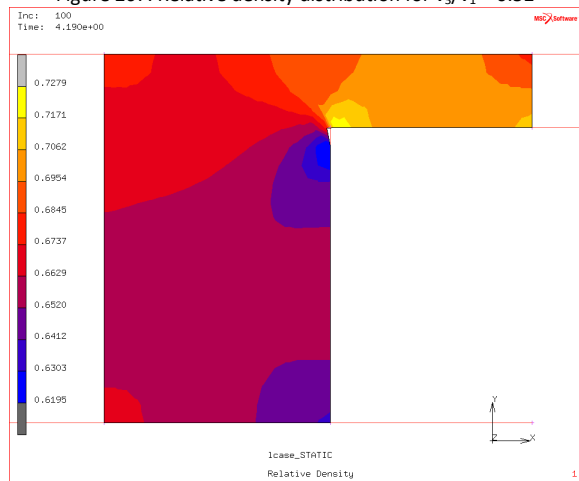


Figure 269. Relative density distribution for $v_3/v_1 = 0.54$

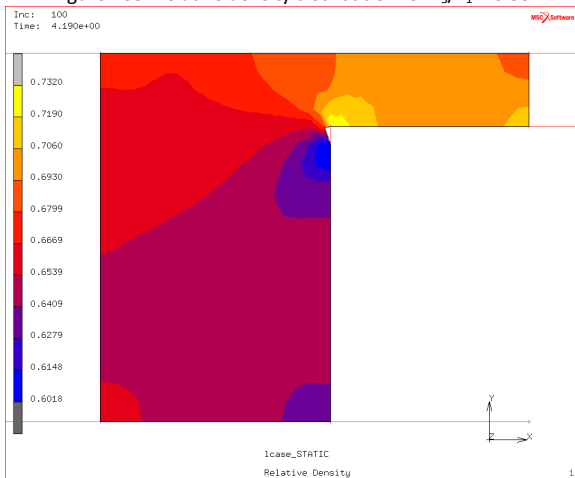


Figure 270. Relative density distribution for $v_3/v_1 = 0.55$

D.2.4 Using Variable Friction Coefficient, $\mu(\sigma_n, v_r)$

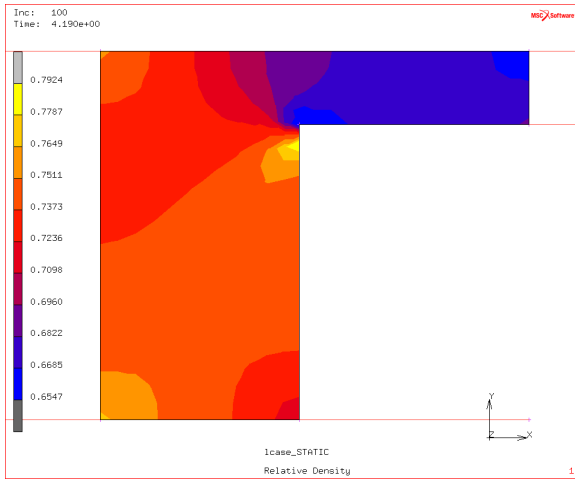


Figure 271. Relative density distribution for $v_3/v_1 = 0.45$

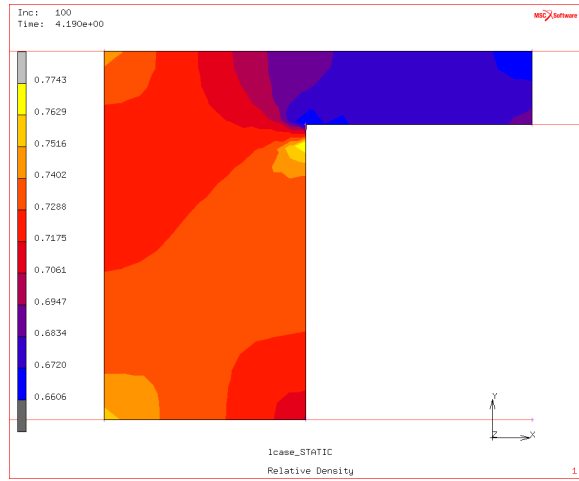


Figure 272. Relative density distribution for $v_3/v_1 = 0.46$

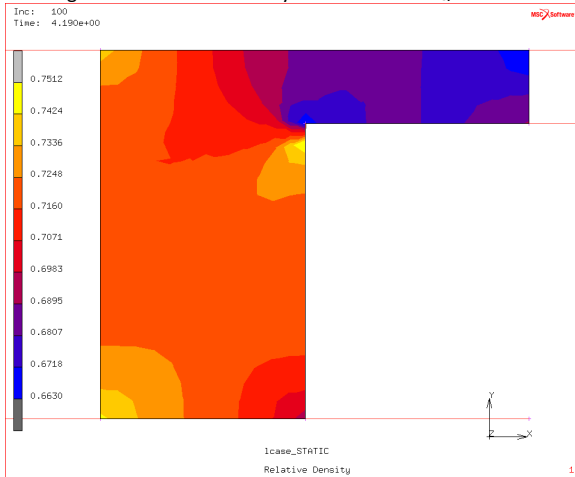


Figure 273. Relative density distribution for $v_3/v_1 = 0.47$

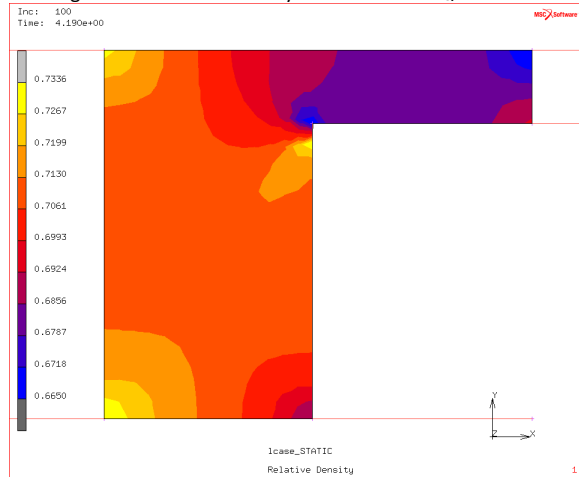


Figure 274. Relative density distribution for $v_3/v_1 = 0.48$

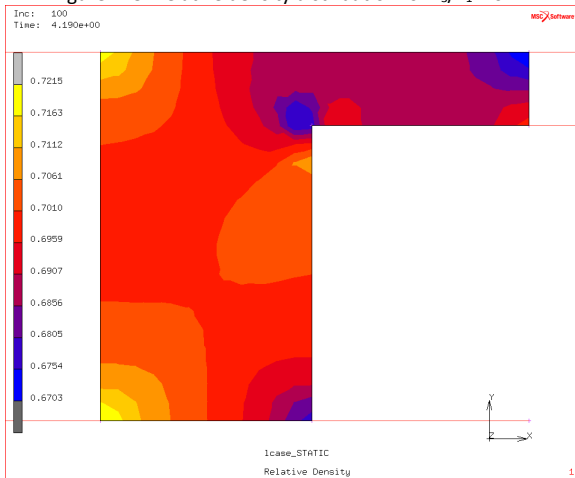


Figure 275. Relative density distribution for $v_3/v_1 = 0.49$

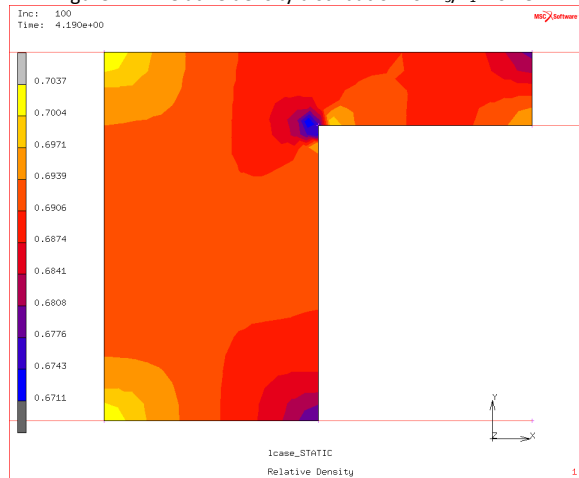


Figure 276. Relative density distribution for $v_3/v_1 = 0.50$

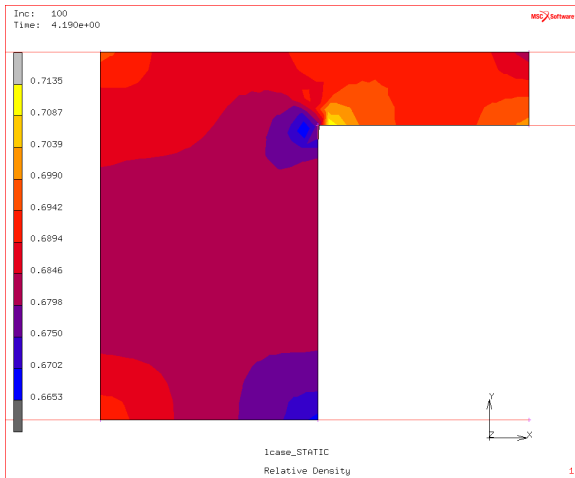


Figure 277. Relative density distribution for $v_3/v_1 = 0.51$

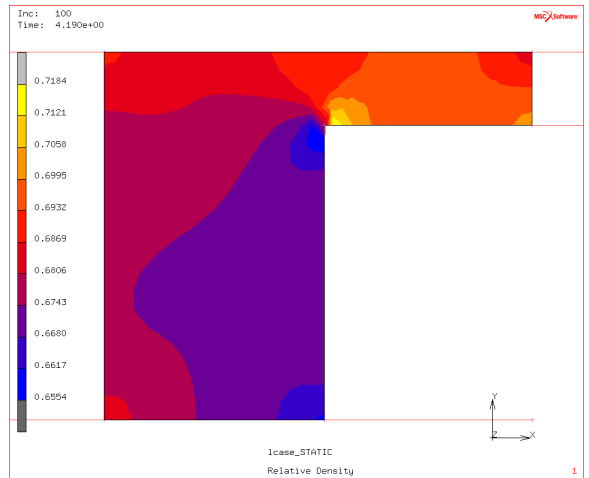


Figure 278. Relative density distribution for $v_3/v_1 = 0.52$

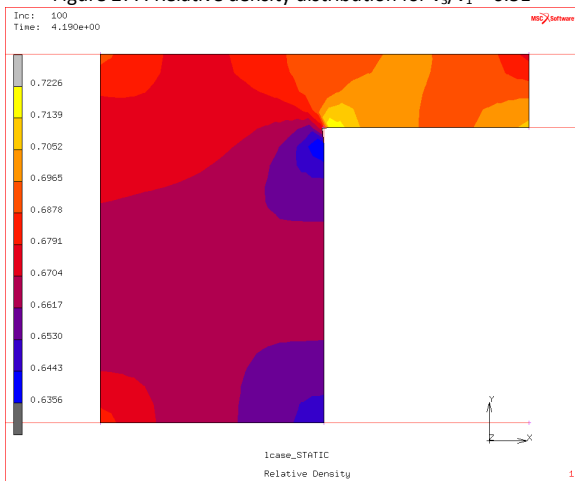


Figure 279. Relative density distribution for $v_3/v_1 = 0.53$

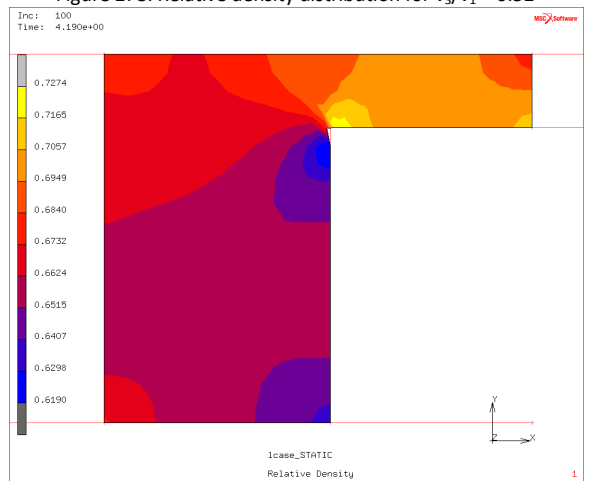


Figure 280. Relative density distribution for $v_3/v_1 = 0.54$

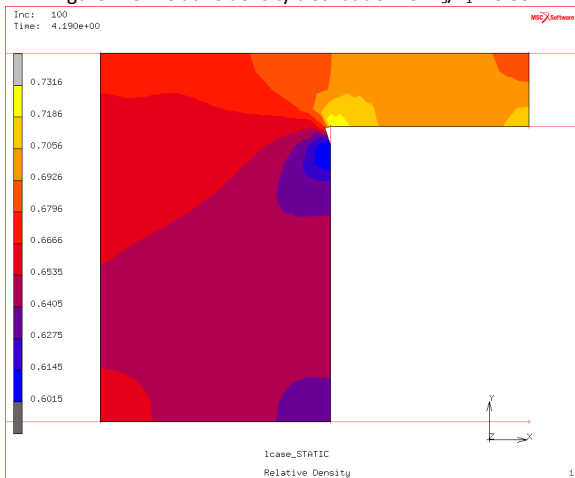


Figure 281. Relative density distribution for $v_3/v_1 = 0.55$

D.3 Using Material Properties Provided by Koval'chenko [54]

D.3.1 Using Constant Friction Coefficient of 0.08

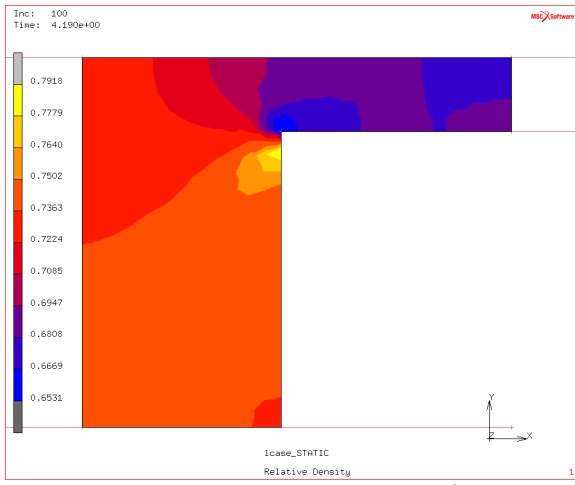


Figure 282. Relative density distribution for $v_3/v_1 = 0.45$

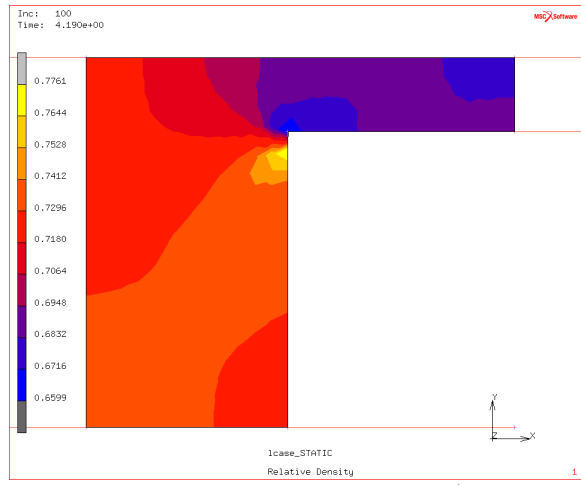


Figure 283. Relative density distribution for $v_3/v_1 = 0.46$

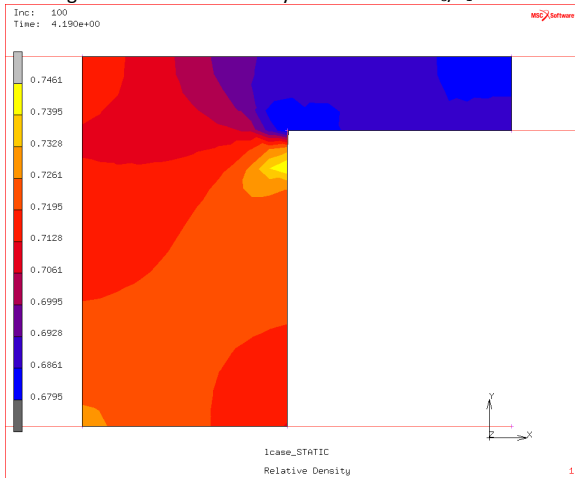


Figure 284. Relative density distribution for $v_3/v_1 = 0.47$

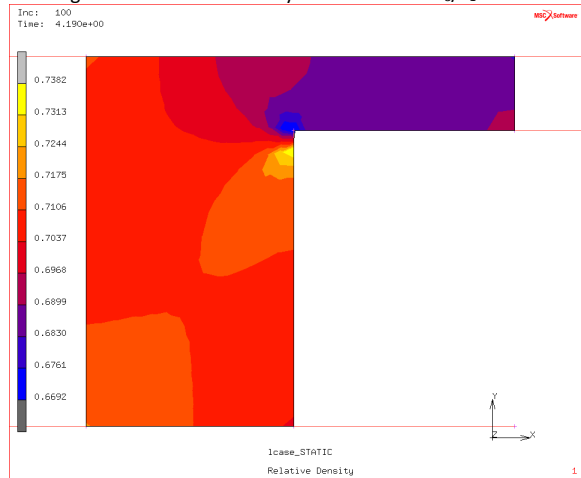


Figure 285. Relative density distribution for $v_3/v_1 = 0.48$

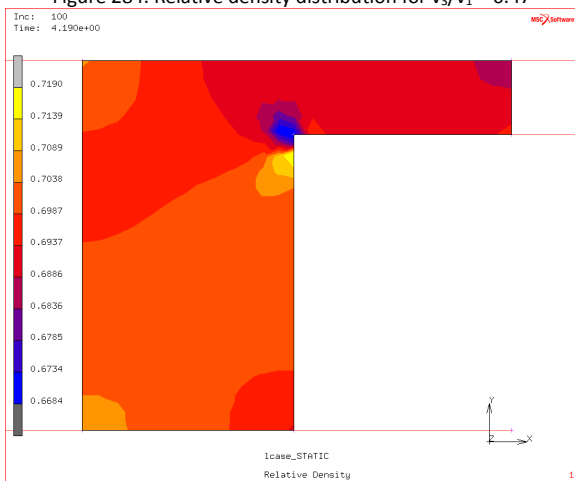


Figure 286. Relative density distribution for $v_3/v_1 = 0.49$

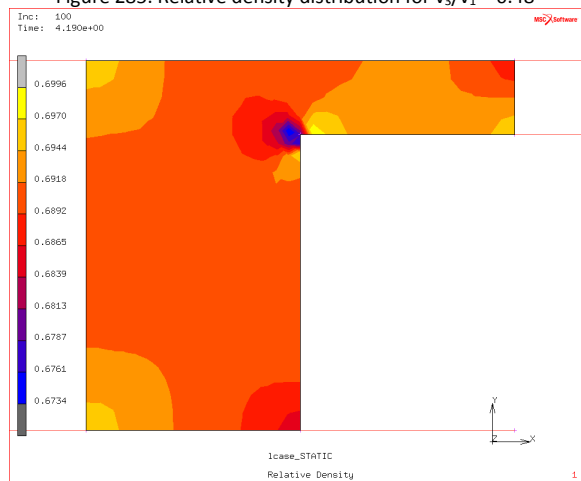


Figure 287. Relative density distribution for $v_3/v_1 = 0.50$

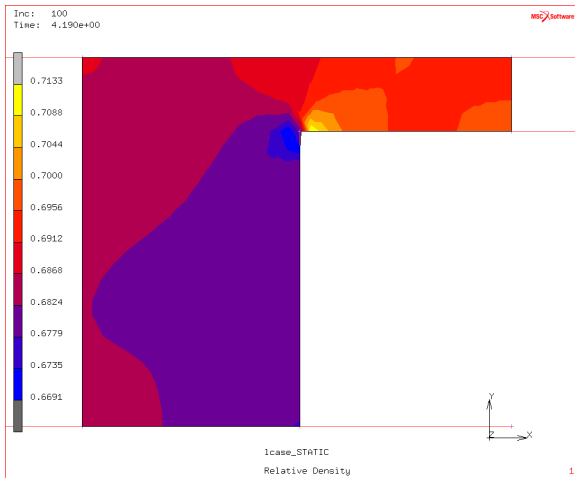


Figure 288. Relative density distribution for $v_3/v_1 = 0.51$

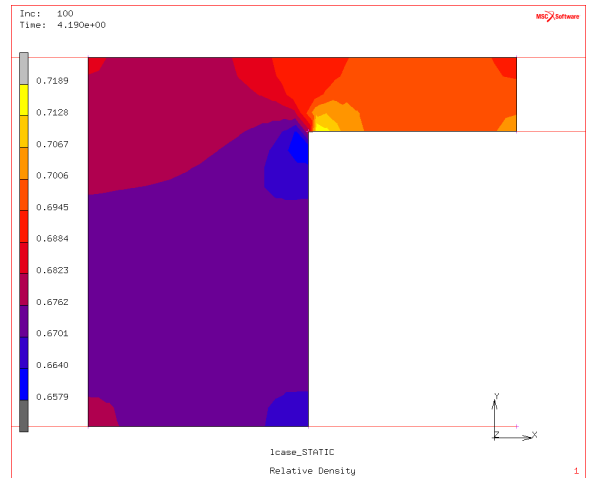


Figure 289. Relative density distribution for $v_3/v_1 = 0.52$

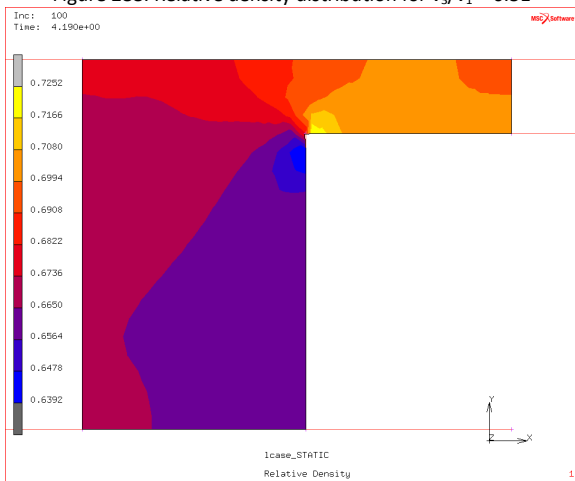


Figure 290. Relative density distribution for $v_3/v_1 = 0.53$

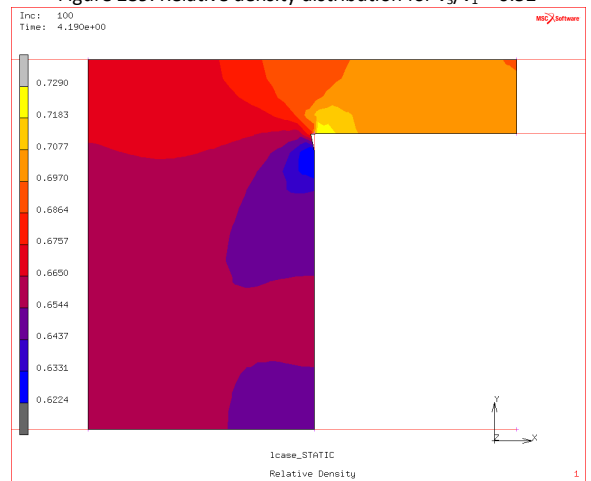


Figure 291. Relative density distribution for $v_3/v_1 = 0.54$

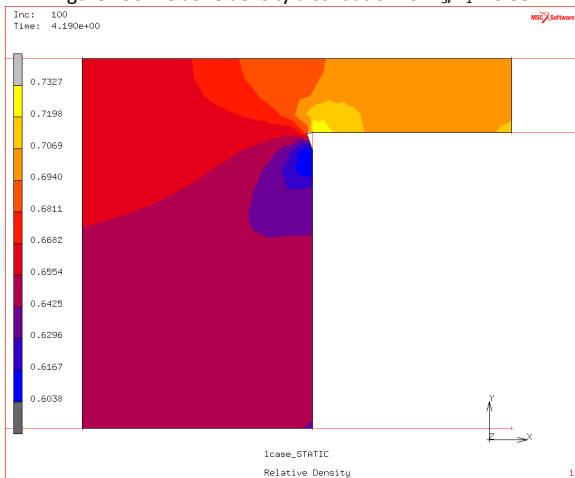


Figure 292. Relative density distribution for $v_3/v_1 = 0.55$

D.3.2 Using Constant Friction Coefficient of 0.12

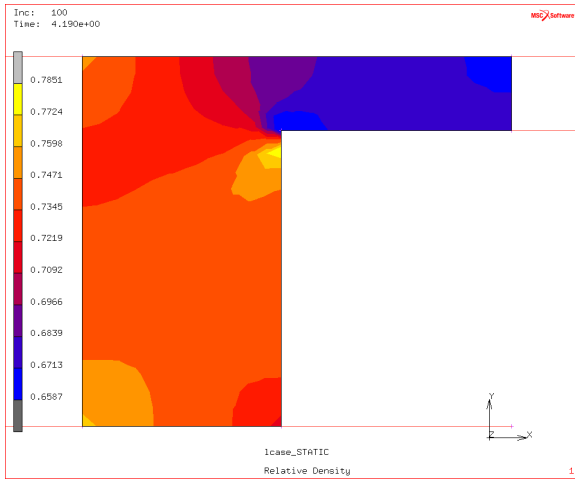


Figure 293. Relative density distribution for $v_3/v_1 = 0.45$

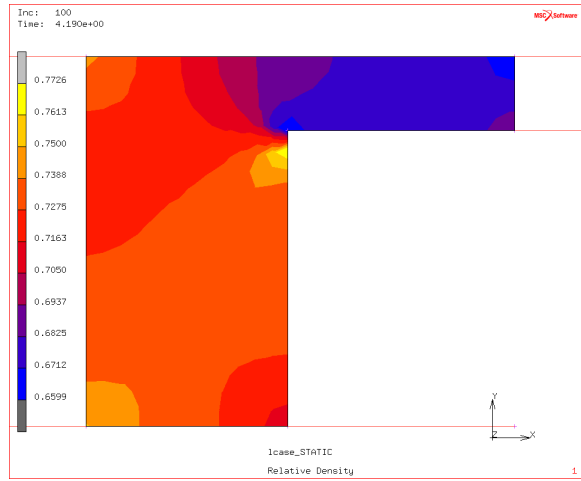


Figure 294. Relative density distribution for $v_3/v_1 = 0.46$

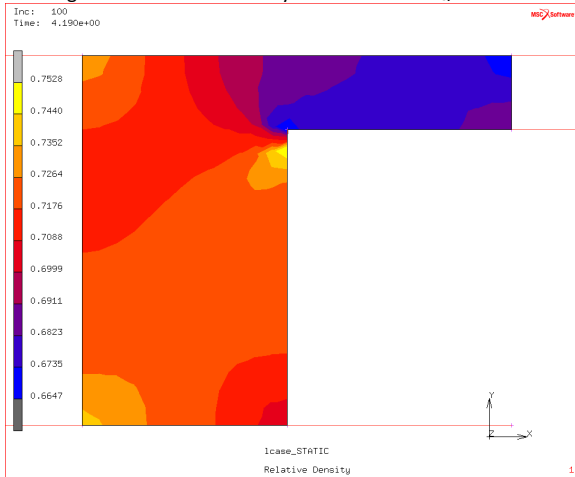


Figure 295. Relative density distribution for $v_3/v_1 = 0.47$

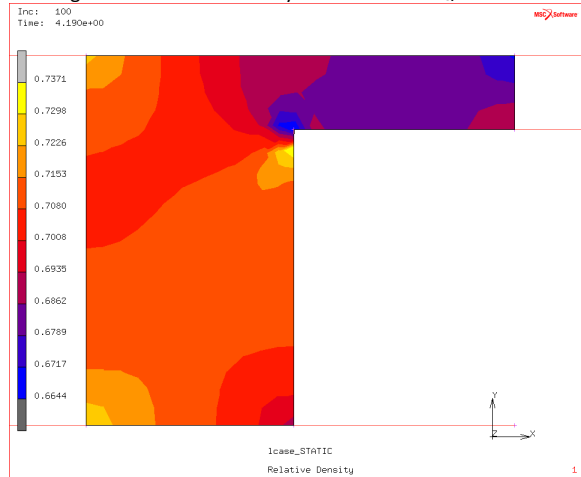


Figure 296. Relative density distribution for $v_3/v_1 = 0.48$

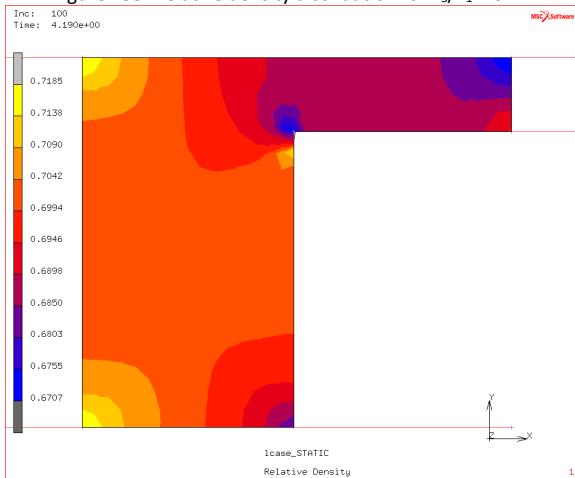


Figure 297. Relative density distribution for $v_3/v_1 = 0.49$

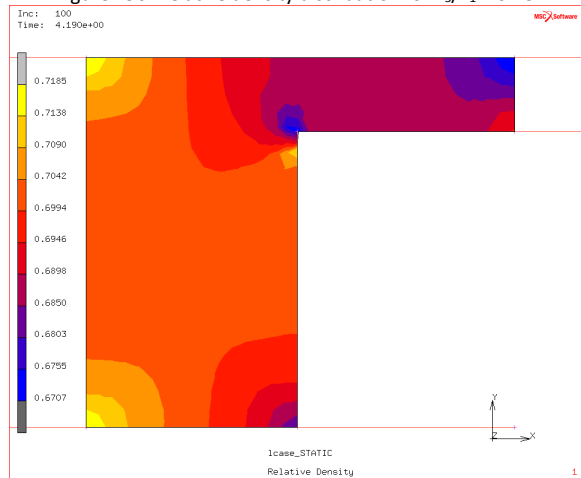


Figure 298. Relative density distribution for $v_3/v_1 = 0.50$

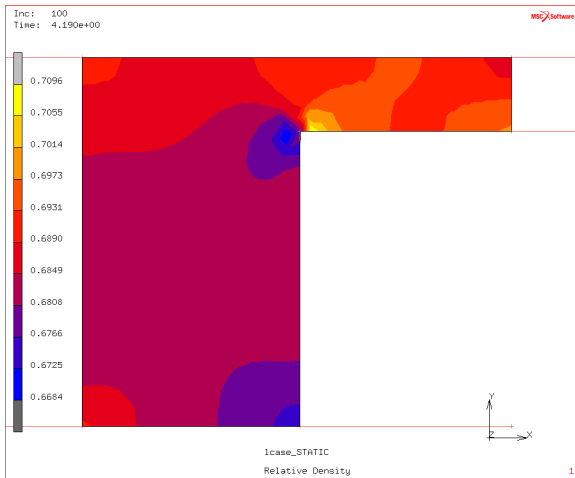


Figure 299. Relative density distribution for $v_3/v_1 = 0.51$

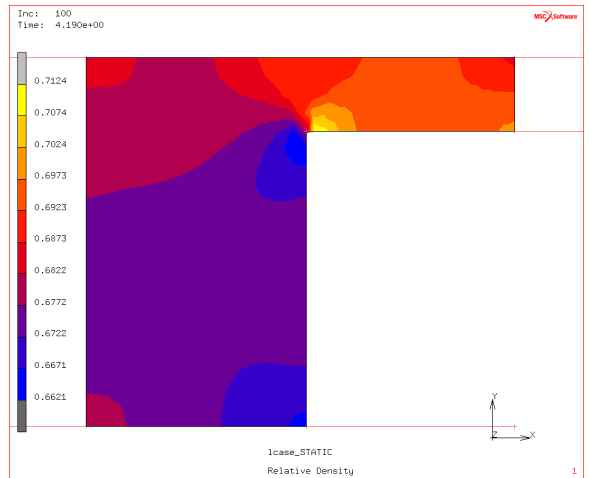


Figure 300. Relative density distribution for $v_3/v_1 = 0.52$

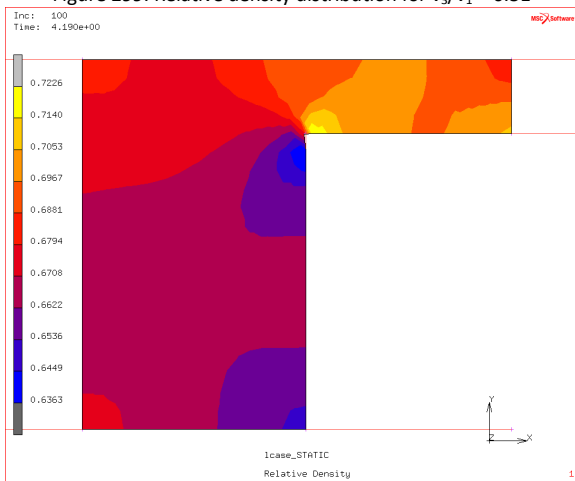


Figure 301. Relative density distribution for $v_3/v_1 = 0.53$

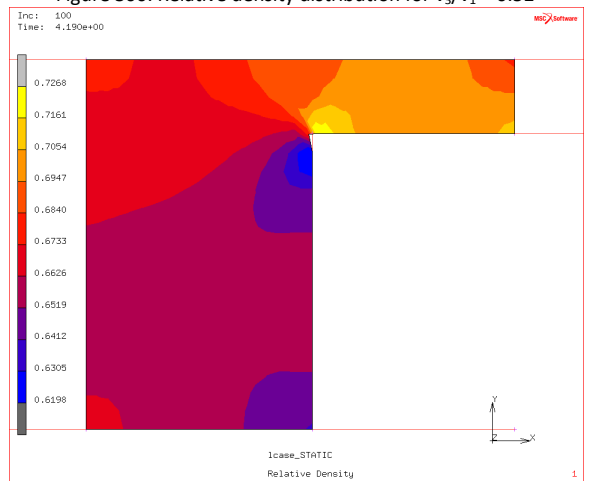


Figure 302. Relative density distribution for $v_3/v_1 = 0.54$

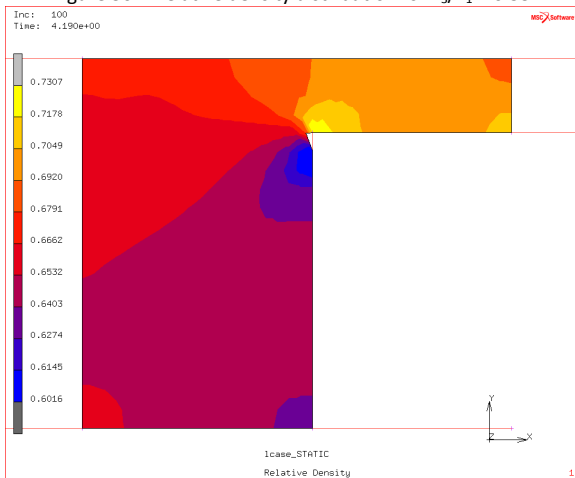


Figure 303. Relative density distribution for $v_3/v_1 = 0.55$

D.3.3 Using Constant Friction Coefficient of 0.20

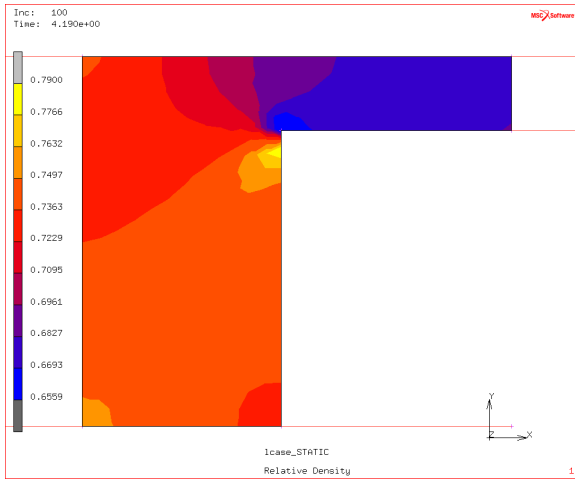


Figure 304. Relative density distribution for $v_3/v_1 = 0.45$

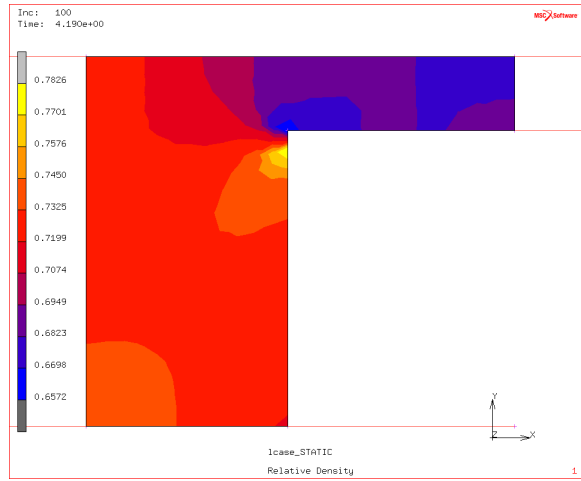


Figure 305. Relative density distribution for $v_3/v_1 = 0.46$

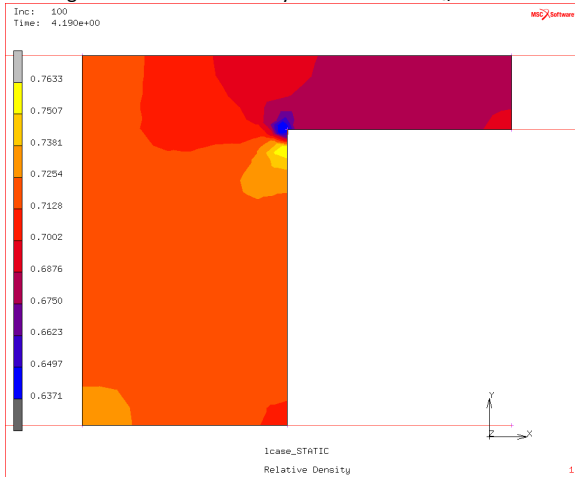


Figure 306. Relative density distribution for $v_3/v_1 = 0.47$

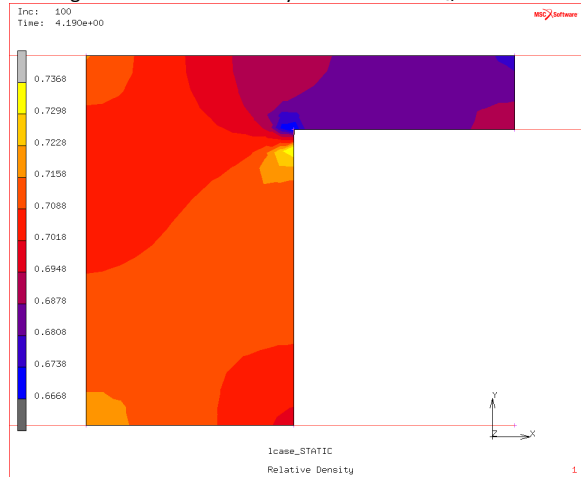


Figure 307. Relative density distribution for $v_3/v_1 = 0.48$

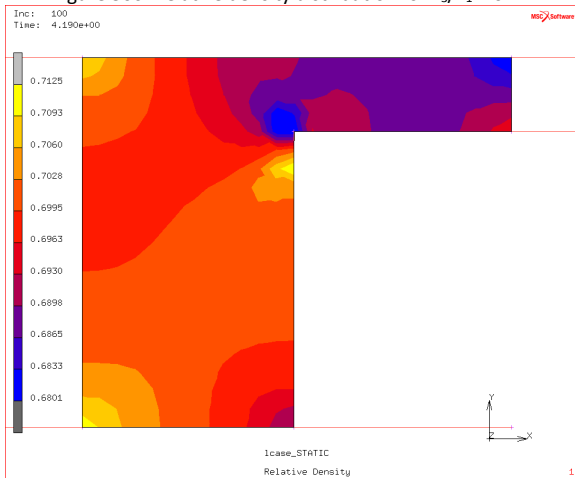


Figure 308. Relative density distribution for $v_3/v_1 = 0.49$

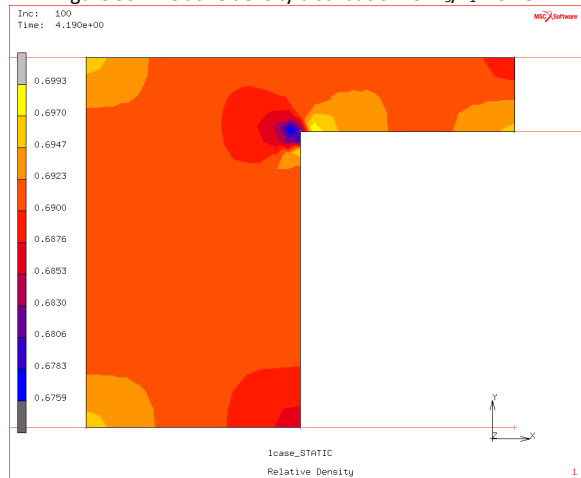


Figure 309. Relative density distribution for $v_3/v_1 = 0.50$

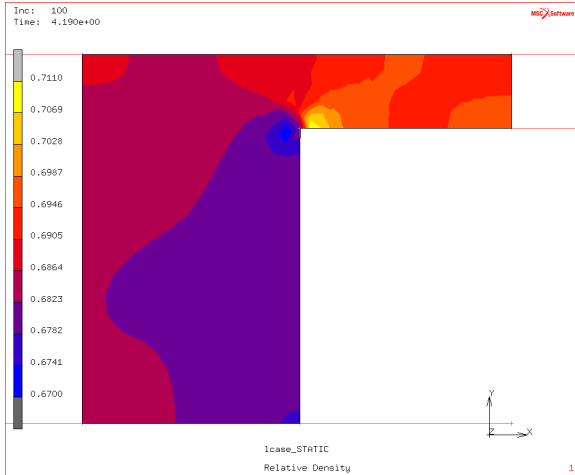


Figure 310. Relative density distribution for $v_3/v_1 = 0.51$

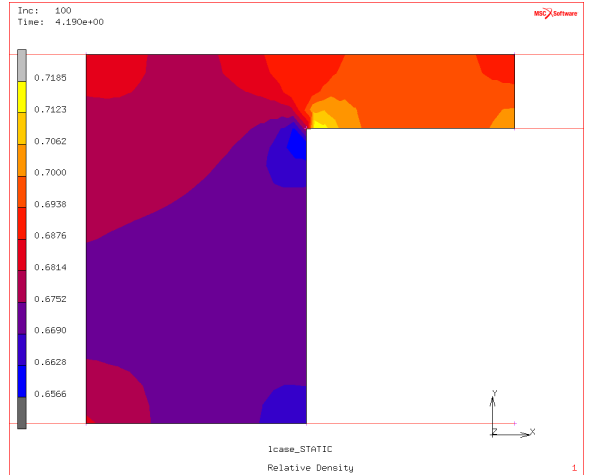


Figure 311. Relative density distribution for $v_3/v_1 = 0.52$

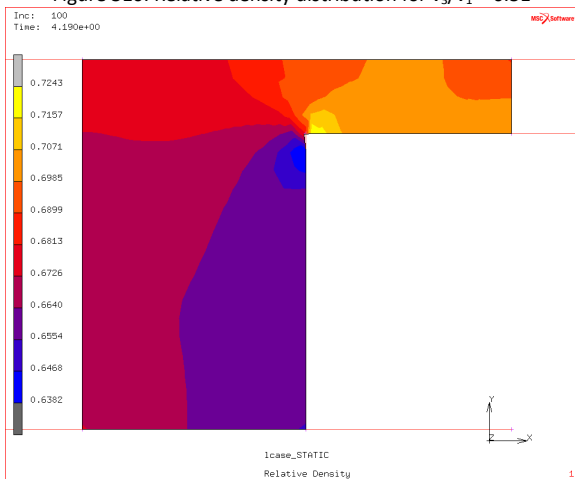


Figure 312. Relative density distribution for $v_3/v_1 = 0.53$

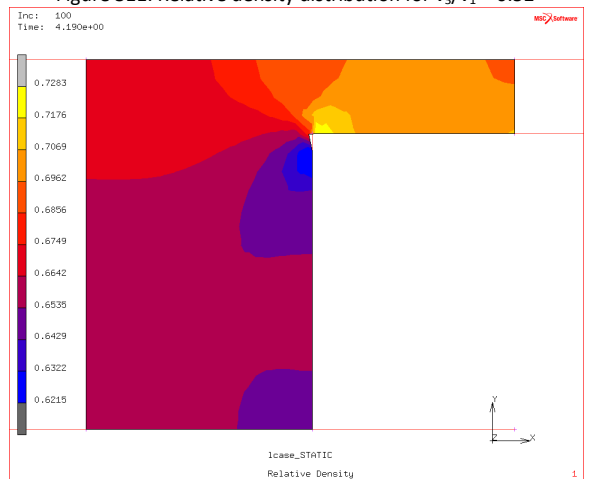


Figure 313. Relative density distribution for $v_3/v_1 = 0.54$

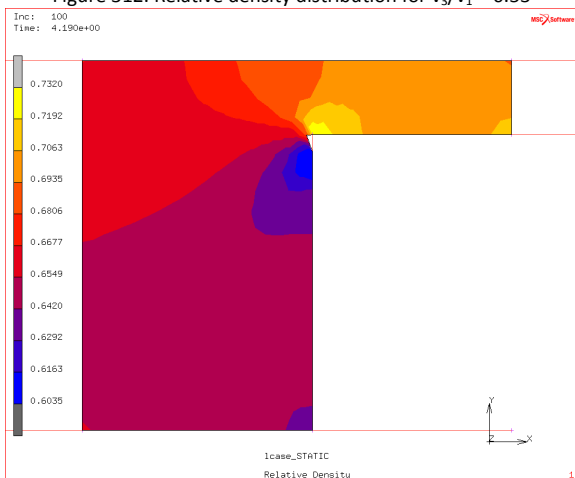


Figure 314. Relative density distribution for $v_3/v_1 = 0.55$

D.3.4 Using Variable Friction Coefficient, $\mu(\sigma_n, v_r)$

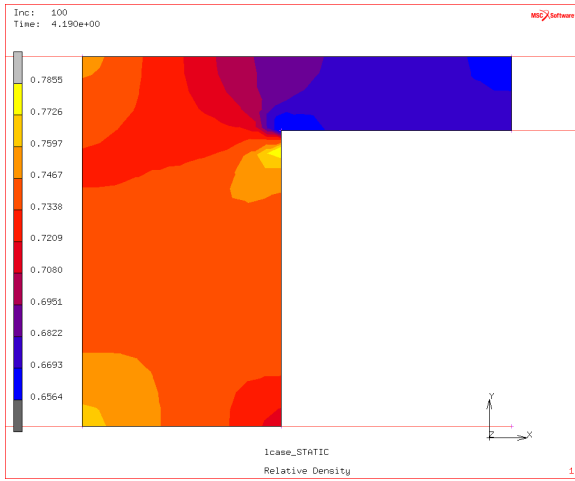


Figure 315. Relative density distribution for $v_3/v_1 = 0.45$

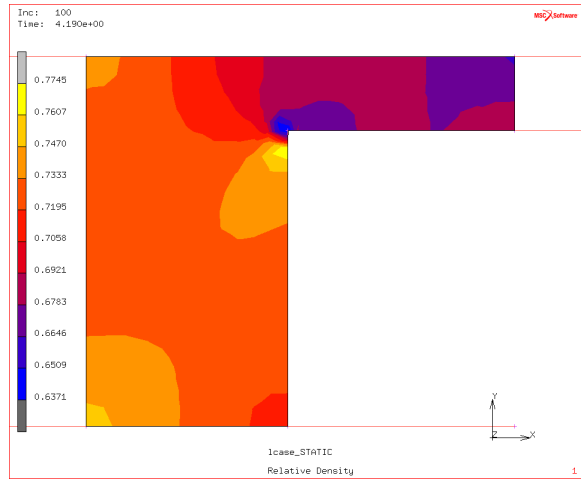


Figure 316. Relative density distribution for $v_3/v_1 = 0.46$

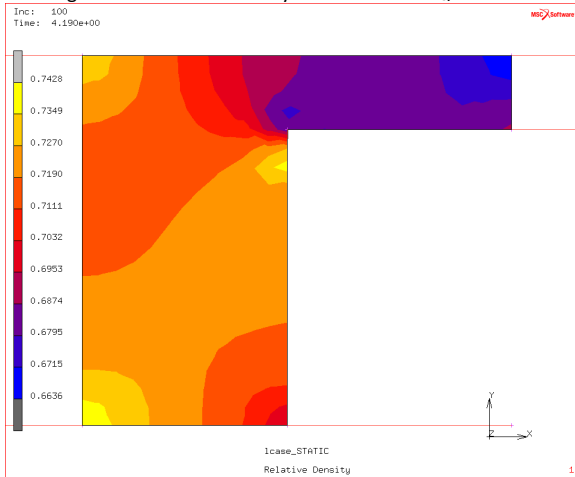


Figure 317. Relative density distribution for $v_3/v_1 = 0.47$

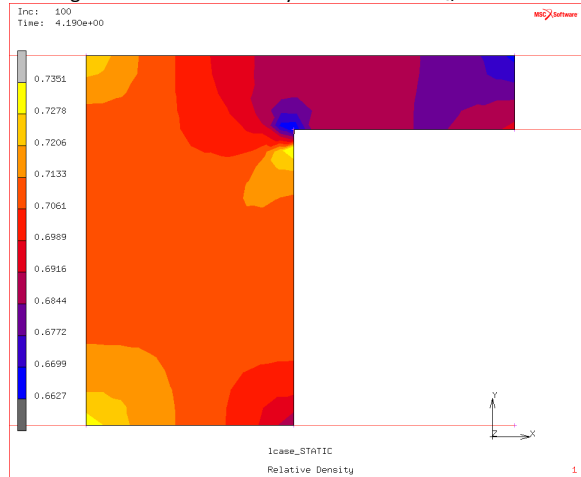


Figure 318. Relative density distribution for $v_3/v_1 = 0.48$

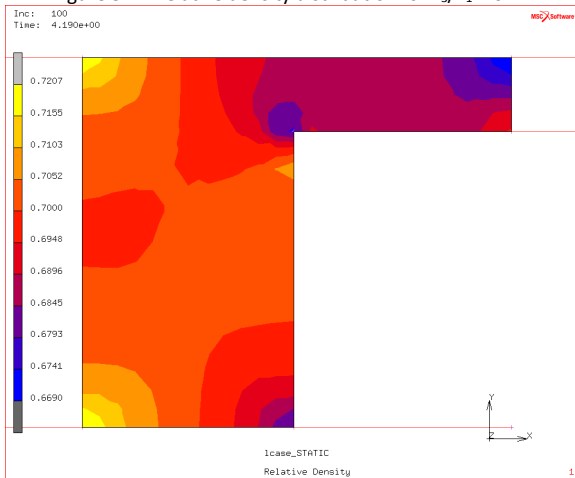


Figure 319. Relative density distribution for $v_3/v_1 = 0.49$

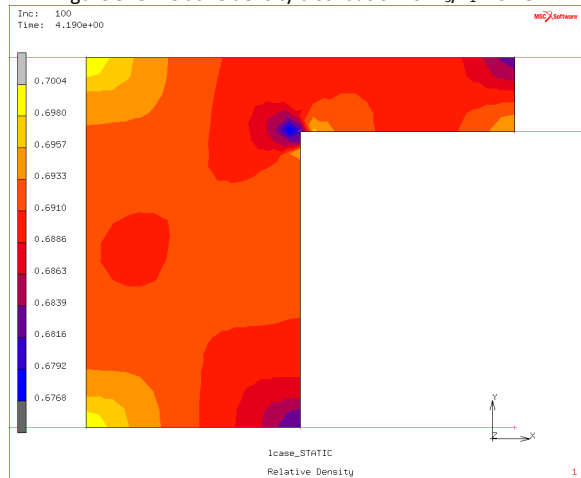


Figure 320. Relative density distribution for $v_3/v_1 = 0.50$

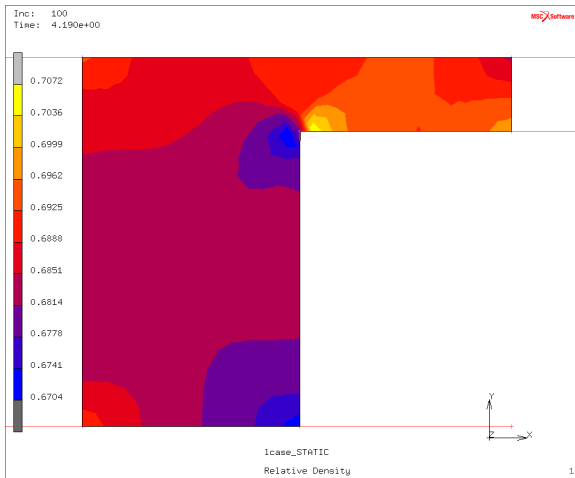


Figure 321. Relative density distribution for $v_3/v_1 = 0.51$

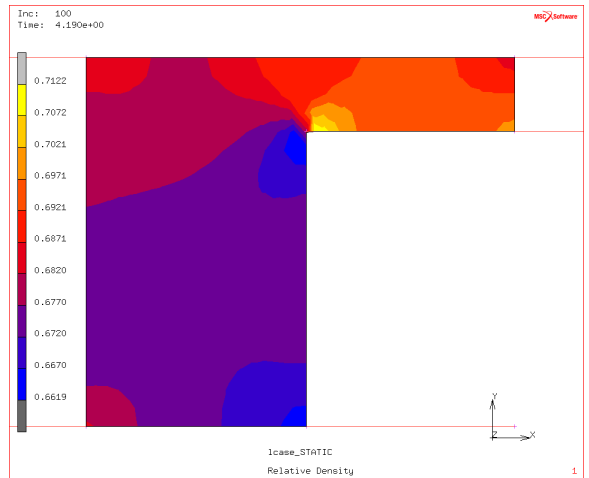


Figure 322. Relative density distribution for $v_3/v_1 = 0.52$

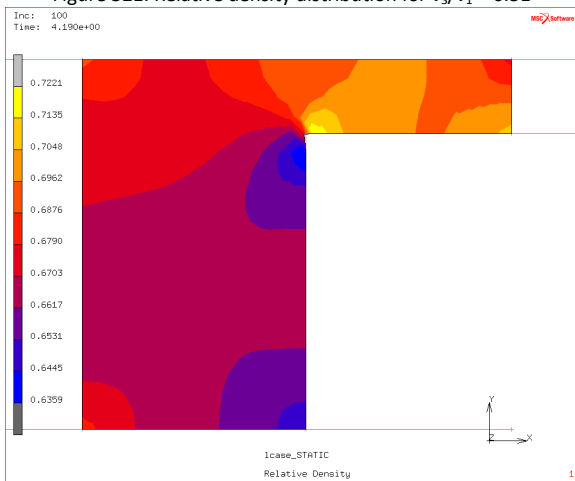


Figure 323. Relative density distribution for $v_3/v_1 = 0.53$

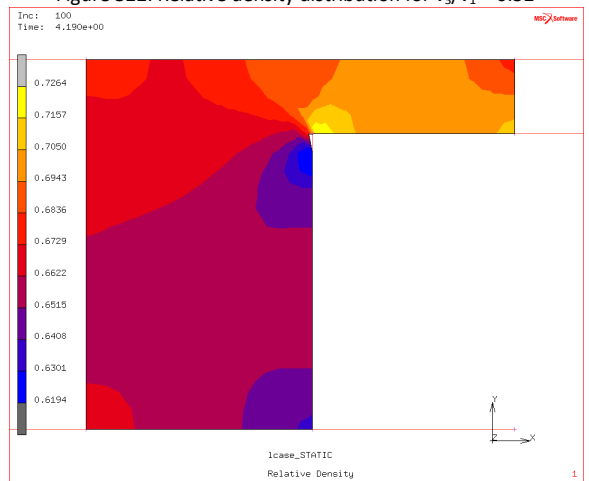


Figure 324. Relative density distribution for $v_3/v_1 = 0.54$

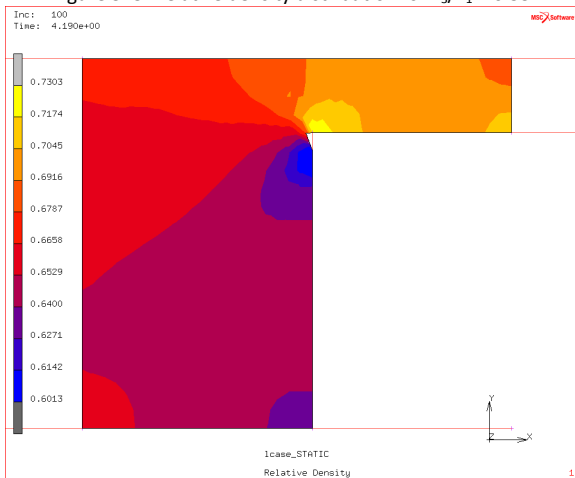


Figure 325. Relative density distribution for $v_3/v_1 = 0.55$

Appendix E. Effect of Die to Upper-Punch Velocity Ratio on Density Distribution of a Multi-stepped Part

E.1 Using Material Properties Provided by Shima [101, 102]

E.1.1 Using Constant Friction Coefficient of 0.08

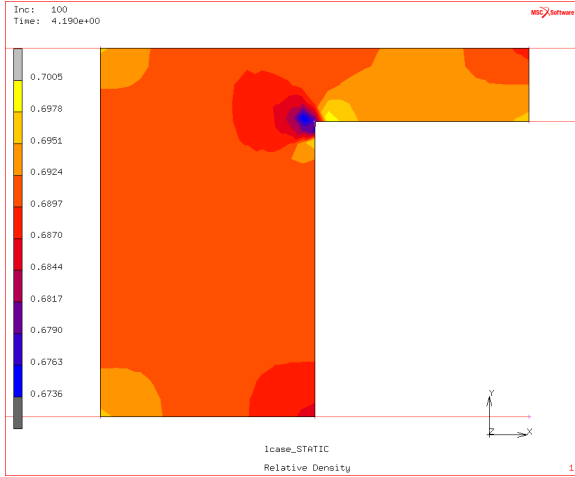


Figure 326. Relative density distribution for $v_4/v_1 = 0$

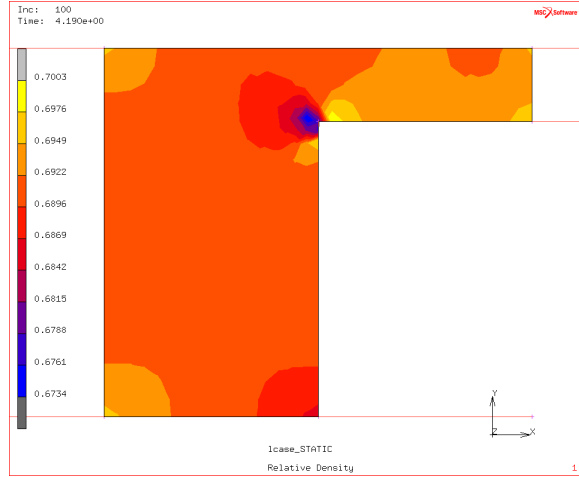


Figure 327. Relative density distribution for $v_4/v_1 = 0.1$

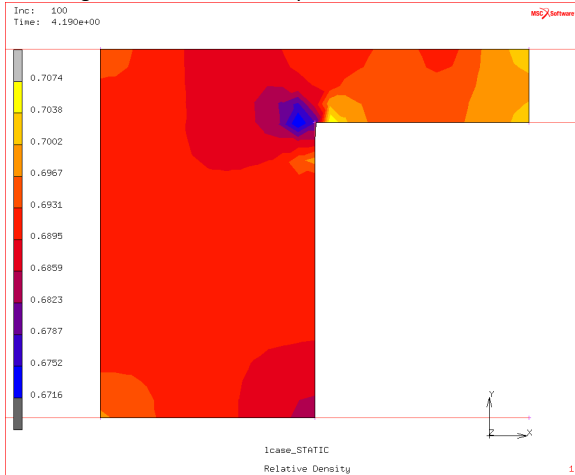


Figure 328. Relative density distribution for $v_4/v_1 = 0.2$

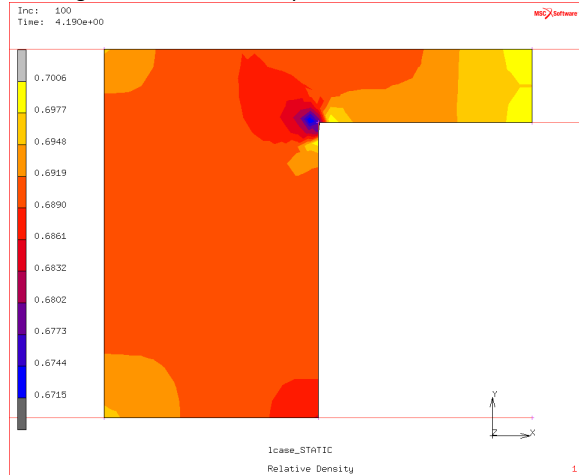


Figure 329. Relative density distribution for $v_4/v_1 = 0.3$

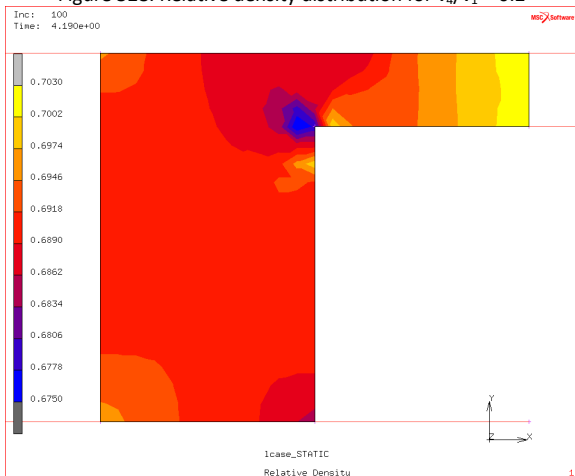


Figure 330. Relative density distribution for $v_4/v_1 = 0.4$

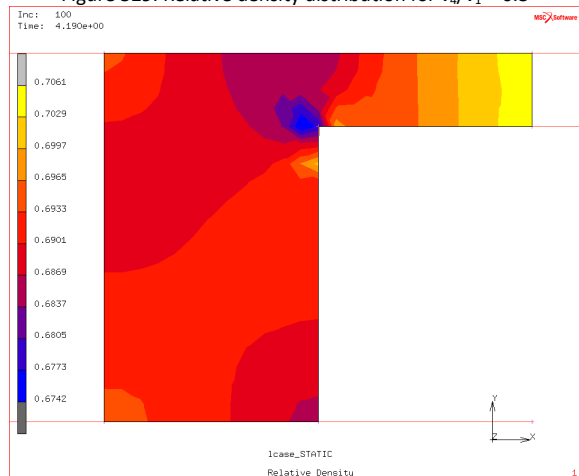


Figure 331. Relative density distribution for $v_4/v_1 = 0.5$

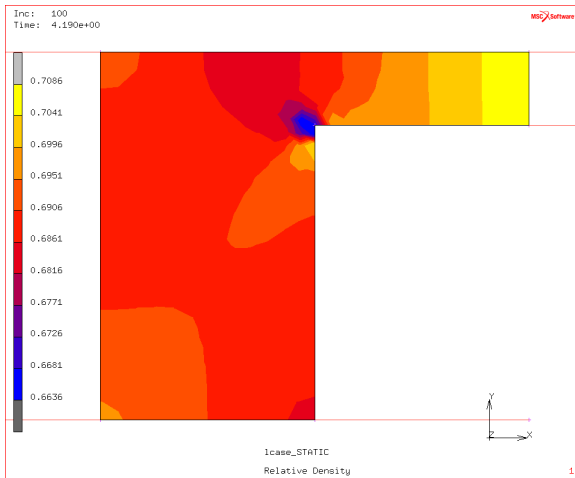


Figure 332. Relative density distribution for $v_4/v_1 = 0.6$

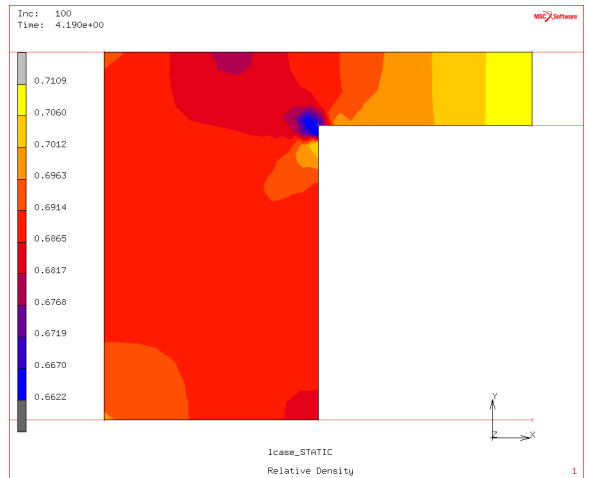


Figure 333. Relative density distribution for $v_4/v_1 = 0.7$

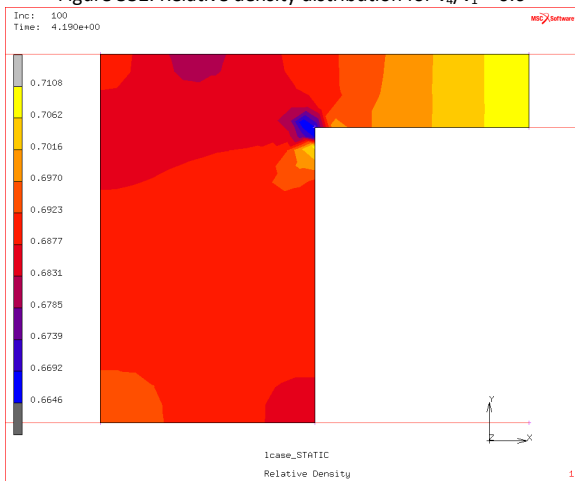


Figure 334. Relative density distribution for $v_4/v_1 = 0.8$

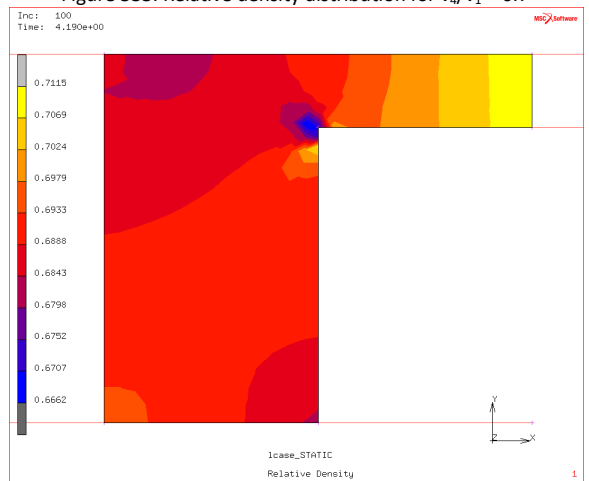


Figure 335. Relative density distribution for $v_4/v_1 = 0.9$

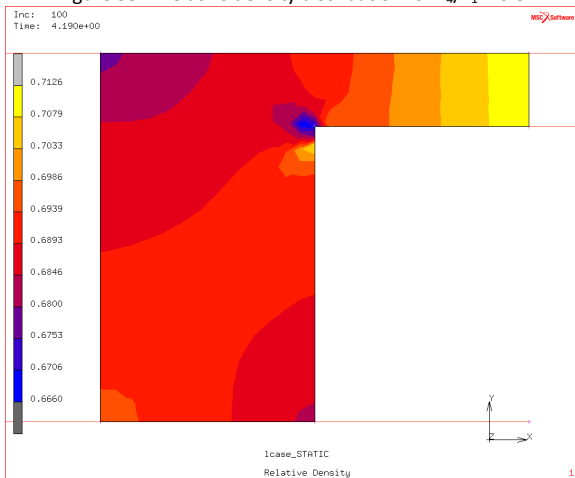


Figure 336. Relative density distribution for $v_4/v_1 = 1.0$

E.1.2 Using Constant Friction Coefficient of 0.12

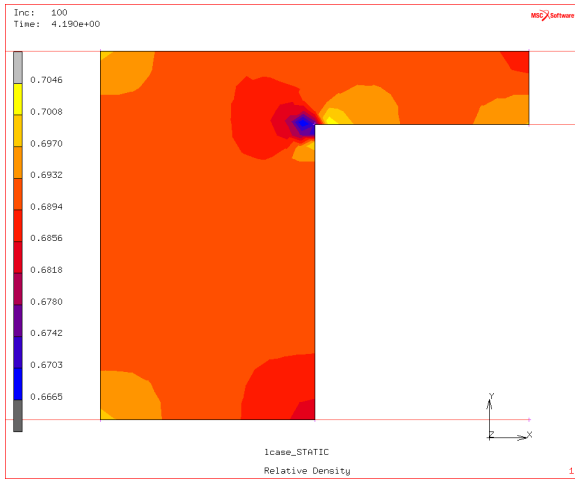


Figure 337. Relative density distribution for $v_4/v_1 = 0$

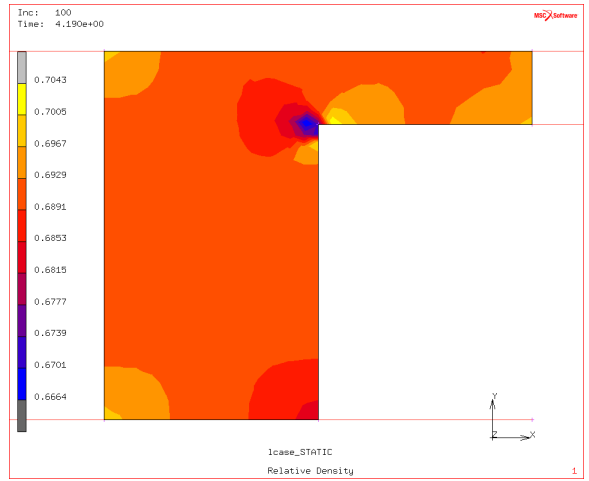


Figure 338. Relative density distribution for $v_4/v_1 = 0.1$

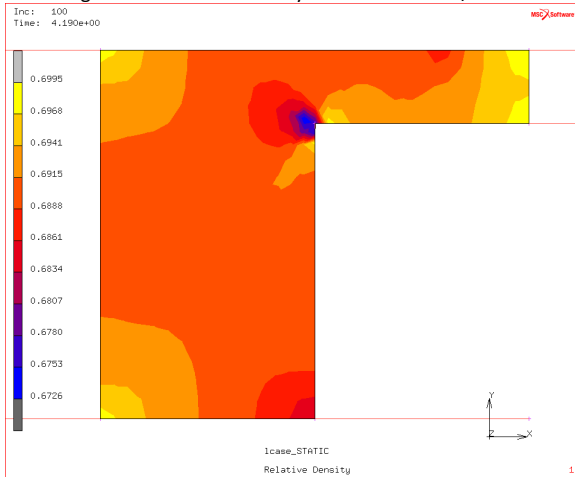


Figure 339. Relative density distribution for $v_4/v_1 = 0.2$

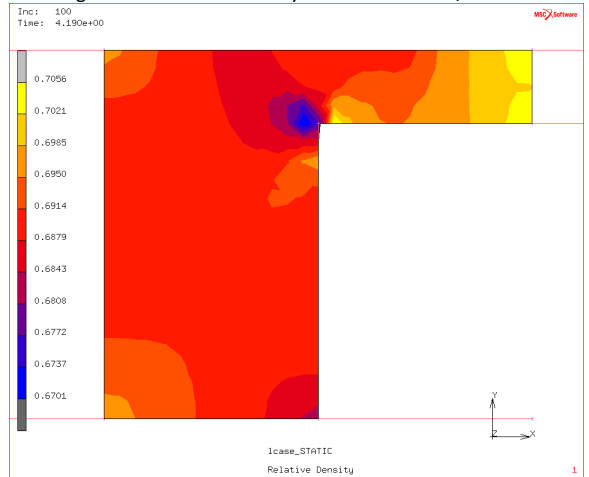


Figure 340. Relative density distribution for $v_4/v_1 = 0.3$

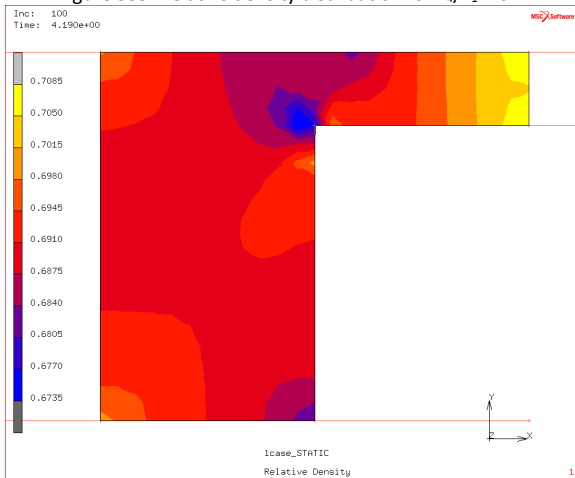


Figure 341. Relative density distribution for $v_4/v_1 = 0.4$

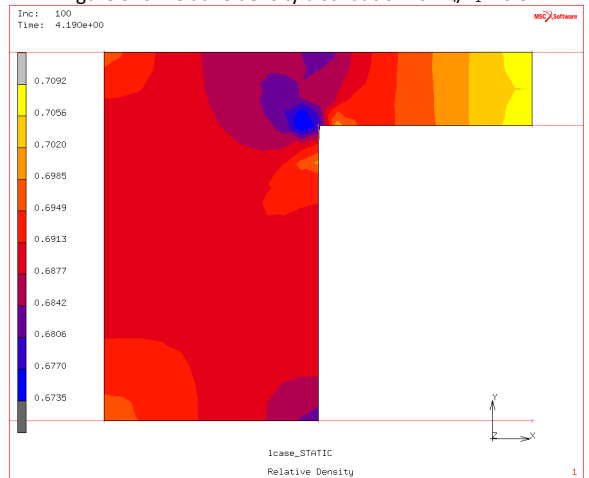


Figure 342. Relative density distribution for $v_4/v_1 = 0.5$

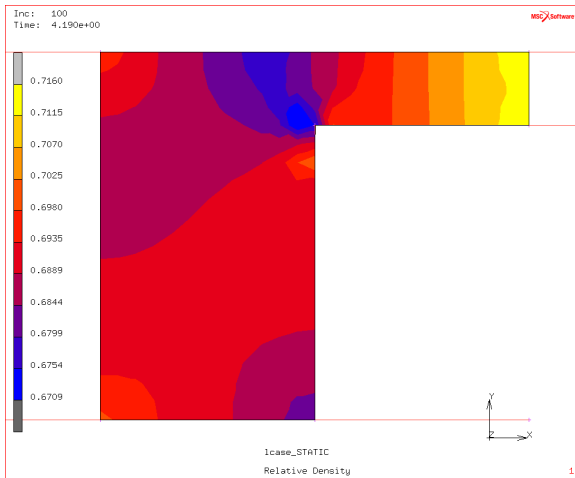


Figure 343. Relative density distribution for $v_4/v_1 = 0.6$

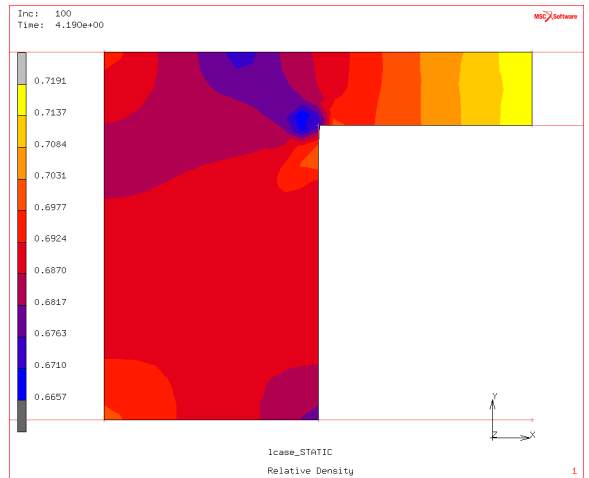


Figure 344. Relative density distribution for $v_4/v_1 = 0.7$

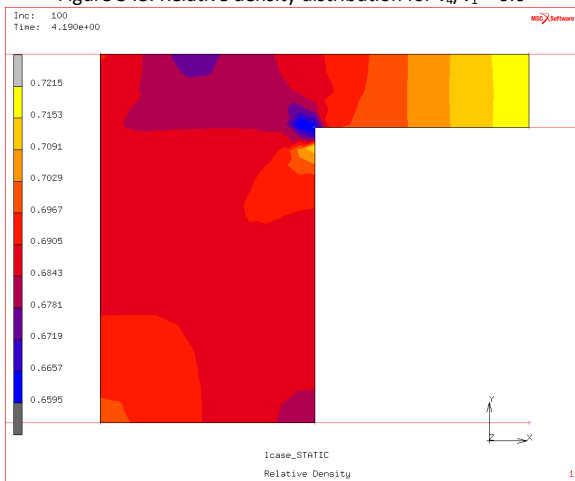


Figure 345. Relative density distribution for $v_4/v_1 = 0.8$

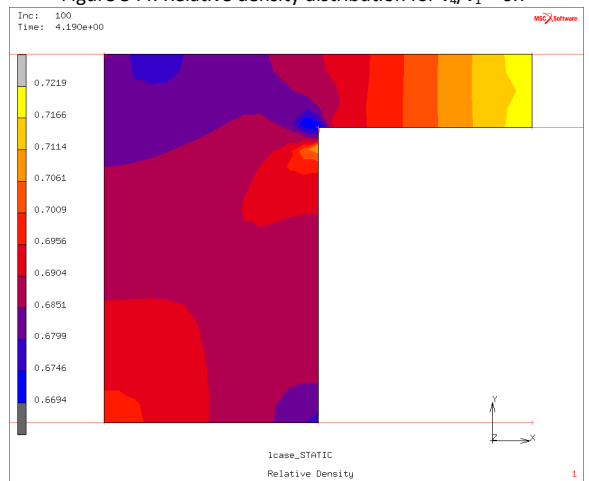


Figure 346. Relative density distribution for $v_4/v_1 = 0.9$

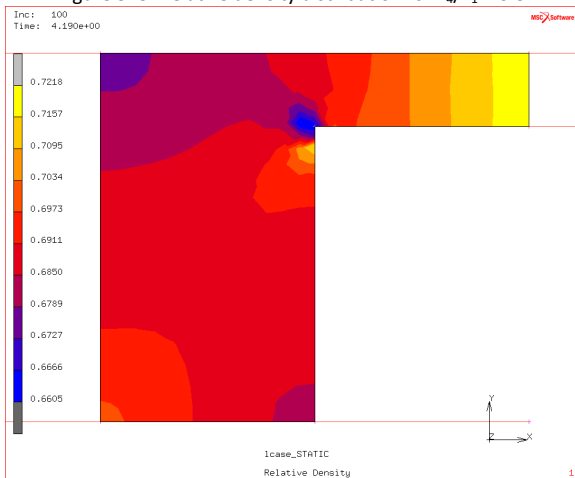


Figure 347. Relative density distribution for $v_4/v_1 = 1.0$

E.1.3 Using Constant Friction Coefficient of 0.20

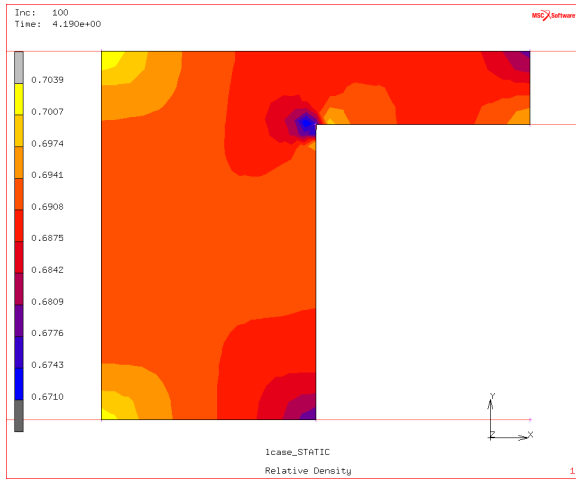


Figure 348. Relative density distribution for $v_4/v_1 = 0$

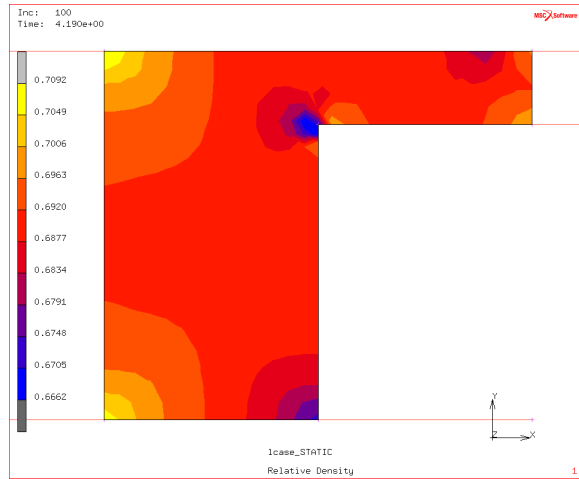


Figure 349. Relative density distribution for $v_4/v_1 = 0.1$

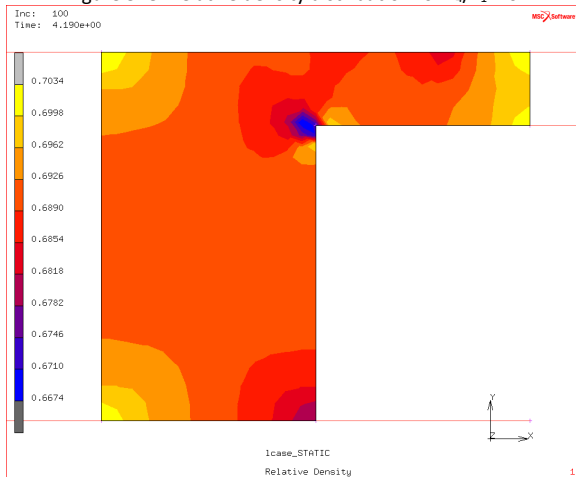


Figure 350. Relative density distribution for $v_4/v_1 = 0.2$

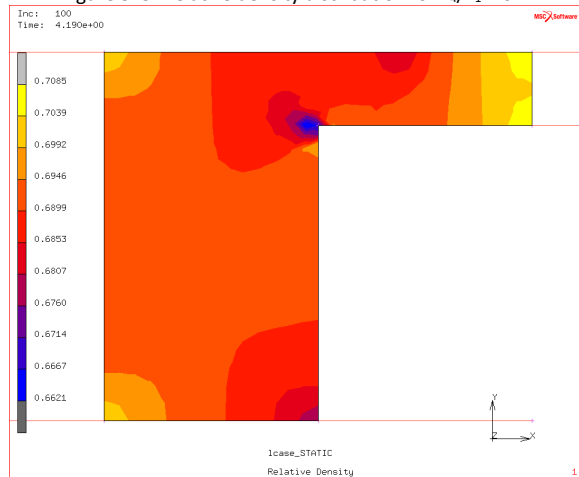


Figure 351. Relative density distribution for $v_4/v_1 = 0.3$

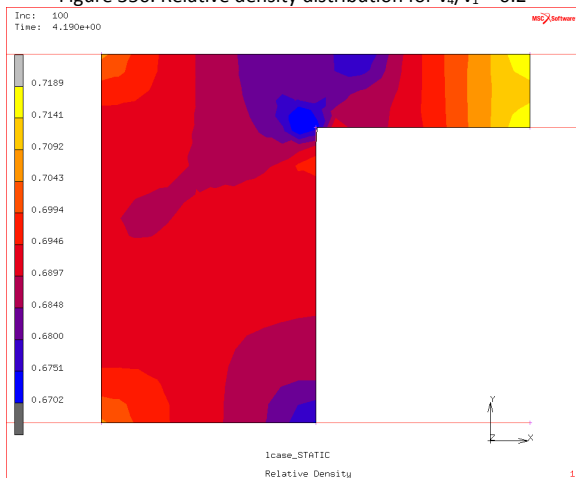


Figure 352. Relative density distribution for $v_4/v_1 = 0.4$

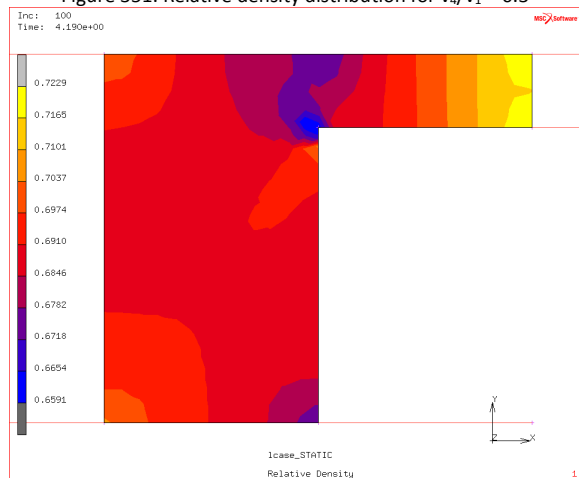


Figure 353. Relative density distribution for $v_4/v_1 = 0.5$

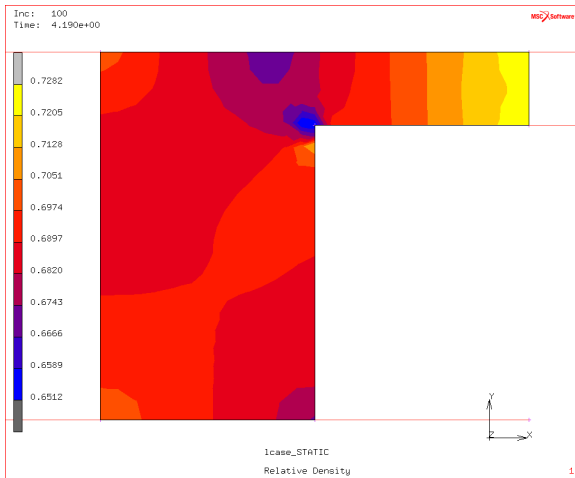


Figure 354. Relative density distribution for $v_4/v_1 = 0.6$

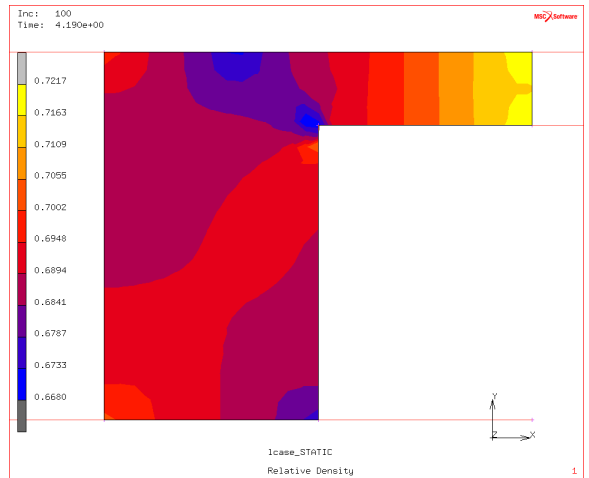


Figure 355. Relative density distribution for $v_4/v_1 = 0.7$

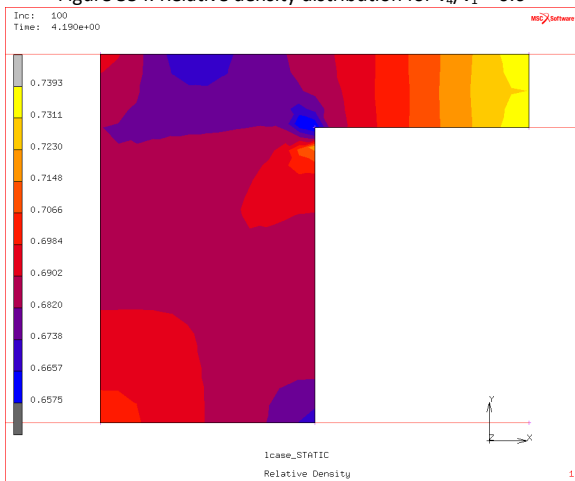


Figure 356. Relative density distribution for $v_4/v_1 = 0.8$

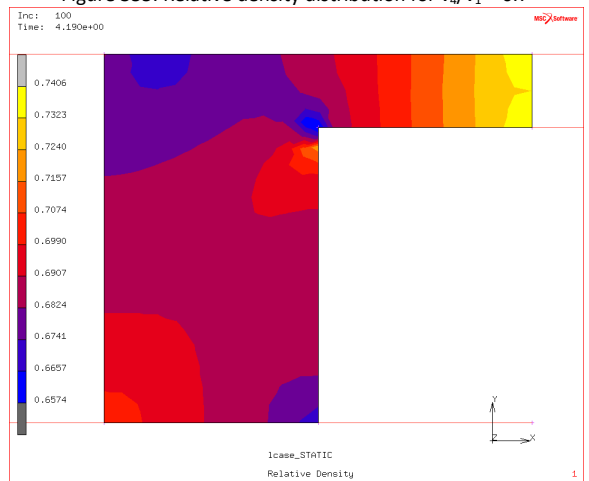


Figure 357. Relative density distribution for $v_4/v_1 = 0.9$

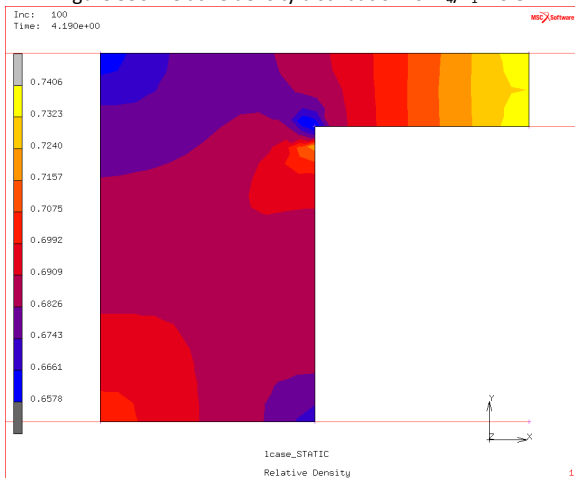


Figure 358. Relative density distribution for $v_4/v_1 = 1.0$

E.1.4 Using Variable Friction Coefficient, $\mu(\sigma_n, v_r)$

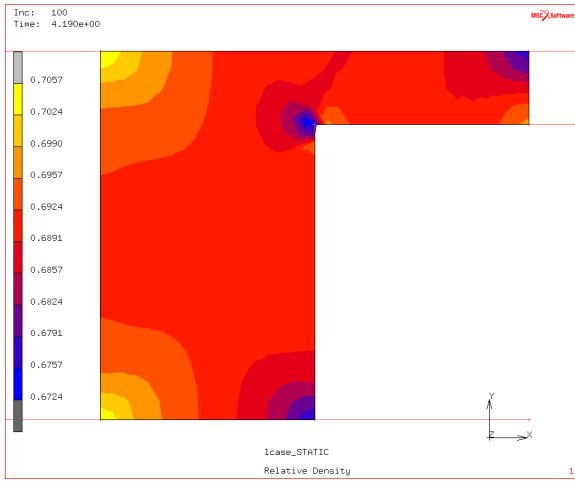


Figure 359. Relative density distribution for $v_4/v_1 = 0$

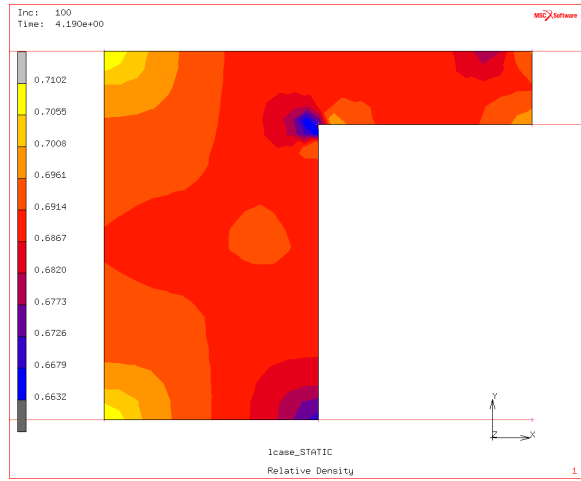


Figure 360. Relative density distribution for $v_4/v_1 = 0.1$

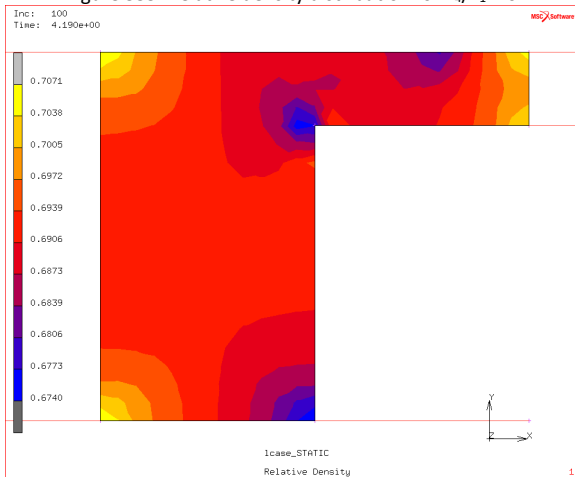


Figure 361. Relative density distribution for $v_4/v_1 = 0.2$

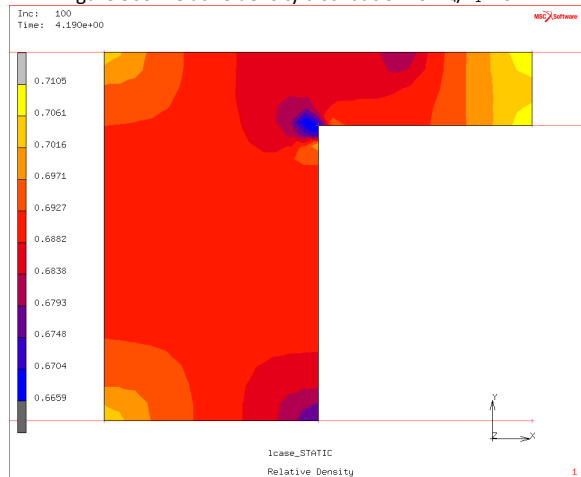


Figure 362. Relative density distribution for $v_4/v_1 = 0.3$

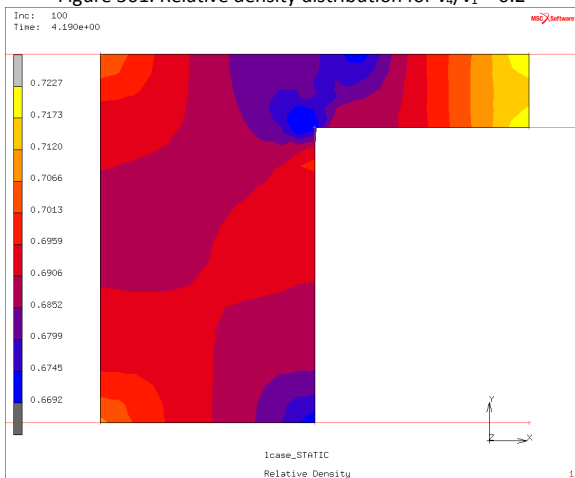


Figure 363. Relative density distribution for $v_4/v_1 = 0.4$

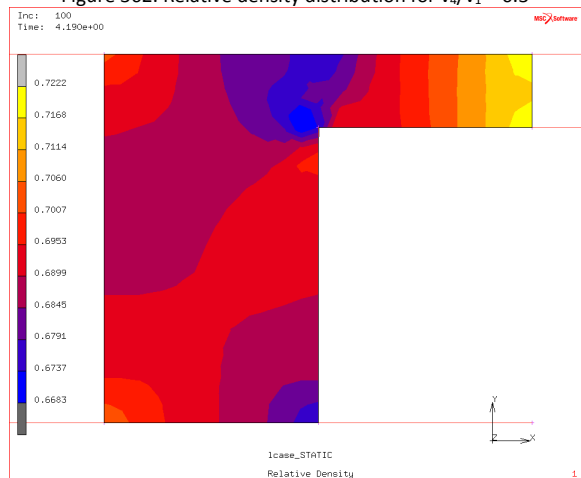


Figure 364. Relative density distribution for $v_4/v_1 = 0.5$

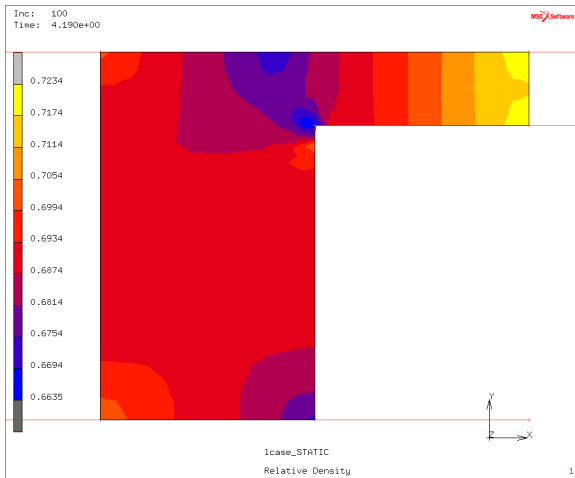


Figure 365. Relative density distribution for $v_4/v_1 = 0.6$

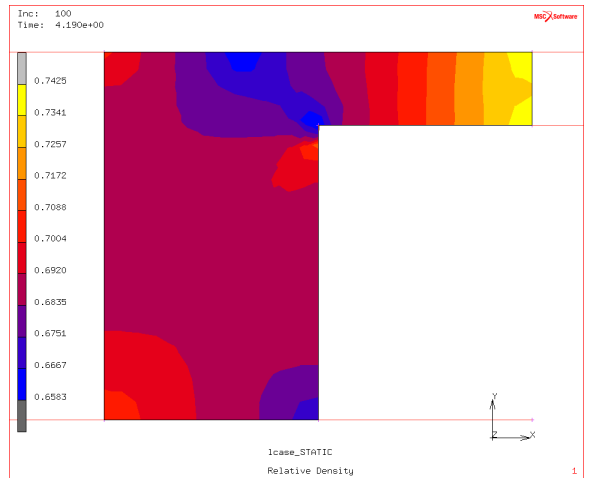


Figure 366. Relative density distribution for $v_4/v_1 = 0.7$

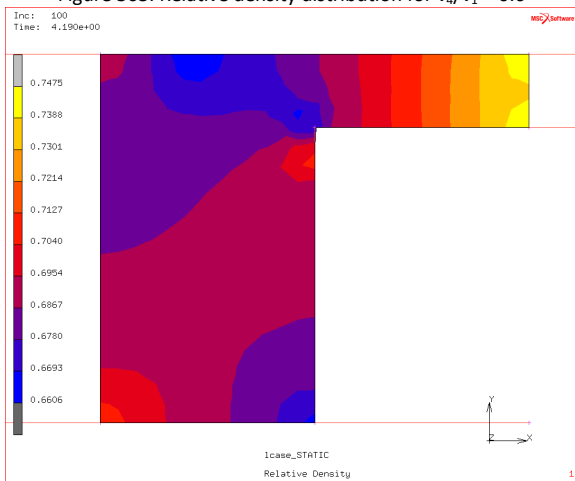


Figure 367. Relative density distribution for $v_4/v_1 = 0.8$

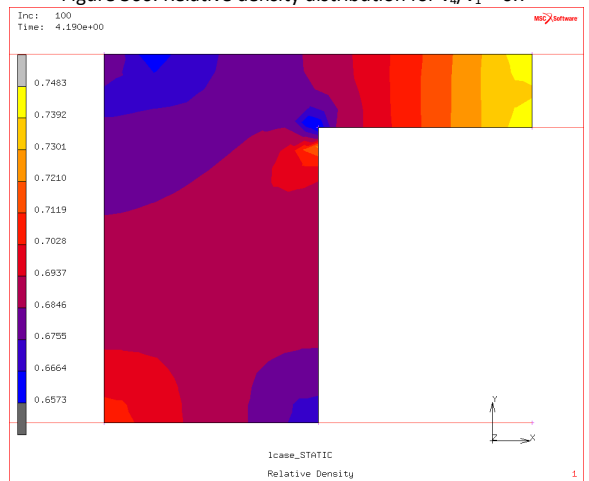


Figure 368. Relative density distribution for $v_4/v_1 = 0.9$

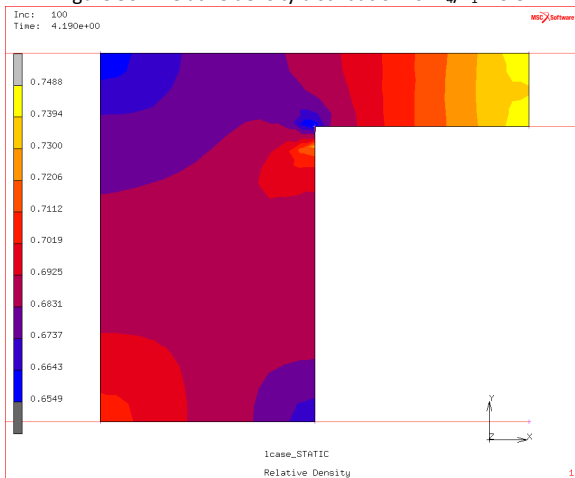


Figure 369. Relative density distribution for $v_4/v_1 = 1.0$

E.2 Using Material Properties Provided by Pavier and Doremus [10, 84]

E.2.1 Using Constant Friction Coefficient of 0.08

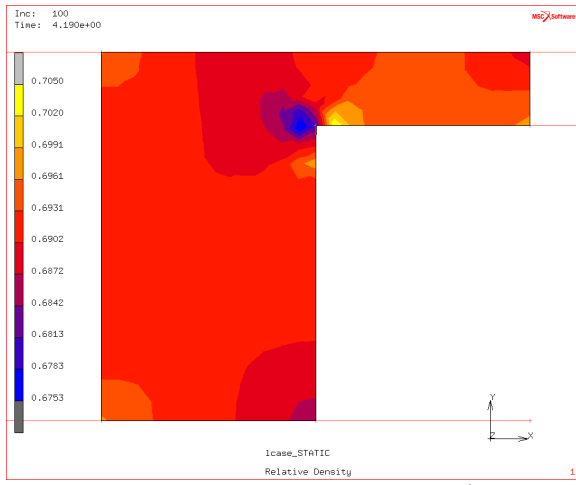


Figure 370. Relative density distribution for $v_4/v_1 = 0$

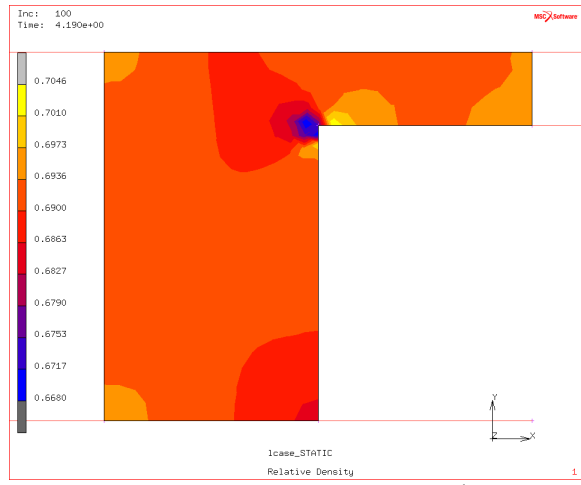


Figure 371. Relative density distribution for $v_4/v_1 = 0.1$

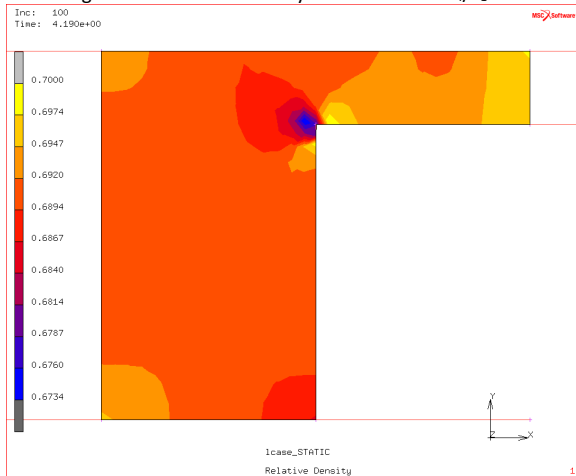


Figure 372. Relative density distribution for $v_4/v_1 = 0.2$

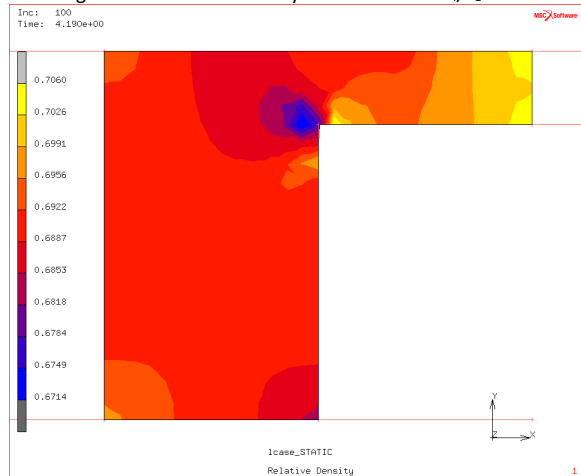


Figure 373. Relative density distribution for $v_4/v_1 = 0.3$

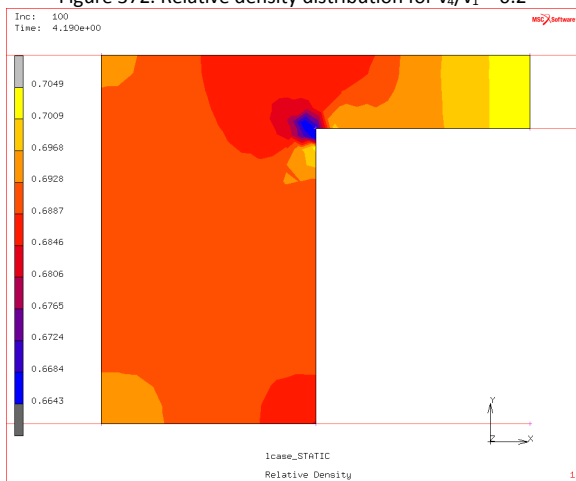


Figure 374. Relative density distribution for $v_4/v_1 = 0.4$

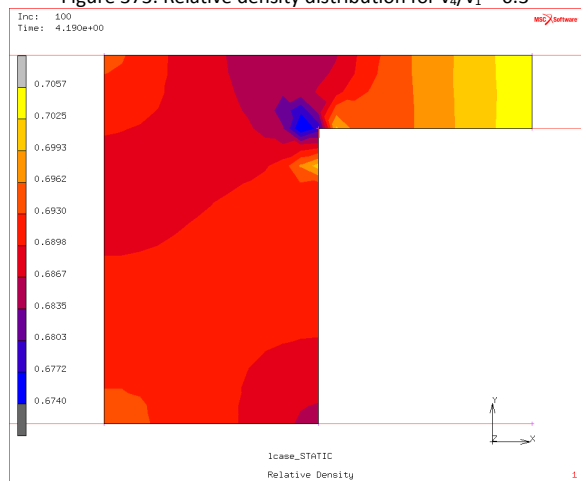


Figure 375. Relative density distribution for $v_4/v_1 = 0.5$

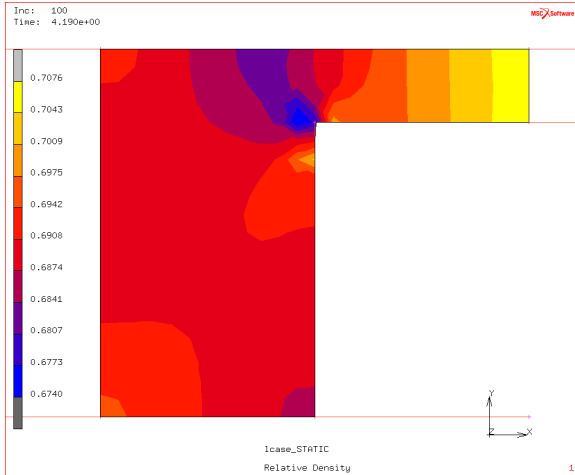


Figure 376. Relative density distribution for $v_4/v_1 = 0.6$

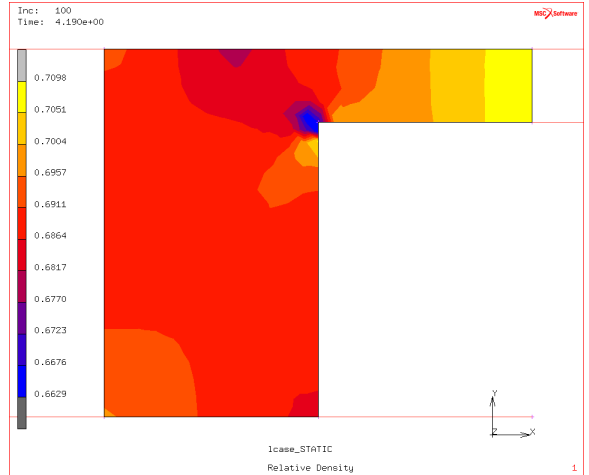


Figure 377. Relative density distribution for $v_4/v_1 = 0.7$

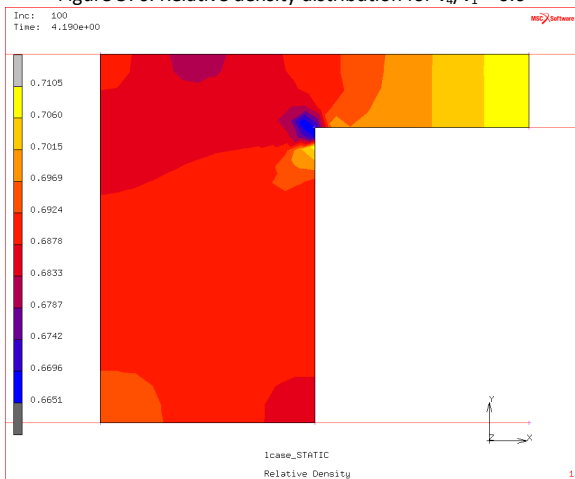


Figure 378. Relative density distribution for $v_4/v_1 = 0.8$

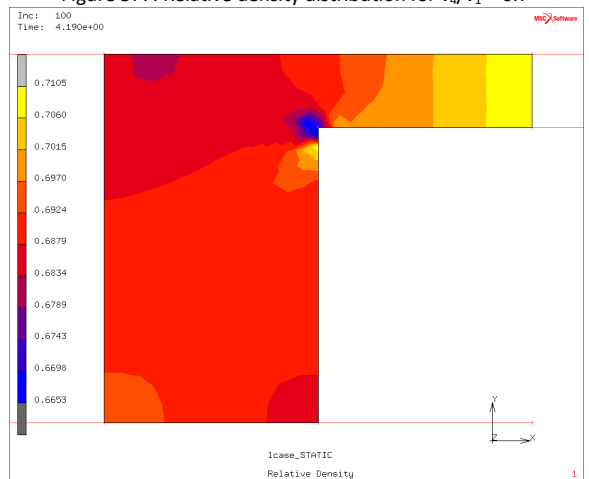


Figure 379. Relative density distribution for $v_4/v_1 = 0.9$

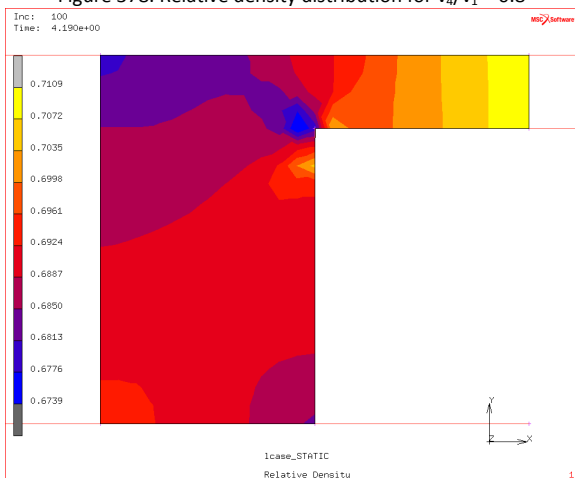


Figure 380. Relative density distribution for $v_4/v_1 = 1.0$

E.2.2 Using Constant Friction Coefficient of 0.12

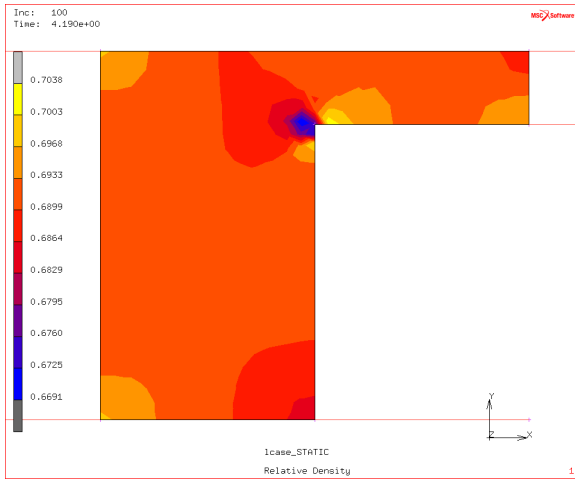


Figure 381. Relative density distribution for $v_4/v_1 = 0$

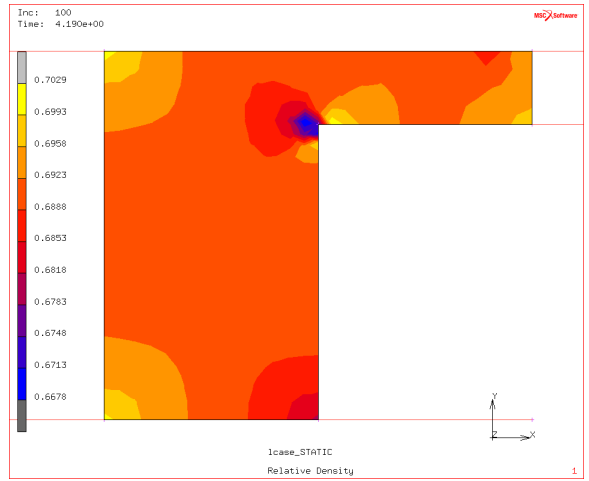


Figure 382. Relative density distribution for $v_4/v_1 = 0.1$

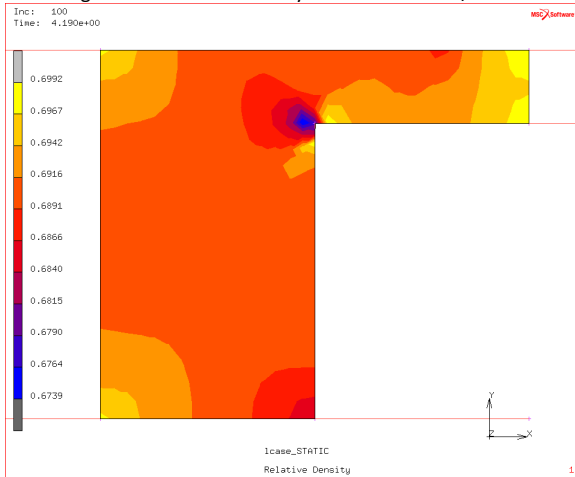


Figure 383. Relative density distribution for $v_4/v_1 = 0.2$

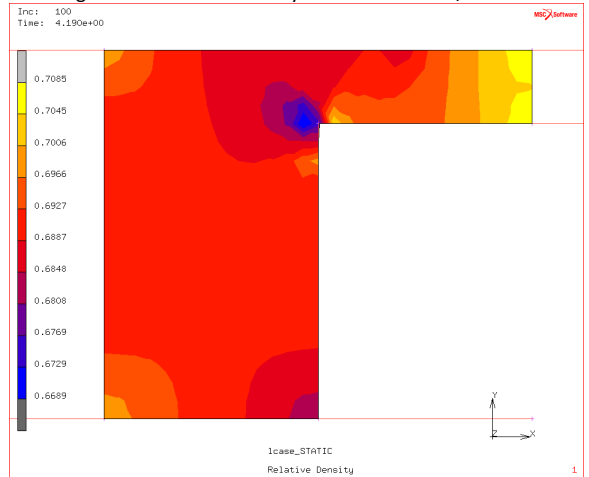


Figure 384. Relative density distribution for $v_4/v_1 = 0.3$

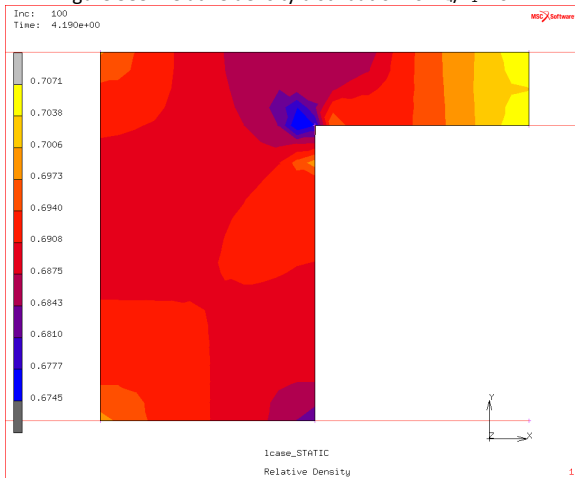


Figure 385. Relative density distribution for $v_4/v_1 = 0.4$

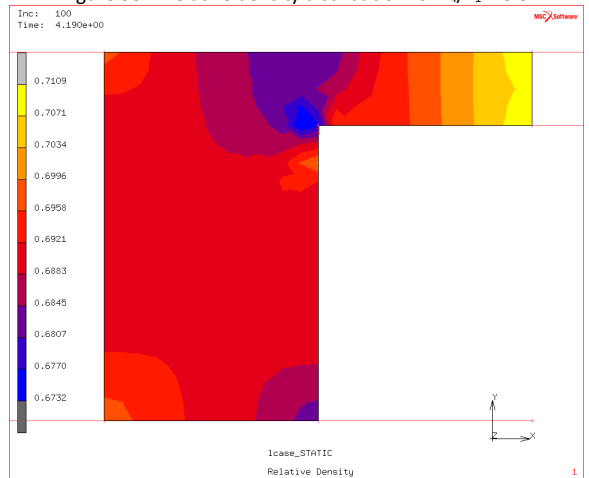


Figure 386. Relative density distribution for $v_4/v_1 = 0.5$

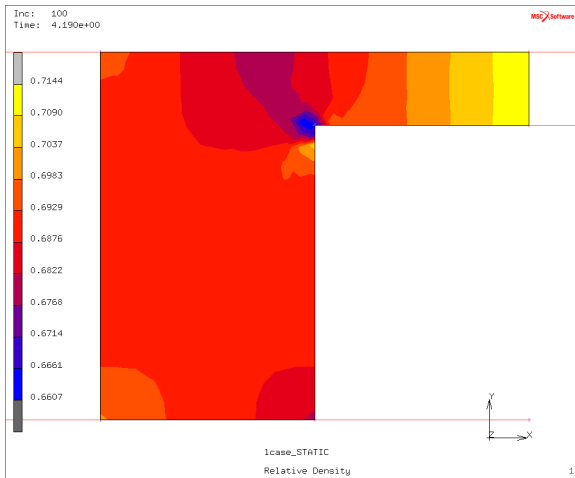


Figure 387. Relative density distribution for $v_4/v_1 = 0.6$

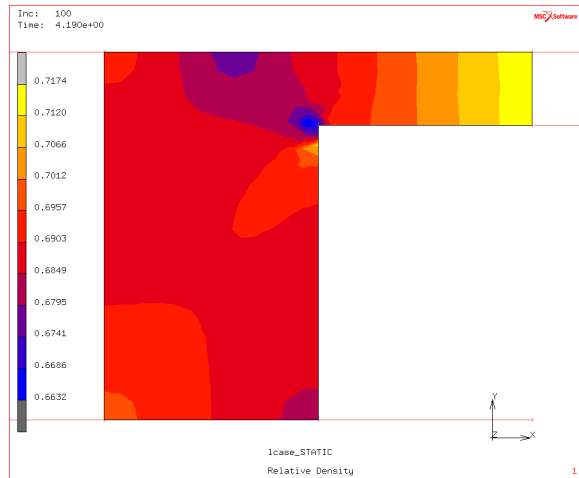


Figure 388. Relative density distribution for $v_4/v_1 = 0.7$

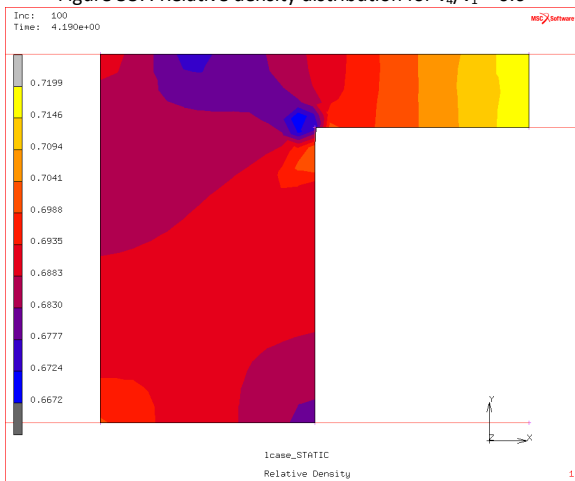


Figure 389. Relative density distribution for $v_4/v_1 = 0.8$

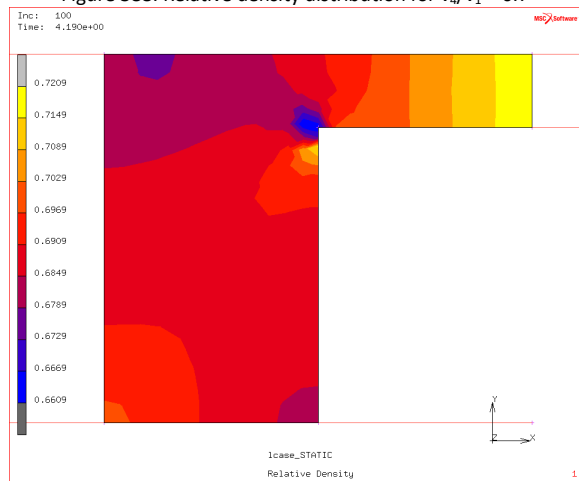


Figure 390. Relative density distribution for $v_4/v_1 = 0.9$

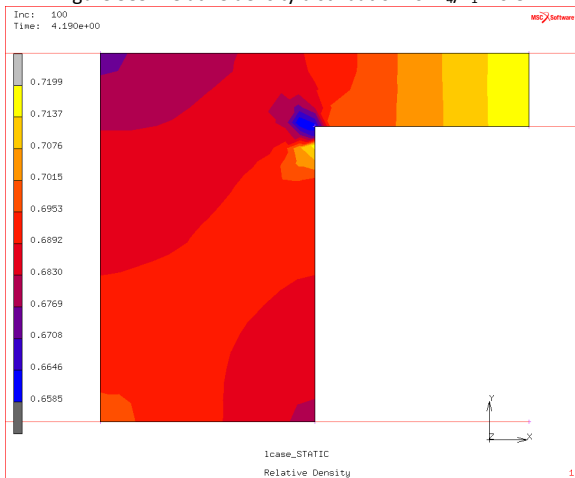


Figure 391. Relative density distribution for $v_4/v_1 = 1.0$

E.2.3 Using Constant Friction Coefficient of 0.20

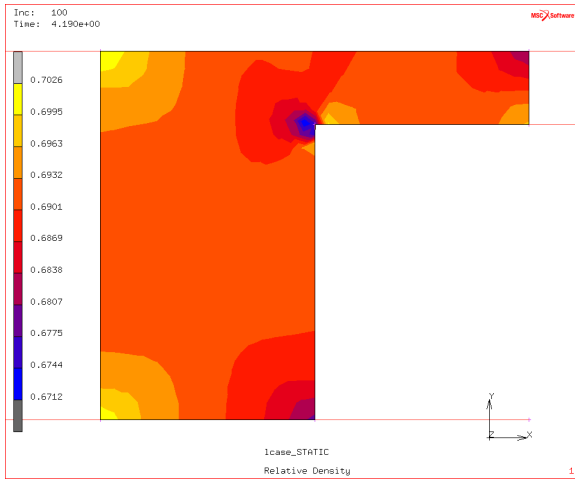


Figure 392. Relative density distribution for $v_4/v_1 = 0$

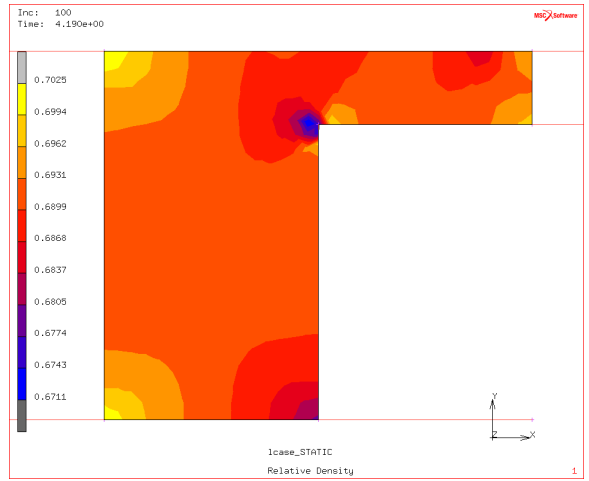


Figure 393. Relative density distribution for $v_4/v_1 = 0.1$

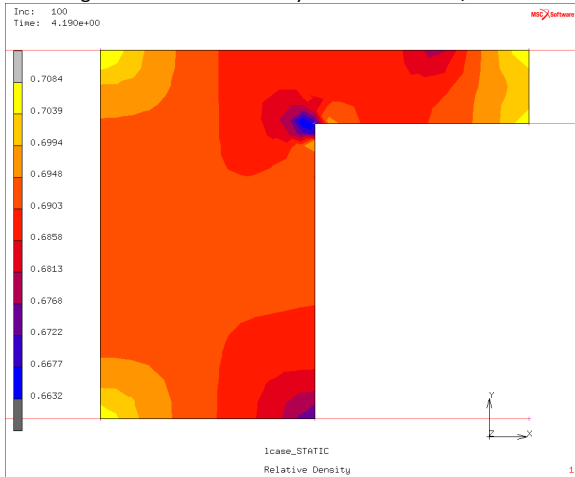


Figure 394. Relative density distribution for $v_4/v_1 = 0.2$

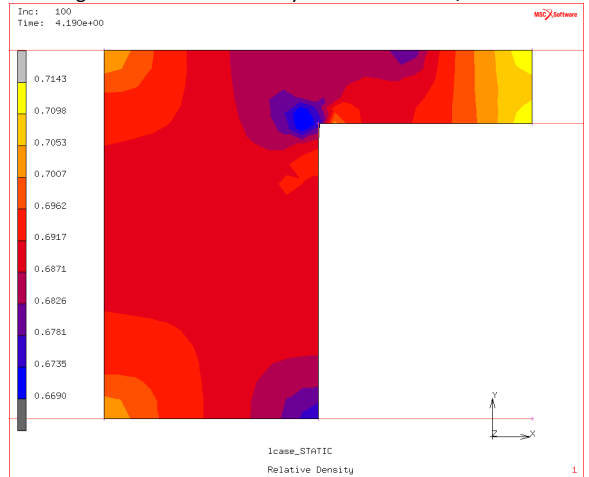


Figure 395. Relative density distribution for $v_4/v_1 = 0.3$

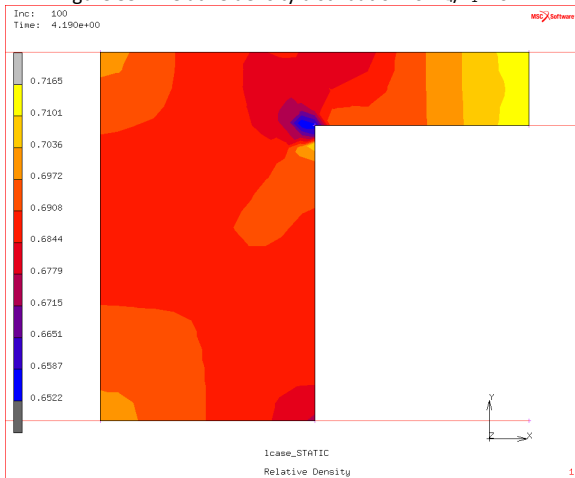


Figure 396. Relative density distribution for $v_4/v_1 = 0.4$

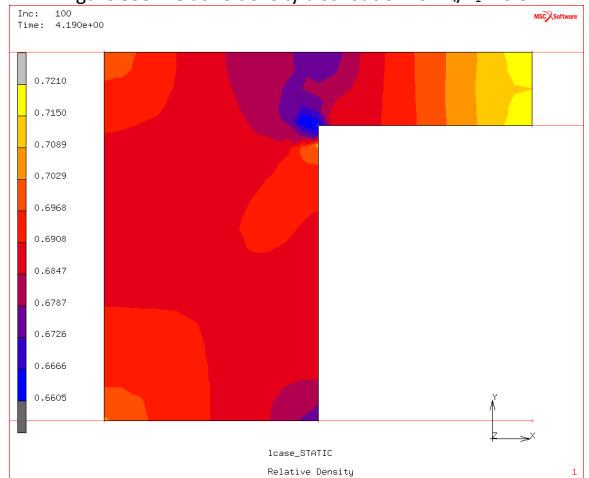


Figure 397. Relative density distribution for $v_4/v_1 = 0.5$

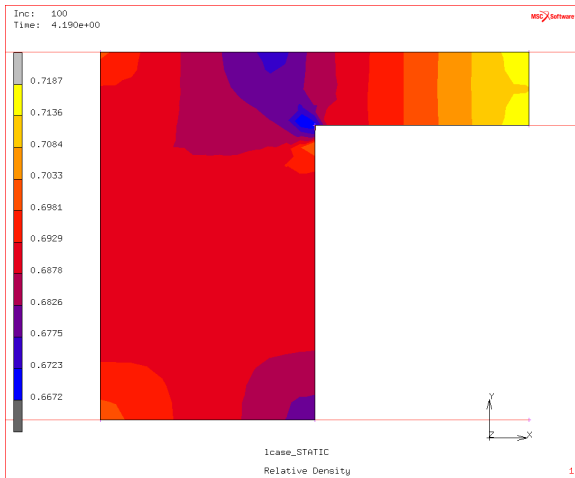


Figure 398. Relative density distribution for $v_4/v_1 = 0.6$

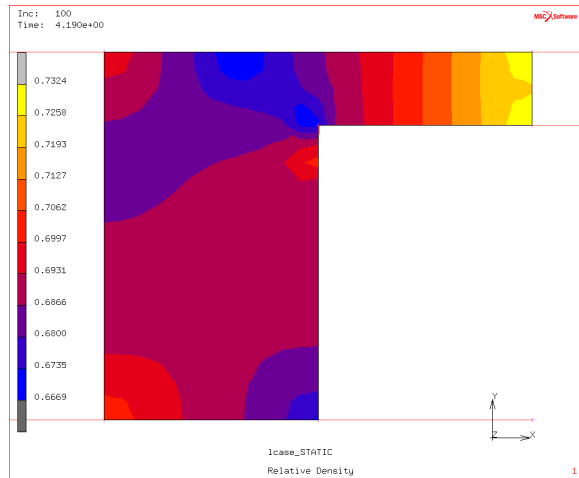


Figure 399. Relative density distribution for $v_4/v_1 = 0.7$

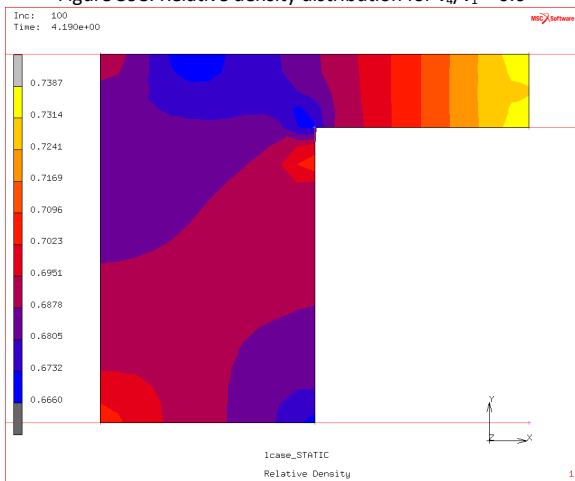


Figure 400. Relative density distribution for $v_4/v_1 = 0.8$

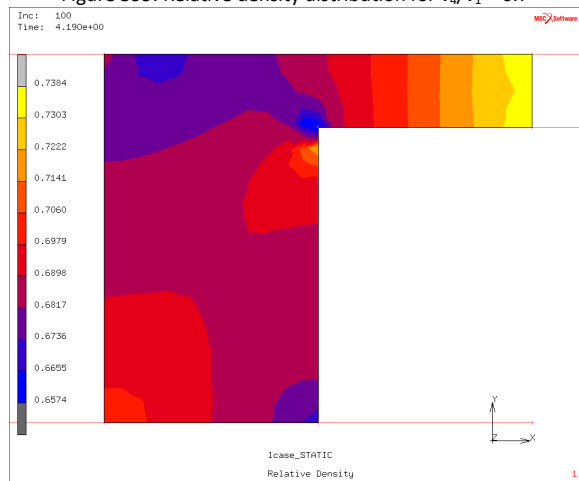


Figure 401. Relative density distribution for $v_4/v_1 = 0.9$

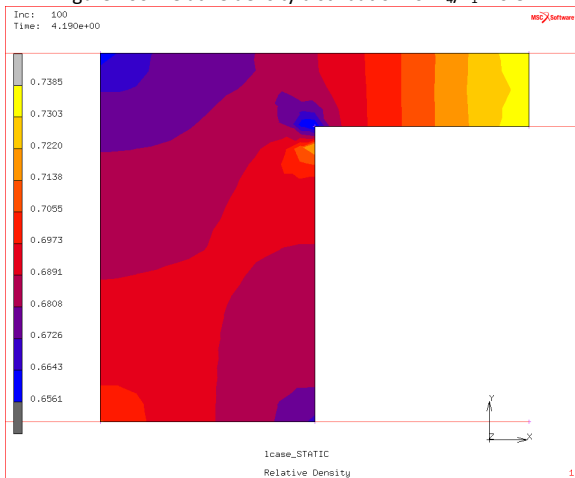


Figure 402. Relative density distribution for $v_4/v_1 = 1.0$

E.2.4 Using Variable Friction Coefficient, $\mu(\sigma_n, v_r)$

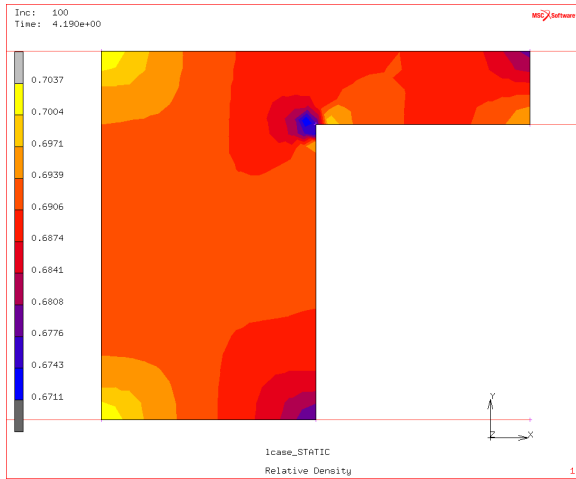


Figure 403. Relative density distribution for $v_4/v_1 = 0$

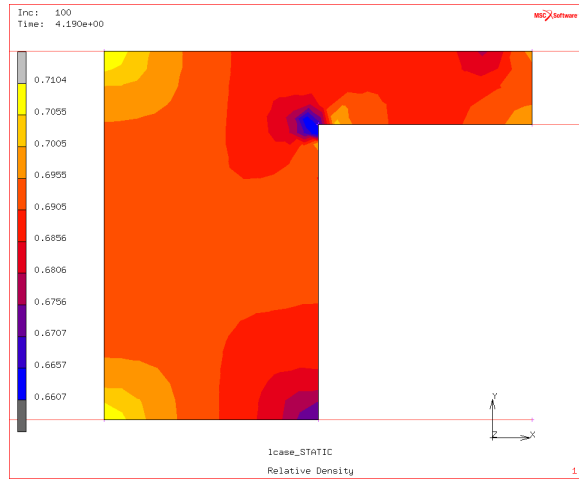


Figure 404. Relative density distribution for $v_4/v_1 = 0.1$

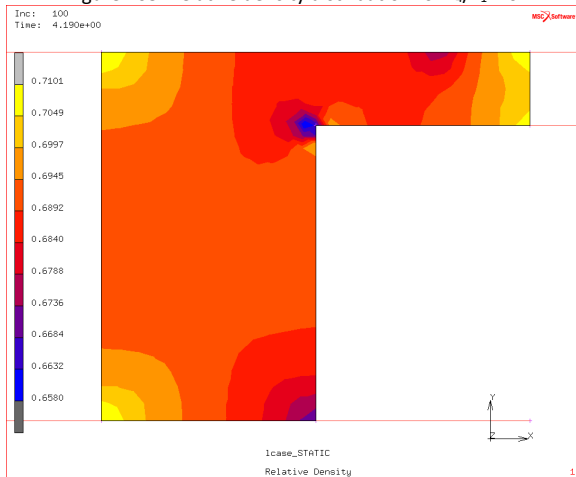


Figure 405. Relative density distribution for $v_4/v_1 = 0.2$

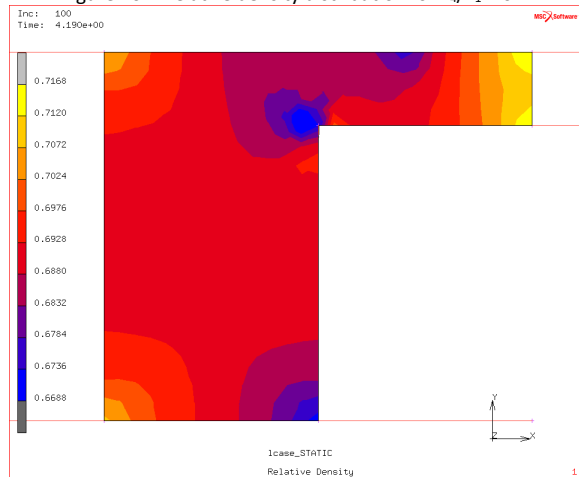


Figure 406. Relative density distribution for $v_4/v_1 = 0.3$

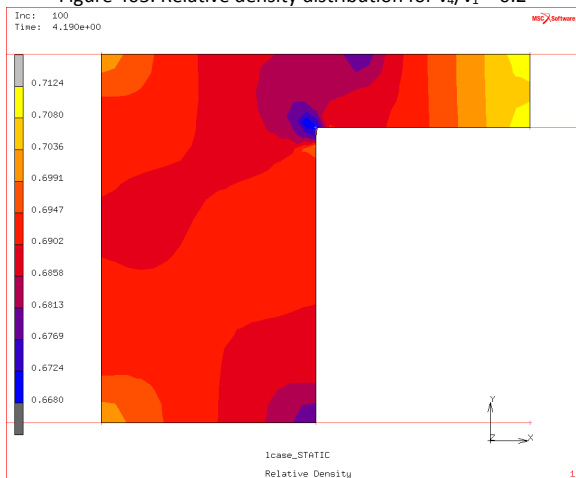


Figure 407. Relative density distribution for $v_4/v_1 = 0.4$

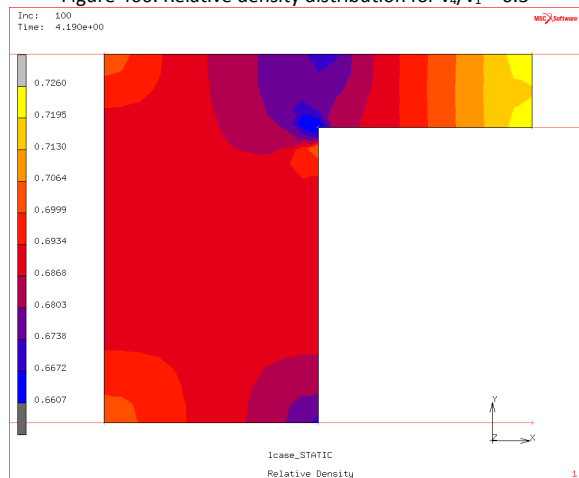


Figure 408. Relative density distribution for $v_4/v_1 = 0.5$

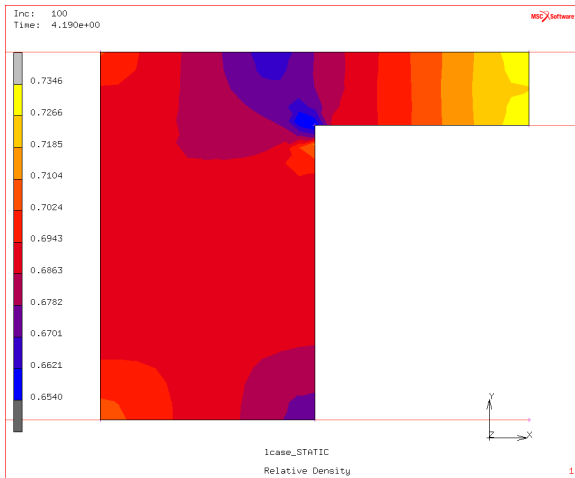


Figure 409. Relative density distribution for $v_4/v_1 = 0.6$

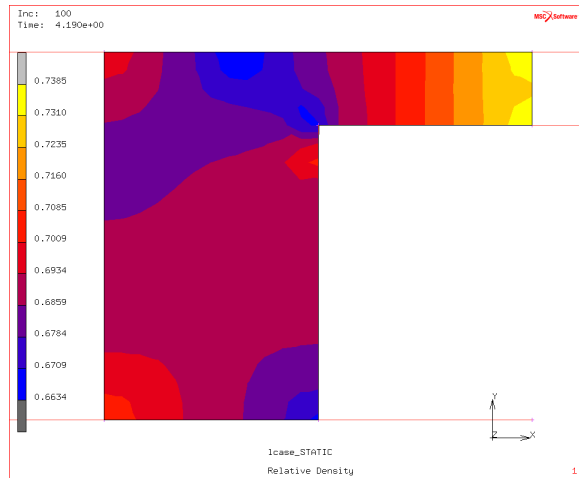


Figure 410. Relative density distribution for $v_4/v_1 = 0.7$

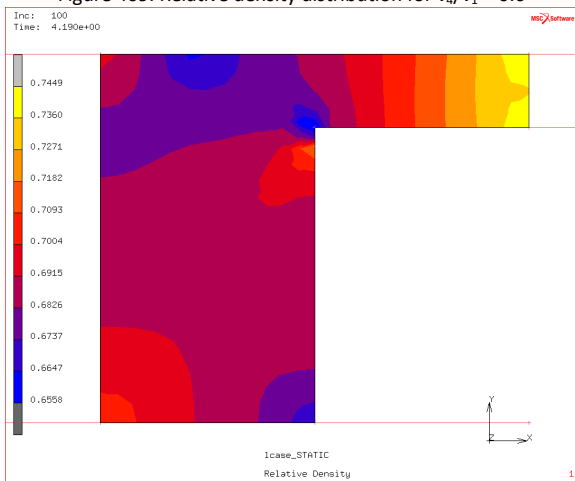


Figure 411. Relative density distribution for $v_4/v_1 = 0.8$

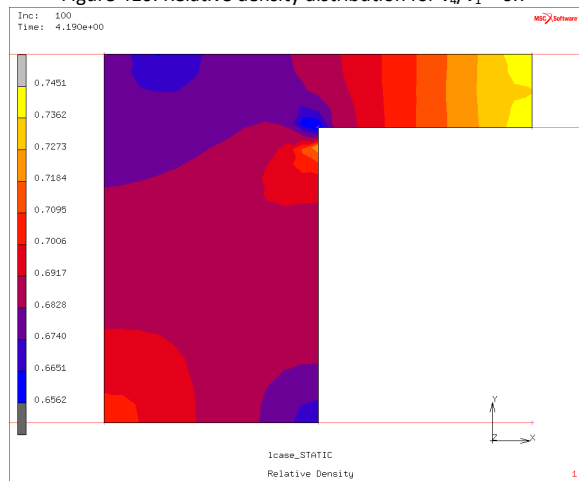


Figure 412. Relative density distribution for $v_4/v_1 = 0.9$

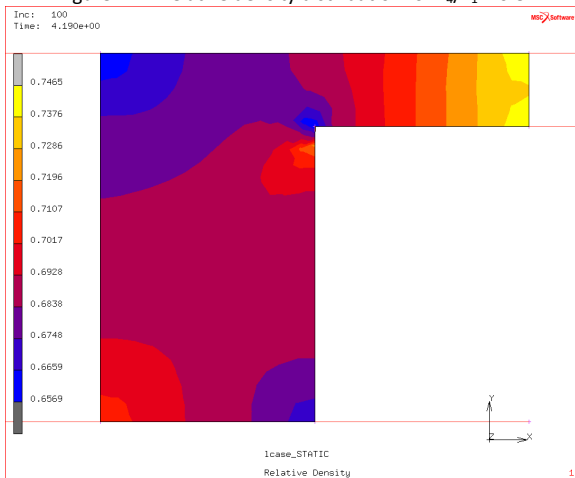


Figure 413. Relative density distribution for $v_4/v_1 = 1.0$

E.3 Using Material Properties Provided by Koval'chenko [54]

E.3.1 Using Constant Friction Coefficient of 0.08

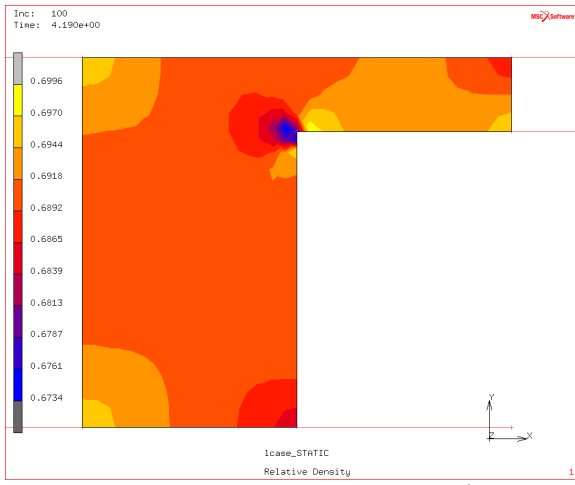


Figure 414. Relative density distribution for $v_4/v_1 = 0$

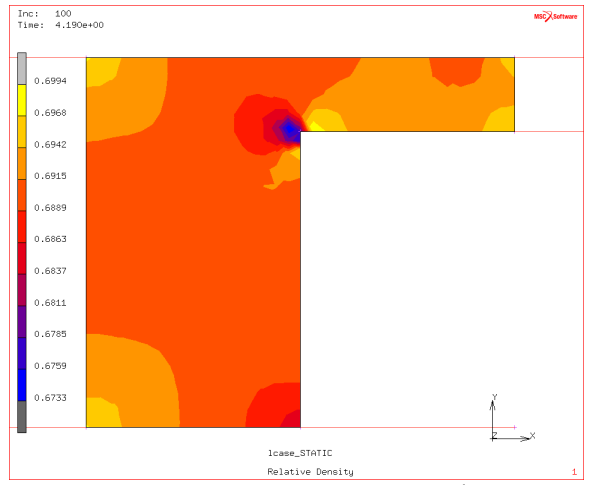


Figure 415. Relative density distribution for $v_4/v_1 = 0.1$

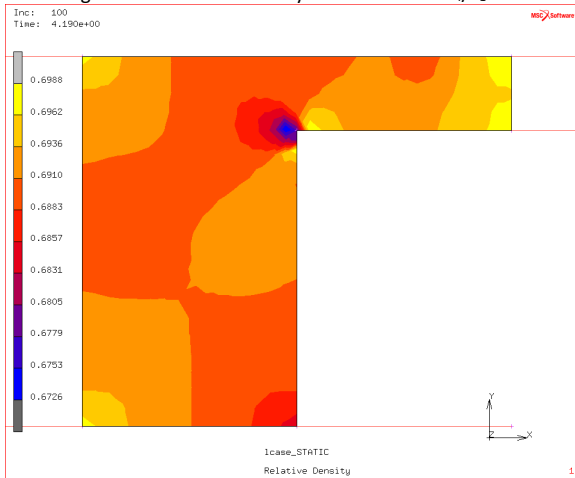


Figure 416. Relative density distribution for $v_4/v_1 = 0.2$

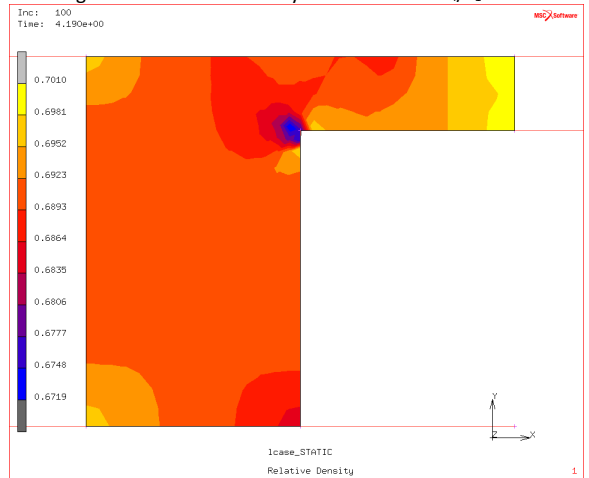


Figure 417. Relative density distribution for $v_4/v_1 = 0.3$

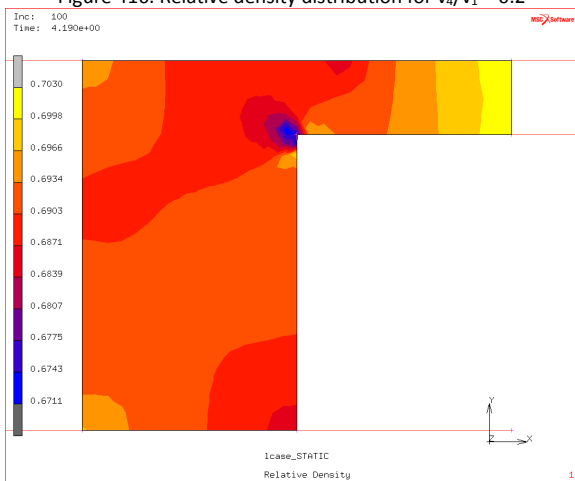


Figure 418. Relative density distribution for $v_4/v_1 = 0.4$

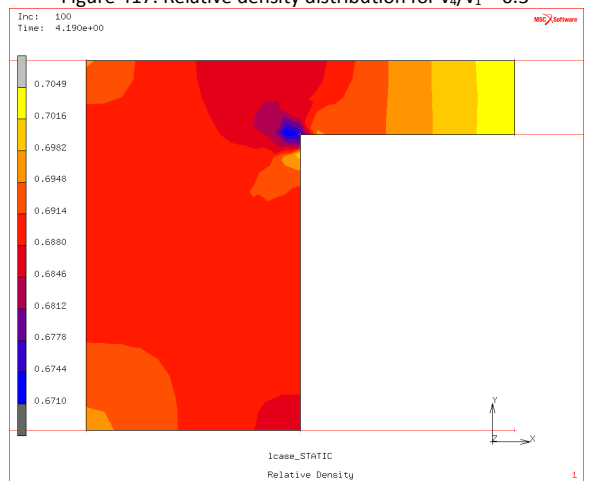


Figure 419. Relative density distribution for $v_4/v_1 = 0.5$

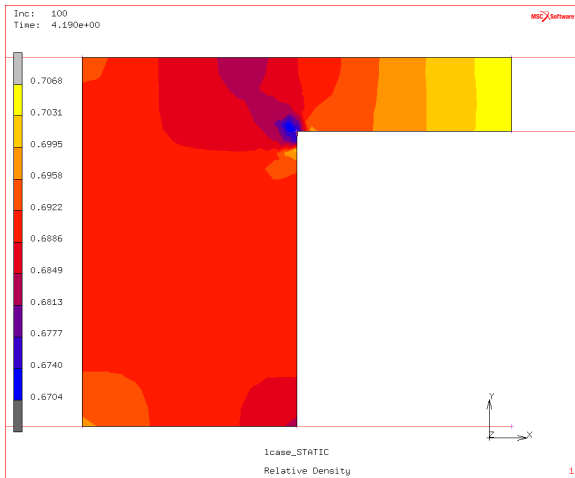


Figure 420. Relative density distribution for $v_4/v_1 = 0.6$

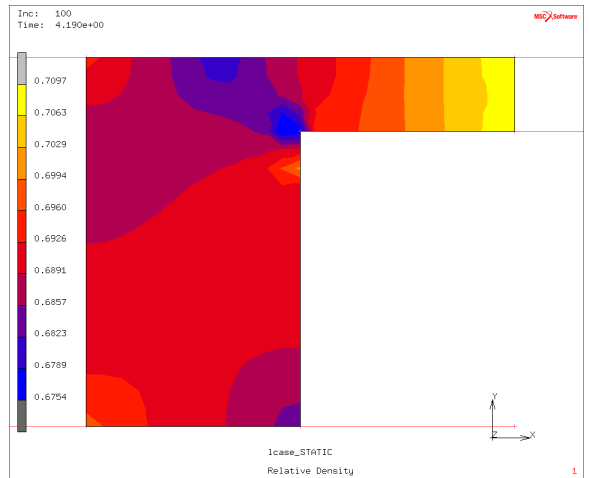


Figure 421. Relative density distribution for $v_4/v_1 = 0.7$

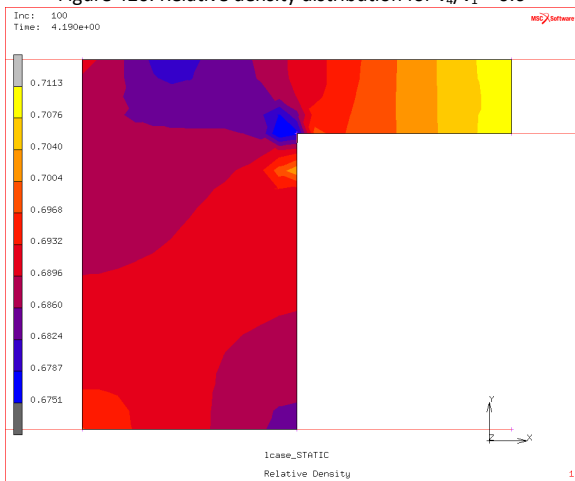


Figure 422. Relative density distribution for $v_4/v_1 = 0.8$

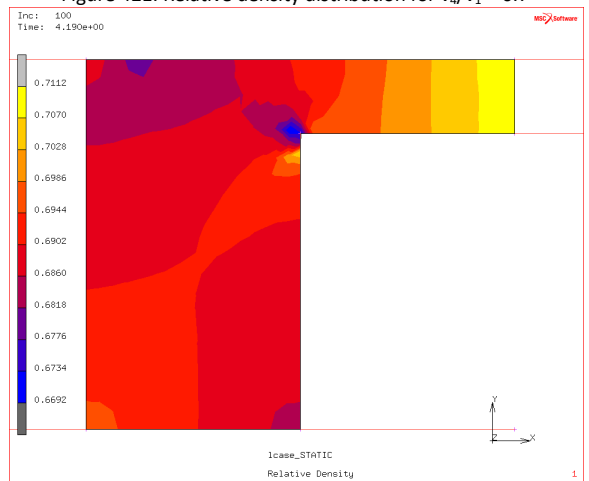


Figure 423. Relative density distribution for $v_4/v_1 = 0.9$

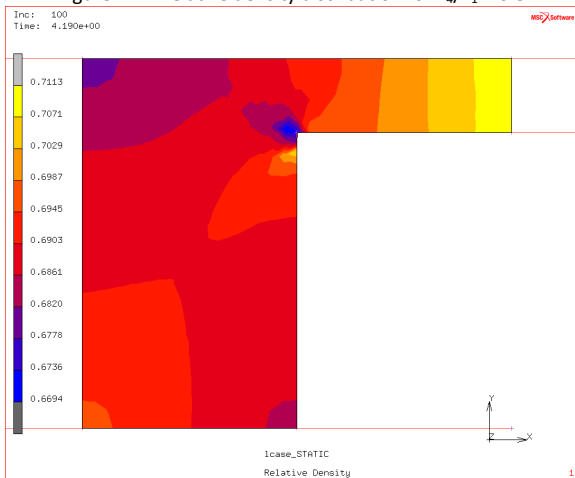


Figure 424. Relative density distribution for $v_4/v_1 = 1.0$

E.3.2 Using Constant Friction Coefficient of 0.12

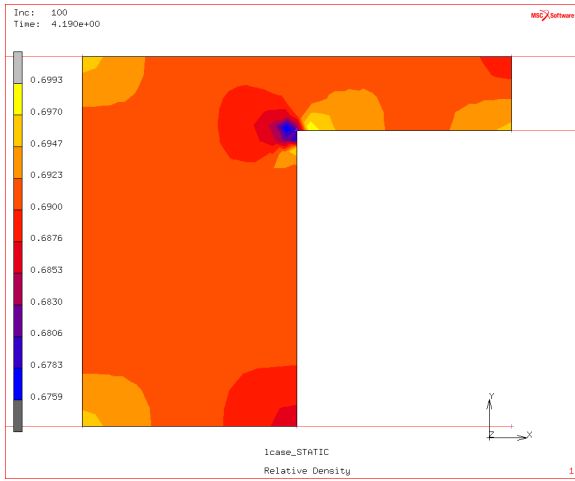


Figure 425. Relative density distribution for $v_4/v_1 = 0$

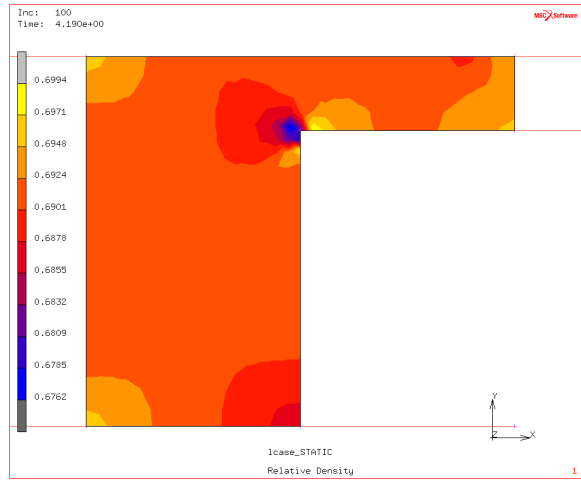


Figure 426. Relative density distribution for $v_4/v_1 = 0.1$

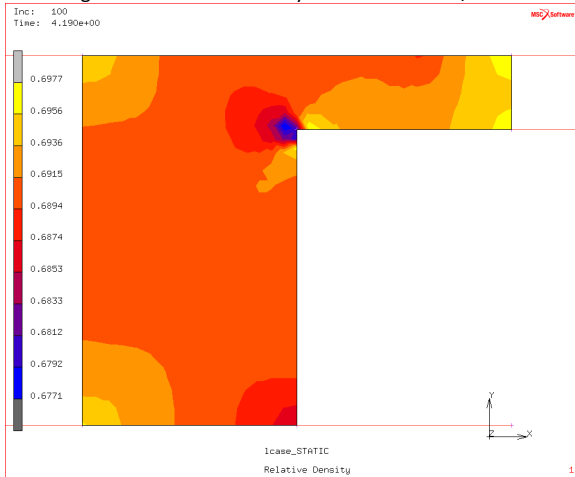


Figure 427. Relative density distribution for $v_4/v_1 = 0.2$

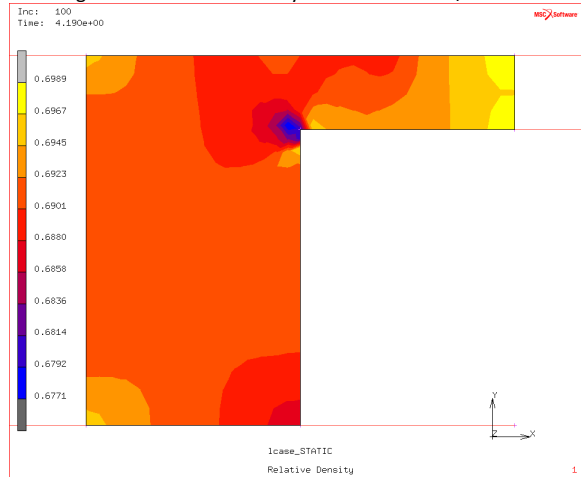


Figure 428. Relative density distribution for $v_4/v_1 = 0.3$

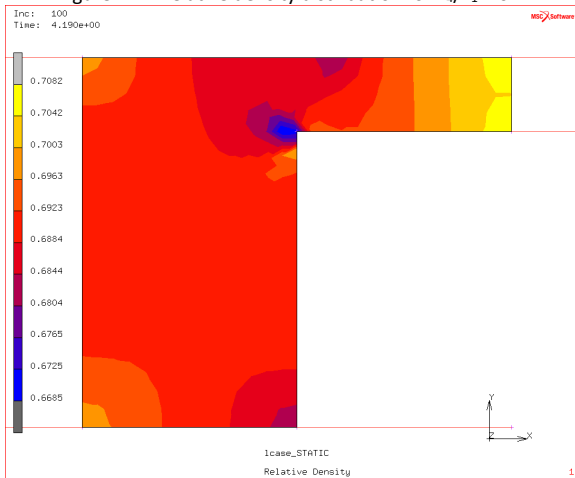


Figure 429. Relative density distribution for $v_4/v_1 = 0.4$

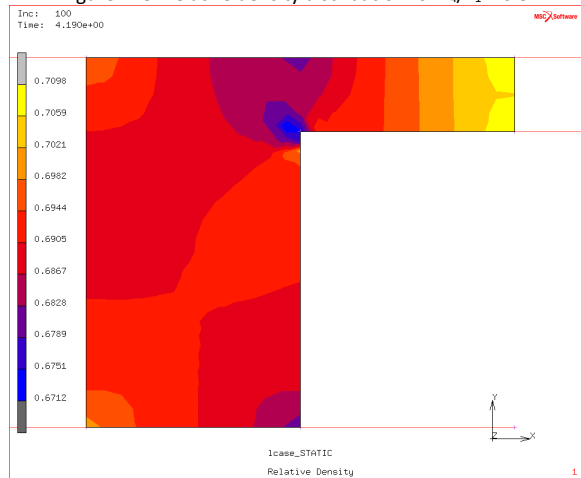


Figure 430. Relative density distribution for $v_4/v_1 = 0.5$

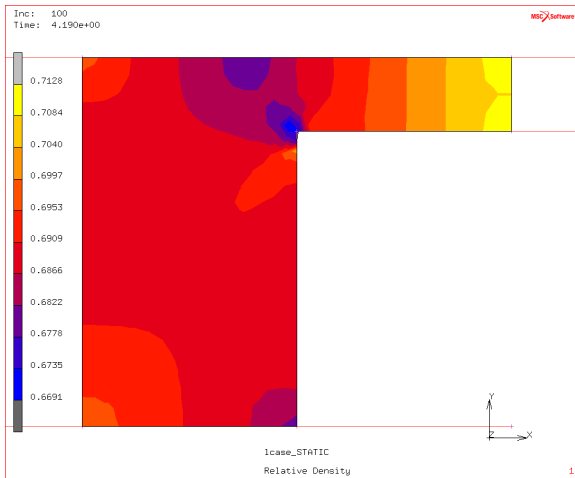


Figure 431. Relative density distribution for $v_4/v_1 = 0.6$

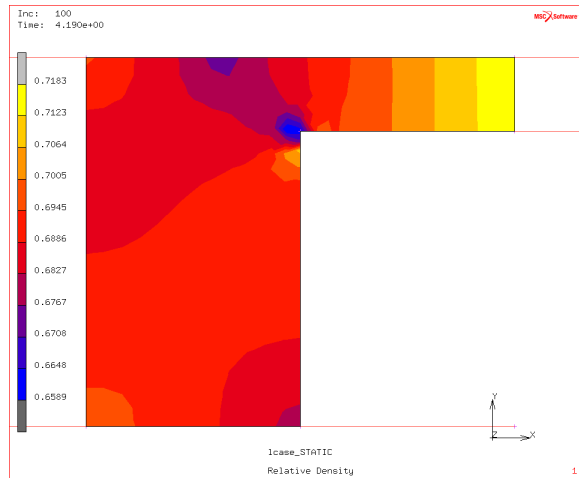


Figure 432. Relative density distribution for $v_4/v_1 = 0.7$

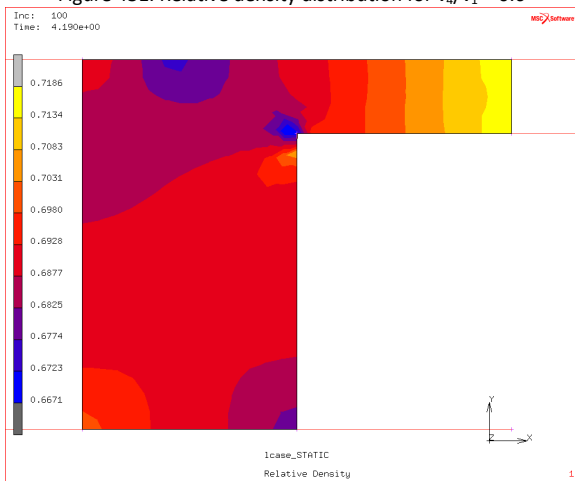


Figure 433. Relative density distribution for $v_4/v_1 = 0.8$

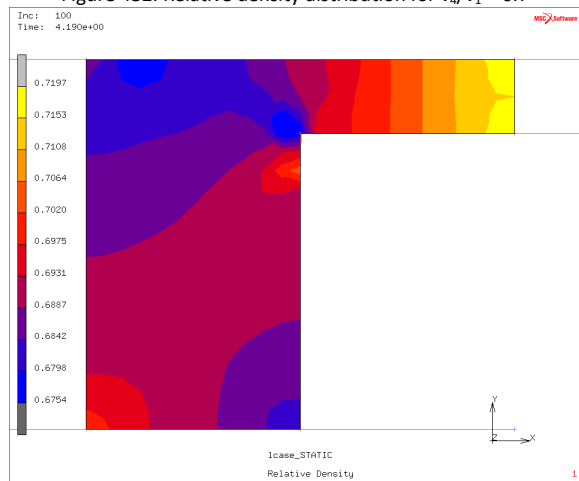


Figure 434. Relative density distribution for $v_4/v_1 = 0.9$

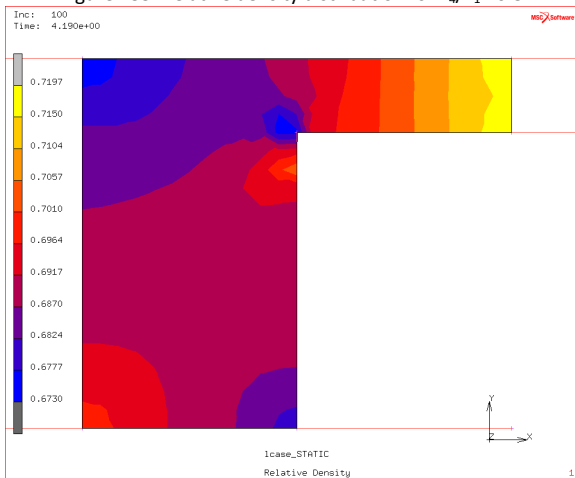


Figure 435. Relative density distribution for $v_4/v_1 = 1.0$

E.3.3 Using Constant Friction Coefficient of 0.20

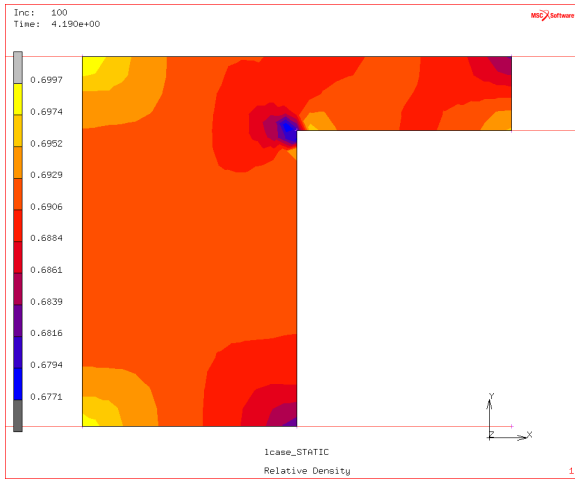


Figure 436. Relative density distribution for $v_4/v_1 = 0$

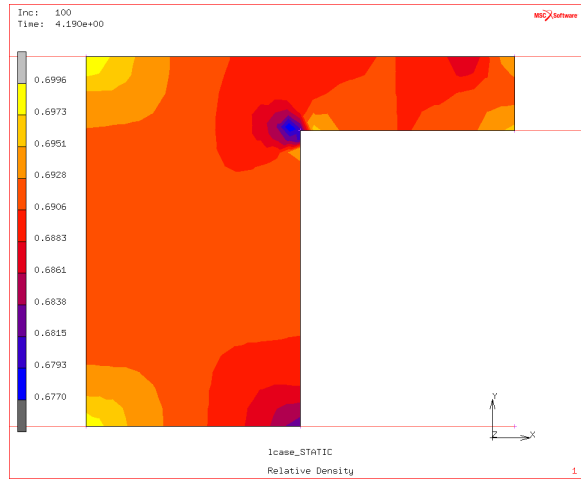


Figure 437. Relative density distribution for $v_4/v_1 = 0.1$

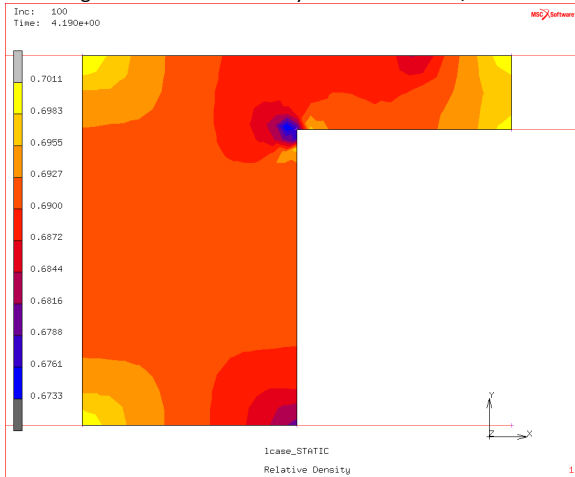


Figure 438. Relative density distribution for $v_4/v_1 = 0.2$

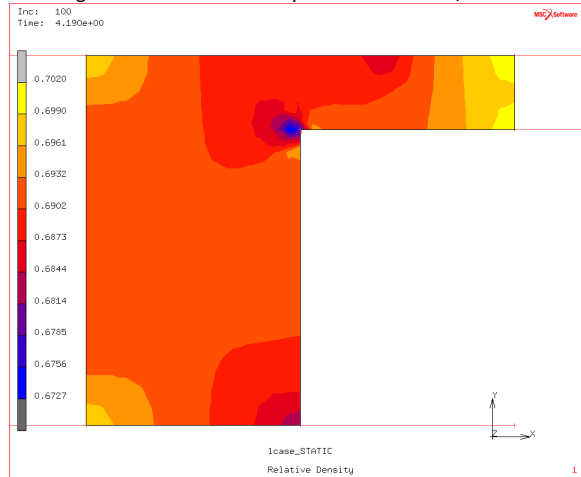


Figure 439. Relative density distribution for $v_4/v_1 = 0.3$

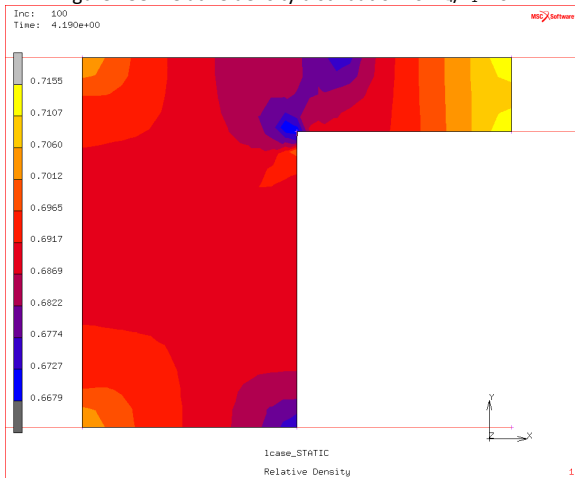


Figure 440. Relative density distribution for $v_4/v_1 = 0.4$

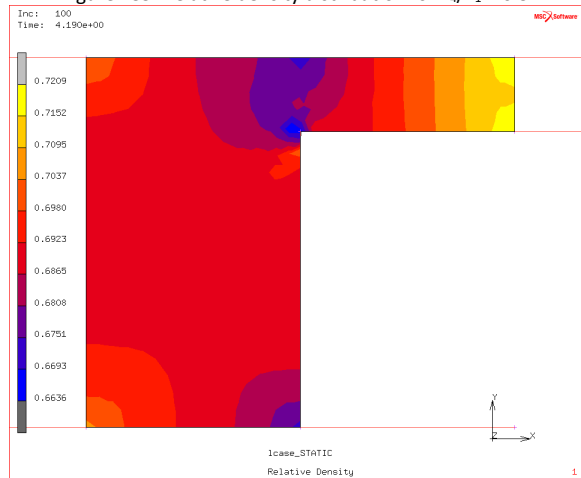


Figure 441. Relative density distribution for $v_4/v_1 = 0.5$

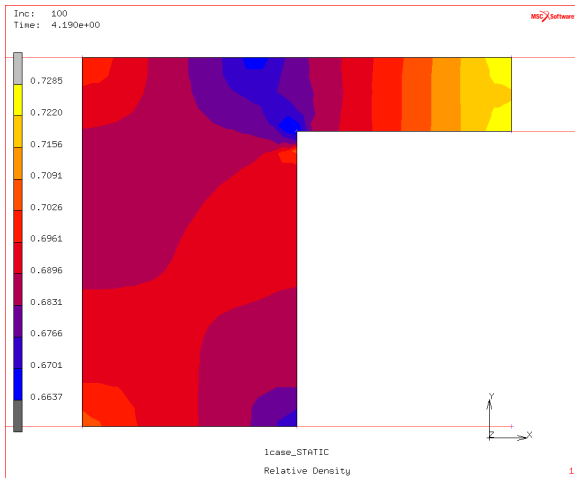


Figure 442. Relative density distribution for $v_4/v_1 = 0.6$

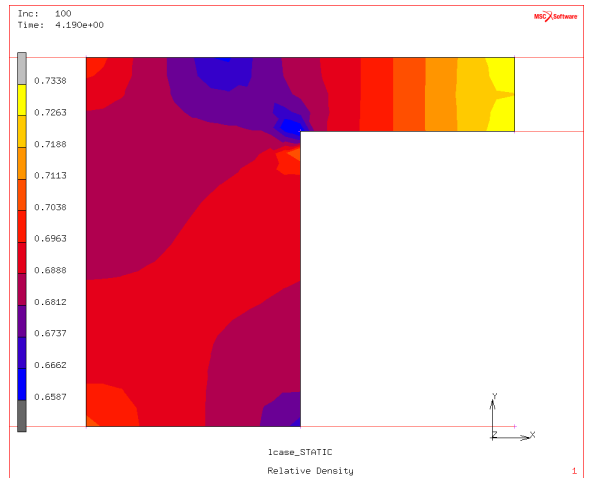


Figure 443. Relative density distribution for $v_4/v_1 = 0.7$

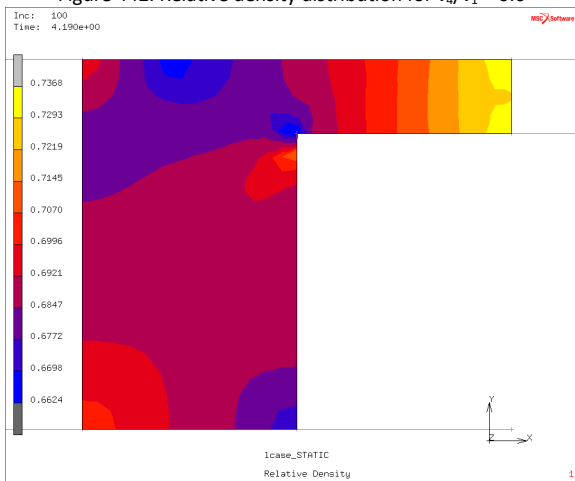


Figure 444. Relative density distribution for $v_4/v_1 = 0.8$

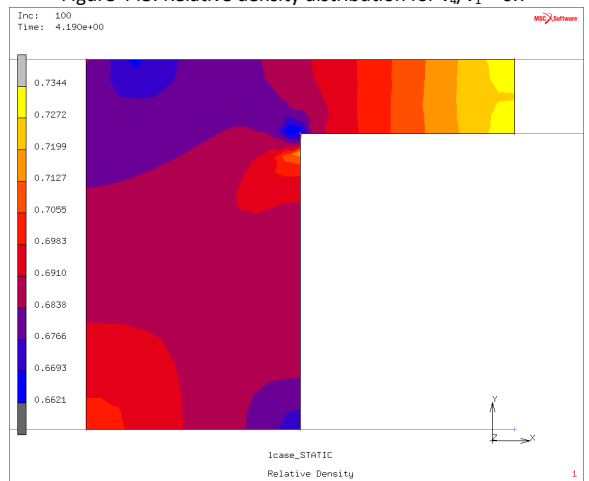


Figure 445. Relative density distribution for $v_4/v_1 = 0.9$

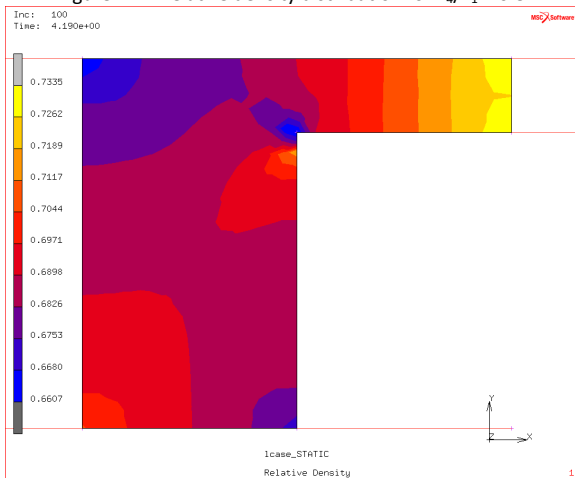


Figure 446. Relative density distribution for $v_4/v_1 = 1.0$

E.3.4 Using Variable Friction Coefficient, $\mu(\sigma_n, v_r)$

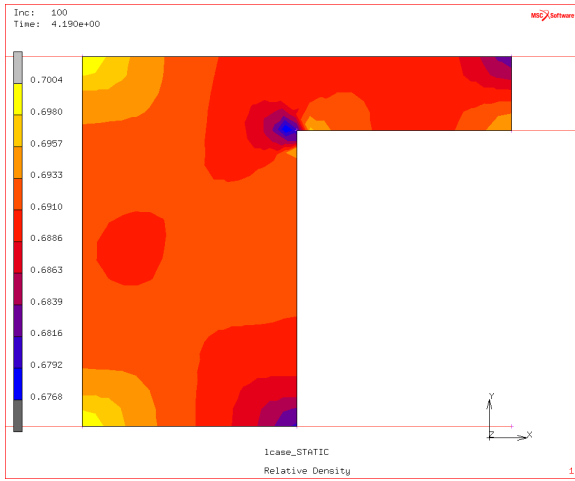


Figure 447. Relative density distribution for $v_4/v_1 = 0$

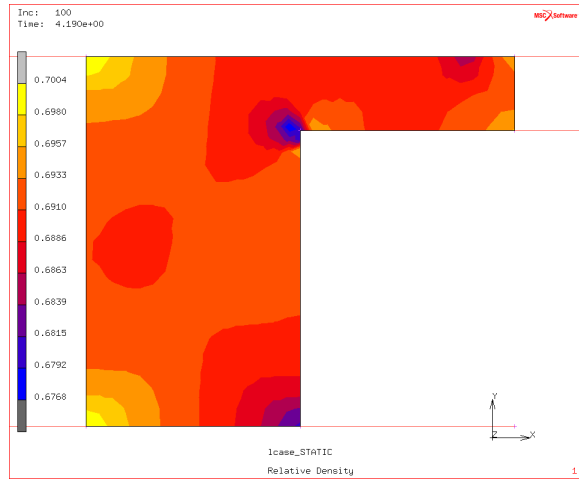


Figure 448. Relative density distribution for $v_4/v_1 = 0.1$

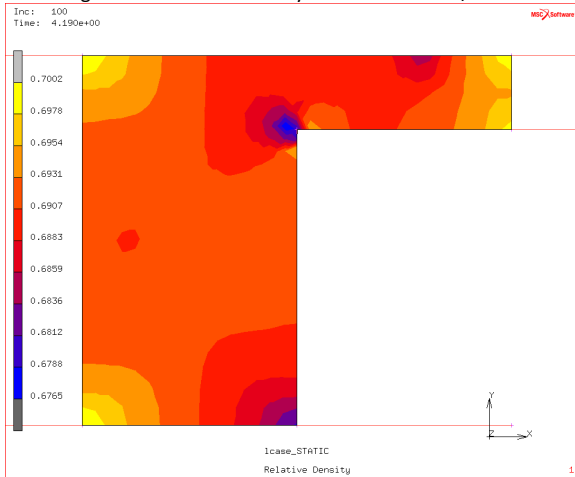


Figure 449. Relative density distribution for $v_4/v_1 = 0.2$

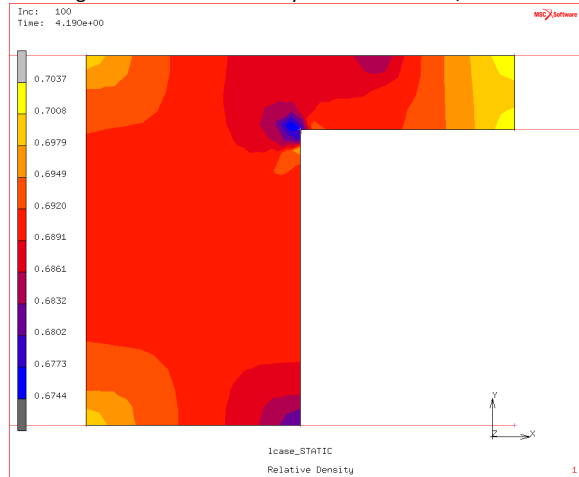


Figure 450. Relative density distribution for $v_4/v_1 = 0.3$

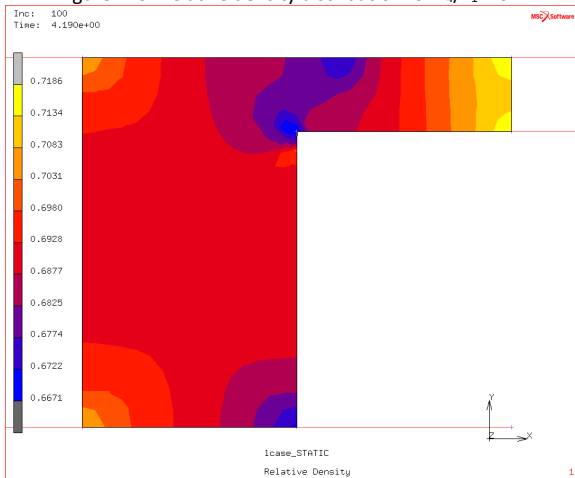


Figure 451. Relative density distribution for $v_4/v_1 = 0.4$

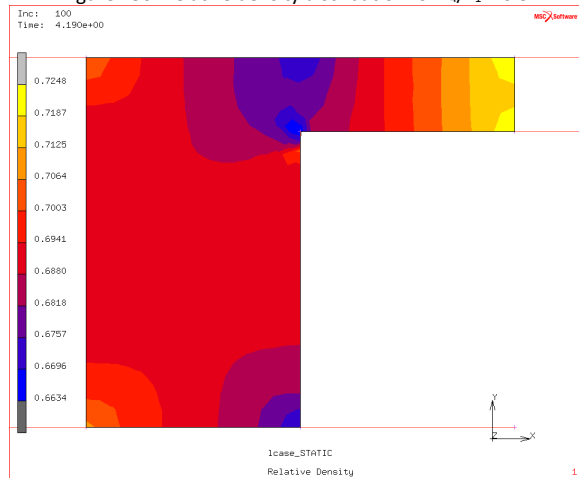


Figure 452. Relative density distribution for $v_4/v_1 = 0.5$

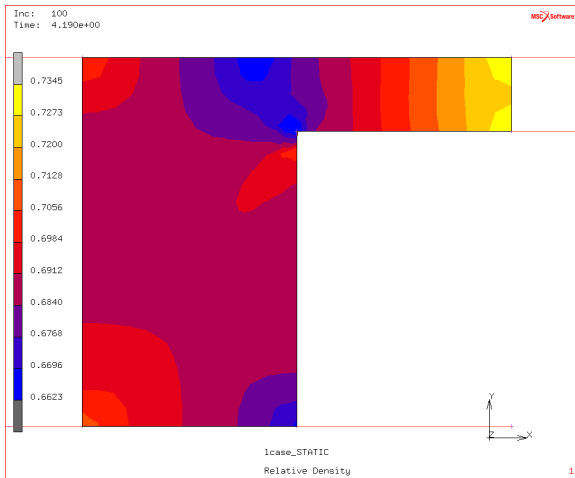


Figure 453. Relative density distribution for $v_4/v_1 = 0.6$

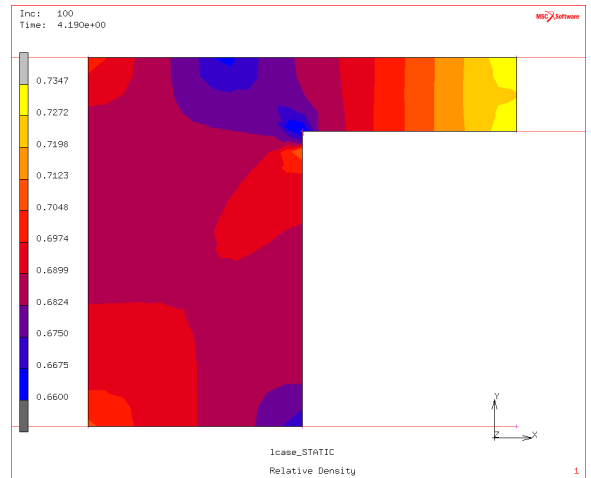


Figure 454. Relative density distribution for $v_4/v_1 = 0.7$

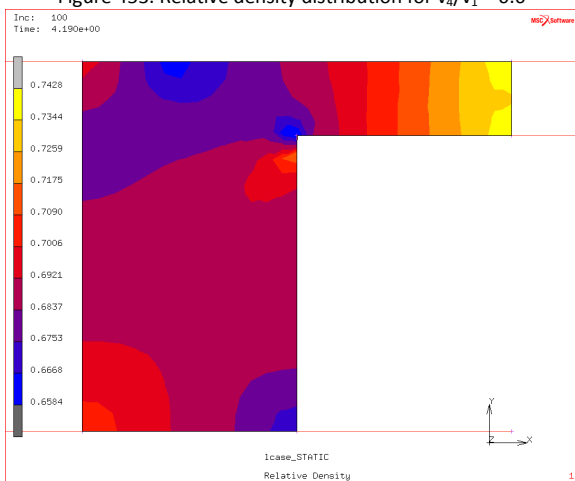


Figure 455. Relative density distribution for $v_4/v_1 = 0.8$

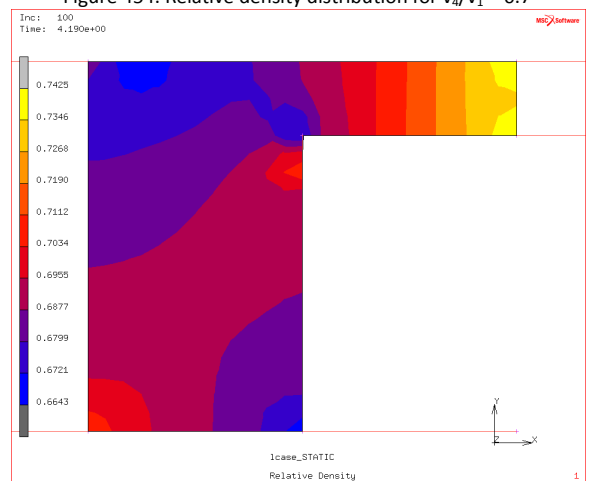


Figure 456. Relative density distribution for $v_4/v_1 = 0.9$

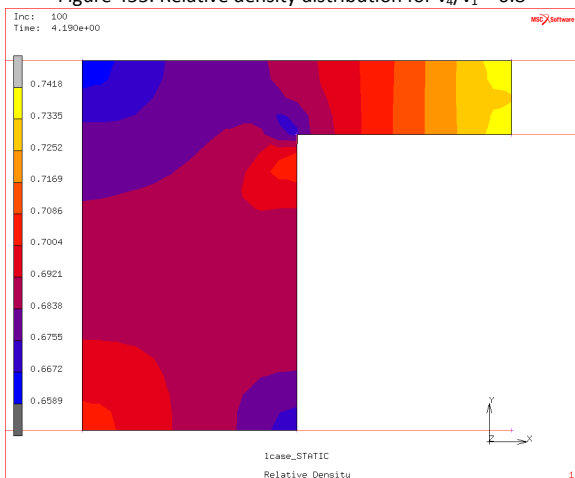


Figure 457. Relative density distribution for $v_4/v_1 = 1.0$

Appendix F. Effect of Die & Core-Rod to Upper-Punch Velocity Ratio on Density Distribution of a Multi-stepped Part

F.1 Using Material Properties Provided by Shima [101, 102]

F.1.1 Using Constant Friction Coefficient of 0.08

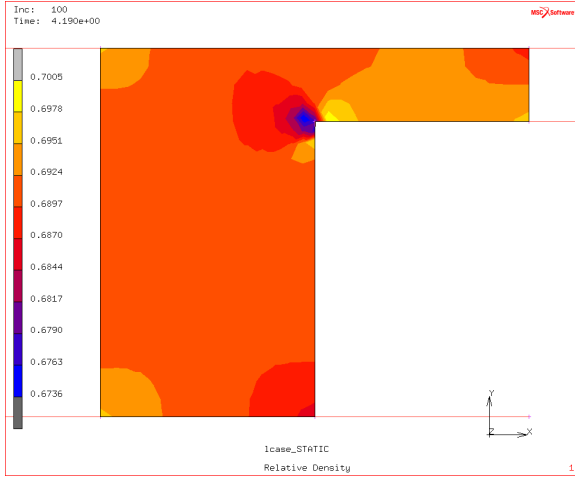


Figure 458. Relative density distribution for $v_{4,5}/v_1 = 0$

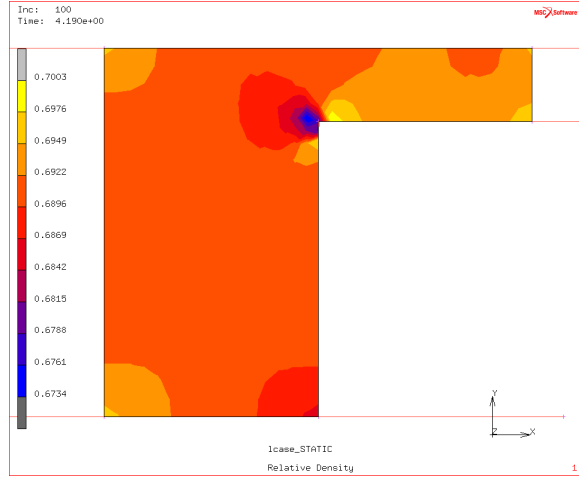


Figure 459. Relative density distribution for $v_{4,5}/v_1 = 0.1$

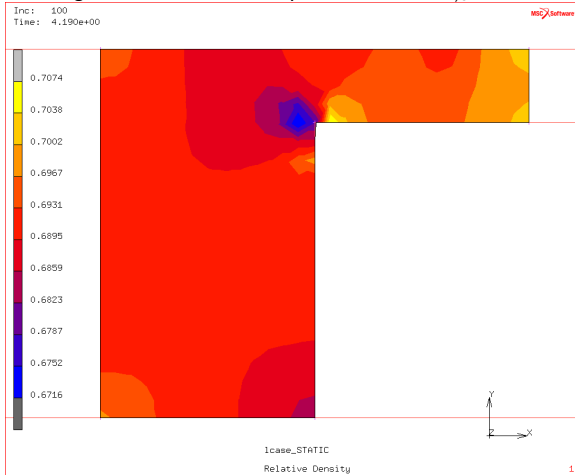


Figure 460. Relative density distribution for $v_{4,5}/v_1 = 0.2$

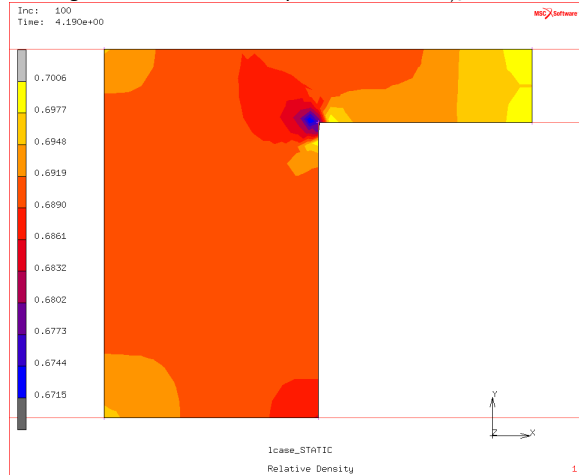


Figure 461. Relative density distribution for $v_{4,5}/v_1 = 0.3$

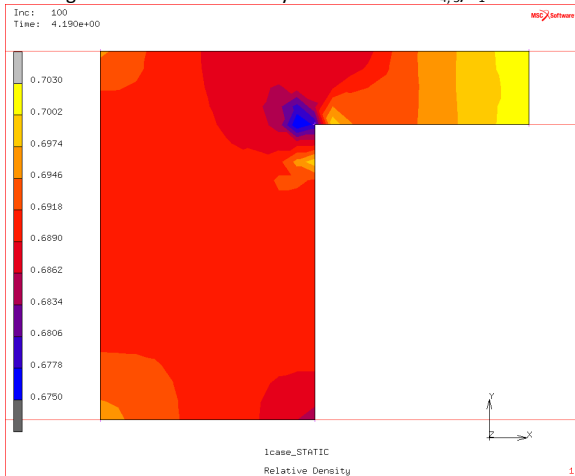


Figure 462. Relative density distribution for $v_{4,5}/v_1 = 0.4$

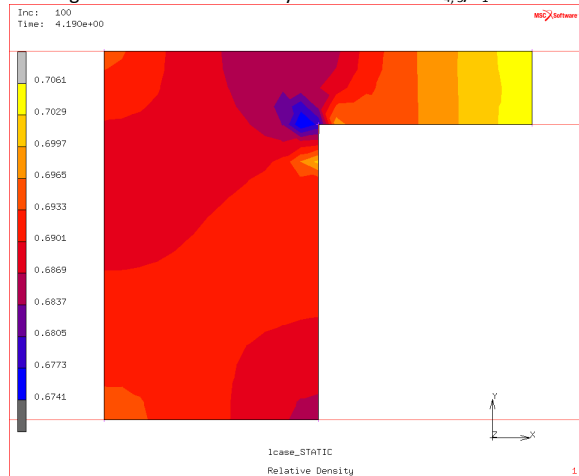


Figure 463. Relative density distribution for $v_{4,5}/v_1 = 0.5$

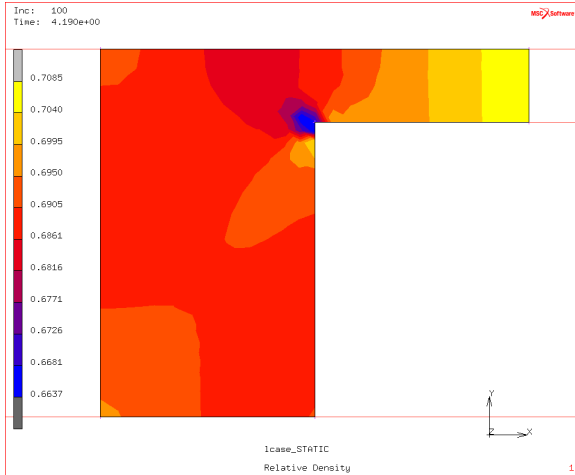


Figure 464. Relative density distribution for $v_{4,5}/v_1 = 0.6$

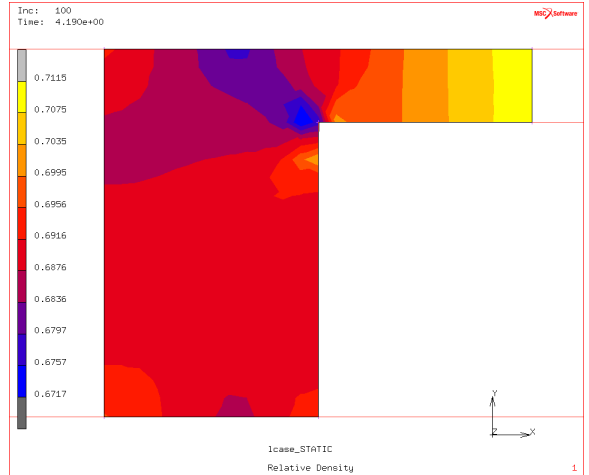


Figure 465. Relative density distribution for $v_{4,5}/v_1 = 0.7$

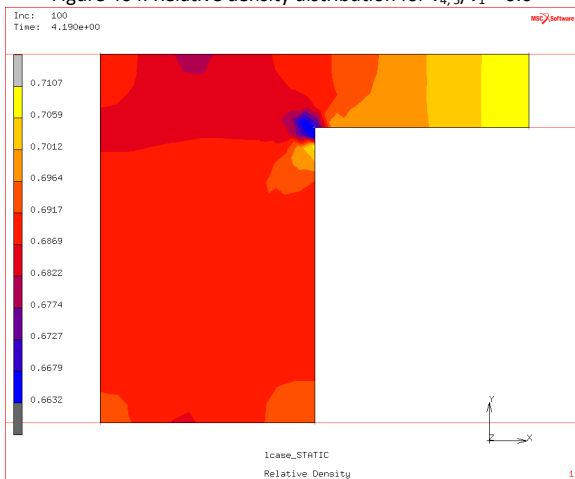


Figure 466. Relative density distribution for $v_{4,5}/v_1 = 0.8$

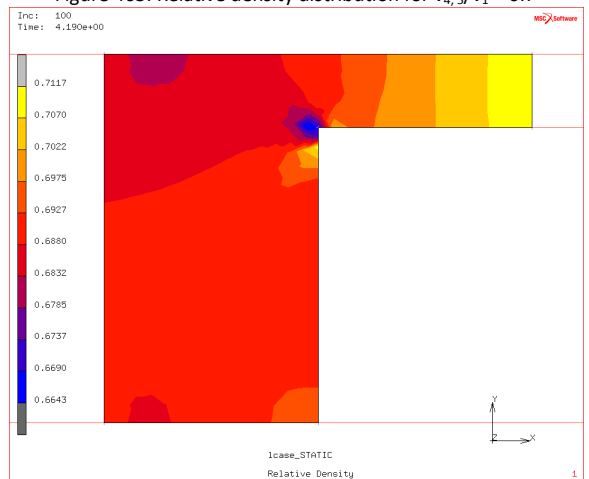


Figure 467. Relative density distribution for $v_{4,5}/v_1 = 0.9$

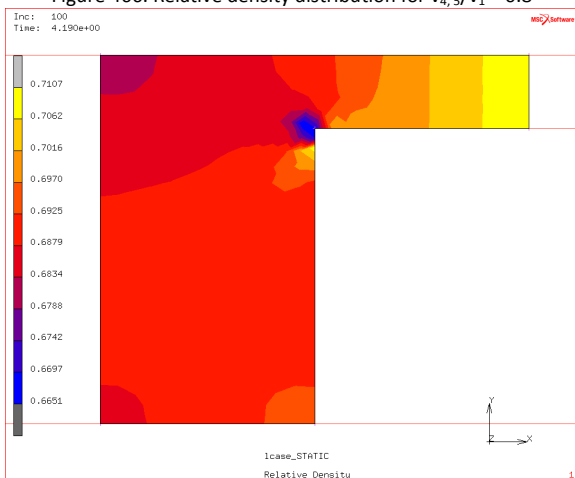


Figure 468. Relative density distribution for $v_{4,5}/v_1 = 1.0$

F.1.2 Using Constant Friction Coefficient of 0.12

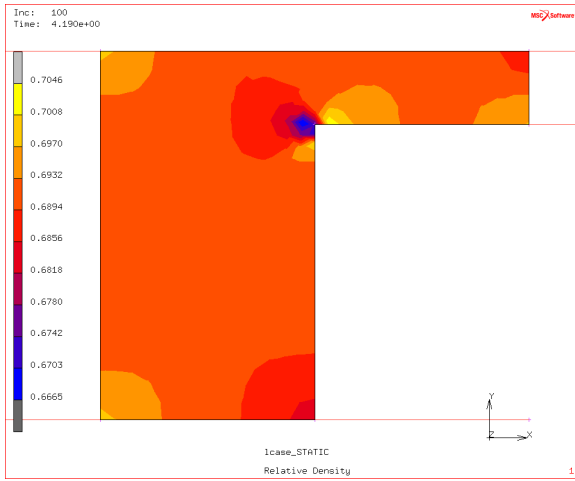


Figure 469. Relative density distribution for $v_{4,5}/v_1 = 0$

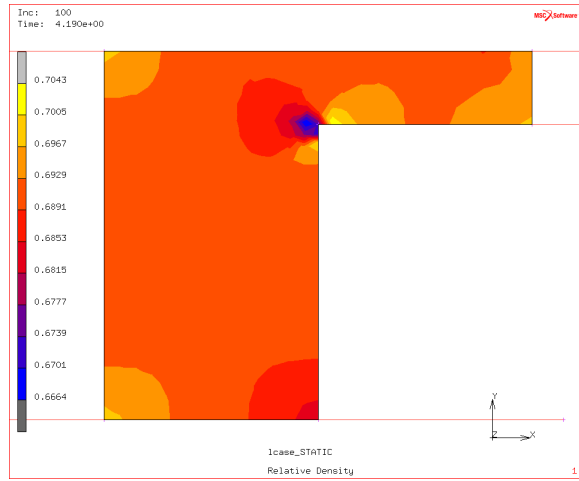


Figure 470. Relative density distribution for $v_{4,5}/v_1 = 0.1$

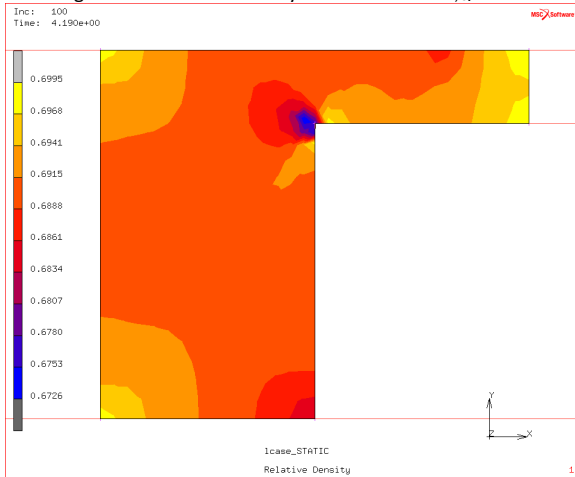


Figure 471. Relative density distribution for $v_{4,5}/v_1 = 0.2$

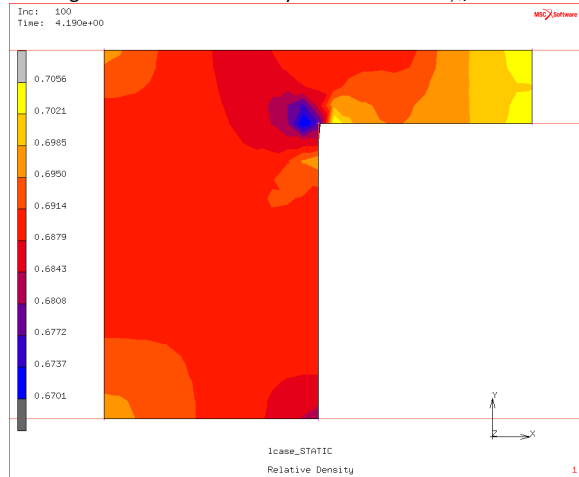


Figure 472. Relative density distribution for $v_{4,5}/v_1 = 0.3$

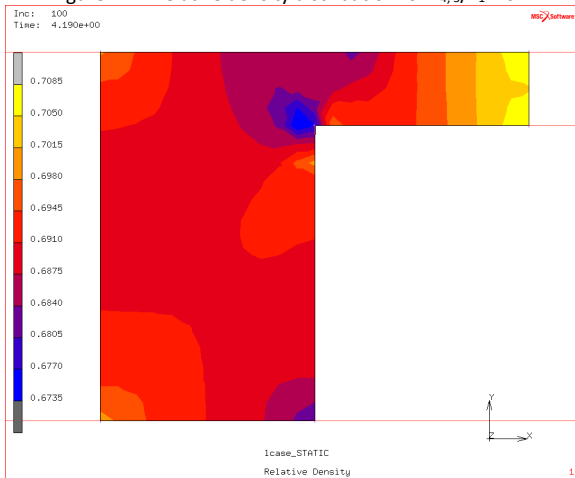


Figure 473. Relative density distribution for $v_{4,5}/v_1 = 0.4$

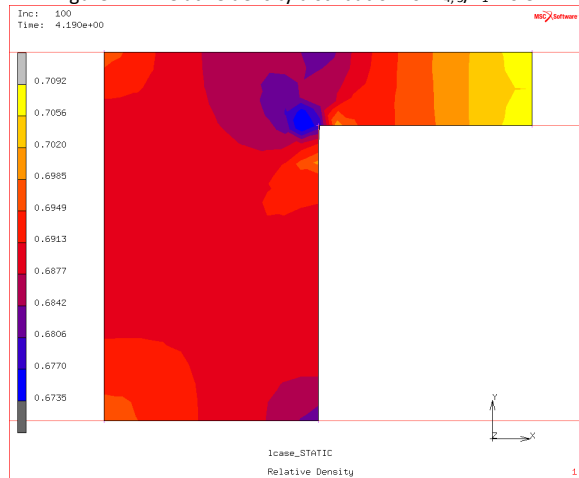


Figure 474. Relative density distribution for $v_{4,5}/v_1 = 0.5$

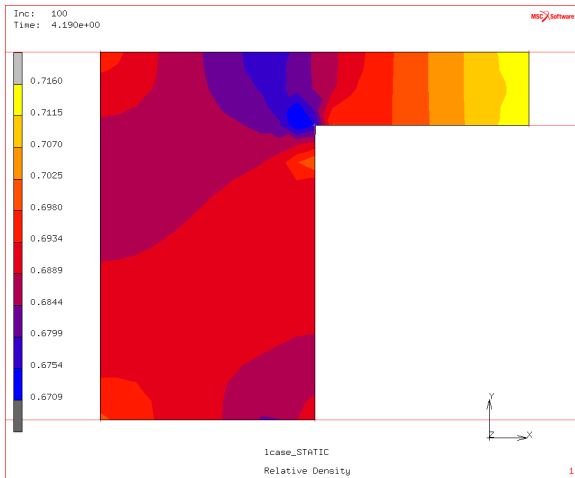


Figure 475. Relative density distribution for $v_{4,5}/v_1 = 0.6$

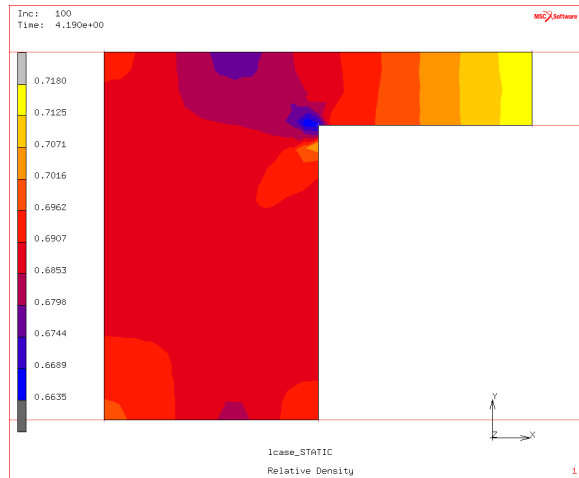


Figure 476. Relative density distribution for $v_{4,5}/v_1 = 0.7$

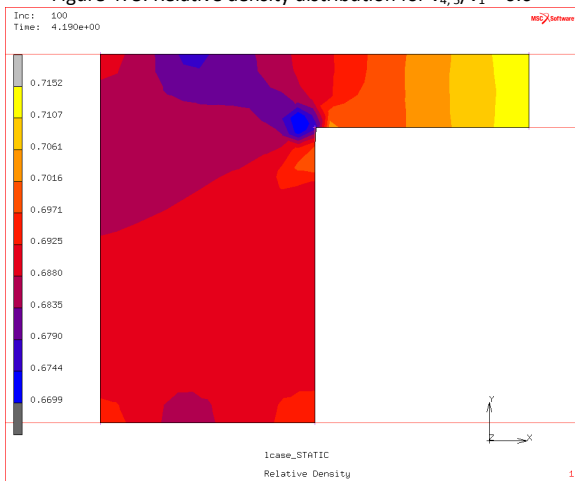


Figure 477. Relative density distribution for $v_{4,5}/v_1 = 0.8$

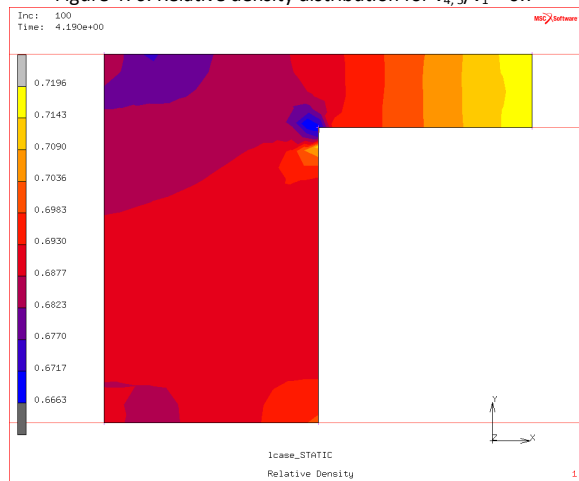


Figure 478. Relative density distribution for $v_{4,5}/v_1 = 0.9$

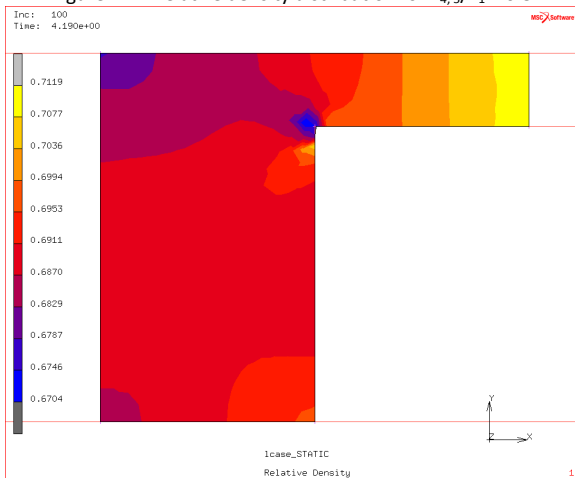


Figure 479. Relative density distribution for $v_{4,5}/v_1 = 1.0$

F.1.3 Using Constant Friction Coefficient of 0.20

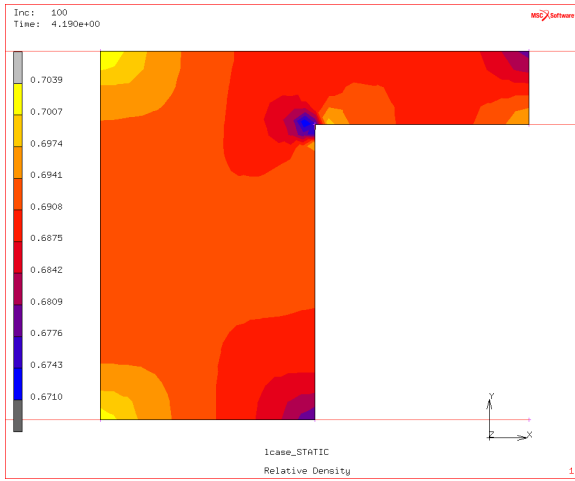


Figure 480. Relative density distribution for $v_{4,5}/v_1 = 0$

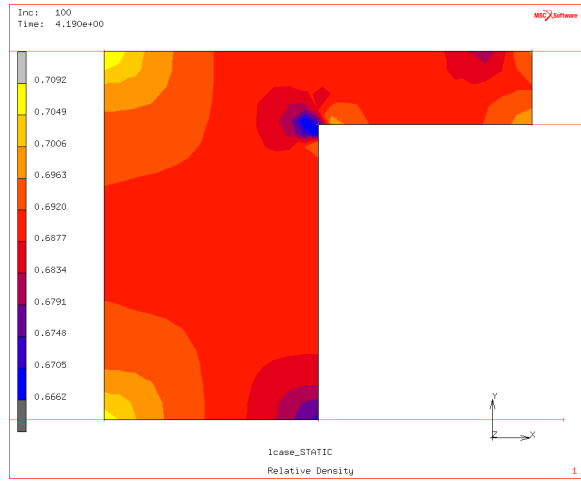


Figure 481. Relative density distribution for $v_{4,5}/v_1 = 0.1$

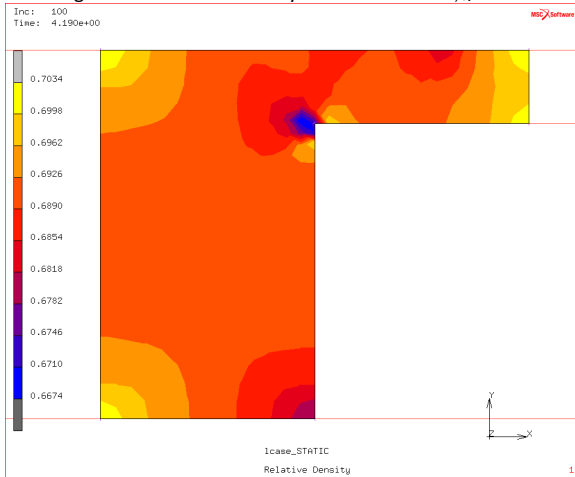


Figure 482. Relative density distribution for $v_{4,5}/v_1 = 0.2$

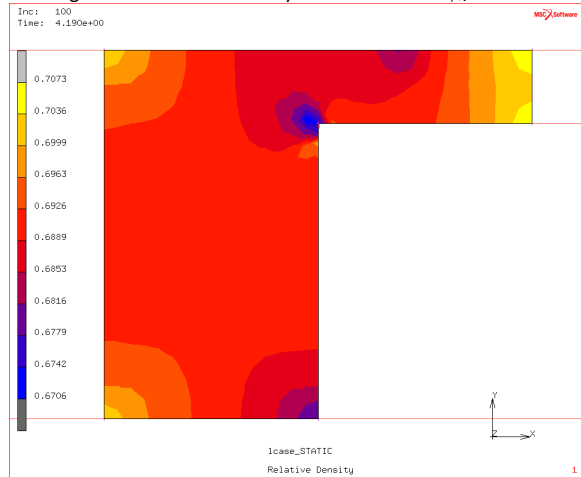


Figure 483. Relative density distribution for $v_{4,5}/v_1 = 0.3$

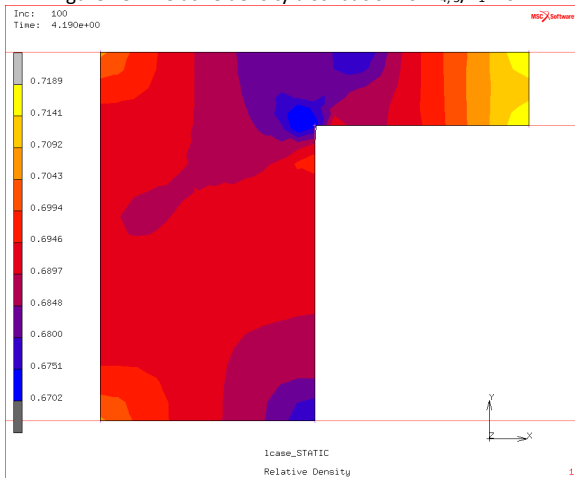


Figure 484. Relative density distribution for $v_{4,5}/v_1 = 0.4$

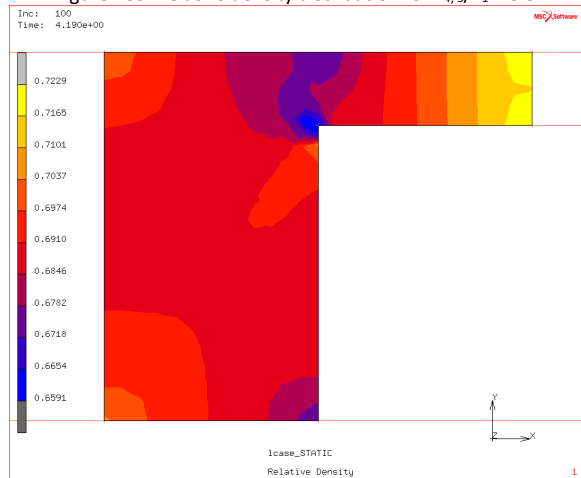


Figure 485. Relative density distribution for $v_{4,5}/v_1 = 0.5$

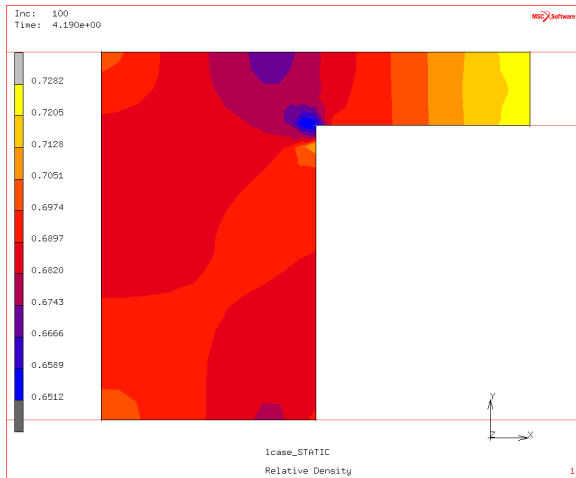


Figure 486. Relative density distribution for $v_{4,5}/v_1 = 0.6$

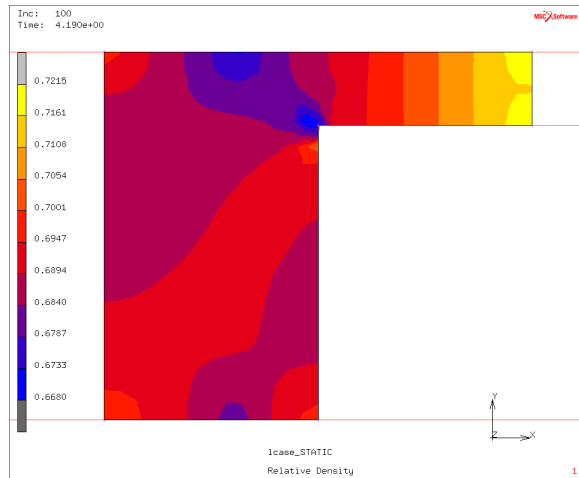


Figure 487. Relative density distribution for $v_{4,5}/v_1 = 0.7$

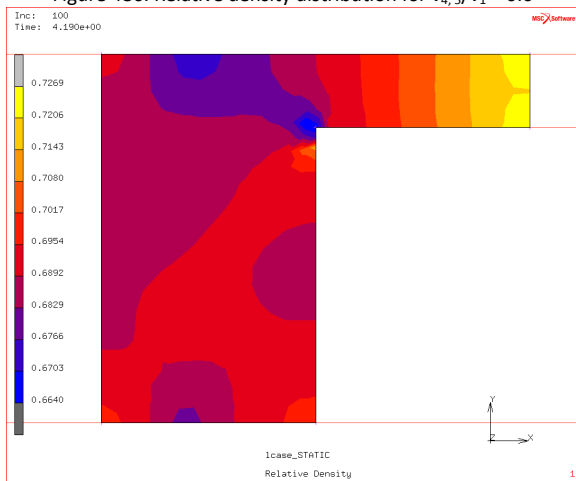


Figure 488. Relative density distribution for $v_{4,5}/v_1 = 0.8$

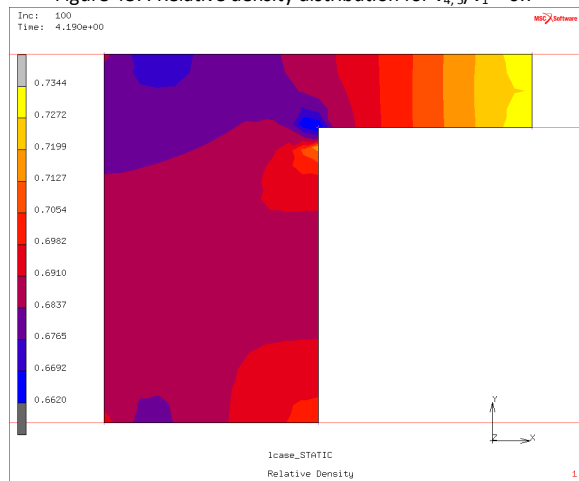


Figure 489. Relative density distribution for $v_{4,5}/v_1 = 0.9$

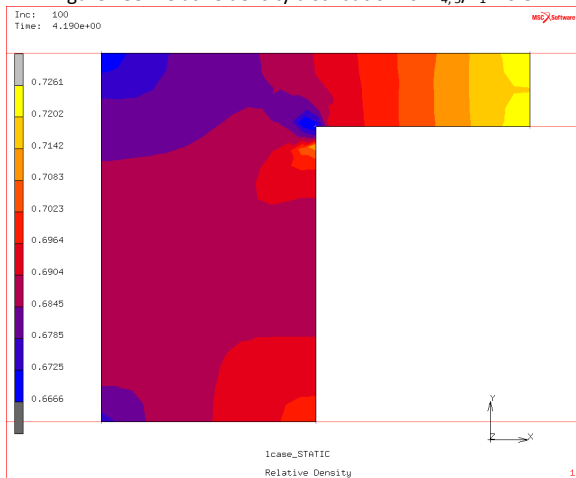


Figure 490. Relative density distribution for $v_{4,5}/v_1 = 1.0$

F.1.4 Using Variable Friction Coefficient, $\mu(\sigma_n, v_r)$

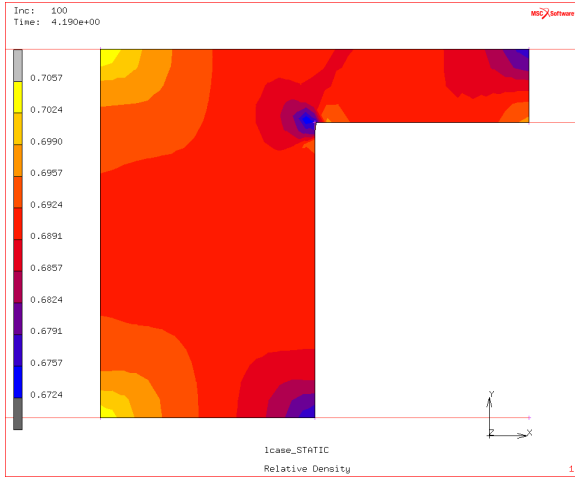


Figure 491. Relative density distribution for $v_{4,5}/v_1 = 0$

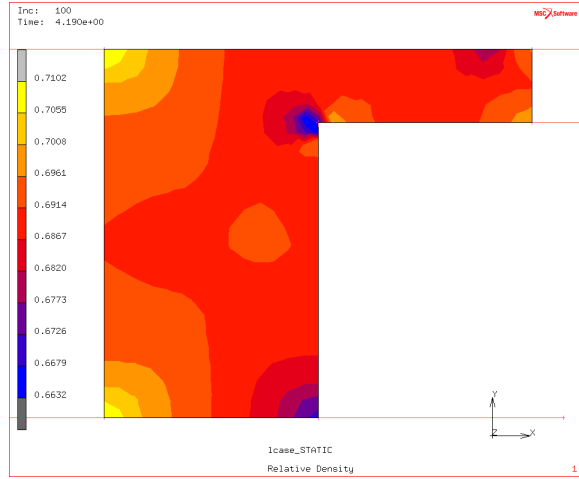


Figure 492. Relative density distribution for $v_{4,5}/v_1 = 0.1$

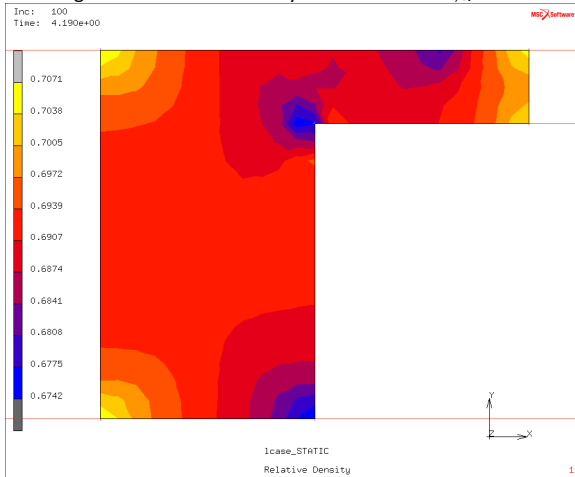


Figure 493. Relative density distribution for $v_{4,5}/v_1 = 0.2$

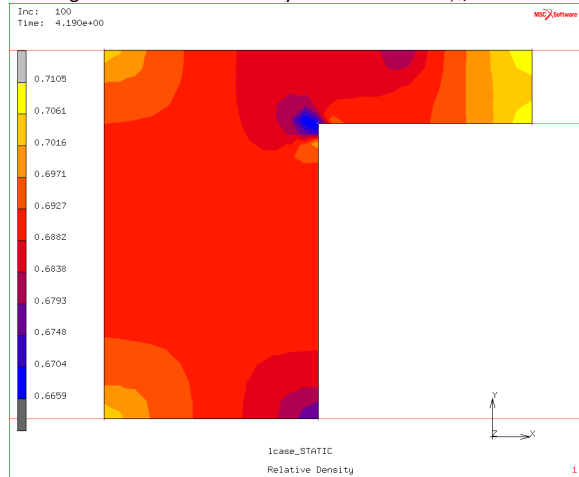


Figure 494. Relative density distribution for $v_{4,5}/v_1 = 0.3$

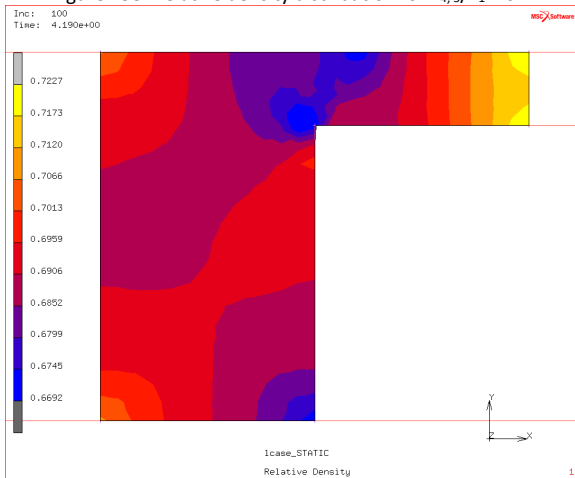


Figure 495. Relative density distribution for $v_{4,5}/v_1 = 0.4$

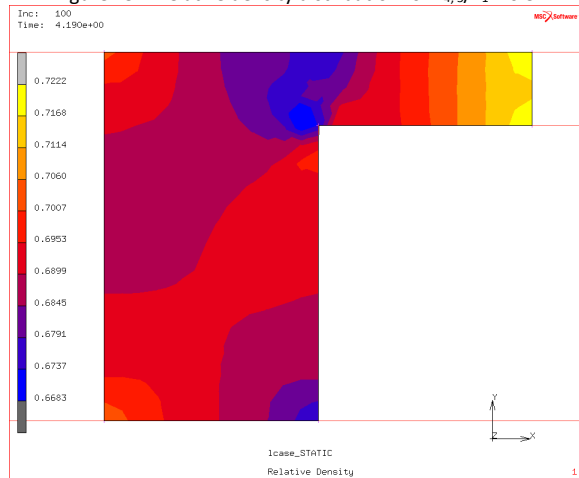


Figure 496. Relative density distribution for $v_{4,5}/v_1 = 0.5$

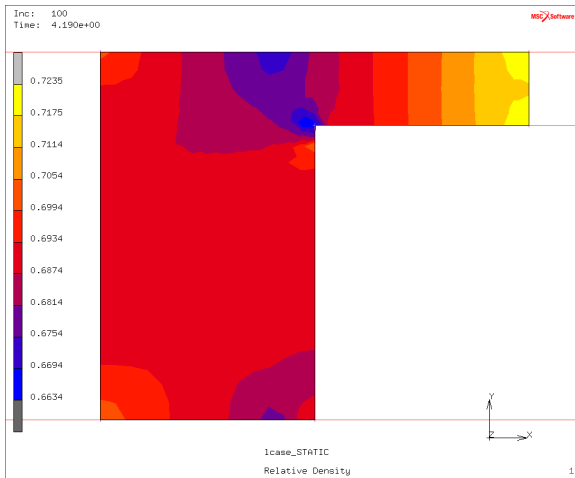


Figure 497. Relative density distribution for $v_{4,5}/v_1 = 0.6$

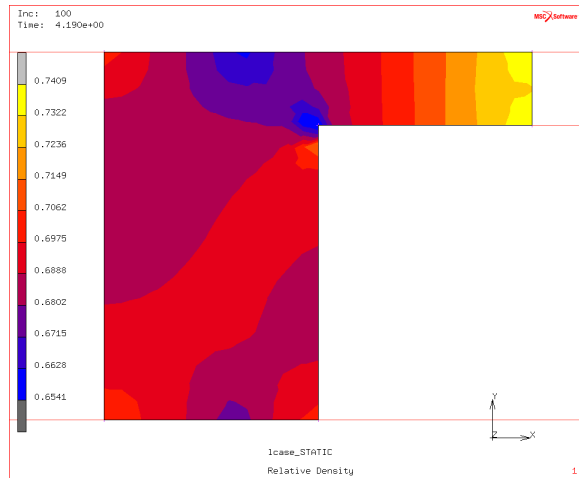


Figure 498. Relative density distribution for $v_{4,5}/v_1 = 0.7$

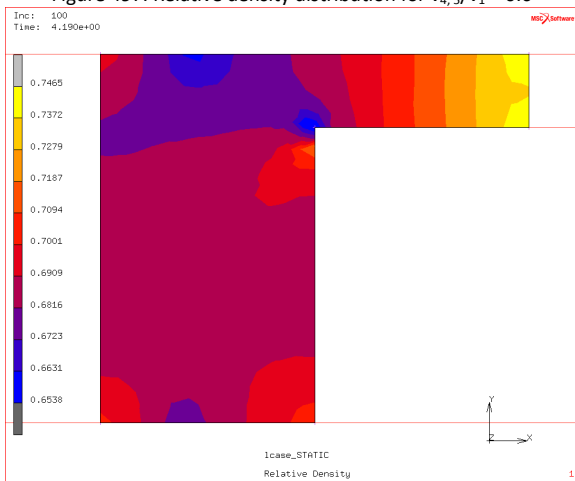


Figure 499. Relative density distribution for $v_{4,5}/v_1 = 0.8$

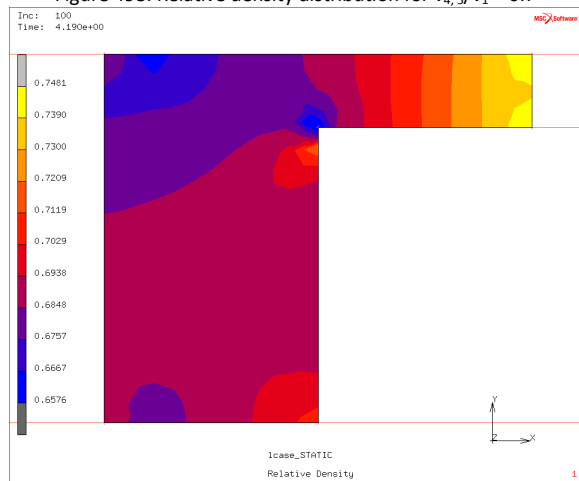


Figure 500. Relative density distribution for $v_{4,5}/v_1 = 0.9$

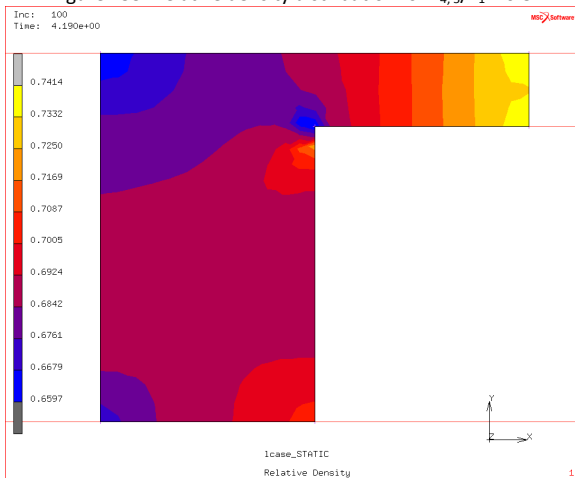


Figure 501. Relative density distribution for $v_{4,5}/v_1 = 1.0$

F.2 Using Material Properties Provided by Pavier and Doremus [10, 84]

F.2.1 Using Constant Friction Coefficient of 0.08

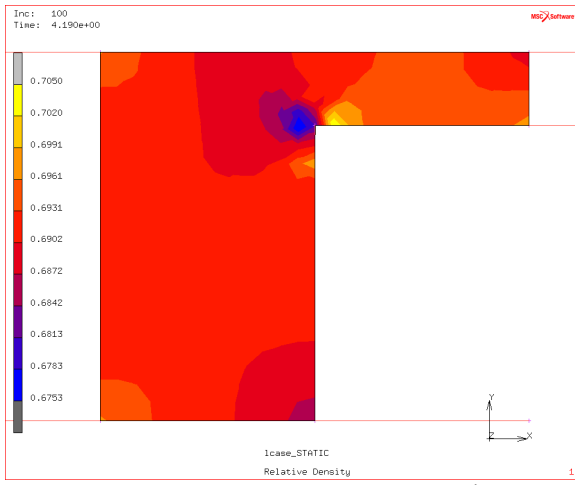


Figure 502. Relative density distribution for $v_{4,5}/v_1 = 0$

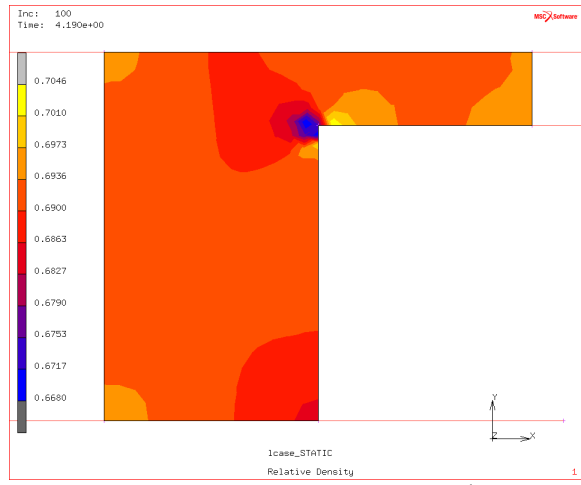


Figure 503. Relative density distribution for $v_{4,5}/v_1 = 0.1$

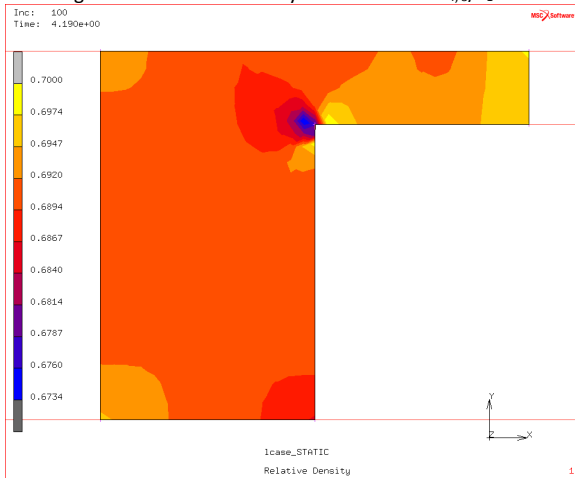


Figure 504. Relative density distribution for $v_{4,5}/v_1 = 0.2$

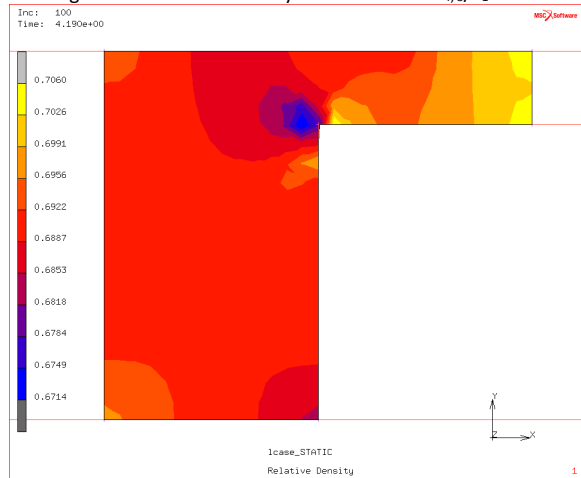


Figure 505. Relative density distribution for $v_{4,5}/v_1 = 0.3$

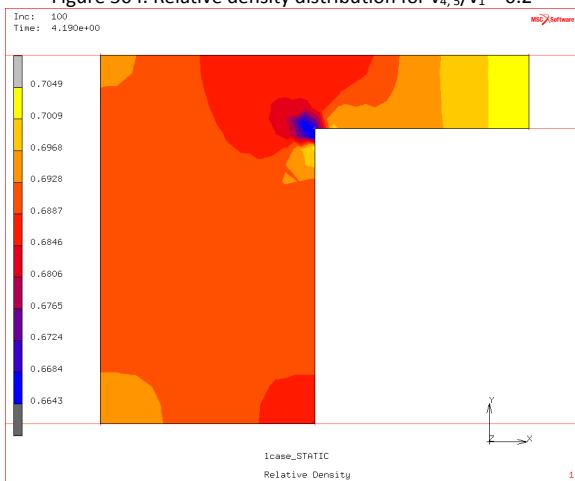


Figure 506. Relative density distribution for $v_{4,5}/v_1 = 0.4$

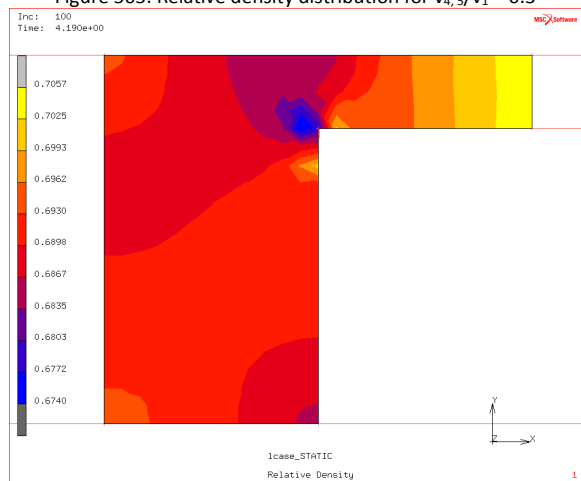


Figure 507. Relative density distribution for $v_{4,5}/v_1 = 0.5$

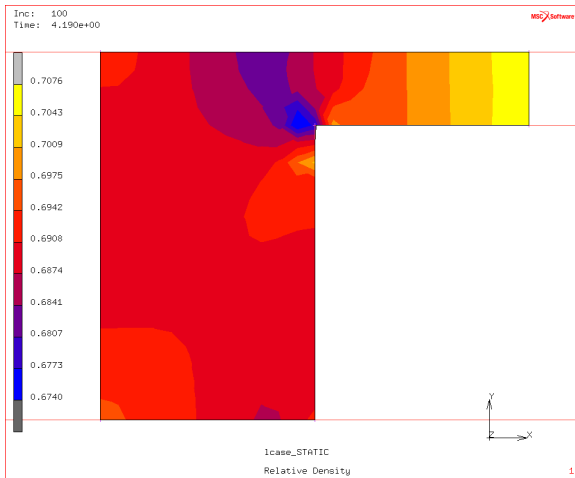


Figure 508. Relative density distribution for $v_{4,5}/v_1 = 0.6$

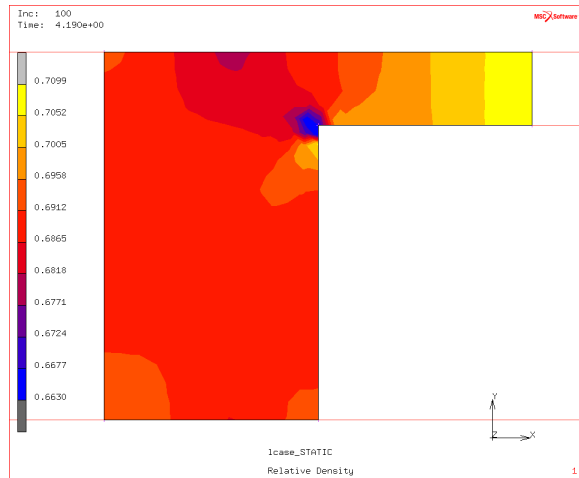


Figure 509. Relative density distribution for $v_{4,5}/v_1 = 0.7$

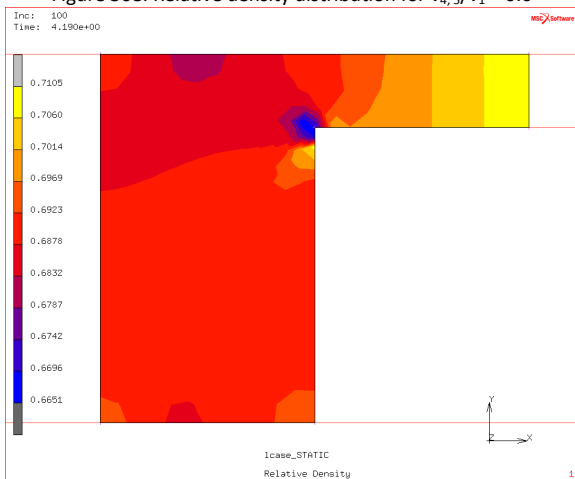


Figure 510. Relative density distribution for $v_{4,5}/v_1 = 0.8$

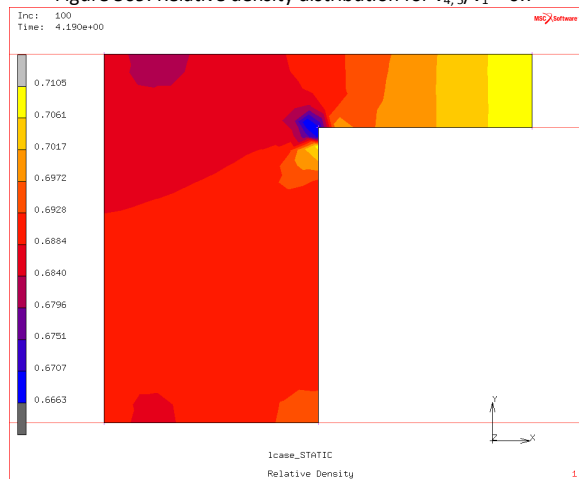


Figure 511. Relative density distribution for $v_{4,5}/v_1 = 0.9$

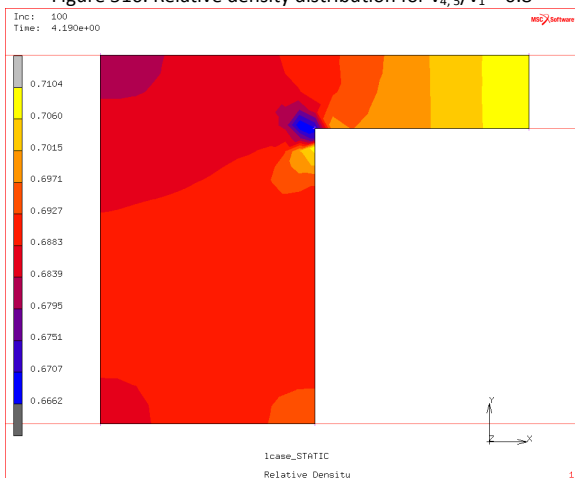


Figure 512. Relative density distribution for $v_{4,5}/v_1 = 1.0$

F.2.2 Using Constant Friction Coefficient of 0.12

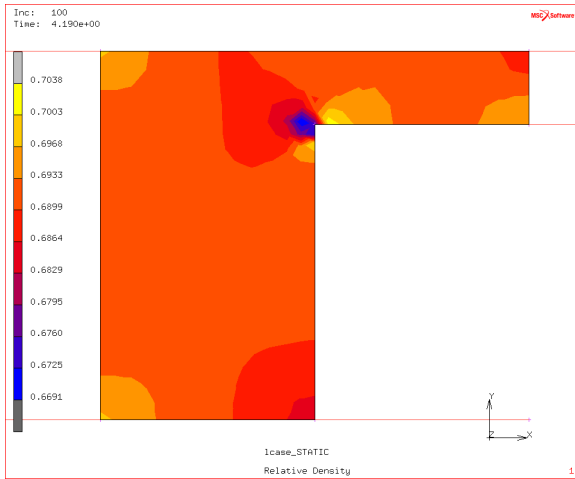


Figure 513. Relative density distribution for $v_{4,5}/v_1 = 0$

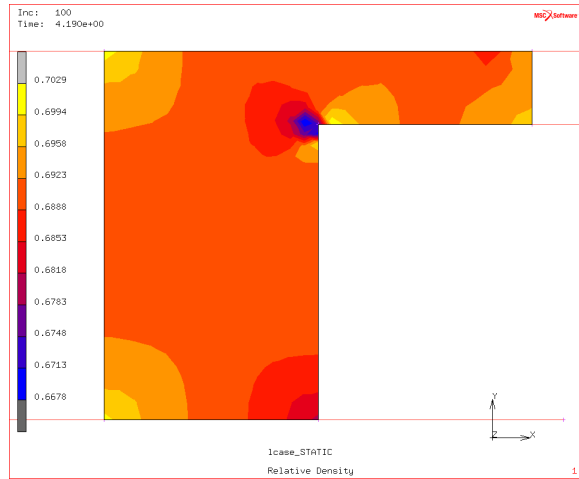


Figure 514. Relative density distribution for $v_{4,5}/v_1 = 0.1$

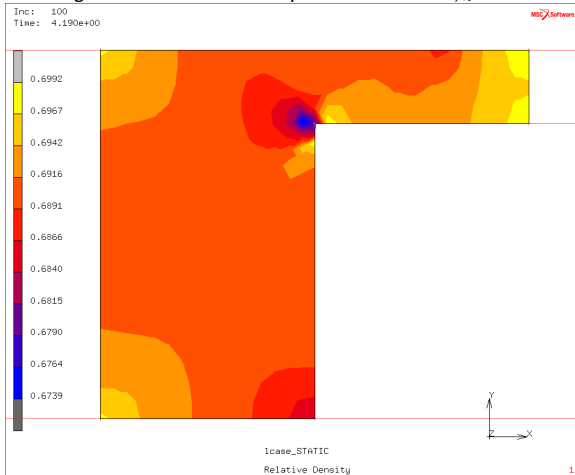


Figure 515. Relative density distribution for $v_{4,5}/v_1 = 0.2$

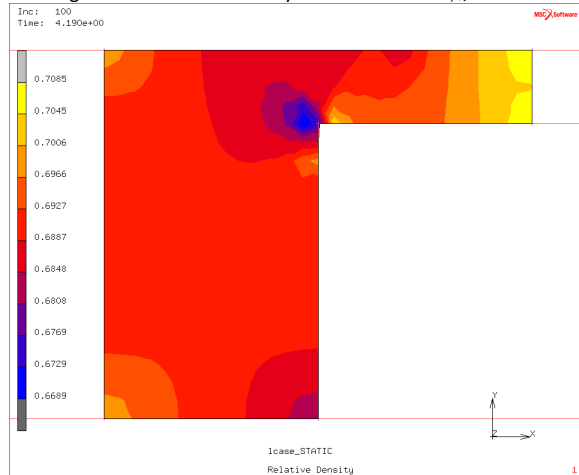


Figure 516. Relative density distribution for $v_{4,5}/v_1 = 0.3$

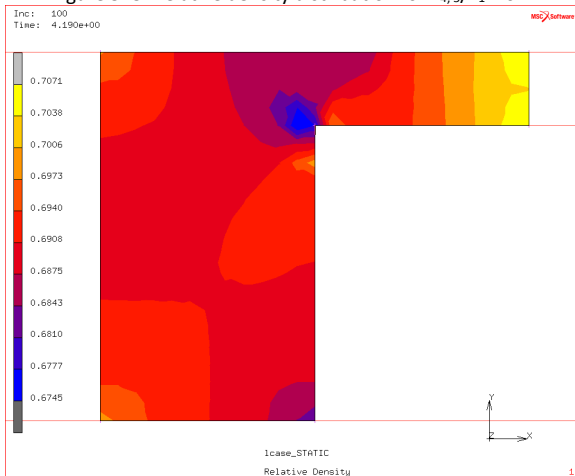


Figure 517. Relative density distribution for $v_{4,5}/v_1 = 0.4$

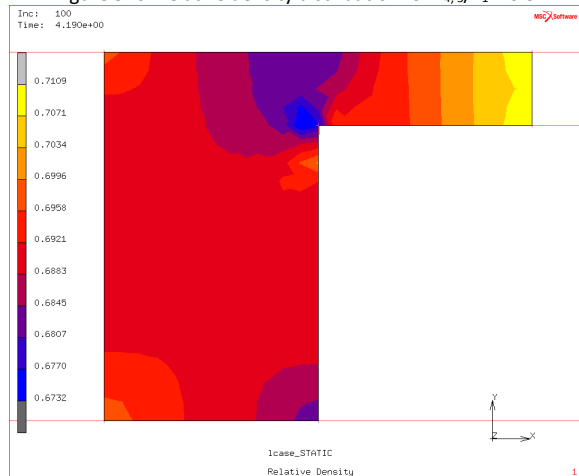


Figure 518. Relative density distribution for $v_{4,5}/v_1 = 0.5$

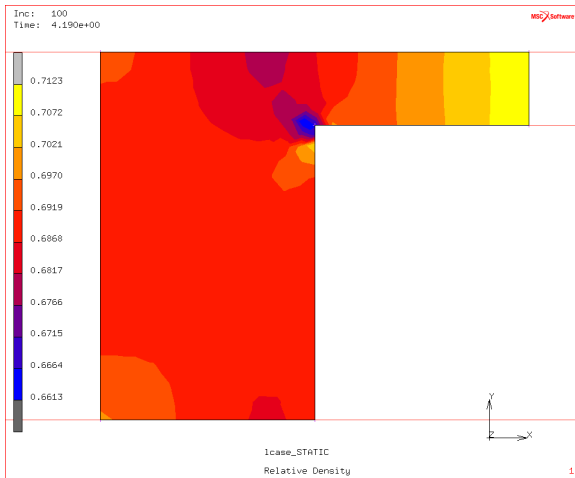


Figure 519. Relative density distribution for $v_{4,5}/v_1 = 0.6$

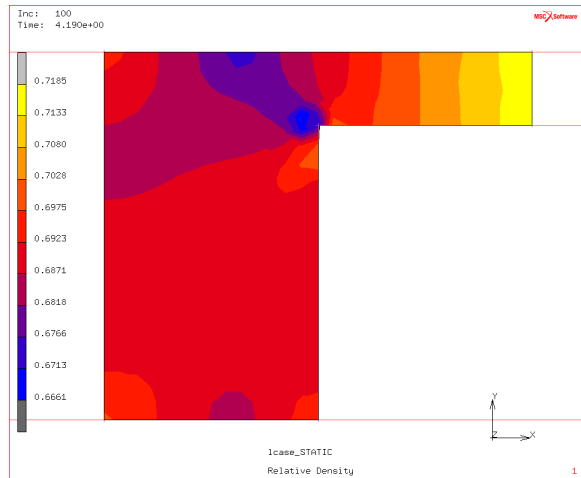


Figure 520. Relative density distribution for $v_{4,5}/v_1 = 0.7$

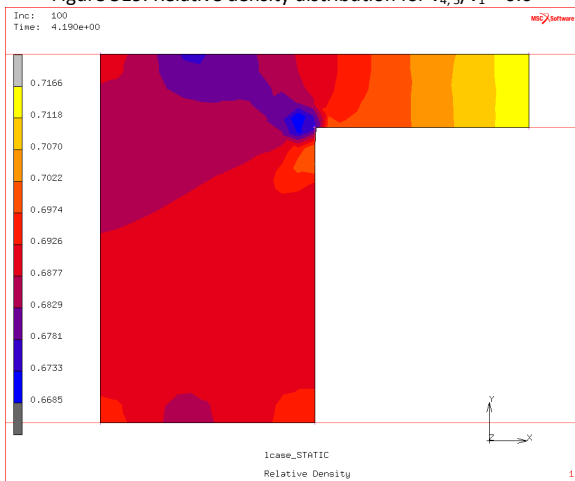


Figure 521. Relative density distribution for $v_{4,5}/v_1 = 0.8$

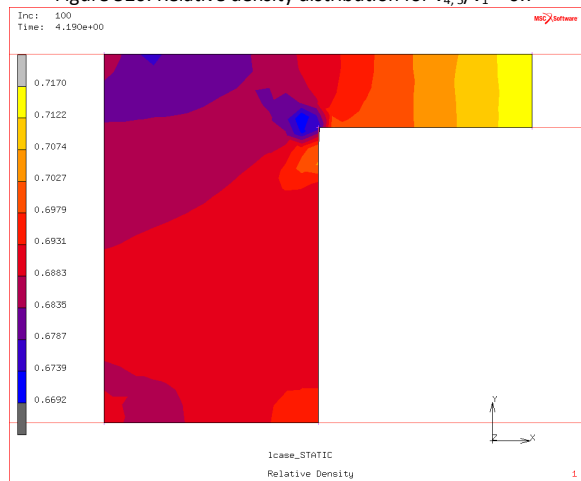


Figure 522. Relative density distribution for $v_{4,5}/v_1 = 0.9$

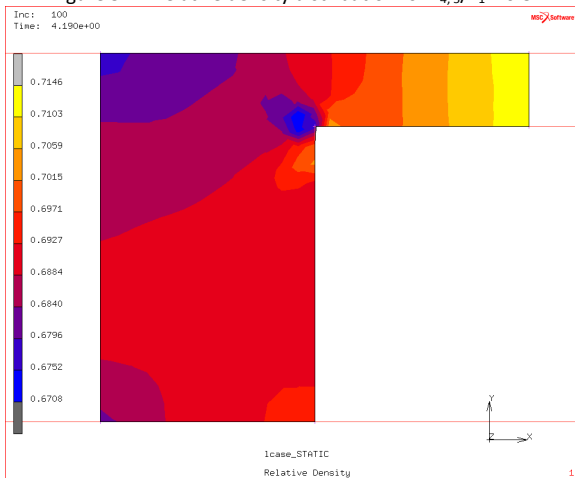


Figure 523. Relative density distribution for $v_{4,5}/v_1 = 1.0$

F.2.3 Using Constant Friction Coefficient of 0.20

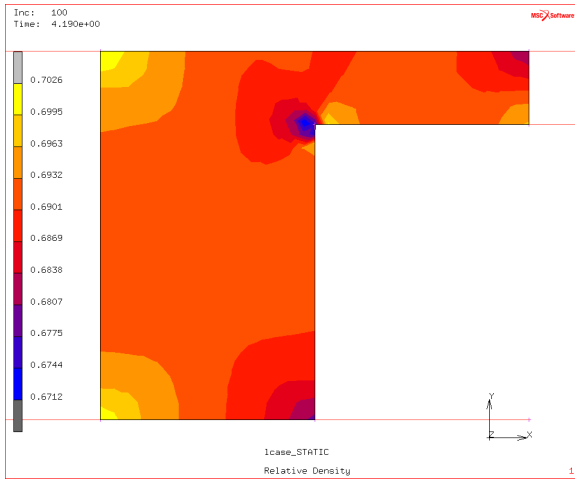


Figure 524. Relative density distribution for $v_{4,5}/v_1 = 0$

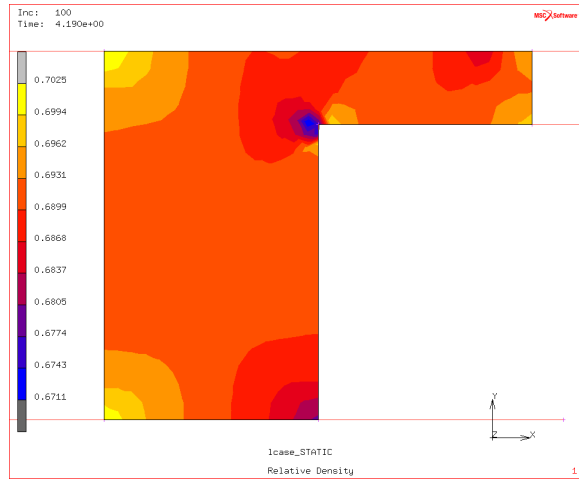


Figure 525. Relative density distribution for $v_{4,5}/v_1 = 0.1$

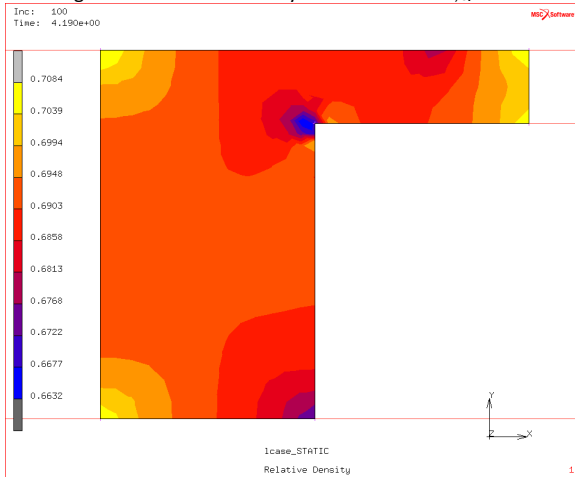


Figure 526. Relative density distribution for $v_{4,5}/v_1 = 0.2$

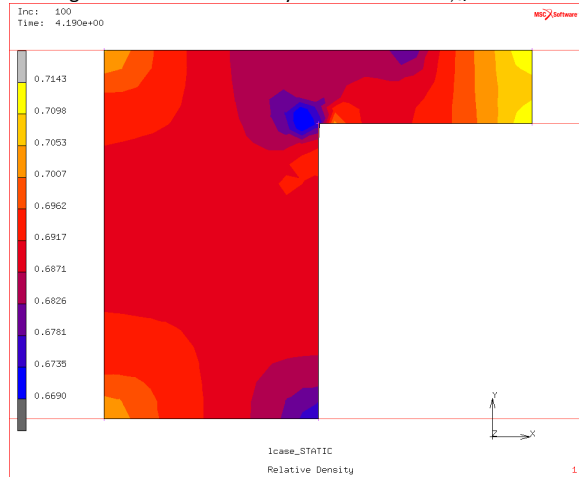


Figure 527. Relative density distribution for $v_{4,5}/v_1 = 0.3$

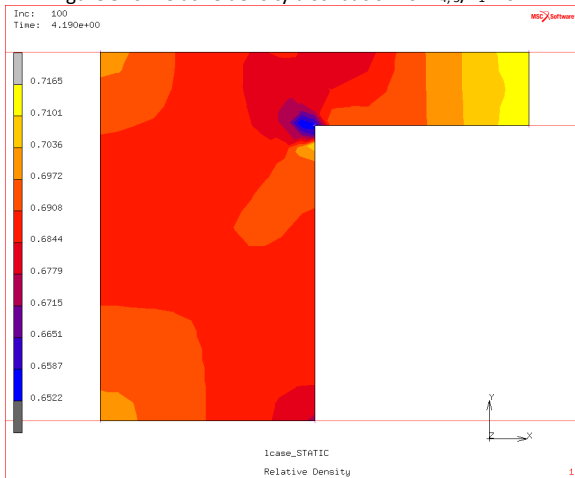


Figure 528. Relative density distribution for $v_{4,5}/v_1 = 0.4$

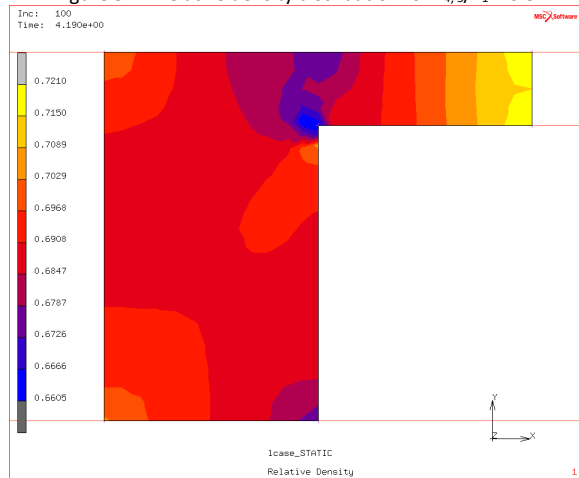


Figure 529. Relative density distribution for $v_{4,5}/v_1 = 0.5$

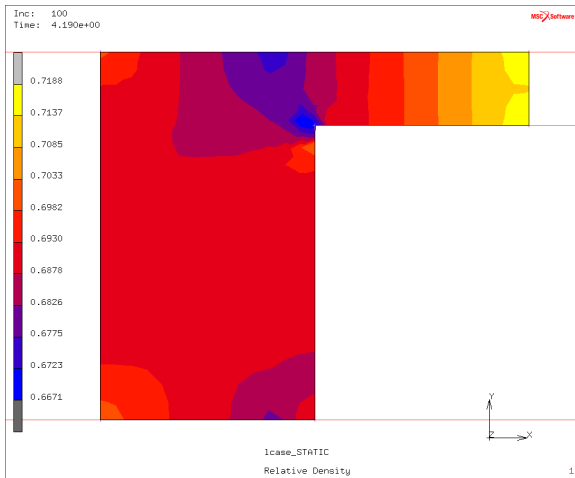


Figure 530. Relative density distribution for $v_{4,5}/v_1 = 0.6$

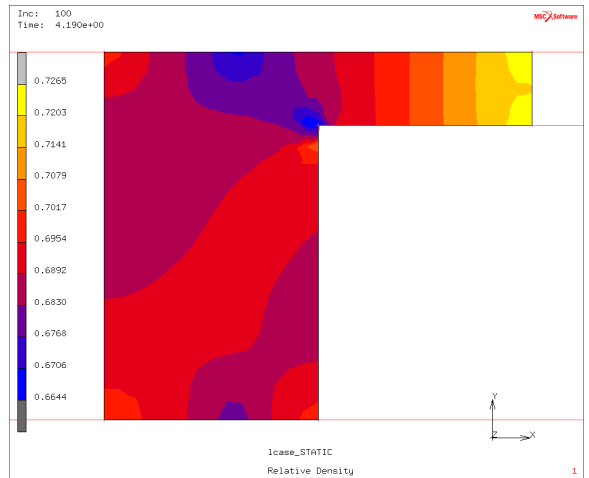


Figure 531. Relative density distribution for $v_{4,5}/v_1 = 0.7$

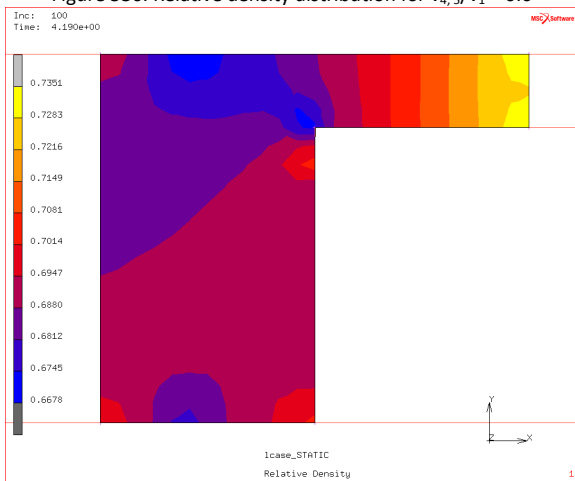


Figure 532. Relative density distribution for $v_{4,5}/v_1 = 0.8$

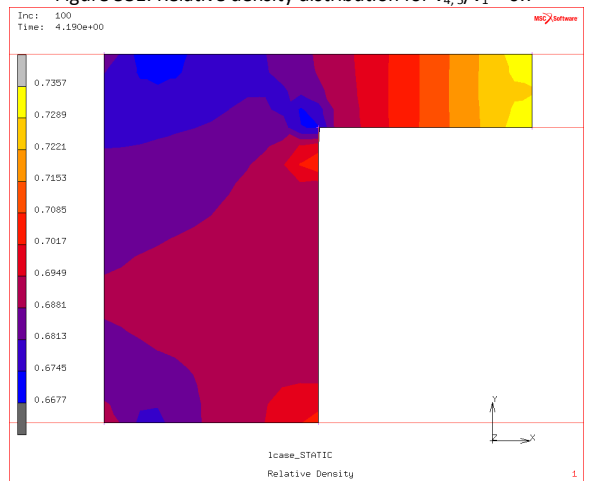


Figure 533. Relative density distribution for $v_{4,5}/v_1 = 0.9$

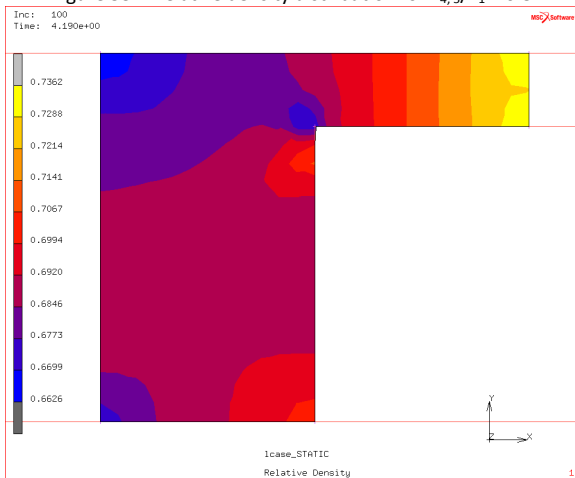


Figure 534. Relative density distribution for $v_{4,5}/v_1 = 1.0$

F.2.4 Using Variable Friction Coefficient, $\mu(\sigma_n, v_r)$

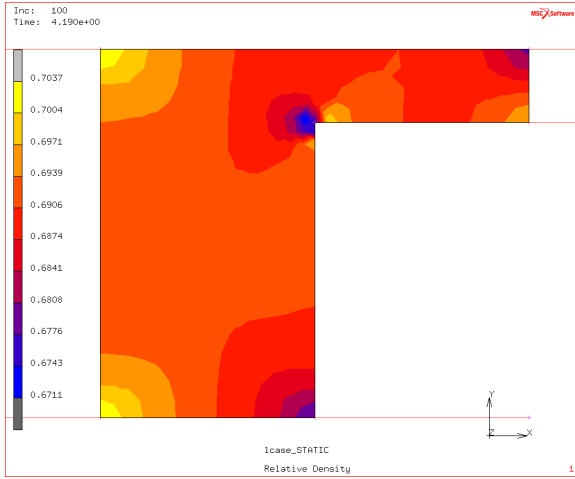


Figure 535. Relative density distribution for $v_{4,5}/v_1 = 0$

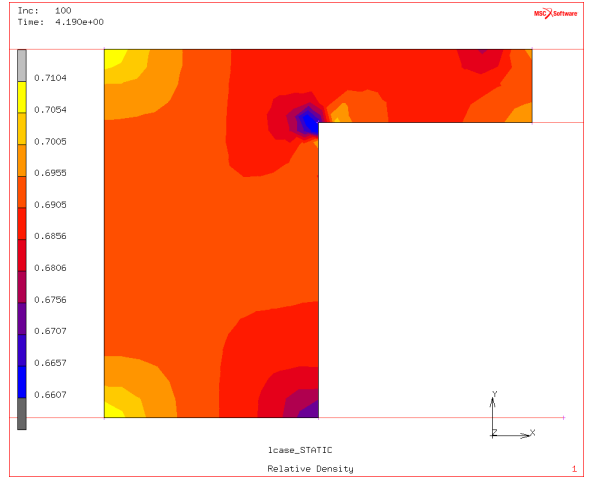


Figure 536. Relative density distribution for $v_{4,5}/v_1 = 0.1$

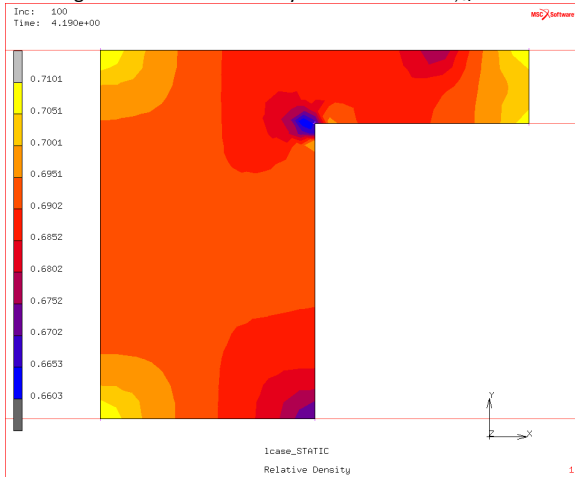


Figure 537. Relative density distribution for $v_{4,5}/v_1 = 0.2$

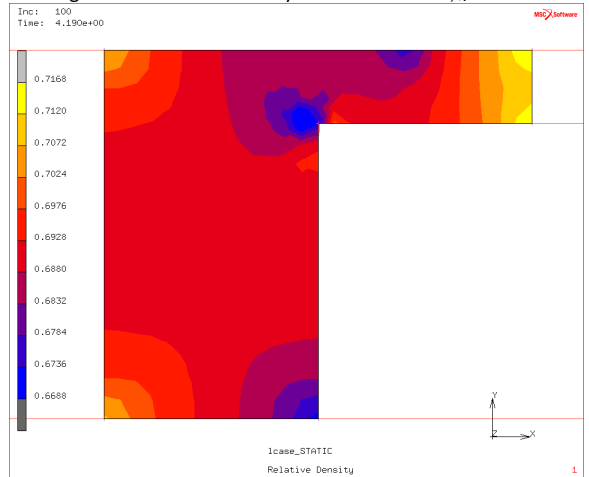


Figure 538. Relative density distribution for $v_{4,5}/v_1 = 0.3$

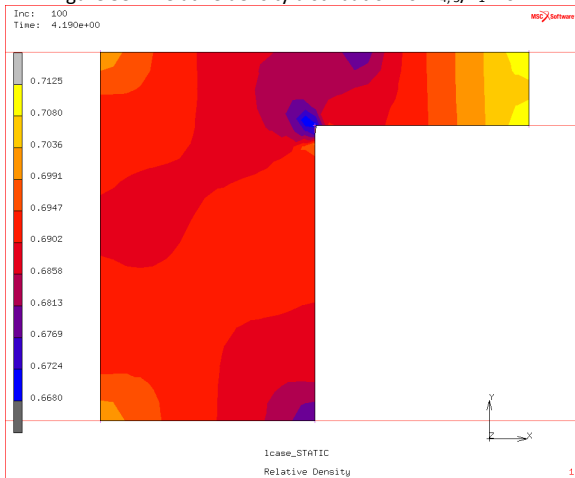


Figure 539. Relative density distribution for $v_{4,5}/v_1 = 0.4$

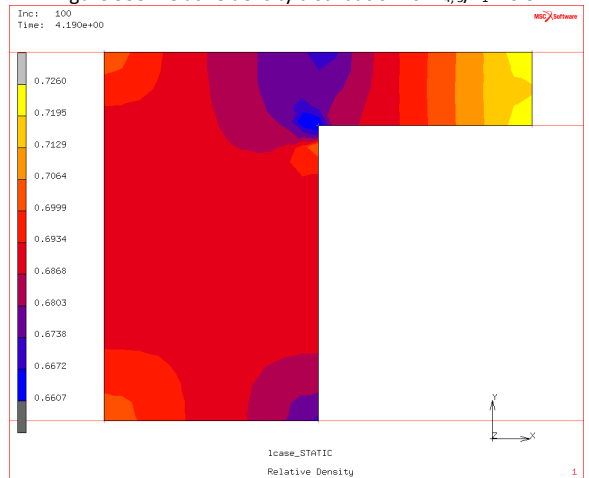


Figure 540. Relative density distribution for $v_{4,5}/v_1 = 0.5$

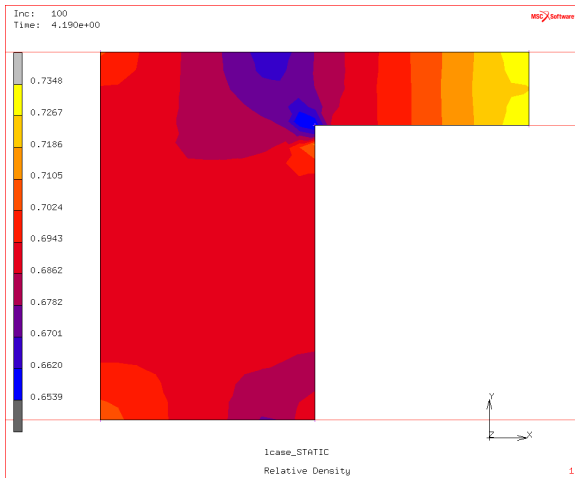


Figure 541. Relative density distribution for $v_{4,5}/v_1 = 0.6$

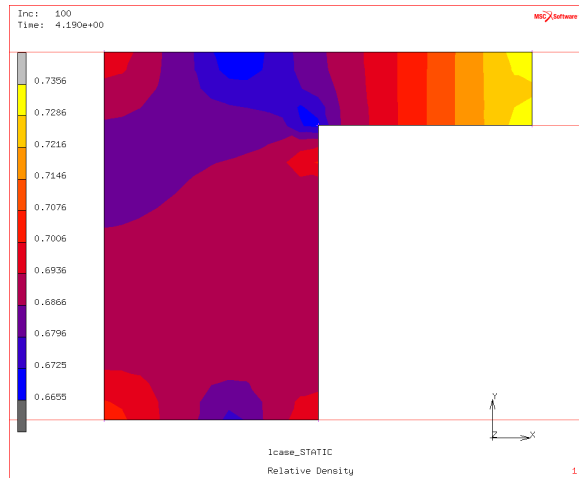


Figure 542. Relative density distribution for $v_{4,5}/v_1 = 0.7$

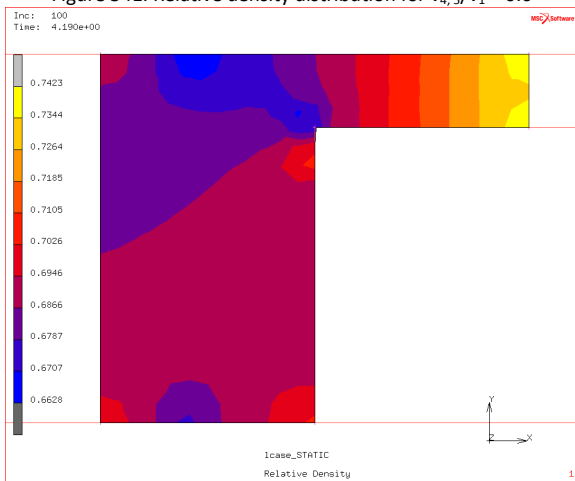


Figure 543. Relative density distribution for $v_{4,5}/v_1 = 0.8$

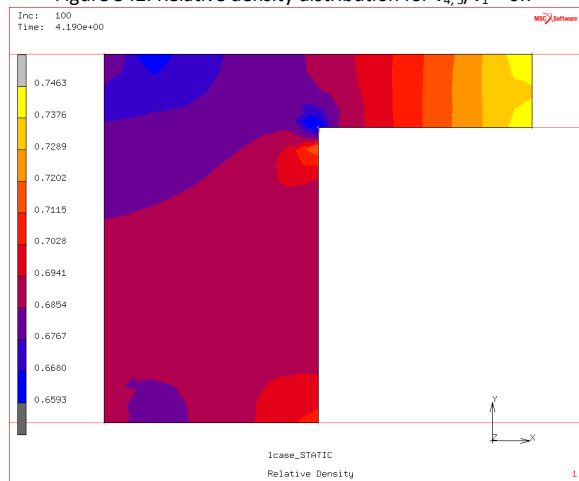


Figure 544. Relative density distribution for $v_{4,5}/v_1 = 0.9$

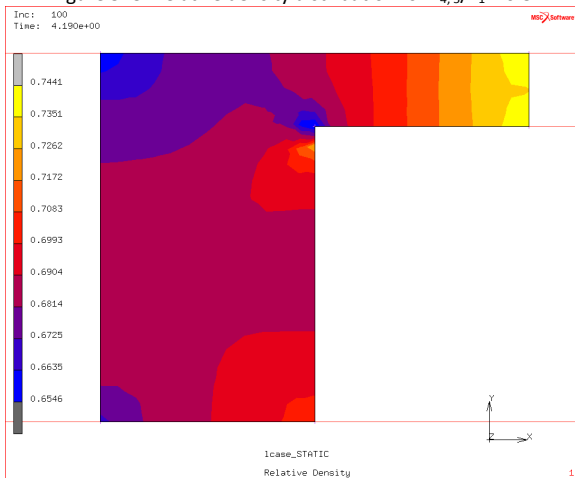


Figure 545. Relative density distribution for $v_{4,5}/v_1 = 1.0$

Appendix G. Conversion Procedure for Material Parameters β and γ for Iron-based Powder

The format employed by MSC.Marc Mental for definition of material parameters β and γ is the following

$$\beta = (b_1 + b_2 \bar{\rho}^{b_3})^{b_4} \quad (\text{G-1a})$$

$$\gamma = (q_1 + q_2 \bar{\rho}^{q_3})^{q_4} \quad (\text{G-1b})$$

However, the corresponding material parameters supplied by Shima et al. are presented in the following format

$$\beta = \frac{1}{g(1 - \bar{\rho})^m} = \frac{1}{2.49(1 - \bar{\rho})^{0.514}} \quad (\text{G-2a})$$

$$\gamma = \bar{\rho}^s = \bar{\rho}^{2.5} \quad (\text{G-2b})$$

The following steps were taken to derive appropriate material parameter constants for implementation into the FE model.

Material Parameter Constants for β

By letting (G-1a) equal (G-2a)

$$\beta = \frac{1}{2.49(1 - \bar{\rho})^{0.514}} = (b_1 + b_2 \bar{\rho}^{b_3})^{b_4} \quad (\text{G-3})$$

By further manipulation (G-2) becomes

$$\left(\frac{1}{2.49}\right)(1 - \bar{\rho})^{-0.514} = b_1^{b_4} \left(1 + \frac{b_2}{b_1}\right)^{b_4} \quad (\text{G-4})$$

Based on observation

$$b_1^{b_4} = \frac{1}{2.49} \quad (\text{G-5a})$$

$$b_4 = -0.514 \quad (\text{G-5b})$$

$$b_3 = 1 \quad (\text{G-5c})$$

$$\frac{b_2}{b_1} = -1 \quad (\text{G-5d})$$

$$b_2 = -b_1 \quad (\text{G-5e})$$

Now, by substituting (G-5b) into (G-5a)

$$b_1^{-0.514} = \frac{1}{2.49} \quad (\text{G-6})$$

Solving (G-6) for b_1 and substituting into equations (G-5a) to (G-5e)

$$b_1 = 5.8995087606021 \quad (\text{G-7a})$$

$$b_2 = -5.8995087606021 \quad (\text{G-7b})$$

$$b_3 = 1 \quad (\text{G-7c})$$

$$b_4 = -0.514 \quad (\text{G-7d})$$

Material Parameter Constants for γ

By letting (G-1b) equal (G-2b)

$$\gamma = \bar{\rho}^{2.5} = (q_1 + q_2\bar{\rho}^{q_3})^{q_4} \quad (\text{G-8})$$

Based on observation, the material parameter constants for γ are the following

$$q_1 = 0 \quad (\text{G-9a})$$

$$q_2 = 1 \quad (\text{G-9b})$$

$$q_3 = 1 \quad (\text{G-9c})$$

$$q_4 = 2.5 \quad (\text{G-9d})$$

Check

For β :

$$\beta(0.42) = \frac{1}{2.49(1 - (0.42))^{0.514}} = 0.53137199774165 \quad (\text{G-10a})$$

$$\begin{aligned}\beta(0.42) &= (5.8995087606021)^{-0.514} \times \left(1 + \frac{-5.8995087606021}{5.8995087606021} (0.42)^1\right)^{-0.514} \\ &= 0.53137199774163\end{aligned}\quad (\text{G-10b})$$

For γ :

$$\gamma(0.42) = (0.42)^{2.5} = 0.11432026591991 \quad (\text{G-11a})$$

$$\gamma(0.42) = (0 + 1(0.42)^1)^{2.5} = 0.11432026591991 \quad (\text{G-11b})$$

Appendix H. UFRIC User-subroutine

The following FORTRAN code was employed for the implementation of the variable friction coefficient, $\mu(\sigma_n, v_r)$, using UFRIC user-subroutine:

```
SUBROUTINE UFRIC (MIBODY,X, FN,VREL,TEMP,YIEL,FRIC,TIME,INC,NSURF)
```

```
    IMPLICIT REAL *8 (A-H, O-Z)
```

```
    DIMENSION X(2), MIBODY(4), VREL(1), TEMP(2), FN(1)
```

```
        FRIC=exp(-FN(1)/(1169*201.06192982975))*(0.224)*
```

```
9      1.437*tanh(VREL(1)/12.6+0.886)
```

```
    return
```

```
    end
```